Einfluss extrinsischer und intrinsischer Faktoren auf die Funktionalität des Endothels

Inaugural-Dissertation

zur Erlangung des Doktorgrades
der Mathematisch-Naturwissenschaftlichen Fakultät
der Heinrich-Heine-Universität Düsseldorf

vorgelegt von

Jan Greulich
aus Wuppertal

Düsseldorf, Juli 2024

aus dem Zentralinstitut für Klinische Chemie und Laboratoriumsdiagnostik
der Heinrich-Heine-Universität Düsseldorf

Gedruckt mit der Genehmigung der
Mathematisch-Naturwissenschaftlichen Fakultät der
Heinrich-Heine-Universität Düsseldorf

Berichterstatter:

1. Prof. Dr. Joachim Altschmied

2. Prof. Dr. William F. Martin

Tag der mündlichen Prüfung: 24.10.2024

Erklärung

Ich versichere an Eides statt, dass die Dissertation von mir selbstständig und ohne unzulässige fremde Hilfe unter Beachtung der „Grundsätze zur Sicherung guter wissenschaftlicher Praxis an der Heinrich-Heine-Universität Düsseldorf“ erstellt worden ist.

_____

(Jan Greulich)

Düsseldorf, Juli 2024

„Our time here is brief, our risk enormous.
Don't waste the one or increase the other, if you please.“

aus „The Dark Tower“
von Stephen King

Inhaltsverzeichnis

Kardiovaskuläre Erkrankungen

Nach Angaben der Weltgesundheitsorganisation (WHO) sind kardiovaskuläre Erkrankungen weltweit die häufigste Todesursache. 2019 sind schätzungsweise 17,9 Millionen Menschen daran gestorben, was 32 % aller Todesfälle weltweit entspricht. (https://www.who.int/news-room/fact-sheets/detail/cardiovascular-diseases-(cvds)). Der Begriff kardiovaskuläre Erkrankungen beschreibt im Allgemeinen Zustände, die das Herz oder die Blutgefäße betreffen. Dies kann sich auf eine Reihe von Erkrankungen beziehen, darunter Schlaganfall oder Herzinsuffizienz, wobei Letztere eine Folge eines durch Gefäßverschluss ausgelösten Herzinfarkts sein kann. Ein solcher Gefäßverschluss kann im Rahmen einer Atherosklerose entstehen, welche durch chronische Entzündungen und Lipidansammlungen in den Arterien gekennzeichnet ist, die letztlich den Blutfluss im Gefäß einschränken (Libby et al. 2019). Von besonderer Bedeutung ist dabei das Endothel, die innerste Auskleidung der Blutgefäße. Nach der Exposition gegenüber atherogenen Stimuli, die von *oxidized low-density lipoprotein* (oxLDL), Cholesterinkristallen, Entzündungsreizen, oxidativem Stress und gestörtem Blutfluss ausgehen, werden Endothelzellen aktiviert. Nach der Aktivierung exprimieren Endothelzellen verschiedene Adhäsionsmoleküle wie *Intercellular Adhesion Molecule 1* (ICAM1), *Vascular Cell Adhesion Molecule 1* (VCAM1), P-Selektin und E-Selektin sowie Zytokine wie *Monocyte Chemoattractant Protein 1* (MCP1). Diese Moleküle locken Neutrophile und Monozyten an und bieten ihnen die Möglichkeit zur Adhäsion, sodass diese sich an die aktivierten Endothelzellen anlagern und in die Arterienwand eindringen können (Chistiakov et al. 2018). Die eingedrungenen Monozyten differenzieren zu Makrophagen und nehmen oxLDL auf, wodurch nach und nach sogenannte Schaumzellen entstehen können. Diese häufen sich immer weiter an und bilden atherosklerotische Plaques. Durch phänotypisch veränderte glatte Muskelzellen kann es zudem zur Bildung einer fibrotischen Kappe kommen, was – im Gegensatz zu der weichen Plaque ohne fibrotische Kappe – eine harte Plaque charakterisiert. Je nach Größe des Lipidkerns und Dicke der fibrotischen Kappe kann eine Plaque anfällig für eine Ruptur sein, welche anschließend zu einem Gefäßverschluss führen kann. Man spricht dann von einer instabilen Plaque, wobei diese desto vulnerabler ist, je dicker der Lipidkern und je dünner die Kappe ist. Dem gegenüber steht eine stabile Plaque, die nicht rupturiert (Hafiane 2019). Atherogene Stimuli führen auch zur Seneszenz von Endothelzellen (Minamino et al. 2002). Seneszente Endothelzellen spielen eine wichtige Rolle in endothelialer Dysfunktion und werden in nachfolgenden Kapiteln noch genauer behandelt.

Interessanterweise sind die wichtigsten Risikofaktoren für kardiovaskuläre Erkrankungen verhaltensbedingte Faktoren, darunter ungesunde Ernährung, Bewegungsmangel, Tabak- und Alkoholkonsum. Daher könnte das Risiko, Gefäß- und Herzerkrankungen zu entwickeln, durch Maßnahmen wie die Einstellung des Tabakkonsums, eine gesündere Ernährung, regelmäßige körperliche Betätigung und den Verzicht auf Alkohol erheblich gesenkt werden. Dennoch sind, global gesehen, kardiovaskuläre Erkrankungen nach wie vor die überwiegende Sterbeursache. Aber auch erbliche Faktoren sowie das Alter tragen zur Entstehung von kardiovaskulären Erkrankungen bei (https://www.who.int/news-room/fact-

sheets/detail/cardiovascular-diseases-(cvds); https://www.nhs.uk/conditions/cardiovascular-disease/). Insbesondere das Alter spielt hierbei eine wichtige Rolle, da mit steigendem Alter sowohl die Frequenz als auch die Schwere kardiovaskulärer Erkrankungen zunimmt (Vaduganathan et al. 2022; Aidoud et al. 2023)

Eine der wichtigsten Ursachen für die Entstehung von kardiovaskulären Erkrankungen ist die endotheliale Dysfunktion, die als eines der Hauptmerkmale fast aller menschlicher vaskulärer Pathologien gilt (Xu et al. 2021). Im Folgenden werden das Endothel und die endotheliale Dysfunktion im Detail erörtert.

Das Endothel

Das Endothel, eine Einzelschicht aus Endothelzellen, bildet die innere zelluläre Auskleidung von Blutgefäßen wie Arterien, Venen, Kapillaren, sowie des lymphatischen Systems und steht daher in direktem Kontakt mit Blut bzw. Lymphe und den zirkulierenden Zellen. Diese Schicht wird auch als Tunica intima bezeichnet. Sie ist umgeben von der Tunica media, welche von den glatten Muskelzellen gebildet wird und von den Endothelzellen durch die interne elastische Lamina abgegrenzt ist. Die Tunica media ihrerseits wird von der Tunica externa, einer Bindegewebsschicht, umschlossen (Abb. 1).

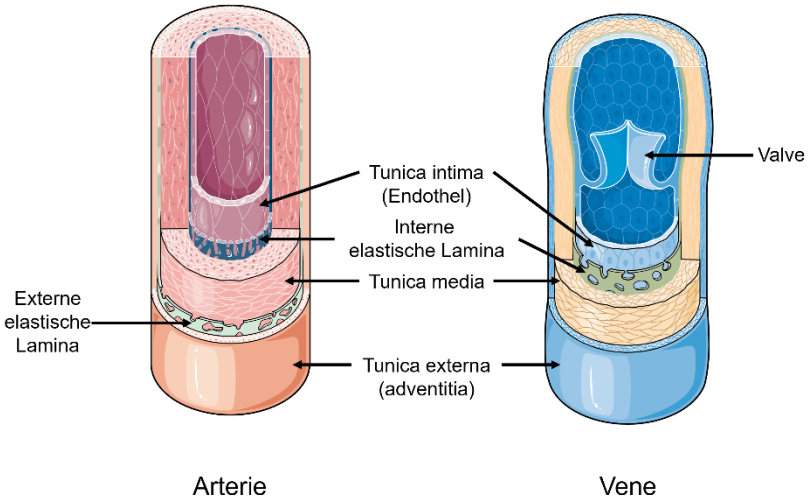

Abbildung 1: Schematischer Aufbau von Arterien und Venen. Die Tunica intima bildet die Abgrenzung zum Lumen; sie besteht aus einer einzelnen Schicht von Endothelzellen. Die nach außen folgende Tunica media besteht aus glatten Muskelzellen; bei Venen ist sie wesentlich dünner ist als bei Arterien. Vom Endothel ist sie durch die interne elastische Lamina abgegrenzt; nach außen nur bei Arterien durch eine externe elastische Lamina. Die folgende, aus Bindegewebe bestehende Tunica externa bildet die äußerste Lage der Gefäßwand.

Das Endothel ist ein wichtiger Akteur bei der Verhinderung der Thrombozytenaggregation, welche ansonsten zu einem Verschluss der Blutgefäße durch das Verklumpen der Thrombozyten führen könnte. Weiterhin spielt das Endothel für das Immunsystem eine wichtige Rolle, indem es, sofern es nicht im Rahmen eines Entzündungsprozesses aktiviert wird, die Extravasation von Leukozyten verhindert. Außerdem setzt das Endothel Mediatoren frei, die zur Induktion von Angiogenese benötigt werden, wie etwa *Vascular Endothelial Growth*

Factor (VEGF). Endothelzellen steuern auch den Gefäßtonus und damit den Blutfluss, indem sie entspannende Faktoren wie etwa Stickstoffmonoxid (NO), Adenosin, reaktive Sauerstoffspezies (*reactive oxygen species*, ROS), und kontrahierende Faktoren wie Endotheline synthetisieren und freisetzen.

Für die Funktionalität des Endothels ist die Redox-Homöostase essenziell. Diese wird vor allem durch die Oxidoreduktase Thioredoxin-1 (Trx-1) sichergestellt, die eines der wichtigsten antioxidativen Systeme des Endothels ist (Haendeler 2006; Altschmied und Haendeler 2009). Die Aufrechterhaltung des Trx-1-Spiegels ist somit für Endothelzellen von zentraler Bedeutung (Altschmied und Haendeler 2009).

Eine Beeinträchtigung der Endothelzellfunktionalität, typischerweise als endotheliale Dysfunktion bezeichnet, wird bei fast allen kardiovaskulären Erkrankungen beobachtet. Eine endotheliale Dysfunktion ist mit einem erhöhten Risiko für kardiovaskuläre Ereignisse verbunden (Medina-Leyte et al. 2021) und stellt häufig ein Schlüsselereignis bei der Entwicklung und dem Fortschreiten kardiovaskulärer Pathologien dar, wie etwa Bluthochdruck oder Atherosklerose (Xu et al. 2021). Die endotheliale Dysfunktion ist durch verminderte NO-Bioverfügbarkeit charakterisiert (Cyr et al. 2020). Endotheliales NO spielt eine entscheidende Rolle bei der Induktion der Vasodilatation, der Zellproliferation und -migration, sowie der Verhinderung der Leukozytenadhäsion und der Thrombozytenaggregation (Förstermann und Münzel 2006) . Ebenfalls ist der Schutz der Endothelzellen vor Apoptose NO-abhängig (Ziche et al. 1994; Tzeng et al. 1998), was die essenzielle Rolle dieses Moleküls im Endothel noch einmal verdeutlicht.

In Endothelzellen katalysiert die endotheliale NO-Synthase (eNOS, oder auch NOS3) die Umsetzung von L-Arginin und molekularem Sauerstoff zu NO und Citrullin. Die katalytisch aktive Form von eNOS ist ein Homodimer. Dabei enthält jedes der identischen Monomere eine Reduktase-Domäne, welche Bindungsstellen für Nikotinamid-Adenin-Dinukleotid-Phosphat (NADPH), Flavin-Mononukleotid (FMN) und Flavin-Adenin-Dinukleotid (FAD) aufweist, eine Oxidase-Domäne und die Bindungsstellen für eine Häm-Gruppe, an die molekularer Sauerstoff bindet, reduziert und schließlich in L-Arginin eingebaut wird, um NO und L-Citrullin zu bilden (Fleming und Busse 1999; Verhaar et al. 2004). Ein Zn^{2+} Ion stabilisiert das Homodimer über die Bindung an zwei Cysteinthiole in jedem der beiden Monomere (Raman et al. 1998; Li et al. 1999). Weiterhin enthält jedes Monomer ein Molekül des Kofaktors Tetrahydrobiopterin (BH_4) (Qian und Fulton 2013). Die Bindung dieses Kofaktors ist für eNOS zur effizienten Erzeugung von NO unerlässlich (Dudzinski et al. 2006). Ist dieser Kofaktor zu Dihydrobiopterin (BH_2) oxidiert, geht eNOS von einer dimeren in eine monomere Form über und wird entkoppelt (Maron und Michel 2012). In dieser Konformation produziert eNOS statt NO Superoxid-Anionen. Diese hochreaktiven freien Radikale können Makromoleküle wie Proteine, DNA und Lipide oxidieren, was schädliche Folgen unter anderem auch für das kardiovaskuläre System hat (Araki und Kitaoka 2001). Die Reduktase-Domäne ist über eine Calmodulin-bindende Sequenz mit der Oxidase-Domäne verbunden (Alderton et al. 2001). Die

Bindung von Calmodulin an diese Sequenz ermöglicht schlussendlich den Elektronenfluss von der Reduktase- zur Oxidasedomäne und somit die Produktion von NO (Sessa 2004).

Die katalytisch aktive Form von eNOS zeichnet sich durch eine Phosphorylierung an Serin 1177 aus, welche die Aktivität erhöht (Dimmeler et al. 1999). Im Gegensatz dazu führt eine Phosphorylierung an Threonin 495 zu einer reduzierten Aktivität (Chen et al. 1999).

Wie bereits erwähnt, ist die NO-Bioverfügbarkeit in der endothelialen Dysfunktion verringert. Dies ist ebenfalls in zellulärer Seneszenz von Endothelzellen der Fall, weshalb diese zu endothelialer Dysfunktion und damit auch zur Entstehung und dem Fortschreiten von kardiovaskulären Erkrankungen beiträgt. Seneszente Endothelzellen wurden bereits 2002 *in vivo* nachgewiesen (Minamino et al. 2002). In seneszenten Endothelzellen ist die Redox-Homöostase gestört, was maßgeblich durch reduzierte Level an Trx-1 bedingt ist (Goy et al. 2014). Trx-1 wird im Endothel durch die lysosomale Protease Cathepsin D abgebaut (Haendeler et al. 2005), deren Aktivität in seneszenten Endothelzellen erhöht ist (Goy et al. 2014), was den Verlust von Trx-1 erklären kann. Zudem sind auch die Level der NADPH-Oxidase 4 (NOX4) in seneszenten Endothelzellen erhöht (Goy et al. 2014). NOX-Enzyme produzieren ROS, wobei NOX4 das vorwiegende Enzym in Endothelzellen darstellt (Ago et al. 2004).

Für die Funktionalität des Endothels spielen auch Faktoren, wie z.B. Ernährung, eine wesentliche Rolle. Teil einer ungesunden, jedoch häufig üblichen Ernährung besonders in westlichen Ländern ist ein hoher Gehalt an Cholesterin. Dieses wird im Blutplasma durch *low-density lipoprotein* (LDL) zu den Geweben und Organen transportiert. Durch die Oxidation von LDL entsteht oxLDL. Dieses steht, wie bereits früher erwähnt, im Zusammenhang mit kardiovaskulären Erkrankungen, da in mehreren Studien eine signifikante Erhöhung des zirkulierenden oxLDL im Plasma bei Patienten mit Herz-Kreislauf-Erkrankungen gezeigt wurde (Ehara et al. 2001; Itabe und Ueda 2007). So ist es auch an der Entstehung atherosklerotischer Läsionen beteiligt (Witztum 1993; Itabe 2003). Oxidierte Lipide stehen zudem im Zusammenhang mit der Entstehung von Krankheiten in anderen Organen, wie etwa der Leber, die im folgenden Kapitel näher beleuchtet werden.

Gentherapie gegen oxidierte Phosphatidylcholine bei Mäusen mit etablierter Lebersteatose verhindert das Fortschreiten der Fibrose

Die übermäßige Bildung von ROS in steatotischen Lebern, umgangssprachlich auch „Fettleber“ genannt, führt zur Bildung von Lipidoxidationsprodukten, einschließlich oxidierter Phosphatidylcholine (oxPCs) (Podrez et al. 2002; Bochkov et al. 2002; Kadl et al. 2010; Kadl et al. 2011). Die Oxidation mehrfach ungesättigter Fettsäuren, die in Phospholipiden enthalten sind, bildet chemisch einzigartige Klassen oxidierter Spezies, die in die Regulation spezifischer zellulärer Reaktionen eingreifen. Hierzu zählen z.B. die Integrität der endothelialen Barriere (Karki et al. 2018; Ke et al. 2019), die Zellmigration und der Stoffwechsel von Immunzellen

(Kadl et al. 2009; Serbulea et al. 2018), die Aktivierung von Endothelzellen (Kadl et al. 2010; Kadl et al. 2011), die Knochenhomöostase (Ambrogini et al. 2018) sowie die Apoptose (Borisenko et al. 2003; Kagan et al. 2017). Folglich wird angenommen, dass oxPCs eine zentrale Rolle bei der Entstehung und dem Verlauf von akuten Erkrankungen wie Sepsis (Bochkov et al. 2002) und Lungenverletzungen (Imai et al. 2008; Birukov und Karki 2018; Ke et al. 2019) sowie bei chronischen Krankheiten, einschließlich des metabolischen Syndroms (Serbulea et al. 2018; Sun et al. 2020), spielen. Darüber hinaus stellen die Plasmaspiegel von oxPCs, die durch die Reaktivität mit E06, einem natürlichen Immunglobulin M, das oxidierte Phosphatidylcholine bindet (Tsimikas et al. 2006), gemessen werden können, einen Biomarker für den Schweregrad der menschlichen Karotis- und Femoralarteriosklerose dar (Horkko et al. 1999).

Zur möglichen Prävention der durch oxPCs ausgelösten Krankheiten haben wir eine therapeutische Anwendung der Virus-vermittelten Expression des variablen Antikörperfragments von E06 (*single-chain variable fragment of E06*, scFv-E06) mittels Adeno-assoziierter Viren (AAV) untersucht. Da anzunehmen ist, dass oxPCs auch in der Leber selbst Effekte hervorrufen, haben wir in diesem Zusammenhang analysiert, ob und wie sich die hepatische Expression von scFv-E06 auf das Auftreten von nicht-alkoholischer Fettleber (*non-alcoholic fatty liver disease*, NAFLD), die eng mit dem metabolischen Syndrom verknüpft ist (Yki-Jarvinen 2014), und das Fortschreiten zu nicht-alkoholischer Steatohepatitis (*non-alcoholic steatohepatitis,* NASH) und Leberfibrose auswirkt. Wir konnten zeigen, dass die AAV8-vermittelte Leber-spezifische Expression von scFv-E06 in Mäusen auch zur Sekretion des Proteins in das Plasma führt. Dies veränderte die normale Physiologie der Mäuse nicht, was die Möglichkeit bot zu untersuchen, wie sich die Eliminierung von oxPCs auf Auftreten und Verlauf der Krankheit auswirkt. Wir konnten zeigen, dass die hepatische Expression von scFv-E06 vor Beginn einer Fütterung mit Fructose-, Palmitat- und Cholesterin-reicher (FPC) Ernährung, die normalerweise gewählt wird, um NASH zu induzieren, zu einer deutlichen Verringerung der Spiegel einzelner oxPC-Spezies im Plasma der Mäuse führt und die Tiere vor diätbedingter Lebersteatose schützt. Angesichts der Wirksamkeit von scFv-E06 bei der Eliminierung von Plasma-oxPCs und dem damit einhergehenden Schutz vor Lebersteatose nutzten wir die Flexibilität des virusvermittelten Gentransfers, um nach Etablierung der Lebersteatose mit der Expression von scFv-E06 therapeutisch einzugreifen. Mit diesem Ansatz konnten wir zeigen, dass die Expression von scFv-E06 in einem klinisch relevanten Interventionsmodell weitere ernährungsbedingte Leberschäden und Leberfibrose trotz bestehender Fettleibigkeit und Insulinresistenz abschwächen kann. Unabhängig davon reichte auch hierbei die Expression von scFv-E06 aus, um die Level einer Vielzahl von oxPC-Spezies im Plasma zu reduzieren. Mithilfe von Massenspektrometrie identifizierten wir einzelne oxPC-Spezies, deren Konzentrationen durch die Expression von scFv-E06 in Mäusen auch nach bereits etablierter Steatose am Übergang zu NASH verringert werden. Die Behandlung von Hepatozyten und Sternzellen mit den so identifizierten oxPC-Spezies *in vitro* induzierte metabolische Veränderungen in diesen Zelltypen. Zusätzlich veränderten diese oxPCs in dem

therapeutischen Modell *in vivo* die hepatische Genexpression. Die hierbei herabregulierten *Gene Ontology* (GO) *Termini* deuten auf reduzierte Fibrose und Entzündung in den Lebern von Mäusen hin, welche scFv-E06 exprimieren. Diese Daten zeigen, dass Plasma-oxPCs die Leberfunktion in verschiedenen Stadien des Krankheitsverlaufs in einzigartiger Weise regulieren. So schützte die Expression von scFv-E06 vor Beginn der FPC-Diät die Mäuse vor Lebersteatose, während die Intervention mit scFv-E06 nach Auftreten der Steatose die Lipidbelastung in der Leber nicht verringerte. Obwohl die Lipidbelastung insgesamt nicht abnahm, wiesen die scFv-E06-exprimierenden Mäuse kleinere hepatische Lipidtröpfchen auf, deren Größe invers mit intrazellulärem Stress in Hepatozyten korreliert (Chin et al. 2020). Dies könnte als Indiz dafür gewertet werden, dass oxPCs an der Dysregulation der zellulären Lipidspeicherung beteiligt sind, die für den Beginn der Lebersteatose, nicht aber für deren Aufrechterhaltung entscheidend ist. Zusammengenommen deuten die Daten darauf hin, dass die Senkung der Plasma-Konzentrationen der identifizierten oxPC-Spezies ausreicht, um die Entstehung einer Lebersteatose und das Fortschreiten der Fibrose in einem Mausmodell der ernährungsbedingten NAFLD zu verhindern. Mit diesem Ansatz liefern wir den ersten Beweis dafür, dass eine therapeutische Intervention mit hepatischer scFv-E06-Expression nach der Entwicklung einer ernährungsbedingten Steatose das Fortschreiten der hepatischen Fibrose in einem klinisch relevanten Modell der NAFLD aufhält (Upchurch, … **Greulich** et al. 2022).

Interessanterweise können oxPCs zu einer Dysregulation der Mitochondrienfunktion in hepatischen Sternzellen (Upchurch, … **Greulich** et al. 2022) sowie generell des mitochondriellen Stoffwechsels führen (Perez-Carreras et al. 2003; Rector et al. 2010; Gluchowski et al. 2017). Auf die Wichtigkeit der mitochondriellen Funktion und ihrer Rolle in Erkrankungen, insbesondere des Herz-Kreislauf-Systems, werde ich in den folgenden Kapiteln gesondert eingehen.

Mitochondrien

Mitochondrien erfüllen diverse biochemische Funktionen und verbrauchen dabei beträchtliche Ressourcen. Sie sind an anabolen und katabolen Reaktionen beteiligt und produzieren beispielsweise Adenosintriphosphat (ATP) sowie viele Biosynthese-Zwischenprodukte und tragen gleichzeitig zu zellulären Stressreaktionen wie Autophagie und Apoptose bei (Spinelli und Haigis 2018). Mitochondrien sind entgegen der landläufigen Vorstellung keine einzelnen Organellen, sondern bilden ein dynamisches, zusammenhängendes Netzwerk.

Eine ordnungsgemäße Funktion der Mitochondrien ist wesentlich für viele normale Funktionen eines Organismus. Mitochondrien reagieren sehr empfindlich auf die Nährstoff- und Sauerstoffversorgung und passen ihren Stoffwechsel an die sich verändernden Bedingungen an. Ist diese Anpassung beeinträchtigt und können Mitochondrien ihre Funktion nicht mehr wahrnehmen, spricht man von mitochondrialer Dysfunktion. Diese tritt bei weit verbreiteten Krankheiten wie z.B. neurodegenerativen Störungen, metabolischem Syndrom, Fettleibigkeit und kardiovaskulären Erkrankungen auf (Nunnari und Suomalainen 2012).

Im Folgenden wird insbesondere auf die Rolle von mitochondrialer Dysfunktion bei kardiovaskulären Erkrankungen eingegangen.

Mitochondriale Dysfunktion in kardiovaskulären Erkrankungen

Mitochondriale Dysfunktion konnte in verschiedensten kardiovaskulären Erkrankungen beobachtet werden, wie etwa bei Herzinsuffizienz (Sharov et al. 1998), Aneurysmen (Navas-Madronal et al. 2019), und Atherosklerose (Peng et al. 2019). Dies lässt sich dadurch erklären, dass Kardiomyozyten, glatte Muskelzellen der Gefäßwand, Endothelzellen, und kardiale Fibroblasten abhängig von funktionellen Mitochondrien sind. Kardiomyozyten benötigen für die permanente Kontraktion große Mengen an Energie, die von Mitochondrien bereitgestellt wird. Die glatten Muskelzellen der Gefäßwände sind auf funktionale Mitochondrien zur Kontrolle der Proliferation angewiesen, um Hypertonie zu verhindern (Chen et al. 2004). In Endothelzellen ist die Migration, die eine essenzielle Rolle in der Angiogenese spielt, von intakten Mitochondrien abhängig (Spyridopoulos et al. 2008; Shen et al. 2015), während diese in kardialen Fibroblasten für die Differenzierung zu Myofibroblasten benötigt werden (Negmadjanov et al. 2015; Ale-Agha, … **Greulich** et al. 2021). Daher könnte der Erhalt bzw. die Wiederherstellung der Mitochondrienfunktionalität ein therapeutischer Ansatzpunkt bei kardiovaskulären Erkrankungen sein.

Im nächsten Kapitel werde ich auf die Funktion von mitochondrialer Telomerase Reverse Transkriptase eingehen, welche verschiedene Aspekte der Mitochondrienbiologie beeinflusst und zudem protektive Funktionen im Herz-Kreislauf-System hat.

Mitochondriale Telomerase Reverse Transkriptase verringert den myokardialen Ischämie/Reperfusions-Schaden durch Verbesserung der Komplex-I-Zusammensetzung und -Funktion

Es wurde lange angenommen, dass das Telomerase Holoenzym nach der Geburt nur noch in hochproliferativen Zellen und Stammzellen vorhanden ist (Forsyth et al. 2002). In jüngster Vergangenheit wurde jedoch gezeigt, dass die katalytische Untereinheit, Telomerase Reverse Transkriptase (TERT), auch in Zellen mit geringer Proliferationskapazität und post-mitotischen Geweben vorzufinden ist (Eitan et al. 2012; Spilsbury et al. 2015), darunter auch im kardiovaskulären System (Minamino und Kourembanas 2001; Haendeler et al. 2004; Richardson et al. 2012). Es gibt einige Hinweise darauf, dass TERT eine schützende Wirkung gegen kardiovaskuläre Erkrankungen hat (Zurek et al. 2016). In den vergangenen Jahren wurde TERT, neben ihrer kanonischen Lokalisation im Nukleus, ebenfalls in Mitochondrien nachgewiesen (Santos et al. 2004; Ahmed et al. 2008; Haendeler et al. 2009). Dabei konnte unter anderem gezeigt werden, dass TERT dort die Atmungskettenaktivität erhöht, sowie an mitochondriale DNA bindet und diese vor Schädigungen schützt (Haendeler et al. 2009).

Nach der Entdeckung, dass TERT nicht nur im Zellkern, sondern auch in den Mitochondrien lokalisiert ist, fehlten jedoch bislang die Möglichkeiten, um zwischen den Funktionen von nukleärer und mitochondrialer TERT zu unterscheiden. Um dieses Problem zu lösen, haben wir Mäuse generiert, die TERT ubiquitär ausschließlich im Zellkern (nucTERT) oder in den Mitochondrien (mitoTERT) enthalten. Bei der Messung der Atmungskettenaktivitäten dieser Mäuse wiesen die Herzmitochondrien von mitoTERT-Mäusen eine erhöhte Aktivität von Komplex I gegenüber den gleichen Organellen von TERT-defizienten und nucTERT-Mäusen auf, was zeigt, dass mitochondrial lokalisierte, nicht aber nukleäre TERT essenziell für Mitochondrienfunktionen in kardialen Zellen ist. Zudem haben wir die Rolle der Lokalisierung von TERT bei akuter Ischämie/Reperfusion, einem experimentellen Modell für einen Myokardinfarkt, untersucht, da die Funktionalität der Mitochondrien für die Kardioprotektion entscheidend ist (Heusch 2015; Siasos et al. 2018). Mitochondriale TERT, nicht aber nukleäre TERT, konnte die nachteiligen Auswirkungen des Fehlens von TERT in TERT-defizienten Mäusen auf Infarkt- und Narbengröße sowie auf die linksventrikuläre Funktionserholung nach myokardialer Ischämie/Reperfusion verhindern. Nach einem Myokardinfarkt werden Myofibroblasten benötigt, um den nekrotischen Bereich strukturell zu stabilisieren (Fu et al. 2018). Im Rahmen unserer Arbeiten konnten wir zeigen, dass ihre Differenzierung aus kardialen Fibroblasten von der mitochondrialen Atmung abhängt. Zudem zeigte sich das gleiche Phänomen wie bei der Infarkt- und Narbengröße, da die Myofibroblasten-Differenzierung in TERT-defizienten Zellen gestört war und dieser Defekt nur durch mitochondriale TERT kompensiert werden konnte. Aufgrund der Befunde in den Herzmitochondrien ist es möglich, dass auch in diesem Zelltyp eine Verbindung zwischen mitochondrialer TERT und Komplex I-Aktivität besteht und bei der Myofibroblasten-Differenzierung eine Rolle spielt.

Um einen Einblick in den mechanistischen Zusammenhang zwischen mitochondrialer TERT und Komplex I-Aktivität zu erhalten, haben wir zunächst das Proteom von Herzmitochondrien analysiert. Dabei war der auffälligste Unterschied zwischen wildtypischen, TERT-defizienten und mitoTERT Mäusen das Level an mitochondrialem Prohibitin, welches am höchsten in den Herzmitochondrien von TERT-defizienten Mäusen und am niedrigsten in mitoTERT-Mäusen war. Prohibitin beeinflusst die Stöchiometrie der Untereinheiten von Komplex I, wobei gezeigt wurde, dass erhöhte Prohibitin-Level das Verhältnis von Matrixarm- zu Membranuntereinheiten erhöhen und zu einer verringerten Komplex I-Aktivität führen (Miwa et al. 2014).

Auf der Grundlage dieser Beobachtung haben wir die Verhältnisse von zwei Untereinheiten des Komplex I-Matrixarms, nämlich NDUFS3 und NDUFV2, zu den beiden Membranuntereinheiten NDUFA9 und NDUFB9 in kardialen Fibroblasten aus den verschiedenen, oben genannten Mäusen bestimmt. Die TERT-Defizienz führte zu einem Anstieg der Matrixarm-Proteine im Verhältnis zu den Membranuntereinheiten von Komplex I; die gleiche Beobachtung wurde in nucTERT-Fibroblasten gemacht. Dieses Missverhältnis wurde in mitoTERT-Zellen nicht nur abgeschwächt, sondern auch gegenüber Wildtyp-Zellen

weiter verbessert. Somit verhindert mitochondriale TERT ein Ungleichgewicht zwischen Matrixarm- und Membranuntereinheiten von Komplex I, was die in den Herzmitochondrien von mitoTERT-Mäusen beobachtete verbesserte Atmung im Zustand 4 und im Zustand 3 erklärt (Ale-Agha, … **Greulich** et al. 2021).

Anhand dieser Ergebnisse lag es nahe, dass eine Erhöhung der mitochondrialen TERT-Level therapeutisch von Interesse sein könnte. Daher haben wir untersucht, ob der Telomeraseaktivator TA-65 dazu in der Lage ist. Tatsächlich konnten wir eine Erhöhung des Levels an mitochondrialer TERT in Endothelzellen nach Behandlung mit TA-65 sowie funktionell eine Verbesserung ihrer Migrationsfähigkeit feststellen. Interessanterweise wurde auch die Myofibroblasten-Differenzierung von kardialen Fibroblasten aus Wildtyp-Tieren durch TA-65 verbessert (Ale-Agha, … **Greulich** et al. 2021).

Zusammenfassend konnten wir feststellen, dass nur mitochondriale, nicht aber nukleäre TERT eine kardioprotektive Wirkung hat. Die mitochondriale Funktion, die durch mitochondriale TERT erhöht wird, ist für Kardiomyozyten, Fibroblasten und Endothelzellen entscheidend, um ihren Funktionsverlust bei akuter myokardialer Ischämie/Reperfusion zu verringern.

Auf mechanistischer Ebene konnten wir zeigen, dass mitochondriale TERT, nicht aber nukleäre TERT, die Komplex I-Aktivität verbessert, indem sie die optimale Stöchiometrie von Matrixarm- zu Membranuntereinheiten des Komplexes I der mitochondrialen Elektronentransportkette erhält, was für seine ordnungsgemäße Funktion erforderlich ist (Ale-Agha, … **Greulich** et al. 2021).

Mitochondrien und ihre Funktionalität sind essenziell für alle Zellen des Herz-Kreislauf-Systems, so auch für Endothelzellen. Obwohl Endothelzellen die erste Barriere zwischen potenziell schädlichen zirkulierenden Stoffen und umliegendem Gewebe darstellen, haben diese auch signifikante Auswirkungen auf diverse weitere Zelltypen, so etwa zirkulierende Zellen wie Makrophagen, wie zuvor im Kontext von Endothelzellaktivierung beschrieben. Gleichzeitig nehmen die durch diese Zellen mit ausgelösten Entzündungsreaktionen wiederum Einfluss auf das Endothel. Daher werde ich im nächsten Kapitel auf die Regulation von Entzündungen durch Stoffwechselprozesse in Makrophagen eingehen.

Makrophagen Acetyl-CoA-Carboxylase reguliert akute Entzündungen durch Kontrolle des Glukose- und Lipidstoffwechsels

Als Reaktion auf Infektionen oder Gewebeschäden müssen Immunzellen, einschließlich Makrophagen, welche zu den myeloischen Zellen gehören, ihren intrazellulären Stoffwechsel rapide anpassen, um eine wirksame Entzündungsreaktion einzuleiten (O'Neill et al. 2016; O'Neill und Pearce 2016; Van den Bossche et al. 2017). Dabei ist die Regulation des Lipidstoffwechsels sowohl für die Auslösung als auch für die Beendigung der Entzündungsreaktion von wesentlicher Bedeutung (Wei et al. 2016; Carroll et al. 2018; Liebergall et al. 2020). Dementsprechend könnten Enzyme eine Rolle spielen, die an der

Lipogenese beteiligt sind, wie etwa die Acetyl-CoA-Carboxylase (ACC), das geschwindigkeitsbestimmende Enzym der *de novo* Lipogenese. Von diesem Enzym gibt es 2 unterschiedliche Isoformen, ACC1 und ACC2. Es konnte bereits gezeigt werden, dass der Verlust dieses Enzyms die Bildung von T-Gedächtniszellen verbessert (Lee et al. 2014; Stuve et al. 2018; Endo et al. 2019), jedoch ist seine Rolle in myeloischen Zellen noch unerforscht. Myeloische Zellen umfassen alle Zellen des blutbildenden Systems, welche nicht dem lymphatischen System zugeordnet werden, wie etwa rote Blutkörperchen, Blutplättchen, oder auch Makrophagen. Wir haben ein Mausmodell mit einem *knockout* sowohl von ACC1 als auch ACC2 in myeloischen Zellen entwickelt, um die Auswirkungen des Verlusts von ACC auf die Makrophagenaktivierung zu untersuchen.

Dabei haben wir eine unerwartete Rolle der ACC im Zusammenhang von metabolischer Umprogrammierung und Aktivierung von Makrophagen in Entzündungsreaktionen identifiziert. Die Umprogrammierung kann entweder zu pro-inflammatorischen M1-Makrophagen oder zu anti-inflammatorischen M2-Makrophagen erfolgen, abhängig von den jeweiligen Erfordernissen und Signalen aus deren Mikromilieu. Unter Verwendung des Mausmodells und pharmakologischer Ansätze *in vivo* sowie bioenergetischer, lipidomischer und transkriptionsanalytischer Methoden *in vitro* fanden wir heraus, dass der Verlust von ACC in Makrophagen zur Umstellung auf einen hyperglykolytischen Stoffwechsel mit erhöhter Glukose-Aufnahme führt. Durch diese basal erhöhte Glukose-Aufnahme wird die Fähigkeit der Makrophagen zur Verbesserung der Glukoseverwertung und zur Blockierung der Lipidakkumulation als Reaktion auf Stimulation des *Toll-like receptor 2* und *4* eingeschränkt, was in Summe für die verschlechterte metabolische Flexibilität durch den ACC-Verlust spricht. Zusätzlich konnten wir beobachten, dass die Ausschaltung von ACC die Transkription von Genen für pro-inflammatorische Mediatoren reduzierte, was die Zytokinsekretion der Makrophagen, die Phagozytose und die Zerstörung von Krankheitserregern beeinträchtigte und zu einer geringeren Entzündungsreaktion führte (Yeudall, … **Greulich** et al. 2022).

Diese Ergebnisse weisen auf eine essenzielle Rolle der ACC für eine normale Entzündungsreaktion hin, welche bei Verlust der ACC kompromittiert ist. Unsere Beobachtungen unterstreichen die Verbindungen zwischen der Kontrolle des Zellstoffwechsels und der Menge an pro-inflammatorischen M1-Makrophagen.

Bei Entzündungsreaktionen sind nicht nur Effektorzellen, wie beispielsweise Makrophagen wichtig, sondern auch Reaktionen des Endothels, das direkt mit inflammatorischen Mediatoren oder anderen Entzündungs-auslösenden Substanzen im Blutstrom konfrontiert ist. Zu Letzteren gehört z.B. Lipopolysaccharid (LPS), ein Membranbestandteil gramnegativer Bakterien, das in hohen Dosen im Blutkreislauf zu einer Endotoxämie führt, auf welche im folgenden Kapitel genauer eingegangen wird.

Selenoprotein T schützt Endothelzellen vor Lipopolysaccharid-induzierter Aktivierung und Apoptose

Als Endotoxämie wird das Vorhandensein von hohen Endotoxin-Spiegeln, beispielsweise LPS, einem Membranbestandteil gram-negativer Bakterien, im Blut bezeichnet. Dabei können 1 bis 2 mg in der Blutbahn tödlich sein, welche infolge einer systemischen bakteriellen Infektion auftreten können, da LPS ein serologisch reaktives Bakterientoxin ist. Dies kann schlussendlich zu einer Sepsis, einer lebensbedrohlichen Dysfunktion eines oder mehrerer Organe als Folge einer überschießenden Immunreaktion führen. Bei einem septischen Schock tritt dabei eine massive arterielle Hypotonie auf, die eine Hypoperfusion innerer Organe nach sich zieht. Jedes Jahr erleiden fast 50 Mio. Menschen eine Sepsis. Damit ist sie eine der häufigsten Erkrankungen weltweit. Circa 20 % aller Todesfälle werden mit Sepsis assoziiert (Fleischmann-Struzek et al. 2022).

Die meisten bakteriellen LPS-Moleküle sind thermostabil und stellen einen entzündungsfördernden Stimulus für das menschliche Immunsystem dar. Aufgrund der Zirkulation von LPS in der Blutbahn sind aber auch Endothelzellen diesem direkt ausgesetzt. LPS induziert deren Aktivierung und löst schlussendlich Endothelzell-Apoptose aus, was wiederum zu Gefäßleckagen führt. Dieser Verlust der Integrität der endothelialen Barriere ist ein Hauptgrund für das Auftreten eines septischen Schocks (Joffre et al. 2020). Die effektive Behandlung einer Sepsis stellt sich weiterhin als schwierig dar. Abgesehen von der Einführung von Vasopressoren zur Aufrechterhaltung des arteriellen Drucks als Hauptbehandlungsmethode vor 40 Jahren ist bis heute kein neues therapeutisches Prinzip zur Behandlung der Sepsis entwickelt worden (Brunkhorst et al. 2020). Insofern wären adjuvante Therapien, die den Endothelzellverlust verringern oder sogar verhindern und damit die Barrierefunktion des Endothels erhalten könnten, von enormem Wert für die Patienten.

Unsere Arbeitsgruppe konnte in früheren Arbeiten zeigen, dass die apurininische/apyrimidinische Endodeoxyribonuklease 1 (APEX1) H_2O_2-induzierte Apoptose in Endothelzellen hemmt. Interessanterweise reichten hierfür die ersten 20 Aminosäuren von APEX1 – im Folgenden als APEX1(1-20) bezeichnet – aus (Dyballa-Rukes et al. 2017). Da die molekularen Mechanismen, die durch einen apoptotischen Stimulus induziert werden, unabhängig vom Auslöser sind, stellten wir die Hypothese auf, dass APEX1(1-20) auch die LPS-induzierte Apoptose hemmen könnte.

In dieser Studie wollten wir untersuchen, ob APEX1(1-20) einen Einfluss auf Signalwege hat, die durch LPS in Endothelzellen induziert werden, um aus den darauffolgenden Signalweganalysen neue Optionen für therapeutische Ansätze zu entwickeln. LPS selbst beeinflusst das endotheliale Transkriptom, indem es das Level zahlreicher Transkripte reguliert, nicht nur von proteincodierenden RNAs, sondern auch von nichtcodierenden RNAs wie microRNAs und langen nicht-kodierenden RNAs (Zhao et al. 2001; Ho et al. 2016). Allerdings gab es zum Zeitpunkt dieser Studie keine RNA-Deep-Sequencing Daten zu LPS-induzierten Transkriptomveränderungen im Endothel in den etablierten Datenbanken wie dem

Gene Expression Omnibus (GEO), dem European Nucleotide Archive (ENA), Sequence Read Archive (SRA) oder ArrayExpress. Da eine solche Transkriptom-Analyse in Kombination mit Signalweganalysen neue Zielmoleküle für die Entwicklung therapeutischer Ansätze zur Behandlung von Sepsis, insbesondere zum Schutz des Endothels, liefern könnte, haben wir ein RNA-Deep-Sequencing von LPS-behandelten primären Endothelzellen durchgeführt und dabei auch Zellen eingeschlossen, die permanent APEX1(1-20) exprimieren.

Zu diesem Zweck wurden primäre menschliche Endothelzellen mit einem lentiviralen Expressionsvektor für APEX1(1-20) transduziert, um eine permanente Expression des Peptids zu gewährleisten. Die Zellen wurden dann mit 150 ng/ml aktivem LPS behandelt. Als Kontrollen wurden Zellen mit einem Leervirus transduziert sowie mit detoxifiziertem LPS behandelt. Die RNA aus diesen Zellen wurde für RNA-Deep-Sequencing verwendet und auf differentielle Genexpression untersucht.

Das Transkriptom in Zellen, die APEX1(1-20) exprimieren und mit detoxifiziertem LPS behandelt wurden, war gegenüber Leervirus-transduzierten, gleichartig behandelten Zellen unverändert. Daraus lässt sich schließen, dass APEX1(1-20) in intakten Endothelzellen keine Nebenwirkungen hat.

Zudem induzierte die Behandlung von Zellen, die kein APEX1(1-20) exprimieren, mit aktivem LPS – wie erwartet – typische, bei Sepsis bekannte Signalwege. In diesen Zellen wurde die Expression von Genen hochreguliert, die beispielsweise unter die GO-Begriffe *response to interferon alpha*, *cellular response to tumor necrosis factor* und *tumor necrosis factor-mediated signaling pathway* fallen. Die Aktivierung dieser Signalwege, die zelluläre Antworten auf Entzündungen umschreiben, ist typisch für die Reaktion des Endothels auf LPS. Interessanterweise unterdrückte die Expression von APEX1(1-20) diese LPS-induzierten Transkriptomveränderungen und führte sogar zu einer signifikanten Herabregulation der Expression von Genen mit der GO-Klassifizierung *cellular response to tumor necrosis factor*. Dies wies darauf hin, dass APEX1(1-20) der LPS-induzierten Endothelzellaktivierung und -apoptose durch Veränderungen des zellulären Transkriptoms entgegenwirkt (Merk, … **Greulich** et al. 2021).

Basierend auf den differentiellen Genexpressionsanalysen wählten wir zunächst Kandidatengene für eine erste Validierung mittels semi-quantitativer real-time PCR und eine spätere funktionelle Charakterisierung hinsichtlich Endothelzellaktivierung und -apoptose aus. Dabei wurden folgende Selektionskriterien angewendet: die Gene sollten den Sequenzierungsdaten zufolge hinreichend stark exprimiert sein, um ihre Transkripte zuverlässig nachweisen und quantifizieren zu können. Zudem sollte ihre Expression nur nach LPS-Behandlung von Zellen, die das APEX1-Peptid exprimieren, erhöht sein. Die Grundlage hierfür war die Annahme, dass die von derartigen Transkripten codierten Proteine die protektive Wirkung von APEX1(1-20) in Endothelzellen vermitteln und somit therapeutisch von Interesse sein könnten.

Die drei Gene, die diesen Kriterien am besten entsprachen, waren *IL1RL*, welches für ein Interleukin-1-Rezeptor-ähnliches Protein codiert, *PXDN* (Peroxidasin) und *SELENOT* (SELENOT oder Selenoprotein T). Interleukin-1-Rezeptoren sind eine Familie von 10 strukturell verwandten Proteinen mit teilweise unterschiedlichen Funktionen (Boraschi et al. 2018). Insofern könnte die Interferenz mit diesem Netzwerk von Signaltransduktionsmolekülen unerwünschte Nebenwirkungen haben, weswegen *IL1RL* für weitergehende Analysen nicht in Betracht gezogen wurde. Die beiden anderen Gene, *PXDN* und *SELENOT* hingegen, wurden für weitere Validierungen ausgewählt. Peroxidasin ist im Herz und der Gefäßwand hoch exprimiert (Cheng et al. 2008), fördert Angiogenese (Medfai et al. 2019) und ist essenziell für das Überleben von Endothelzellen (Lee et al. 2020). SELENOT, das evolutionär höchstkonservierte Selenoprotein (Pothion et al. 2020), ist im Endoplasmatischen Retikulum (ER) lokalisiert und damit, wie die anderen Selenoproteine des ERs, kritisch für zelluläre Stressantworten (Addinsall et al. 2018). Allerdings waren bisher keine Funktionen dieses Proteins bei der endothelialen Aktivierung und Apoptose beschrieben worden.

Die Validierung der Deep-Sequencing Daten in der real-time PCR zeigte keine signifikante Herabregulation der *SELENOT*- und *PXDN*-Expression in LPS-behandelten Endothelzellen, obwohl es einen Trend in diese Richtung zu geben scheint. Im Gegenteil zeigten die Zellen, die APEX1(1-20) exprimieren, nach der LPS-Behandlung einen signifikanten Anstieg der *SELENOT*- und *PXDN*-RNA-Spiegel. Die protektive Wirkung von *PXDN* in Endothelzellen war allerdings bereits beschrieben worden (Lee et al. 2020), weswegen *PXDN* nicht in die funktionellen Analysen einbezogen wurde. Nichtsdestotrotz stellt der Nachweis der *PXDN*-Regulation in der real-time PCR eine unabhängige Bestätigung der Validität unseres experimentellen Ansatzes dar.

Um die Auswirkungen von SELENOT auf die durch LPS beeinflussten Funktionen von Endothelzellen zu untersuchen, haben wir einen Expressionsvektor für SELENOT mit einem FLAG-Epitop-Tag kloniert, welches die Identifizierung des überexprimierten Proteins ermöglicht. Bei der Klonierung dieses Expressionsvektors musste ein für Selenoproteine einzigartiger Aspekt berücksichtigt werden. Selenocystein (Sec)-Reste in Selenoproteinen sind nicht das Produkt einer posttranslationalen Modifikation, sondern werden bereits während der Translation eingebaut, indem eines der Translationsterminationscodons, nämlich UGA, zur Bindung der Selenocystein-tRNA (tRNASec) an die mRNA verwendet wird. Diese translationale Umcodierung des UGA-Codons benötigt eine sogenannte Selenocystein-Insertionssequenz (SECIS) in der 3′-untranslatierten Region (UTR) des Transkripts. Die SECIS, die auf Sequenzebene nicht hoch konserviert ist, bildet eine Haarnadel-Struktur, die für die Rekrutierung der tRNASec an das UGA-Codon erforderlich ist (Tujebajeva et al. 2000). Folglich führt das Fehlen einer SECIS zu einem vorzeitigen Abbruch der Translation, wenn das Ribosom auf das erste UGA innerhalb des offenen Leserasters trifft. Daher haben wir - neben dem offenen Leseraster für SELENOT - einen Teil seiner 3′-UTR einschließlich der SECIS in den Expressionsvektor aufgenommen. In unserer Studie konnten wir zeigen, dass

die Überexpression von SELENOT die LPS-induzierte Aktivierung und Apoptose in humanen primären Endothelzellen vollständig hemmt (Merk, … **Greulich** et al. 2021).

Unsere Daten deuten darauf hin, dass das APEX1(1-20) Peptid sowie SELENOT Endothelzellen vor LPS-induzierter Aktivierung und Apoptose schützen und somit die Beeinträchtigung der Integrität der Endothelbarriere im Verlauf einer Sepsis verhindern könnten. Die Umsetzung dieser Befunde in Konzepte für eine adjuvante Therapie könnte somit die Zahl der Fälle von Patienten mit septischem Schock, multiplem Organversagen und Todesfällen verringern.

Während hohe Konzentrationen von LPS in der Blutbahn aufgrund einer akuten Infektion zu einer Sepsis führen und somit potenziell akut letal enden können, führen permanent vorhandene, niedrige LPS-Level zu einer sogenannten niedriggradigen Entzündung. Diese subklinischen Entzündungen können chronische Erkrankungen als Folgen haben (Cani et al. 2012; Mohammad und Thiemermann 2020). Die niedrigen, aber messbaren Konzentrationen an LPS können beispielsweise die Folge einer ungesunden Ernährung sein, die, wie eingangs erwähnt, in westlichen Ländern heutzutage weit verbreitet ist. Auf den Einfluss von Ernährung und Nahrungsbestandteilen und den Implikationen für das Endothel werde ich im folgenden Kapitel näher eingehen.

Koffein inhibiert Endothelzellseneszenz

Wie in der Einleitung bereits erwähnt, trägt die zelluläre Seneszenz von Endothelzellen zu endothelialer Dysfunktion und somit auch der Entstehung und dem Fortschreiten kardiovaskulärer Erkrankungen bei. Dies kann unter anderem durch die Erhöhung an reaktiven Sauerstoffspezies während der Alterung sowie durch diverse Erkrankungen bedingt sein (Minamino et al. 2002). Zelluläre Seneszenz ist durch einen stabilen Zellzyklus-Arrest gekennzeichnet, der bei diploiden Zellen auftritt und ihre proliferative Lebensdauer begrenzt. Dabei unterscheidet man zwischen zwei Arten von Seneszenz. Eine Form ist die replikative Seneszenz. Die erste Beschreibung dieses Phänomens stammt aus den 1960er Jahren, als Leonard Hayflick beobachtete, dass menschliche diploide Fibroblasten in Kultur eine maximale Anzahl von Zellteilungen erreichen können, bevor ihr Wachstum zum Stillstand kommt (Hayflick 1965). Diese biologische Uhr, die als "Hayflick-Grenze" bekannt ist, basiert unter anderem auf einer fortschreitenden Verkürzung der Telomere bei jeder Zellteilung (Harley et al. 1990). Der Verlust der Telomersequenzen begünstigt wiederum Chromosomenfusionen. Zudem kann es im Verlauf von Zellteilungen trotz vorhandener Reparaturmechanismen zu Mutationen, fehlerhafter Chromosomensegregation und genomischer Instabilität kommen. Diese Veränderungen führen im schlechtesten Fall zum Verlust der Proliferationskontrolle und Tumorentstehung. Zelluläre Seneszenz wird daher als ein Mechanismus diskutiert, der dafür sorgt, dass sich Zellen mit derartigen Veränderungen nicht weiter teilen können, so dass Seneszenz Tumor-suppressiv wirkt (Campisi 2001). Allerdings ist es äußerst unwahrscheinlich, dass es in sich langsam teilenden Zellen, wie z.B. Endothelzellen, und post-

mitotischen Organen, überhaupt zur replikativen Seneszenz kommen kann, da die hierfür notwendige Anzahl an Zellteilungen im Verlauf der menschlichen Lebensspanne nicht erreicht wird. Zelluläre Seneszenz kann jedoch auch unabhängig von der Telomerverkürzung in einem wesentlich kürzeren Zeitrahmen durch verschiedenste Stressoren, wie z.B. permanenten milden oxidativen Stress (Toussaint et al. 2000), aber auch durch Onkogene (Courtois-Cox et al. 2008) induziert werden. Dies wird dann als vorzeitige oder Stress-induzierte Seneszenz bezeichnet. Endothelzellen sind als erste Barriere zum Blutkreislauf einer Vielzahl verschiedener Stimuli, darunter einigen Stressoren inklusive erhöhten ROS-Leveln, ausgesetzt. Insofern ist es nicht verwunderlich, dass sich Seneszenz in primären humanen Endothelzellen durch eine zweiwöchige, repetitive Behandlung mit geringen Konzentrationen von H_2O_2 induzieren lässt (Haendeler et al. 2004).

In seneszenten Zellen geht der Zellzyklus-Arrest mit einer erhöhten Konzentration von Zellzyklusinhibitoren aus der Familie der Cyclin-abhängigen Kinase Inhibitoren wie z.B. p16 und p21 und/oder ihrer verstärkten Translokation in den Zellkern einher. Außerdem wird eine erhöhte Aktivität der Seneszenz-assoziierten β-Galaktosidase (SA-β-Gal) beobachtet. Daher werden sowohl SA-β-Gal, als auch p16 und p21 als Biomarker für zelluläre Seneszenz verwendet (Wang und Dreesen 2018).

Wie ebenfalls in der Einleitung bereits erwähnt, weisen seneszente Endothelzellen eine verringerte NO-Bioverfügbarkeit auf, was durch verringerte Mengen an eNOS bedingt ist (Buchner et al. 2013; Gonnissen et al. 2019). Dies führt zu Einschränkungen der Endothelzellfunktionalität (Goy et al. 2014). Ebenfalls sind in seneszenten Endothelzellen die ROS-Level erhöht, was sich durch verringerte Level an Trx-1, erhöhte Level der lysosomalen Protease Cathepsin D, welche Trx-1 abbaut (Haendeler et al. 2005), sowie erhöhte Level des ROS-produzierenden Enzyms NOX4 (Goy et al. 2014) erklären lässt. Funktionell wurde eine eingeschränkte Mitochondrienfunktion sowie eine verringerte Migrationsfähigkeit beobachtet (Buchner et al. 2013; Gonnissen et al. 2019), wobei anzumerken ist, dass die Migration von Endothelzellen funktionelle Mitochondrien benötigt (Gonnissen et al. 2019).

Koffein in physiologischen Konzentrationen von 30-50 µM, die nach dem Konsum von 4 Tassen Kaffee im Blut gesunder Probanden gemessen werden können, verbessert die Migrationsfähigkeit und die mitochondriale Funktionalität von Endothelzellen (Spyridopoulos et al. 2008; Ale-Agha et al. 2018). Allerdings wurde die Wirkung von Koffein auf Endothelzellseneszenz noch nie zuvor untersucht. Daher haben wir in einem etablierten Modell zur Auslösung von Stress-induzierter Endothelzellseneszenz mittels repetitiver Behandlung mit H_2O_2 (Goy et al. 2014) den Einfluss von Koffein untersucht. Wir konnten zeigen, dass die gleichzeitige Gabe von Koffein mit H_2O_2 die Induktion von Seneszenz verhindert, indem es die Erhöhung der p21-Level und dessen nukleäre Akkumulation inhibiert (Merk*, **Greulich*** et al. 2023). Dies spiegelt sich auch im für Endothelzellen relevanten Spiegel an eNOS wider, da es bei paralleler Behandlung mit Koffein nicht zu einem Verlust

von eNOS kommt (Abb. 2, diese Untersuchungen wurden in Zusammenarbeit mit cand. med. Annika Vierkant durchgeführt) (Merk*, **Greulich*** et al. 2023).

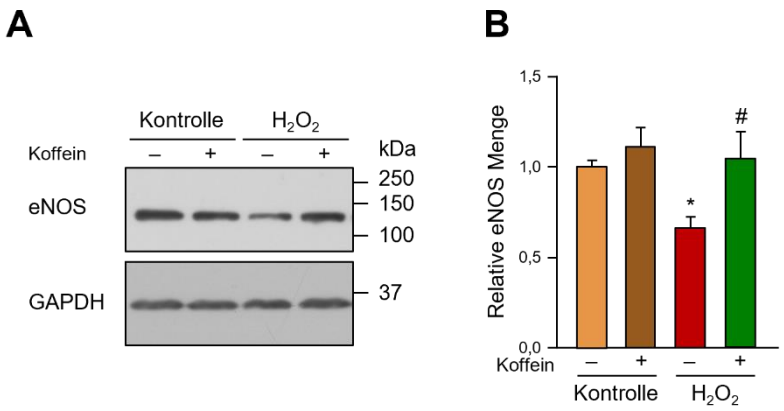

Abbildung 2: Koffein verhindert den Verlust von eNOS nach repetitiver Behandlung von Endothelzellen mit H_2O_2. (**A**,**B**) Endothelzellen wurden zwei Wochen lang jeden zweiten Tag mit 50 µM H_2O_2 behandelt, unbehandelte Zellen dienten als Kontrolle. Beide Gruppen erhielten zu den gleichen Zeitpunkten 10 µM Koffein (+) oder nicht (-) wie angegeben. eNOS wurde mittels Immunoblot nachgewiesen, GAPDH diente als Ladekontrolle. (**A**) Repräsentative Immunoblots für eNOS und GAPDH. (**B**) Semi-quantitative Analyse der relativen Mengen von eNOS (Daten sind Mittelwerte ± Stichprobenfehler, n = 5, *p < 0,05 vs. Kontrolle, #p< 0,05 vs. H_2O_2 ohne Koffein, einseitiger ANOVA mit post hoc Tukey LSD Test).

Allerdings kann Endothelzellseneszenz nicht nur durch oxidativen Stress hervorgerufen werden, sondern auch durch die Art der Ernährung. Wie bereits erwähnt, ist ein hoher Gehalt an Cholesterin Teil einer ungesunden, jedoch häufig üblichen Ernährung, besonders in westlichen Ländern. Cholesterin wird im Blutplasma durch LDL zu den Geweben und Organen transportiert und kann zur Endothelzellseneszenz führen (Buchner et al. 2013). Bemerkenswerterweise führt dies auch zu niedrigen, nachweisbaren LPS-Spiegeln von etwa 1 ng/ml im Blut; in diesem Fall spricht man zur Abgrenzung gegenüber den bei einer Sepsis beobachteten Mengen von einer metabolischen Endotoxämie (Merk et al. 2024). Aufgrund des Zusammenhangs zwischen LDL, welches nachgewiesenermaßen Endothelzellseneszenz induziert, und metabolischer Endotoxämie haben wir untersucht, ob auch eine Exposition gegenüber diesen niedrigen LPS-Dosen Seneszenz in Endothelzellen induziert, und ob Koffein diesen Prozess verhindern oder sogar umkehren kann.

Interessanterweise induzierte die repetitive Behandlung von Endothelzellen mit 1 ng/mL LPS über einen Zeitraum von 2 Wochen tatsächlich Seneszenz, wie sich an einem Anstieg des p21-Spiegels und seiner nukleären Akkumulation zeigte (Merk*, **Greulich*** et al. 2023). Analog zu unseren Beobachtungen in H_2O_2-induzierter Endothelzellseneszenz war der eNOS-Spiegel in LPS-induzierter Endothelzellseneszenz ebenfalls verringert. Dieser Verlust konnte jedoch auch in diesem Modell durch die gleichzeitige Gabe von Koffein verhindert werden (Abb. 3) (Merk*, **Greulich*** et al. 2023).

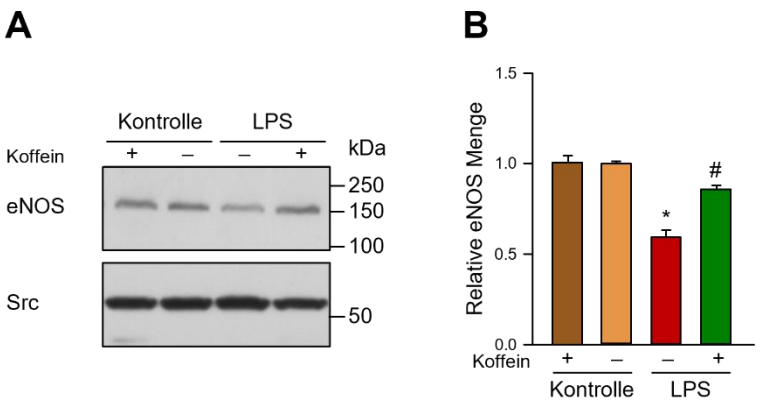

Abbildung 3: Koffein verhindert den Verlust von eNOS nach repetitiver Behandlung von Endothelzellen mit niedrigen LPS-Dosen. (**A**,**B**) Endothelzellen wurden zwei Wochen lang jeden zweiten Tag mit 1 ng/ml LPS behandelt, unbehandelte Zellen dienten als Kontrolle. Beide Gruppen erhielten zu den gleichen Zeitpunkten 10 µM Koffein (+) oder nicht (-) wie angegeben. eNOS wurde mittels Immunoblot nachgewiesen, Src diente als Ladekontrolle. (**A**) Repräsentative Immunoblots für eNOS und Src. (**B**) Semi-quantitative Analyse der relativen Mengen von eNOS (Daten sind Mittelwerte ± Stichprobenfehler, n = 4, *p < 0,05 vs. Kontrolle, #p< 0,05 vs. LPS ohne Koffein, einseitiger ANOVA mit post hoc Tukey LSD Test).

Wie bereits erwähnt, spiegelt auch die Migrationsfähigkeit die Funktionalität von Endothelzellen wider und ist in seneszenten Endothelzellen eingeschränkt (Buchner et al. 2013; Gonnissen et al. 2019). Dies konnten wir ebenfalls in unserem Modell der LPS-induzierten Endothelzellseneszenz beobachten. Interessanterweise kann die gleichzeitige Gabe von Koffein den Verlust der Migrationsfähigkeit ebenfalls vollständig verhindern (Abb. 4) (Merk*, **Greulich*** et al. 2023).

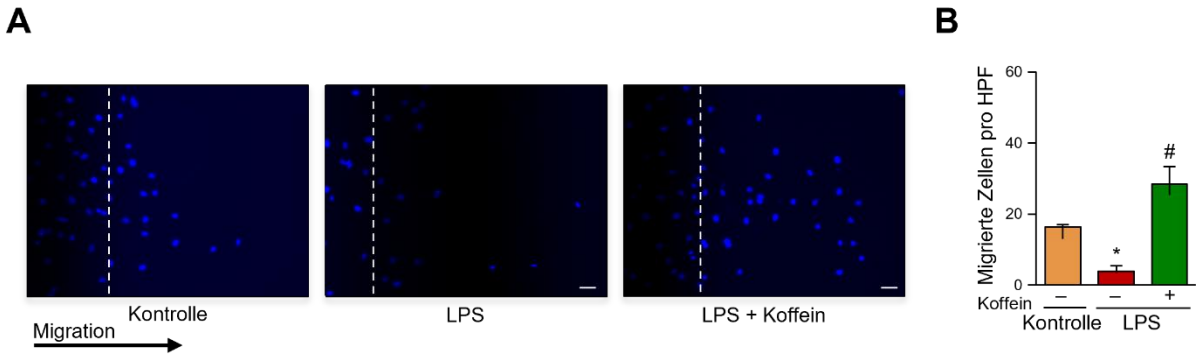

Abbildung 4: Koffein verhindert den Verlust der Migrationsfähigkeit nach repetitiver Behandlung von Endothelzellen mit niedrigen LPS-Dosen (**A**,**B**) Endothelzellen wurden zwei Wochen lang jeden zweiten Tag mit 1 ng/ml LPS behandelt, unbehandelte Zellen dienten als Kontrolle. Die mit LPS-behandelten Zellen erhielten zu den gleichen Zeitpunkten 10 µM Koffein (+) oder nicht (-) wie angegeben. Die Migrationskapazität wurde mittels eines *Scratch-Wound*-Assays untersucht. Zur Auszählung der migrierten Zellen, wurden die Zellkerne mit 4′,6-Diamidin-2-phenylindol (DAPI) gefärbt. (**A**) Repräsentative DAPI-Färbungen (Maßstabsbalken = 50 µM). (**B**) Semi-quantitative Analyse der migrierten Zellen pro Hauptgesichtsfeld (*High-Power Field*, HPF) (Daten sind Mittelwerte ± Stichprobenfehler, n = 4, *p < 0,05 vs. Kontrolle, #p< 0,05 vs. LPS ohne Koffein, einseitiger ANOVA mit post hoc Tukey LSD Test).

Gleichzeitig war auch das Level an Trx-1-verringert, was auf eine gestörte Redox-Homöostase hinweist. Auch dieser Effekt wurde durch die gleichzeitige Behandlung mit Koffein vollständig blockiert (Merk*, **Greulich*** et al. 2023).

In vorangegangenen Arbeiten hat unsere Arbeitsgruppe den molekularen Mechanismus entschlüsselt, der der positiven Wirkung von Koffein im Herz-Kreislauf-System zugrunde liegt. In diesen Untersuchungen wurde gezeigt, dass Koffein die verstärkte Translokation von p27, dem Cyclin-abhängigen Kinase-Inhibitor 1B, in die Mitochondrien induziert. Der Befund, dass die durch Koffein erhöhte mitochondriale Atmungskettenaktivität in Mausherzen vollständig von p27 abhängig war, legte nahe, dass mitochondriales p27 die Koffeineffekte vermittelt. Dies konnte dadurch bewiesen werden, dass sowohl die Stimulation mit Koffein als auch die Expression von exklusiv in Mitochondrien lokalisiertem p27 die Endothelzellmigration verstärkten, es aber keine additiven Effekte gab. (Ale-Agha et al. 2018). Endothelzellseneszenz geht, wie bereits eingangs erwähnt, nachweislich mit einer verschlechterten Mitochondrienfunktion und einer verringerten Migrationsfähigkeit einher. Daher haben wir untersucht, ob mitochondriales p27 den gleichen Einfluss auf die LPS-induzierte Seneszenz wie Koffein hat. In der Tat konnten wir zeigen, dass die permanente Expression von exklusiv mitochondrial lokalisiertem p27 die LPS-induzierte Hochregulation und Kerntranslokation von p21 verhindert, und damit die Induktion von Endothelzellseneszenz blockiert (Merk*, **Greulich*** et al. 2023) (Abb. 5).

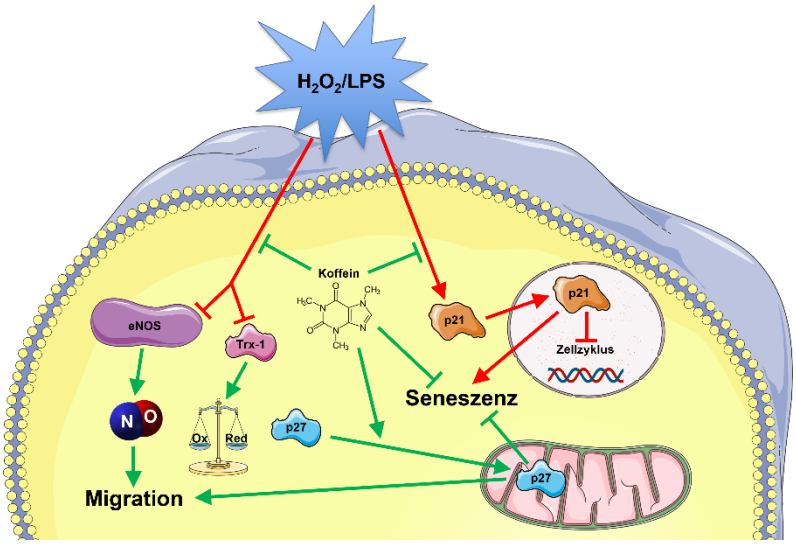

Abbildung 5: Koffein verhindert die Induktion von Endothelzellseneszenz und verstärkt die mitochondriale Translokation von p27. Koffein verhindert die Induktion von Endothelzellseneszenz, indem es der Erhöhung der p21 Level entgegenwirkt. Zudem hält es den eNOS-Spiegel und damit die NO-Produktion sowie die Migrationsfähigkeit aufrecht. Die wahrscheinlichste Erklärung hierfür ist die durch Koffein induzierte Erhöhung der Menge an mitochondrialem p27, da die permanente Expression von mitochondrial lokalisiertem p27 gleiche Konsequenzen im Hinblick auf die Seneszenzinduktion hat.

(Die Abbildung wurde mit Servier Medical Art generiert, die von Servier bereitgestellt wird, und unter einer Creative Commons Attribution 3.0 Unported License (https://creativecommons.org/licenses/by/3.0/) zum freien Gebrauch lizensiert ist).

In den bisher beschriebenen Experimenten wurde ein ausschließlich präventiver Ansatz zur Verhinderung der Seneszenz verwendet, indem die Zellen parallel zur H_2O_2- oder LPS-Exposition mit Koffein behandelt wurden. Oftmals wird Seneszenz als irreversibler Zellzyklusarrest beschrieben, jedoch gibt es bereits einige Berichte über einen erneuten Zellzykluseintritt nach vorherigem Arrest (Galanos et al. 2016; Patel et al. 2016; Milanovic et al. 2018; Saleh et al. 2019). Insofern stellte sich uns die Frage, ob Koffein einen bereits manifestierten seneszenten Phänotyp revertieren kann. Um dies zu untersuchen, haben wir Endothelzellen, in denen bereits Seneszenz mittels LPS-Behandlung über 12 Tage induziert worden war, einmalig für 2 Tage mit Koffein behandelt. Hierfür wurde im Gegensatz zu dem

zuvor geschilderten präventiven Ansatz mit 10 µM Koffein eine Konzentration von 50 µM gewählt, da diese in Kurzzeitbehandlungen von Endothelzellen zu positiven Effekten geführt hatte (Spyridopoulos et al. 2008; Ale-Agha et al. 2018). Dieser einzelne Bolus von Koffein reichte aus, um das bereits stark angestiegene p21-Level wieder zu verringern. Gleichzeitig normalisierte er den Trx-1-Spiegel, was darauf hindeutet, dass die Umkehrung der Seneszenz eng mit der Wiederherstellung einer intakten Redox-Homöostase verknüpft ist (Merk*, **Greulich*** et al. 2023).

Mit diesen Arbeiten konnte von uns erstmals gezeigt werden, dass geringe Dosen LPS, wie sie etwa bei schlechter Ernährung und damit verbundener metabolischer Endotoxämie nachweisbar sind, Seneszenz in Endothelzellen induzieren. Dieser Prozess kann durch konstante Zufuhr von Koffein verhindert werden, und ist darüber hinaus durch einmalige Behandlung mit einer höheren Koffeinmenge revertierbar (Merk*, **Greulich*** et al. 2023).

In seneszenten, Funktions-eingeschränkten Endothelzellen ist das eNOS-Level verringert. Tatsächlich sind einige der wichtigsten Funktionen des Endothels – etwa Migrationsfähigkeit und Apoptoseschutz – abhängig von dem von eNOS synthetisierten Molekül NO und dessen Bioverfügbarkeit. Im folgenden Kapitel werde ich auf die Rolle des Transkriptionsfaktors Grainyhead-like 3 (GRHL3) in der Endothelzellfunktionalität und im Speziellen auf seinen Einfluss auf eNOS eingehen.

Der Transkriptionsfaktor Grainyhead-like 3 besitzt extranukleäre Funktionen im Endothel und interagiert mit eNOS

Eine zentrale Rolle in der Funktion und Adaptation von Zellen an sich verändernde Bedingungen nehmen Transkriptionsfaktoren ein, da jeder einzelne die Expression einer Vielzahl von Genen regulieren kann. In früheren Arbeiten hat unsere Arbeitsgruppe in einem *gene trapping* für Gene, welche durch Tumornekrosefaktor-α reguliert werden, den Transkriptionsfaktor GRHL3 identifiziert und nachgewiesen, dass er eine pro-migratorische Funktion in Endothelzellen hat (Guardiola-Serrano et al. 2008). GRHL3 ist ein Mitglied einer Proteinfamilie, welche die Säugerhomologe zu dem namensgebenden Protein Grainyhead aus der Taufliege *Drosophila melanogaster* darstellen (Bray und Kafatos 1991). In Säugern umfasst diese Familie drei Homologe, GRHL1, GRHL2, und GRHL3, die teils unterschiedliche, nicht-redundante Funktionen haben (Wilanowski et al. 2002; Ting et al. 2003). Allen gemeinsam ist jedoch, dass sie eine evolutionär hoch konservierte Rolle in der Aufrechterhaltung der epidermalen Integrität spielen (Ting et al. 2005; Wang und Samakovlis 2012).

Später wurde von unserer Arbeitsgruppe gezeigt, dass GRHL3 nicht nur nach Überexpression die Endothelzellmigration stimuliert, wobei dies unabhängig vom *Vascular Endothelial Growth Factor* geschieht, sondern auch eine zentrale Rolle bei der Migration spielt, da diese durch eine Herunterregulation von GRHL3 inhibiert wird (Lukosz et al. 2011). Dies steht im Einklang

mit Befunden aus Keratinozyten, in denen GRHL3 ebenfalls eine essenzielle Rolle bei der Migration spielt (Yu et al. 2008; Caddy et al. 2010). Unsere Arbeitsgruppe konnte in Endothelzellen auf verschiedenen Ebenen auch einen direkten Zusammenhang zwischen GRHL3 und NO nachweisen. Zum einen wurde gezeigt, dass der pro-migratorische Effekt von NO abhängig von GRHL3 ist, zum anderen, dass NO die Expression von GRHL3 erhöht. Letztendlich nimmt GRHL3 auch Einfluss auf die endotheliale NO-Produktion, da es die Phosphorylierung von eNOS an Serin 1177 erhöht und somit deren Aktivität steigert (Lukosz et al. 2011). Diese Phosphorylierung wird vermittelt durch die Proteinkinase Bα (Akt1) (Dimmeler et al. 1999), deren Aktivität ihrerseits durch eine verstärkte Phosphorylierung an Serin 473 durch GRHL3 erhöht wird. Im gleichen Zug konnte von unserer Gruppe gezeigt werden, dass GRHL3 nicht nur Migration von Endothelzellen positiv beeinflusst, sondern auch deren Apoptose inhibiert, was ebenfalls NO-abhängig ist (Lukosz et al. 2011). Somit nimmt GRHL3 eine zentrale Rolle in der Funktionalität von Endothelzellen ein.

Beim Menschen gibt es neben dem als Isoform 2 bezeichneten direkten Homolog zu dem Mausprotein zwei weitere Isoformen von GRHL3. Die zugehörigen Transkripte entstehen durch Nutzung eines alternativen ersten Exons, das im Mausgenom nicht vorhanden ist, und alternatives Splicing dieser prä-mRNA; alle anderen Exons sind bei den drei Isoformen identisch (Ting et al. 2003). Aus der Translation der beiden reifen mRNA-Moleküle mit dem alternativen Exon 1 entsteht mit Isoform 1 ein Protein, das bis auf wenige Aminosäuren am N-Terminus identisch zu Isoform 2 ist, und mit Isoform 3 ein N-terminal verkürztes Protein. Unsere Arbeitsgruppe konnte zeigen, dass alle GRHL3-Isoformen in primären menschlichen Endothelzellen exprimiert werden, wo die Isoformen 1 und 2 pro-migratorisch und anti-apoptotisch wirken, wohingegen die verkürzte Isoform 3 gegenteilige Effekte hat (Guardiola-Serrano et al. 2008; Lukosz et al. 2011; Haendeler et al. 2013).

Alle bisher beschriebenen Untersuchungen waren *ex vivo* in Primärkulturen humaner Endothelzellen durchgeführt worden. Um zu untersuchen, in welchen Zelltypen der Gefäßwand GRHL3 *in vivo* vorkommt, haben wir Immunfluoreszenzfärbungen an *en face* Präparationen aus verschiedenen Gefäßbetten der Maus durchgeführt. Da in Mäusen wie bereits erwähnt nur Isoform 2 vorkommt, konnten wir mit eindeutigen Ergebnissen rechnen, auch wenn der Antikörper alle 3 menschlichen Isoformen erkennt. Mit diesen ersten Untersuchungen zur Lokalisierung von GRHL3 *in vivo* konnten wir zeigen, dass sich GRHL3 nur im Endothel, nicht jedoch in den glatten Muskelzellen befindet. Wesentlich interessanter noch war der Befund, dass sowohl in der thorakalen Aorta, als auch in Mesenterialarterien ein großer Anteil von GRHL3 außerhalb des Zellkerns lokalisiert ist, vor allem in sogenannten myoendothelialen Projektionen (MEPs) (Abb. 6) (Jander*, **Greulich***, Gonnissen* et al. 2021). MEPs sind Ausstülpungen von Endothelzellen, welche durch Aussparungen in der internen elastischen Lamina (IEL) physischen Kontakt zu den glatten Muskelzellen in Gefäßen herstellen. Dadurch stellen MEPs eine Mikrodomäne für zahlreiche Signalprozesse dar, indem dort wichtige Komponenten für Signalwege der Zellen konzentriert und organisiert werden.

Somit kann unter anderem der Austausch wichtiger Signalmoleküle stattfinden, etwa zur Regulation des Gefäßtonus (Kerr et al. 2012; Straub et al. 2014).

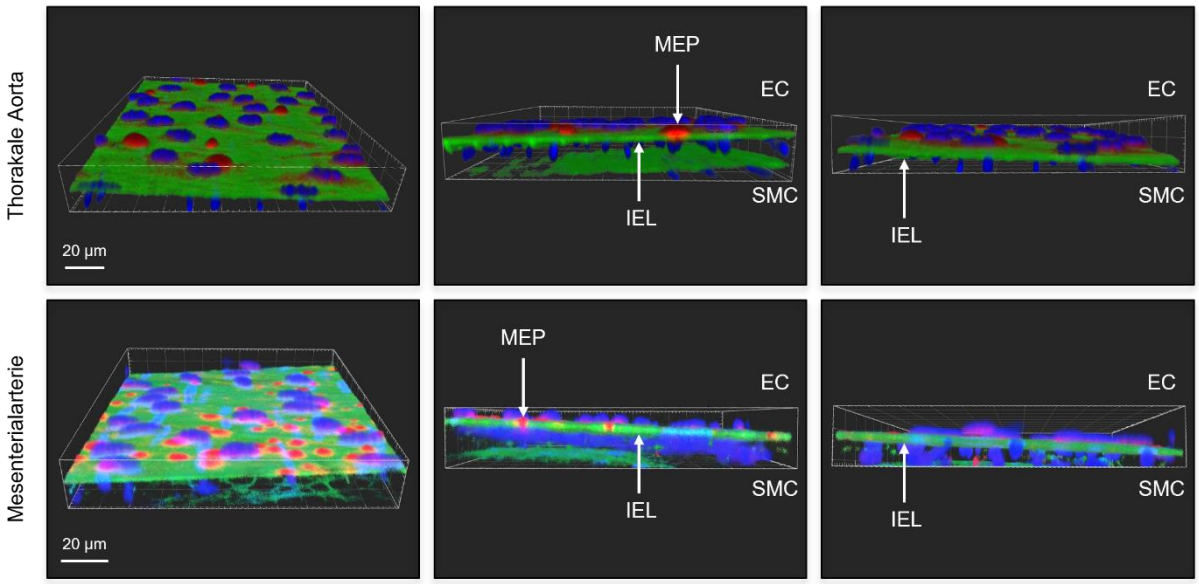

Abbildung 6: Lokalisierung des Transkriptionsfaktors Grainyhead-like 3 (GRHL3) in der Gefäßwand der thorakalen Aorta und von Mesenterialarterien der Maus. Gezeigt sind dreidimensionale Rekonstruktionen von Immunfluoreszenzfärbungen von *en face* Präparationen der thorakalen Aorta und einer Mesenterialarterie. Die Endothelzellschicht (*endothelial cells*, EC, oben) ist von der glatten Muskelzellschicht (*smooth muscle cells*, SMC, unten) durch die aufgrund von Autofluoreszenz grün erscheinende interne elastische Lamina (IEL) getrennt. In den mittleren Feldern sind die myoendothelialen Projektionen (MEP) durch Pfeile gekennzeichnet. Die rote Färbung steht für GRHL3, die blaue Färbung zeigt die mit DAPI gefärbten Zellkerne.

Die Lokalisation in MEPs legte nahe, dass GRHL3 neben seinen kanonischen Funktionen als Transkriptionsfaktor im Zellkern auch extranukleäre Funktionen besitzt.

Um diese möglichen extranukleären Funktionen zu untersuchen, haben wir zunächst das Kernlokalisierungssignal (*nuclear localization signal*, NLS) mittels Generierung mehrerer Deletionsmutanten der Isoform 2 basierend auf beschriebenen funktionellen Domänen (Ting et al. 2003) und einem mit dem Programm cNLS Mapper (Kosugi et al. 2009) vorhergesagten Kernlokalisierungssignal identifiziert. Dabei wurde als erster Indikator für die Lokalisierung im Zellkern die transkriptionelle Aktivität der einzelnen Deletionsvarianten mithilfe eines GRHL3-spezifischen Luciferase Reporter-Assays (Lukosz et al. 2011) herangezogen. Hierbei zeigte sich, dass schon die Deletion des nur 31 Aminosäure großen zweiteiligen Kernlokalisierungssignals (*bipartite* NLS) im C-Terminus die Translokation in den Zellkern verhindert, was dann durch Zellfraktionierung bestätigt wurde (Jander*, **Greulich***, Gonnissen* et al. 2021).

Nach erfolgreicher Beschreibung des NLS konnten wir zeigen, dass nicht nur das komplette GRHL3 Protein, sondern auch die strikt extranukleäre Variante ΔbiNLS, der das Kernlokalisierungssignal fehlt, die Funktionalität von humanen Endothelzellen verbessert, was sich an verschiedenen Parametern nachweisen ließ. So reduziert extranukleäres GRHL3 die Apoptose von Endothelzellen. Dies wurde anhand der verringerten proteolytischen Spaltung

der Pro-Caspase-3 zur aktiven Caspase-3, einer Effektorcaspase der Apoptose, gezeigt. Zudem erhöht extranukleäres GHRL3 die Fähigkeit zur Migration der Zellen, was mittels eines *Scratch-Wound*-Assays und eines Boyden-Kammer-Assays nachgewiesen wurde. Außerdem erhöht es die aktivierende Phosphorylierung von eNOS und die NO-Bioverfügbarkeit (Abb. 7) (Jander*, **Greulich***, Gonnissen* et al. 2021).

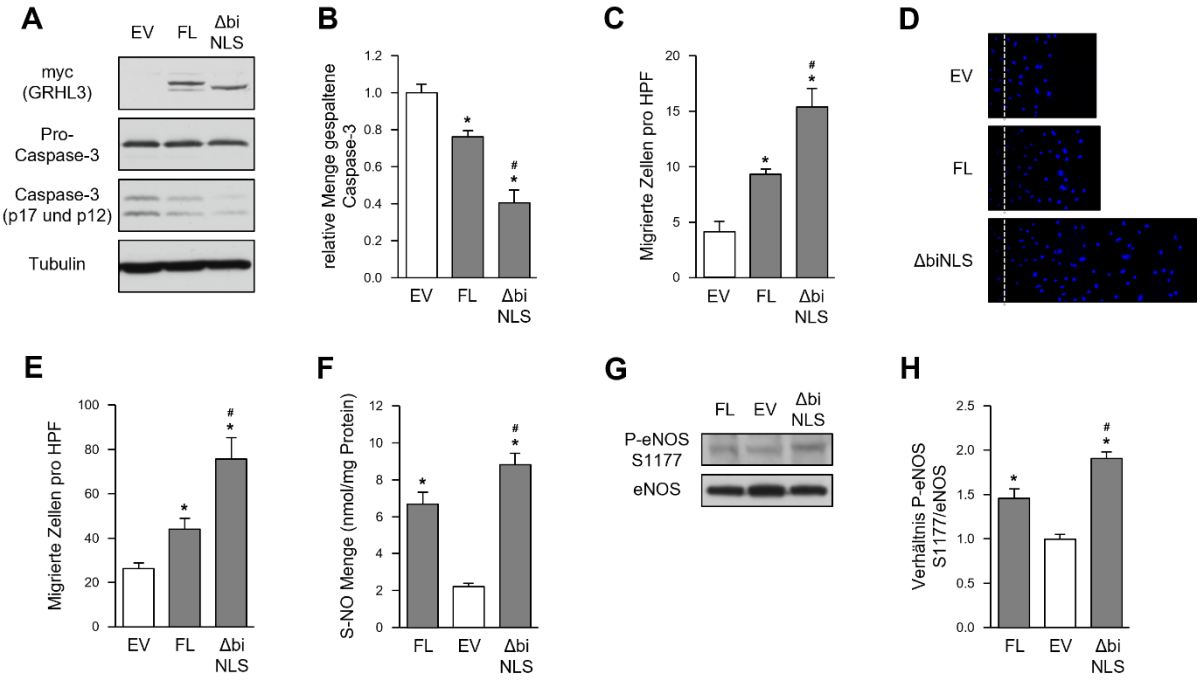

Abbildung 7: Auswirkungen von GRHL3 und extranukleärem GRHL3 auf Endothellzellapoptose, -migration, und NO-Bioverfügbarkeit. (**A-H**) Primäre humane Endothelzellen wurden mit einem Leervektor (*empty vector*, EV), oder Expressionsvektoren für das komplette GRHL3 Protein (*full length*, FL) bzw. die Variante, der das zweiteilige Kernlokalisierungssignal fehlt (ΔbiNLS), transfiziert. (**A, B**) Nachweis der Prozessierung von Pro-Caspase 3 mittels Immunoblot. (**A**) Repräsentativer Immunoblot. myc bezeichnet GRHL3 FL und GRHL3 ΔbiNLS, Pro-Caspase-3 steht für die unprozessierte Pro-Caspase 3, Caspase-3 (p17 und p12) für deren Spaltprodukte, die die aktive Caspase bilden, Tubulin diente als Ladekontrolle. (**B**) Semiquantitative Analyse der relativen Menge an gespaltener Caspase-3 (Daten sind Mittelwerte ± SEM, n = 6, *p< 0,05 vs. EV, #p< 0,05 vs. FL). (**C)** Die Migrationsfähigkeit wurde in einem Boyden-Kammer-Assay gemessen. Die Anzahl der migrierten Zellen pro *high-power-field* (HPF) wurde nach Anfärbung der Zellkerne mit DAPI mit Image J bestimmt (Daten sind Mittelwerte ± SEM, n = 5, *p< 0,05 vs. EV, #p< 0,05 vs. FL). (**D, E**) Die Migrationsfähigkeit wurde in einem *Scratch-Wound*-Assay gemessen, die Zellkerne wurden mit DAPI gefärbt. (**D**) Repräsentative fluoreszenzmikroskopische Aufnahmen. Die Wunden wurden an den gestrichelten Linien gesetzt; links der Linien sind die unverletzten Bereiche. Die Bereiche rechts von den Linien zeigen die Wunden mit den Zellen, die in sie eingewandert sind. (**E**) Image J-Analysen der migrierten Zellen pro *high-power-field* (HPF) (Daten sind Mittelwerte ± SEM, n = 5, *p< 0,05 vs. EV, #p< 0,05 vs. FL). (**F**) Der S-NO-Gehalt als Surrogatmarker für die NO-Bioverfügbarkeit wurde mittels eines modifizierten Saville-Griess-Assays gemessen (Daten sind Mittelwerte ± SEM, n = 5, *p< 0,05 vs. EV, #p< 0,05 vs. FL). (**G, H**) Die Phosphorylierung von eNOS an Serin 1177 wurde mittels Immunoblot gemessen. (**G**) Repräsentativer Immunoblot. Oben: Nachweis von an Serin 1177 phosphorylierter eNOS; unten: Nachweis von Gesamt-eNOS. (**H**) Semiquantitative Analyse des Verhältnisses von an Serin 1177 phosphorylierter eNOS zu Gesamt-eNOS (Daten sind Mittelwerte ± SEM, n = 5, *p< 0,05 vs. EV, #p< 0,05 vs. FL).

Hierbei fällt auf, dass die extranukleäre Form von GRHL3 in allen betrachteten Aspekten die Endothelzellfunktionalität in noch höherem Maße als das vollständige GRHL3-Protein verbessert. Dies ist höchstwahrscheinlich darauf zurückzuführen, dass bei der Expression von nativem GRHL3 nur ein geringer Anteil nicht in den Zellkern importiert wird, wohingegen im Fall der Variante ΔbiNLS das gesamte Protein extranukleär vorliegt. Zudem legt dies die

Vermutung nahe, dass diese Effekte auch bei endogenem GRHL3 von der außerhalb des Zellkerns lokalisierten Fraktion des Proteins vermittelt werden.

Interessanterweise wurde auch bereits gezeigt, dass sich ein Teil der zellulären eNOS, insbesondere der aktiven phosphorylierten Form, ebenfalls in MEPs befindet und als Quelle der NO-Produktion und somit etwa der heterozellulären Kommunikation und Regulation des Gefäßtonus dient (Straub et al. 2011; Straub et al. 2012; Straub et al. 2014). Wir konnten zudem zeigen, dass GRHL3, insbesondere das extranukleär lokalisierte Protein, die Interaktion zwischen Akt1 und eNOS verstärkt (Jander*, **Greulich***, Gonnissen* et al. 2021). Aufgrund der gemeinsamen Lokalisation in den MEPs vermuteten wir, dass es dort zu einer Interaktion zwischen GRHL3 und eNOS in einem möglicherweise größeren Komplex, der die Aktivierung von eNOS durch Akt1-vermittelte Phosphorylierung begünstigt, kommen könnte.

Tatsächlich konnten wir mittels eines *Proximity Ligation*-Assays (PLA) zeigen, dass GRHL3 mit eNOS *ex vivo* außerhalb des Zellkerns interagiert (Abb. 8) (Jander*, **Greulich***, Gonnissen* et al. 2021).

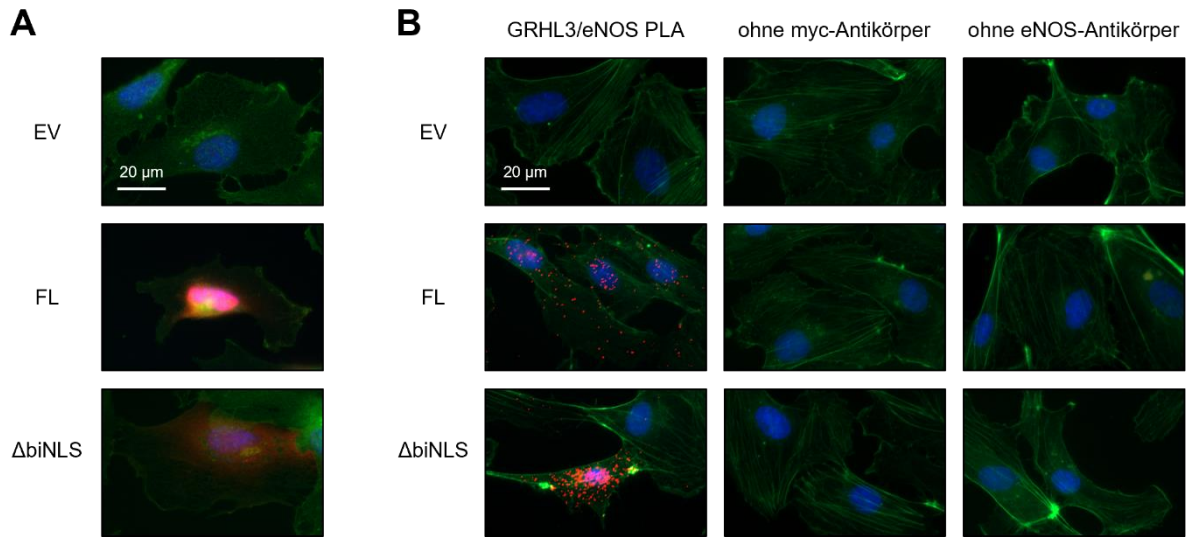

Abbildung 8: GRHL3-/eNOS-Interaktion in primären humanen Endothelzellen. (**A,B**) Primäre humane Endothelzellen wurden mit einem Leervektor (*empty vector*, EV), oder Expressionsvektoren für das komplette GRHL3 Protein (*full length*, FL) bzw. die Variante, der das zweiteilige Kernlokalisierungssignal fehlt (ΔbiNLS), transfiziert. (**A**) Repräsentative Co-Immunfluoreszenzfärbungen. Die Färbungen wurden mit einem myc-tag-Antikörper zur Detektion der überexprimierten GRHL3 Proteine (rot) und einem eNOS-Antikörper (grün) durchgeführt, die Zellkerne wurden mit DAPI (blau) gefärbt. Gezeigt sind die Überlagerungen aller Fluoreszenzkanäle. (**B**) Der *Proximity Ligation*-Assay (PLA) wurde mit Antikörpern gegen das myc-tag und eNOS durchgeführt (GRHL3/eNOS PLA, linkes Feld). Als Negativkontrollen wurden PLAs durchgeführt, bei denen entweder der myc-Antikörper (mittlere Felder) oder der eNOS-Antikörper (rechte Felder) weggelassen wurde. Die roten Punkte stellen eNOS- und GRHL3-Interaktionen dar. Das Aktin-Zytoskelett wurde mit Phalloidin (grün) und die Zellkerne mit DAPI (blau) gefärbt. Gezeigt sind die Überlagerungen aller Fluoreszenzkanäle.

Wie bereits bei den Funktionsparametern von Endothelzellen beschrieben, war der Effekt mit der extranukleären GRHL3-Variante aus den dort aufgeführten Gründen wesentlich drastischer als mit dem kompletten Protein. Da Interaktionen mit eNOS aber auch mit diesem nachweisbar waren, führt dies wiederum zu dem Schluss, dass der nicht im Kern lokalisierte Anteil des endogenen GRHL3 Proteins mit eNOS interagieren kann. Tatsächlich konnten wir

die GRHL3/eNOS Interaktion mittels PLA auch in den Gefäßwänden der thorakalen Aorta und der Mesenterialarterien der Maus nachweisen (Jander*, **Greulich***, Gonnissen* et al. 2021).

Wir zeigen hier zum ersten Mal, dass der Transkriptionsfaktors GRHL3 in der Blutgefäßwand ausschließlich im Endothel vorhanden ist, und dort nicht nur im Zellkern. Seine Funktionen außerhalb des Zellkerns werden durch die Lokalisation in MEPs, die Interaktion mit eNOS und Steigerung ihrer Aktivität sowie durch die anti-apoptotische und pro-migratorische Wirkung einer extranukleären GRHL3-Variante belegt. Somit trägt nicht nur die an den Zellkern gebundene transkriptionelle Aktivität von GRHL3 (Lukosz et al. 2011), sondern auch seine Funktion außerhalb des Zellkerns zu einer verbesserten Funktionalität von Endothelzellen bei (Abb. 9) (Jander*, **Greulich***, Gonnissen* et al. 2021).

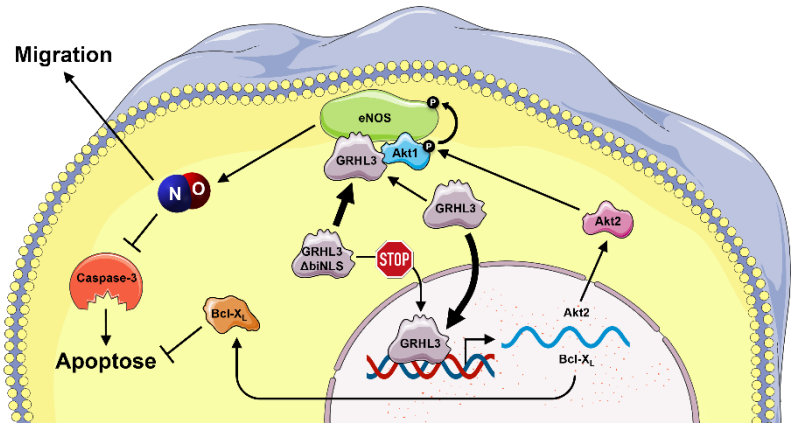

Abbildung 9: Nukleäre und extranukleäre Funktionen von GRHL3 verbessern die Endothelzellfunktionalität. Außerhalb des Zellkerns interagiert GRHL3 mit eNOS. Dies verstärkt die Akt1/eNOS Interaktion und die Aktivierung von eNOS über Phosphorylierung an Serin 1177. Die dadurch erhöhte NO-Bioverfügbarkeit resultiert in gesteigerter Migrationsfähigkeit und verringerter Apoptose. Diese Effekte sind bei ausschließlich extranukleärem GRHL3 noch verstärkt. Im Zellkern induziert GRHL3 als Transkriptionsfaktor unter anderem die Expression des anti-apoptotischen Proteins Bcl-X_L und die der Proteinkinase Akt2, welche wiederum Akt1 durch Phosphorylierung aktiviert und damit auch zur gesteigerten eNOS-Aktivität beiträgt.

Ausblick

Im Rahmen dieser Doktorarbeit wurden extrinsische und intrinsische Faktoren, die sich direkt oder indirekt auf die Funktionalität des Endothels auswirken, untersucht. In der zuerst vorgestellten Publikation konnten wir zeigen, dass die hepatische Expression von scFv-E06 bei einer FPC-Fütterung von Mäusen die oxPC-Konzentrationen im Plasma senkt, und das Entstehen einer Lebersteatose bzw. das Fortschreiten der Fibrose verhindert (Upchurch, … **Greulich** et al. 2022). Oxidierte Lipide haben ebenfalls negative Auswirkungen auf das Endothel. Daher bietet sich das hier gezeigte Modell für zukünftige Untersuchungen an, wie sich eine FPC-Fütterung auf Endothelfunktionen auswirkt und ob scFv-E06 in der Lage ist, das Endothel gegenüber diesen Einflüssen zu schützen. Hierzu könnte man die Aktivierung des Endothels infolge dieser Fütterung mittels histologischer Schnitte betrachten oder etwa *in vivo* Messungen von Endothel-abhängiger Vasodilatation durchführen (Schuler et al. 2014).

In einer zweiten Publikation haben wir nachgewiesen, dass mitochondriale TERT die Aktivität von Komplex I der Atmungskette in Mausherzmitochondrien verbessert und mechanistische Grundlagen bezüglich der Stöchiometrie der Komplexuntereinheiten aufgeklärt. Zudem konnten wir zeigen, dass mitochondriale TERT den Schaden nach einem experimentellen Herzinfarkt sowohl strukturell als auch funktionell verringert. Ein pharmakologischer Ansatz mit TA-65 zeigte, dass dieser Telomeraseaktivator *ex vivo* die mitochondrialen TERT-Level erhöht und sowohl Endothelzellmigration als auch Myofibroblasten-Differenzierung verbessert (Ale-Agha, … **Greulich** et al. 2021). Insofern wäre es in Zukunft interessant, TA-65 *in vivo* einzusetzen und die Auswirkungen auf Endothelfunktionen generell, wie z.B. zuvor beschrieben, sowie auch im Myokardinfarkt, etwa anhand der Revaskularisierung, zu untersuchen.

Im Kontext von Entzündungsprozessen, die auch immer das Endothel betreffen, haben wir gezeigt, dass ein ACC-*knockout* in myeloischen Zellen die LPS-induzierte Makrophagenaktivierung durch eine Veränderung des zellulären Glukose- und Lipidstoffwechsels reduziert. Dies hatte eine gestörte Makrophagenfunktion und verringerte Sekretion von inflammatorischen Zytokinen zur Folge (Yeudall, … **Greulich** et al. 2022). In diesem Zusammenhang stellt sich die Frage, inwieweit sich die Funktionseinschränkung der Makrophagen evtl. auch auf die Aktivierung von Endothelzellen auswirkt, was man *in vivo* in dem ACC-*knockout* Mausmodell untersuchen könnte.

In einer weiteren Veröffentlichung haben wir intrinsische LPS-induzierte Veränderungen in primären humanen Endothelzellen und die schützende Rolle von APEX1(1-20) auf Transkriptomebene untersucht. Dabei haben wir SELENOT als einen protektiven Faktor identifiziert, dessen Expression nach LPS-Gabe abhängig von APEX1(1-20) hochreguliert wird. In der Folge haben wir gezeigt, dass SELNEOT vor LPS-induzierter Endothelzellaktivierung und -apoptose schützt (Merk, … **Greulich** et al. 2021). Diese Daten deuten darauf hin, dass basierend auf APEX1(1-20) und SELENOT therapeutische Optionen für die adjuvante Behandlung von Sepsis entwickelt werden könnten, um das Endothel zu schützen und seine Barrierefunktion aufrecht zu erhalten. Dies wäre von großem Nutzen für die Patienten und könnte die Zahl der Fälle von septischem Schock, multiplem Organversagen und Todesfällen verringern, weshalb in Zukunft die Effektivität noch kleinerer Peptide untersucht werden sollte, um gegebenenfalls niedermolekulare Wirkstoffe basierend auf deren Struktur zu entwerfen. Alternativ könnte man APEX1(1-20) mit einem sogenannten *cell-penetrating peptide* (CPP) fusionieren und dieses direkt als Wirkstoff nutzen (Dinca et al. 2016). Dafür muss aber zunächst untersucht werden, ob ein CPP nicht mit der Funktion von APEX1(1-20) interferiert, was man zunächst in Endothelzellen testen kann. Alternativ könnte man Wege suchen, die SELENOT-Menge in Endothelzellen zu erhöhen, etwa durch die Supplementation mit Selen, was in verschiedenen Modellen bereits Erfolg gezeigt hat. So führte eine Selengabe zur Hochregulation von Selenoproteinen in einer Makrophagen-Zelllinie (Wang et al. 2018) bzw. zum Schutz vor LPS-induzierter myokardialer Dysfunktion in Mäusen (Wang et al. 2021).

Neben den Untersuchungen, wie man den negativen Auswirkungen hoher LPS-Konzentrationen auf das Endothel, wie man sie bei Sepsis findet, entgegenwirken kann, konnten wir auch erstmals nachweisen, dass geringe Dosen LPS, die beispielsweise bei schlechter Ernährung und der damit verbundenen metabolischen Endotoxämie vorzufinden sind, Endotheldysfunktion hervorrufen, indem sie Endothelzellseneszenz induzieren. In diesem Kontext haben wir gezeigt, dass Koffein die Seneszenzinduktion durch LPS hemmt und darüber hinaus selbst bei therapeutischer Verabreichung, d.h. nach der Seneszenzinduktion durch LPS, zur Reversion des seneszenten Phänotyps führt (Merk*, **Greulich*** et al. 2023). Die Koffeinwirkung wird auch im Seneszenzmodell über die mitochondriale Translokation von p27 vermittelt, allerdings ist der zugrunde liegende molekulare Mechanismus noch nicht bekannt. Dessen Aufklärung könnte möglicherweise neue Ansatzpunkte zu einer gezielten Intervention liefern, mit der man der Seneszenzinduktion vorbeugen oder dieser entgegenwirken kann.

Schlussendlich konnte im Rahmen dieser Arbeit ein Zell-intrinsischer Mechanismus aufgeklärt werden, der relevant für die Funktionalität von Endothelzellen ist. Nach dem Nachweis, dass der Transkriptionsfaktor GRHL3, der Endothelzellfunktionen verbessert (Lukosz et al. 2011; Haendeler et al. 2013), *in vivo* in MEPs lokalisiert ist, konnten wir der extranukleär lokalisierten Fraktion dieses Proteins Funktionen zuweisen, welche die Endothelzellfunktionalität verbessern. Diese beruhen höchstwahrscheinlich auf der Interaktion mit eNOS und der damit verbundenen Aktivierung dieses Enzyms (Jander*, **Greulich***, Gonnissen* et al. 2021). Die zugrunde liegenden Mechanismen werden Gegenstand zukünftiger Untersuchungen sein. Dabei soll auch die Regulation der Verteilung von GRHL3 zwischen Zellkern und MEPs untersucht werden, um daraus mögliche therapeutische Optionen zur Verbesserung der Endothelfunktionalität ableiten zu können.

Zusammenfassung

Kardiovaskuläre Erkrankungen sind weltweit die häufigste Todesursache. Eine ihrer wichtigsten Ursachen ist die endotheliale Dysfunktion. Sowohl extrinsische als auch intrinsische Faktoren können einen Einfluss auf die Funktionalität des Endothels haben.

Ziel dieser Arbeit war es, verschiedene dieser extrinsischen und intrinsischen Faktoren zu untersuchen, um langfristig sowohl präventive als auch therapeutische Strategien zur Verbesserung oder Aufrechterhaltung der Funktionalität des Endothels zu entwickeln. Zu den Faktoren, die das Endothel negativ beeinflussen, gehören oxidierte Lipide. In Publikation I (Upchurch, … **Greulich** et al. 2022) konnten wir zunächst im Kontext der Leber zeigen, dass die hepatische Expression eines Antikörperfragments die oxPC-Konzentration im Plasma senkt und das Entstehen einer Lebersteatose bzw. das Fortschreiten der Fibrose verhindert. Da oxPCs auch Mitochondrienfunktionen verschlechtern, haben wir in Publikation II (Ale-Agha, … **Greulich** et al. 2021) untersucht wie sich die Verbesserung der Aktivität von Komplex I der Atmungskette durch mitochondriale TERT auswirkt und die mechanistischen Grundlagen aufgeklärt. Wir konnten nachweisen, dass mitochondriale TERT den Schaden nach einem experimentellen Herzinfarkt verringert sowie dass der Telomeraseaktivator TA-65 die mitochondrialen TERT-Level erhöht und unter anderem Endothelzellmigration verbessert. Das Endothel als Grenzschicht zum Blutkreislauf ist direkt von Entzündungsreaktionen betroffen. In Publikation III (Yeudall, … **Greulich** et al. 2022) haben wir gezeigt, dass ein ACC-*knockout* in myeloischen Zellen die Makrophagenaktivierung beeinträchtigt, was die Induktion von inflammatorischen Zytokinen abschwächt. Entzündungen lösen auch Reaktionen im Endothel aus. In Publikation IV (Merk, … **Greulich** et al. 2021) haben wir LPS-induzierte Transkriptomveränderungen in Endothelzellen in Abhängigkeit von APEX1(1-20) untersucht und SELENOT als einen Endothel-protektiven Faktor identifiziert. In Publikation V (Merk*, **Greulich*** et al. 2023) konnten wir zeigen, dass wesentlich geringere LPS-Dosen, wie sie etwa bei metabolischer Endotoxämie vorzufinden sind, Endothelzellseneszenz induzieren. Koffein ist in der Lage die Seneszenzinduktion zu verhindern und kann bei therapeutischer Verabreichung sogar den seneszenten Phänotyp revertieren. In Publikation VI (Jander*, **Greulich***, Gonnissen* et al. 2021) haben wir nachgewiesen, dass der Transkriptionsfaktor GRHL3 *in vivo* in MEPs lokalisiert ist. *Ex vivo* konnten wir der extranukleär lokalisierten Fraktion des Proteins Funktionen zuweisen, welche die Endothelzellfunktionalität verbessern, was höchstwahrscheinlich auf einer Interaktion mit eNOS beruht.

Die Ergebnisse dieser Arbeit beleuchten unterschiedliche Facetten extrinsischer und intrinsischer Faktoren in der Endothelfunktionalität und liefern erste mechanistische Grundlagen zur Entwicklung neuer therapeutischer Ansatzpunkte zur Verbesserung oder zum Erhalt der Endothelfunktion.

Summary

Cardiovascular diseases are the most common cause of death worldwide. One of its most important determinants is endothelial dysfunction. Both extrinsic and intrinsic factors can have an influence on the functionality of the endothelium.

The aim of this work was to investigate several of these extrinsic and intrinsic factors in order to develop both preventive and therapeutic strategies to improve or maintain the functionality of the endothelium in the long term. Factors that negatively affect the endothelium include oxidized lipids. In publication I (Upchurch, ... **Greulich** et al. 2022), we were initially able to show in the context of the liver that hepatic expression of an antibody fragment reduces the oxPC concentration in plasma and prevents the development of hepatic steatosis or the progression of fibrosis. Since oxPCs also impair mitochondrial functions, we investigated in publication II (Ale-Agha, ... **Greulich** et al. 2021) the impact of improved respiratory chain complex I activity conveyed by mitochondrial TERT and elucidated the mechanistic basis. We were able to demonstrate that mitochondrial TERT reduces damage after experimental myocardial infarction and that the telomerase activator TA-65 increases mitochondrial TERT levels and – amongst others – improves endothelial cell migration. The endothelium as the boundary to the circulation is directly affected by inflammatory reactions. In publication III (Yeudall, ... **Greulich** et al. 2022), we have shown that a knockout of ACC in myeloid cells impairs macrophage activation, which attenuates the induction of inflammatory cytokines. Inflammation also triggers reactions in the endothelium itself. In publication IV (Merk, ... **Greulich** et al. 2021), we investigated LPS-induced transcriptome changes in endothelial cells dependent on APEX1(1-20) and identified SELENOT as an endothelium-protective factor. In publication V (Merk*, **Greulich*** et al. 2023), we were able to show that much lower doses of LPS, such as those found in metabolic endotoxemia, induce endothelial cell senescence. Caffeine is able to prevent senescence induction and can even reverse the senescent phenotype when administered therapeutically. In publication VI (Jander*, **Greulich***, Gonnissen* et al. 2021), we demonstrated that the transcription factor GRHL3 is localized in MEPs *in vivo*. *Ex vivo*, we were able to assign functions to the extranuclear localized fraction of the protein that improve endothelial cell functionality, most likely based on an interaction with eNOS.

The results of this work shed light on different facets of extrinsic and intrinsic factors in endothelial functionality and provide first mechanistic bases for the development of new therapeutic targets to improve or maintain endothelial function.

Literaturverzeichnis

Addinsall, A. B., C. R. Wright, S. Andrikopoulos, C. van der Poel, und N. Stupka. 2018. 'Emerging roles of endoplasmic reticulum-resident selenoproteins in the regulation of cellular stress responses and the implications for metabolic disease', *Biochem J*, 475: 1037-57.

Ago, T., T. Kitazono, H. Ooboshi, T. Iyama, Y. H. Han, J. Takada, M. Wakisaka, S. Ibayashi, H. Utsumi, und M. Iida. 2004. 'Nox4 as the major catalytic component of an endothelial NAD(P)H oxidase', *Circulation*, 109: 227-33.

Ahmed, S., J. F. Passos, M. J. Birket, T. Beckmann, S. Brings, H. Peters, M. A. Birch-Machin, T. von Zglinicki, und G. Saretzki. 2008. 'Telomerase does not counteract telomere shortening but protects mitochondrial function under oxidative stress', *J Cell Sci*, 121: 1046-53.

Aidoud, A., W. Gana, F. Poitau, C. Debacq, V. Leroy, J. A. Nkodo, P. Poupin, D. Angoulvant, und B. Fougere. 2023. 'High Prevalence of Geriatric Conditions Among Older Adults With Cardiovascular Disease', *J Am Heart Assoc*, 12: e026850.

Alderton, W. K., C. E. Cooper, und R. G. Knowles. 2001. 'Nitric oxide synthases: structure, function and inhibition', *Biochem J*, 357: 593-615.

Ale-Agha, N., C. Goy, P. Jakobs, I. Spyridopoulos, S. Gonnissen, N. Dyballa-Rukes, K. Aufenvenne, F. von Ameln, M. Zurek, T. Spannbrucker, O. Eckermann, S. Jakob, S. Gorressen, M. Abrams, M. Grandoch, J. W. Fischer, K. Kohrer, R. Deenen, K. Unfried, J. Altschmied, und J. Haendeler. 2018. 'CDKN1B/p27 is localized in mitochondria and improves respiration-dependent processes in the cardiovascular system-New mode of action for caffeine', *PLoS Biol*, 16: e2004408.

Ale-Agha, N., P. Jakobs, C. Goy, M. Zurek, J. Rosen, N. Dyballa-Rukes, S. Metzger, J. Greulich, F. von Ameln, O. Eckermann, K. Unfried, F. Brack, M. Grandoch, M. Thielmann, M. Kamler, N. Gedik, P. Kleinbongard, A. Heinen, G. Heusch, A. Godecke, J. Altschmied, und J. Haendeler. 2021. 'Mitochondrial Telomerase Reverse Transcriptase Protects From Myocardial Ischemia/Reperfusion Injury by Improving Complex I Composition and Function', *Circulation*, 144: 1876-90.

Altschmied, J., und J. Haendeler. 2009. 'Thioredoxin-1 and endothelial cell aging: role in cardiovascular diseases', *Antioxid Redox Signal*, 11: 1733-40.

Ambrogini, E., X. Que, S. Wang, F. Yamaguchi, R. S. Weinstein, S. Tsimikas, S. C. Manolagas, J. L. Witztum, und R. L. Jilka. 2018. 'Oxidation-specific epitopes restrain bone formation', *Nat Commun*, 9: 2193.

Araki, T., und H. Kitaoka. 2001. 'The mechanism of reaction of ebselen with superoxide in aprotic solvents as examined by cyclic voltammetry and ESR', *Chem Pharm Bull (Tokyo)*, 49: 541-5.

Birukov, K. G., und P. Karki. 2018. 'Injured lung endothelium: mechanisms of self-repair and agonist-assisted recovery (2017 Grover Conference Series)', *Pulm Circ*, 8: 2045893217752660.

Bochkov, V. N., A. Kadl, J. Huber, F. Gruber, B. R. Binder, und N. Leitinger. 2002. 'Protective role of phospholipid oxidation products in endotoxin-induced tissue damage', *Nature*, 419: 77-81.

Boraschi, D., P. Italiani, S. Weil, und M. U. Martin. 2018. 'The family of the interleukin-1 receptors', *Immunol Rev*, 281: 197-232.

Borisenko, G. G., T. Matsura, S. X. Liu, V. A. Tyurin, J. Jianfei, F. B. Serinkan, und V. E. Kagan. 2003. 'Macrophage recognition of externalized phosphatidylserine and phagocytosis of apoptotic Jurkat cells--existence of a threshold', *Arch Biochem Biophys*, 413: 41-52.

Bray, S. J., und F. C. Kafatos. 1991. 'Developmental function of Elf-1: an essential transcription factor during embryogenesis in Drosophila', *Genes Dev*, 5: 1672-83.

Brunkhorst, F. M., M. A. Weigand, M. Pletz, P. Gastmeier, S. W. Lemmen, A. Meier-Hellmann, M. Ragaller, A. Weyland, G. Marx, M. Bucher, H. Gerlach, B. Salzberger, B. Grabein, T. Welte, K. Werdan, S. Kluge, H. G. Bone, C. Putensen, R. Rossaint, M. Quintel, C. Spies, B. Weiss, S. John, M. Oppert, A. Jorres, T. Brenner, G. Elke, M. Grundling, K. Mayer, A. Weimann, T. W. Felbinger, H. Axer, T. Heller, N. Gagelmann, und V. Deutsche Sepsis Gesellschaft e. 2020. '[S3 guideline sepsis-prevention, diagnosis, treatment, and aftercare : Summary of the strong recommendations]', *Med Klin Intensivmed Notfmed*, 115: 178-88.

Buchner, N., N. Ale-Agha, S. Jakob, U. Sydlik, K. Kunze, K. Unfried, J. Altschmied, und J. Haendeler. 2013. 'Unhealthy diet and ultrafine carbon black particles induce senescence and disease associated phenotypic changes', *Exp Gerontol*, 48: 8-16.

Caddy, J., T. Wilanowski, C. Darido, S. Dworkin, S. B. Ting, Q. Zhao, G. Rank, A. Auden, S. Srivastava, T. A. Papenfuss, J. N. Murdoch, P. O. Humbert, V. Parekh, N. Boulos, T. Weber, J. Zuo, J. M. Cunningham, und S. M. Jane. 2010. 'Epidermal wound repair is regulated by the planar cell polarity signaling pathway', *Dev Cell*, 19: 138-47.

Campisi, J. 2001. 'Cellular senescence as a tumor-suppressor mechanism', *Trends Cell Biol*, 11: S27-31.

Cani, P. D., M. Osto, L. Geurts, und A. Everard. 2012. 'Involvement of gut microbiota in the development of low-grade inflammation and type 2 diabetes associated with obesity', *Gut Microbes*, 3: 279-88.

Carroll, R. G., Z. Zaslona, S. Galvan-Pena, E. L. Koppe, D. C. Sevin, S. Angiari, M. Triantafilou, K. Triantafilou, L. K. Modis, und L. A. O'Neill. 2018. 'An unexpected link between fatty acid synthase and cholesterol synthesis in proinflammatory macrophage activation', *J Biol Chem*, 293: 5509-21.

Chen, K. H., X. Guo, D. Ma, Y. Guo, Q. Li, D. Yang, P. Li, X. Qiu, S. Wen, R. P. Xiao, und J. Tang. 2004. 'Dysregulation of HSG triggers vascular proliferative disorders', *Nat Cell Biol*, 6: 872-83.

Chen, Z. P., K. I. Mitchelhill, B. J. Michell, D. Stapleton, I. Rodriguez-Crespo, L. A. Witters, D. A. Power, P. R. Ortiz de Montellano, und B. E. Kemp. 1999. 'AMP-activated protein kinase phosphorylation of endothelial NO synthase', *FEBS Lett*, 443: 285-9.

Cheng, G., J. C. Salerno, Z. Cao, P. J. Pagano, und J. D. Lambeth. 2008. 'Identification and characterization of VPO1, a new animal heme-containing peroxidase', *Free Radic Biol Med*, 45: 1682-94.

Chin, L., N. D. Theise, A. E. Loneker, P. A. Janmey, und R. G. Wells. 2020. 'Lipid droplets disrupt mechanosensing in human hepatocytes', *Am J Physiol Gastrointest Liver Physiol*, 319: G11-G22.

Chistiakov, D. A., A. A. Melnichenko, A. V. Grechko, V. A. Myasoedova, und A. N. Orekhov. 2018. 'Potential of anti-inflammatory agents for treatment of atherosclerosis', *Exp Mol Pathol*, 104: 114-24.

Courtois-Cox, S., S. L. Jones, und K. Cichowski. 2008. 'Many roads lead to oncogene-induced senescence', *Oncogene*, 27: 2801-9.

Cyr, A. R., L. V. Huckaby, S. S. Shiva, und B. S. Zuckerbraun. 2020. 'Nitric Oxide and Endothelial Dysfunction', *Crit Care Clin*, 36: 307-21.

Dimmeler, S., I. Fleming, B. Fisslthaler, C. Hermann, R. Busse, und A. M. Zeiher. 1999. 'Activation of nitric oxide synthase in endothelial cells by Akt-dependent phosphorylation', *Nature*, 399: 601-5.

Dinca, A., W. M. Chien, und M. T. Chin. 2016. 'Intracellular Delivery of Proteins with Cell-Penetrating Peptides for Therapeutic Uses in Human Disease', *Int J Mol Sci*, 17: 263.

Dudzinski, D. M., J. Igarashi, D. Greif, und T. Michel. 2006. 'The regulation and pharmacology of endothelial nitric oxide synthase', *Annu Rev Pharmacol Toxicol*, 46: 235-76.

Dyballa-Rukes, N., P. Jakobs, A. Eckers, N. Ale-Agha, V. Serbulea, K. Aufenvenne, T. C. Zschauer, L. L. Rabanter, S. Jakob, F. von Ameln, O. Eckermann, N. Leitinger, C. Goy, J. Altschmied, und J. Haendeler. 2017. 'The Anti-Apoptotic Properties of APEX1 in the Endothelium Require the First 20 Amino Acids and Converge on Thioredoxin-1', *Antioxid Redox Signal*, 26: 616-29.

Ehara, S., M. Ueda, T. Naruko, K. Haze, A. Itoh, M. Otsuka, R. Komatsu, T. Matsuo, H. Itabe, T. Takano, Y. Tsukamoto, M. Yoshiyama, K. Takeuchi, J. Yoshikawa, und A. E. Becker. 2001. 'Elevated levels of oxidized low density lipoprotein show a positive relationship with the severity of acute coronary syndromes', *Circulation*, 103: 1955-60.

Eitan, E., A. Tichon, G. Daniel, und E. Priel. 2012. 'Telomerase expression in adult and old mouse Purkinje neurons', *Rejuvenation Res*, 15: 206-9.

Endo, Y., A. Onodera, K. Obata-Ninomiya, R. Koyama-Nasu, H. K. Asou, T. Ito, T. Yamamoto, T. Kanno, T. Nakajima, K. Ishiwata, H. Kanuka, D. J. Tumes, und T. Nakayama. 2019. 'ACC1 determines memory potential of individual CD4(+) T cells by regulating de novo fatty acid biosynthesis', *Nat Metab*, 1: 261-75.

Fleischmann-Struzek, C., D. Schwarzkopf, und K. Reinhart. 2022. 'Inzidenz der Sepsis in Deutschland und weltweit', *Medizinische Klinik - Intensivmedizin und Notfallmedizin*, 117: 264-68.

Fleming, I., und R. Busse. 1999. 'Signal transduction of eNOS activation', *Cardiovasc Res*, 43: 532-41.

Förstermann, Ulrich, und Thomas Münzel. 2006. 'Endothelial Nitric Oxide Synthase in Vascular Disease', *Circulation*, 113: 1708-14.

Forsyth, N. R., W. E. Wright, und J. W. Shay. 2002. 'Telomerase and differentiation in multicellular organisms: turn it off, turn it on, and turn it off again', *Differentiation*, 69: 188-97.

Fu, X., H. Khalil, O. Kanisicak, J. G. Boyer, R. J. Vagnozzi, B. D. Maliken, M. A. Sargent, V. Prasad, I. Valiente-Alandi, B. C. Blaxall, und J. D. Molkentin. 2018. 'Specialized fibroblast differentiated states underlie scar formation in the infarcted mouse heart', *J Clin Invest*, 128: 2127-43.

Galanos, P., K. Vougas, D. Walter, A. Polyzos, A. Maya-Mendoza, E. J. Haagensen, A. Kokkalis, F. M. Roumelioti, S. Gagos, M. Tzetis, B. Canovas, A. Igea, A. K. Ahuja, R. Zellweger, S. Havaki, E. Kanavakis, D. Kletsas, I. B. Roninson, S. D. Garbis, M. Lopes, A. Nebreda, D. Thanos, J. J. Blow, P. Townsend, C. S. Sorensen, J. Bartek, und V. G. Gorgoulis. 2016. 'Chronic p53-independent p21 expression causes genomic instability by deregulating replication licensing', *Nat Cell Biol*, 18: 777-89.

Gluchowski, N. L., M. Becuwe, T. C. Walther, und R. V. Farese, Jr. 2017. 'Lipid droplets and liver disease: from basic biology to clinical implications', *Nat Rev Gastroenterol Hepatol*, 14: 343-55.

Gonnissen, S., J. Ptok, C. Goy, K. Jander, P. Jakobs, O. Eckermann, W. Kaisers, F. von Ameln, J. Timm, N. Ale-Agha, J. Haendeler, H. Schaal, und J. Altschmied. 2019. 'High Concentration of Low-Density Lipoprotein Results in Disturbances in Mitochondrial Transcription and Functionality in Endothelial Cells', *Oxid Med Cell Longev*, 2019: 7976382.

Goy, C., P. Czypiorski, J. Altschmied, S. Jakob, L. L. Rabanter, A. C. Brewer, N. Ale-Agha, N. Dyballa-Rukes, A. M. Shah, und J. Haendeler. 2014. 'The imbalanced redox status in senescent endothelial cells is due to dysregulated Thioredoxin-1 and NADPH oxidase 4', *Exp Gerontol*, 56: 45-52.

Guardiola-Serrano, F., J. Haendeler, M. Lukosz, K. Sturm, Hv Melchner, und J. Altschmied. 2008. 'Gene trapping identifies a putative tumor suppressor and a new inducer of cell migration', *Biochem Biophys Res Commun*, 376: 748-52.

Haendeler, J. 2006. 'Thioredoxin-1 and posttranslational modifications', *Antioxid Redox Signal*, 8: 1723-8.

Haendeler, J., S. Drose, N. Buchner, S. Jakob, J. Altschmied, C. Goy, I. Spyridopoulos, A. M. Zeiher, U. Brandt, und S. Dimmeler. 2009. 'Mitochondrial telomerase reverse transcriptase binds to and protects mitochondrial DNA and function from damage', *Arterioscler Thromb Vasc Biol*, 29: 929-35.

Haendeler, J., J. Hoffmann, J. F. Diehl, M. Vasa, I. Spyridopoulos, A. M. Zeiher, und S. Dimmeler. 2004. 'Antioxidants inhibit nuclear export of telomerase reverse transcriptase and delay replicative senescence of endothelial cells', *Circ Res*, 94: 768-75.

Haendeler, J., A. Mlynek, N. Buchner, M. Lukosz, M. Graf, C. Guettler, S. Jakob, S. Farrokh, K. Kunze, C. Goy, F. Guardiola-Serrano, H. Schaal, M. Cortese-Krott, R. Deenen, K. Kohrer, C. Winkler, und J. Altschmied. 2013. 'Two isoforms of Sister-Of-Mammalian Grainyhead have opposing functions in endothelial cells and in vivo', *Arterioscler Thromb Vasc Biol*, 33: 1639-46.

Haendeler, J., R. Popp, C. Goy, V. Tischler, A. M. Zeiher, und S. Dimmeler. 2005. 'Cathepsin D and H2O2 stimulate degradation of thioredoxin-1: implication for endothelial cell apoptosis', *J Biol Chem*, 280: 42945-51.

Haendeler, Judith, Arne Mlynek, Nicole Büchner, Margarete Lukosz, Martin Graf, Christopher Guettler, Sascha Jakob, Sabrina Farrokh, Kerstin Kunze, Christine Goy, Francisca

Guardiola-Serrano, Heiner Schaal, Miriam Cortese-Krott, René Deenen, Karl Köhrer, Christoph Winkler, und Joachim Altschmied. 2013. 'Two Isoforms of Sister-of-Mammalian Grainyhead Have Opposing Functions in Endothelial Cells and In Vivo', *Arteriosclerosis, Thrombosis, and Vascular Biology*, 33: 1639-46.

Hafiane, A. 2019. 'Vulnerable Plaque, Characteristics, Detection, and Potential Therapies', *J Cardiovasc Dev Dis*, 6.

Harley, C. B., A. B. Futcher, und C. W. Greider. 1990. 'Telomeres shorten during ageing of human fibroblasts', *Nature*, 345: 458-60.

Hayflick, L. 1965. 'The Limited in Vitro Lifetime of Human Diploid Cell Strains', *Exp Cell Res*, 37: 614-36.

Heusch, G. 2015. 'Molecular basis of cardioprotection: signal transduction in ischemic pre-, post-, and remote conditioning', *Circ Res*, 116: 674-99.

Ho, Jeffery, Hung Chan, Sunny H. Wong, Maggie H. T. Wang, Jun Yu, Zhangang Xiao, Xiaodong Liu, Gordon Choi, Czarina C. H. Leung, Wai T. Wong, Zheng Li, Tony Gin, Matthew T. V. Chan, und William K. K. Wu. 2016. 'The involvement of regulatory non-coding RNAs in sepsis: a systematic review', *Critical Care*, 20.

Horkko, S., D. A. Bird, E. Miller, H. Itabe, N. Leitinger, G. Subbanagounder, J. A. Berliner, P. Friedman, E. A. Dennis, L. K. Curtiss, W. Palinski, und J. L. Witztum. 1999. 'Monoclonal autoantibodies specific for oxidized phospholipids or oxidized phospholipid-protein adducts inhibit macrophage uptake of oxidized low-density lipoproteins', *J Clin Invest*, 103: 117-28.

Imai, Y., K. Kuba, G. G. Neely, R. Yaghubian-Malhami, T. Perkmann, G. van Loo, M. Ermolaeva, R. Veldhuizen, Y. H. Leung, H. Wang, H. Liu, Y. Sun, M. Pasparakis, M. Kopf, C. Mech, S. Bavari, J. S. Peiris, A. S. Slutsky, S. Akira, M. Hultqvist, R. Holmdahl, J. Nicholls, C. Jiang, C. J. Binder, und J. M. Penninger. 2008. 'Identification of oxidative stress and Toll-like receptor 4 signaling as a key pathway of acute lung injury', *Cell*, 133: 235-49.

Itabe, H. 2003. 'Oxidized low-density lipoproteins: What is understood and what remains to be clarified', *Biological & Pharmaceutical Bulletin*, 26: 1-9.

Itabe, H., und M. Ueda. 2007. 'Measurement of plasma oxidized low-density lipoprotein and its clinical implications', *Journal of Atherosclerosis and Thrombosis*, 14: 1-11.

Jander, K., J. Greulich, S. Gonnissen, N. Ale-Agha, C. Goy, P. Jakobs, S. Farrokh, C. Marziano, S. K. Sonkusare, J. Haendeler, und J. Altschmied. 2021. 'Extra-Nuclear Functions of the Transcription Factor Grainyhead-Like 3 in the Endothelium-Interaction with Endothelial Nitric Oxide Synthase', *Antioxidants (Basel)*, 10.

Joffre, J., J. Hellman, C. Ince, und H. Ait-Oufella. 2020. 'Endothelial Responses in Sepsis', *Am J Respir Crit Care Med*, 202: 361-70.

Kadl, A., E. Galkina, und N. Leitinger. 2009. 'Induction of CCR2-dependent macrophage accumulation by oxidized phospholipids in the air-pouch model of inflammation', *Arthritis Rheum*, 60: 1362-71.

Kadl, A., A. K. Meher, P. R. Sharma, M. Y. Lee, A. C. Doran, S. R. Johnstone, M. R. Elliott, F. Gruber, J. Han, W. Chen, T. Kensler, K. S. Ravichandran, B. E. Isakson, B. R. Wamhoff, und N. Leitinger. 2010. 'Identification of a novel macrophage phenotype that develops in response to atherogenic phospholipids via Nrf2', *Circ Res*, 107: 737-46.

Kadl, A., P. R. Sharma, W. Chen, R. Agrawal, A. K. Meher, S. Rudraiah, N. Grubbs, R. Sharma, und N. Leitinger. 2011. 'Oxidized phospholipid-induced inflammation is mediated by Toll-like receptor 2', *Free Radic Biol Med*, 51: 1903-9.

Kagan, V. E., G. Mao, F. Qu, J. P. Angeli, S. Doll, C. S. Croix, H. H. Dar, B. Liu, V. A. Tyurin, V. B. Ritov, A. A. Kapralov, A. A. Amoscato, J. Jiang, T. Anthonymuthu, D. Mohammadyani, Q. Yang, B. Proneth, J. Klein-Seetharaman, S. Watkins, I. Bahar, J. Greenberger, R. K. Mallampalli, B. R. Stockwell, Y. Y. Tyurina, M. Conrad, und H. Bayir. 2017. 'Oxidized arachidonic and adrenic PEs navigate cells to ferroptosis', *Nat Chem Biol*, 13: 81-90.

Karki, P., A. Meliton, A. Shah, Y. Tian, T. Ohmura, N. Sarich, A. A. Birukova, und K. G. Birukov. 2018. 'Role of truncated oxidized phospholipids in acute endothelial barrier dysfunction caused by particulate matter', *PLoS One*, 13: e0206251.

Ke, Y., P. Karki, J. Kim, S. Son, E. Berdyshev, V. N. Bochkov, A. A. Birukova, und K. G. Birukov. 2019. 'Elevated truncated oxidized phospholipids as a factor exacerbating ALI in the aging lungs', *FASEB J*, 33: 3887-900.

Kerr, P. M., R. Tam, K. Ondrusova, R. Mittal, D. Narang, C. H. Tran, D. G. Welsh, und F. Plane. 2012. 'Endothelial feedback and the myoendothelial projection', *Microcirculation*, 19: 416-22.

Kosugi, S., M. Hasebe, M. Tomita, und H. Yanagawa. 2009. 'Systematic identification of cell cycle-dependent yeast nucleocytoplasmic shuttling proteins by prediction of composite motifs', *Proc Natl Acad Sci U S A*, 106: 10171-6.

Lee, J., M. C. Walsh, K. L. Hoehn, D. E. James, E. J. Wherry, und Y. Choi. 2014. 'Regulator of fatty acid metabolism, acetyl coenzyme a carboxylase 1, controls T cell immunity', *J Immunol*, 192: 3190-9.

Lee, S. W., H. K. Kim, P. Naidansuren, K. A. Ham, H. S. Choi, H. Y. Ahn, M. Kim, D. H. Kang, S. W. Kang, und Y. A. Joe. 2020. 'Peroxidasin is essential for endothelial cell survival

and growth signaling by sulfilimine crosslink-dependent matrix assembly', *FASEB J*, 34: 10228-41.

Li, H., C. S. Raman, C. B. Glaser, E. Blasko, T. A. Young, J. F. Parkinson, M. Whitlow, und T. L. Poulos. 1999. 'Crystal structures of zinc-free and -bound heme domain of human inducible nitric-oxide synthase. Implications for dimer stability and comparison with endothelial nitric-oxide synthase', *J Biol Chem*, 274: 21276-84.

Libby, P., J. E. Buring, L. Badimon, G. K. Hansson, J. Deanfield, M. S. Bittencourt, L. Tokgözoğlu, und E. F. Lewis. 2019. 'Atherosclerosis', *Nat Rev Dis Primers*, 5: 56.

Liebergall, S. R., J. Angdisen, S. H. Chan, Y. Chang, T. F. Osborne, A. F. Koeppel, S. D. Turner, und I. G. Schulman. 2020. 'Inflammation Triggers Liver X Receptor-Dependent Lipogenesis', *Mol Cell Biol*, 40.

Lukosz, M., A. Mlynek, P. Czypiorski, J. Altschmied, und J. Haendeler. 2011. 'The transcription factor Grainyhead like 3 (GRHL3) affects endothelial cell apoptosis and migration in a NO-dependent manner', *Biochem Biophys Res Commun*, 412: 648-53.

Maron, B. A., und T. Michel. 2012. 'Subcellular localization of oxidants and redox modulation of endothelial nitric oxide synthase', *Circ J*, 76: 2497-512.

Medfai, H., A. Khalil, A. Rousseau, V. Nuyens, M. Paumann-Page, B. Sevcnikar, P. G. Furtmüller, C. Obinger, N. Moguilevsky, O. Peulen, M. Herfs, V. Castronovo, M. Amri, P. Van Antwerpen, L. Vanhamme, und K. Zouaoui Boudjeltia. 2019. 'Human peroxidasin 1 promotes angiogenesis through ERK1/2, Akt, and FAK pathways', *Cardiovasc Res*, 115: 463-75.

Medina-Leyte, Diana Jhoseline, Oscar Zepeda-García, Mayra Domínguez-Pérez, Antonia González-Garrido, Teresa Villarreal-Molina, und Leonor Jacobo-Albavera. 2021. 'Endothelial Dysfunction, Inflammation and Coronary Artery Disease: Potential Biomarkers and Promising Therapeutical Approaches', *International Journal of Molecular Sciences*, 22: 3850.

Merk, D., F. F. Cox, P. Jakobs, S. Promel, J. Altschmied, und J. Haendeler. 2024. 'Dose-Dependent Effects of Lipopolysaccharide on the Endothelium-Sepsis versus Metabolic Endotoxemia-Induced Cellular Senescence', *Antioxidants (Basel)*, 13.

Merk, D., J. Greulich, A. Vierkant, F. Cox, O. Eckermann, F. von Ameln, N. Dyballa-Rukes, J. Altschmied, N. Ale-Agha, P. Jakobs, und J. Haendeler. 2023. 'Caffeine Inhibits Oxidative Stress- and Low Dose Endotoxemia-Induced Senescence-Role of Thioredoxin-1', *Antioxidants (Basel)*, 12.

Merk, D., J. Ptok, P. Jakobs, F. von Ameln, J. Greulich, P. Kluge, K. Semperowitsch, O. Eckermann, H. Schaal, N. Ale-Agha, J. Altschmied, und J. Haendeler. 2021.

'Selenoprotein T Protects Endothelial Cells against Lipopolysaccharide-Induced Activation and Apoptosis', *Antioxidants (Basel)*, 10.

Milanovic, M., D. N. Y. Fan, D. Belenki, J. H. M. Dabritz, Z. Zhao, Y. Yu, J. R. Dorr, L. Dimitrova, D. Lenze, I. A. Monteiro Barbosa, M. A. Mendoza-Parra, T. Kanashova, M. Metzner, K. Pardon, M. Reimann, A. Trumpp, B. Dorken, J. Zuber, H. Gronemeyer, M. Hummel, G. Dittmar, S. Lee, und C. A. Schmitt. 2018. 'Senescence-associated reprogramming promotes cancer stemness', *Nature*, 553: 96-100.

Minamino, T., und S. Kourembanas. 2001. 'Mechanisms of telomerase induction during vascular smooth muscle cell proliferation', *Circ Res*, 89: 237-43.

Minamino, Tohru, Hideaki Miyauchi, Toshihiko Yoshida, Yasuo Ishida, Hideo Yoshida, und Issei Komuro. 2002. 'Endothelial Cell Senescence in Human Atherosclerosis', *Circulation*, 105: 1541-44.

Miwa, S., H. Jow, K. Baty, A. Johnson, R. Czapiewski, G. Saretzki, A. Treumann, und T. von Zglinicki. 2014. 'Low abundance of the matrix arm of complex I in mitochondria predicts longevity in mice', *Nat Commun*, 5: 3837.

Mohammad, S., und C. Thiemermann. 2020. 'Role of Metabolic Endotoxemia in Systemic Inflammation and Potential Interventions', *Front Immunol*, 11: 594150.

Navas-Madronal, M., C. Rodriguez, M. Kassan, J. Fite, J. R. Escudero, L. Canes, J. Martinez-Gonzalez, M. Camacho, und M. Galan. 2019. 'Enhanced endoplasmic reticulum and mitochondrial stress in abdominal aortic aneurysm', *Clin Sci (Lond)*, 133: 1421-38.

Negmadjanov, U., Z. Godic, F. Rizvi, L. Emelyanova, G. Ross, J. Richards, E. L. Holmuhamedov, und A. Jahangir. 2015. 'TGF-beta1-mediated differentiation of fibroblasts is associated with increased mitochondrial content and cellular respiration', *PLoS One*, 10: e0123046.

Nunnari, J., und A. Suomalainen. 2012. 'Mitochondria: in sickness and in health', *Cell*, 148: 1145-59.

O'Neill, L. A., R. J. Kishton, und J. Rathmell. 2016. 'A guide to immunometabolism for immunologists', *Nat Rev Immunol*, 16: 553-65.

O'Neill, L. A., und E. J. Pearce. 2016. 'Immunometabolism governs dendritic cell and macrophage function', *J Exp Med*, 213: 15-23.

Patel, P. L., A. Suram, N. Mirani, O. Bischof, und U. Herbig. 2016. 'Derepression of hTERT gene expression promotes escape from oncogene-induced cellular senescence', *Proc Natl Acad Sci U S A*, 113: E5024-33.

Peng, W., G. Cai, Y. Xia, J. Chen, P. Wu, Z. Wang, G. Li, und D. Wei. 2019. 'Mitochondrial Dysfunction in Atherosclerosis', *DNA Cell Biol*, 38: 597-606.

Perez-Carreras, M., P. Del Hoyo, M. A. Martin, J. C. Rubio, A. Martin, G. Castellano, F. Colina, J. Arenas, und J. A. Solis-Herruzo. 2003. 'Defective hepatic mitochondrial respiratory chain in patients with nonalcoholic steatohepatitis', *Hepatology*, 38: 999-1007.

Podrez, E. A., E. Poliakov, Z. Shen, R. Zhang, Y. Deng, M. Sun, P. J. Finton, L. Shan, M. Febbraio, D. P. Hajjar, R. L. Silverstein, H. F. Hoff, R. G. Salomon, und S. L. Hazen. 2002. 'A novel family of atherogenic oxidized phospholipids promotes macrophage foam cell formation via the scavenger receptor CD36 and is enriched in atherosclerotic lesions', *J Biol Chem*, 277: 38517-23.

Pothion, H., C. Jehan, H. Tostivint, D. Cartier, C. Bucharles, A. Falluel-Morel, L. Boukhzar, Y. Anouar, und I. Lihrmann. 2020. 'Selenoprotein T: An Essential Oxidoreductase Serving as a Guardian of Endoplasmic Reticulum Homeostasis', *Antioxid Redox Signal*, 33: 1257-75.

Qian, J., und D. Fulton. 2013. 'Post-translational regulation of endothelial nitric oxide synthase in vascular endothelium', *Front Physiol*, 4: 347.

Raman, C. S., H. Li, P. Martasek, V. Kral, B. S. Masters, und T. L. Poulos. 1998. 'Crystal structure of constitutive endothelial nitric oxide synthase: a paradigm for pterin function involving a novel metal center', *Cell*, 95: 939-50.

Rector, R. S., J. P. Thyfault, G. M. Uptergrove, E. M. Morris, S. P. Naples, S. J. Borengasser, C. R. Mikus, M. J. Laye, M. H. Laughlin, F. W. Booth, und J. A. Ibdah. 2010. 'Mitochondrial dysfunction precedes insulin resistance and hepatic steatosis and contributes to the natural history of non-alcoholic fatty liver disease in an obese rodent model', *J Hepatol*, 52: 727-36.

Richardson, G. D., D. Breault, G. Horrocks, S. Cormack, N. Hole, und W. A. Owens. 2012. 'Telomerase expression in the mammalian heart', *FASEB J*, 26: 4832-40.

Saleh, T., L. Tyutyunyk-Massey, und D. A. Gewirtz. 2019. 'Tumor Cell Escape from Therapy-Induced Senescence as a Model of Disease Recurrence after Dormancy', *Cancer Res*, 79: 1044-46.

Santos, J. H., J. N. Meyer, M. Skorvaga, L. A. Annab, und B. Van Houten. 2004. 'Mitochondrial hTERT exacerbates free-radical-mediated mtDNA damage', *Aging Cell*, 3: 399-411.

Schuler, D., R. Sansone, T. Freudenberger, A. Rodriguez-Mateos, G. Weber, T. Y. Momma, C. Goy, J. Altschmied, J. Haendeler, J. W. Fischer, M. Kelm, und C. Heiss. 2014. 'Measurement of endothelium-dependent vasodilation in mice--brief report', *Arterioscler Thromb Vasc Biol*, 34: 2651-7.

Serbulea, V., C. M. Upchurch, K. W. Ahern, G. Bories, P. Voigt, D. E. DeWeese, A. K. Meher, T. E. Harris, und N. Leitinger. 2018. 'Macrophages sensing oxidized DAMPs reprogram their metabolism to support redox homeostasis and inflammation through a TLR2-Syk-ceramide dependent mechanism', *Mol Metab*, 7: 23-34.

Serbulea, V., C. M. Upchurch, M. S. Schappe, P. Voigt, D. E. DeWeese, B. N. Desai, A. K. Meher, und N. Leitinger. 2018. 'Macrophage phenotype and bioenergetics are controlled by oxidized phospholipids identified in lean and obese adipose tissue', *Proc Natl Acad Sci U S A*, 115: E6254-E63.

Sessa, W. C. 2004. 'eNOS at a glance', *J Cell Sci*, 117: 2427-9.

Sharov, V. G., A. Goussev, M. Lesch, S. Goldstein, und H. N. Sabbah. 1998. 'Abnormal mitochondrial function in myocardium of dogs with chronic heart failure', *J Mol Cell Cardiol*, 30: 1757-62.

Shen, T., N. Wang, X. Yu, J. Shi, Q. Li, C. Zhang, L. Fu, S. Wang, Y. Xing, X. Zheng, L. Yu, und D. Zhu. 2015. 'The Critical Role of Dynamin-Related Protein 1 in Hypoxia-Induced Pulmonary Vascular Angiogenesis', *J Cell Biochem*, 116: 1993-2007.

Siasos, G., V. Tsigkou, M. Kosmopoulos, D. Theodosiadis, S. Simantiris, N. M. Tagkou, A. Tsimpiktsioglou, P. K. Stampouloglou, E. Oikonomou, K. Mourouzis, A. Philippou, M. Vavuranakis, C. Stefanadis, D. Tousoulis, und A. G. Papavassiliou. 2018. 'Mitochondria and cardiovascular diseases-from pathophysiology to treatment', *Ann Transl Med*, 6: 256.

Spilsbury, A., S. Miwa, J. Attems, und G. Saretzki. 2015. 'The role of telomerase protein TERT in Alzheimer's disease and in tau-related pathology in vitro', *J Neurosci*, 35: 1659-74.

Spinelli, J. B., und M. C. Haigis. 2018. 'The multifaceted contributions of mitochondria to cellular metabolism', *Nat Cell Biol*, 20: 745-54.

Spyridopoulos, I., S. Fichtlscherer, R. Popp, S. W. Toennes, B. Fisslthaler, T. Trepels, A. Zernecke, E. A. Liehn, C. Weber, A. M. Zeiher, S. Dimmeler, und J. Haendeler. 2008. 'Caffeine enhances endothelial repair by an AMPK-dependent mechanism', *Arterioscler Thromb Vasc Biol*, 28: 1967-74.

Straub, A. C., M. Billaud, S. R. Johnstone, A. K. Best, S. Yemen, S. T. Dwyer, R. Looft-Wilson, J. J. Lysiak, B. Gaston, L. Palmer, und B. E. Isakson. 2011. 'Compartmentalized connexin 43 s-nitrosylation/denitrosylation regulates heterocellular communication in the vessel wall', *Arterioscler Thromb Vasc Biol*, 31: 399-407.

Straub, A. C., J. T. Butcher, M. Billaud, S. M. Mutchler, M. V. Artamonov, A. T. Nguyen, T. Johnson, A. K. Best, M. P. Miller, L. A. Palmer, L. Columbus, A. V. Somlyo, T. H. Le, und B. E. Isakson. 2014. 'Hemoglobin alpha/eNOS coupling at myoendothelial

junctions is required for nitric oxide scavenging during vasoconstriction', *Arterioscler Thromb Vasc Biol*, 34: 2594-600.

Straub, A. C., A. W. Lohman, M. Billaud, S. R. Johnstone, S. T. Dwyer, M. Y. Lee, P. S. Bortz, A. K. Best, L. Columbus, B. Gaston, und B. E. Isakson. 2012. 'Endothelial cell expression of haemoglobin alpha regulates nitric oxide signalling', *Nature*, 491: 473-7.

Straub, A. C., A. C. Zeigler, und B. E. Isakson. 2014. 'The myoendothelial junction: connections that deliver the message', *Physiology (Bethesda)*, 29: 242-9.

Stuve, P., L. Minarrieta, H. Erdmann, C. Arnold-Schrauf, M. Swallow, M. Guderian, F. Krull, A. Holscher, P. Ghorbani, J. Behrends, W. R. Abraham, C. Holscher, T. D. Sparwasser, und L. Berod. 2018. 'De Novo Fatty Acid Synthesis During Mycobacterial Infection Is a Prerequisite for the Function of Highly Proliferative T Cells, But Not for Dendritic Cells or Macrophages', *Front Immunol*, 9: 495.

Sun, X., J. S. Seidman, P. Zhao, T. D. Troutman, N. J. Spann, X. Que, F. Zhou, Z. Liao, M. Pasillas, X. Yang, J. A. Magida, T. Kisseleva, D. A. Brenner, M. Downes, R. M. Evans, A. R. Saltiel, S. Tsimikas, C. K. Glass, und J. L. Witztum. 2020. 'Neutralization of Oxidized Phospholipids Ameliorates Non-alcoholic Steatohepatitis', *Cell Metab*, 31: 189-206 e8.

Ting, S. B., J. Caddy, N. Hislop, T. Wilanowski, A. Auden, L. L. Zhao, S. Ellis, P. Kaur, Y. Uchida, W. M. Holleran, P. M. Elias, J. M. Cunningham, und S. M. Jane. 2005. 'A homolog of Drosophila grainy head is essential for epidermal integrity in mice', *Science*, 308: 411-3.

Ting, S. B., T. Wilanowski, L. Cerruti, L. L. Zhao, J. M. Cunningham, und S. M. Jane. 2003. 'The identification and characterization of human Sister-of-Mammalian Grainyhead (SOM) expands the grainyhead-like family of developmental transcription factors', *Biochem J*, 370: 953-62.

Toussaint, O., E. E. Medrano, und T. von Zglinicki. 2000. 'Cellular and molecular mechanisms of stress-induced premature senescence (SIPS) of human diploid fibroblasts and melanocytes', *Exp Gerontol*, 35: 927-45.

Tsimikas, S., S. Kiechl, J. Willeit, M. Mayr, E. R. Miller, F. Kronenberg, Q. Xu, C. Bergmark, S. Weger, F. Oberhollenzer, und J. L. Witztum. 2006. 'Oxidized phospholipids predict the presence and progression of carotid and femoral atherosclerosis and symptomatic cardiovascular disease: five-year prospective results from the Bruneck study', *J Am Coll Cardiol*, 47: 2219-28.

Tujebajeva, R. M., P. R. Copeland, X. M. Xu, B. A. Carlson, J. W. Harney, D. M. Driscoll, D. L. Hatfield, und M. J. Berry. 2000. 'Decoding apparatus for eukaryotic selenocysteine insertion', *EMBO Rep*, 1: 158-63.

Tzeng, E., T. R. Billiar, D. L. Williams, J. Li, A. Lizonova, I. Kovesdi, und Y. M. Kim. 1998. 'Adenovirus-mediated inducible nitric oxide synthase gene transfer inhibits hepatocyte apoptosis', *Surgery*, 124: 278-83.

Upchurch, C. M., S. Yeudall, C. M. Pavelec, D. Merk, J. Greulich, M. Manjegowda, S. S. Raghavan, I. M. Bochkis, M. M. Scott, E. Perez-Reyes, und N. Leitinger. 2022. 'Targeting oxidized phospholipids by AAV-based gene therapy in mice with established hepatic steatosis prevents progression to fibrosis', *Sci Adv*, 8: eabn0050.

Vaduganathan, M., G. A. Mensah, J. V. Turco, V. Fuster, und G. A. Roth. 2022. 'The Global Burden of Cardiovascular Diseases and Risk: A Compass for Future Health', *J Am Coll Cardiol*, 80: 2361-71.

Van den Bossche, J., L. A. O'Neill, und D. Menon. 2017. 'Macrophage Immunometabolism: Where Are We (Going)?', *Trends Immunol*, 38: 395-406.

Verhaar, M. C., P. E. Westerweel, A. J. van Zonneveld, und T. J. Rabelink. 2004. 'Free radical production by dysfunctional eNOS', *Heart*, 90: 494-5.

Wang, A. S., und O. Dreesen. 2018. 'Biomarkers of Cellular Senescence and Skin Aging', *Front Genet*, 9: 247.

Wang, L., J. Jing, H. Yan, J. Tang, G. Jia, G. Liu, X. Chen, G. Tian, J. Cai, H. Shang, und H. Zhao. 2018. 'Selenium Pretreatment Alleviated LPS-Induced Immunological Stress Via Upregulation of Several Selenoprotein Encoding Genes in Murine RAW264.7 Cells', *Biol Trace Elem Res*, 186: 505-13.

Wang, S., und C. Samakovlis. 2012. 'Grainy head and its target genes in epithelial morphogenesis and wound healing', *Curr Top Dev Biol*, 98: 35-63.

Wang, X., B. Yang, H. L. Cao, R. Y. Wang, Z. Y. Lu, R. F. Chi, und B. Li. 2021. 'Selenium Supplementation Protects Against Lipopolysaccharide-Induced Heart Injury via Sting Pathway in Mice', *Biol Trace Elem Res*, 199: 1885-92.

Wei, X., H. Song, L. Yin, M. G. Rizzo, R. Sidhu, D. F. Covey, D. S. Ory, und C. F. Semenkovich. 2016. 'Fatty acid synthesis configures the plasma membrane for inflammation in diabetes', *Nature*, 539: 294-98.

Wilanowski, T., A. Tuckfield, L. Cerruti, S. O'Connell, R. Saint, V. Parekh, J. Tao, J. M. Cunningham, und S. M. Jane. 2002. 'A highly conserved novel family of mammalian

developmental transcription factors related to Drosophila grainyhead', *Mech Dev*, 114: 37-50.

Witztum, J. L. 1993. 'Role of Oxidized Low-Density-Lipoprotein in Atherogenesis', *British Heart Journal*, 69: S12-S18.

Xu, S., I. Ilyas, P. J. Little, H. Li, D. Kamato, X. Zheng, S. Luo, Z. Li, P. Liu, J. Han, I. C. Harding, E. E. Ebong, S. J. Cameron, A. G. Stewart, und J. Weng. 2021. 'Endothelial Dysfunction in Atherosclerotic Cardiovascular Diseases and Beyond: From Mechanism to Pharmacotherapies', *Pharmacol Rev*, 73: 924-67.

Yeudall, S., C. M. Upchurch, P. V. Seegren, C. M. Pavelec, J. Greulich, M. C. Lemke, T. E. Harris, B. N. Desai, K. L. Hoehn, und N. Leitinger. 2022. 'Macrophage acetyl-CoA carboxylase regulates acute inflammation through control of glucose and lipid metabolism', *Sci Adv*, 8: eabq1984.

Yki-Jarvinen, H. 2014. 'Non-alcoholic fatty liver disease as a cause and a consequence of metabolic syndrome', *Lancet Diabetes Endocrinol*, 2: 901-10.

Yu, Z., A. Bhandari, J. Mannik, T. Pham, X. Xu, und B. Andersen. 2008. 'Grainyhead-like factor Get1/Grhl3 regulates formation of the epidermal leading edge during eyelid closure', *Dev Biol*, 319: 56-67.

Zhao, B., R. A. Bowden, S. A. Stavchansky, und P. D. Bowman. 2001. 'Human endothelial cell response to gram-negative lipopolysaccharide assessed with cDNA microarrays', *Am J Physiol Cell Physiol*, 281: C1587-95.

Ziche, M., L. Morbidelli, E. Masini, S. Amerini, H. J. Granger, C. A. Maggi, P. Geppetti, und F. Ledda. 1994. 'Nitric oxide mediates angiogenesis in vivo and endothelial cell growth and migration in vitro promoted by substance P', *J Clin Invest*, 94: 2036-44.

Zurek, M., J. Altschmied, S. Kohlgruber, N. Ale-Agha, und J. Haendeler. 2016. 'Role of Telomerase in the Cardiovascular System', *Genes (Basel)*, 7.

Eigene Veröffentlichungen

I **Targeting oxidized phospholipids by AAV-based gene therapy in mice with established hepatic steatosis prevents progression to fibrosis**
Upchurch CM, Yeudall S, Pavelec CM, Merk D, **Greulich J**, Manjegowda M, Raghavan SS, Bochkis IM, Scott MM, Perez-Reyes E, Leitinger N
Science Advances. 2022; 8, eabn0050

II **Mitochondrial Telomerase Reverse Transcriptase Protects From Myocardial Ischemia/Reperfusion Injury by Improving Complex I Composition and Function**
Ale-Agha N*, Jakobs P*, Goy C, Zurek M, Rosen J, Dyballa-Rukes N, Metzger S, **Greulich J**, von Ameln F, Eckermann O, Unfried K, Brack F, Grandoch M, Thielmann M, Kamler M, Gedik N, Kleinbongard P, Heinen A, Heusch G, Gödecke A, Altschmied J[#], Haendeler J[#]
Circulation. 2021; 144, 1876-1890
*gleichberechtigte Erstautoren, [#]gleichberechtigete Seniorautoren

III **Macrophage acetyl-CoA carboxylase regulates acute inflammation through control of glucose and lipid metabolism**
Yeudall S, Upchurch CM, Seegren PV, Pavelec CM, **Greulich J**, Lemke MC, Harris TE, Desai BN, Hoehn KL, Leitinger N
Science Advances. 2022; 8, eabq1984

IV **Selenoprotein T Protects Endothelial Cells against Lipopolysaccharide-Induced Activation and Apoptosis**
Merk D*, Ptok J*, Jakobs P*, von Ameln F, **Greulich J**, Kluge P, Semperowitsch K, Eckermann O, Schaal H, Ale-Agha N[#], Altschmied J[#], Haendeler J[#]
Antioxidants. 2021; 10, 1427
*gleichberechtigte Erstautoren, [#]gleichberechtigete Seniorautoren

V **Caffeine Inhibits Oxidative Stress- and Low Dose Endotoxemia-Induced Senescence – Role of Thioredoxin-1**
Merk D*, **Greulich J***, Vierkant A, Cox F, Eckermann O, von Ameln F, Dyballa-Rukes N, Altschmied J, Ale-Agha N[#], Jakobs P[#], Haendeler J[#]
Antioxidants. 2023; 12, 1244
*gleichberechtigte Erstautoren, [#]gleichberechtigete Seniorautoren

VI **Extra-Nuclear Functions of the Transcription Factor Grainyhead-Like 3 in the Endothelium-Interaction with Endothelial Nitric Oxide Synthase**
Jander K*, **Greulich J***, Gonnissen S*, Ale-Agha N, Goy C, Jakobs P, Farrokh S, Marziano C, Sonkusare SK, Haendeler J[#], Altschmied J[#]
Antioxidants. 2021; 10, 428
*gleichberechtigte Erstautoren, [#]gleichberechtigete Seniorautoren

Targeting oxidized phospholipids by AAV-based gene therapy in mice with established hepatic steatosis prevents progression to fibrosis

Upchurch CM, Yeudall S, Pavelec CM, Merk D, **Greulich J**, Manjegowda M, Raghavan SS, Bochkis IM, Scott MM, Perez-Reyes E, Leitinger N

Science Advances. 2022; 8, eabn0050

Publikation I

Beteiligung der Autoren:

Upchurch CM: Erstautor, war an der Planung und Durchführung aller Versuche beteiligt, führte die Datenanalyse durch und war am Entwurf des Manuskripts beteiligt.

Yeudall S: Führte Experimente zur inflammatorischen Aktivierung und Signaltransduktion in Leberzellen durch.

Pavelec CM: Führte metabolische Messungen mittels Seahorse-Analyzer durch und analysierte die Daten.

Merk D: Führte Analysen von AAV8-scFv-E06 Konzentrationen im Plasma mittels kompetitivem Sandwich ELISA durch.

Greulich J: Führte Immunoblots und Immunfluoreszenzfärbungen durch.

Manjegowda M: Führte Datenanalysen von RNAseq und Chip Experimenten durch.

Raghavan SS: Führte das Clinical Scoring von Leberschnitten aus NASH-Tierversuchen durch.

Bochkis IM: Führte Chip Experimente und Datenanalysen durch.

Scott MM: Erstellte zusammen mit Ed Perez-Reyes das Konzept für den AAV8-scFv-E06 Expressionsvektor.

Perez-Reyes E: Erstellte das Konzept für den AAV8-scFv-E06 Expressionsvektor und produzierte die AAV8-scFv-E06 Viren.

Leitinger N: Seniorautor, konzipierte die Studie, war an der Versuchsplanung beteiligt, finalisierte das Manuskript.

GENETICS

Targeting oxidized phospholipids by AAV-based gene therapy in mice with established hepatic steatosis prevents progression to fibrosis

Clint M. Upchurch[1], Scott Yeudall[1], Caitlin M. Pavelec[1,2], Dennis Merk[3], Jan Greulich[3,4], Mohan Manjegowda[1], Shyam S. Raghavan[5], Irina M. Bochkis[1], Michael M. Scott[1], Edward Perez-Reyes[1], Norbert Leitinger[1,2]*

Oxidized phosphatidylcholines (OxPCs) are implicated in chronic tissue damage. Hyperlipidemic LDL-R−/− deficient mice transgenic for an OxPC-recognizing IgM fragment (scFv-E06) are protected against nonalcoholic fatty liver disease (NAFLD). To examine the effect of OxPC elimination at different stages of NAFLD progression, we used cre-dependent, adeno-associated virus serotype 8–mediated expression of the single-chain variable fragment of E06 (AAV8-scFv-E06) in hepatocytes of albumin-cre mice. AAV8-induced expression of scFv-E06 at the start of FPC diet protected mice from developing hepatic steatosis. Independently, expression of scFv-E06 in mice with established steatosis prevented the progression to hepatic fibrosis. Mass spectrometry–based oxophospho-lipidomics identified individual OxPC species that were reduced by scFv-E06 expression. In vitro, identified OxPC species dysregulated mitochondrial metabolism and gene expression in hepatocytes and hepatic stellate cells. We demonstrate that individual OxPC species independently affect disease initiation and progression from hepatic steatosis to steatohepatitis, and that AAV-mediated expression of scFv-E06 is an effective therapeutic intervention.

INTRODUCTION

Nonalcoholic fatty liver disease (NAFLD) is a multistage disease that affects approximately 30% of the global population (*1*, *2*). Hepatic steatosis is the hallmark of NAFLD, which, in a subset of patients, will progress into nonalcoholic steatohepatitis (NASH). Steatosis can arise as a result of caloric overload, which dysregulates hepatocyte bioenergetics and metabolism (*3*) and increases reactive oxygen species (*4*) and hepatic triglyceride accumulation (*5*, *6*), resulting in organ damage indicated by elevated plasma alanine aminotransferase (ALT) and aspartate aminotransferase (AST) (*4*, *7*–*11*). The culmination of multiple hepatic insults leads to the development of NASH, which is characterized by inflammation (*12*) and activation of hepatic stellate cells, ultimately leading to irreversible hepatic fibrosis (*12*–*17*). In the absence of U.S. Food and Drug Administration–approved pharmacological interventions and suitable biomarkers for NASH, there is an urgent need for new therapeutic and diagnostic tools (*18*).

Excess radical oxygen species generation in steatotic livers leads to the formation of lipid oxidation products, including oxidized phosphatidylcholines (OxPCs) (*19*–*22*). Free radical–driven and enzymatically driven oxidation of polyunsaturated fatty acids contained in phospholipids forms chemically unique classes of oxidized species whose location and chemical functionalization dictate the regulation of specific cellular responses, including endothelial barrier integrity (*23*–*27*); immune cell migration (*28*), activation (*19*, *20*), and metabolism (*29*); bone homeostasis (*30*); and regulated cell death (*31*, *32*). Consequently, OxPCs are thought to play a central role in acute pathologies such as sepsis (*21*) and lung injury (*23*, *24*, *33*), as well as in chronic diseases including those of the metabolic syndrome (*34*, *35*). Moreover, plasma levels of OxPCs, as measured by reactivity with E06, a natural immunoglobulin M (IgM) that binds oxidized phosphorylcholine (*36*), predict severity of human carotid and femoral atherosclerosis (*37*).

Recent work from the Witztum laboratory has demonstrated that constitutive transgenic expression of a single-chain variable fragment of E06 (scFv-E06) protects hypercholesterolemic *Ldlr*$^{-/-}$ mice from diet-induced hepatic steatosis and subsequent NASH (*35*, *37*, *38*). While these studies demonstrated that targeting OxPCs in general is sufficient to improve clinical outcomes in a mouse model of chronic disease, the identity of individual OxPC species that are eliminated by scFv-E06 in vivo remains unknown. Furthermore, it is unknown whether OxPC sequestration by scFv-E06 is sufficient to independently halt the progression to NASH and the transition to hepatic fibrosis, and it is necessary to identify the cellular targets and the pathological mechanisms by which OxPCs drive hepatic steatosis and fibrosis.

Here, we show that adeno-associated virus serotype 8–mediated hepatic expression of scFv-E06 (AAV8-E06) eliminates defined plasma OxPC species derived from oxidation of 1-palmitoyl-2-arachidonyl-*sn*-glycero-3-phosphocholine (PAPC) and 1-palmitoyl-2-linoleoyl-*sn*-glycero-3-phosphocholine (PLPC), which protects mice from diet-induced hepatic steatosis. Identified OxPC species regulate hepatocyte gene expression and shift cellular metabolism toward a bioenergetically impaired state, which results in reduced oxygen consumption and increased lipid droplet accumulation. Moreover, intervention with AAV8-scFv-E06 in mice with established hepatic steatosis prevents the progression to NASH and hepatic fibrosis. OxPC species that were reduced during the progression phase regulate hepatic stellate cell bioenergetics and gene expression. Together, we identify specific pathology-driving OxPC species in plasma that

[1]Department of Pharmacology, University of Virginia School of Medicine, Charlottesville, VA 22904, USA. [2]Robert M. Berne Cardiovascular Research Center, University of Virginia School of Medicine, Charlottesville, VA 22904, USA. [3]Environmentally-Induced Cardiovascular Degeneration, Clinical Chemistry and Laboratory Diagnostics, Medical Faculty, University Hospital and Heinrich-Heine University Düsseldorf, 40225 Düsseldorf, Germany. [4]IUF-Leibniz Research Institute for Environmental Medicine, 40225 Düsseldorf, Germany. [5]Department of Pathology, University of Virginia, Charlottesville, VA 22904, USA.
*Corresponding author. Email: nl2q@virginia.edu

may be used as noninvasive biomarkers to diagnose distinct stages of NAFLD, and we demonstrate efficacy of AAV8-mediated gene transfer of scFv-E06 as an intervention-based therapeutic measure that attenuates the initiation of hepatic steatosis and the progression to fibrotic steatohepatitis in mice.

RESULTS

AAV8-mediated gene transfer for cre recombinase–dependent expression of scFv-E06 in mice

Previous reports demonstrated that constitutive transgenic expression of scFv-E06 via the *Apoe* promoter protected *Ldlr*$^{-/-}$ mice fed a high-cholesterol diet from hepatic steatosis and ensuing steatohepatitis (*35*, *38*). To investigate the effect of scFv-E06 at different stages of disease progression and to establish a therapeutic approach using virus-mediated gene transfer of scFv-E06, we developed an AAV8 construct containing a myc- and 6xHis-tagged scFv-E06 flanked by double-inverse orientation flox sites (AAV8-scFv-E06) for cre-dependent expression (Fig. 1A). Speer6-ps1$^{Tg(Alb\text{-}cre)21Mgn}$/J (Alb-cre) mice, which express cre recombinase specifically in hepatocytes, were injected via tail vein with AAV8-scFv-E06 or a control AAV8 expressing green fluorescent protein (AAV8-GFP). Viral transduction resulted in incorporation of the scFv-E06 vector predominantly in the liver and, to some extent, in adipose tissue, kidney, and spleen, while it was not detected in the heart or lungs (Fig. 1B). Messenger RNA and protein expression of scFv-E06 was restricted to the liver, demonstrating that expression was dependent on cre recombinase (Fig. 1, C and D). scFv-E06 protein was secreted into the plasma with detectable levels as early as 10 days after AAV administration (Fig. 1J).

AAV8-mediated hepatic expression of scFv-E06 had no observable effect on total body weight, and liver, gonadal adipose tissue, heart, kidney, or spleen mass (fig. S1). There were also no differences in levels of ALT (Fig. 1E) and AST (Fig. 1F) in plasma, or esterified (Fig. 1G), free (Fig. 1H), and total cholesterol (Fig. 1I) in livers of mice given AAV8-scFv-E06 compared to AAV-GFP controls. Together, these data demonstrate that AAV8-mediated hepatic expression of scFv-E06 in mice leads to accumulation of scFv-E06 protein in the liver and plasma without inducing overt physiological changes.

Using a high fructose, palmitate, and cholesterol (FPC) diet supplemented with 4.2% sugar water (55/45 glucose/fructose), we establish a progressive model NAFLD defined by distinct stages of hepatic steatosis and subsequent inflammation and fibrosis (*39*). These stages were evident in histopathological assessment of livers from mice fed FPC diet compared to chow-fed controls (fig. S1, G to J). This allowed us to assess the impact of scFv-E06 expression at different stages of NAFLD progression.

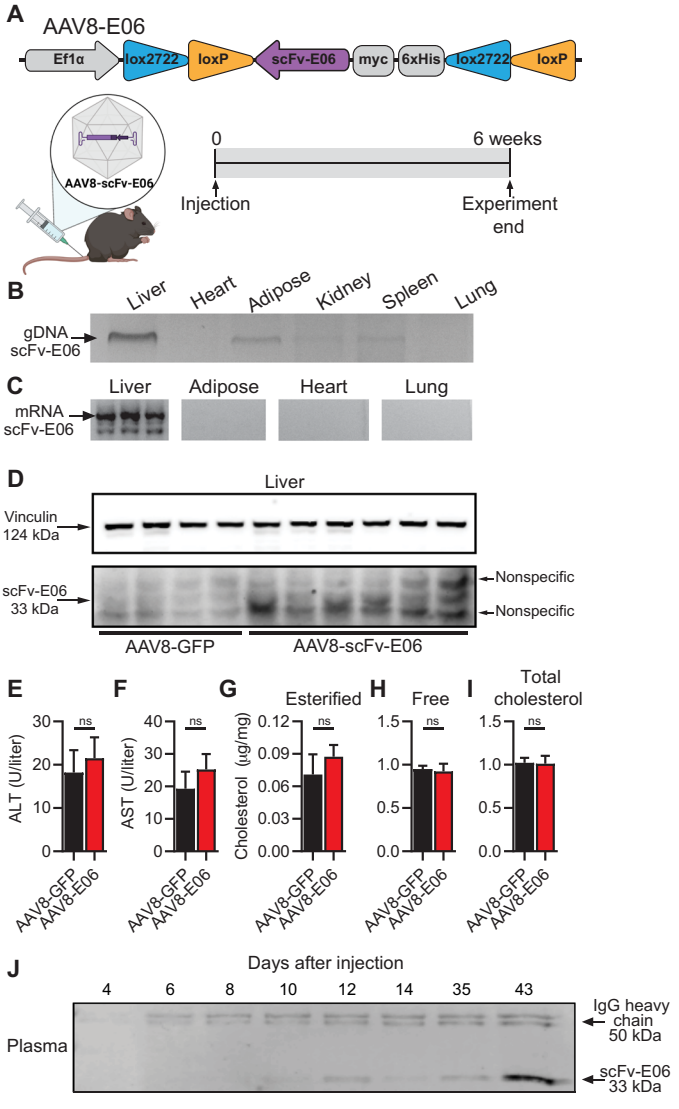

Fig. 1. Virus-mediated gene transfer for cre-dependent expression of scFv-E06 in a murine model. (**A**) Schematic of experimental design. Mice were injected via tail vein with AAV8-E06 or AAV-GFP and fed chow diet for 6 weeks (created with BioRender.com). Viral transduction of AAV8-scFv-E06 was assessed by (**B**) polymerase chain reaction (PCR) of genomic DNA and (**C**) reverse transcription PCR of mRNA. scFv-E06 expression in the (**D**) liver was confirmed via Western blotting 6 weeks after injection. Vinculin was used as a loading control. There were no significant changes in (**E**) ALT, (**F**) AST, and (**G**) esterified, (**H**) free, and (**I**) total liver cholesterol between scFv-E06– and GFP-expressing mice (AAV8-GFP, $n = 5$; AAV8-E06, $n = 6$). (**J**) scFv-E06 was detectable in plasma 12 days after injection and remained elevated after 6 weeks. Nonspecific IgG heavy chain staining was used as a loading control. ns, not significant.

AAV8-mediated expression of scFv-E06 protects mice from diet-induced hepatic steatosis and reduces oxidized phospholipids in plasma

To determine whether induced expression of scFv-E06 could be used as a therapeutic approach to prevent hepatic steatosis in mice, we inoculated Speer6-ps1$^{Tg(Alb\text{-}cre)21Mgn}$/J (Alb-cre) mice via tail vein with AAV8-scFv-E06 or AAV8-GFP 2 weeks before feeding mice FPC diet for 6 weeks to induce hepatic steatosis (Fig. 2A). After 6 weeks, we confirmed the expression of myc-tagged scFv-E06 in the liver by Western blot (Fig. 2B) and mRNA by quantitative reverse transcription polymerase chain reaction (qRT-PCR) in the liver (fig. S2A) and confirmed detectable titers of scFv-E06 in the plasma by enzyme-linked immunosorbent assay (ELISA) (Fig. 2C). scFv-E06–expressing mice exhibited no difference in weight gain compared to GFP-expressing mice over 6 weeks (fig. S2B); however, scFv-E06 expression reduced body fat percentage starting at 4 weeks on FPC diet (fig. S2C). FPC diet feeding increased liver and adipose mass; however, there was no difference in organ mass between GFP- and scFv-E06–expressing mice (fig. S2, D to I). Histological assessment

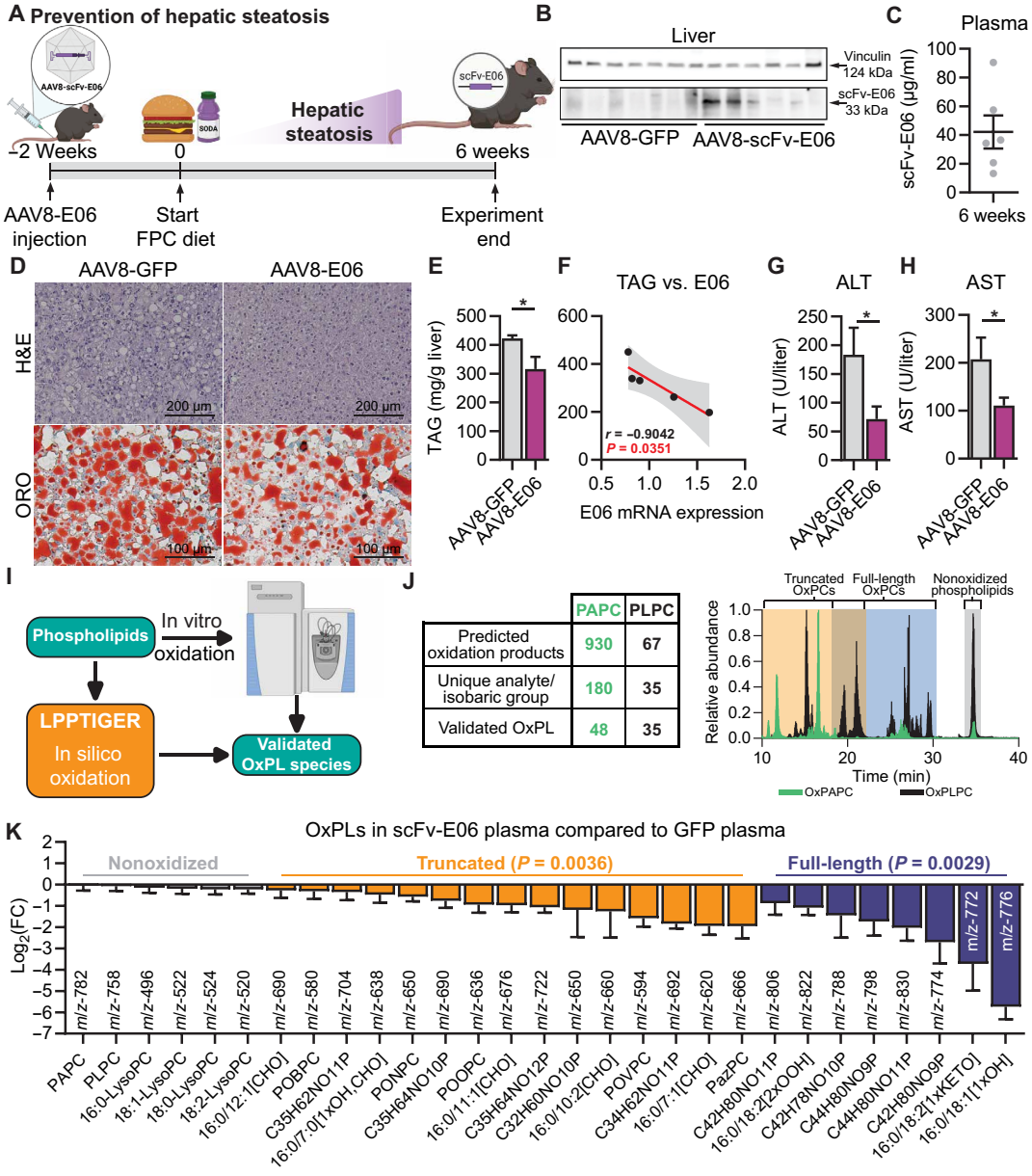

Fig. 2. Virus-mediated hepatic expression of scFv-E06 prevented development of diet-induced hepatic steatosis. (**A**) Schematic of experimental design. Mice were injected via tail vein with AAV8-E06 or AAV8-GFP 2 weeks before the start of 6-week FPC diet challenge (created with BioRender.com). (**B**) scFv-E06 protein expression in mouse liver 8 weeks after injection. (**C**) scFv-E06 titer concentrations were estimated in plasma by competitive sandwich enzyme-linked immunosorbent assay (ELISA). (**D**) Hematoxylin and eosin (H&E) and Oil red O (ORO) staining revealed decreased hepatic lipid burden in mice expressing scFv-E06 and was confirmed by (**E**) quantification of hepatic triglycerides (GFP, $n = 6$; scFv-E06, $n = 5$). (**F**) Hepatic triglyceride concentrations negatively correlated with hepatic mRNA expression of scFv-E06 (scFv-E06, $n = 5$). scFv-E06 expression protected mice from diet-induced liver toxicity resulting in significantly lower (**G**) ALT and (**H**) AST (GFP, $n = 6$; scFv-E06, $n = 6$). (**I**) Schema demonstrating strategy for mass spectrometry method development and validation. (**J**) Forty-eight analytes/isobaric groups from PAPC and 35 analytes/isobaric groups from PLPC were validated. (**K**) Both truncated and full-length OxPC species were significantly reduced in mice expressing scFv-E06 (GFP, $n = 7$; scFv-E06, $n = 6$). Statistical significance was determined by two-way analysis of variance (ANOVA), Spearman's rank correlation, and Student's t test (*$P < 0.05$).

of liver sections by hematoxylin and eosin (H&E) or Oil red O staining revealed that treatment with AAV8-scFv-E06 reduced hepatic tissue damage and lipid accumulation compared to GFP controls (Fig. 2D). Hepatic triglyceride levels were significantly reduced in scFv-E06–expressing mice and negatively correlated with hepatic mRNA expression of scFv-E06 (Fig. 2, E and F). Moreover, plasma ALT (Fig. 2G) and AST (Fig. 2H) levels were significantly decreased in mice expressing scFv-E06, while alkaline phosphatase (ALP), cholesterol, low-density lipoprotein (LDL) and high-density lipoprotein (HDL) cholesterol, plasma triglycerides, albumin, and total protein were unchanged (fig. S2, J to R). These data demonstrate that AAV8-mediated expression of scFv-E06 protects mice from diet-induced hepatic lipid accumulation and liver damage.

Previously published studies have demonstrated that constitutive scFv-E06 expression reduced overall plasma reactivity with IgM E06 (*35*, *38*), indicative of reduced OxPC levels in plasma. However,

the identity of OxPC species that are reduced by scFv-E06 expression and the degree of reduction remain unknown.

To identify OxPC species that are affected by scFv-E06 in plasma, we used an in silico platform, LPPTiger (*40*), to predict structures of possible oxidation products that can be generated from oxidation of PAPC and PLPC. We then validated predicted OxPC species by electrospray ionization liquid chromatography–mass spectrometry (ESI–LC-MS) using air- or copper (I) chloride–oxidized PAPC (OxPAPC) and PLPC (OxPLPC) (fig. S3, A and B), which resulted in validation of 48 PAPC- and 35 PLPC-derived oxidized individual analytes or groups of isobaric compounds (Fig. 2, I and J). Next, we assessed the presence of validated compounds in the plasma of GFP- or scFv-E06–expressing mice after 6 weeks on FPC diet (fig. S3, C and D). We identified 23 individual OxPC species and isobaric groups containing OxPCs and 6 nonoxidized PC and lyso-PC species in mouse plasma. Levels of nonoxidized PCs and lyso-PCs were not different in GFP- and scFv-E06–expressing mice; however, all identified OxPC species, including truncated and full-length OxPCs, were markedly decreased in plasma of mice expressing scFv-E06 (Fig. 2K). A similar pattern was observed in the liver; however, the differences in OxPC species were less pronounced between the two groups (fig. S2S).

In the plasma, the truncated and full-length OxPCs that were substantially decreased in scFv-E06–expressing mice included several previously described biologically active compounds containing specific functional groups: Among decreased truncated OxPC species were γ-keto/hydroxy OxPCs [mass/charge ratio (*m/z*) 650] (*22*, *41*), the aldehyde-containing 1-palmitoyl-2-(5′-oxo-valeroyl)-*sn*-glycero-3-phosphocholine (POVPC; *m/z* 594) (*42*), the 4-carbon aldehyde 1-palmitoyl-2-(4′-oxo-butanoyl)-*sn*-glycero-3-phosphocholine (POBPC; *m/z* 580) (*43*), the 8-carbon aldehyde 1-palmitoyl-2-(8′-oxo-octanoyl)-*sn*-glycero-3-phosphocholine (POOPC; *m/z* 636), the 9-carbon aldehyde 1-palmitoyl-2-(9′-oxo-nonanoyl)-*sn*-glycero-3-phosphocholine (*m/z* 650) (*44*, *45*), and the carboxylic acid–containing 1-palmitoyl-2-azelaoyl-*sn*-glycero-3-phosphocholine (PazPC; *m/z* 666) (Fig. 2J) (*45*, *46*). Among the most substantially reduced full-length OxPC were 1-palmitoyl-2-((E)-8′-hydroxyoctadec-12′-enoyl)-*sn*-glycero-3-phosphocholine (HODE-PC; *m/z* 776), an isobaric group with an *m/z* of 798 containing 1-palmitoyl-2-((5E,8E,11E,14E)-4′-hydroxyicosa-5′,8′,11′,14′-tetraenoyl (HETE-PC) (*47*), and an isobaric group with an *m/z* of 830 containing isoprostane-PC (Fig. 2K) (*48*, *49*). The structures of the identified compounds with the corresponding *m/z* values are represented in table S1.

Together, these data demonstrate that AAV8-dependent hepatic expression of scFv-E06 results in its secretion into the plasma, decreased plasma levels of defined OxPC species, and protection from diet-induced hepatic. scFv-E06 showed specificity toward OxPCs, but not nonoxidized phospholipids, recognizing a variety of oxidation-specific functional groups that are associated with previously reported biological functions (*50*, *51*).

OxPCs regulate hepatocyte gene expression and mitochondrial bioenergetics

These data imply a role of OxPCs in the development of hepatic steatosis; however, it is unknown if hepatocytes recognize and respond to OxPCs. To investigate whether OxPCs regulate hepatocyte function, we treated a murine hepatocyte cell line (AML12) with a mixture of full-length and truncated OxPCs (OxPAPC) (*42*) for 4 hours and analyzed changes in gene expression by RNA sequencing (RNA-seq). OxPAPC regulated the expression of 1367 genes in AML12 hepatocytes [fold change > 1.5, false discovery rate (FDR) < 0.05], of which 782 were up-regulated and 585 were down-regulated compared to vehicle-treated cells (Fig. 3A and table S2). EnrichR (*52*, *53*) Gene Ontology (GO) pathway analysis revealed that OxPAPC induced pathways associated with oxidative stress, including the "NRF2-mediated oxidative stress response," the "unfolded protein response," and the "aryl hydrocarbon receptor signaling pathway," as well as the "superpathway of cholesterol biosynthesis" (fig. S4A), suggesting that OxPCs contribute to dysregulating cholesterol metabolism, a hallmark of NAFLD (*54*).

Since our data showed that levels of both truncated and full-length OxPCs were decreased by scFv-E06, we separated OxPAPC into two fractions enriched for either truncated or full-length OxPC species using a strong anionic solid phase exchange chromatography method that we previously described (*34*). Treatment of AML12 cells with truncated OxPCs resulted in regulation of 720 genes (427 up-regulated, 293 down-regulated), while full-length OxPCs regulated the expression of 259 (204 up-regulated, 55 down-regulated) genes (Fig. 3B). Of those, truncated OxPCs uniquely regulated 78 genes (30 up/45 down), while full-length OxPCs uniquely down-regulated 2 genes (Fig. 3B and table S2). Both truncated and full-length OxPAPC up-regulated genes associated with oxidative stress such as *Hmox1*, *Gsta1*, *Txnrd1*, *Hspa1a*, and *Hspa1b*, as well as *Ptgs2* (cyclooxygenase 2) (table S2). In addition, qRT-PCR confirmed that full-length OxPCs, truncated OxPCs, and OxPAPC up-regulated the expression of *Hmox1* (fig. S4D) and *Pgd* (fig. S4E), while only truncated OxPCs up-regulated *Acly* (fig. S4F), *Hmgcoas* (fig. S4G), and *Hmgcoar* (fig. S4H). GO Biological Pathway analysis revealed that, like OxPAPC, both truncated OxPCs and full-length OxPCs induced the "NRF2-mediated oxidative stress pathway"; however, only truncated OxPCs induced the "superpathway of cholesterol biosynthesis" (Fig. 3, D and E, and fig. S4A). Moreover, truncated OxPAPC down-regulated the expression of *Cav1* (caveolin 1), which has been shown to increase hepatic lipid droplet size in NAFLD (*55*–*57*), and up-regulated *Slc25a1*, which has recently been associated with hepatic steatosis and glucose intolerance by dysregulation of hepatocyte metabolism (*58*).

To investigate the effect of OxPCs on hepatocyte metabolism, we treated AML12 cells with OxPAPC or the fractions enriched for truncated or full-length OxPCs for 4 hours and measured oxygen consumption rate via extracellular flux analysis. Treatment with OxPAPC significantly decreased maximal oxygen consumption rate (Fig. 4A), which was mimicked by truncated OxPCs (Fig. 4B). Impaired oxygen consumption in hepatocytes is indicative of mitochondrial dysfunction that precedes the transition from steatosis to NASH (*9*, *59*). To investigate whether this metabolic dysregulation would lead to increased lipid accumulation, we treated AML12 hepatocytes with OxPAPC, truncated OxPCs, or full-length OxPCs for 48 hours and then stained cells with Nile red to quantify lipid droplet numbers and size (*60*). Consistent with the effects on hepatocyte mitochondrial function, OxPAPC (Fig. 4C) and truncated OxPCs (Fig. 4D) increased average lipid droplet size in cells compared to vehicle, while full-length OxPCs (Fig. 4E) did not alter lipid droplet size (Fig. 4F). However, both fractions increased the number of lipid droplets per cell compared to vehicle control (Fig. 4G).

Together, these data demonstrate that distinct OxPC species differently regulate hepatocyte gene expression and metabolic function in vitro. While both truncated and full-length OxPCs regulate

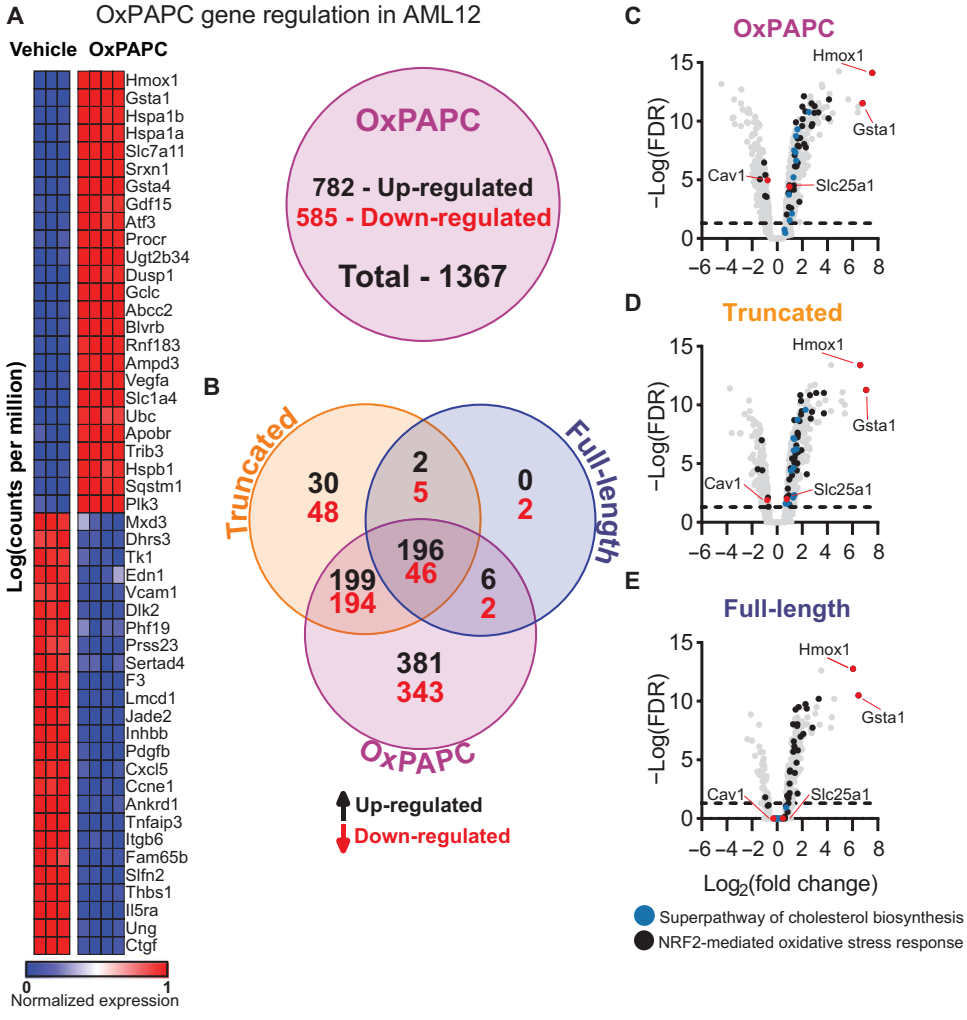

Fig. 3. Truncated OxPLs shift AML12 hepatocytes to an anabolic metabolic programming. AML12 hepatocytes were treated with OxPAPC (100 μg/ml) for 4 hours, and gene expression was measured via RNA-seq. (**A**) OxPAPC regulated 1367 genes (782 up-regulated/585 down-regulated, fold change > |1.5| and adjusted $P < 0.05$; vehicle, $n = 3$; OxPAPC; $n = 4$). (**B**) Truncated OxPLs uniquely regulated 78 genes (30 up-regulated/48 down-regulated) compared to 2 down-regulated genes in full-length OxPL and 724 (381 up-regulated/343 down-regulated) in OxPAPC treatment with 242 regulated by all three treatments (196 up-regulated/46 down-regulated) (fold change > |1.5| and adjusted $P < 0.05$, $n = 3$ to 4). Volcano plot analysis of (**C**) OxPAPC, (**D**) truncated OxPAPC, and (**E**) full-length OxPAPC revealed that *Hmox1* and *Gsta1* were the most highly up-regulated genes in all three treatments along with genes associated with the NRF2-mediated oxidative stress response. *Slc25a1* and *Cav1* were regulated in OxPAPC and truncated OxPL treatment, but not in full-length OxPL treatment. The same pattern was observed for genes associated with the superpathway of cholesterol biosynthesis. Statistical significance was determined by one-way ANOVA and Student's *t* test. Multiple comparisons were corrected by FDR or Dunnett's multiple comparison correction.

redox transcriptomic programming, only truncated OxPCs regulate anabolic gene programming, such as the superpathway of cholesterol biosynthesis, and inhibit mitochondrial oxygen consumption, resulting in increased lipid droplets.

scFv-E06 after development of hepatic steatosis halts disease progression to fibrosis

To test whether elimination of OxPCs through inducible expression of scFv-E06 during the transition from steatosis to NASH could halt the progression to fibrosis, we first fed age-matched Alb-cre mice an FPC diet for 6 weeks (Fig. 5A), which established hepatic steatosis without signs of fibrosis. Then, weight-randomized mice were injected with AAV8-scFv-E06 or AAV8-GFP via tail vein. To induce fibrosis, mice were fed FPC diet for an additional 14 weeks (Fig. 5A). Sustained scFv-E06 gene expression was confirmed in the liver (fig. S5A), and scFv-E06 protein was detected in the liver by Western blot and in the plasma by ELISA (Fig. 5, B and C) at the end of the experiment (20 weeks). As expected, FPC diet significantly elevated body mass and body fat percentage compared to chow control (fig. S5, B and C); however, there were no differences in body mass (fig. S5B); body fat percentage (fig. S5C); liver, adipose, lung, heart, kidney, and spleen mass (fig. S5, D to I); and fasting glucose and insulin tolerance between AAV8-scFv-E06– or AAV8-GFP–treated mice at 20 weeks (fig. S5, Q to S).

Notably, intervention with AAV8-scFv-E06 protected mice with established hepatic steatosis from further liver injury as evidenced by significantly reduced plasma AST (Fig. 5D), ALT (Fig. 5E), ALP (Fig. 5F), LDL:HDL ratio (fig. S5J), and cholesterol:HDL ratio

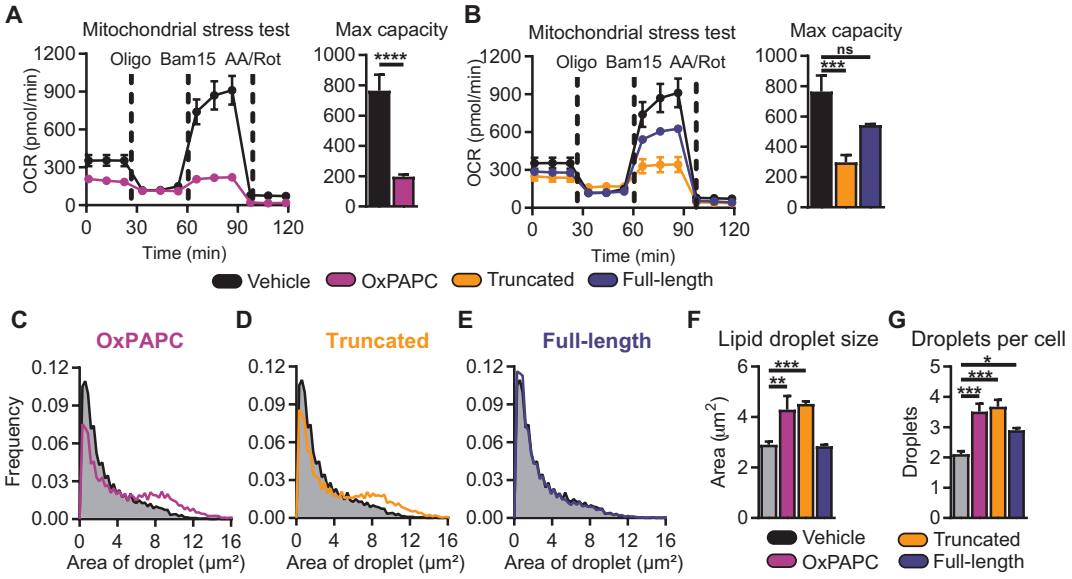

Fig. 4. Truncated oxidized phospholipids dysregulate hepatocyte metabolism resulting in lipid droplet accumulation. (**A**) Mitochondrial stress test analysis of AML12 murine hepatocytes treated with OxPAPC (100 μg/ml) for 4 hours significantly inhibited maximum oxygen consumption in hepatocytes ($n = 5$). (**B**) Truncated, but not full-length, OxPLs significantly inhibited maximum mitochondrial oxygen consumption rate ($n = 5$). AML12 cells were treated with (**C**) OxPAPC (100 μg/ml), (**D**) truncated OxPAPC, and (**E**) full-length OxPAPC for 48 hours. (**F**) Lipid droplet size and (**G**) number were significantly increased in AML12 cells treated with OxPAPC and truncated OxPLs. Full-length OxPLs increased droplet number per cell ($n = 4$, three fields of view per biological replicate). Statistical significance was determined by one-way ANOVA and Mann-Whitney *U* test. Multiple comparisons were corrected by FDR or Dunnett's multiple comparison correction (*$P < 0.05$, **$P < 0.01$, ***$P < 0.001$, and ****$P < 0.0001$). OCR, oxygen consumption rate.

(fig. S5K), indicating significantly improved liver function compared to control mice. Plasma cholesterol (fig. S5L), LDL (fig. S5M), HDL (fig. S5N), triglycerides (fig. S5O), and albumin (fig. S5P) were not changed by expression of scFv-E06. Total hepatic triglyceride levels were not affected by AAV8-E06 (Fig. 5G); however, histological analysis by H&E and Oil red O staining revealed a decrease in average lipid droplet size and a concomitant increase in lipid droplet number (Fig. 5, H and I) in the livers of mice expressing scFv-E06, a pattern of lipid droplet morphology suggestive of improved liver health (*6*).

To examine whether intervention with AAV8-scFv-E06 affects hepatic gene expression in mice with established steatosis during NASH progression, we performed RNA-seq in bulk liver tissue from mice that were treated with either AAV8-scFv-E06 or AAV8-GFP. Notably, 701 genes (154 up-regulated and 547 down-regulated in scFv-E06–expressing mice) were differentially expressed (fold change > 1.5, FDR < 0.05) between AAV8-scFv-E06– and AAV8-GFP–treated mice. EnrichR and GO Pathway Analysis for Biological Processes revealed that the most significantly down-regulated GO term in the scFv-E06–expressing group was "Extracellular Matrix Organization," indicating down-regulation of genes associated with matrix production and consequently hepatic fibrosis (Fig. 5J). In addition, "Regulation of Cell Migration," "PDGFR Signaling Pathway," "Cell Matrix Adhesion," and "Regulation of Macrophage Cytokine Production" were all down-regulated, suggesting a reduced fibrotic and inflammatory tone in the liver of mice expressing scFv-E06. Extracellular matrix protein (ECM) gene regulation was confirmed by qRT-PCR. Overall, expression of a panel of ECM proteins was significantly lower in livers of scFv-E06–expressing mice (fig. S6). To assess the extent of hepatic fibrosis in mice expressing scFv-E06, we quantified picrosirius red staining in livers after 20 weeks of FPC diet, which revealed a trend toward a decrease in positive staining in mice that received intervention with scFv-E06 (Fig. 5K). Liver hydroxyproline concentration was significantly increased in GFP-expressing mice fed FPC diet for 20 weeks compared to chow (Fig. 5L), and the FPC-induced increase in hydroxyproline was attenuated by intervention with scFv-E06 after 6 weeks on diet (Fig. 5M). Together, these data demonstrate that intervention with scFv-E06 in mice with established steatosis protects mice from further diet-induced liver damage and hepatic fibrosis.

Biologically active oxidized phospholipids are reduced by interventional expression of scFv-E06 during the progression to hepatic fibrosis

To identify OxPC species that are affected by intervention with AAV8-scFv-E06 in the plasma of mice during the progression to fibrosis, we performed LC-MS as described above, using the in silico–predicted and in vitro–validated compound list (Fig. 2, I and J). We identified 29 OxPC analytes or groups of isobaric compounds and 6 nonoxidized PCs in the plasma of mice with hepatic fibrosis (Fig. 6A). A similar but less pronounced reduction in OxPCs was observed in the liver of scFv-E06 mice compared to GFP controls (sup. Fig. 6B). In addition, there was a slight but statistically significant decrease in nonoxidized PCs in the scFv-E06 liver (fig. S6B). In the plasma, the majority of both truncated and full-length OxPCs were significantly decreased in scFv-E06–expressing mice and included several previously described biologically active compounds containing specific functional groups. Among decreased truncated OxPC species were the carboxylic acid–containing 1-palmitoyl-2-glutaryl-*sn*-glycero-3-phosphocholine (PGPC; *m/z* 610) as well as PazPC (*m/z* 666) (*45*, *46*), a group of γ-keto/hydroxy OxPCs [C32H60NO10P

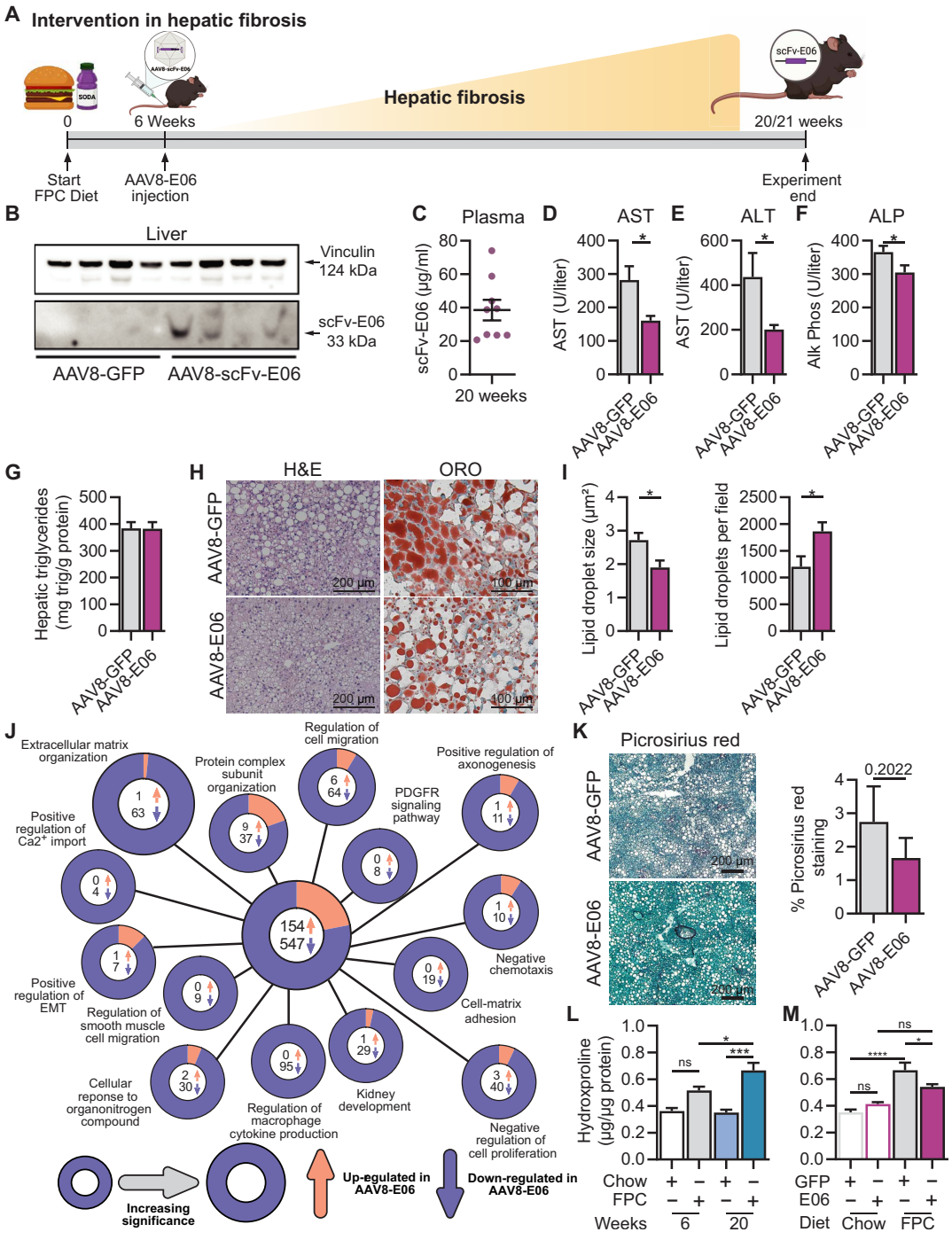

Fig. 5. Passive genetic immunization against oxidized phospholipids inhibits liver fibrogenesis. (**A**) Schematic of experimental design. Mice were challenged with FPC diet for 6 weeks. After 6 weeks, mice were injected with AAV8-GFP or AAV8-E06 and fed FPC diet for an additional 14 weeks (total: 20 weeks) (created with BioRender.com). (**B**) Expression of scFv-E06 in mouse liver 14 weeks after injection. (**C**) scFv-E06 titer concentrations were estimated in plasma by competitive sandwich ELISA. (**D**) Plasma AST, (**E**) ALT, and (**F**) ALP levels were decreased in mice expressing scFv-E06 ($n = 6$). (**G** and **H**) H&E and ORO staining revealed no difference in hepatic triglycerides with an (**I**) increased droplet size but reduced number in mice expressing scFv-E06 (GFP, $n = 6$; scFv-E06, $n = 6$; 15 fields of view per biological replicate). (**J**) Pathway analysis of differential gene expression in bulk liver tissue identified 701 genes (154 up-regulated/547 down-regulated) that were significantly regulated by scFv-E06 expression (GFP, $n = 3$; scFv-E06, $n = 3$; fold change > |1.5| and FDR < 0.05). Extracellular matrix organization was the most significantly down-regulated pathway in scFv-E06–expressing mice. (**K**) Representative picrosirius red staining of livers from mice expressing GFP or scFv-E06 after 20 weeks of FPC diet. (**L**) Hydroxyproline concentration was measured in liver tissue from mice fed chow or FPC diet for 6 or 20 weeks. (**M**) Liver hydroxyproline concentration was decreased in mice expressing scFv-E06 after 20 weeks on FPC diet compared to GFP-expressing controls. Quantification of picrosirius red confirmed reduced staining in scFv-E06 mice ($n = 4$). Statistical significance was determined by one-way ANOVA, two-way ANOVA, Spearman's correlation, and Student's *t* test with Dunnett's multiple comparisons correction (*$P < 0.05$). Statistical outliers were excluded using ROUT test with $Q = 2\%$.

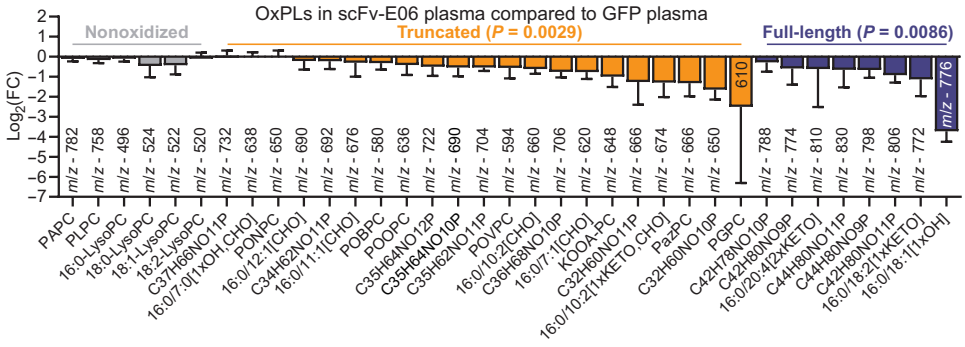

Fig. 6. scFv-E06 expression decreases plasma OxPL levels in mice with hepatic fibrosis. OxPL levels were measured in the plasma by LC-MS. Both truncated and full-length OxPLs were significantly reduced by scFv-E06 expression. Nonoxidized phospholipids were unaffected by scFv-E06 expression. Statistical significance was determined by two-way ANOVA. Multiple comparisons were corrected by FDR.

(isobaric group containing HOOA-PC), *m/z* 650]; HODA-PC [1-palmitoyl-2-(9-hydroxy-12-oxo-10E-dodecenoyl)-*sn*-glycero-3-phosphocholine] (*m/z* 706); KOOA-PC (*m/z* 648); C32H60NO11P (isobaric group containing HOdiA-PC) (*m/z* 666) (*22*, *41*), the aldehyde-containing POVPC (*m/z* 594) (*42*), POBPC (*m/z* 580) (*43*), and POOPC (*m/z* 636) (Fig. 6A) (*44*, *45*). Among the most substantially reduced full-length OxPCs were HOME-PC (*m/z* 776) and three isobaric species containing HODE-PC (*m/z* 774), an isobaric group with an *m/z* of 798, containing HETE-PC (*61*), and an isobaric group with an *m/z* of 830, containing isoprostane-PC (Fig. 6A) (*48*, *49*). The predicted structures of the identified compounds with corresponding *m/z* values are shown in table S3.

Selectivity of scFv-E06 for oxidized PCs was further illustrated by the fact that expression of scFv-E06 specifically decreased levels of truncated and full-length OxPC species, while none of the other lipid classes were significantly affected, as demonstrated by comparison of the overall plasma lipidome between scFv-E06– and GFP-expressing mice after either 6 (steatosis) or 20 (fibrosis) weeks of FPC feeding (fig. S7A). Comparing the OxPC profiles at the different stages of disease progression not only demonstrated that individual OxPC species are differentially affected by scFv-E06 but also indicated that levels of OxPCs may be selectively affected during disease progression.

To study the changes in the levels of the different OxPC classes during the progression from hepatic steatosis to fibrosis, we compared OxPC levels in control mice (expressing AAV8-GFP) that had been fed FPC diet for 6 and 20 weeks to their chow-fed counterparts. Of the nonoxidized species, PAPC and 16:0 LysoPC were decreased after 6, but not 20, weeks on diet, while PLPC and 18:0, 18:1, and 18:2 LysoPC were increased after both 6 and 20 weeks on FPC diet (Fig. 7A). Of the truncated OxPC species, levels of a subset of aldehyde-containing OxPCs, including POVPC, were lower at both 6 and 20 weeks, while carboxylic acid–containing and other aldehyde-containing OxPCs, including POBPC, were increased in response to FPC diet (Fig. 7A).

Full-length OxPC species were differentially regulated at different time points. At 6 weeks, levels of 16:0/18:1[1xOH] trended to be lower compared to chow but higher at 20 weeks. 16:0/18:2[1xKETO] was higher at 6 weeks compared to chow and lower at 20 weeks. Isobaric groups C44H80NO10P and C42H80NO9P, which contain HETE-PCs and HODE-PCs, were significantly higher at 20 weeks. Together, these data show that levels of plasma nonoxidized and individual OxPC species are differently regulated at defined stages of NAFLD progression.

Comparison of OxPCs that were affected by AAV8-scFv-E06 in the plasma of mice at the initiation of hepatic steatosis (Fig. 2K) and during the progression to hepatic fibrosis (Fig. 6A) revealed 28 OxPC species that were decreased in both settings, while 1 OxPC was uniquely identified in hepatic steatosis and 7 OxPC species were uniquely detected in mice with hepatic fibrosis (fig. S7B). Of the seven unique species identified in hepatic fibrosis, four were decreased by more than 50% by scFv-E06. These four species include two previously identified biologically active OxPCs: KOOA-PC and the isobaric group C32H60NO11P containing HOdiA-PC (*41*).

To elucidate at which stage of disease progression these identified OxPC species may exert pathologic activity, we took a closer look at the timeline of scFv-E06–mediated reduction of their plasma levels. The aldehyde-containing species POVPC, POOPC, and 16:0/7:1[CHO] were preferentially reduced by scFv-E06 after 6 weeks on FPC diet (Fig. 7B), implying a role in the initiation of hepatic steatosis. To test whether aldehyde-containing OxPCs affect hepatocyte lipid storage, we treated AML12 hepatocytes with POVPC for 48 hours and assessed lipid droplet size and number per cell. POVPC significantly increased the number and size of lipid droplets (Fig. 7C). On the other hand, carboxylic acid–containing OxPC species (PazPC and C35H62NO11P) were affected by scFv-E06 predominantly after 20 weeks of FPC diet (Fig. 7D), implying a role for these compounds in NAFLD progression to NASH. Treatment of AML12 cells with PGPC (a carboxylic acid–containing OxPC) significantly decreased maximum oxygen consumption rate (Fig. 7E) and increased lipid droplet size and number in a concentration-dependent manner (fig. S8, A and B). Of the γ-keto/hydroxy OxPC species, the levels of KOOA-PC and isobaric group C32H60NO10P (containing HOOA-PC) were reduced by scFv-E06 specifically at 20 weeks of FPC diet (Fig. 7F). Treatment of AML12 hepatocytes for 4 hours with 1-palmitoyl-2-(5-keto-6-octene-dioyl)-*sn*-glycero-3-phosphocholine (KOdiA-PC), a representative γ-keto/hydroxy OxPC, significantly decreased maximum oxygen consumption rate of hepatocytes in a concentration-dependent manner (Fig. 7G). These data show that identified truncated OxPC species that are reduced by scFv-E06 promote a hepatocyte phenotype in vitro that is observed in hepatic steatosis and steatohepatitis.

Hepatic stellate cells are the primary cell niche in the liver that produce fibrotic matrix in response to liver injury (*15*, *62*). To determine

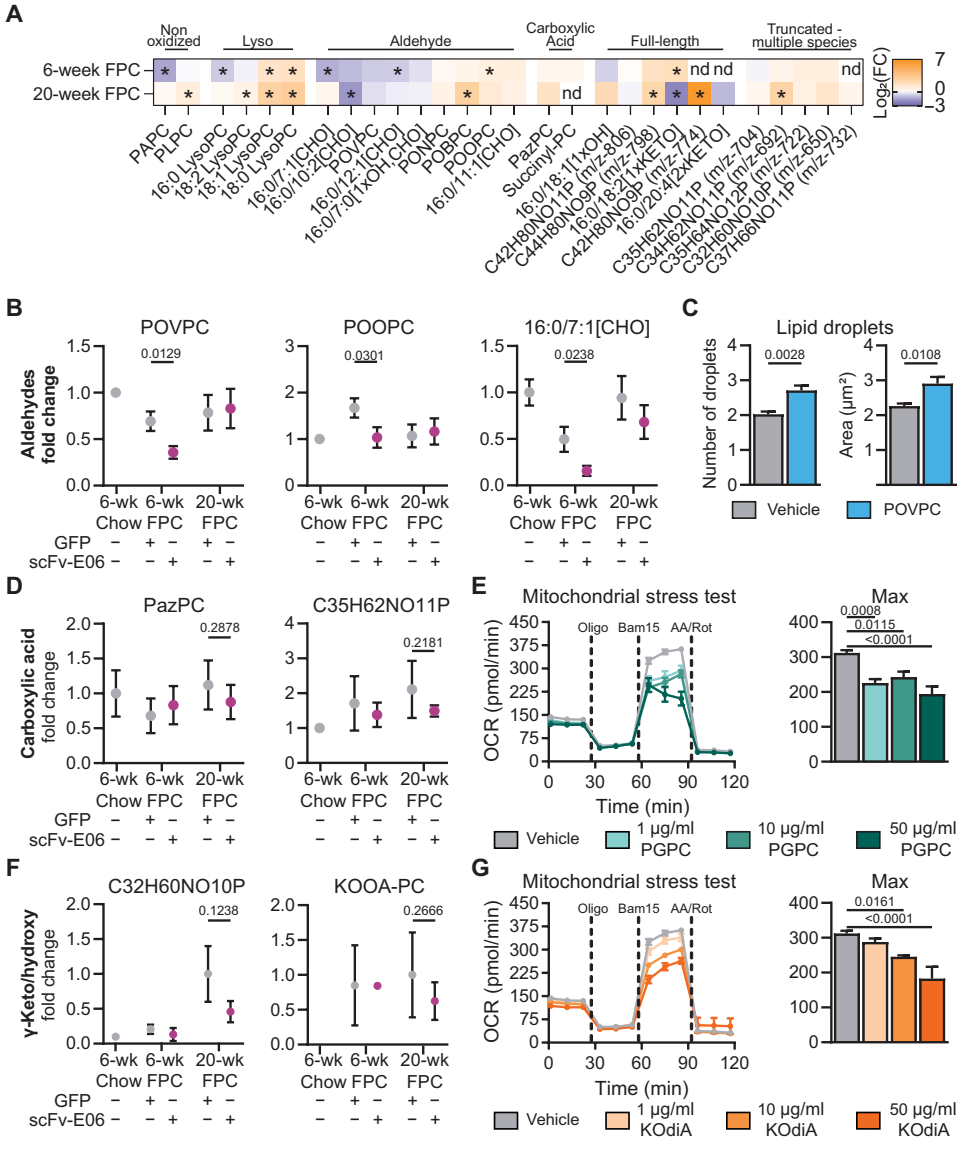

Fig. 7. Bioactive oxidized phospholipids are differentially regulated during hepatic steatosis and fibrosis. (**A**) Semiquantitative analysis of OxPL species normalized to their chow counterparts demonstrates a complex, pathology-specific pattern. (**B**) Aldehyde-containing OxPLs, POVPC (6-week Chow GFP, $n = 3$; 6-week FPC GFP, $n = 7$; 6-week FPC scFv-E06, $n = 6$; 20-week FPC GFP, $n = 10$; 20-week FPC scFv-E06, $n = 10$), POOPC (6-week Chow GFP, $n = 3$; 6-week FPC GFP, $n = 7$; 6-week FPC scFv-E06, $n = 6$; 20-week FPC GFP, $n = 10$; 20-week FPC scFv-E06, $n = 10$), and 16:0/7:1[CHO] (6-week Chow GFP, $n = 3$; 6-week FPC GFP, $n = 5$; 6-week FPC scFv-E06, $n = 5$; 20-week FPC GFP, $n = 7$; 20-week FPC scFv-E06, $n = 8$), were decreased by scFv-E06 expression at 6 weeks. (**C**) POVPC, a representative of the aldehyde class, increased lipid droplet size and number after 48 hours in AML12 hepatocytes ($n = 4$). (**D**) Carboxylic acid–containing OxPLs were decreased by scFv-E06 after 20 weeks on diet (6-week Chow GFP, $n = 3/1$; 6-week FPC GFP, $n = 7/4$; 6-week FPC scFv-E06, $n = 5/2$; 20-week FPC GFP, $n = 9/5$; 20-week FPC scFv-E06, $n = 9/6$). (**E**) PGPC, a representative of the carboxylic acid class, decreased maximum oxygen consumption of AML12 hepatocytes after 4 hours ($n = 8$; 50 μg/ml, $n = 6$). (**F**) γ-Keto/hydroxy–containing OxPLs were decreased after 20 weeks on diet (6-week Chow GFP, $n = 1/0$; 6-week FPC GFP, $n = 5/2$; 6-week FPC scFv-E06, $n = 2/1$; 20-week FPC GFP, $n = 9/2$; 20-week FPC scFv-E06, $n = 8/4$), and (**G**) KOdiA-PC, a class representative, decreased maximum oxygen consumption in AML12 hepatocytes in a dose-dependent manner ($n = 8$). Statistical significance was determined by Student's *t* test.

whether individual OxPC species that were targeted by scFv-E06 could activate hepatic stellate cells, we challenged LX-2 human hepatic stellate cells with OxPAPC, full-length OxPCs, truncated OxPCs, POVPC, or KOdiA-PC. Treatment of LX-2 hepatic stellate cells for 4 hours with KOdiA-PC, OxPAPC, or POVPC significantly decreased maximum oxygen consumption rate of hepatic stellate cells (fig. S8C).

Previously, *Hmox1* has been implicated in fibrotic activation of hepatic stellate cells (*63*). We found that truncated OxPCs and OxPAPC increased the expression of the NRF2-dependent genes *Hmox1* and *Gclm* in LX-2 human hepatic stellate cells (fig. S8D).

Together, these data demonstrate that expression of scFv-E06 decreases levels of individual OxPCs in plasma. FPC diet results in multivariate changes in the OxPC lipidome, which suggest complex

regulation of OxPC species in pathology. Identified OxPC species that were decreased by scFv-E06, including aldehyde-, carboxylic acid–, and γ-keto/hydroxy–containing OxPCs, regulate metabolism and gene expression in hepatocytes and hepatic stellate cells, suggesting that they are actively involved in the initiation and progression of hepatic steatosis and fibrosis (Fig. 8A).

DISCUSSION

Here, we examined a potential therapeutic application of AAV-mediated hepatic expression of the oxidized phospholipid-binding antibody fragment scFv-E06 for the prevention of the initiation of NAFLD and, independently, of the progression to NASH and hepatic fibrosis. We show that AAV8-mediated gene transfer of scFv-E06 is sufficient to express scFv-E06 in a cre-dependent manner in the liver, which by itself leads to secretion of scFv-E06 protein into the plasma. Expression of scFv-E06 in mice fed a chow diet did not alter normal mouse physiology, which provided an excellent tool to interrogate the effect of OxPCs on diet-induced NAFLD initiation and disease progression, without secondary effects on mouse physiology or development, while providing a way to regulate dosing and timing of expression. We demonstrated that hepatic expression of scFv-E06 before the start of FPC diet feeding resulted in a marked reduction in individual OxPC species in plasma, which was sufficient to protect mice from diet-induced hepatic steatosis. Given the efficacy of this model in eliminating plasma OxPCs and subsequent protection from diet-induced hepatic steatosis, we leveraged the flexibility of virus-mediated gene transfer to intervene therapeutically with scFv-E06 expression after the establishment of diet-induced hepatic steatosis. We showed that, in a clinically relevant intervention model, scFv-E06 expression prevented further diet-induced liver damage and hepatic fibrosis independent of obesity and insulin resistance. Separately, scFv-E06 expression was sufficient to reduce a variety of OxPC species in plasma. At present, it is unclear whether reduction of OxPCs is protective in NASH pathogenesis or simply a biomarker of the therapeutic effect of scFv-E06. Using mass spectrometry, we identified individual OxPC species that are decreased by expression of scFv-E06 in mice. Identified OxPC species induced gene expression and metabolic changes in hepatocytes and stellate cells in vitro. These data suggest that plasma OxPCs regulate liver function uniquely at different stages of disease progression. For instance, expression of scFv-E06 before the start of FPC diet protected mice from hepatic steatosis, while intervention with scFv-E06 after established steatosis did not reduce lipid burden in the liver. Despite no overall decrease in lipid burden, scFv-E06–expressing mice had smaller hepatic lipid droplets. This may suggest that OxPCs are involved in dysregulation of cellular lipid storage vital to initiation of hepatic steatosis but not maintenance of steatosis. Together, this suggests that lowering the concentration of identified plasma OxPC species is necessary for preventing hepatic steatosis and progression to fibrosis in a normolipidemic mouse model of diet-induced NAFLD without genetic lipodystrophy. Using this approach, we provide the first evidence that therapeutic intervention after the development of diet-induced steatosis with virus-induced scFv-E06 expression halts progression to hepatic fibrosis in a clinically relevant model of NAFLD.

The natural IgM E06 has been shown to recognize oxidized products of PAPC in vitro and has been used clinically to assess total plasma OxPC levels (*36*, *64*). However, individual OxPC species that are eliminated by E06 in vivo had not been identified. Our findings demonstrate that scFv-E06 recognizes a variety of OxPC species irrespective of the type of oxidative modification or *sn*-1 position acyl-chain length while not affecting plasma levels of nonoxidized lipids in vivo. Further research is necessary to investigate binding affinities and specificity of scFv-E06 among OxPC species and to demonstrate the potency of scFv-E06 as a potential therapeutic in the context of NAFLD and other oxidative stress–induced diseases.

Oxidized phospholipids have previously been shown to regulate numerous cellular functions and biological processes (*20*, *21*, *27*, *29*, *30*, *34*, *35*, *38*, *65*–*67*). We show that individual OxPCs that are targeted by scFv-E06 activate hepatocytes, resulting in up-regulation of the evolutionarily conserved NRF2-dependent antioxidant program and metabolic dysregulation. While both truncated

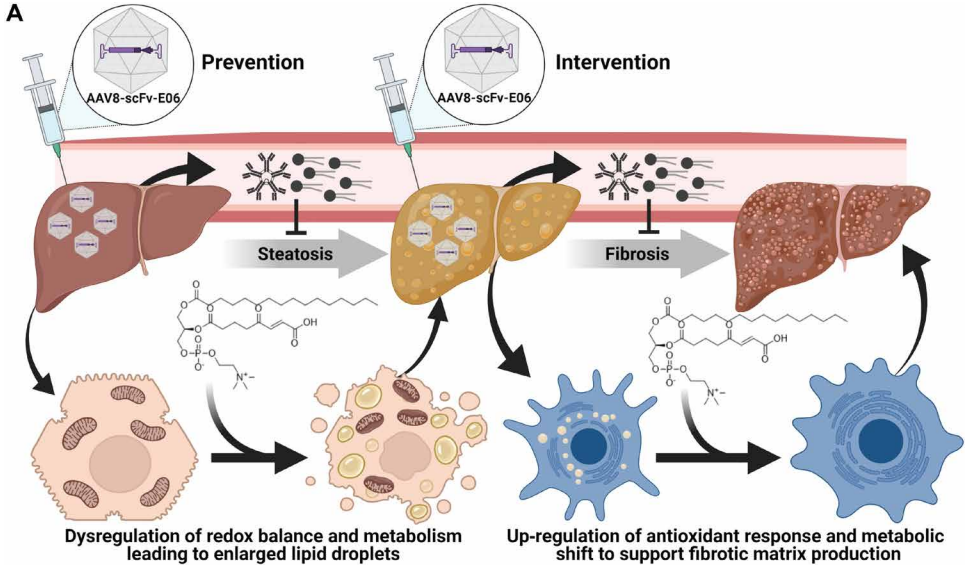

Fig. 8. scFv-E06 expression protects mice from hepatic steatosis, and intervention with viral expression of scFv-E06 halts disease progression. (Created with BioRender.com)

and full-length OxPCs up-regulated genes related to oxidative stress, only truncated OxPCs up-regulated prosteatotic anabolic pathways including cholesterol biosynthesis. Induction of de novo cholesterol synthesis leading to cholesterol accumulation has been shown to promote transition from hepatic steatosis to NASH (*68*) and may be one mechanism through which OxPCs promote disease progression. Furthermore, identified OxPCs inhibited mitochondrial oxygen consumption in hepatocytes, consistent with a switch to an anabolic cellular phenotype, and resulted in increased lipid droplet formation, a hallmark of hepatic steatosis (*6*). Together, our findings demonstrate that hepatocytes recognize and respond to OxPCs, and treatment of hepatocytes in vitro with truncated OxPCs phenocopies pathological alterations in mitochondrial bioenergetics and lipid droplet regulation seen during the development of hepatic steatosis. Differences in regulation of the transcriptome in mice expressing scFv-E06 compared to GFP during development of diet-induced hepatic steatosis may give key insights into the mechanisms by which OxPCs drive early metabolic changes in hepatocytes that promote disease initiation.

Levels of truncated OxPCs containing a γ-keto/hydroxy functional group were also reduced by scFv-E06 in vivo. Several biological functions have been described for these lipids (*22*, *41*); however, it is unknown if γ-keto/hydroxy–containing OxPCs play a role in NASH and hepatic fibrosis. Here, we show that KOdiA-PC inhibits mitochondrial oxygen consumption and extracellular acidification rate in hepatic stellate cells. In addition, truncated OxPCs induced expression of the NRF2-dependent genes *Hmox1* and *Gclm* in hepatic stellate cells. These data demonstrate that individual truncated OxPCs that are targeted by scFv-E06 regulate hepatic stellate cell bioenergetics and gene expression and may polarize the cells toward a redox-regulatory state.

Plasma levels of both truncated and full-length OxPC species were significantly reduced by scFv-E06 either at the initiation of hepatic steatosis or during the progression to hepatic fibrosis. These data demonstrate that scFv-E06 specifically recognizes individual oxidized phosphorylcholine phospholipids in vivo, without affecting levels of OxPCs or lyso-PCs, which builds on previous studies that have demonstrated similar specificity of E06 in vitro (*37*, *69*). We identified one unique OxPC species in the setting of hepatic steatosis and seven unique OxPC species in the setting of hepatic fibrosis that are targeted by scFv-E06. Identification of specific OxPC species that are eliminated by scFv-E06 during the different stages of disease progression suggests that plasma OxPCs could serve as noninvasive biomarkers of NAFLD severity. In human plasma, oxidized phospholipids are carried on LDLs and previous work has shown that the ratio of OxPCs to apoB-100 or apo(a) correlates with cardiovascular disease, calcific aortic valve disease, and aortic valve stenosis (*70*, *71*). These risk factors are assessed from lipoprotein-bound OxPCs. Our method assesses free or "unconjugated" OxPCs. Considering the pathologic role of OxPCs in NAFLD and the dearth of viable noninvasive biomarkers for NASH, analysis of individual unconjugated OxPC species may provide an additional diagnostic metric and possible alternative to more invasive techniques like liver biopsy.

In this study, we limited our analysis to validated OxPC species predicted by LPPTiger (*40*) and identified in air- and copper-oxidized PAPC and PLPC. Combining an in silico–based approach with in vitro validation allowed us to assess 83 validated analytes (individual lipid species and isobaric groups); however, this accounts for only a fraction of the possible oxidation species present in vivo. Given the numerous possible oxidative modifications that can arise as products of oxidation, many oxidized phospholipid species are isobaric requiring additional metrics to accurately distinguish individual species. In this study, we leverage both mass and chromatographic retention time to distinguish between OxPC species. Consequently, isobaric species with similar retention times were not uniquely identified. Future studies are necessary to identify unique fragmentation patterns for isobaric species that overlap chromatographically to confidently identify each species. In addition, expanding the OxPL panel to include not only other OxPC species but also phospholipids with other head groups, which have been shown to play critical roles in diverse biological processes ranging from thrombus formation (*72*) to ferroptosis (*31*) and apoptosis (*73*), is essential to understand how OxPLs regulate complex pathologies. Currently, our method is limited to semiquantitation of OxPL species because of the lack of deuterated and nondeuterated OxPL standards. Synthesis of OxPL standards is necessary to directly quantify the concentration of pathology-driving OxPLs in the plasma. In addition, our method measures OxPCs that can be isolated by liquid-liquid organic extraction, which likely reflects the free OxPC lipidome as it is likely that some electrophilic lipid species bind covalently with proteins. For example, POVPC has previously been shown to bind manganese superoxide dismutase (*35*).

We demonstrate that scFv-E06 expression lowers levels of OxPCs in the plasma, which are necessary for pathogenesis of both hepatic steatosis and fibrosis. Furthermore, although OxPC levels are lowered by scFv-E06 expression as measured by mass spectrometry, the mechanism through which this occurs remains unclear. We propose two possible mechanisms that will require further study: (i) elimination from the biological system by enzymatic activity or excretion or (ii) masking of OxPC inhibiting their biological effects. Distinguishing whether it is necessary to lower both plasma and liver OxPC species to inhibit disease progression as well as understanding the mechanism through which OxPC species are lowered by scFv-E06 expression will provide a deeper understanding of the role of OxPC species in NAFLD pathology and guide future therapeutic approaches.

In conclusion, our study establishes the translational potential of plasma OxPC elimination using AAV8-mediated gene transfer of scFv-E06 in a clinically relevant NAFLD model. This approach to target plasma OxPCs provides multimodal control over oxidized lipid-driven pathologies. Temporal and spatial regulation of scFv-E06 expression will allow for exploration of previously inaccessible OxPC-mediated biology and pathology. Last, assessment of plasma levels of individually identified, pathology-driving OxPC species during NAFLD initiation and progression may lead to the discovery of urgently needed noninvasive biomarkers.

MATERIALS AND METHODS

Study design

The objective of this study was to determine whether AAV8-induced expression of scFv-E06 was sufficient to prevent hepatic steatosis by decreasing plasma OxPCs, and further to intervene in progression from hepatic steatosis to hepatic fibrosis by decreasing plasma OxPCs. Group size was selected on the basis of similar studies previously reported in the literature. The number of mice included in all groups was selected before the start of study and not altered throughout the study. End points to assess hepatic steatosis (6 weeks on diet)

and hepatic fibrosis (20 weeks on FPC diet) were defined before the start of the study. Mice were randomized into each group based on body mass and excluded from analysis if they did not gain weight in response to FPC diet feeding. The study was blinded for the duration of FPC diet feeding and after for all subjective analyses. All animal experiments were approved by the University of Virginia's Animal Care and Use Committee (protocol #3444). For each analysis, statistical outliers were assessed using the robust regression and outlier removal method (ROUT) method ($Q = 5\%$). Outliers were excluded from final analysis and determination of statistical significance. All in vitro experiments were conducted, at minimum, in duplicate, and representative results were reported.

Generation of AAV8-scFV-E06

We developed a cre-dependent adeno-associated viral construct for expression of scFv-E06. The E06 coding region was synthesized by GenScript from the publicly available, published sequence (Piscataway, NJ, USA), containing a C-terminal myc- and His-tag and flanking 5′ Mlu I and 3′ Nhe I restriction sites. This DNA fragment was then cloned into the unique Nhe I–Asc I restriction sites of pAAV-EF1a-double floxed-hChR2(H134R)-EYFP-WPRE-HGHpA (gift from K. Deisseroth—Addgene, plasmid #20298). The subsequent construct contained the scFv-E06 fusion in the inverse orientation from the EF1a promoter. Cre recombinase expression then reverses the orientation of scFv-E06 and allows expression. AAV viral particles using serotype 8 were then prepared by the University of Pennsylvania Vector Core Facility.

Mice

B6.Cg-Speer6-ps1$^{Tg(Alb\text{-}cre)21Mgn}$/J (The Jackson Laboratory, 003574) (Alb-cre) were obtained from The Jackson Laboratory (Bar Harbor, ME) and housed in the Pinn vivarium at the University of Virginia Center for Comparative Medicine. Unless otherwise stated, animals were maintained in pathogen-free housing with a 12-hour light/dark cycle with ad libitum access to food and water. All animal experiments were approved by the University of Virginia's Animal Care and Use Committee (protocol #3444). To assess the impact of scFv-E06 on hepatic steatosis, 6-week-old mice were injected with either AAV8-GFP (UNC Vector Core) or AAV8-scFv-E06 [10^{11} genome copies/100 μl of sterile phosphate-buffered saline (PBS)]. Mice, 8 weeks of age, were fed a high FPC diet (Teklad TD.190142) supplemented with 4.2% glucose (Thermo Fisher Scientific, D12-500)/fructose (Thermo Fisher Scientific, L95-500) water (55%/45%, w/w) for 6 weeks. At the end of the experiment, mice were euthanized via CO_2 inhalation and cardiac puncture. To assess the impact of scFv-E06 expression on fibrosis and whether expression of scFv-E06 after the onset of hepatic steatosis could mitigate progression to hepatic fibrosis, mice, 6 weeks of age, were fed FPC diet for 6 weeks. After 6 weeks of feeding, mice were injected via tail vein with AAV8-GFP or AAV8-scFv-E06. Mice continued FPC diet for an additional 14 weeks, at which point they were euthanized via CO_2 inhalation. Control mice were fed chow diet (Teklad 7912).

Histology

PBS-perfused liver tissue was either fixed in 10% formalin (w/v) for 24 hours and transferred to 200 proof ethanol or cryopreserved in NEG-50 (Richard Allan Scientific, 6502) and stored at −80°C. Tissue samples were processed for histology at the Robert M. Berne Cardiovascular Research Center Histology Facility at the University of Virginia. Briefly, samples were embedded in paraffin, and 10-μm serial sections were stained with H&E, picrosirius red, or Oil red O. Images were collected using Olympus BX51 or Leica Thunder with a total internal reflection fluorescence microscope operating in bright field. Picrosirius red counterstained with Fast Green was quantified using ImageJ (*74*) to assess stained area in three sections from the liver tissue of each mouse. Positive staining was determined by thresholding while blinded after exclusion of perivascular collagen: Threshold settings were kept constant for all samples assessed.

Triglyceride assay

Hepatic triglyceride concentration was quantified using triglyceride colorimetric assay (Pointe Scientific, T7532500). Liver tissue (20 to 30 mg) was lysed in 400 μl of 0.6% NaCl using Qiagen TissueLyser II (30 Hz for 15 min). Samples were diluted 1:4 in 0.6% NaCl and mixed with 4.4 parts chloroform (EMD UN1888/Fisher Scientific, C607-1) and 2.2 parts methanol (Sigma-Aldrich, 646377-1 L). Samples were vortexed vigorously and centrifuged for 10 min at 3000*g* to accelerate phase separation. The organic phase (500 μl) of each sample was transferred to a new tube and dried under N_2 purge. The dried organic phase was resuspended in 200 μl of 95% ethanol (200 μl) (Fisher Scientific, 04-0355-223). Samples from mice on FPC diet were diluted 1:5 in 95% ethanol. Assay was conducted in triplicate according to the manufacturer's recommendations.

Plasma liver biomarkers

Whole blood was collected from mice after euthanasia via cardiac puncture and dispensed into heparin-coated plasma collection tubes (Becton Dickinson, 365985) and stored on ice. Plasma was separated via centrifugation at 2000*g* for 15 min at 4°C. Plasma was stored at −80°C. Plasma was diluted 1:1 in sterile 0.9% saline, and liver biomarkers were analyzed by UVA Clinical Laboratories.

Cell culture

AML12 murine hepatocytes (American Type Culture Collection, CRL-2254) were cultured in Dulbecco's modified Eagle's medium (DMEM):F12 supplemented with 10% fetal bovine serum (FBS) (R&D Systems, S12450/Atlanta Biologicals, S11150) and 1% Anti-Anti (Gibco, 15240-062) and grown at 37°C with 5% CO_2. Cells were passaged when they reached 90% confluency using 0.5% trypsin (Gibco, 15400-054). LX-2 human hepatic stellate cells (MilliporeSigma, SCC064) were cultured in DMEM supplemented with 2% FBS (R&D Systems,S12450/Atlanta Biologicals, S11150) and 1% penicillin-streptomycin (Gibco, 15140-122) and grown in DMEM (Gibco, 11965-092) at 37°C with 5% CO_2. Cells were passaged when they reached 90% confluency using 0.25% trypsin (Gibco, 25200-056). For all experiments using the LX-2 cell line, cells were cultured on Matrigel (83 μg/ml) (Fisher Scientific, CB-40230) for 24 hours in DMEM containing 1% penicillin-streptomycin before the start of the experiment.

Mitochondrial and glycolytic stress test

XF24 seahorse bioenergetics assay

AML12 hepatocytes (75,000 cells per well) were plated in complete medium in XF24 cell culture microplates (Agilent, 100777-004) and allowed to settle overnight. The following day, cells were treated for 4 hours with oxidized phospholipids (10 to 100 μg/ml) in DMEM:F12 supplemented as described. At the end of the experimental treatment, the medium was removed and replaced with assay appropriate

medium: mitochondrial stress test medium (Corning, 50-003-PB). Oxygen consumption was measured via mitochondrial stress test. The rate of PO_2 (partial pressure of oxygen) consumption was measured every 10 min for a 4-min interval preceded by a 3-min mixing and 3-min waiting interval. Oligomycin A (Sigma-Aldrich, 75351) (0.91 μM), BAM15 (Cayman Chemical Company 17811) (1.667 μM), antimycin A (Sigma-Aldrich, A8674) (7.692 μM), and rotenone (Sigma-Aldrich, R88751G) (7.692 μM) were used to interrogate basal, reserve, and maximum oxygen consumption capacity.

XFe96 seahorse bioenergetics assay

AML12 hepatocytes were plated (25,000 cells per well) in complete medium in XFe96 cell culture microplates (Agilent, 101085-004) and incubated for 1 hour at room temperature before settling overnight at 37°C. The following day, cells were treated for 4 hours with oxidized phospholipids (10 to 100 μg/ml) in DMEM:F12 supplemented as previously described. After treatment, the medium was removed and replaced with assay appropriate medium: mitochondrial stress test medium (Corning, 50-003-PB) and glycolytic stress test medium (Sigma-Aldrich, D5030) supplemented with 143 mM NaCl (Thermo Fisher Scientific, S671-3) and 2 mM L-glutamine (Gibco, 25030-081). Oxygen consumption was measured via mitochondrial stress test. The rate of PO_2 consumption was measured every 10 min for a 4-min interval for 30 min before sequential challenge with (i) oligomycin A (Sigma-Aldrich 75351) (1 μM), (ii) BAM15 (Cayman Chemical Company, 17811) (2 μM), and (iii) antimycin A (Sigma-Aldrich, A8674) (10 μM) and rotenone (Sigma-Aldrich, R88751G) (10 μM). PO_2 consumption was measured as described previously to analyze basal, reserve, and maximum oxygen consumption capacity. Glycolytic rate was measured via extracellular acidification rate. The rate of pH change was measured every 10 min for a 4-min interval for 30 min before sequential challenge with (i) glucose (Sigma-Aldrich, D9434) (20 mM), (ii) oligomycin A (Sigma-Aldrich, 75351) (1 μM), and (iii) 2-deoxyglucose (Sigma-Aldrich, D8375) (80 mM) to interrogate basal, reserve, and stressed glycolytic rate.

Quantitative real-time PCR

In vitro

RNA was isolated from cells lysed in RLT lysis buffer using the RNeasy Mini Kit (Qiagen 74106). The manufacturer's recommendations were followed for RNA isolation. RNA quantity and purity were analyzed by spectrometric analysis. cDNA was synthesized from 250 ng of total RNA using an iScript cDNA synthesis kit (Bio-Rad, 1708891) according to the manufacturer's recommendations. SensiMIX SYBR Green (Bioline, QT615-05) was used to quantify gene expression. Relative gene expression was calculated using the ΔΔCq method normalized to cyclophilin A in AML12 cells and *Hprt* in LX-2 cells.

Ex vivo

Liver tissue was stored at −80°C in RNAlater (Sigma-Aldrich, R0901) until analysis. Liver tissue was lysed using Qiagen TissueLyser II (30 Hz for 15 min) in RLT lysis buffer. The manufacturer's recommendations were followed for RNA isolation using the RNeasy Mini Kit. RNA quantity and purity were analyzed by spectrometric analysis (260/280, >1.8 and <2.2; 260/230, >1.8 and <2.2). cDNA was synthesized from 250 ng of total RNA using an iScript cDNA synthesis kit according to the manufacturer's recommendations. SensiMIX SYBR Green was used to quantify gene expression. Relative gene expression was calculated using the ΔΔCq method normalized to β-2-microglobulin. Primer sequences were generated using NCBI Primer Blast and span an exon-exon junction to ensure mRNA specificity and synthesized by Eurofins or Integrated DNA Technologies (table S4).

Air oxidation of PAPC

One milligram of PAPC (Avanti Polar Lipids, 850459C) was dried in a 13 × 100 borosilicate glass tube (Corning, 99445-13) with nitrogen, covered loosely with aluminum foil to allow gas exchange, and oxidized by exposure to air for 7 to 12 days to generate the oxidized phospholipid mixture, OxPAPC. Level of oxidation was monitored by LC-MS to maintain a consistent oxidation profile.

Copper oxidation of PLPC

Ten micrograms of PLPC (Avanti Polar Lipids, 850458) was transferred to a tube and dried under N_2. PLPC was resuspended in water containing CuCl (10.547 mM) and H_2O_2 (659 mM) and oxidized for 19 hours at 37°C to generate oxidized PLPC (OxPLPC). OxPLPC was extracted via liquid-liquid extraction using chloroform:methanol: water (1:1:1). Briefly, chloroform, methanol, and water were added to a glass tube. The extraction mixture was vortex vigorously and centrifuged at 805*g* for 10 min at 20°C. After centrifugation, the organic layer was transferred to a new a tube and dried under nitrogen. OxPLPC was resuspended in methanol.

Oxidized phospholipid quantification by LC-MS/MS

OxPL extraction from plasma

Plasma was collected from mice as described above and stored at −80°C in 50 μM butylated hydroxytoluene to prevent ex vivo oxidation. Twenty-five microliters of plasma was added to 1.975 ml of high-performance LC (HPLC) water (Tedia, WS2211-001) in a 13 × 100 borosilicate glass tube (Corning, 99445-13). Two milliliters of chloroform (EMD, UN1888/Fisher Scientific, C607-1) and 2 ml of methanol (Sigma-Aldrich, 646377-1L) containing 16.24 nM 1-palmitoyl-2-glutaryl-*sn*-glycerol-3-phosphocholine-*d6* (Cayman Chemical, 25746) were added and vortexed vigorously. Samples were centrifuged at 805*g* (20°C) for 10 min to accelerate phase separation. The organic phase was transferred to a new tube, and 2 ml of chloroform was added to the original tube. The extraction was repeated twice more for a total of three times. Samples were dried under nitrogen and resuspended in 200 μl of methanol and vortexed vigorously. Samples were transferred to sample vials for LC-MS analysis.

OxPL extraction from liver

Liver tissue was collected from mice and stored at −80°C in 50 μM in butylated hydroxytoluene to prevent ex vivo oxidation. Liver tissue was homogenized using Qiagen TissueLyser II (30 Hz for 15 min) in water. Thirty-five milligrams of tissue was used for extraction as described previously (see the previous section). Samples were resuspended in 200 μl of HPLC butanol (PHARMCO-AAPER 13050-03).

In silico phospholipid oxidation and method development

LPPTiger (*40*) was used to predict possible oxidation products of PAPC and PLPC. Oxidation level was set to level 3. Maximum modification site was set to 8, max keto was set to 8, max peroxy was set to 3, and max epoxy was set to 3. Nine hundred eighty oxidation species were predicted for PAPC, and 67 oxidation species were predicted for PLPC. Isobaric species were combined as a single analyte recording corresponding to the chemical formula. After combining isobaric species, there were 180 potential analytes for PAPC and 35 potential analytes for PLPC. Predicted analytes were validated by mass [<5-ppm (parts per million) variance from predicted mass] using PAPC oxidized by air and PLPC oxidized by copper (I) chloride.

Lipid analysis

Oxidized phospholipids were measured using Thermo Fisher Scientific Q Exactive coupled with a Vanquish UHPLC. Samples were separated by reversed-phase chromatography using C18 Phenomenex 4.6 μm × 100 mm with 69% methanol–31% water with 10 mM ammonium acetate (mobile phase A) and 50% methanol–50% isopropanol with 10 mM ammonium acetate (mobile phase B) at a flow rate of 0.5 ml/min using the following gradient: 0 to 4 min 0% B, 4 to 6 min 0 to 17.5% B, 6 to 12 min 17.5% B, 12 to 14 min 17.5 to 25% B, 14 to 21 min 25% B, 21 to 24 min 25 to 60% B, 24 to 33 min 60% B, 33 to 36 min 60 to 65% B, 36 to 40 min 65% B, 40 to 43 min 65 to 0% B, and 43 to 50 min 0% B. Q Exactive was operated in positive mode using parallel reaction monitoring mode with an inclusion list and the following settings: MS^2 resolution, 17,500; automatic gain control (AGC) target, 1×10^5; maximum injection time (IT), 100 ms; isolation window, 1.0 *m/z*; normalized collision energy, 27. Analyte detection was limited to inclusion list within a specified retention window determined from in vitro OxPAPC and PLPC. Peaks corresponding to individual oxidized phospholipid species or isobaric groups were identified using Xcalibur (v4.1) QuanBrowser based on mass (<5-ppm variance from predicted mass) and validated retentions times. Peak areas were normalized to PGPC-*d*6. Biological replicates were excluded from analysis for an individual analyte if the analyte was not detected.

Lipidomics LC-MS and data analysis

The plasma lipidome was assessed using Thermo Fisher Scientific Q Exactive coupled with a Vanquish UHPLC. Samples were separated by reversed-phase chromatography using Thermo Scientific Acclaim 120 (C18 5 μm 120 Å 4.6 × 100 mm) with 50% acetonitrile, 50% water, and 0.1% formic acid with 10 mM ammonium formate (mobile phase A) and 88% isopropanol, 10% acetonitrile, 2% water, and 0.02% formic acid with 2 mM ammonium formate (mobile phase B) at a flow rate of 400 μl/min using the following gradient: 0 to 4 min 30 to 60% B, 4 to 10 min 60 to 80% B, 10 to 15 min 80 to 90% B, 15 to 24 min 90 to 100% B, 24 to 27 min 100% B, 27 to 27.1 min 100 to 30% B, 27.1 to 31 30% B. Q Exactive was operated in positive mode and collected spectra using full MS data-dependent MS^2 mode with an inclusion list containing analytes in Splash Lipidomix Mass Spec Standard (Avanti, 330707) using the following settings: full MS settings: resolution, 35,000; AGC target, 1×10^5, max IT, 128 ms; scan range, 200 to 1500 *m/z*; dd-MS^2 settings: resolution, 17,500; AGC target, 2×10^5; max IT, 64 ms, loop count, 5; normalized collision energy (NCE), 40. Data were analyzed using LipidSearch (version 4.1.16) with the following settings: search—database: Q Exactive, precursor tolerance, 5.0 ppm; product tolerance, 8.0 ppm; alignment—alignment method, mean; retention time tolerance, 0.25 min. Samples were normalized to the internal standard PGPC-*d*6 to control for extraction efficiency.

In vitro quantification of lipid droplet

AML12 cells were fixed with 4% paraformaldehyde (diluted from 16%, Alfa Aesar, 43368-9M) and stained with Hoechst blue (Invitrogen, 953557) and Nile red (Invitrogen, N1142). Two images (Zeiss Axiovert 200 with QICAM Fast 1394), one of 4′,6-diamidino-2-phenylindole (DAPI) and one of Nile red, were taken at three locations in each well. Lipid droplet size and quantity were calculated from epifluorescent widefield micrographs using an ImageJ plugin, MRI Lipid Droplets (*75*). Lipid droplets were identified as areas larger than five pixels. MRI Lipid Droplets ImageJ plugin was used to identify nuclei in DAPI staining and count total cell number.

In vitro and ex vivo RNA-seq

In vitro

AML12 hepatocytes (100,000 cells per well) were treated with OxPAPC (100 μg/ml), truncated OxPAPC (100 μg/m), and full-length OxPAPC (100 μg/ml) for 4 hours. RNA was isolated using the RNeasy Mini Kit (Qiagen 74106). RNA quantity and purity were analyzed by spectrometric analysis (260/280, >1.8 and <2.2; 260/230, >1.8 and <2.2; RNA integrity number ≥ 8). cDNA libraries were generated using the NEBNext Ultra II Directional RNA Library Prep Kit (New England Biosciences, E7760S). cDNA library fragment size was verified using Bioanalyzer 2100. Samples were sequenced by the UVA Genomics and Technology core with a read length of 75 base pairs (bp) and a target depth of 10 million reads using the Illumina NextSeq 500 Sequencing System.

Ex vivo

After dissection, liver tissue was stored at −80°C in RNAlater (Sigma-Aldrich, R0901) until use. Liver tissue was lysed using Qiagen TissueLyser II (30 Hz for 15 min) in RLT lysis buffer (Qiagen, 1015762). The manufacturer's recommendations were followed for RNA isolation using the RNeasy Mini Kit (Qiagen, 74106). RNA quantity and purity were analyzed by spectrometric analysis (260/280, >1.8 and <2.2; 260/230, >1.8 and <2.2). RNA was shipped to GeneWiz (South Plainfield, NJ). RNA was sequenced in a strand-specific manner with a read length of 150 bp and a target depth of 20 million to 30 million reads.

Data analysis

Reads were aligned using UVA Rivanna Supercluster using Spliced Transcripts Alignment to a Reference (STAR) (*76*). Reads were trimmed and aligned to the mouse reference genome (mm10) with either single- or pair-end alignment where appropriate. Aligned reads were counted, and differential gene expression was calculated if reads exceeded 1 read per million using EdgeR (*77*) and RStudio. Genes were considered differentially expressed if they deviated from the control condition by 50% with a *P* value less than 0.05 (in vitro) or 0.1 (in vivo). EnrichR (*53*) was used to identify pathways that were up- or down-regulated on the basis of differentially regulated genes.

Magnetic resonance imaging

Body composition analysis was performed by EchoMRI-100H on mice before the start of FPC diet feeding and weekly for the duration of feeding.

Western blot

Tissue

Tissues were lysed using Qiagen TissueLyser II (30 Hz for 15 min) in radioimmunoprecipitation assay (RIPA) lysis buffer containing cOmplete Mini protease inhibitors (Roche, 37439120) and phosphatase inhibitors (Sigma-Aldrich, P5726 and P0044). Protein concentration was quantified via Pierce BCA Protein Assay (Thermo Fisher Scientific, 23225). Total protein (25 to 75 μg) was separated by SDS–polyacrylamide gel electrophoresis (PAGE) (8 to 12%) and transferred to nitrocellulose or polyvinylidene difluoride membranes. Membranes were blocked with Intercept Blocking Buffer (LI-COR Biosciences, 927-70001) or 5% bovine serum albumin in tris-buffered saline (TBS) or 5% milk powder in TBS with 0.1% Tween 20 for 1 hour at room temperature. Membranes were

stained with goat anti-myc [horseradish peroxidase (HRP)] antibody (1:30,000; NovusBio, NB600-341) or rabbit anti-vinculin antibody (1:1000; CST, E1E9V) diluted in 1% milk powder in TBS with 0.1% Tween 20 overnight at 4°C. Next, membranes were washed in TBS containing 0.1% Tween 20, followed by incubation for 1 hour at room temperature with HRP-conjugated secondary antibodies (1:10,000 dilution in 1% milk in TBS with 0.1% Tween 20, CST), except for membranes incubated with the goat anti-myc [HRP] antibody. Membranes were washed in TBS containing 0.1% Tween 20 and imaged on the Odyssey Imager (LI-COR Biosciences) or incubated with ECL substrate (Thermo Scientific SuperSignal, 34580) for 5 min at room temperature and imaged using Amersham ImageQuant 800.

Plasma

Plasma was diluted in loading dye (150 μl/ml) and denatured at 95°C for 10 min. Heat-denatured samples were separated by SDS-PAGE gel and transferred to nitrocellulose membranes. Membranes were blocked with PBS Blocking Buffer (LI-COR Biosciences) and for 1 hour at room temperature and stained with a 1:1000 dilution of mouse anti-myc antibody (Millipore, 05-724) overnight at 4°C. The blot was washed three times for 15 min with PBS Blocking Buffer. The blot was stained with the secondary antibody IRDye 800CW Goat anti-Rabbit (1:10,000 in PBS) (LI-COR Biosciences, 926-32211) for 1 hour at room temperature followed by three washes with LI-COR PBS Blocking Buffer. The resulting blot was visualized using the Odyssey Imager (LI-COR Biosciences).

HIS/myc competitive sandwich ELISA

Ninety-six–well Nunc MaxiSorp flat-bottom plates (Thermo Fisher Scientific) were coated with rabbit anti HIS-Tag antibody (1:250 in 1× PBS; CST, 2365S) overnight at 4°C. Coated wells were then aspirated and washed three times with 1× PBS (~1-min soaking in between). After blocking for 1 hour at room temperature with 1× ELISA/Elispot Diluent (Invitrogen, 19045636) diluted in double-distilled water, wells were washed as previously described. Plasma samples were diluted 1:20 in double-distilled water and added into the wells. For the HIS-competitive standard curve, 2 μg of HIS-protein ELISA standard (stock, 50 μg/ml; Cayman Chemical, 0556338) was serially diluted in double-distilled water and E06 plasma sample was added (1:20). The E06 plasma standard curve was generated by serial dilution of plasma. A HIS-protein competitive standard curve was generated by serial dilution of HIS-tagged 4EBP1 (11.1 mg/ml). Blanks were incubated with 1× ELISA/Elispot Diluent. Plates were sealed and incubated overnight at 4°C. Following five washing steps, the detection antibody goat anti–c-Myc HRP-coupled (1:5000 in 1× ELISA/Elispot Diluent; Novus P26) was added to the plates and incubated for 1 hour at room temperature. After washing seven times, 1× TMB ELISA Substrate Solution (eBioscience Inc., E00008-1655) was pipetted into the wells and incubated for 35 min. Absorbance was measured using Plate Reader (BioTek) at 450 and 570 nm.

Glucose and insulin tolerance tests

Intraperitoneal glucose (GTT) and insulin tolerance tests (ITT) were performed on fasted mice at time points indicated. Mice were fasted for 6 hours, and body mass and basal blood glucose were measured via tail vein nick using a glucometer (CVS Health). For GTT, glucose (1 mg/g) in sterile water was administered by intraperitoneal injection, and blood glucose was recorded 15, 30, 45, 60, 90, and 120 min after injection. For ITT, Humulin R (100 U/ml, Lilly) was diluted in sterile 0.9% saline, 0.75 U/kg was administered by intraperitoneal injection, and blood glucose was recorded 15, 30, 45, 60, 90, and 120 min after injection.

Cholesterol assay

Hepatic cholesterol was assessed using the Amplex Red Cholesterol Assay Kit (Invitrogen, A12216). Liver tissue was weighed and lysed in 400 μl of RIPA lysis buffer (EMD Millipore 20-188) using TissueLyser II. The protein concentration of the lysate was determined by Pierce BCA Protein Assay (Thermo Fisher Scientific, 23225). Lysates were diluted (15 μg per reaction) and analyzed in triplicate for free, esterified, and total cholesterol according to the manufacturer's recommendations. Final hepatic cholesterol concentrations were reported as micrograms of cholesterol per milligram of liver protein.

Hydroxyproline assay

Liver tissue (20 to 30 mg) was lysed in 200 μl of HPLC water (Sigma-Aldrich, 270733) using TissueLyser II shaking at 30 Hz for 15 min. Lysates were centrifuged at 20,817*g* at 4°C for 15 min. Supernatants were collected, and protein concentration was assessed by Pierce BCA Protein Assay (Thermo Fisher Scientific, 23225). Five hundred micrograms of protein was diluted 1:1 in 37% HCl (12.1 M) to a final concentration of 1.89 mg/ml in ~6 M HCl. The lysates were incubated at 95°C for 20 hours. After 20 hours, samples were cooled to room temperature and centrifuged at 13,000*g* for 10 min. Supernatants were collected and diluted to 4 M HCl. Hydroxyproline content was assessed using QuickZyme Sensitive Tissue Hydroxyproline Assay (QuickZyme Biosciences QZBTISHYP1) according to the manufacturer's recommendations.

Statistical analysis

Statistical analysis was performed using GraphPad Prism 9. Data are represented as the mean ± SEM. Statistical tests were applied as described in the figure legends. Statistical outliers were identified using the ROUT method ($Q = 2$ or 5%) and excluded from analyses.

SUPPLEMENTARY MATERIALS

Supplementary material for this article is available at https://science.org/doi/10.1126/sciadv.abn0050

View/request a protocol for this paper from *Bio-protocol*.

REFERENCES AND NOTES

1. Z. M. Younossi, Non-alcoholic fatty liver disease—A global public health perspective. *J. Hepatol.* **70**, 531–544 (2019).
2. R. Loomba, A. J. Sanyal, The global NAFLD epidemic. *Nat. Rev. Gastroenterol. Hepatol.* **10**, 686–690 (2013).
3. K. K. Bence, M. J. Birnbaum, Metabolic drivers of non-alcoholic fatty liver disease. *Mol. Metab.* **50**, 101143 (2020).
4. Z. Chen, R. Tian, Z. She, J. Cai, H. Li, Role of oxidative stress in the pathogenesis of nonalcoholic fatty liver disease. *Free Radic. Biol. Med.* **152**, 116–141 (2020).
5. D. H. Ipsen, J. Lykkesfeldt, P. Tveden-Nyborg, Molecular mechanisms of hepatic lipid accumulation in non-alcoholic fatty liver disease. *Cell. Mol. Life Sci.* **75**, 3313–3327 (2018).
6. N. L. Gluchowski, M. Becuwe, T. C. Walther, R. V. Farese, Lipid droplets and liver disease: From basic biology to clinical implications. *Nat. Rev. Gastroenterol. Hepatol.* **14**, 343–355 (2017).
7. M. H. Wehmeyer, B. C. Zyriax, B. Jagemann, E. Roth, E. Windler, J. S. Z. Wiesch, A. W. Lohse, J. Kluwe, Nonalcoholic fatty liver disease is associated with excessive calorie intake rather than a distinctive dietary pattern. *Medicine (Baltimore)* **95**, e3887 (2016).
8. B. A. Neuschwander-Tetri, Hepatic lipotoxicity and the pathogenesis of nonalcoholic steatohepatitis: The central role of nontriglyceride fatty acid metabolites. *Hepatology* **52**, 774–788 (2010).

9. R. S. Rector, J. P. Thyfault, G. M. Uptergrove, E. M. Morris, S. P. Naples, S. J. Borengasser, C. R. Mikus, M. J. Laye, M. H. Laughlin, F. W. Booth, J. A. Ibdah, Mitochondrial dysfunction precedes insulin resistance and hepatic steatosis and contributes to the natural history of non-alcoholic fatty liver disease in an obese rodent model. *J. Hepatol.* **52**, 727–736 (2010).
10. Y. Wei, R. S. Rector, J. P. Thyfault, J. A. Ibdah, Nonalcoholic fatty liver disease and mitochondrial dysfunction. *World J. Gastroenterol.* **14**, 193–199 (2008).
11. F. Nassir, J. Ibdah, Role of mitochondria in nonalcoholic fatty liver disease. *Int. J. Mol. Sci.* **15**, 8713–8742 (2014).
12. S. Schuster, D. Cabrera, M. Arrese, A. E. Feldstein, Triggering and resolution of inflammation in NASH. *Nat. Rev. Gastroenterol. Hepatol.* **15**, 349–364 (2018).
13. T. Kisseleva, D. Brenner, Molecular and cellular mechanisms of liver fibrosis and its regression. *Nat. Rev. Gastroenterol. Hepatol.* **18**, 151–166 (2021).
14. S. Caldwell, Y. Ikura, D. Dias, K. Isomoto, A. Yabu, C. Moskaluk, P. Pramoonjago, W. Simmons, H. Scruggs, N. Rosenbaum, T. Wilkinson, P. Toms, C. K. Argo, A. M. S. Al-Osaimi, J. A. Redick, Hepatocellular ballooning in NASH. *J. Hepatol.* **53**, 719–723 (2010).
15. T. Tsuchida, S. L. Friedman, Mechanisms of hepatic stellate cell activation. *Nat. Rev. Gastroenterol. Hepatol.* **14**, 397–411 (2017).
16. K. Kazankov, S. M. D. Jørgensen, K. L. Thomsen, H. J. Møller, H. Vilstrup, J. George, D. Schuppan, H. Grønbæk, The role of macrophages in nonalcoholic fatty liver disease and nonalcoholic steatohepatitis. *Nat. Rev. Gastroenterol. Hepatol.* **16**, 145–159 (2019).
17. Y. Takahashi, T. Fukusato, Histopathology of nonalcoholic fatty liver disease/nonalcoholic steatohepatitis. *World J. Gastroenterol.* **20**, 15539–15548 (2014).
18. V. A. Piazzolla, A. Mangia, Noninvasive diagnosis of NAFLD and NASH. *Cell* **9**, 1005 (2020).
19. A. Kadl, A. K. Meher, P. R. Sharma, M. Y. Lee, A. C. Doran, S. R. Johnstone, M. R. Elliott, F. Gruber, J. Han, W. Chen, T. Kensler, K. S. Ravichandran, B. E. Isakson, B. R. Wamhoff, N. Leitinger, Identification of a novel macrophage phenotype that develops in response to atherogenic phospholipids via Nrf2. *Circ. Res.* **107**, 737–746 (2010).
20. A. Kadl, P. R. Sharma, W. Chen, R. Agrawal, A. K. Meher, S. Rudraiah, N. Grubbs, R. Sharma, N. Leitinger, Oxidized phospholipid-induced inflammation is mediated by Toll-like receptor 2. *Free Radic. Biol. Med.* **51**, 1903–1909 (2011).
21. V. N. Bochkov, A. Kadl, J. Huber, F. Gruber, B. R. Binder, N. Leitinger, Protective role of phospholipid oxidation products in endotoxin-induced tissue damage. *Nature* **419**, 77–81 (2002).
22. E. A. Podrez, E. Poliakov, Z. Shen, R. Zhang, Y. Deng, M. Sun, P. J. Finton, L. Shan, M. Febbraio, D. P. Hajjar, R. L. Silverstein, H. F. Hoff, R. G. Salomon, S. L. Hazen, A novel family of atherogenic oxidized phospholipids promotes macrophage foam cell formation via the scavenger receptor CD36 and is enriched in atherosclerotic lesions. *J. Biol. Chem.* **277**, 38517–38523 (2002).
23. Y. Ke, P. Karki, J. Kim, S. Son, E. Berdyshev, V. N. Bochkov, A. A. Birukova, K. G. Birukov, Elevated truncated oxidized phospholipids as a factor exacerbating ALI in the aging lungs. *FASEB J.* **33**, 3887–3900 (2019).
24. K. G. Birukov, P. Karki, Injured lung endothelium: Mechanisms of self-repair and agonist-assisted recovery (2017 Grover Conference Series). *Pulm. Circ.* **8**, 2045893217752660 (2018).
25. P. Karki, A. Meliton, A. Shah, Y. Tian, T. Ohmura, N. Sarich, A. A. Birukova, K. G. Birukov, Role of truncated oxidized phospholipids in acute endothelial barrier dysfunction caused by particulate matter. *PLOS ONE* **13**, e0206251 (2018).
26. K. G. Birukov, V. N. Bochkov, A. A. Birukova, K. Kawkitinarong, A. Rios, A. Leitner, A. D. Verin, G. M. Bokoch, N. Leitinger, J. G. Garcia, Epoxycyclopentenone-containing oxidized phospholipids restore endothelial barrier function via Cdc42 and Rac. *Circ. Res.* **95**, 892–901 (2004).
27. S. Nonas, I. Miller, K. Kawkitinarong, S. Chatchavalvanich, I. Gorshkova, V. N. Bochkov, N. Leitinger, V. Natarajan, J. G. N. Garcia, K. G. Birukov, Oxidized phospholipids reduce vascular leak and inflammation in rat model of acute lung injury. *Am. J. Respir. Crit. Care Med.* **173**, 1130–1138 (2006).
28. A. Kadl, E. Galkina, N. Leitinger, Induction of CCR2-dependent macrophage accumulation by oxidized phospholipids in the air-pouch model of inflammation. *Arthritis Rheum.* **60**, 1362–1371 (2009).
29. V. Serbulea, C. M. Upchurch, K. W. Ahern, G. Bories, P. Voigt, D. E. DeWeese, A. K. Meher, T. E. Harris, N. Leitinger, Macrophages sensing oxidized DAMPs reprogram their metabolism to support redox homeostasis and inflammation through a TLR2-Syk-ceramide dependent mechanism. *Mol. Metab.* **7**, 23–34 (2018).
30. E. Ambrogini, X. Que, S. Wang, F. Yamaguchi, R. S. Weinstein, S. Tsimikas, S. C. Manolagas, J. L. Witztum, R. L. Jilka, Oxidation-specific epitopes restrain bone formation. *Nat. Commun.* **9**, 2193 (2018).
31. V. E. Kagan, G. Mao, F. Qu, J. P. Angeli, S. Doll, C. S. Croix, H. H. Dar, B. Liu, V. A. Tyurin, V. B. Ritov, A. A. Kapralov, A. A. Amoscato, J. Jiang, T. Anthonymuthu, D. Mohammadyani, Q. Yang, B. Proneth, J. Klein-Seetharaman, S. Watkins, I. Bahar, J. Greenberger, R. K. Mallampalli, B. R. Stockwell, Y. Y. Tyurina, M. Conrad, H. Bayir, Oxidized arachidonic and adrenic PEs navigate cells to ferroptosis. *Nat. Chem. Biol.* **13**, 81–90 (2017).
32. T. M. Grigory, G. Borisenko, Macrophage recognition of externalized phosphatidylserine and phagocytosis of apoptotic Jurkat cells—Existence of a threshold. *Arch. Biochem. Biophys.* **413**, 41–52 (2003).
33. Y. Imai, K. Kuba, G. G. Neely, R. Yaghubian-Malhami, T. Perkmann, G. Van Loo, M. Ermolaeva, R. Veldhuizen, Y. H. C. Leung, H. Wang, H. Liu, Y. Sun, M. Pasparakis, M. Kopf, C. Mech, S. Bavari, J. S. M. Peiris, A. S. Slutsky, S. Akira, M. Hultqvist, R. Holmdahl, J. Nicholls, C. Jiang, C. J. Binder, J. M. Penninger, Identification of oxidative stress and toll-like receptor 4 signaling as a key pathway of acute lung injury. *Cell* **133**, 235–249 (2008).
34. V. Serbulea, C. M. Upchurch, M. S. Schappe, P. Voigt, D. E. DeWeese, B. N. Desai, A. K. Meher, N. Leitinger, Macrophage phenotype and bioenergetics are controlled by oxidized phospholipids identified in lean and obese adipose tissue. *Proc. Natl. Acad. Sci. U.S.A.* **115**, E6254–E6263 (2018).
35. X. Sun, J. S. Seidman, P. Zhao, T. D. Troutman, N. J. Spann, X. Que, F. Zhou, Z. Liao, M. Pasillas, X. Yang, J. A. Magida, T. Kisseleva, D. A. Brenner, M. Downes, R. M. Evans, A. R. Saltiel, S. Tsimikas, C. K. Glass, J. L. Witztum, Neutralization of oxidized phospholipids ameliorates non-alcoholic steatohepatitis. *Cell Metab.* **31**, 189–206.e8 (2020).
36. S. Tsimikas, S. Kiechl, J. Willeit, M. Mayr, E. R. Miller, F. Kronenberg, Q. Xu, C. Bergmark, S. Weger, F. Oberhollenzer, J. L. Witztum, Oxidized phospholipids predict the presence and progression of carotid and femoral atherosclerosis and symptomatic cardiovascular disease: Five-year prospective results from the Bruneck study. *J. Am. Coll. Cardiol.* **47**, 2219–2228 (2006).
37. S. Hörkkö, D. A. Bird, E. Miller, H. Itabe, N. Leitinger, G. Subbanagounder, J. A. Berliner, P. Friedman, E. A. Dennis, L. K. Curtiss, W. Palinski, J. L. Witztum, Monoclonal autoantibodies specific for oxidized phospholipids or oxidized phospholipid–protein adducts inhibit macrophage uptake of oxidized low-density lipoproteins. *J. Clin. Investig.* **103**, 117–128 (1999).
38. X. Que, M.-Y. Hung, C. Yeang, A. Gonen, T. A. Prohaska, X. Sun, C. Diehl, A. Määttä, D. E. Gaddis, K. Bowden, J. Pattison, J. G. Macdonald, S. Ylä-Herttuala, P. L. Mellon, C. C. Hedrick, K. Ley, Y. I. Miller, C. K. Glass, K. L. Peterson, C. J. Binder, S. Tsimikas, J. L. Witztum, Oxidized phospholipids are proinflammatory and proatherogenic in hypercholesterolaemic mice. *Nature* **558**, 301–306 (2018).
39. X. Wang, Z. Zheng, J. M. Caviglia, K. E. Corey, T. M. Herfel, B. Cai, R. Masia, R. T. Chung, J. H. Lefkowitch, R. F. Schwabe, I. Tabas, Hepatocyte TAZ/WWTR1 promotes inflammation and fibrosis in nonalcoholic steatohepatitis. *Cell Metab.* **24**, 848–862 (2016).
40. Z. Ni, G. Angelidou, R. Hoffmann, M. Fedorova, LPPtiger software for lipidome-specific prediction and identification of oxidized phospholipids from LC-MS datasets. *Sci. Rep.* **7**, 15138 (2017).
41. E. A. Podrez, E. Poliakov, Z. Shen, R. Zhang, Y. Deng, M. Sun, P. J. Finton, L. Shan, B. Gugiu, P. L. Fox, H. F. Hoff, R. G. Salomon, S. L. Hazen, Identification of a novel family of oxidized phospholipids that serve as ligands for the macrophage scavenger receptor CD36. *J. Biol. Chem.* **277**, 38503–38516 (2002).
42. A. D. Watson, N. Leitinger, M. Navab, K. F. Faull, S. Hörkkö, J. L. Witztum, W. Palinski, D. Schwenke, R. G. Salomon, W. Sha, G. Subbanagounder, A. M. Fogelman, J. A. Berliner, Structural identification by mass spectrometry of oxidized phospholipids in minimally oxidized low density lipoprotein that induce monocyte/endothelial interactions and evidence for their presence in vivo. *J. Biol. Chem.* **272**, 13597–13607 (1997).
43. M. Hiraoka, A. Abe, An increase of oxidized phospholipids and the role of macrophages in intraocular inflammation. *Investig. Opthalmol. Vis. Sci.* **61**, 23 (2020).
44. Z. Ahmed, A. Ravandi, G. F. Maguire, A. Emili, D. Draganov, B. N. La Du, A. Kuksis, P. W. Connelly, Multiple substrates for paraoxonase-1 during oxidation of phosphatidylcholine by peroxynitrite. *Biochem. Biophys. Res. Commun.* **290**, 391–396 (2002).
45. K. Sabatini, J. P. Mattila, F. M. Megli, P. K. Kinnunen, Characterization of two oxidatively modified phospholipids in mixed monolayers with DPPC. *Biophys. J.* **90**, 4488–4499 (2006).
46. J.-P. Mattila, K. Sabatini, P. K. J. Kinnunen, Interaction of Cytochrome c with 1-Palmitoyl-2-azelaoyl-sn-glycero-3-phosphocholine: Evidence for acyl chain reversal. *Langmuir* **24**, 4157–4160 (2008).
47. C. P. Thomas, L. T. Morgan, B. H. Maskrey, R. C. Murphy, H. Kühn, S. L. Hazen, A. H. Goodall, H. A. Hamali, P. W. Collins, V. B. O'Donnell, Phospholipid-esterified eicosanoids are generated in agonist-activated human platelets and enhance tissue factor-dependent thrombin generation. *J. Biol. Chem.* **285**, 6891–6903 (2010).
48. K. Kayganich-Harrison, D. Rose, R. Murphy, J. Morrow, L. Roberts, Collision-induced dissociation of F2-isoprostane-containing phospholipids. *J. Lipid Res.* **34**, 1229–1235 (1993).
49. A. D. Watson, G. Subbanagounder, D. S. Welsbie, K. F. Faull, M. Navab, M. E. Jung, A. M. Fogelman, J. A. Berliner, Structural identification of a novel pro-inflammatory epoxyisoprostane phospholipid in mildly oxidized low density lipoprotein. *J. Biol. Chem.* **274**, 24787–24798 (1999).
50. V. Bochkov, B. Gesslbauer, C. Mauerhofer, M. Philippova, P. Erne, O. V. Oskolkova, Pleiotropic effects of oxidized phospholipids. *Free Radic. Biol. Med.* **111**, 6–24 (2017).

51. V. N. Bochkov, O. V. Oskolkova, K. G. Birukov, A.-L. Levonen, C. J. Binder, J. Stöckl, Generation and biological activities of oxidized phospholipids. *Antioxid. Redox Signal.* **12**, 1009–1059 (2010).
52. M. V. Kuleshov, M. R. Jones, A. D. Rouillard, N. F. Fernandez, Q. Duan, Z. Wang, S. Koplev, S. L. Jenkins, K. M. Jagodnik, A. Lachmann, M. G. McDermott, C. D. Monteiro, G. W. Gundersen, A. Ma'ayan, Enrichr: A comprehensive gene set enrichment analysis web server 2016 update. *Nucleic Acids Res.* **44**, W90–W97 (2016).
53. E. Y. Chen, C. M. Tan, Y. Kou, Q. Duan, Z. Wang, G. Meirelles, N. R. Clark, A. Ma'Ayan, Enrichr: Interactive and collaborative HTML5 gene list enrichment analysis tool. *BMC Bioinformatics* **14**, 128 (2013).
54. H. K. Min, A. Kapoor, M. Fuchs, F. Mirshahi, H. Zhou, J. Maher, J. Kellum, R. Warnick, M. J. Contos, A. J. Sanyal, Increased hepatic synthesis and dysregulation of cholesterol metabolism is associated with the severity of nonalcoholic fatty liver disease. *Cell Metab.* **15**, 665–674 (2012).
55. W. Xue, J. Wang, W. Jiang, C. Shi, X. Wang, Y. Huang, C. Hu, Caveolin-1 alleviates lipid accumulation in NAFLD associated with promoting autophagy by inhibiting the Akt/mTOR pathway. *Eur. J. Pharmacol.* **871**, 172910 (2020).
56. M. Li, D. Chen, H. Huang, J. Wang, X. Wan, C. Xu, C. Li, H. Ma, C. Yu, Y. Li, Caveolin1 protects against diet induced hepatic lipid accumulation in mice. *PLOS ONE* **12**, e0178748 (2017).
57. M. Han, W. Pioronska, S. Wang, Z. C. Nwosu, C. Sticht, S. Wang, Y. Gao, M. P. Ebert, S. Dooley, C. Meyer, Hepatocyte caveolin-1 modulates metabolic gene profiles and functions in non-alcoholic fatty liver disease. *Cell Death Dis.* **11**, 104 (2020).
58. M. Tan, R. Mosaoa, G. T. Graham, A. Kasprzyk-Pawelec, S. Gadre, E. Parasido, O. Catalina-Rodriguez, P. Foley, G. Giaccone, A. Cheema, B. Kallakury, C. Albanese, C. Yi, M. L. Avantaggiati, Inhibition of the mitochondrial citrate carrier, Slc25a1, reverts steatosis, glucose intolerance, and inflammation in preclinical models of NAFLD/NASH. *Cell Death Differ.* **27**, 2143–2157 (2020).
59. M. Pérez-Carreras, P. Del Hoyo, M. A. Martín, J. C. Rubio, A. Martín, G. Castellano, F. Colina, J. Arenas, J. A. Solis-Herruzo, Defective hepatic mitochondrial respiratory chain in patients with nonalcoholic steatohepatitis. *Hepatology* **38**, 999–1007 (2003).
60. P. Greenspan, E. P. Mayer, S. D. Fowler, Nile red: A selective fluorescent stain for intracellular lipid droplets. *J. Cell Biol.* **100**, 965–973 (1985).
61. B. H. Maskrey, A. Bermúdez-Fajardo, A. H. Morgan, E. Stewart-Jones, V. Dioszeghy, G. W. Taylor, P. R. S. Baker, B. Coles, M. J. Coffey, H. Kühn, V. B. O'Donnell, Activated platelets and monocytes generate four hydroxyphosphatidylethanolamines via lipoxygenase. *J. Biol. Chem.* **282**, 20151–20163 (2007).
62. P. Trivedi, S. Wang, S. L. Friedman, The power of plasticity-metabolic regulation of hepatic stellate cells. *Cell Metab.* **33**, 242–257 (2021).
63. X. Liu, S. B. Rosenthal, N. Meshgin, J. Baglieri, S. G. Musallam, K. Diggle, K. Lam, R. Wu, S. Q. Pan, Y. Chen, K. Dorko, S. Presnell, C. Benner, M. Hosseini, H. Tsukamoto, D. Brenner, T. Kisseleva, Primary alcohol-activated human and mouse hepatic stellate cells share similarities in gene-expression profiles. *Hepatol. Commun.* **4**, 606–626 (2020).
64. P. X. Shaw, S. Hörkkö, M.-K. Chang, L. K. Curtiss, W. Palinski, G. J. Silverman, J. L. Witztum, Natural antibodies with the T15 idiotype may act in atherosclerosis, apoptotic clearance, and protective immunity. *J. Clin. Investig.* **105**, 1731–1740 (2000).
65. I. Zanoni, Y. Tan, M. Di Gioia, A. Broggi, J. Ruan, J. Shi, C. A. Donado, F. Shao, H. Wu, J. R. Springstead, J. C. Kagan, An endogenous caspase-11 ligand elicits interleukin-1 release from living dendritic cells. *Science* **352**, 1232–1236 (2016).
66. C. Erridge, S. Kennedy, C. M. Spickett, D. J. Webb, Oxidized phospholipid inhibition of toll-like receptor (TLR) signaling is restricted to TLR2 and TLR4: Roles for CD14, LPS-binding protein, and MD2 as targets for specificity of inhibition. *J. Biol. Chem.* **283**, 24748–24759 (2008).
67. L. Wang, Y. Chai, C. Li, H. Liu, W. Su, X. Liu, B. Yu, W. Lei, B. Yu, J. L. Crane, X. Cao, M. Wan, Oxidized phospholipids are ligands for LRP6. *Bone Res.* **6**, 22 (2018).
68. G. N. Ioannou, The role of cholesterol in the pathogenesis of NASH. *Trends Endocrinol. Metab.* **27**, 84–95 (2016).
69. P. Friedman, S. Horkko, D. Steinberg, J. L. Witztum, E. A. Dennis, Correlation of antiphospholipid antibody recognition with the structure of synthetic oxidized phospholipids. Importance of Schiff base formation and aldol condensation. *J. Biol. Chem.* **277**, 7010–7020 (2002).
70. K. L. Gillotte, S. Hörkkö, J. L. Witztum, D. Steinberg, Oxidized phospholipids, linked to apolipoprotein B of oxidized LDL, are ligands for macrophage scavenger receptors. *J. Lipid Res.* **41**, 824–833 (2000).
71. P. R. Kamstrup, M. Y. Hung, J. L. Witztum, S. Tsimikas, B. G. Nordestgaard, Oxidized phospholipids and risk of calcific aortic valve disease: The copenhagen general population study. *Arterioscler. Thromb. Vasc. Biol.* **37**, 1570–1578 (2017).
72. D. A. Slatter, C. L. Percy, K. Allen-Redpath, J. M. Gajsiewicz, N. J. Brooks, A. Clayton, V. J. Tyrrell, M. Rosas, S. N. Lauder, A. Watson, M. Dul, Y. Garcia-Diaz, M. Aldrovandi, M. Heurich, J. Hall, J. H. Morrissey, S. Lacroix-Desmazes, S. Delignat, P. V. Jenkins, P. W. Collins, V. B. O'Donnell, Enzymatically oxidized phospholipids restore thrombin generation in coagulation factor deficiencies. *JCI Insight* **3**, e98459 (2018).
73. V. E. Kagan, B. Gleiss, Y. Y. Tyurina, V. A. Tyurin, C. Elenström-Magnusson, S.-X. Liu, F. B. Serinkan, A. Arroyo, J. Chandra, S. Orrenius, B. Fadeel, A role for oxidative stress in apoptosis: Oxidation and externalization of phosphatidylserine is required for macrophage Clearance of cells undergoing fas-mediated apoptosis. *J. Immunol.* **169**, 487–499 (2002).
74. C. A. Schneider, W. S. Rasband, K. W. Eliceiri, NIH Image to ImageJ: 25 years of image analysis. *Nat. Methods* **9**, 671–675 (2012).
75. V. Bäcker, ImageJ macro tool sets of biological image analysis. *Proc. ImageJ User Dev. Conf. Luxembourg* **24**, 1–6 (2012).
76. A. Dobin, C. A. Davis, F. Schlesinger, J. Drenkow, C. Zaleski, S. Jha, P. Batut, M. Chaisson, T. R. Gingeras, STAR: Ultrafast universal RNA-seq aligner. *Bioinformatics* **29**, 15–21 (2013).
77. M. D. Robinson, D. J. Mccarthy, G. K. Smyth, edgeR: A Bioconductor package for differential expression analysis of digital gene expression data. *Bioinformatics* **26**, 139–140 (2010).

Acknowledgments: AAV8-scFv-E06 was synthesized by the Penn Vector Core. RNA-seq analysis was supported by the UVA Genome Analysis and Technology Core. We thank M. Bevard (UVA CVRC Histology Core) for her expertise and preparation of histological samples. RNA sequencing of in vitro OxPAPC-treated hepatocytes was performed in the Genome Analysis and Technology Core at UVA. We thank J. Gatesman (UVA Center for Comparative Medicine) for technical assistance with viral injections. **Funding:** This work was funded by NIH grants T32GM007055 (to C.M.U.), F30HL154554 (to S.Y.), T32GM007267 (to S.Y.), T32GM007055 (to S.Y.), T32HL007284 (to C.M.P.), , R01DK121055 (to I.M.B.), R01MH116694 (to M.M.S.), R01NS097726 (to E.P.-R.), and P01HL120840 (N.L.) and Deutsche Forschungsgemeinschaft IRTG 1902-2 (to D.M.) and IRTG 1902-1 (to J.G.). **Author contributions:** Conceptualization: C.M.U., M.M.S., E.P.-R., and N.L. Methodology: C.M.U., S.Y., C.M.P., D.M., J.G., M.M., I.M.B., M.M.S., E.P.-R., and N.L. Investigation: C.M.U., S.Y., C.M.P., M.M., D.M., J.G., and S.S.R. Visualization: C.M.U. and N.L. Funding acquisition: C.M.U., S.Y., C.M.P., I.M.B., M.M.S., and N.L. Project administration: N.L. Supervision: N.L. Writing—original draft: C.M.U. and N.L. Writing—review and editing: C.M.U., S.Y., C.M.P., M.M., I.M.B., M.M.S., E.P.-R., and N.L. **Competing interests:** C.M.U., N.L., E.P.-R., and M.M.S. have applied for a provisional patent on the application of AAV8-mediated transduction of scFv-E06 for use in a therapeutic capacity in chronic disease. The authors declare no other competing interests. **Data and materials availability:** All data needed to evaluate the conclusions in the paper are present in the paper and/or the Supplementary Materials. The plasmid used to generate the viral construct AAV8-scFv-E06 was provided to the authors via an MTA agreement with genOway. Requests for the plasmid should be submitted to N.L. or E.P.-R. Genomic data for this manuscript have been deposited in the NCBI Genomic Expression Omnibus (accession number: GSE202984—in vitro RNA-seq; GSE202982—in vivo RNA-seq).

Submitted 27 October 2021
Accepted 3 June 2022
Published 15 July 2022
10.1126/sciadv.abn0050

Science Advances
AAAS

Supplementary Materials for

Targeting oxidized phospholipids by AAV-based gene therapy in mice with established hepatic steatosis prevents progression to fibrosis

Clint M. Upchurch *et al.*

Corresponding author: Norbert Leitinger, nl2q@virginia.edu

Sci. Adv. **8**, eabn0050 (2022)
DOI: 10.1126/sciadv.abn0050

The PDF file includes:

Other Supplementary Material for this manuscript includes the following:

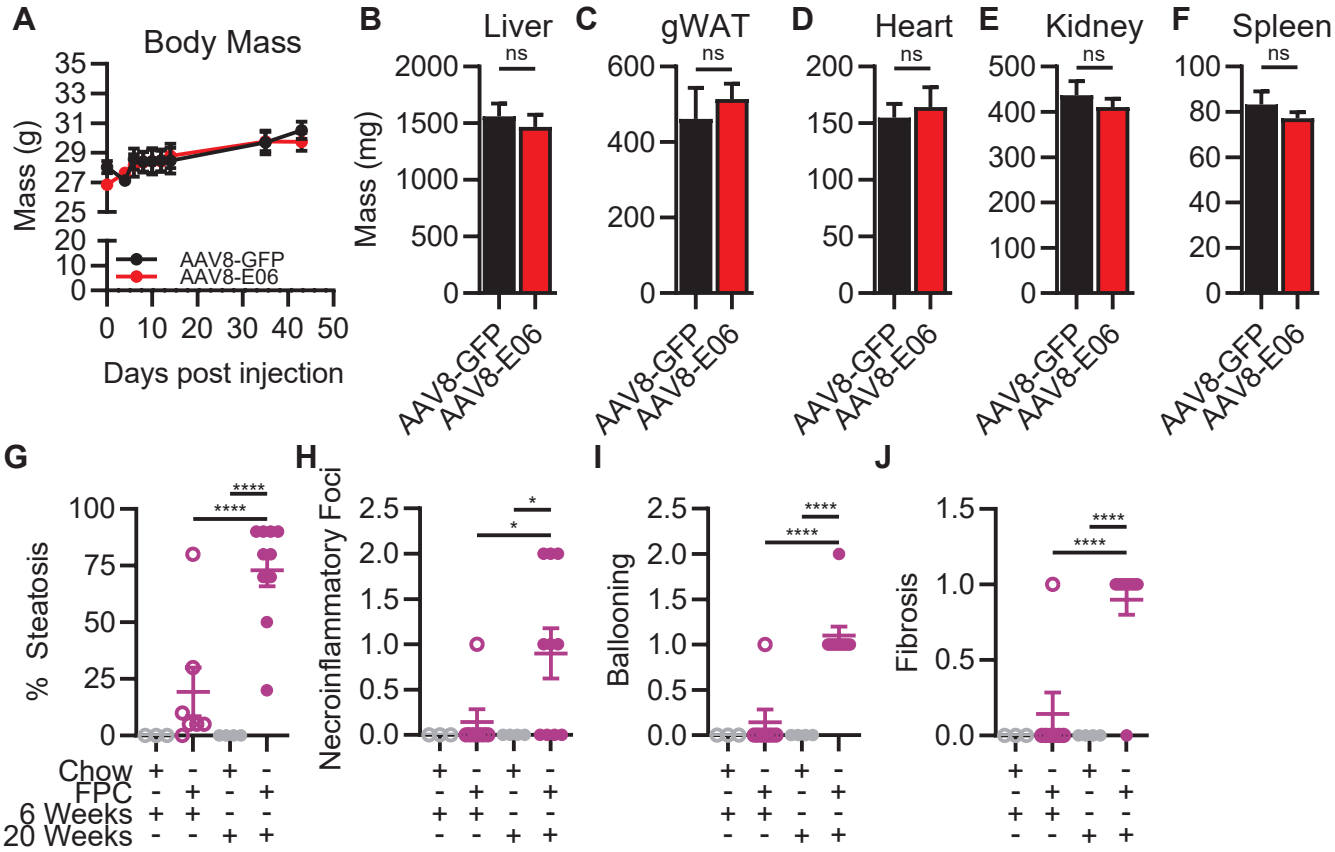
A
Body Mass
Mass (g)
Days post injection
AAV8-GFP
AAV8-E06
B
Liver
C
gWAT
D
Heart
E
Kidney
F
Spleen
Mass (mg)
ns
AAV8-GFP
AAV8-E06
G
% Steatosis
H
Necroinflammatory Foci
I
Ballooning
J
Fibrosis
****
*
Chow
FPC
6 Weeks
20 Weeks

Supplemental Figure 1. Adeno-associated virus serotype 8 scFv-E06 and FPC diet verification.

Mice were injected with either AAV8-GFP or AAV8-E06. There were no differences in **(A)** body mass, or mass of **(B)** liver, **(C)** gonadal white adipose tissue, **(D)** heart, **(E)** kidney, and **(F)** spleen (AAV8-GFP – n=5; AAV8-E06 – n=6). Mice injected with AAV8-GFP were fed chow or FPC diet for 6 or 20 weeks and histopathological assessment of **(G)** percent steatosis, **(H)** necroinflammatory foci, **(I)** hepatocellular ballooning, and **(J)** fibrosis was performed by a clinical pathologist. Statistical significance was determined by 2-way ANOVA (*=$p<0.05$, ****=$p<0.0001$).

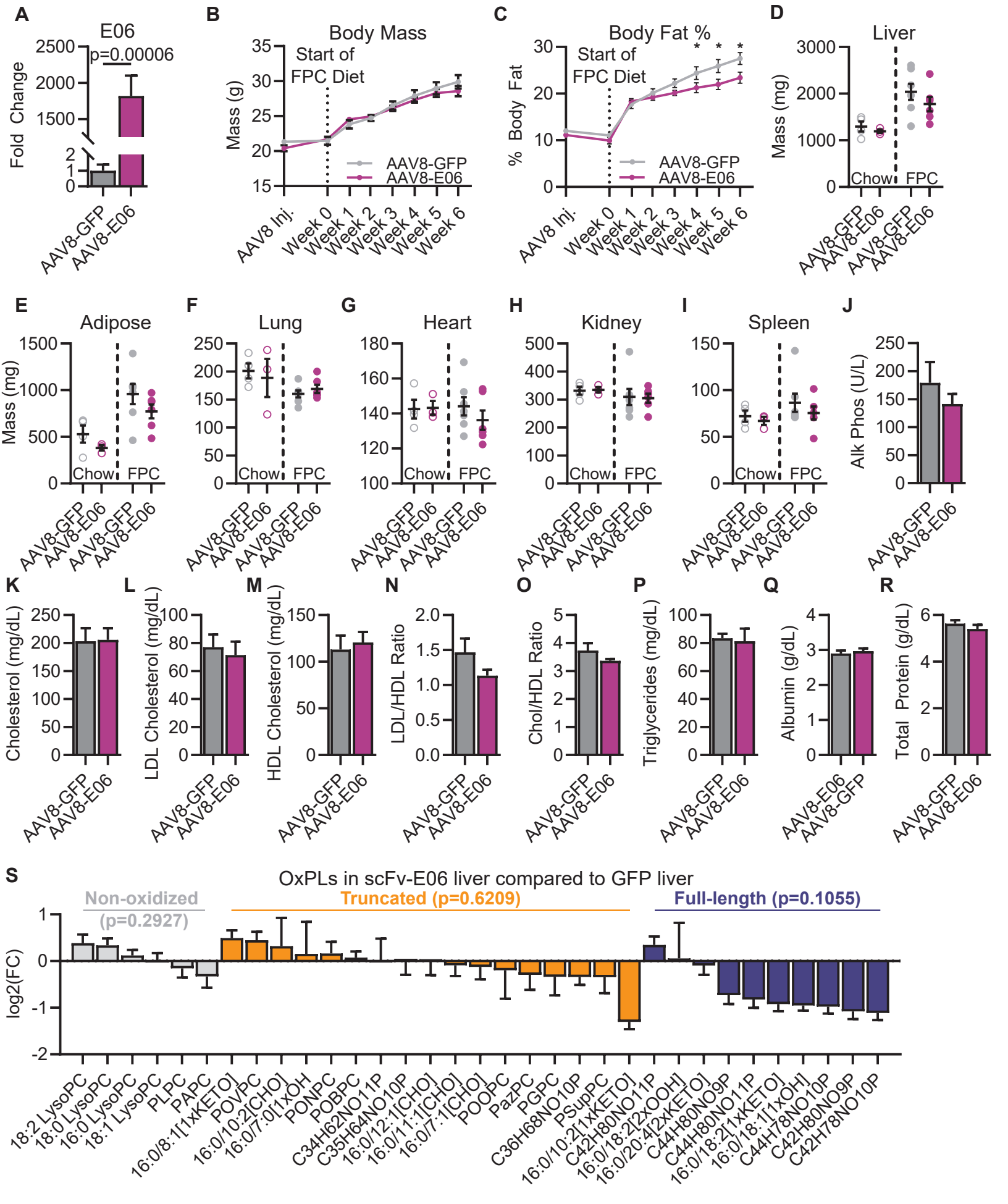
A
E06
p=0.00006
Fold Change
AAV8-GFP
AAV8-E06
B
Body Mass
Start of FPC Diet
Mass (g)
AAV8-GFP
AAV8-E06
AAV8 Inj.
Week 0
Week 1
Week 2
Week 3
Week 4
Week 5
Week 6
C
Body Fat %
Start of FPC Diet
% Body Fat
D
Liver
Mass (mg)
Chow
FPC
E
Adipose
F
Lung
G
Heart
H
Kidney
I
Spleen
J
Alk Phos (U/L)
K
Cholesterol (mg/dL)
L
LDL Cholesterol (mg/dL)
M
HDL Cholesterol (mg/dL)
N
LDL/HDL Ratio
O
Chol/HDL Ratio
P
Triglycerides (mg/dL)
Q
Albumin (g/dL)
R
Total Protein (g/dL)
S
OxPLs in scFv-E06 liver compared to GFP liver
Non-oxidized (p=0.2927)
Truncated (p=0.6209)
Full-length (p=0.1055)
log2(FC)
18:2 LysoPC
18:0 LysoPC
16:0 LysoPC
18:1 LysoPC
PLPC
PAPC
16:0/8:1[1xKETO]
POVPC
16:0/10:2[CHO]
16:0/7:0[1xOH
PONPC
POBPC
C34H62NO11P
C35H64NO10P
16:0/12:1[CHO]
16:0/11:1[CHO]
16:0/7:1[CHO]
POOPC
PazPC
PGPC
C36H68NO10P
PSupPC
16:0/10:2[1xKETO]
C42H80NO11P
16:0/18:2[2xOOH]
16:0/20:4[2xKETO]
C44H80NO9P
C44H80NO11P
16:0/18:2[1xKETO]
16:0/18:1[1xOH]
C44H78NO10P
C44H78NO9P
C42H80NO10P
C42H78NO10P

Supplemental Figure 2. Characterization of mice treated with AAV8-scFv-E06 after six weeks of FPC diet.

Speer6-ps1$^{Tg(Alb\text{-}cre)21Mgn}$/J mice were injected with AAV8-GFP or AAV8-scFv-E06. Two weeks after injection, mice were fed FPC diet for six weeks (FPC AAV8-GFP, n=7; FPC AAV8-E06, n=6). **(A)** scFv-E06 mRNA expression was significantly increased in mice injected with AAV8-scFv-E06 (AAV8-GFP – n=6; AAV8-E06 – n=6). **(B)** Body mass (FPC AAV8-GFP, n=7; FPC AAV8-E06, n=6) and **(C)** body fat percentage (FPC AAV8-GFP, n=6; FPC AAV8-E06, n=6) were recorded weekly. While there was no difference in body mass, there was a significant decrease in body fat percentage between FPC diet-fed mice expressing scFv-E06 compared to mice expressing GFP after four weeks on diet. There was significant increase in body fat percentage between chow fed and FPC diet-fed mice after six weeks. After six weeks, mouse plasma was collected, and hepatic function and lipid profile were measured. (**D-I)** There were no significant differences in organ mass between AAV8-GFP and AAV8-scFv-E06 in either chow-fed or FPC-fed mice (FPC AAV8-GFP, n=7; FPC AAV8-E06, n=6). There was no significant difference in **(J)** alkaline phosphatase, **(K)** cholesterol, **(L)** LDL cholesterol, **(M)** HDL cholesterol, **(N)** LDL/HDL ratio, **(O)** cholesterol/HDL ratio, **(P)** triglycerides, **(Q)** albumin, and **(R)** total protein in the plasma of FPC diet-fed mice expressing scFv-E06 compared to GFP-expressing mice (AAV8-GFP – n=6; AAV8-E06 – n=6). **(S)** Truncated and full-length OxPCs extracted from liver tissue demonstrate a similar pattern to that observed in the plasma. Statistical significance was determined by 1-way and 2-way ANOVA and Student's T-test. Multiple comparisons were corrected by Dunnet or Tukey multiple comparisons correction (*=$p<0.05$, **=$p<0.01$, ***=$p<0.001$, ****=$p<0.0001$). Statistical outliers were excluded based on the ROUT test (Q=5%).

A

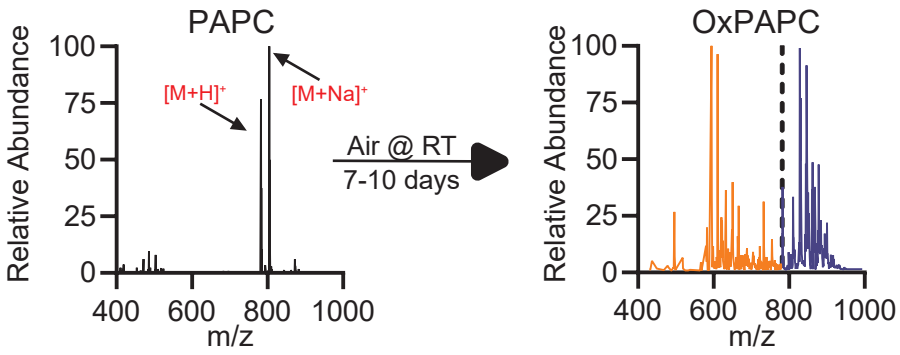

B

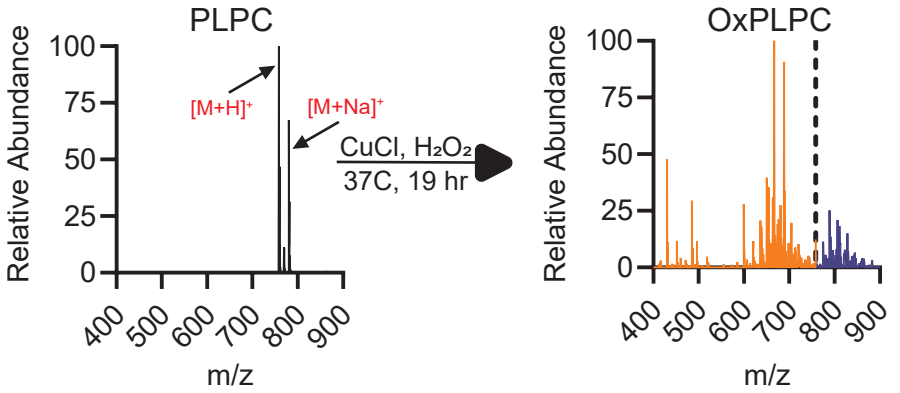

C

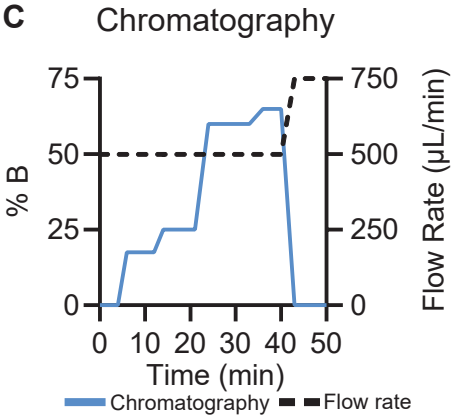

D

	Solvent A	Solvent B
Water	31%	---
Methanol	69%	50%
Isopropanol	---	50%
Ammonium acetate	10 mM	10 mM

Supplemental Figure 3. Oxidation and detection of oxidation products of PAPC and PLPC. Oxidized phospholipids were prepared for LCMS by *in vitro* oxidation. **(A)** PAPC was oxidized by air for 7-10 days. **(B)** PLPC was oxidized by Fenton-like copper reaction for 18 hours. **(C)** Schematic of chromatography for analysis mass spectrometric analysis of oxidized phospholipids. **(D)** Solvent system for separation of OxPL species by HPLC.

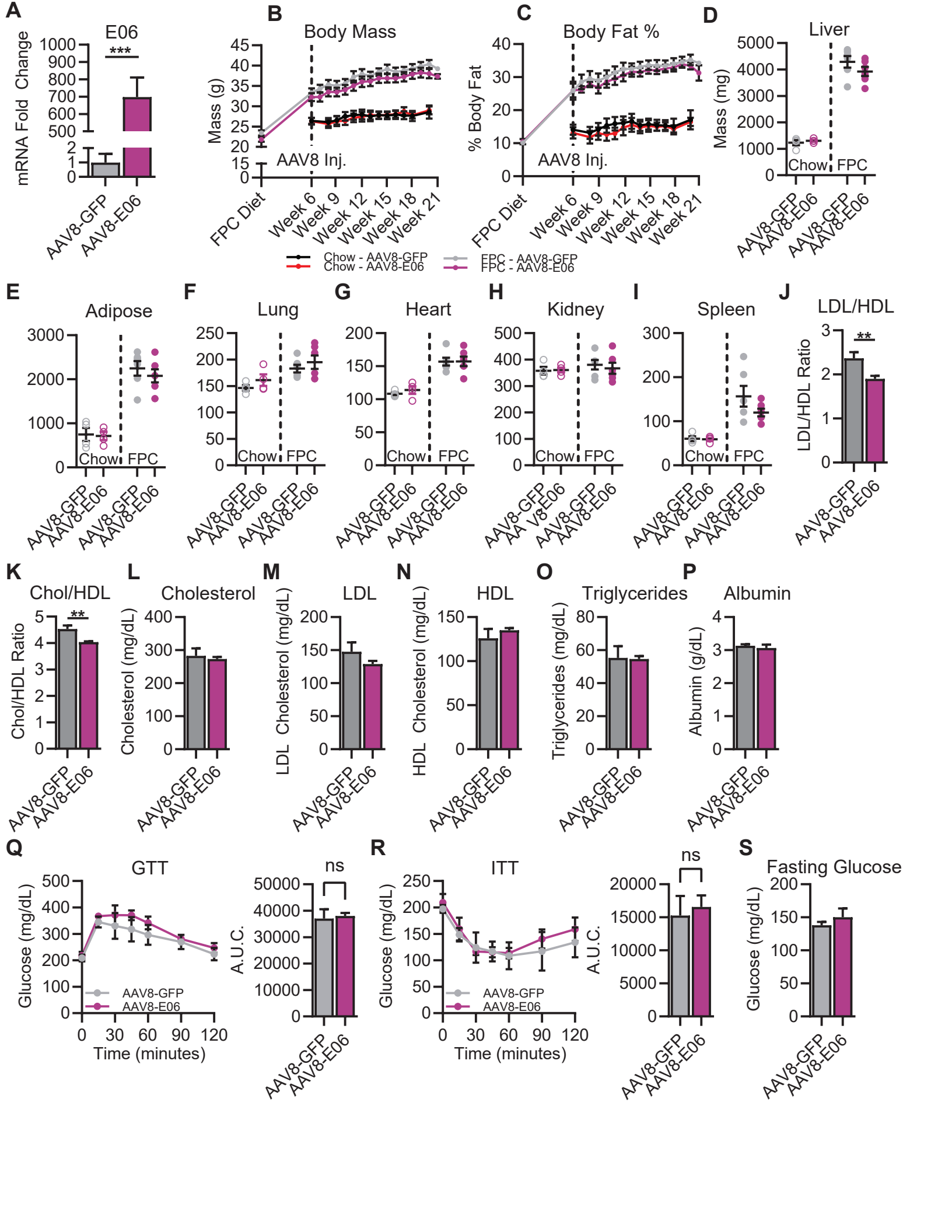
A
E06
***
mRNA Fold Change
AAV8-GFP
AAV8-E06
B
Body Mass
Mass (g)
AAV8 Inj.
FPC Diet
Week 6
Week 9
Week 12
Week 15
Week 18
Week 21
C
Body Fat %
% Body Fat
D
Liver
Mass (mg)
Chow
FPC
Chow - AAV8-GFP
Chow - AAV8-E06
FPC - AAV8-GFP
FPC - AAV8-E06
E
Adipose
F
Lung
G
Heart
H
Kidney
I
Spleen
J
LDL/HDL
LDL/HDL Ratio
**
K
Chol/HDL
Chol/HDL Ratio
L
Cholesterol
Cholesterol (mg/dL)
M
LDL
LDL Cholesterol (mg/dL)
N
HDL
HDL Cholesterol (mg/dL)
O
Triglycerides
Triglycerides (mg/dL)
P
Albumin
Albumin (g/dL)
Q
GTT
Glucose (mg/dL)
Time (minutes)
A.U.C.
ns
R
ITT
S
Fasting Glucose

Supplemental Figure 4. Gene ontology and gene expression of AML12 hepatocytes treated with truncated OxPAPC, full-length OxPAPC, and OxPAPC.

AML12 murine hepatocytes were treated with either OxPAPC, truncated OxPAPC, and full-length OxPAPC (100 μg/mL) for 4 hours and gene expression was measured via RNA-seq. GO Biological processes of upregulated genes (fold change > |1.5| and adjusted p-value < 0.05) identified by EnrichR for **(A)** OxPAPC, **(B)** truncated OxPAPC, and **(C)** full-length OxPAPC. Expression of **(D)** *Hmox1,* **(E)** *Pgd,* **(F)** *Acly,* **(G)** *Hmgcoas,* and **(H)** *Hmgcoar* in AML12 hepatocytes were confirmed by RT-qPCR (n=4). *Hmox1* and *Pgd* were regulated by all three oxidized phospholipid treatments; however, *Acly*, *Hmgcoas*, and *Hmgcoar* were exclusively upregulated by truncated OxPAPC. Statistical significance was determined by 1-way ANOVA. Multiple comparisons were corrected by Dunnet's multiple comparisons correction (*=$p<0.05$, **=$p<0.01$, ****=$p<0.0001$).

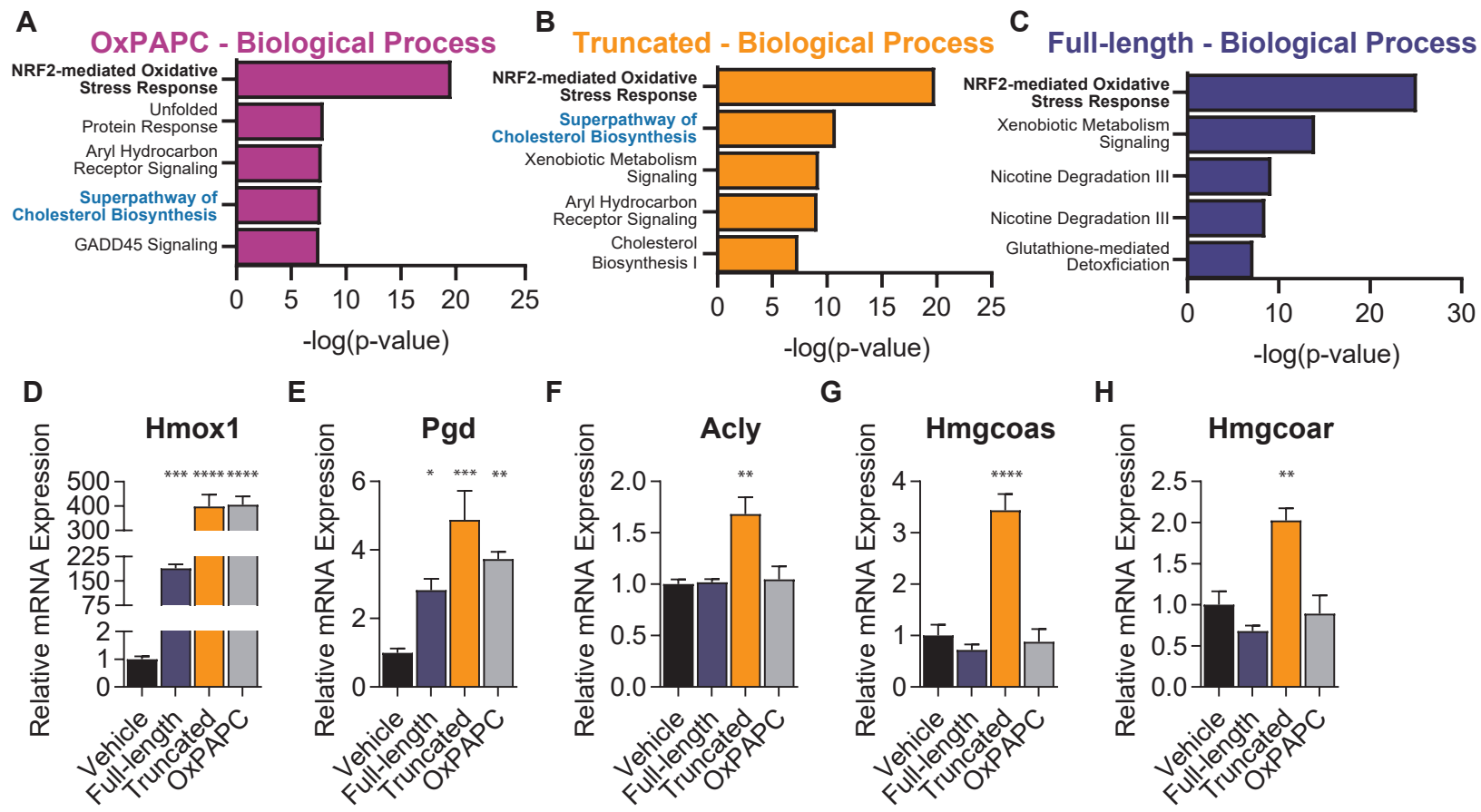
A
OxPAPC - Biological Process
NRF2-mediated Oxidative Stress Response
Unfolded Protein Response
Aryl Hydrocarbon Receptor Signaling
Superpathway of Cholesterol Biosynthesis
GADD45 Signaling
0 5 10 15 20 25
-log(p-value)
B
Truncated - Biological Process
NRF2-mediated Oxidative Stress Response
Superpathway of Cholesterol Biosynthesis
Xenobiotic Metabolism Signaling
Aryl Hydrocarbon Receptor Signaling
Cholesterol Biosynthesis I
0 5 10 15 20 25
-log(p-value)
C
Full-length - Biological Process
NRF2-mediated Oxidative Stress Response
Xenobiotic Metabolism Signaling
Nicotine Degradation III
Nicotine Degradation III
Glutathione-mediated Detoxification
0 10 20 30
-log(p-value)

D
Hmox1
Relative mRNA Expression
*** **** ****
500
400
300
225
150
75
2
1
0
Vehicle
Full-length
Truncated
OxPAPC
E
Pgd
Relative mRNA Expression
* *** **
6
4
2
0
Vehicle
Full-length
Truncated
OxPAPC
F
Acly
Relative mRNA Expression
**
2.0
1.5
1.0
0.5
0.0
Vehicle
Full-length
Truncated
OxPAPC
G
Hmgcoas
Relative mRNA Expression
****
4
3
2
1
0
Vehicle
Full-length
Truncated
OxPAPC
H
Hmgcoar
Relative mRNA Expression
**
2.5
2.0
1.5
1.0
0.5
0.0
Vehicle
Full-length
Truncated
OxPAPC

Supplemental Figure 5. Characterization of mice treated with AAV8-scFv-E06 after 20 weeks on FPC diet.

Speer6-ps1$^{Tg(Alb\text{-}cre)21Mgn}$/J mice were fed FPC or chow diet for six weeks. After six weeks mice were injected with either AAV8-GFP or AAV8-scFv-E06. Mice continued diet for a total of 20/21 weeks. **(A)** scFv-E06 gene expression was significantly increased in mice injected with AAV8-scFv-E06 ((FPC AAV8-GFP, n=5; FPC AAV8-E06, n=6). There were no significant differences in **(B)** body mass or **(C)** body fat percentage between GFP and scFv-E06 expressing mice on FPC or chow diet; however, there were a significant increase in both body mass and body fat percentage between diet groups (n=10). At the end of the experiment, plasma was collected, and hepatic function and lipid profile were measured. **(D-I)** There were no differences in organ mass between scFv-E06- and GFP-expressing mice fed chow or FPC diet (n=6). Ratios of **(J)** LDL/HDL and **(K)** Cholesterol/HDL in plasma were significantly reduced in mice expressing scFv-E06 compared to GFP after FPC diet feeding (n=6). **(L)** Cholesterol, **(M)** LDL, **(N)** HDL, **(O)** triglycerides, and **(P)** albumin levels in plasma were not significantly changed between scFv-E06 and GFP-expressing mice fed FPC diet (n=6). There were no differences in **(Q)** 6-hour fasted glucose and **(R)** insulin tolerance and **(S)** 18-hour fasting glucose in mice expressing GFP or scFv-E06 after 20 weeks FPC diet feeding (FPC AAV8-GFP, n=3; FPC AAV8-E06, n=4). Statistical significance was determined by 1-way and 2-way ANOVA and Student's T-test. Multiple comparisons were corrected by Dunnet or Tukey multiple comparisons correction (*=$p<0.05$, **=$p<0.01$, ****=$p<0.0001$).

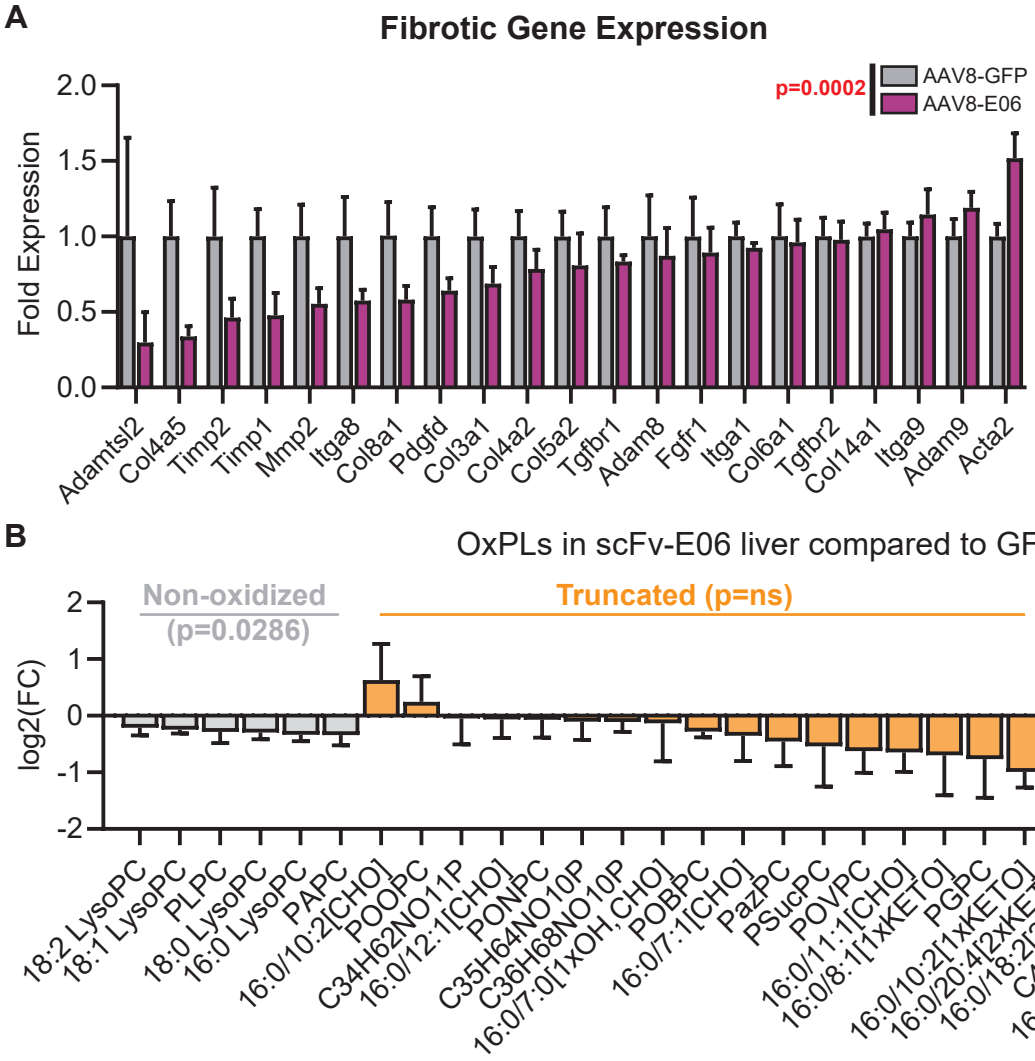
A
Fibrotic Gene Expression
p=0.0002
AAV8-GFP
AAV8-E06
Fold Expression
2.0
1.5
1.0
0.5
0.0
Adamtsl2
Col4a5
Timp2
Timp1
Mmp2
Itga8
Col8a1
Pdgfd
Col3a1
Col4a2
Col5a2
Tgfbr1
Adam8
Fgfr1
Itga1
Col6a1
Tgfbr2
Col14a1
Itga9
Adam9
Acta2

B
OxPLs in scFv-E06 liver compared to GFP liver
Non-oxidized
(p=0.0286)
Truncated (p=ns)
Full-length (p=ns)
log2(FC)
2
1
0
-1
-2
18:2 LysoPC
18:1 LysoPC
PLPC
18:0 LysoPC
16:0 LysoPC
PAPC
16:0/10:2[CHO]
POOPC
C34H62NO11P
16:0/12:1[CHO]
PONPC
C35H64NO10P
C36H68NO10P
16:0/7:0[1xOH,CHO]
POBPC
16:0/7:1[CHO]
PazPC
PSucPC
POVPC
16:0/11:1[CHO]
16:0/8:1[1xKETO]
PGPC
16:0/10:2[1xKETO]
16:0/20:4[2xKETO]
16:0/18:2[2xKETO]
C42H80NO9P
16:0/18:2[2xOOH]
C44H78NO10P
16:0/18:2[1xKETO]
C42H78NO10P
C44H80NO11P
C42H80NO11P
C44H80NO10P
C42H78NO10P
C44H80NO9P
16:0/18:1[1xOH]

Supplemental Figure 6. Fibrotic gene expression in mice treated with AAV8-scFv-E06. **(A)** Hepatic gene expression of fibrogenic genes were confirmed by RT-qPCR (GFP – n=6, scFv – n=6). **(B)** Truncated and full-length OxPCs extracted from liver tissue demonstrate a similar pattern to that observed in the plasma, while non-oxidized phospholipids were significantly decreased. Statistical significance was determined by 2-way ANOVA with Dunnet's multiple comparisons correction. Statistical outliers were excluded with the ROUT test (Q=5%)

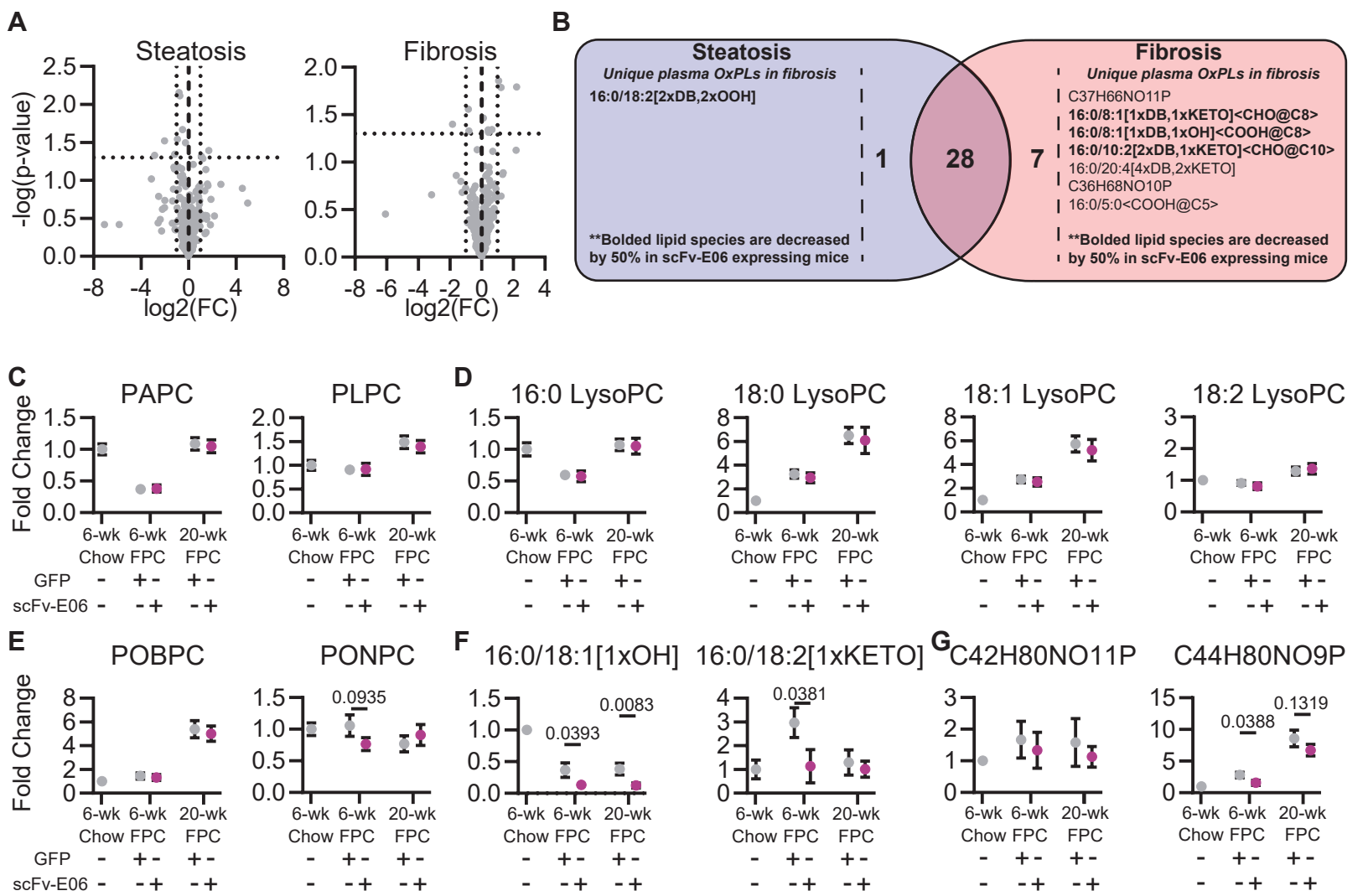
A
Steatosis
Fibrosis
-log(p-value)
log2(FC)
log2(FC)
B
Steatosis
Unique plasma OxPLs in fibrosis
16:0/18:2[2xDB,2xOOH]
1
28
7
**Bolded lipid species are decreased by 50% in scFv-E06 expressing mice
Fibrosis
Unique plasma OxPLs in fibrosis
C37H66NO11P
16:0/8:1[1xDB,1xKETO]<CHO@C8>
16:0/8:1[1xDB,1xOH]<COOH@C8>
16:0/10:2[2xDB,1xKETO]<CHO@C10>
16:0/20:4[4xDB,2xKETO]
C36H68NO10P
16:0/5:0<COOH@C5>
**Bolded lipid species are decreased by 50% in scFv-E06 expressing mice
C
PAPC
PLPC
D
16:0 LysoPC
18:0 LysoPC
18:1 LysoPC
18:2 LysoPC
Fold Change
6-wk Chow
6-wk FPC
20-wk FPC
GFP
scFv-E06
E
POBPC
PONPC
0.0935
F
16:0/18:1[1xOH]
16:0/18:2[1xKETO]
0.0393
0.0083
0.0381
G
C42H80NO11P
C44H80NO9P
0.0388
0.1319

Supplemental Figure 7. Untargeted and targeted lipid analysis reveal a changing oxo-phospholipidome but no change in the overall lipidome.

The plasma lipidome of mice after **(A)** six (GFP – n=7, scFv-E06 – n=6) and twenty weeks (GFP – n=10, scFv-E06 – n=10) of FPC diet were unaffected by expression of scFv-E06. **(B)** Comparison of oxidized phospholipids species detected in steatosis and fibrosis revealed 1 unique plasma oxidized phospholipid in steatotic mice and 7 unique oxidized phospholipids in mice with hepatic fibrosis. **(C)** Non-oxidized phospholipids PAPC and PLPC were unaffected by expression of scFv-E06; though their levels were altered by FPC diet duration (6-wk Chow GFP – n=3, 6-wk FPC GFP – n=7, 6-wk FPC scFv-E06 – n=6, 20-wk FPC GFP – n=10, 20-wk FPC scFv-E06 – n=10). **(D)** 16:0 LysoPC (6-wk Chow GFP – n=3, 6-wk FPC GFP – n=7, 6-wk FPC scFv-E06 – n=6, 20-wk FPC GFP – n=10, 20-wk FPC scFv-E06 – n=10) decreased after 6-weeks of FPC diet feeding while 18:0, 18:1 (6-wk Chow GFP – n=3, 6-wk FPC GFP – n=7, 6-wk FPC scFv-E06 – n=6, 20-wk FPC GFP – n=7/6, 20-wk FPC scFv-E06 – n=7), and 18:2 LysoPC (6-wk Chow GFP – n=2, 6-wk FPC GFP – n=7, 6-wk FPC scFv-E06 – n=6, 20-wk FPC GFP – n=6, 20-wk FPC scFv-E06 – n=7) increased after 6 and 20 weeks on FPC diet compared to 6-week, chow-fed controls. **(E)** POBPC (6-wk Chow GFP – n=3, 6-wk FPC GFP – n=7, 6-wk FPC scFv-E06 – n=6, 20-wk FPC GFP – n=10, 20-wk FPC scFv-E06 – n=10) increased with longer duration FPC-feeding but was unaffected by scFv-E06, while PONPC (6-wk Chow GFP – n=3, 6-wk FPC GFP – n=7, 6-wk FPC scFv-E06 – n=6, 20-wk FPC GFP – n=10, 20-wk FPC scFv-E06 – n=10) was unaffected by feeding and scFv-E06 expression. **(F)** 16:0/18:1[1xOH] (6-wk Chow GFP – n=1, 6-wk FPC GFP – n=5, 6-wk FPC scFv-E06 – n=6, 20-wk FPC GFP – n=9, 20-wk FPC scFv-E06 – n=10) was decreased by expression of scFv-E06 at both 6-weeks and 20-weeks of FPC-diet feeding, while 16:0/18:2[1xKETO] was only decreased by scFv-E06 after six

weeks of feeding (6-wk Chow GFP – n=3, 6-wk FPC GFP – n=7, 6-wk FPC scFv-E06 – n=6, 20-wk FPC GFP – n=10, 20-wk FPC scFv-E06 – n=8). **(G)** The isobaric group C42H80NO11P (6-wk Chow GFP – n=3, 6-wk FPC GFP – n=7, 6-wk FPC scFv-E06 – n=6, 20-wk FPC GFP – n=10, 20-wk FPC scFv-E06 – n=10) was unaffected by diet and scFv-E06 expression while C44H80NO9P was increased after six and 20 weeks of FPC diet. scFv-E06 expression decreased levels of C44H80NO9P after 20 weeks of FPC diet (6-wk Chow GFP – n=3, 6-wk FPC GFP – n=7, 6-wk FPC scFv-E06 – n=6, 20-wk FPC GFP – n=10, 20-wk FPC scFv-E06 – n=10). Statistical significance was determined by 2-way ANOVA with Tukey multiple comparison correction or Student's t-test.

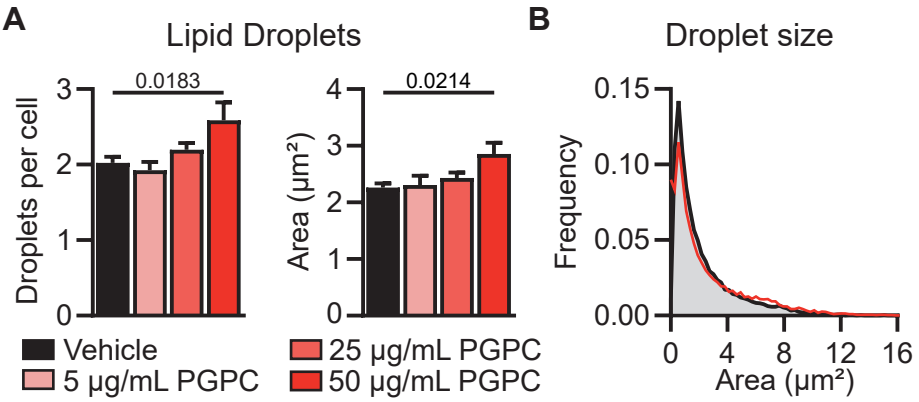
A
Lipid Droplets
Droplets per cell
0.0183
Area (µm²)
0.0214
Vehicle
5 µg/mL PGPC
25 µg/mL PGPC
50 µg/mL PGPC
B
Droplet size
Frequency
Area (µm²)

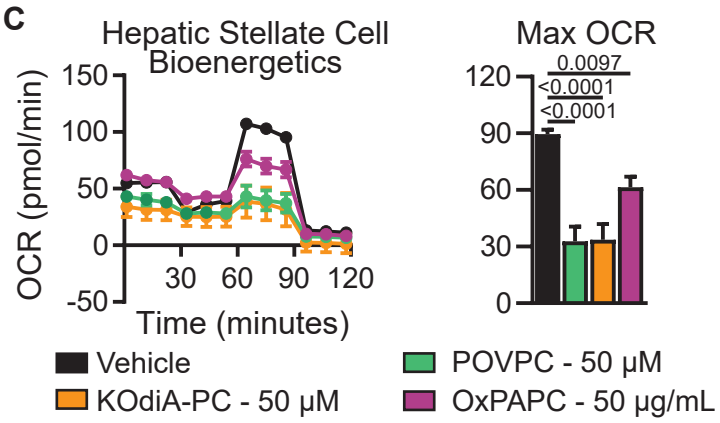
C
Hepatic Stellate Cell Bioenergetics
OCR (pmol/min)
Time (minutes)
Max OCR
0.0097
<0.0001
<0.0001
Vehicle
KOdiA-PC - 50 µM
POVPC - 50 µM
OxPAPC - 50 µg/mL

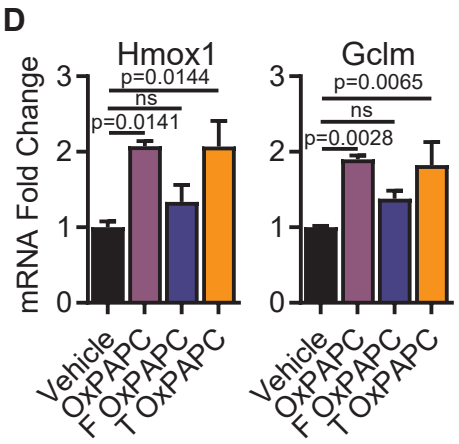
D
Hmox1
Gclm
mRNA Fold Change
p=0.0144
ns
p=0.0141
p=0.0065
ns
p=0.0028
Vehicle
OxPAPC
FOxPAPC
TOxPAPC

Supplemental Figure 8. Pathology-driving OxPCs regulate hepatocyte and hepatic stellate cell function *in vitro*.

AML12 hepatocytes treated with an increasing concentration of PGPC exhibited increased **(A)** lipid droplet number per cell and size resulting in a shift toward **(B)** a higher frequency of larger lipid droplets (n=4). **(C)** LX-2 hepatic stellate cell oxygen consumption rate was significantly decreased by POVPC, KOdiA-PC, and OxPAPC after 4 hours (Vehicle, n=6; POVPC, n=5; KOdiA-PC, n=5; OxPAPC, n=6), while **(D)** OxPAPC and truncated OxPAPC increased expression of *Hmox1* and *Gclm* after 4 hours (n=4). Statistical significance was determined by 1-way ANOVA with Dunnet's Multiple Comparison Correction or Student's t-test.

LPPTiger Nomenclature (previously identified species)	Parent Lipid	*m/z*	Formula	LPPTiger Predicted Structure(s)
1. PAPC	---	782	$C_{44}H_{80}NO_8P$	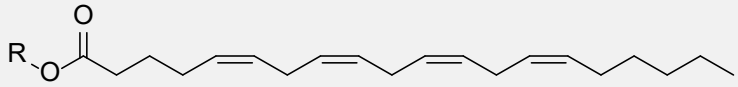
2. PLPC	---	758	$C_{42}H_{80}NO_8P$	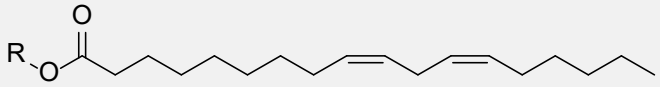
3. 16:0 LysoPC	---	496	$C_{24}H_{50}NO_7P$	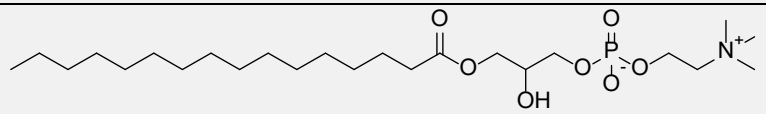
4. 18:1 LysoPC	---	522	$C_{26}H_{52}NO_7P$	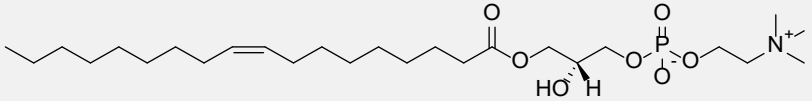
5. 18:2 LysoPC	---	520	$C_{26}H_{54}NO_7P$	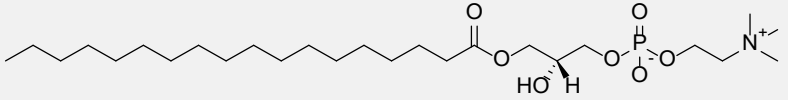
6. 18:0 LysoPC	---	524	$C_{26}H_{54}NO_7P$	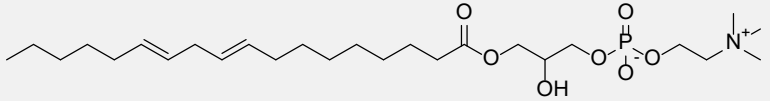
7. 16:0/12:1[CHO]	PLPC	690	$C_{36}H_{68}NO_9P$	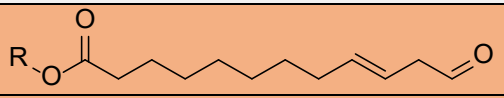
8. POBPC	PAPC	580	$C_{28}H_{54}NO_9P$	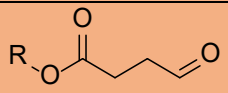
9. C35H62NO11P	PAPC	704	$C_{35}H_{62}NO_{11}P$	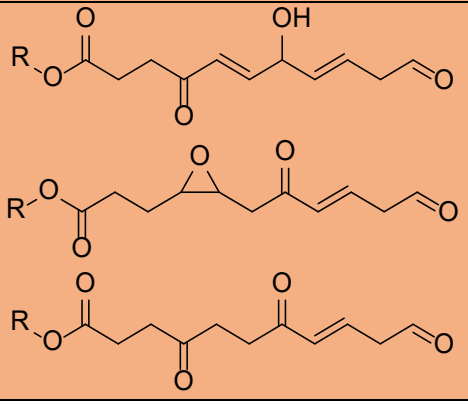

				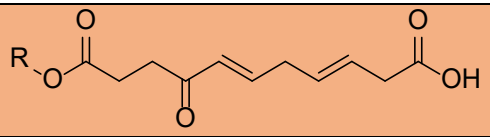
10. 16:0/7:0[1xOH,CHO]	PAPC	638	$C_{31}H_{60}NO_{10}P$	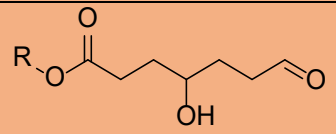
11. PONPC	PLPC	650	$C_{33}H_{64}NO_9P$	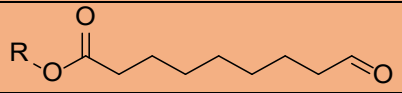
12. C35H64NO10P	PAPC	690	$C_{35}H_{64}NO_{10}P$	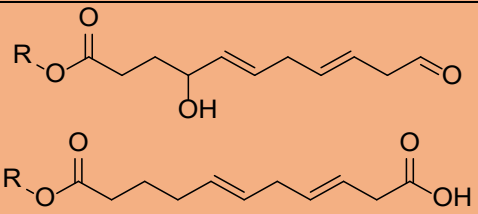
13. 16:0/11:1[CHO]	PLPC	676	$C_{35}H_{66}NO_9P$	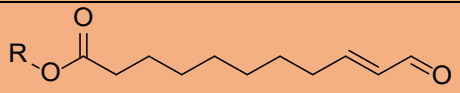
14. 16:0/8:0[CHO] (POOPC)	PLPC	636	$C_{32}H_{62}NO_9P$	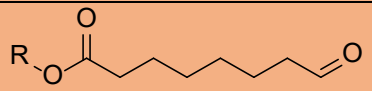
15. C35H64NO12P	PAPC	722	$C_{35}H_{64}NO_{12}P$	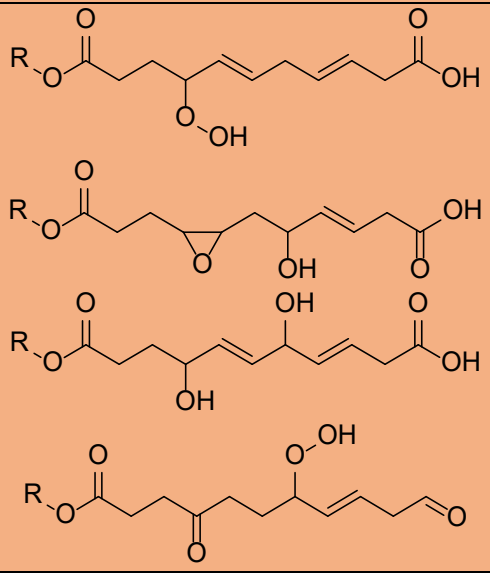

				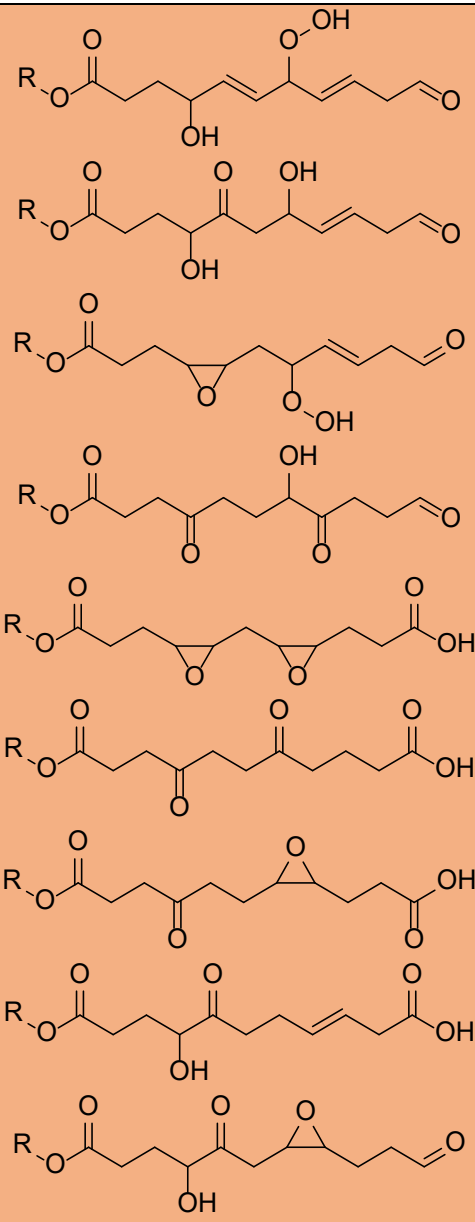
16. C32H60NO10P	PAPC	650	$C_{32}H_{60}NO_{10}P$	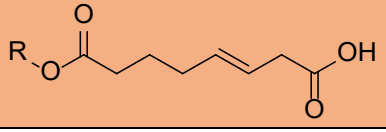

				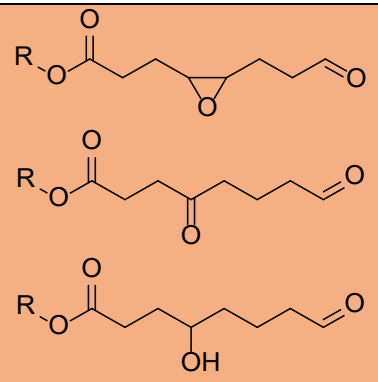
17. 16:0/10:2[CHO]	PAPC	660	$C_{34}H_{62}NO_9P$	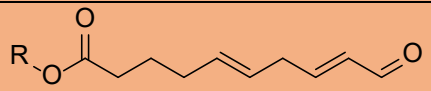
18. POVPC	PAPC	594	$C_{29}H56NO_9P$	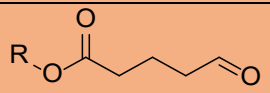
19. C34H62NO11P	PAPC	692	$C_{34}H_{62}NO_{11}P$	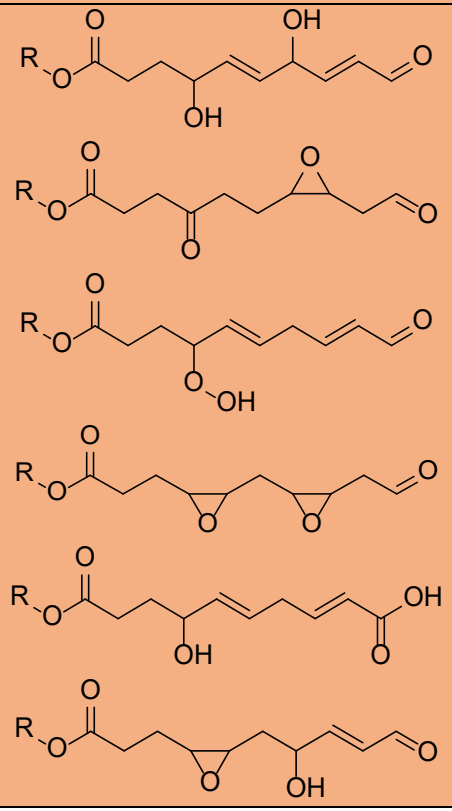

				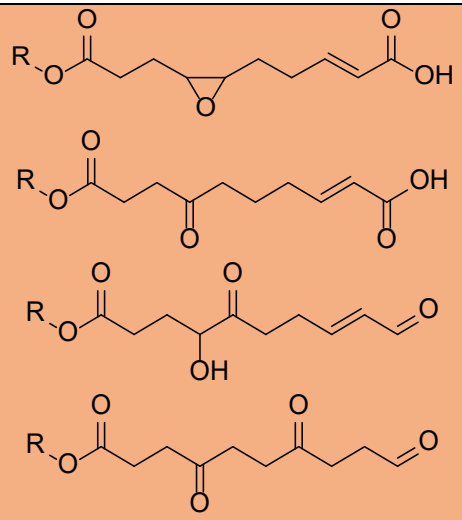
20. 16:0/7:1[CHO]	PAPC	620	$C_{31}H_{58}NO_9P$	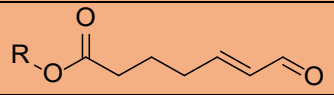
21. PazPC	PLPC	666	$C_{33}H_{64}NO_{10}P$	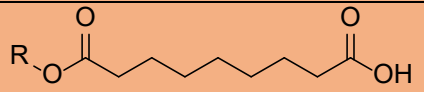
22. C42H80NO11P (HPODE-PC)	PLPC	806	$C_{42}H_{80}NO_{11}P$	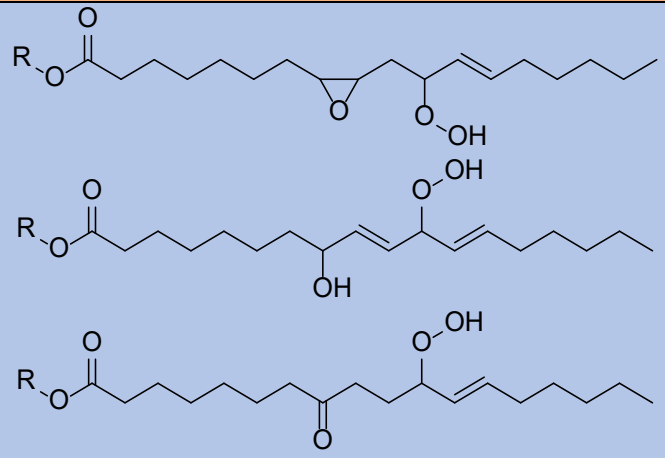
23. 16:0/18:2[2xOOH]	PLPC	822	$C_{42}H_{80}NO_{12}P$	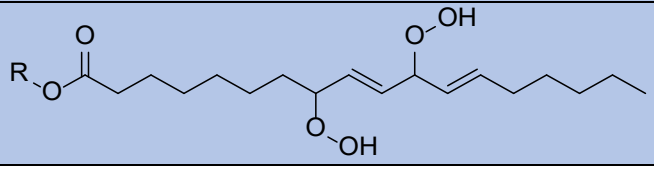

24. C42H78NO10P	PLPC	788	$C_{42}H_{78}NO_{10}P$	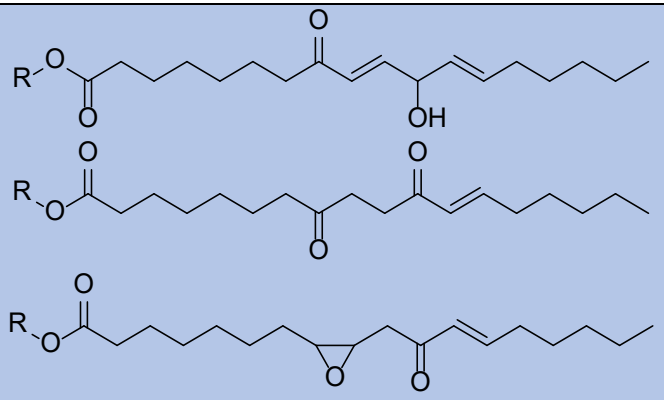
25. C44H80NO9P (HETE-PC)	PAPC	798	$C_{44}H_{80}NO_9P$	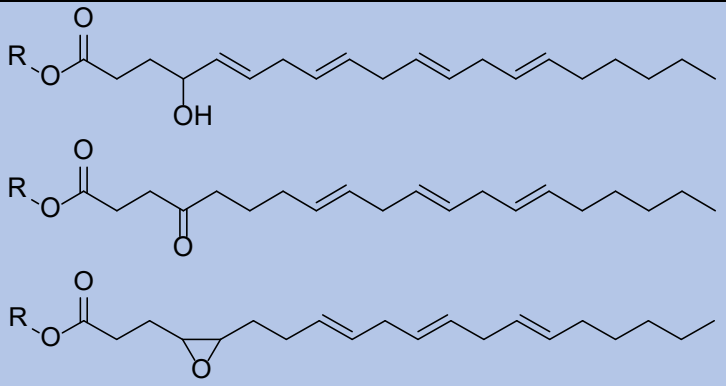
26. C44H80NO11P (Isoprostane-PC, Isoketal-PC)	PAPC	830	$C_{44}H_{80}NO_{11}P$	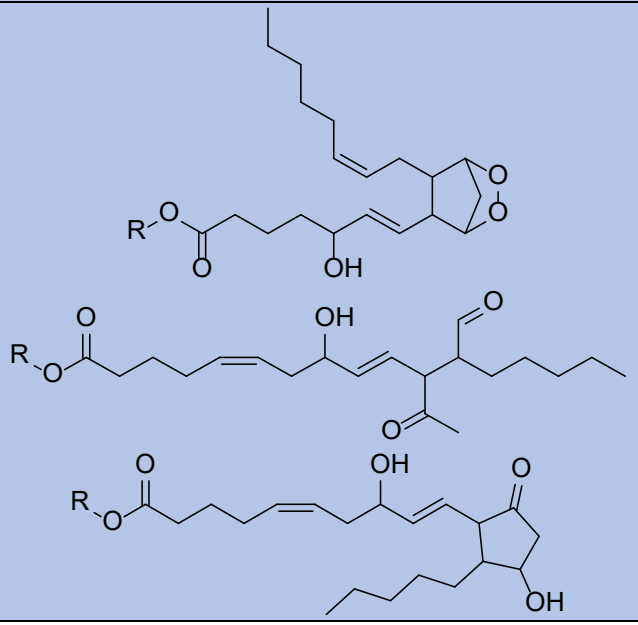

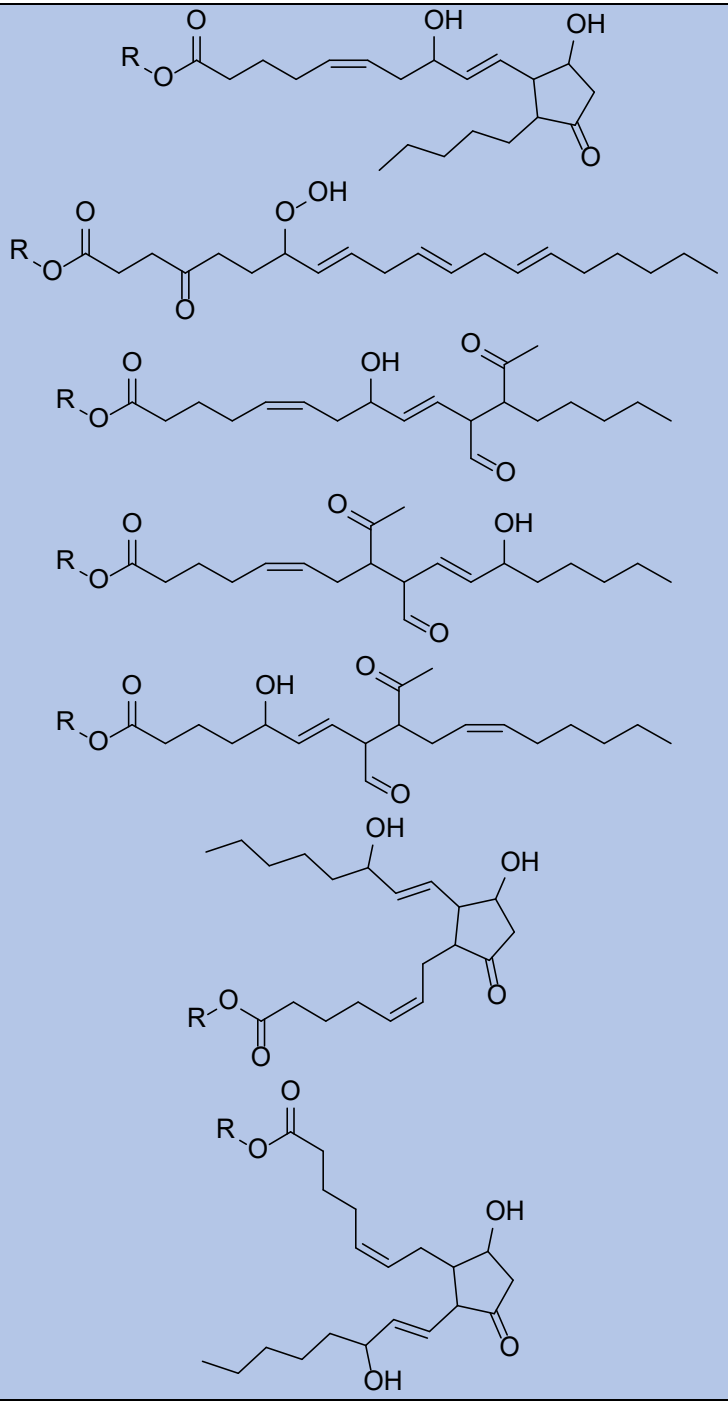
O
OH
OH
R
O
O
O
OH
R
O
O
O
O
OH
R
O
O
O
O
OH
R
O
O
O
O
OH
R
O
O
O
OH
OH
R
O
O
O
R
O
O
OH
O
OH

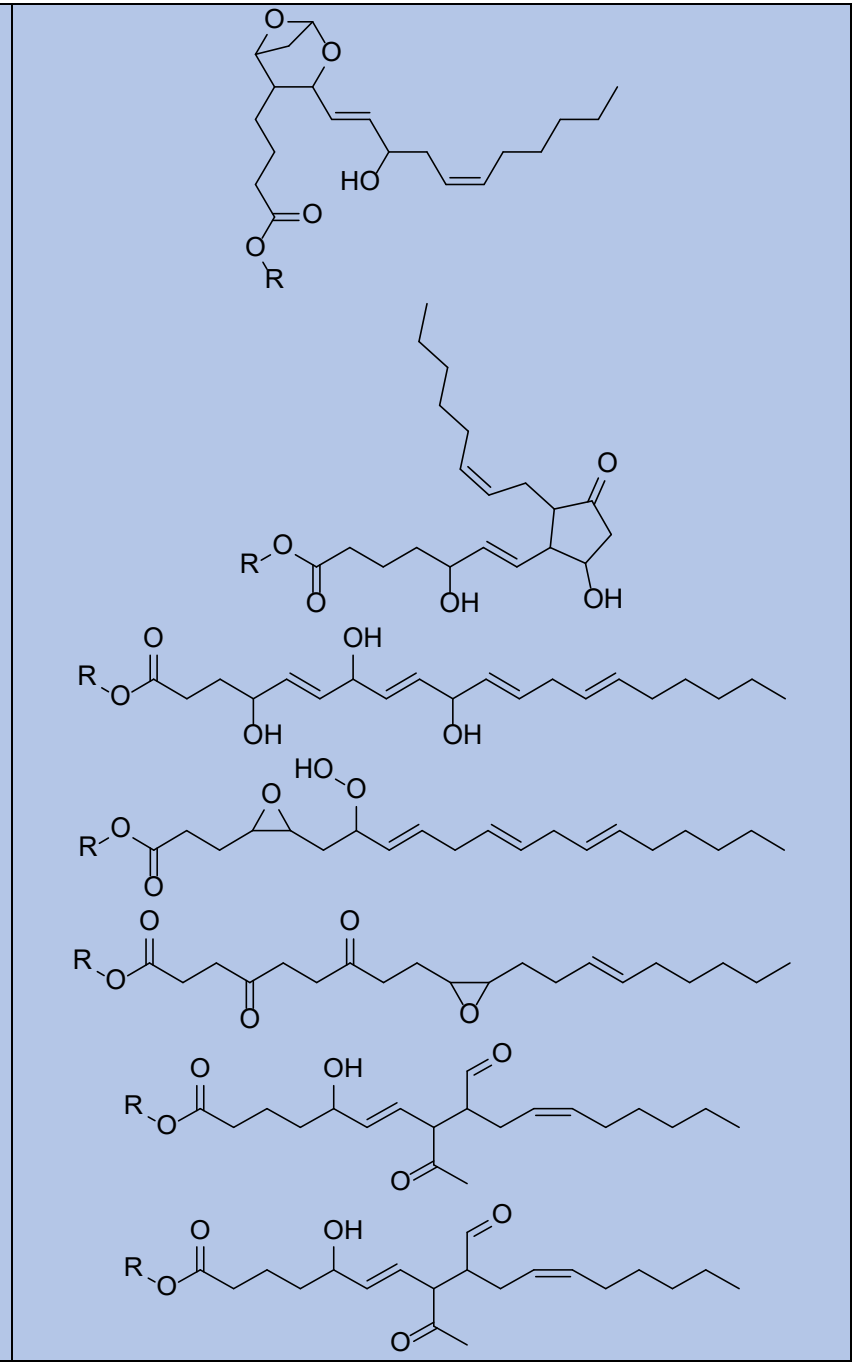
O
O
HO
O
O
R
O
O
R
O
O
OH
OH
O
R
O
O
OH
OH
HO
O
R
O
O
O
R
O
O
O
O
O
R
O
OH
O
O
O
R
O
OH
O
O

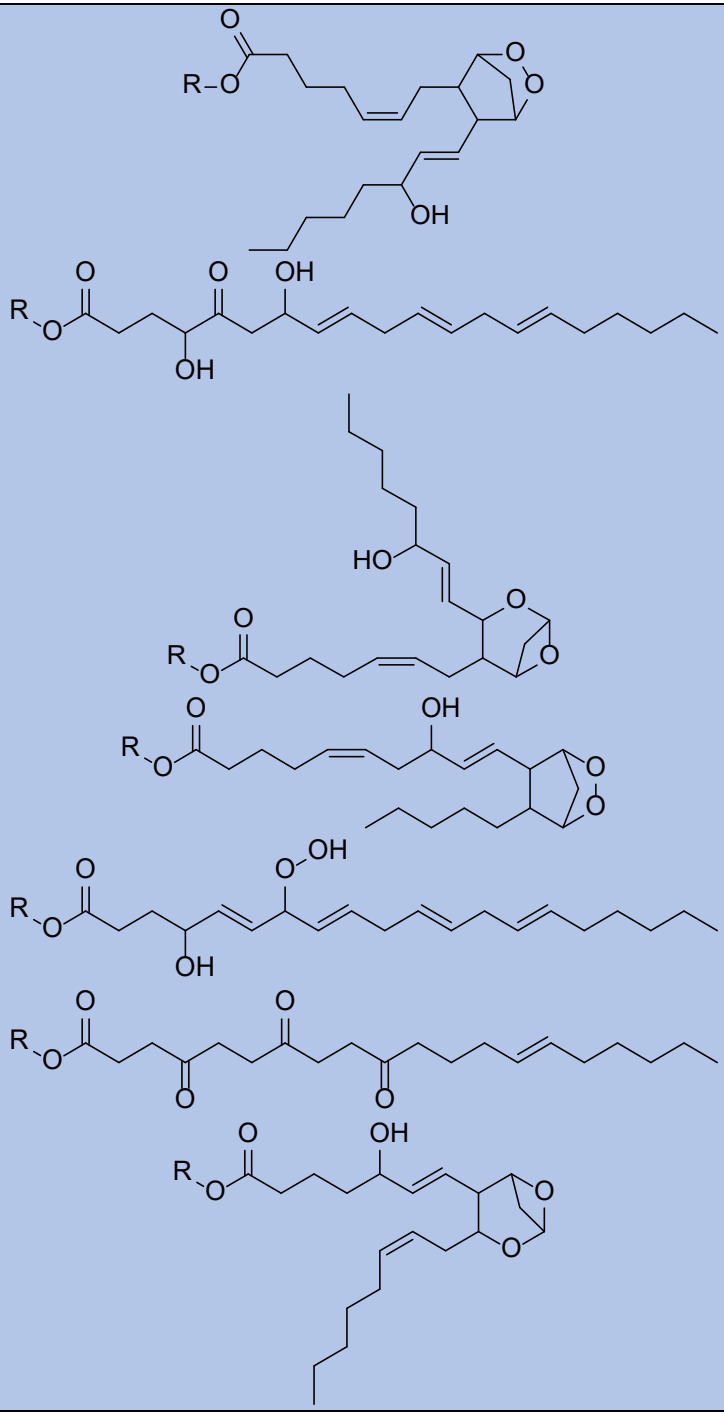
O
R–O
O
O
OH
O
O
OH
R
O
O
OH
HO
O
R
O
O
O
OH
R
O
O
O
OH
R
O
O
OH
O
O
R
O
O
O
O
R
O
OH
O

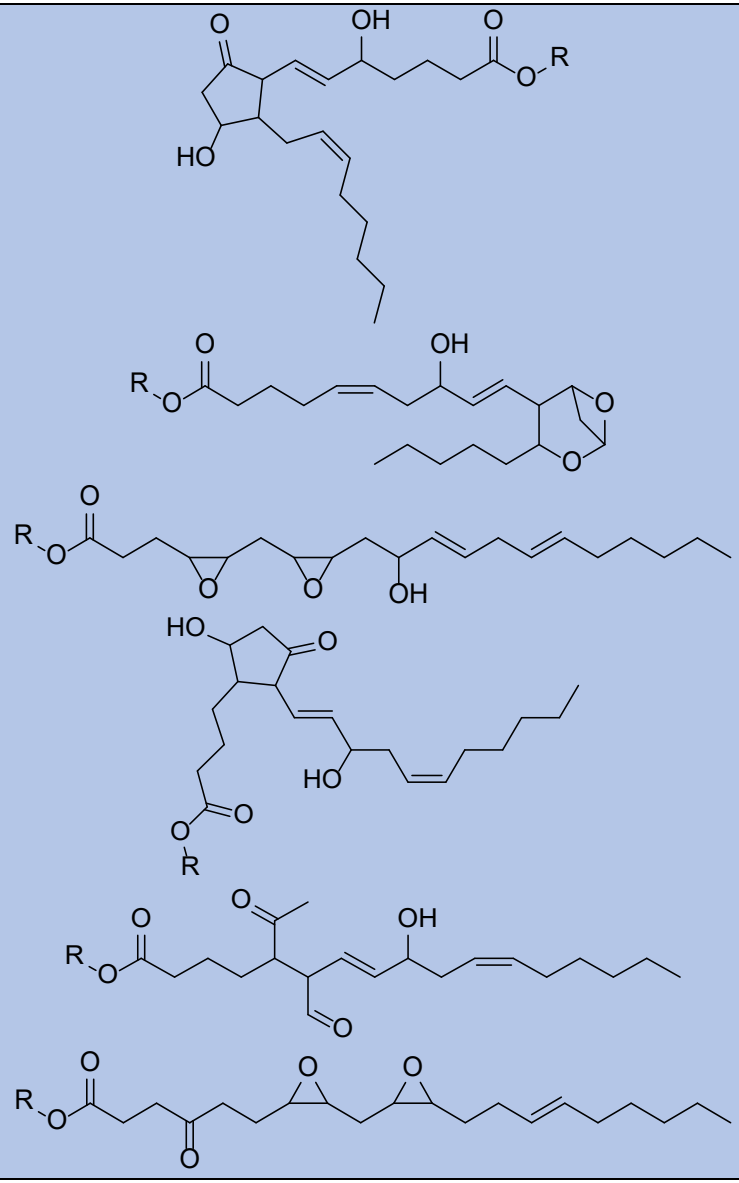
O
OH
O
R
O
HO
O
OH
R
O
O
O
R
O
O
O
OH
HO
O
HO
O
O
R
O
O
OH
R
O
O
O
R
O
O
O
O

				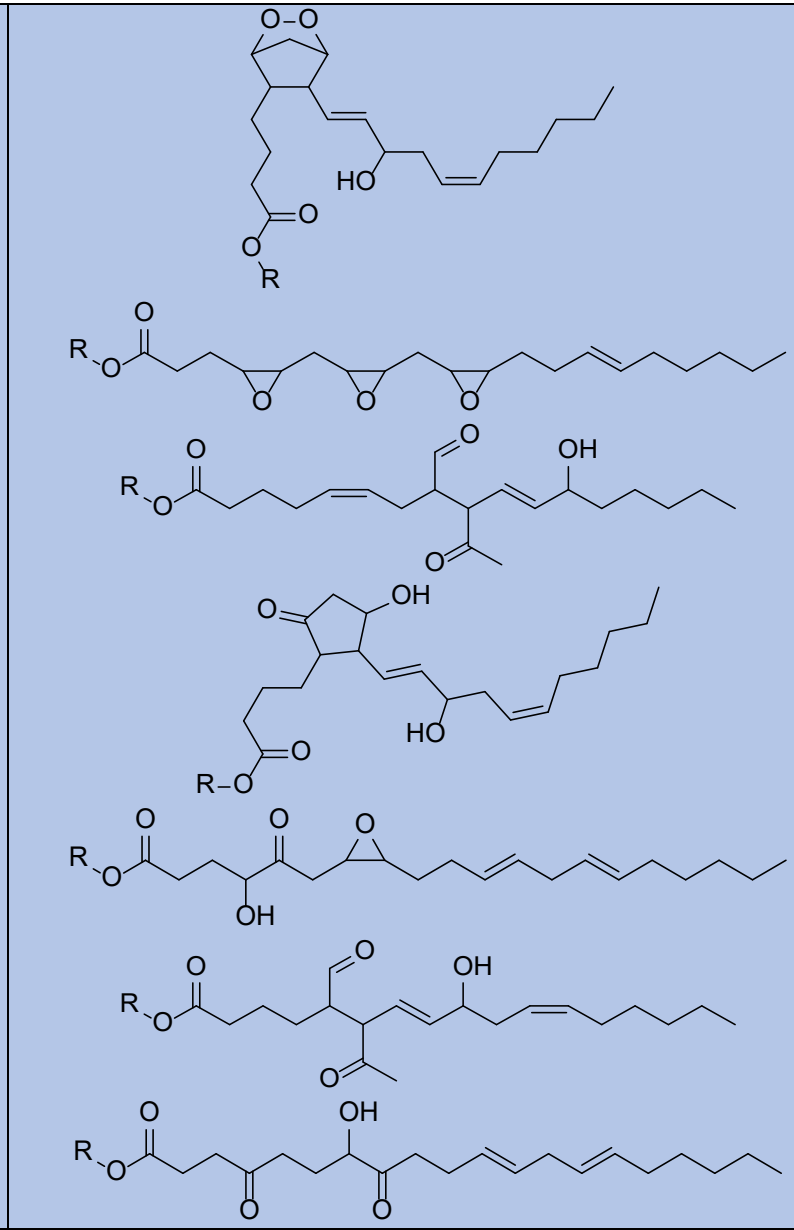
27. C42H80NO9P (HODE-PC)	PLPC	774	$C_{42}H_{80}NO_9P$	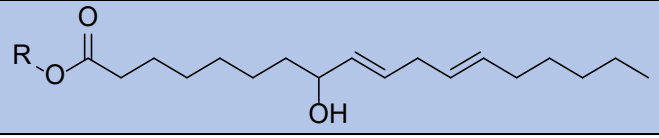

				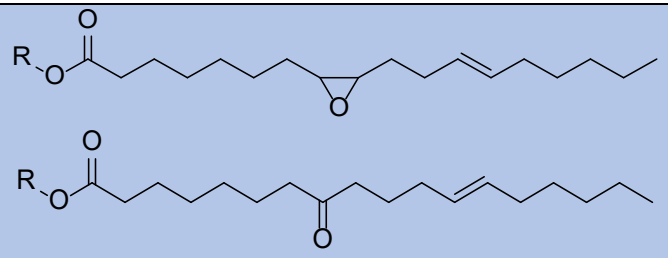
28. 16:0/18:2[2xDB,1xKETO] (KODE-PC)	PLPC	772	$C_{42}H_{78}NO_9P$	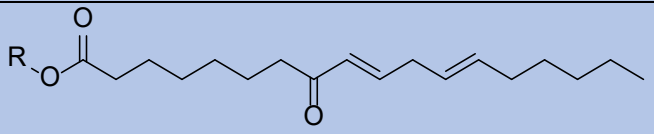
29. 16:0/18:1[1xDB,1xOH] (HOME-PC)	PLPC	776	$C_{42}H_{82}NO_9P$	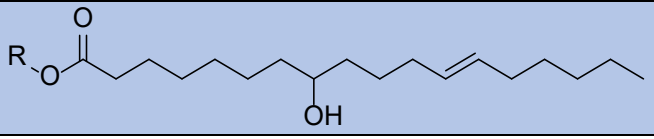

Supplemental Table 1. Oxidized phospholipids detected after development of hepatic steatosis. *In silico* predicted structures of oxidized phospholipids derived from PAPC or PLPC detected in mouse plasma after six weeks on FPC diet. CHO – aldehyde, COOH – carboxylic acid, OH – hydroxy, OOH – hydroperoxy, KETO – ketone, EPOXY – epoxide.

Gene Symbol	Trun-cated	Full-length	Ox-PAPC
1110002E22Rik	---	---	-1.06
1700011H14Rik	---	---	-0.83
1700066M21Rik	---	---	-0.74
1810011O10Rik	-1.11	---	---
2010111I01Rik	0.86	---	---
2310007B03Rik	---	---	-1.15
2310022B05Rik	---	---	-0.68
2410131K14Rik	0.77	---	0.86
2810417H13Rik	-0.77	---	-1.13
3010026O09Rik	---	---	-1.62
3110002H16Rik	---	---	0.72
3110043O21Rik	0.78	---	1.14
4921536K21Rik	---	---	1.63
4930427A07Rik	---	---	-0.82
4930430F08Rik	0.79	---	---
5031439G07Rik	---	---	0.75
5730508B09Rik	---	---	-0.97
9230110C19Rik	1.26	---	---
9330159F19Rik	---	---	0.97
9930012K11Rik	---	---	-0.95
AA415398	---	---	0.82
Aasdhppt	---	---	-0.75
Abca8b	2.50	1.43	2.74
Abcb6	2.03	1.35	1.77
Abcc1	1.90	1.58	2.02
Abcc2	3.72	2.81	4.08
Abcc4	1.53	1.37	1.71
Abcc5	1.03	---	1.04
Abcd4	---	---	0.87
Abhd4	1.36	1.03	1.64
Abhd5	---	---	0.92
Ablim1	-0.80	---	-0.77
Abr	1.05	---	1.20
Abtb1	1.24	---	1.02
Acan	-0.91	---	---
Acot2	1.01	---	1.38
Acox2	1.12	---	1.72
Acrbp	---	---	0.92
Actb	---	---	-0.67
Actg1	-0.72	---	-0.95
Actn1	-0.78	---	-0.72
Adamts1	-1.17	-1.36	---
Adamts6	-1.50	-1.58	-1.50
Adamts9	-1.73	-1.22	-1.73
Adap2	---	---	-1.26
Adgra2	-1.03	---	-0.81
Adgrg1	---	---	1.14
Adh7	2.75	1.86	1.86
Adprm	1.08	---	1.31
Adra1a	2.56	1.79	2.50
Adrm1	0.81	---	1.13
Afap1	---	---	0.85
Ahnak2	1.14	0.81	1.16
Ahr	-1.54	-0.92	-1.52
Ahsa1	0.79	---	0.84
Ahsa2	1.42	0.77	1.39
AI846148	---	---	0.88
Ajuba	---	---	-0.96
Akap1	---	---	-0.96
Akap12	-0.86	---	-0.99
Akap8l	0.79	---	1.05
Akr1c13	0.80	---	---
Akr1c14	2.30	1.37	1.73
Akr1c19	3.31	2.39	3.16
Akt1s1	---	---	0.78
Alas1	0.91	0.81	0.96
Aldh18a1	---	---	0.67
Aldh1a1	2.27	1.50	1.70
Aldh1l2	---	---	1.06
Aldh2	---	---	0.71
Aldh3a2	0.83	---	0.92
Aldoa	---	---	0.85
Alg6	---	---	-0.96
Als2	0.75	---	0.79
Amacr	---	---	-0.88
Ammecr1	---	---	-0.75
Amotl2	-0.86	---	-1.58
Ampd3	3.35	3.12	3.67
Anapc16	---	---	0.79
Angptl4	-0.97	---	-1.40
Angptl6	---	---	1.34
Ankle1	---	---	-1.24
Ankrd1	-2.23	-0.98	-2.75
Ankrd11	---	---	0.91
Ankrd12	---	---	1.05
Ankrd40	---	---	-0.63
Ankrd49	---	---	-0.80
Anln	-0.73	---	-0.91
Antxr2	-0.79	---	---
Anxa7	---	---	0.75
Aox1	2.67	2.07	2.79
Ap1ar	---	---	-0.76
Ap1s3	---	---	-0.84
Apba3	---	---	0.78
Apobr	2.59	1.14	3.37
Aqp9	1.84	---	2.08
Areg	---	---	1.37
Arhgap18	---	---	-0.82
Arhgap19	---	---	-1.35
Arhgap27	---	---	0.72
Arhgap8	-1.23	---	-1.22
Arhgef39	---	---	-1.01
Arid4b	---	---	0.70
Arid5a	---	---	1.36
Arih2	---	---	0.80
Arl4a	---	---	0.79
Arl4c	-1.13	-0.85	-1.65
Arl4d	1.19	---	---
Arl5b	---	---	0.93
Arl8a	---	---	0.95
Armcx3	---	---	0.96
Arrdc2	1.08	---	0.91
Arrdc3	0.66	---	---
Asns	0.69	---	0.78
Aspm	---	---	-1.38
Atad5	---	---	-1.02
Atf3	1.39	---	4.41
Atf4	---	---	1.11
Atf5	1.01	---	1.15
Atg12	---	---	0.65
Atg14	0.97	---	1.17
Atp10a	-1.01	---	---
Atp5sl	0.85	---	0.87
Atp6v0a1	---	---	1.09
Atp7a	---	---	0.79
Atxn1	---	---	-0.81
Atxn7l2	---	---	0.77
Aurkb	-0.73	---	-1.09
Avl9	---	---	0.82
B2m	---	---	0.73
B4galt7	---	---	0.75
B4gat1	---	---	-0.78
Bach1	1.63	1.01	1.98
Bag3	1.62	1.42	2.57
Bahcc1	-0.99	---	-1.36
Bahd1	---	---	0.65
Bbc3	---	---	0.86
Bbs12	---	---	-0.98

BC005537	0.71	---	0.92
BC025446	-0.88	---	-0.77
BC055324	---	---	-0.65
Bcar1	-1.31	---	-1.47
Bcl3	-0.86	---	---
Blcap	---	---	1.03
Blvrb	3.83	3.03	3.95
Bmf	---	---	-0.94
Bnip3	0.97	---	0.91
Bok	---	---	-1.16
Bora	-0.97	---	-1.31
Borcs5	---	---	-0.81
Brd2	---	---	0.89
Bsdc1	0.79	---	1.13
Btc	---	---	1.01
Bub1b	---	---	-0.88
C2cd4c	1.04	---	---
C2cd5	---	---	-0.80
Cachd1	2.24	1.67	2.61
Cacna1h	---	-1.03	-0.95
Cacnb2	-1.06	---	---
Cacybp	---	---	0.85
Cad	---	---	-0.83
Calcoco1	1.15	---	1.11
Calr3	2.88	2.24	2.91
Camkk1	---	---	-1.43
Camkk2	-0.89	---	-1.16
Camkmt	---	---	0.90
Capn5	-0.92	---	-0.74
Car15	---	---	1.41
Card10	-0.75	---	-1.45
Casc4	-0.97	---	---
Casp8ap2	---	---	-0.89
Cat	1.64	1.36	1.62
Cav1	-0.79	---	-0.76
Cav2	-0.88	---	-1.12
Cbr1	1.60	0.89	1.32
Cbx4	---	---	-0.81
Cbx6	---	---	-1.00
Cc2d2a	---	---	-0.86
Ccbe1	-1.42	---	-1.21
Ccdc117	0.83	---	0.75
Ccdc186	---	---	0.80
Ccdc28a	---	---	0.75
Ccdc71l	---	---	0.74
Ccdc88a	1.06	0.99	1.43
Ccdc92	---	---	0.79
Ccl2	-1.21	-1.12	-1.78

Ccna2	---	---	-0.99
Ccnb1	---	---	-1.05
Ccnb2	---	---	-0.84
Ccnd1	-0.96	---	-1.21
Ccnd3	-0.73	---	-0.93
Ccne1	-1.99	---	-2.41
Ccne2	-1.25	---	-1.64
Ccnf	---	---	-0.85
Ccng2	0.96	---	1.31
Ccsap	---	---	-1.36
Cd3eap	---	---	-1.11
Cd44	-0.88	---	---
Cd59a	0.94	---	1.06
Cd9	---	---	0.70
Cdc20	---	---	-0.87
Cdc25b	---	---	-0.74
Cdc25c	---	---	-0.91
Cdc42ep2	1.79	1.56	1.69
Cdc42ep5	---	---	0.93
Cdc6	-1.13	---	-1.35
Cdc7	-0.74	---	-0.99
Cdca2	---	---	-0.65
Cdca7	-1.22	---	-1.77
Cdca7l	---	---	-1.16
Cdk2	-0.75	---	-0.72
Cdk6	-0.84	---	-0.86
Cdkn1a	---	---	0.74
Cdkn2aipnl	---	---	-0.88
Cdkn2b	1.75	1.24	2.02
Cdkn2c	---	---	-0.79
Cdkn2d	---	---	-1.62
Cdr2l	---	---	0.95
Cds2	0.97	---	0.87
Cdt1	-0.87	---	-0.67
Cebpa	1.59	---	1.67
Cebpb	---	---	1.27
Cenpa	---	---	-1.10
Cenpf	---	---	-0.74
Cenpl	---	---	-0.78
Cep55	---	---	-0.85
Cep78	---	---	-0.71
Cep85l	---	---	1.61
Cep89	---	---	-0.69
Cfap43	-0.72	---	---
Cgn	---	---	-1.52
Cgnl1	1.48	1.15	1.53
Chac1	---	---	2.38
Chaf1b	-0.74	---	---

Chchd10	---	---	1.33
Chd2	---	---	1.12
Chka	-0.99	-0.76	-0.70
Chmp1b	---	---	0.73
Chn2	-0.86	---	---
Chordc1	0.97	0.82	1.06
Chpf2	2.13	1.39	2.03
Chrnb2	1.29	---	1.39
Chst15	---	---	-0.70
Cish	---	---	1.01
Ckap2	-0.77	---	-0.87
Clcf1	---	---	0.84
Clcn2	---	---	0.88
Clcn6	---	---	0.90
Cldn2	-0.80	---	-0.89
Clic4	---	---	0.93
Clip2	---	---	0.81
Clk1	---	---	0.82
Clk3	---	---	0.67
Clk4	---	---	0.80
Clmn	---	---	-0.79
Clspn	---	---	-0.73
Cnn2	-0.95	---	-1.18
Cnnm2	0.86	---	---
Cnot6	---	---	-0.68
Cnppd1	0.98	---	1.14
Cobl	---	---	0.93
Coil	---	---	-0.90
Col11a2	1.41	---	1.46
Col4a5	---	---	-0.80
Coro2a	---	---	1.01
Cotl1	---	---	-0.72
Cpeb2	---	---	1.13
Cpt1a	0.92	---	0.83
Cpt1b	---	---	0.87
Crb2	---	---	-1.19
Crebrf	---	---	0.90
Creg1	2.32	2.00	2.58
Creld1	0.90	---	---
Crem	0.84	---	1.41
Crim1	-0.72	---	-0.82
Crlf1	---	0.97	1.24
Crocc	---	---	-0.88
Crocc2	---	---	-1.12
Crtc1	1.05	0.94	1.34
Cryab	---	---	1.15
Csf1	---	---	0.73
Csnk1e	---	---	0.76

Csrnp2	0.72	---	0.80
Cstb	---	---	0.72
Ctdsp2	---	---	-0.67
Ctdspl	---	---	-0.90
Ctgf	-3.76	-2.09	-4.45
Cth	1.17	---	1.35
Ctns	---	---	0.97
Ctps	---	---	-1.04
Ctsb	---	---	0.65
Ctsd	0.92	---	1.07
Cxcl1	-1.26	---	---
Cxcl5	-1.53	-1.17	-2.39
Cyb5a	1.76	1.63	1.97
Cyb5r1	---	---	0.97
Cyld	---	---	-1.08
Cyp1a1	2.61	1.97	---
Cyp2j6	0.85	---	1.00
Cyp3a13	---	---	0.94
Cyp51	2.25	---	2.51
Cyr61	-1.36	---	-1.75
Cys1	---	---	1.17
D630003M21Rik	---	---	-1.42
D930048N14Rik	---	---	-1.10
Dact2	1.33	---	0.88
Dbt	---	---	-0.87
Dck	---	---	-0.84
Dcun1d3	---	---	1.01
Ddit3	1.60	---	2.82
Ddit4	0.98	---	2.10
Ddx11	---	---	-1.01
Ddx20	---	---	-0.88
Ddx41	---	---	-0.81
Ddx51	---	---	-0.72
Dedd2	2.46	1.48	2.77
Dennd4a	---	---	1.07
Depdc1a	---	---	-1.04
Depdc7	1.05	---	1.49
Deptor	1.06	---	0.91
Dgat2	---	---	1.09
Dhcr24	0.67	---	---
Dhodh	---	---	-0.86
Dhrs13	---	---	-1.09
Dhrs3	-1.34	-1.18	-1.91
Dhrs9	-1.26	---	---
Dimt1	-0.78	---	-1.08
Dip2b	---	---	0.81
Dkc1	-0.74	---	-0.80

Dlg5	---	---	0.99
Dlgap4	---	---	0.98
Dlk2	-1.04	---	-1.98
Dna2	-1.13	---	-1.22
Dnaja1	1.20	0.88	1.63
Dnaja4	1.51	0.99	2.74
Dnajb1	1.38	0.99	2.96
Dnajb2	1.47	0.84	1.41
Dnajb4	1.96	1.60	2.23
Dnajb9	---	---	1.48
Dnajc27	-1.16	---	-1.15
Dnase2a	1.46	1.19	1.40
Dnhd1	---	---	1.14
Dnph1	---	---	-1.00
Dock5	---	---	0.84
Dpp7	---	---	0.90
Dpy19l1	---	---	-0.97
Dsel	---	---	-0.79
Dtl	-1.29	---	-1.29
Dtx2	---	---	0.78
Dusp1	2.31	2.06	4.15
Dusp10	-0.79	---	-0.66
Dusp14	-1.07	---	-1.03
Dusp18	1.46	1.08	1.44
Dusp4	1.36	0.80	1.86
Dusp5	-1.21	---	---
Dusp6	---	---	0.98
Dusp7	-1.22	---	-0.84
Dut	---	---	-0.86
Dync1h1	---	---	0.77
Dync1li1	---	---	0.67
Dyrk1b	1.12	---	1.44
Dzip1l	---	---	-0.76
E2f6	0.96	0.89	1.08
E2f7	-0.88	---	-0.95
E2f8	-1.51	---	-1.61
E330009J07Rik	1.11	---	1.19
Eaf1	---	---	0.89
Ecm1	---	---	0.74
Ect2	-0.76	---	-1.03
Edn1	---	---	-1.95
Eea1	---	---	0.83
Eef2kmt	---	---	-0.71
Eepd1	-0.83	---	-1.18
Efcab8	---	---	0.95
Efnb1	1.00	---	1.22
Efnb2	-1.42	-0.68	-1.13

Egfr	-0.96	---	---
Egr1	-3.62	-2.38	---
Eid3	1.97	1.82	2.33
Eif2s2	---	---	0.83
Eif4ebp1	0.83	---	1.16
Elf1	---	---	1.01
Elmo1	---	---	0.97
Eml4	-0.86	---	-0.83
Emp1	-0.89	---	-0.80
Enc1	-1.22	---	-1.05
Endod1	---	---	-0.66
Engase	---	---	-1.29
Enpp1	-0.88	-0.84	-0.86
Enpp4	---	---	-0.83
Entpd5	1.52	1.07	1.46
Epb41	---	---	0.86
Epha7	---	---	-1.04
Ephx1	1.63	1.29	1.82
Eprs	---	---	0.73
Ercc6l	---	---	-0.80
Ereg	---	---	0.81
Eri1	---	---	-0.70
Eri2	---	---	-0.79
Ern1	---	---	1.00
Ero1l	---	---	0.77
Ero1lb	1.15	0.86	1.12
Errfi1	-1.20	-0.89	---
Esd	1.61	1.40	1.54
Espl1	---	---	-1.03
Esyt1	---	---	0.72
Etaa1	---	---	-0.97
Ets1	-0.84	---	-0.83
Exo1	-0.74	---	-1.01
Ext1	-0.78	---	-0.79
Eya2	---	---	1.14
Ezr	---	---	0.71
F2rl1	-1.35	---	-1.29
F3	-2.17	-0.89	-2.19
Faap100	-0.84	---	-0.98
Faap24	---	---	-0.84
Fadd	---	---	-0.83
Fads1	---	---	0.89
Fads2	0.99	---	1.23
Fam102a	---	---	1.09
Fam102b	-1.32	-0.87	-1.06
Fam118a	---	---	-0.78
Fam126a	---	---	0.74
Fam13a	2.35	1.44	2.43

Fam21	0.91	---	1.07
Fam214b	1.04	---	1.17
Fam219a	1.98	1.44	2.02
Fam63a	---	---	0.72
Fam64a	---	---	-1.08
Fam65b	-1.92	-1.29	-2.88
Fam73b	---	---	-0.76
Fam83d	---	---	-1.10
Fam83g	---	---	1.29
Fam83h	---	---	0.87
Fam84b	---	-0.83	---
Fanca	---	---	-0.80
Fancb	---	---	-0.92
Fancd2	---	---	-0.68
Fbxl20	0.77	---	0.76
Fbxo11	---	---	0.72
Fbxo30	1.01	---	1.11
Fbxo31	0.98	---	1.03
Fbxo32	1.06	---	0.89
Fbxo48	---	---	-1.23
Fbxo5	-1.08	---	-1.55
Fbxo9	1.06	0.82	0.82
Fchsd1	0.97	---	---
Fchsd2	-1.08	---	-1.09
Fdft1	1.32	---	1.44
Fech	---	0.79	0.80
Fen1	---	---	-0.93
Fermt1	-1.00	-0.75	-1.14
Fermt2	-0.73	---	-0.87
Fermt3	---	---	1.73
Fgd3	1.18	0.93	---
Fgf1	2.37	1.98	2.17
Fgfrl1	---	---	0.77
Fhdc1	---	---	1.10
Fhl2	-0.96	---	-1.22
Fhl3	-0.79	---	---
Fignl1	-0.71	---	-1.34
Fip1l1	---	---	0.74
Fjx1	---	---	-0.80
Flcn	---	---	0.77
Flrt2	-2.03	---	-1.72
Flrt3	---	---	0.91
Flywch1	1.13	---	1.00
Fndc4	---	---	-0.94
Fopnl	1.14	1.00	0.98
Fosl2	---	---	0.91
Foxj1	---	---	-1.10
Foxn3	---	---	1.02
Foxo3	---	---	0.88
Foxq1	1.74	1.46	1.45
Fpgt	0.78	---	---
Frmd4a	-0.85	---	---
Frmd6	-1.32	-0.80	-1.24
Fth1	1.66	1.64	2.14
Ftl1	1.37	0.89	1.52
Fxyd5	---	---	1.00
Fzd4	---	---	-0.90
Fzd7	1.09	0.75	1.06
G0s2	---	---	-1.12
G6pdx	0.79	---	1.23
Gaa	0.72	---	0.93
Gabarapl1	2.43	1.61	2.64
Gabpb2	---	---	-0.76
Gadd45a	1.68	---	2.29
Gadd45b	---	---	-1.32
Gart	---	---	-0.81
Gas2l3	---	---	-0.88
Gata3	---	---	1.52
Gba	---	---	0.73
Gbe1	1.44	0.91	1.60
Gch1	1.32	---	1.60
Gclc	3.72	3.31	4.12
Gclm	2.61	2.26	2.72
Gcnt2	---	---	0.76
Gcnt3	---	---	-0.91
Gdf11	---	---	0.89
Gdf15	1.93	1.48	4.41
Gemin4	---	---	-0.95
Gemin8	-1.11	---	-0.99
Ggta1	-0.71	---	-0.75
Ghdc	---	---	0.80
Ghitm	---	---	0.66
Gimd1	---	---	-0.79
Gjb1	1.21	1.18	1.59
Gjb3	-0.89	---	-1.55
Gla	0.95	---	1.11
Glis2	---	---	-0.92
Glmp	---	---	0.77
Glul	1.12	0.77	1.28
Glyat	2.50	2.01	2.81
Gm10073	---	---	1.23
Gm21949	---	---	-1.15
Gm21972	---	---	0.93
Gm42878	---	---	0.72
Gm42906	---	---	-1.22
Gm43518	---	---	-0.86
Gm43552	1.15	0.82	1.10
Gm45208	---	---	0.69
Gm7694	1.05	---	1.08
Gm8797	---	---	1.26
Gm9938	---	---	-0.94
Gmnn	---	---	-0.90
Gnal	---	---	0.77
Gpam	-0.77	---	-1.19
Gpcpd1	1.72	1.12	1.93
Gpd1l	---	---	-0.70
Gpi1	---	---	0.76
Gpr137b	0.81	0.88	1.12
Gpr180	---	---	-0.98
Gprc5a	-1.34	---	---
Gpt2	---	---	0.88
Gpx1	0.82	---	---
Gramd1a	---	---	0.79
Gramd3	---	---	0.96
Gramd4	-0.91	-0.71	-0.88
Grasp	---	---	0.80
Grik5	---	---	1.01
Grina	---	---	0.72
Grk6	---	---	-0.81
Grn	0.78	---	0.82
Gsg2	-0.99	---	-1.51
Gsr	1.36	1.26	1.48
Gss	2.37	1.60	2.38
Gsta1	7.09	6.46	6.79
Gsta3	3.11	2.35	2.96
Gsta4	5.13	4.49	4.69
Gstm1	1.91	1.55	2.28
Gsto1	---	---	0.77
Gstp1	2.35	1.63	1.76
Gtf2ird1	---	---	0.99
Gxylt2	-1.18	---	-1.13
H1f0	-1.11	---	-1.51
H2-DMa	1.39	---	1.40
Hap1	---	---	-0.90
Haus5	---	---	-1.07
Havcr1	-1.50	-0.92	-1.54
Hax1	---	---	0.87
Hbegf	-1.10	---	-0.90
Hbp1	0.97	---	1.24
Hdac4	---	---	0.74
Heatr3	---	---	-0.68
Heca	---	---	0.95
Hells	-1.38	---	-1.41
Herpud1	---	---	1.16

Hes1	-0.97	---	-1.41
Hfe	2.39	1.88	2.22
Hgs	---	---	0.87
Hhipl1	---	---	1.31
Hid1	---	---	1.39
Hist1h1c	1.16	---	1.05
Hist3h2a	0.96	---	0.81
Hivep2	-1.05	---	---
Hk2	-1.17	---	---
Hmga2	-0.84	---	---
Hmgcr	1.29	---	1.48
Hmgcs1	1.37	---	1.35
Hmmr	---	---	-0.87
Hmox1	6.60	6.03	7.55
Hnf1b	-1.02	---	---
Hnrnpr	---	---	-0.75
Homer3	0.97	0.71	1.13
Hook1	---	---	-0.76
Hpdl	---	---	-1.05
Hr	---	---	1.12
Hs3st3b1	1.17	---	---
Hsd17b7	---	---	0.87
Hsf2	---	---	0.81
Hsp90aa1	1.19	0.86	1.71
Hsp90ab1	0.81	---	1.21
Hspa1a	5.39	4.26	6.42
Hspa1b	5.38	4.36	6.45
Hspa2	---	---	0.80
Hspa4l	1.17	---	1.12
Hspa8	1.14	1.00	1.61
Hspb1	2.25	1.58	3.30
Hspb8	1.84	1.47	2.11
Hsph1	2.12	1.46	2.65
Htatip2	2.00	1.05	1.66
Htr1b	-1.25	---	-1.37
Hyal1	1.03	---	1.15
Hyal3	1.09	0.83	1.37
Icam1	-1.15	---	-0.85
Ick	1.64	1.52	2.04
Id2	-1.00	---	-1.45
Idh1	2.64	1.48	2.54
Idi1	1.27	---	0.98
Ier3	---	---	0.67
Iffo2	-0.72	---	-0.74
Ifi202b	0.85	---	1.47
Ifi203	---	---	1.03
Ifi47	---	---	-1.20
Ifit2	---	---	-1.44
Ifngr1	---	---	-0.74
Ifnlr1	---	---	-1.01
Igfbp3	-0.86	---	-0.67
Igip	---	---	-1.15
Igsf9	-0.90	---	-1.16
Igtp	1.52	1.24	1.33
Ikbkg	1.45	1.06	1.06
Ikzf2	---	---	-1.38
Il11	---	---	1.26
Il18rap	---	---	-1.01
Il1r1	---	---	-1.17
Il24	-2.11	---	-1.70
Il33	---	---	0.72
Il4ra	0.96	0.91	1.15
Il5ra	-2.91	-2.00	-3.48
Il7	---	---	0.99
Impact	1.41	1.00	1.75
Inhba	-1.43	---	-0.87
Inhbb	-1.15	---	-2.33
Inpp4b	-1.81	---	-1.21
Inpp5j	0.91	---	1.25
Insig1	2.28	---	3.06
Ipp	---	---	-0.93
Iqck	---	---	0.89
Iqgap3	-0.77	---	-0.89
Irs2	1.09	1.03	0.75
Itga3	-0.81	---	---
Itga6	---	---	-0.64
Itga7	1.33	1.09	1.84
Itgb6	-1.59	-1.04	-2.88
Itpripl1	---	---	-0.75
Itsn1	---	---	0.70
Jade2	-1.78	-1.07	-2.28
Jade3	0.85	---	1.07
Jag1	-1.18	-0.78	-1.12
Jmjd6	---	---	0.75
Jrk	---	---	-0.82
Jun	---	---	2.46
Junb	-1.18	---	-0.97
Jup	---	---	0.74
Kank3	---	---	-1.40
Kbtbd8	---	---	-1.19
Kcmf1	---	---	0.91
Kcnab1	---	---	-0.71
Kcnk5	---	---	-0.84
Kctd18	0.92	---	---
Kdm2a	---	---	0.83
Kdm3a	---	---	0.83
Kdm4a	0.83	---	0.89
Keap1	0.97	---	0.95
Kif11	---	---	-0.82
Kif14	---	---	-1.21
Kif15	---	---	-0.82
Kif18a	-0.81	---	-1.04
Kif1b	0.76	---	0.91
Kif20a	---	---	-0.63
Kif20b	---	---	-0.70
Kif21a	0.94	---	1.32
Kif23	---	---	-0.68
Kif24	---	---	-0.99
Kif2a	1.03	0.94	1.40
Kif2c	---	---	-0.71
Kif3c	0.83	---	1.10
Kif7	---	---	-1.21
Kifc3	---	---	-0.90
Kitl	1.07	0.83	0.85
Klc4	0.91	---	0.78
Klf11	0.89	---	1.17
Klf15	---	---	-1.62
Klf16	-0.95	---	-0.89
Klf4	---	---	1.43
Klf5	---	---	0.81
Klf6	---	---	0.69
Klf7	-0.99	---	-1.00
Klf9	---	---	1.02
Klhl15	---	---	0.73
Klhl21	---	---	0.74
Klhl24	1.46	---	1.58
Klhl26	---	---	0.79
Klhl5	---	---	-0.70
Krt7	---	---	-0.88
Krt80	-1.04	---	-1.83
Ksr1	1.26	0.97	1.19
L2hgdh	---	---	-0.68
L3mbtl2	---	---	-0.86
Lancl2	---	---	-0.63
Lancl3	1.28	1.24	1.13
Lasp1	---	---	-0.71
Layn	1.25	1.05	1.71
Lcmt2	---	---	-0.83
Ldlr	1.51	---	1.72
Lfng	---	---	-1.02
Lgals8	0.77	---	1.26
Lgalsl	---	---	-0.99
Lgr6	-1.36	---	-1.73
Lhfpl2	---	---	0.76

Lif	-1.20	---	-1.04
Lig1	-0.80	---	-0.87
Lin37	---	---	0.85
Lipe	0.95	---	1.03
Lmbr1l	---	---	0.72
Lmcd1	-1.96	-1.15	-2.26
Lmln	---	---	-1.45
Lmnb2	---	---	-0.86
Lonrf3	---	---	0.83
Lpar2	0.69	---	---
Lpcat1	-0.91	---	-1.37
Lpcat4	-0.84	---	-0.74
Lpin1	1.99	---	2.41
Lpin2	1.31	---	1.61
Lrig1	-0.76	---	-0.64
Lrp8	1.38	1.28	1.66
Lrr1	---	---	-1.20
Lrrc49	---	---	0.73
Lrrc8c	-1.21	---	---
Lrrc8d	---	---	0.97
Lrrfip2	---	---	0.94
Lrtm2	1.44	---	---
Lss	1.09	---	0.93
Lurap1l	---	---	-0.80
Ly75	---	---	-0.79
Ly96	---	---	1.27
Lyar	-0.76	---	---
Maff	---	---	1.07
Mafg	1.19	0.80	1.39
Mafk	---	---	0.96
Maml2	-0.96	---	---
Man2a1	---	---	0.68
Maoa	1.08	---	0.90
Map1b	---	---	1.44
Map1lc3b	1.13	---	1.34
Map2k6	-1.55	-0.95	-1.38
Map3k4	---	---	-0.69
Map4k4	---	---	0.78
Mapk9	0.78	---	0.96
Mapkapk5	---	---	0.72
Mars2	---	---	-1.09
Masp1	-0.92	---	-1.08
Mat2a	---	---	-0.97
Mb21d2	---	---	0.91
Mccc2	---	---	-0.90
Mcm2	-0.90	---	-0.87
Mcm3	-0.88	---	-0.91
Mcm4	-0.91	---	-0.90
Mcm6	---	---	-0.69
Mcoln1	---	---	0.73
Mdfic	---	---	0.65
Mdm1	---	---	-1.00
Mdm2	---	---	0.96
Mecom	-1.52	-1.07	-1.55
Mef2d	---	---	0.90
Melk	---	---	-0.79
Mettl21a	---	---	-0.83
Mettl7a1	1.85	1.46	1.76
Mettl7b	1.15	1.18	1.34
Mfsd6	0.90	---	1.25
Mgat3	---	---	-1.35
Mgea5	0.69	---	0.85
Mgst1	1.79	1.33	1.62
Mgst2	1.57	1.41	1.33
Mia3	---	---	0.68
Mib2	---	---	0.82
Mical2	-0.99	---	-0.81
Micall2	---	---	-0.85
Mid1ip1	---	---	-0.93
Mipol1	---	---	-0.70
Mkx	---	---	-1.02
Mlkl	0.85	0.80	1.14
Mllt11	1.13	1.31	2.20
Mlycd	---	---	-0.89
Mmachc	-1.16	---	-1.29
Mmp11	0.82	---	---
Mmp13	---	---	1.14
Mms22l	---	---	-0.83
Mndal	---	---	0.88
Mns1	---	---	-0.89
Mocos	2.53	1.75	2.86
Mocs1	1.11	---	1.23
Mogs	---	---	-1.09
Mplkip	---	---	-0.83
Mpp4	1.14	1.06	1.38
Mpzl3	---	---	0.83
Mras	---	---	0.91
Mrc1	-1.77	-1.04	-1.76
Mre11a	---	---	-0.68
Mrpl14	1.03	---	0.88
Mrps6	0.96	---	1.02
Msantd3	1.15	1.05	1.30
Msantd4	0.73	---	---
Msh6	-1.09	---	-1.53
Msmo1	1.54	---	1.51
Msrb3	---	---	-0.76
Mtcl1	-0.81	---	---
mt-Co1	---	---	1.06
Mthfd1	---	---	-0.71
Mthfr	1.19	---	1.31
Mtmr10	-1.72	-0.75	-1.70
Mtmr3	---	---	0.71
Mttp	---	---	0.88
Mturn	1.45	---	1.32
Mvd	0.92	---	---
Mxd1	---	---	0.95
Mxd3	-1.39	---	-1.89
Mxd4	0.73	---	---
Myc	-0.75	---	-0.63
Myo5c	0.75	---	0.72
N4bp3	---	---	-0.84
Naif1	---	---	0.82
Nampt	1.07	---	1.49
Nanos1	-1.19	---	-1.01
Napa	---	---	0.68
Napb	1.10	---	1.16
Napepld	---	---	-1.02
Narf	0.89	---	0.72
Nars	---	---	0.73
Nat6	1.05	---	1.29
Nbeal2	-0.78	---	-1.01
Ncaph	-0.68	---	-0.80
Ncbp2	---	---	-0.77
Ndel1	---	---	0.75
Ndrg1	1.60	0.85	2.41
Neil3	---	---	-0.81
Nek6	-0.84	---	-0.78
Net1	-0.95	---	-0.70
Neurl1b	---	---	-1.01
Neurl3	---	-1.06	---
Nfatc4	1.18	---	---
Nfe2l1	---	---	0.83
Nfkb2	-0.83	---	---
Nfkbia	-1.00	-0.77	---
Nfkbie	---	---	-0.75
Nfkbiz	-0.85	---	-1.05
Ngf	1.47	1.50	2.29
Nid1	0.95	1.26	1.36
Nif3l1	1.06	---	1.41
Noa1	---	---	-1.06
Nolc1	-0.73	---	---
Notch2	---	---	0.77
Npc1	---	---	0.91
Npcd	---	---	-0.99

Nploc4	---	---	0.94
Npnt	-0.93	---	-0.89
Nr1h4	-1.15	---	-1.29
Nr4a1	-1.21	---	---
Nrarp	---	---	-1.35
Nrep	0.98	---	---
Nrg1	-0.90	---	---
Nsdhl	1.29	---	1.28
Nsfl1c	---	---	0.69
Nuak1	---	---	-0.80
Nuak2	---	---	-1.44
Nub1	0.78	---	0.82
Nucks1	---	---	-0.67
Nudt12	0.95	---	---
Nuf2	-0.75	---	-1.03
Numbl	2.19	1.74	2.31
Nup107	---	---	-0.73
Nup210l	---	---	0.69
Nup37	---	---	-0.97
Nup85	---	---	-0.83
Nupl2	---	---	-1.10
Nupr1	1.55	---	2.14
Nusap1	---	---	-0.93
Nxt1	---	---	-0.83
Nyap1	---	---	1.09
Obfc1	-0.66	---	---
Oip5	---	---	-0.76
Olfr56	---	---	-1.19
Onecut1	---	---	-1.64
Osbpl9	---	---	0.69
Oser1	---	---	1.40
Osgin1	2.10	1.87	2.75
Otud4	-0.93	---	-0.79
P2ry1	---	---	-1.01
P4ha1	1.35	0.79	1.66
P4ha2	---	---	0.74
Pacsin2	---	---	0.72
Padi2	-0.81	---	-1.10
Pafah2	0.91	---	0.68
Pag1	-1.20	---	-1.35
Palld	-1.09	---	-0.85
Palmd	-0.96	---	-1.10
Pank1	---	---	-0.83
Papd5	---	---	0.74
Papd7	---	---	-0.66
Papss2	1.73	---	1.98
Parp1	---	---	-0.66
Parp8	-1.00	---	---
Parpbp	-0.79	---	-1.01
Pax3	---	---	0.97
Pbk	---	---	-1.19
Pcdh1	-0.79	---	---
Pcdh7	-1.60	-0.98	-1.41
Pcdh9	---	---	1.55
Pcsk9	1.50	---	1.35
Pcx	1.54	---	1.31
Pcyt2	0.84	---	0.74
Pdcd4	0.80	---	---
Pddc1	---	---	-0.83
Pde4b	---	1.38	1.09
Pdgfb	-1.72	-1.09	-2.37
Pdk4	1.35	---	1.12
Pdlim7	---	---	1.04
Pdss1	-0.77	---	-0.73
Pdxk	-1.02	-1.03	-1.36
Pex13	1.09	---	1.12
Pfas	---	---	-0.87
Pgd	2.41	1.99	2.39
Pgm2l1	0.91	---	0.77
Phf1	0.99	---	1.19
Phf10	---	---	1.04
Phf19	-1.62	-0.90	-2.02
Phlda1	---	0.84	1.67
Pif1	-0.91	---	-1.59
Pik3ap1	0.92	---	0.74
Pilra	-0.73	---	---
Pilrb1	-0.94	---	---
Pim3	---	---	-0.81
Pla2g4a	1.13	0.91	0.86
Plat	---	---	0.71
Plau	-1.47	---	-1.30
Plaur	---	---	0.85
Pld3	---	---	0.73
Plek2	-1.03	---	-0.80
Plekha2	---	---	-0.75
Plekha7	-0.98	---	-1.00
Plekho1	---	---	0.74
Plekho2	-0.73	---	---
Plk1	-0.72	---	-1.08
Plk3	1.50	1.29	3.27
Plk4	---	---	-0.72
Plod1	---	---	0.68
Plod2	1.32	0.82	1.84
Plscr2	---	---	-1.01
Plxnd1	-0.78	---	---
Pmaip1	---	---	0.77
Pmvk	1.37	---	1.17
Pnpla8	---	---	0.71
Pnrc1	1.07	---	1.81
Pold1	---	---	-0.83
Pole2	-1.01	---	-0.98
Polh	-0.81	---	-1.08
Por	---	---	0.74
Pou6f1	1.04	---	1.22
Ppard	1.09	1.02	1.73
Ppat	-0.76	---	-0.94
Ppl	-0.71	---	-0.96
Ppp1r13b	---	---	0.91
Ppp1r13l	---	---	-0.89
Ppp1r15a	1.17	---	2.72
Ppp1r3e	---	---	-0.87
Ppp3ca	---	---	0.89
Pqlc2	1.22	0.82	1.34
Prc1	---	---	-0.85
Prdm2	---	---	0.90
Prdx1	0.93	---	0.92
Prdx6	2.18	1.58	2.28
Prex2	---	---	-0.88
Prim1	---	---	-0.63
Prim2	-0.81	---	---
Prkci	-0.69	---	-0.84
Prob1	1.01	---	0.84
Procr	3.31	2.74	4.38
Prodh	---	---	-0.99
Prorsd1	---	---	-1.00
Proser2	1.75	1.65	2.02
Prox1	---	---	1.03
Prr13	1.16	1.05	1.67
Prss23	-1.24	-0.90	-2.03
Prx	---	---	0.83
Psap	0.84	---	0.79
Psmb3	---	---	1.00
Psmc6	---	---	0.74
Psmd11	0.90	0.78	1.12
Psmd4	---	---	0.79
Psmd5	0.90	0.72	0.84
Psme4	0.74	---	0.83
Psph	1.01	---	1.06
Ptger4	---	---	1.26
Ptgr1	1.42	---	1.11
Ptgs2	2.08	2.10	3.18
Ptprb	-0.90	---	-1.36
Ptrh2	---	---	-0.89
Purb	---	---	-0.71

Pvr	---	---	1.27
Pxmp2	-1.35	---	-1.31
Pxylp1	---	---	-1.24
Pycr1	---	---	0.73
Rab17	---	---	-1.05
Racgap1	---	---	-0.71
Rad18	---	---	-0.73
Rad23b	---	---	0.76
Rad51ap1	-0.73	---	-0.99
Radil	2.05	1.86	2.30
Raf1	---	---	0.76
Ralgps2	-0.84	---	-0.73
Ranbp6	---	---	-0.75
Rap2b	---	---	0.91
Raph1	---	---	1.32
Rasgrf2	-0.92	---	---
Rasgrp3	---	-0.86	-1.53
Rasl12	---	---	-0.84
Rassf6	1.37	1.18	1.50
Rassf8	0.78	---	0.69
Rbbp6	---	---	0.78
Rbm33	---	---	0.76
Rbpms2	---	---	0.80
Rccd1	---	---	-0.80
Rcl1	---	---	-0.66
Rdh10	---	---	-1.16
Recql	---	---	-0.91
Reep6	---	---	1.48
Relb	-1.21	-1.21	-1.04
Rem2	-1.20	---	-1.17
Reps1	---	---	0.90
Rfc3	-0.88	---	-0.71
Rfc5	-0.73	---	-0.92
Rgs17	---	---	0.83
Rgs20	-0.85	---	---
Rhbdd1	---	---	1.06
Rhbdf2	---	---	1.06
Rhob	---	---	0.89
Rhobtb3	---	---	-0.74
Rhpn2	1.10	0.86	1.14
Riok3	0.73	---	0.84
Rit1	1.46	0.90	1.48
Rmi2	-1.11	---	-1.08
Rnd1	-1.25	---	-0.75
Rnd2	1.09	---	1.04
Rnf115	---	---	0.95
Rnf145	-1.50	-0.76	-1.86
Rnf183	3.14	2.69	3.72
Rnf19b	---	---	1.05
Rnf39	-1.08	---	-1.42
Rnf41	---	---	0.68
Rock2	---	---	0.79
Ror1	-1.36	---	-1.39
Rora	1.38	---	2.18
Rorb	---	---	0.93
RP23-145I16.3	0.94	---	0.99
Rragd	1.36	---	1.28
Rrm1	---	---	-0.64
Rrm2	-0.75	---	-0.82
Rrp12	---	---	-0.93
Rrp1b	-1.06	---	-1.09
Rsrp1	---	---	0.75
Rtkn2	---	---	-1.10
Runx2	-1.10	---	-1.19
Rusc2	---	0.77	1.14
Rybp	---	---	0.95
Ryr3	---	---	1.78
S1pr2	-1.07	---	-1.12
Saraf	0.98	---	0.93
Sars	---	---	0.78
Sat1	---	---	1.13
Sbds	---	---	1.17
Sc5d	---	---	0.89
Scamp5	---	---	-1.00
Scarb1	0.85	---	0.89
Scd2	1.36	---	0.68
Schip1	---	---	-1.15
Scpep1	0.77	---	0.85
Sdpr	-0.84	---	-1.41
Sec24d	---	---	1.29
Sel1l3	0.92	---	1.28
Sema6c	1.06	---	---
Sept10	---	---	-0.73
Sepw1	1.19	---	---
Serinc3	---	---	0.86
Serpinb9	1.48	1.16	1.52
Serpinb9b	1.13	1.06	1.33
Serpind1	-1.63	---	-1.39
Serpinh1	---	---	0.74
Sertad2	---	---	0.80
Sertad3	0.91	---	0.97
Sertad4	-1.77	-1.21	-2.08
Sesn2	---	---	1.38
Sesn3	1.30	0.91	1.39
Sf1	---	---	0.71
Sfxn4	---	---	0.78
Sgk1	1.09	1.13	1.10
Sgk3	---	---	0.82
Sgtb	1.15	---	1.70
Sh3bgrl2	---	---	0.86
Sh3bp1	-1.07	---	-0.90
Sh3bp2	2.10	1.54	2.65
Sh3bp5	-0.72	---	-0.95
Sh3tc1	0.92	---	0.77
Shank2	---	---	-0.93
Shcbp1	---	---	-0.80
Shmt1	-0.89	---	-0.94
Siglecg	---	---	-0.98
Sim2	---	---	0.74
Six4	1.40	1.30	1.29
Six5	---	---	-1.03
Ska1	---	---	-0.84
Ska3	---	---	-0.84
Skp2	---	---	-0.83
Slbp	---	---	-0.80
Slc12a2	---	---	-0.78
Slc16a10	---	---	1.58
Slc16a13	1.05	---	0.82
Slc16a6	1.11	---	1.17
Slc19a2	---	---	0.77
Slc1a4	3.01	2.00	3.54
Slc20a1	---	---	1.09
Slc22a23	1.51	1.27	1.74
Slc22a4	1.91	1.51	2.07
Slc25a1	0.77	---	0.96
Slc25a12	---	---	-0.66
Slc25a15	---	---	-0.99
Slc25a27	---	---	1.04
Slc25a33	0.93	---	1.25
Slc25a45	---	---	1.00
Slc25a48	-1.01	---	-1.63
Slc27a6	-1.31	---	-1.13
Slc29a2	-1.45	---	-1.24
Slc2a1	0.97	0.77	1.72
Slc2a2	---	---	-1.47
Slc30a1	---	---	-1.05
Slc35b2	-0.97	---	-1.15
Slc35d1	---	---	0.95
Slc35e2	---	---	0.81
Slc35e4	---	---	0.96
Slc35g1	---	---	-0.71
Slc36a4	---	---	-0.77
Slc38a2	---	---	0.97

Slc38a3	1.20	1.08	1.16
Slc38a7	0.92	---	1.24
Slc39a4	0.83	---	1.11
Slc3a2	1.83	1.22	2.56
Slc40a1	1.81	1.45	1.46
Slc43a2	0.93	---	0.98
Slc48a1	2.55	2.42	3.04
Slc5a3	1.20	---	1.30
Slc5a6	---	---	-0.96
Slc6a8	---	---	0.65
Slc6a9	2.12	1.32	2.83
Slc7a1	---	---	0.97
Slc7a11	5.19	4.54	5.63
Slc7a5	---	---	0.80
Slc8b1	1.28	---	1.02
Slco3a1	---	---	-0.71
Slco4a1	-1.17	-1.06	-0.98
Slfn2	-2.96	-1.76	-3.38
Slfn9	-1.72	---	-1.77
Sltm	---	---	0.95
Slu7	---	---	0.68
Smad5	---	---	-0.64
Smad7	-0.84	---	-0.84
Smcr8	---	---	0.98
Smim14	0.83	---	0.88
Smim3	---	---	0.97
Smox	---	---	0.75
Smpd3	-0.85	---	-0.99
Smtn	-1.01	---	-0.66
Smtnl2	---	---	-0.85
Smyd4	1.18	0.80	0.80
Snai2	-1.35	---	---
Snca	2.05	1.25	2.21
Snx10	1.33	0.93	1.37
Snx30	0.80	---	1.13
Soat2	1.41	---	2.24
Socs5	-0.84	---	-0.93
Sod1	0.97	---	1.11
Sorbs2	---	---	-0.78
Sord	0.91	---	0.74
Sox13	-0.97	---	-1.00
Spata1	---	---	0.98
Spc25	---	---	-1.02
Spcs3	---	---	-0.88
Spns2	-0.99	---	-1.33
Spns3	---	---	-1.17
Spp1	-0.76	---	-0.67
Sppl2b	---	---	-0.79

Sprr1a	-1.57	---	---
Spry1	---	---	-0.78
Spry2	-0.85	---	-0.95
Spry4	---	---	0.95
Spsb4	-1.12	---	-1.82
Sqle	1.63	---	1.61
Sqrdl	2.25	1.72	2.06
Sqstm1	2.77	1.85	3.27
Srd5a1	-0.89	---	-0.99
Srebf2	---	---	0.78
Srf	-1.01	---	-1.17
Srgap3	-1.87	-1.39	-1.77
Srm	-0.86	---	-0.87
Srr	---	---	1.20
Srrm4	---	---	0.86
Srsf10	---	---	-0.73
Srxn1	4.29	3.51	4.90
Ss18l1	---	---	0.83
Ssbp2	-0.92	---	-0.77
St13	---	---	0.89
Stambpl1	-1.09	---	-0.73
Stard13	-0.82	---	-1.20
Stard4	1.19	---	0.91
Stard9	---	---	0.98
Stat1	---	---	-0.94
Stat2	0.86	---	0.79
Stip1	---	---	1.00
Stk10	0.75	---	1.26
Stk40	---	---	0.68
Stx3	---	---	0.78
Stxbp1	---	---	1.04
Stxbp6	---	---	-0.86
Styk1	0.86	---	0.85
Suv39h2	---	---	-0.75
Swap70	---	---	0.67
Swt1	---	---	0.99
Syvn1	---	---	0.73
Tacc2	1.23	0.72	1.39
Tada1	---	---	-0.75
Tada2a	-0.72	---	-0.72
Taf7	1.46	1.23	2.04
Taldo1	0.91	---	0.87
Tapbpl	0.85	---	0.78
Tbc1d1	-0.77	---	---
Tbc1d9	---	---	0.97
Tbce	---	---	0.67
Tbcel	1.05	0.81	1.15
Tbl2	---	---	-1.04

Tcf19	-1.23	---	-1.44
Tcp11l2	1.00	---	1.26
Tdrp	1.14	---	1.06
Tef	0.86	---	---
Tex9	-1.04	---	-0.92
Tfap2a	1.03	---	1.58
Tfe3	---	---	1.21
Tfrc	-1.90	-1.12	-1.62
Tgif2	---	---	-1.17
Tgoln1	---	---	0.69
Thbs1	-2.60	-1.32	-3.45
Them4	---	---	1.04
Thnsl1	---	---	-0.78
Thrb	1.79	1.67	2.08
Tiam2	-0.74	---	-0.69
Ticam1	---	---	1.00
Ticrr	---	---	-0.98
Tigit	-0.90	---	---
Timeless	-0.79	---	-1.03
Tipin	-1.02	---	-1.31
Tk1	-1.21	---	-1.93
Tkt	0.71	---	0.91
Tlk2	---	---	0.76
Tm4sf4	---	---	-1.40
Tmco4	---	---	1.04
Tmem117	2.23	1.53	2.38
Tmem171	-1.60	---	-1.10
Tmem18	---	---	-0.92
Tmem194b	---	---	-1.03
Tmem2	---	---	-0.73
Tmem216	---	---	-0.76
Tmem37	1.19	1.34	1.25
Tmem38a	---	---	0.93
Tmem41b	0.85	---	1.19
Tmem55a	0.87	---	0.91
Tmem57	---	---	0.76
Tmem63b	---	---	0.71
Tmie	1.62	1.23	1.19
Tmpo	---	---	-0.87
Tmppe	0.75	---	0.69
Tnc	-0.99	-0.78	---
Tnfaip2	-0.83	---	---
Tnfaip3	-2.24	-1.44	-2.86
Tnfrsf1a	---	---	0.84
Tnfsf9	---	---	1.15
Tnnc1	1.41	---	1.85
Tns1	---	---	-1.11
Tob1	---	---	1.12

Tob2	0.67	---	0.97
Tollip	---	---	0.85
Tom1	---	---	1.16
Tom1l1	---	---	0.75
Top2a	-0.69	---	-0.99
Tor1aip2	---	---	0.75
Tor4a	---	---	-0.68
Tox	---	---	0.85
Tpx2	---	---	-0.68
Trdmt1	---	---	-0.79
Trib1	-0.86	---	-0.79
Trib3	2.39	---	3.31
Trim16	---	0.88	1.35
Trim17	0.97	---	0.86
Trim36	---	---	1.40
Trim46	---	---	1.12
Trim59	---	---	-0.76
Trim6	0.92	---	1.08
Trio	---	---	0.88
Trip10	---	---	0.92
Trmt1l	---	---	0.85
Trmt2a	---	---	-0.78
Trnt1	---	---	-0.67
Trp53bp2	---	---	0.70
Trp53inp1	1.51	---	2.05
Trp53inp2	---	---	0.91
Tsc22d1	---	---	-0.78
Tsc22d2	---	---	0.94
Tsc22d3	0.97	---	1.16
Tsfm	---	---	-0.91
Tshz1	1.12	1.12	1.48
Tsku	1.61	1.83	1.60
Tspan8	---	---	-1.01
Tspyl2	0.99	---	1.38
Ttc26	---	---	-0.79
Ttc30b	---	---	-0.79
Ttc7	-0.82	---	-0.74
Ttk	---	---	-0.71
Tuba1a	---	---	1.22
Tuba4a	0.81	0.92	1.19
Tubb2a	1.64	1.09	2.01
Tubb2b	---	---	0.78
Tubb6	-0.87	---	-0.78
Txnrd1	1.90	1.71	2.00
Ubap1	0.87	---	1.36
Ubash3b	-1.14	---	-1.02
Ubb	1.21	1.10	2.20
Ubc	1.72	1.34	3.52
Ube2h	---	---	0.75
Ube2j1	---	---	0.69
Ube2o	1.02	---	1.22
Ube4b	---	---	0.79
Ubl3	0.80	0.78	0.80
Ubqln1	---	---	0.81
Ubr4	---	---	0.87
Ubr7	---	---	-1.13
Ubtd1	---	---	0.96
Ubxn4	1.17	0.95	1.39
Ubxn8	---	---	0.65
Ugdh	1.48	1.17	1.52
Ugt1a1	1.16	0.87	0.94
Ugt1a10	1.10	0.88	0.97
Ugt1a2	1.16	0.87	0.94
Ugt1a5	1.16	0.87	0.95
Ugt1a6a	1.10	0.85	0.93
Ugt1a6b	1.09	0.87	0.96
Ugt1a7c	1.10	0.88	0.97
Ugt1a8	1.10	0.88	0.97
Ugt1a9	1.10	0.88	0.97
Ugt2b34	4.29	3.39	4.22
Uhrf1	-1.04	---	-1.17
Ulk1	0.73	---	0.95
Ung	-3.05	-0.90	-3.56
Usp1	---	---	-0.82
Usp14	---	---	0.67
Usp20	0.91	---	---
Usp22	---	---	0.96
Usp35	1.27	---	1.24
Usp43	-1.03	---	-0.89
Uspl1	---	---	0.69
Uts2b	---	---	-1.56
Vamp1	1.04	---	1.04
Vash2	---	---	0.88
Vasn	1.03	0.77	1.36
Vcam1	-1.86	-1.42	-1.96
Vegfa	2.39	1.74	3.57
Vegfc	-0.99	-0.96	-0.82
Vgll3	-0.96	---	-1.14
Vil1	-1.09	---	-1.31
Vipas39	---	---	0.78
Vldlr	1.07	---	1.16
Vnn1	1.03	---	---
Vps18	1.08	---	1.08
Vps37b	0.85	---	1.63
Vstm5	-1.17	---	-0.92
Wbp2	---	---	0.70
Wbscr27	1.40	---	0.96
Wdhd1	-0.84	---	-1.13
Wdr35	---	---	-0.78
Wdr5b	---	---	-1.27
Wdr6	-0.77	---	-1.50
Wdr76	-0.80	---	-1.14
Wdr77	---	---	-0.70
Wdr81	1.15	---	0.99
Wee1	---	---	-0.92
Whamm	0.97	---	1.12
Wipi2	---	---	0.66
Wnt10a	-0.95	---	-1.22
Wnt4	1.50	1.15	1.33
Wnt7b	-1.42	-0.75	-1.41
Wrb	---	---	-0.99
Xkr9	2.05	1.30	2.05
Xpo1	---	---	0.72
Xpot	---	---	0.65
Xrcc2	---	---	-1.06
Xrcc6	---	---	-0.69
Xrcc6bp1	---	---	-0.92
Xxylt1	---	---	-0.86
Ypel2	---	---	1.10
Ypel5	2.39	1.44	2.61
Ywhag	0.94	---	1.27
Zadh2	0.82	0.69	0.70
Zbtb10	---	---	1.14
Zbtb12	---	---	-0.96
Zbtb2	---	---	1.09
Zbtb21	---	---	1.01
Zbtb37	---	---	-0.94
Zbtb45	---	---	-0.73
Zbtb7b	---	---	0.90
Zc2hc1c	1.16	---	0.92
Zdhhc18	1.52	1.28	1.65
Zeb2	---	---	0.98
Zfand2a	1.90	1.22	3.27
Zfand5	1.43	0.89	1.68
Zfp142	---	---	1.21
Zfp185	---	---	1.14
Zfp324	---	---	-1.46
Zfp36	---	---	1.91
Zfp365	1.19	---	1.23
Zfp367	-0.88	---	-1.06
Zfp385a	---	---	0.74
Zfp39	---	---	-1.02
Zfp395	---	---	-0.86
Zfp41	---	---	-0.82

Zfp418	---	---	0.99
Zfp516	---	---	0.91
Zfp617	---	---	0.72
Zfp651	---	---	-0.89
Zfp703	---	---	0.79
Zfp867	---	---	-0.93
Zfp874a	1.00	---	0.83
Zfp874b	1.04	---	1.36
Zfp945	---	---	0.96
Zfp958	---	---	-0.88
Zfp961	---	---	-0.76
Zfpm1	---	---	1.12
Zfpm2	-1.20	---	---
Zfyve1	0.84	---	1.06
Zgrf1	---	---	-1.07
Zhx3	-0.93	---	-1.09
Zik1	---	---	-1.24
Zmynd19	---	---	-0.74
Zrsr1	2.11	1.61	2.54
Zswim4	---	---	1.01
Zswim6	---	---	1.12
Zwint	0.94	0.82	1.15
Zyx	-1.14	---	---

Supplemental Table 2. Gene expression of AML12 hepatocytes treated with truncated OxPAPC, full-length OxPAPC, and OxPAPC. Gene expression represented as $\log_2$ of the fold change compared to vehicle. Genes regulated single treatment are highlighted in orange (truncated OxPAPC), blue (full-length OxPAPC), and purple (OxPAPC).

LPPTigr Nomenclature (previously known species)	Parent Lipid	*m/z*	Formula	LPPTigr Predicted Structure(s)
1. PAPC	---	782	$C_{44}H_{80}NO_8P$	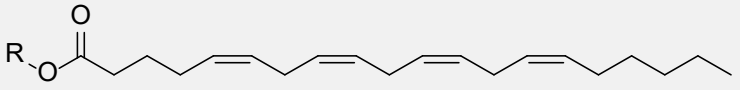
2. PLPC	---	758	$C_{42}H_{80}NO_8P$	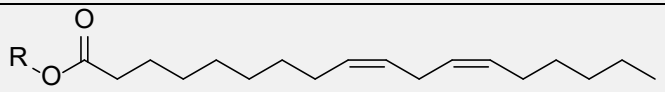
3. 16:0 LysoPC	---	496	$C_{24}H_{50}NO_7P$	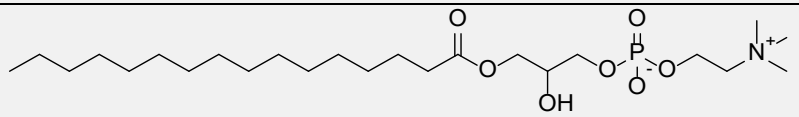
4. 18:0 LysoPC	---	524	$C_{26}H_{54}NO_7P$	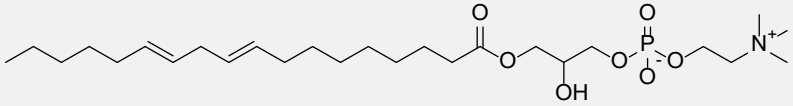
5. 18:1 LysoPC	---	522	$C_{26}H_{52}NO_7P$	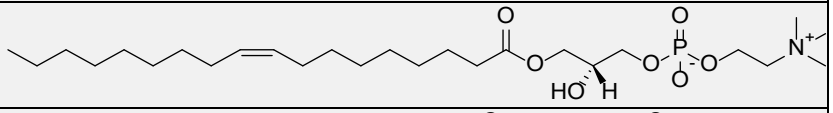
6. 18:2 LysoPC	---	520	$C_{26}H_{54}NO_7P$	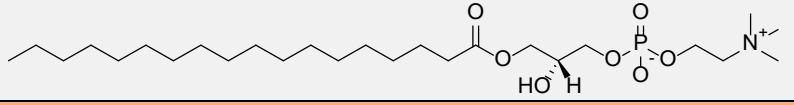
7. C37H66NO11P	PAPC	732	$C_{37}H_{66}NO_{11}P$	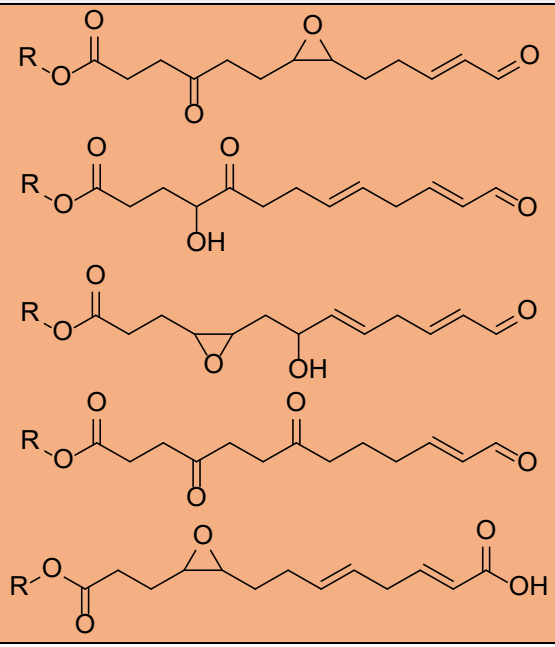

				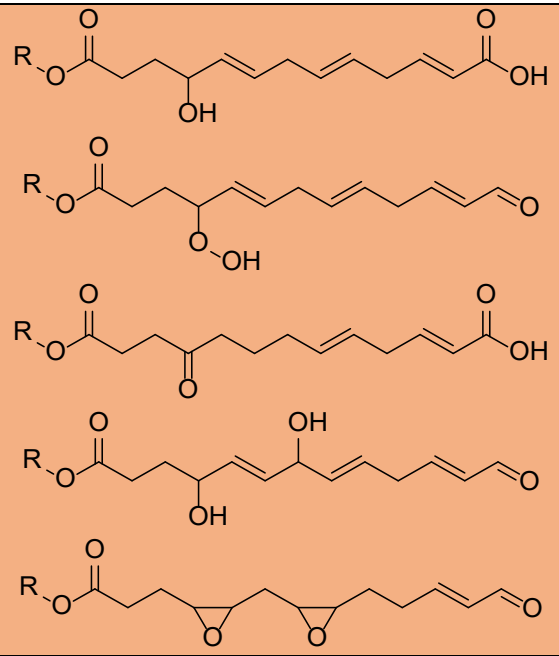
8. 16:0/7:0[1xOH,CHO]	PAPC	638	$C_{31}H_{60}NO_{10}P$	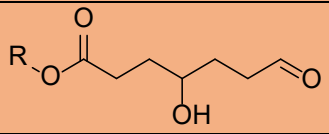
9. PONPC	PLPC	650	$C_{33}H_{64}NO_9P$	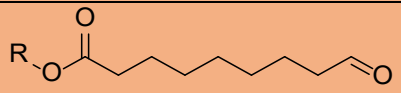
10. 16:0/12:1[CHO]	PLPC	690	$C_{36}H_{68}NO_9P$	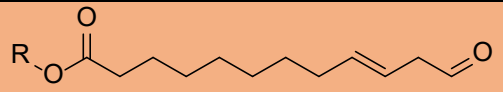
11. C34H62NO11P	PAPC	692	$C_{34}H_{62}NO_{11}P$	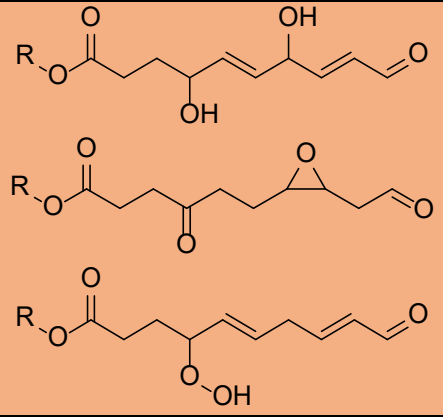

				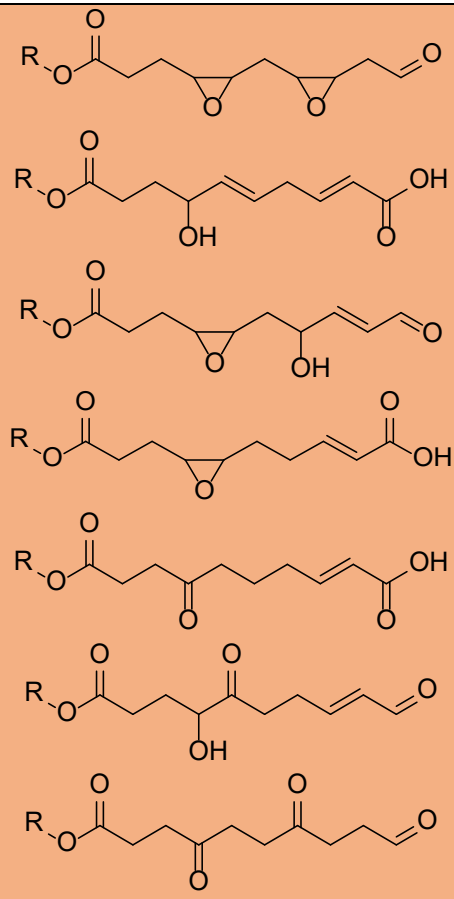
12. 16:0/11:1[CHO]	PLPC	676	$C_{35}H_{66}NO_9P$	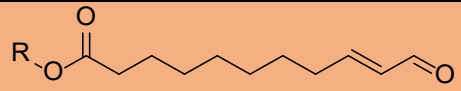
13. POBPC	PAPC	580	$C_{28}H_{54}NO_9P$	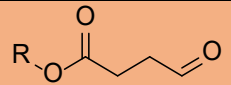
14. 16:0/8:0[CHO] (POOPC)	PLPC	636	$C_{32}H_{62}NO_9P$	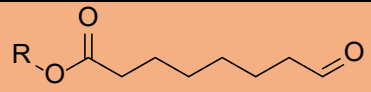
15. C35H64NO12P	PAPC	722	$C_{35}H_{64}NO_{12}P$	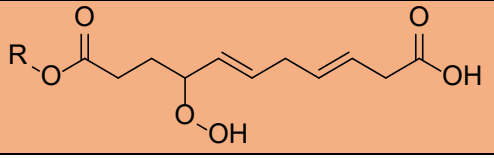

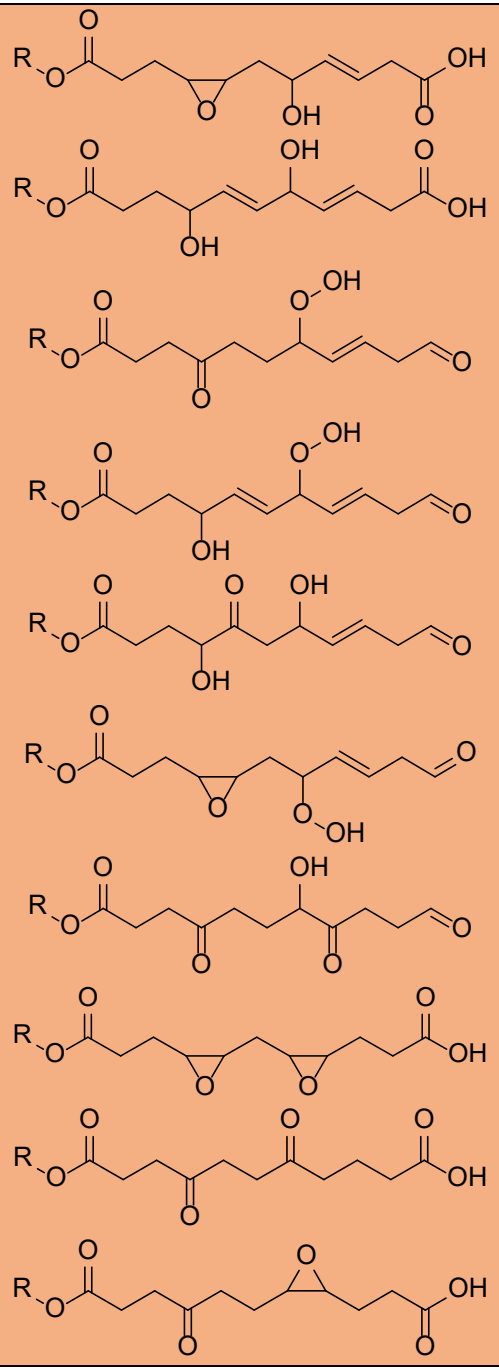

				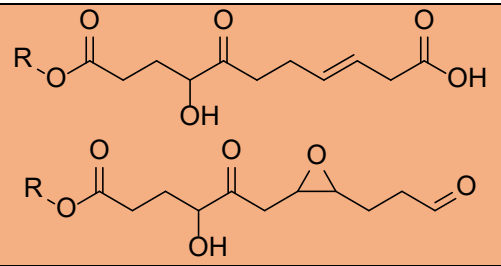
16. C35H64NO10P	PAPC	690	$C_{35}H_{64}NO_{10}P$	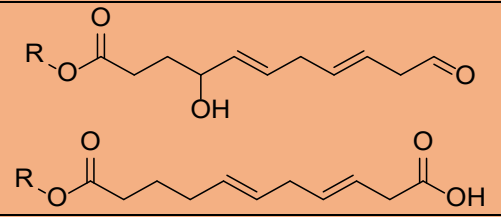
17. C35H62NO11P	PAPC	704	$C_{35}H_{62}NO_{11}P$	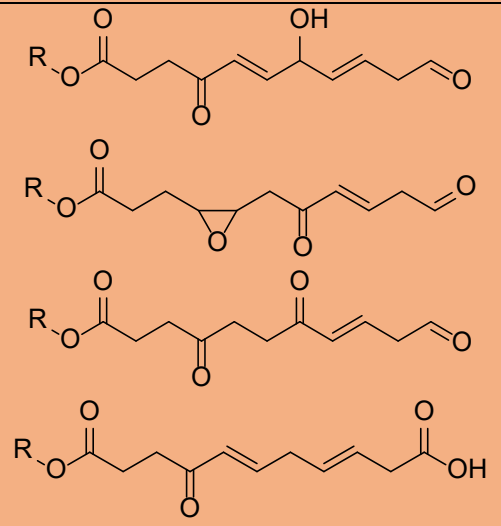
18. POVPC	PAPC	594	$C_{29}H_{56}NO_{9}P$	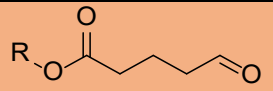
19. 16:0/10:2[CHO]	PAPC	660	$C_{34}H_{62}NO_{9}P$	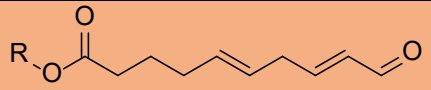
20. C36H68NO10P (HODA-PC)	PLPC	706	$C_{36}H_{68}NO_{10}P$	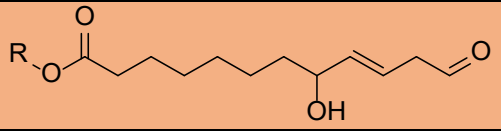

				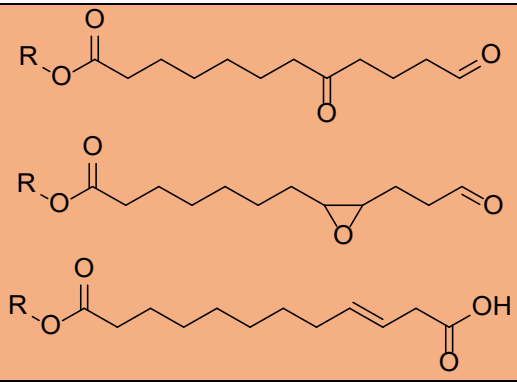
21. 16:0/7:1[CHO]	PAPC	620	$C_{31}H_{58}NO_9P$	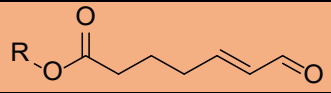
22. KOOA-PC	PAPC	648	$C_{32}H_{58}NO_{10}P$	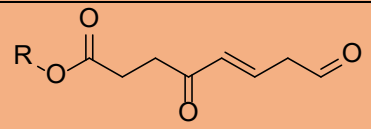
23. C32H60NO11P (HOdiA-PC)	PAPC	666	$C_{32}H_{60}NO_{11}P$	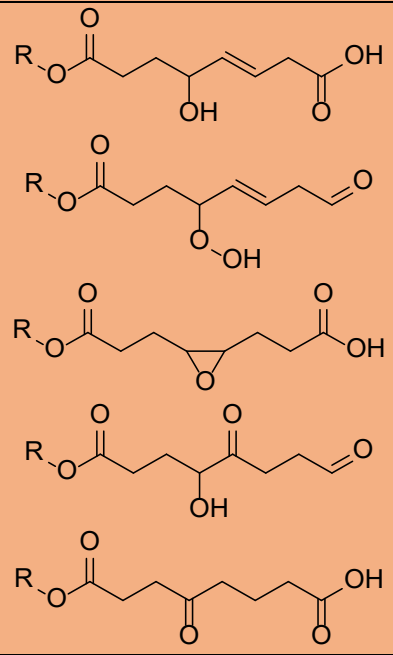
24. 16:0/10:2[1xKETO,CHO]	PAPC	674	$C_{34}H_{60}NO_{10}P$	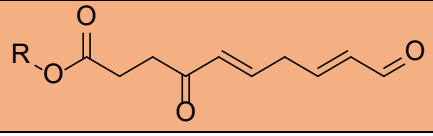

25. PazPC	PLPC	666	$C_{33}H_{64}NO_{10}P$	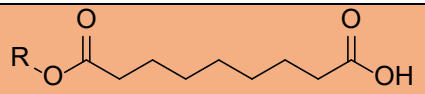
26. C32H60NO10P (HOOA-PC)	PAPC	650	$C_{32}H_{60}NO_{10}P$	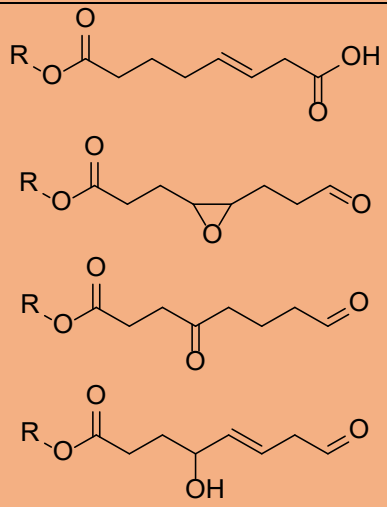
27. PGPC	PAPC	610	$C_{29}H_{56}NO_{10}P$	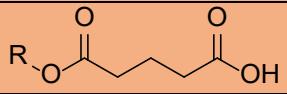
28. C42H78NO10P	PLPC	788	$C_{42}H_{78}NO_{10}P$	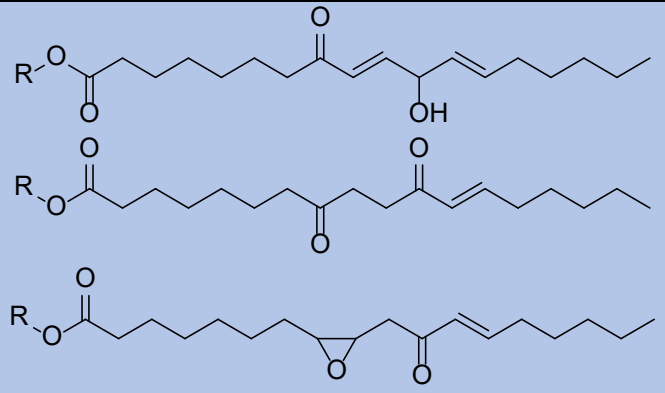
29. C42H80NO9P (HODE-PC)	PLPC	774	$C_{42}H_{80}NO_9P$	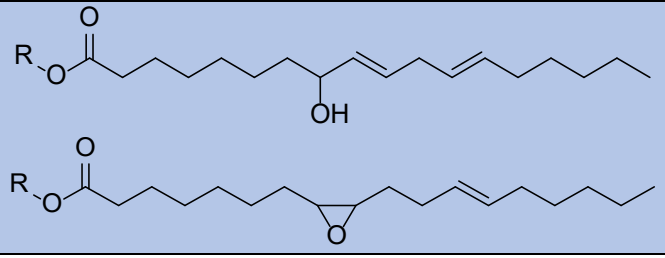

				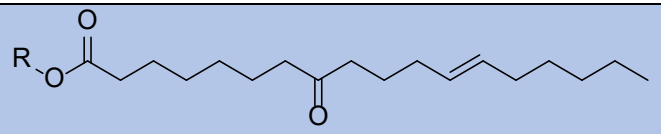
30. 16:0/20:4[2xKETO]	PAPC	810	$C_{44}H_{76}NO_{10}P$	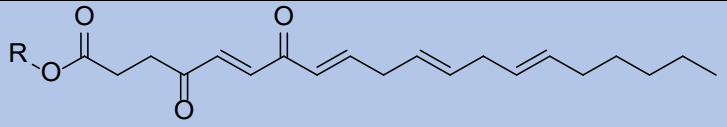
31. C44H80NO11P	PAPC	830	$C_{44}H_{80}NO_{11}P$	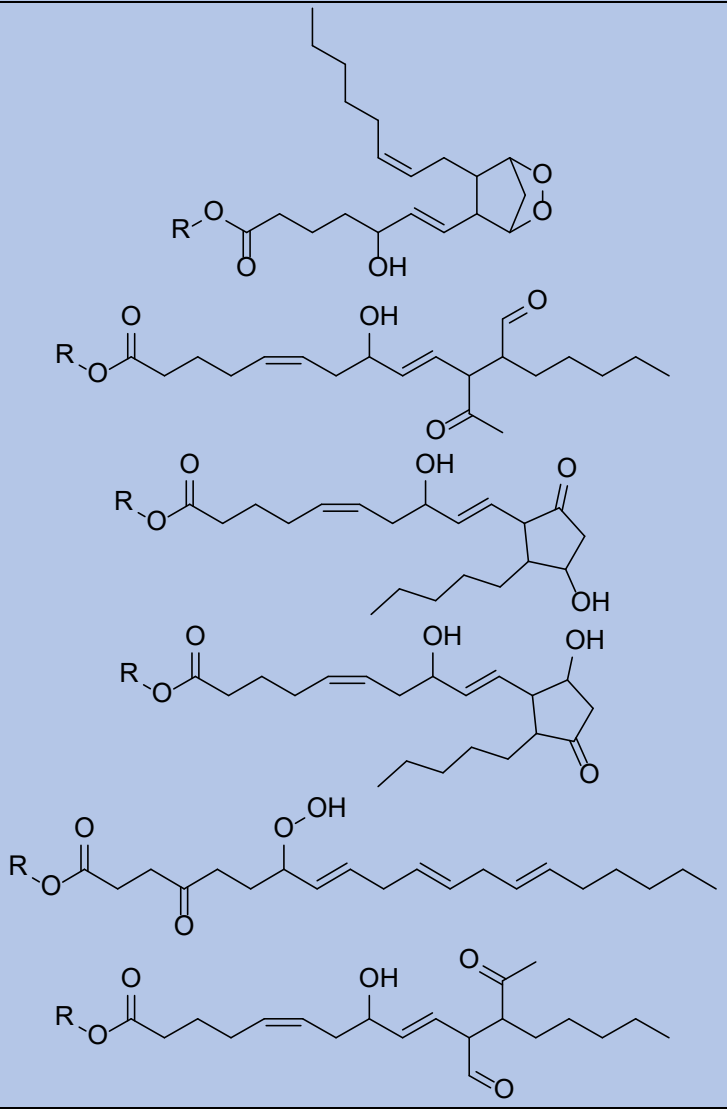

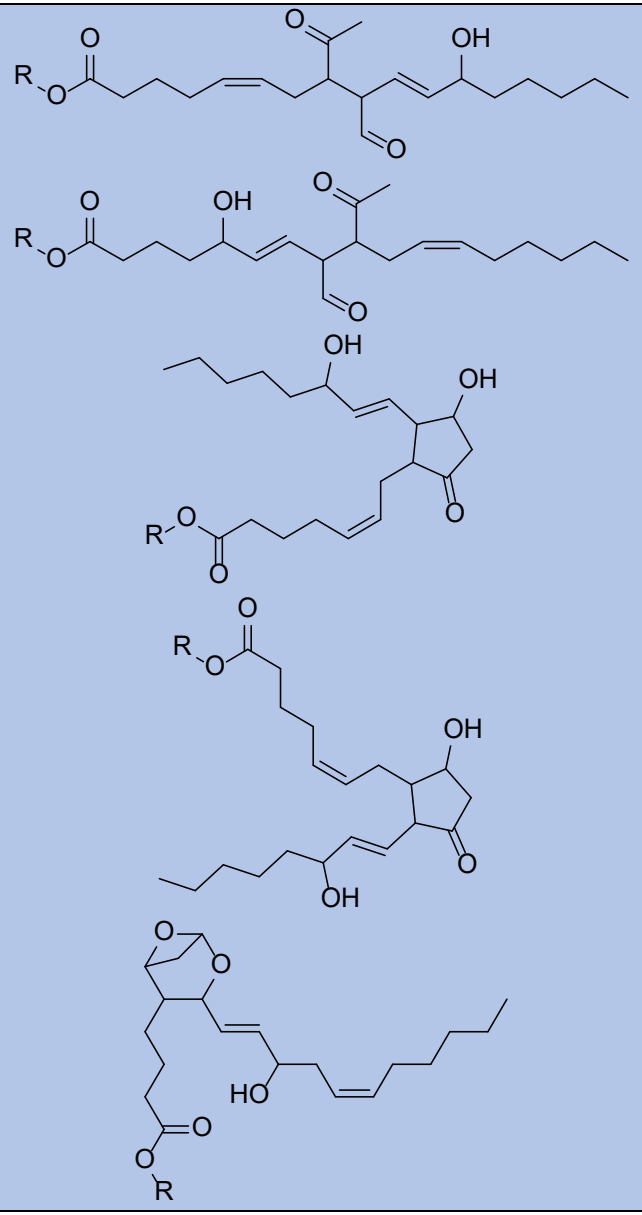
O
R
O
O
OH
O
O
R
O
OH
O
O
OH
OH
R
O
O
O
R
O
O
OH
O
OH
O
O
O
HO
O
O
R

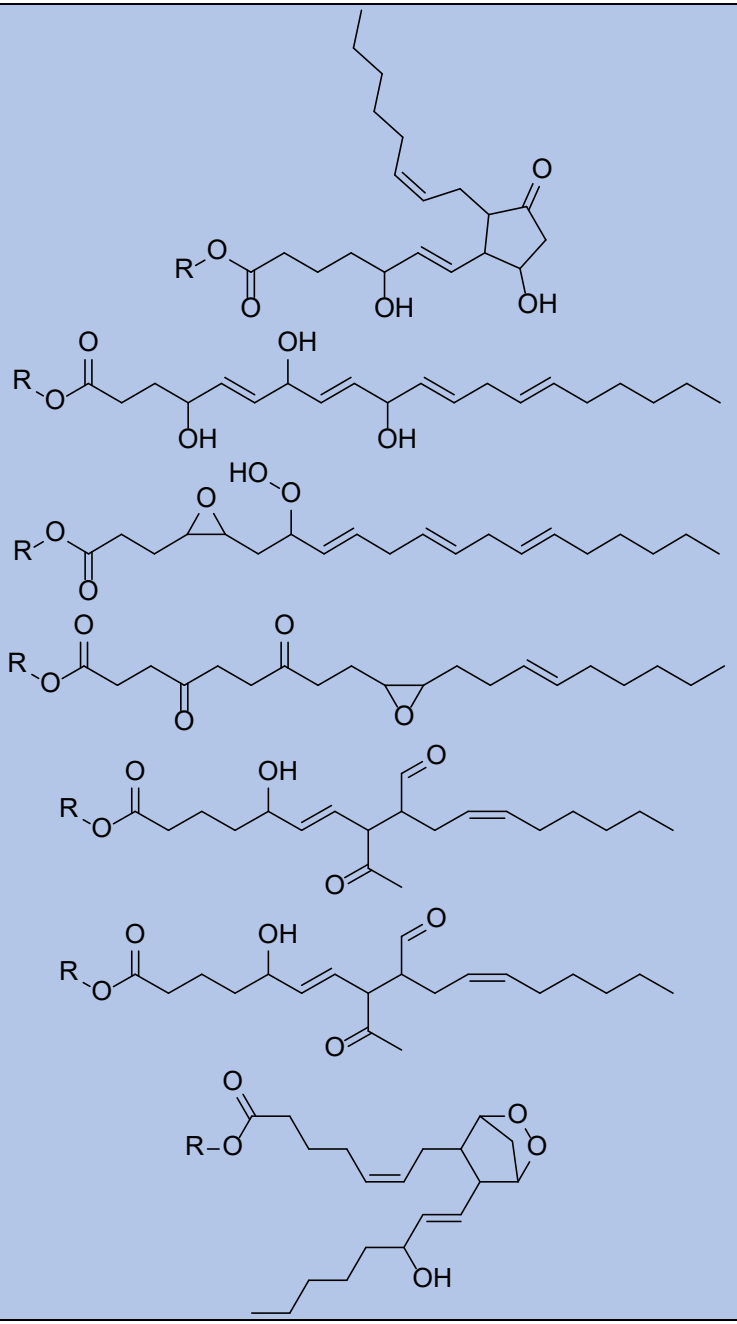
O
R
O
O
OH
OH
O
OH
R
O
OH
OH
HO
O
O
R
O
O
O
R
O
O
O
O
O
OH
R
O
O
O
O
OH
R
O
O
O
O
R
O
O
O
OH

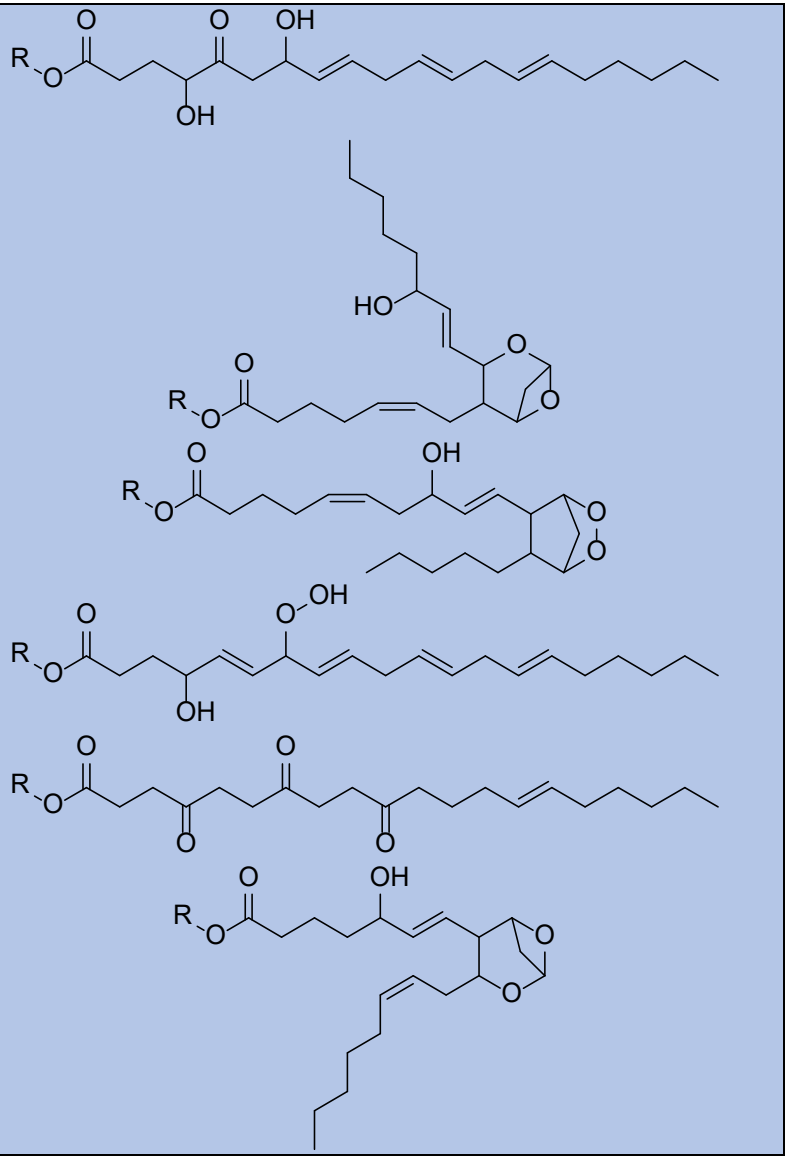
O
O
OH
R
O
OH
HO
O
O
R
O
O
OH
R
O
O
O
OH
O
R
O
OH
O
O
R
O
O
O
O
O
OH
R
O
O
O

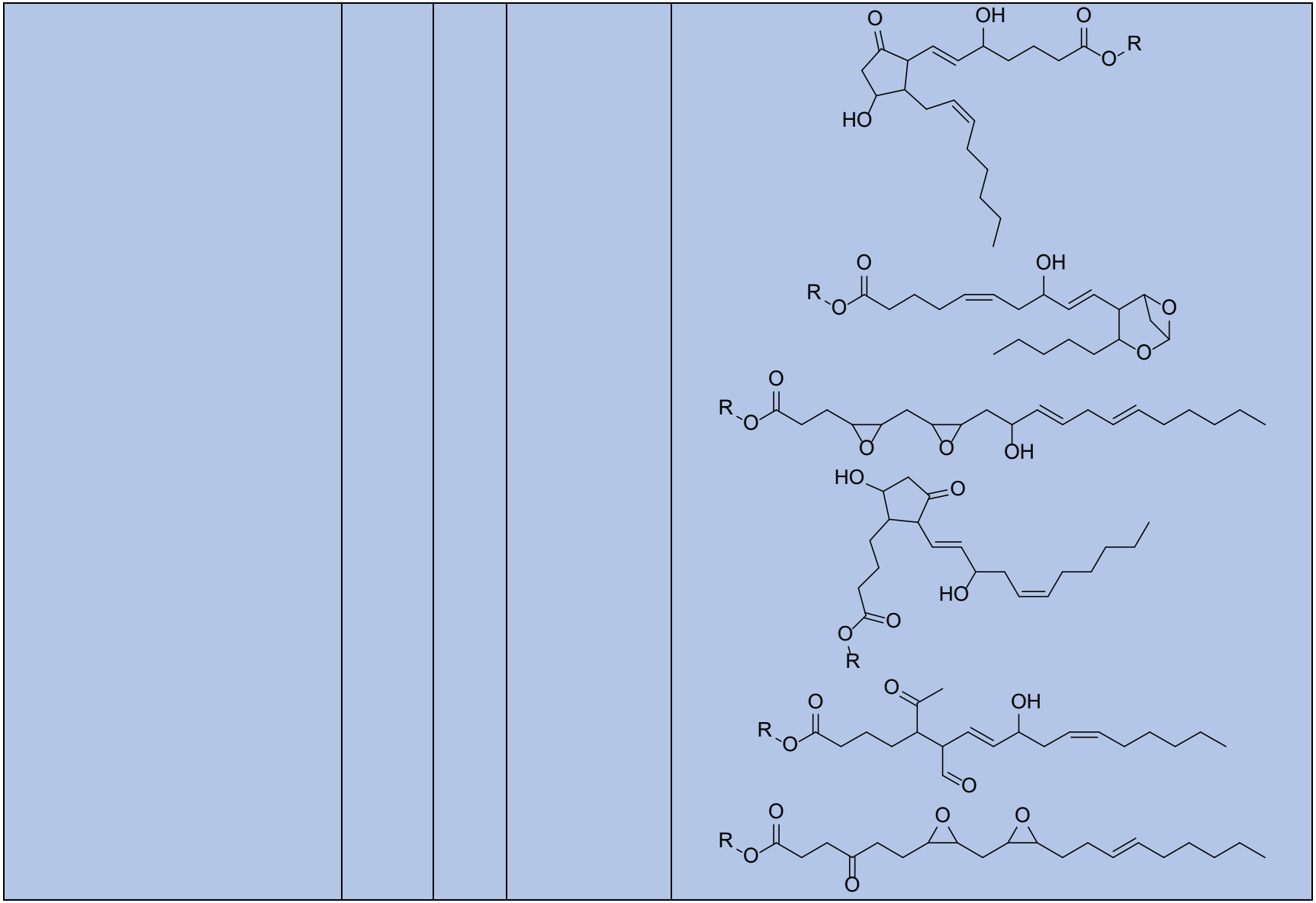
O
OH
O
R
HO
O
OH
R
O
O
O
R
O
O
O
OH
HO
O
HO
O
O
R
O
O
OH
R
O
O
O
O
R
O
O
O
O

				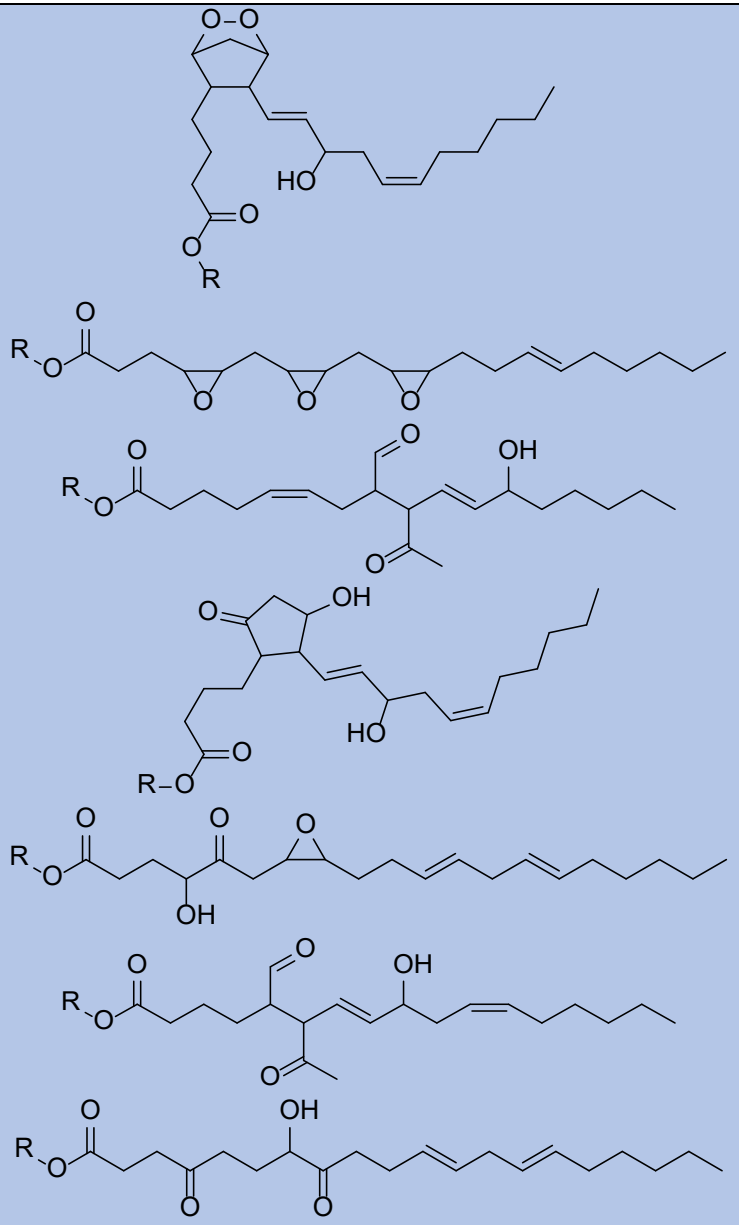
32. C44H80NO9P (HETE-PC)	PAPC	798	$C_{44}H_{80}NO_9P$	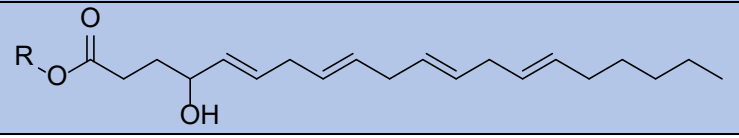

				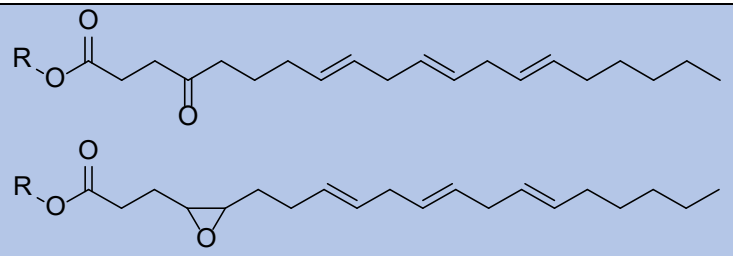
33. C42H80NO11P	PLPC	806	$C_{42}H_{80}NO_{11}P$	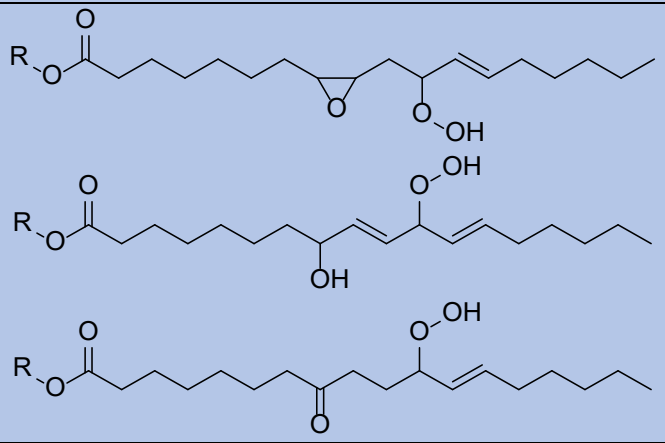
34. 16:0/18:2[1xKETO] (KODE-PC)	PLPC	772	$C_{42}H_{78}NO_9P$	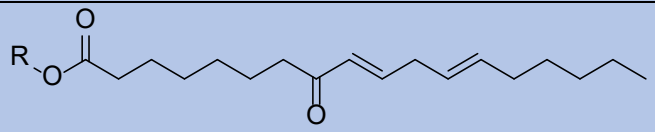
35. 16:0/18:1[1xOH] (HOME-PC)	PLPC	776	$C_{42}H_{82}NO_9P$	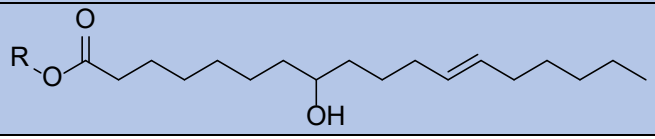

Supplemental Table 3. Oxidized phospholipids detected after development of hepatic fibrosis. *In silico* predicted structures of oxidized phospholipids derived from PAPC or PLPC detected in mouse plasma after twenty weeks on FPC diet. CHO – aldehyde, COOH – carboxylic acid, OH – hydroxy, OOH – hydroperoxy, KETO – ketone, EPOXY – epoxide.

Gene	Species	Primer orientation	Sequence
Hmox1	*Mus musculus*	Forward	ACAGCCCCACCAAGTTCAAA
		Reserve	TCTGCAGGGGCAGTATCTTG
Gclm	*Mus musculus*	Forward	TGGAGCAGCTGTATCAGTGG
		Reserve	AGAGCAGTTCTTTCGGGTCA
Pgd	*Mus musculus*	Forward	CTCCTCGACTCTGCTTCGTC
		Reserve	CGGCATCTTCTTGTCGTGTC
Acly	*Mus musculus*	Forward	TGATGGGAGAAGTTGGGAAG
		Reserve	ATCAGCTCGGGACTCAGAAA
Hmgcoas	*Mus musculus*	Forward	ACAAGCCTGACATGCTCTCC
		Reserve	TTCAGGAACATCCGAGCTAGA
Hmgcoar	*Mus musculus*	Forward	TCTTGTGGAATGCTCTGTGA
		Reserve	AAGCTCTAGGACCAGCGACA
Adamtsl2	*Mus musculus*	Forward	ATGTGAGCCCATTGGCTGTG
		Reserve	TCGGTACTTGACCACTGTGC
Timp2	*Mus musculus*	Forward	ATGGCAACCCCATCAAGAGG
		Reserve	TGGGACAGCGAGTGATCTTG
Timp1	*Mus musculus*	Forward	TCGGACCTGGTCATAAGGC
		Reserve	GTACGCCAGGGAACCAAGAA
Mmp2	*Mus musculus*	Forward	GTGTTCTTCGCAGGGAATGAG
		Reserve	GATGCTTCCAAACTTCACGCT
Itga8	*Mus musculus*	Forward	ACACGTTCCTCAAGAGAAAGAA
		Reserve	GGAGTGGCCCAAATAACCGA
Col15a1	*Mus musculus*	Forward	CTGTCCACTTTCCGAGCCTTT
		Reserve	AAAGCACTTGGCCCTTGAGA

Col8a1	*Mus musculus*	Forward	GGCAAAGAGTACCCACACCTACC
		Reserve	GACCTTGTTCTCCGCGCAAACTG
Col4a2	*Mus musculus*	Forward	TCGTTCAGCCAGGTTGCATT
		Reserve	AAAGCCCTTGAGCCCTTGTT
Col5a2	*Mus musculus*	Forward	TGGGGACTGATGGTACACCT
		Reserve	GGATCACCCGATTGTCCTCG
Adam8	*Mus musculus*	Forward	TGAACAAGCAGCGTCTACGA
		Reserve	CTGGGAGTGGTGAACTGGAC
Fgfr1	*Mus musculus*	Forward	TCCCTGTGGAAGTGGAGTCT
		Reserve	GCTACAGGCCTACGGTTTGG
Tgfbr1	*Mus musculus*	Forward	GGCGAAGGCATTACAGTGTT
		Reserve	TGGTGAATGACAGTGCGGTT
Itga9	*Mus musculus*	Forward	GCTCTCGCTGTAGCCCATC
		Reserve	ACCCACGAGGACCCAGC
Col6a1	*Mus musculus*	Forward	AGGGCTACAAGGAACCATGC
		Reserve	TTTCCTCGCTCCCCCTCATA
Tgfbr2	*Mus musculus*	Forward	CCAAGTCGGATGTGGAAATGG
		Reserve	TGTCGCAAGTGGACAGTCTC
Col14a1	*Mus musculus*	Forward	TGAAGCACCCACAGCCATAG
		Reserve	TCCAGGCACCATAACCACTTC
Itga1	*Mus musculus*	Forward	TCAGTGGAGAGCAGATCGGA
		Reserve	CCCACAGGGCTCATTCTTGT
Adam9	*Mus musculus*	Forward	GGGCCGACGTATAATGCAAAG
		Reserve	CAGGTGGCGGTCTGGAG
CypA	*Mus musculus*	Forward	CGATGACGAGCCCTTGG

		Reserve	TCTGCTGTCTTTGGAACTTTGTC
B2m	*Mus musculus*	Forward	ATTCACCCCCACTGAGACTG
		Reserve	TGCTATTTCTTTCTGCGTGC
Hmox1	*Homo sapiens*	Forward	AAGACTGCGTTCCTGCTCAAC
		Reserve	AAAGCCCTACAGCAACTGTCG
Gclm	*Homo sapiens*	Forward	GCGAGGAGCTTCATGATTGT
		Reserve	TGTGCAACTCCAAGGACTGA
Hprt	*Homo sapiens*	Forward	AGGCGAACCTCTCGGCTTTC
		Reserve	CAAGACGTTCAGTCCTGTCCATA
scFv-E06	*N/A*	Forward	GTACTGCTGCTCTGGGTTCC
		Reserve	CACTGGCCGTGCAACTAATG

Supplemental Table 4. Forward and reserve primer sequences for cDNA and genomic DNA amplification.

Data File S1. Source data.

Mitochondrial Telomerase Reverse Transcriptase Protects From Myocardial Ischemia/Reperfusion Injury by Improving Complex I Composition and Function

Ale-Agha N*, Jakobs P*, Goy C, Zurek M, Rosen J, Dyballa-Rukes N, Metzger S, **Greulich J**, von Ameln F, Eckermann O, Unfried K, Brack F, Grandoch M, Thielmann M, Kamler M, Gedik N, Kleinbongard P, Heinen A, Heusch G, Gödecke A, Altschmied J#, Haendeler J#

Circulation. 2021; 144, 1876-1890

*gleichberechtigte Erstautoren, #gleichberechtigete Seniorautoren

Publikation II

Beteiligung der Autoren:

Ale-Agha N: Erstautorin, war an der Planung und Durchführung der Versuche beteiligt, führte die Datenanalyse durch und war zudem am Entwurf des Manuskripts beteiligt.

Jakobs P: Erstautor, war an der Planung und Durchführung der Versuche beteiligt, führte die Datenanalyse durch und war zudem am Entwurf des Manuskripts beteiligt.

Goy C: Führte Sauerstoffverbrauchsmessungen an Mitochondrien und Migrationsversuche durch.

Zurek M: Führte Isolierung von kardialen Fibroblasten und Immunfluoreszenzanalysen an diesen durch.

Rosen J: Führte Immunoblots und Immunfluoreszenzanalysen an kardialen Fibroblasten durch.

Dyballa-Rukes N: Führte massenspektrometrische Untersuchungen und Immunoblots durch.

Metzger S: Betreute die massenspektrometrischen Untersuchungen und führte Datenanalyse durch.

Greulich J: Führte Immunoblots durch.

von Ameln F: Führte alle Genotypisierungen der Versuchstiere und ATP Messungen durch.

Eckermann O: Führte real-time PCR-Analysen von mitochondrialer DNA und relativer Telomerlänge durch.

Unfried K: Führte Perfusionen und Organentnahme von Mausherzen durch.

Brack F: Führte Fettdepot- und Blutglukosemessungen durch.

Grandoch M: Führte Analysen von Immunzellen und zugehörige Datenanalysen durch.

Thielmann M: Führte Bypass-Operationen und Entnahme humaner Herzaurikel durch.

Kamler M: Führte Bypass-Operationen und Entnahme humaner Herzaurikel durch.

Gedik N: Führte Messungen an isolierten Mitochondrien aus Herzaurikeln von Bypass-Patienten durch.

Kleinbongard P: Stellte isolierte Mitochondrien aus Herzaurikeln von Bypass-Patienten zur Verfügung.

Heinen A: Führte Echokardiografische Untersuchungen an Mäusen und zugehörige Auswertungen durch.

Heusch G: Koordinierte die Studienteile mit Humanmaterial, schrieb zugehörige Teile des Manuskripts.

Gödecke A: Betreute die Durchführung der experimentellen Herzinfarkte an Mäusen, schrieb Teile des Manuskripts für die Revision.

Altschmied J: Seniorautor, war an der Konzeption der Studie federführend beteiligt. Erstellte das Konzept für die Generierung der Mausmodelle, schrieb und finalisierte das Manuskript.

Haendeler J: Seniorautorin, konzipierte die Studie, war an der Versuchsplanung beteiligt, schrieb und finalisierte das Manuskript.

Circulation

ORIGINAL RESEARCH ARTICLE

Mitochondrial Telomerase Reverse Transcriptase Protects From Myocardial Ischemia/Reperfusion Injury by Improving Complex I Composition and Function

Niloofar Ale-Agha, PhD*; Philipp Jakobs, PhD*; Christine Goy, RT; Mark Zurek, MD; Julia Rosen, Cand med; Nadine Dyballa-Rukes, PhD; Sabine Metzger, PhD; Jan Greulich, MSc; Florian von Ameln, RT; Olaf Eckermann, MSc; Klaus Unfried, PhD; Fedor Brack, MSc; Maria Grandoch, MD; Matthias Thielmann, MD; Markus Kamler, MD; Nilgün Gedik, PhD; Petra Kleinbongard, PhD; Andre Heinen, PhD; Gerd Heusch, MD; Axel Gödecke, PhD; Joachim Altschmied, PhD†; Judith Haendeler, PhD†

BACKGROUND: The catalytic subunit of telomerase, telomerase reverse transcriptase (TERT), has protective functions in the cardiovascular system. TERT is not only present in the nucleus but also in mitochondria. However, it is unclear whether nuclear or mitochondrial TERT is responsible for the observed protection, and the appropriate tools are missing to dissect this.

METHODS: We generated new mouse models containing TERT exclusively in the mitochondria (mitoTERT mice) or the nucleus (nucTERT mice) to finally distinguish between the functions of nuclear and mitochondrial TERT. Outcome after ischemia/reperfusion, mitochondrial respiration in the heart, and cellular functions of cardiomyocytes, fibroblasts, and endothelial cells, as well, were determined.

RESULTS: All mice were phenotypically normal. Although respiration was reduced in cardiac mitochondria from TERT-deficient and nucTERT mice, it was increased in mitoTERT animals. The latter also had smaller infarcts than wild-type mice, whereas nucTERT animals had larger infarcts. The decrease in ejection fraction after 1, 2, and 4 weeks of reperfusion was attenuated in mitoTERT mice. Scar size was also reduced and vascularization increased. Mitochondrial TERT protected a cardiomyocyte cell line from apoptosis. Myofibroblast differentiation, which depends on complex I activity, was abrogated in TERT-deficient and nucTERT cardiac fibroblasts and completely restored in mitoTERT cells. In endothelial cells, mitochondrial TERT enhanced migratory capacity and activation of endothelial nitric oxide synthase. Mechanistically, mitochondrial TERT improved the ratio between complex I matrix arm and membrane subunits, explaining the enhanced complex I activity. In human right atrial appendages, TERT was localized in mitochondria and there increased by remote ischemic preconditioning. The telomerase activator TA-65 evoked a similar effect in endothelial cells, thereby increasing their migratory capacity, and enhanced myofibroblast differentiation.

CONCLUSIONS: Mitochondrial, but not nuclear TERT, is critical for mitochondrial respiration and during ischemia/reperfusion injury. Mitochondrial TERT improves complex I subunit composition. TERT is present in human heart mitochondria, and remote ischemic preconditioning increases its level in those organelles. TA-65 has comparable effects ex vivo and improves the migratory capacity of endothelial cells and myofibroblast differentiation. We conclude that mitochondrial TERT is responsible for cardioprotection, and its increase could serve as a therapeutic strategy.

Key Words: mice, transgenic ■ mitochondria ■ myocardial ischemia ■ myofibroblasts ■ reperfusion injury ■ telomerase

Correspondence to: Judith Haendeler, PhD, Environmentally-induced Cardiovascular Degeneration, Clinical Chemistry and Laboratory Diagnostics, Medical Faculty, University Düsseldorf, c/o IUF-Leibniz Research Institute for Environmental Medicine, Auf`m Hennekamp 50, 40225 Düsseldorf, Germany, Email juhae001@uni-duesseldorf.de; or Joachim Altschmied, PhD, c/o IUF-Leibniz Research Institute for Environmental Medicine, Auf`m Hennekamp 50, 40225 Düsseldorf, Germany, Email joalt001@uni-duesseldorf.de

*N. Ale-Agha and P. Jakobs contributed equally.

†J. Altschmied and J. Haendeler contributed equally.

Supplemental Material is available at https://www.ahajournals.org/doi/suppl/10.1161/CIRCULATIONAHA.120.051923.

For Sources of Funding and Disclosures, see page 1889.

Circulation is available at www.ahajournals.org/journal/circ

Clinical Perspective

What Is New?

- Mitochondrial telomerase reverse transcriptase (TERT), not nuclear TERT, is cardioprotective against ischemia/reperfusion injury.
- Mitochondrial TERT improves the ratio between complex I matrix arm and membrane subunits explaining the enhanced complex I activity.
- Mitochondrial TERT protects cardiomyocytes from apoptosis, improves cardiac myofibroblast differentiation, and endothelial cell migration and vascularization.

What Are the Clinical Implications?

- Remote ischemic preconditioning and the telomerase activator TA-65 increase TERT within the mitochondria.
- An increase in mitochondrial TERT levels, possibly induced by remote ischemic preconditioning or by treatment with TA-65, could be beneficial in ischemia/reperfusion injury.

Nonstandard Abbreviations and Acronyms

αSMA	α smooth muscle actin
eNOS	endothelial nitric oxide synthase
mitoTERT mice	mice with TERT exclusively in the mitochondria
mtDNA	mitochondrial DNA
nucTERT mice	mice with TERT exclusively in the nucleus
RIPC	remote ischemic preconditioning
ROS	reactive oxygen species
TERT	telomerase reverse transcriptase
TGFβ1	transforming growth factor β1
TIM23	translocase of inner mitochondrial membrane 23

The enzyme telomerase reverse transcriptase (TERT) has traditionally been viewed as being only expressed in stem cells and highly proliferating cells. However, over the past years, it has become evident that TERT is also detectable in non- or lowly proliferating tissues such as the heart and vasculature (for review, see Zurek et al[1]). TERT exerts protection in the cardiovascular system as evident from reduced cardiomyocyte apoptosis in transgenic mice overexpressing TERT in cardiomyocytes[2] and from the smaller infarct size and better survival in mice with increased expression of TERT by adeno-associated viruses targeted specifically to the heart.[3] Those studies described the potential of TERT to increase the proliferative capacity of the tissue as one of the underlying mechanisms.

Over the past decade, it has become clear that TERT not only is localized in the nucleus, where it protects telomeres, the end of the chromosomes, from shortening, but also is present in mitochondria.[4–6] In both organelles, TERT has noncanonical, telomere-independent functions. We and others have demonstrated that nuclear and mitochondrial TERT, as well, protects from apoptosis in several cell types.[1,4–7] Singhapol et al[8] showed that mitochondrial and not nuclear localization of TERT prevented nuclear DNA damage by decreasing the levels of mitochondrial reactive oxygen species (ROS) in cervical cancer and breast adenocarcinoma cell lines.

Cardiac mitochondria from first-generation TERT-deficient mice, which have no critical telomere shortening, exhibit reduced respiration.[4] It is presently unclear whether it is mitochondrial or nuclear TERT or both that exert protection in the cardiovascular system. To unequivocally distinguish between the functions of mitochondrial and nuclear TERT, we generated mouse models containing TERT exclusively in either of the 2 compartments. To understand for the first time whether mitochondrial TERT or nuclear TERT or both are protective in the cardiovascular system, we performed ischemia/reperfusion experiments in these mice and analyzed animals for 2, 7, 14, and 28 days. Furthermore, we analyzed the effects of mitochondrial and nuclear TERT in the cardiomyocyte cell line HL-1, in cardiac fibroblasts from these mice and human primary endothelial cells. We also provide mechanistic insights shedding light on TERT functions within mitochondria in the cardiovascular system. Moreover, the subcellular localization of TERT in human cardiac tissue has never been investigated. Mitochondrial function is critical to cardioprotection,[9,10] and remote ischemic preconditioning (RIPC) improved mitochondrial and contractile function in patients undergoing coronary artery bypass grafting.[11] Therefore, we also hypothesized that TERT is present in human cardiac mitochondria, is increased by RIPC, and is involved in the protection of the heart from ischemia/reperfusion injury. Moreover, to get a first impression whether the telomerase activator TA-65 can improve cellular characteristics relevant in ischemia/reperfusion injury and, thus, might be of therapeutic interest in the long run, we investigated the effect of TA-65 on endothelial cell migration and myofibroblast activation ex vivo.

METHODS

The data, analytic methods, and study materials will not be made available to other researchers; specific inquiries should be sent to the corresponding authors.

Ethics Statement

The original clinical study[11] conformed to the ethical guidelines of the 1975 Declaration of Helsinki. The local Institutional Review Board (University Hospital Essen 08-3683 and 13-5507)

approved the study, and patients gave written informed consent. In the present study, residual mitochondria from right atrial tissue of 7 patients receiving RIPC and 5 patients receiving placebo were included.[11] All experimental protocols for animal studies were approved by the Animal Ethics Committee of the State Agency for Nature, Environment, and Consumer Protection North Rhine-Westphalia, Düsseldorf (Az.: 84-02.04.2014.A190, Az.: 81-02.04.2020.A030, Az.: 84-02.05.20.12.237).

Experimental Mice

Heterozygous TERT-deficient mice *(B6.129S-Tert^{tm1Yjc}/J)*[12] were originally obtained from The Jackson Laboratory and backcrossed to *C57BL/6N* Tac animals (Taconic Biosciences) for >10 generations. Animals used for breeding were genotyped for the deletion in the *NNT* (nicotinamide nucleotide transhydrogenase) gene,[13] and only individuals without the mutation were used for strain maintenance.

Mice expressing endogenous TERT and TERT targeted to the mitochondria (mitoTERT) or nucleus (nucTERT), respectively, were generated by Taconic Biosciences. Therefore, the TERT coding sequence with an additional mitochondrial targeting sequence or an additional nuclear localization signal was inserted into the *ROSA26* locus.[14] All mice were genotyped by polymerase chain reaction using DNA isolated from tail clips or ear punches; for details, see Supplemental Methods.

Echocardiography

Echocardiography was performed as reported previously by Heinen et al and Gorressen et al[15,16]; for details, see Supplemental Methods.

Myocardial Ischemia and Reperfusion

Male mice (4–8 months old) underwent 45 minutes of coronary occlusion followed by reperfusion. Animals were anesthetized by mask inhalation of isoflurane 2.5% (v/v) and a mixture of oxygen and room air. For details of the exact procedure, see Supplemental Methods.

Infarct Size

For details of the exact procedure, see Supplemental Methods.

Fibrosis

Mice were sacrificed by cervical dislocation 7 days after myocardial infarction; their hearts were explanted, embedded in Tissue-Tek OCT (Sakura Finetek, Science Services), and snap-frozen at −40 °C in isopentane/dry ice. Heart cryosections (4 µm) were stained as described previously by Ale-Agha et al.[17] For detailed information, see Supplemental Methods.

Preparation of Mouse Heart Mitochondria

Mouse heart mitochondria were prepared as described previously by Ale-Agha et al[17]; for details, see Supplemental Methods.

Human Cardiac Mitochondria

Residual mitochondrial preparations from a recently published study[11] were lysed in 100 mmol/L Tris-HCl, pH 7.4, 2% sodium dodecyl sulfate. Lysates were used for immunoblotting. For details on sampling of right atrial appendages and study protocol in patients, see Supplemental Methods.

Respiration of Mouse Mitochondria

The rate of mitochondrial respiration was monitored at 25 °C using an Oxygraph-*2k* system (Oroboros) equipped with 2 chambers and DatLab software[4] as described previously by Ale-Agha et al.[17]

Cardiomyocyte Cell Line HL-1

The murine cardiomyocyte cell line HL-1[18] was a gift from W.C. Claycomb; for cultivation, see Supplemental Methods.

Cardiac Fibroblasts and Induction of Myofibroblast Differentiation

Cardiac fibroblasts were isolated, as described previously by Ale-Agha et al[17]; for details, see Supplemental Methods.

Endothelial Cells

Primary human endothelial cells were obtained from Lonza; for details on cultivation, see Supplemental Methods.

Lentiviral Production and Transduction

For details, see Supplemental Methods.

Transient Transfections

Endothelial cells were transfected on 6-cm culture dishes with 3 µg of plasmid DNA and 25 µL of Superfect (Qiagen) according to the manufacturer's specification with a transfection efficiency of ≈40%.

Scratch-Wound Assay of Endothelial Cells

For detection of cell migration, wounds were created by scraping confluent cell monolayers with a sterile disposable rubber policeman as described previously by Ale-Agha et al[17]; for details, see Supplemental Methods .

Apoptosis

Detection of apoptosis was performed in the cardiomyocyte cell line HL-1 by flow cytometry using annexinV-APC (allophycocyanin) binding and propidium iodide (PI) staining. Only annexinV-APC–positive/PI–negative cells were considered truly apoptotic. Flow cytometry was performed with a BD FACSCalibur (BD Biosciences) by counting 30 000 events. For additional flow cytometry analyses of immune cells, see Supplemental Methods.

Sodium Dodecyl Sulfate-Polyacrylamide Gel Electrophoresis and Immunoblotting

For details, see Supplemental Methods.

Two-Dimensional Gel Electrophoresis and Protein Identification by Mass Spectrometry

For details, see Supplemental Methods.

Immunostaining

For detailed information on direct and indirect immunostaining of cells and tissue sections, see Supplemental Methods.

Mitochondrial DNA Content

Mitochondrial DNA (mtDNA) content was determined by semiquantitative real-time polymerase chain reaction; for details, see Supplemental Methods.

Statistics

The number of experiments (n) given in the figure legends represents independent biological replicates, and the data shown are mean±SEM; for details, see Supplemental Methods.

RESULTS

Generation of Mice Containing TERT Exclusively in the Mitochondria or the Nucleus

The TERT coding sequence was fused to a N-terminal mitochondrial targeting sequence (mitoTERT) or a C-terminal nuclear localization signal (nucTERT), and these fusions were introduced into the ROSA26 locus[14] such that the proteins are expressed from the weak, ubiquitously active ROSA26 promoter (Figure 1A). Mice carrying the mitoTERT or nucTERT allele, respectively, were backcrossed onto a TERT-deficient genetic background (see breeding scheme in Figure S1). mitoTERT or nucTERT mice were phenotypically normal during the 9-month observation period of this study. Because no antibodies for reliable detection of TERT in mouse tissues are available,[19] TERT expression was analyzed on the transcript level and was shown to be higher in these 2 genotypes (Figure S2A). Exclusive localization of TERT in the mitochondria or nuclei in lung and cardiac cells from mitoTERT and nucTERT mice was confirmed by immunostainings (Figure S2). Although we used only first-generation mice of the 4 genotypes (Figure S1), we confirmed that their average telomere lengths were not different (Figure S3). Moreover, we did not observe any obvious signs of hyperproliferation, and mitoTERT and nucTERT mice showed no differences in their body weights or their heart-to-body weight ratios compared with wild-type and TERT-deficient animals from 6 to 9 months of age (body weight: wild-type, 28.3±4.0 g [n=12]; TERT-deficient, 28.0±3.7 g [n=10]; mitoTERT, 28.4±4.1 g [n=11], nucTERT, 27.3±1.3 g [n=13], not significant; heart-to-body weight ratios: wild-type, 5.44±0.21 mg/g [n=10]; TERT-deficient, 5.50±0.27 mg/g [n=7]; mitoTERT, 5.75±0.50 mg/g [n=9]; nucTERT, 5.78±0.21 mg/g [n=7], not significant). To characterize the 4 genotypes more closely, we measured immune cells in the blood and the general metabolic state. As demonstrated in Figure S4, we did not detect any differences in leukocytes, lymphocytes, neutrophils, Ly6C^{high} monocytes, Ly6C^{low} monocytes, and total monocytes. Moreover, white and brown adipose tissue content and fasting blood glucose did not differ between the 4 genotypes (Figure S5A–S5C). We also performed glucose tolerance tests and found no differences (Figure S5D).

Mitochondrial TERT Improves Respiration of Heart Mitochondria

We and others had previously published that TERT is associated mtDNA and protects this DNA from damage.[4,6] Thus, we analyzed mtDNA content in the 4 different mouse lines. Semiquantitative analysis by real-time polymerase chain reaction revealed no differences between the genotypes (relative mtDNA content: wild-type, 60.8±16.6 arbitrary units; TERT-deficient, 52.7±11.5 arbitrary units; mitoTERT, 45.8±15.7 arbitrary units; nucTERT, 42.7±7.3 arbitrary units, n=6, not significant).

Cardiac mitochondria from TERT-deficient mice on a *C57BL/6J* background have reduced mitochondrial respiration.[4] This strain carries a mutation in the *NNT* gene,[13] which results in mitochondrial redox abnormalities.[20] Analysis of the newly generated mitoTERT and nucTERT mice along with wild-type and TERT-deficient animals, all on a *C57BL/6N* background, showed that, independent of the genetic background, cardiac mitochondria from first-generation TERT-deficient mice had reduced state 4 and state 3 respiration compared with those of wild-type mice. Mitochondrial TERT, but not nuclear TERT reversed the respiration impairment observed in cardiac mitochondria of TERT-deficient animals (Figure 1B).

Mitochondrial TERT Protects From Myocardial Ischemia/Reperfusion Injury

We next investigated the effect of TERT localization on infarct size in an ischemia/reperfusion model. After 2 days, the area at risk was comparable in all 4 genotypes (Figure 2A). TERT-deficient mice had larger infarct size than wild-type mice (Figure 2B and 2C). Reintroduction of TERT exclusively into the nucleus did not reduce infarct size. However, mitoTERT mice had smaller infarcts than all other genotypes (Figure 2B and 2C). When we analyzed the death rates of all genotypes after ischemia/reperfusion injury, we noted that 21% of wild-type, 33% of TERT-deficient, and 9% of mitoTERT mice, but 50% of the nucTERT animals died within the first 2 days, indicating that elevated nuclear TERT is harmful for survival after ischemia/reperfusion injury. Moreover, because nucTERT mice did not differ from TERT-deficient animals in infarct size after 2 days (Figure 2B and 2C) and mitochondrial respiration (Figure 1B), we did not perform long-term experiments with those mice.

Wild-type, TERT-deficient, and mitoTERT mice were then analyzed after 7 days of ischemia/reperfusion. Before ischemia/reperfusion, end-diastolic volume, end-systolic volume, stroke volume, and ejection fraction were

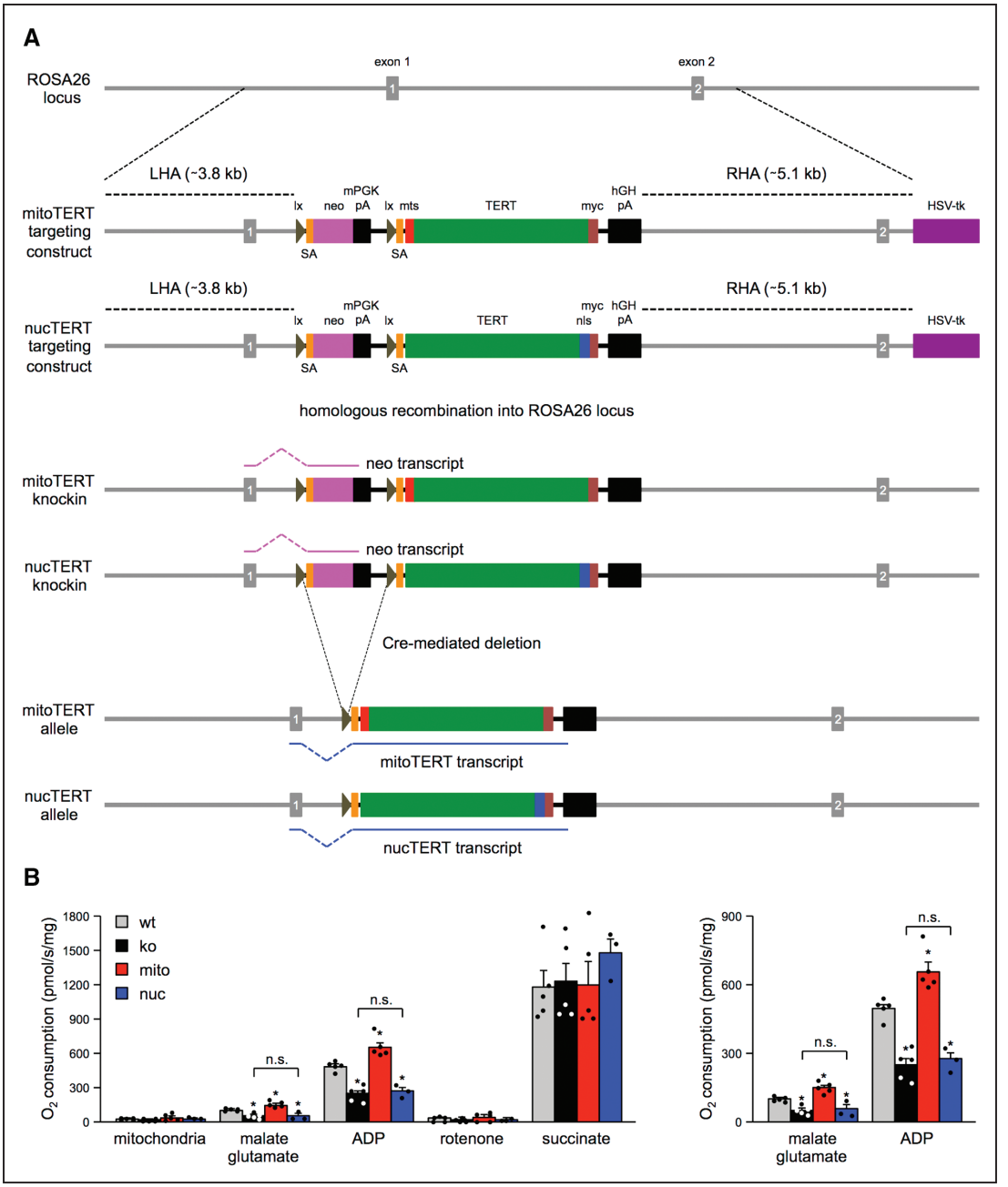

Figure 1. Mitochondrial, but not nuclear TERT (telomerase reverse transcriptase), improves mitochondrial respiration in the heart. **A**, TERT targeted to the mitochondria (mitoTERT) or to the nucleus (nucTERT) was introduced into the ROSA26 locus by homologous recombination such that it is expressed under the control of the ubiquitously active, weak ROSA26 promoter. hGH pA indicates human growth hormone gene polyadenylation signal; HSV-tk, herpes simplex virus thymidine-kinase gene; LHA, left homology arm; lx, loxP site; mPGK pA, mouse phosphoglycerate-kinase gene polyadenylation signal; mts, mitochondrial targeting sequence; myc, myc epitope tag; neo, neomycin resistance gene; nls, nuclear localization signal; RHA, right homology arm; and SA, splice acceptor. **B**, **Left**, O_2 consumption was determined in isolated cardiac mitochondria of adult wild-type (wt), TERT-deficient (ko), mitoTERT (mito), and nucTERT (nuc) mice and after the sequential addition of malate/glutamate, ADP, rotenone, and succinate. **Right**, A magnification of state 4 (malate/glutamate) and state 3 (ADP) respiration (all data are mean±SEM, n=3–5 per group (wt, ko, mito: 5; nuc: 3). *P<0.05 vs wt, n.s. indicates not significant, 1-way ANOVA with post hoc Tukey least significant difference test.

not different in the 3 genotypes. In mitoTERT mice, ejection fraction after 1 week of reperfusion was only slightly reduced from baseline, whereas it was markedly reduced in TERT-deficient and wild-type mice (Figure 3A). End-systolic volume was increased from baseline in wild-type and TERT-deficient animals but not in mitoTERT mice (Figure 3B), and end-diastolic volume was not different among genotypes (Figure 3C). Stroke volume was reduced from baseline in all 3 genotypes, with the largest reduction in TERT-deficient mice (Figure 3D). These animals had the largest scar size 1 week after reperfusion, whereas hearts from mitoTERT mice had even smaller scars than

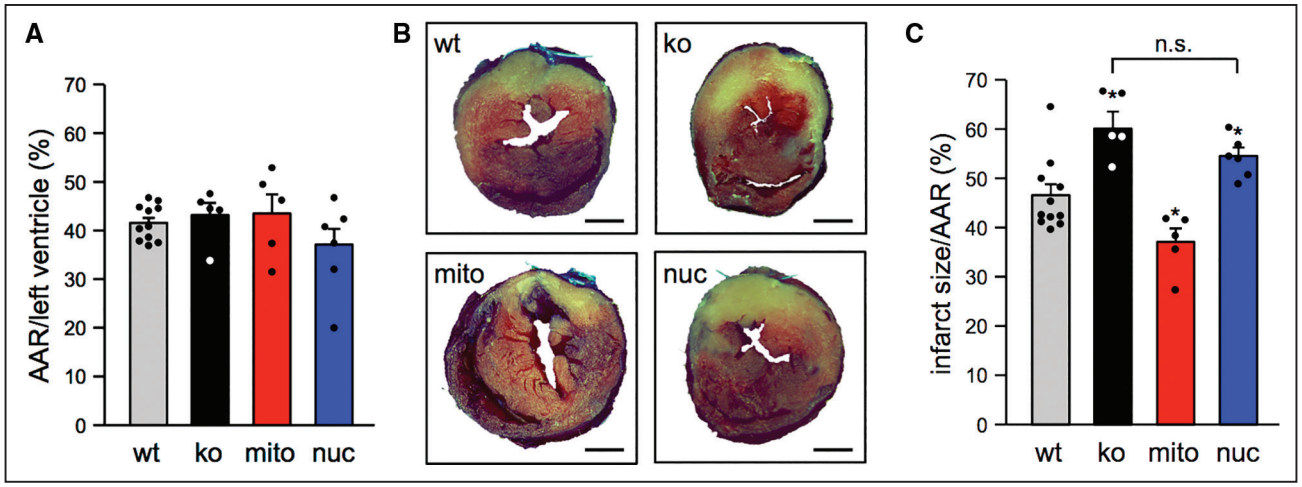

Figure 2. Mitochondrial TERT (telomerase reverse transcriptase) reduces infarct size.
Myocardial ischemia/reperfusion injury was induced in wild-type (wt), TERT-deficient (ko), mitoTERT (mito), and nucTERT (nuc) animals. Two days after infarction, heart sections were stained with Evans blue/2,3,5-triphenyltetrazolium chloride. **A**, Area-at-risk (AAR)/left ventricle. **B**, Representative sections (scale bar=1 mm). **C**, Infarct size/AAR (data are mean±SEM, n=5–11 per group [wt: 11; ko, mito: 5; nuc: 6], **P*<0.05 vs wt, n.s. indicates not significant, Kruskal-Wallis test with post hoc Mann-Whitney test).

wild-type mice (Figure 3E and 3F and Figure S6). Moreover, TERT-deficient mice showed reduced vascularization in the border zone of the infarct (Figure 3G and 3H). In contrast, in mitoTERT mice, CD31-positive cells were significantly increased compared with TERT-deficient and wild-type animals (Figure 3G and 3H). Last, we also confirmed that mitoTERT is still present in the mitochondria even after ischemia/reperfusion injury (Figure S7).

Next, in a new series of mice, we investigated the long-term effects of mitochondrial TERT after ischemia/reperfusion injury by serial echocardiography over 28 days. The decline of ejection fraction was lowest in mitoTERT mice, intermediate in wild-type mice, and worst in TERT-deficient animals (Figure 3I). All groups of mice developed a left ventricular dilation as shown by the gradual increase in end-systolic volume and end-diastolic volume (Figure 3J and 3K). However, the left ventricular dilation was significantly attenuated in mitoTERT mice compared with TERT-deficient mice and was not different from wild-type mice. Moreover, mitoTERT mice showed a significant increase in stroke volume after 28 days compared with TERT-deficient and even wild-type animals (Figure S8A). Heart rates were not changed in all mice at any given time point (Figure S8B). Thus, mitoTERT leads to long-term improvement of cardiac function after ischemia/reperfusion injury.

Mitochondrial TERT Protects the Cardiomyocyte Cell Line HL-1 Against Apoptosis, Is Required for Myofibroblast Differentiation, and Enhances Vascularization and Endothelial Cell Migration and Activity of Endothelial Nitric Oxide Synthase

To assess the effect of mitochondrial and nuclear TERT on cardiomyocyte death in vitro, we expressed mitochondrially or nuclear targeted TERT in the cardiomyocyte cell line HL-1. Increased expression of mitochondrially targeted TERT reduced basal and H_2O_2-induced apoptosis after 24 and 48 hours (Figure 4A). In contrast, nuclear targeted TERT failed to inhibit H_2O_2-induced apoptosis (Figure 4A).

In the early phase after myocardial infarction, the loss of cardiomyocytes is compensated by myofibroblasts, which provide structural stability for the scar.[21] In isolated cardiac fibroblasts of wild-type, TERT-deficient, mitoTERT, and nucTERT mice, myofibroblast differentiation was induced by TGFβ1 (transforming growth factor β1) treatment for 48 hours. TGFβ1 increased the expression of α smooth muscle actin (αSMA), a surrogate marker for myofibroblast differentiation, in fibroblasts from wild-type mice, which also displayed a typical myofibroblast structure. In contrast, TGFβ1 did not increase the expression of αSMA in TERT-deficient fibroblasts or change their phenotype. However, fibroblasts from mitoTERT mice showed stronger upregulation of αSMA (Figure 4B–4D and Figure S9) than those from all other mice along with a more pronounced myofibroblast structure (Figure 4B). In cardiac fibroblasts from nucTERT mice, the basal αSMA levels were already elevated; however, TGFβ1 did not increase expression any further (Figure 4B–4D and Figure S9). Moreover, the typical myofibroblast structure was only weakly apparent (Figure 4B).

As we demonstrated enhanced vascularization in the mitoTERT mice, we investigated the migratory capacity of endothelial cells. Overexpression of untargeted TERT slightly increased migratory capacity in a scratch-wound assay, whereas cells overexpressing nuclear TERT were no different from empty vector transfected cells. In contrast, mitochondrial TERT improved migration over that obtained with untargeted TERT (Figure 4E and 4F). We controlled for the localization of the overexpressed mito-

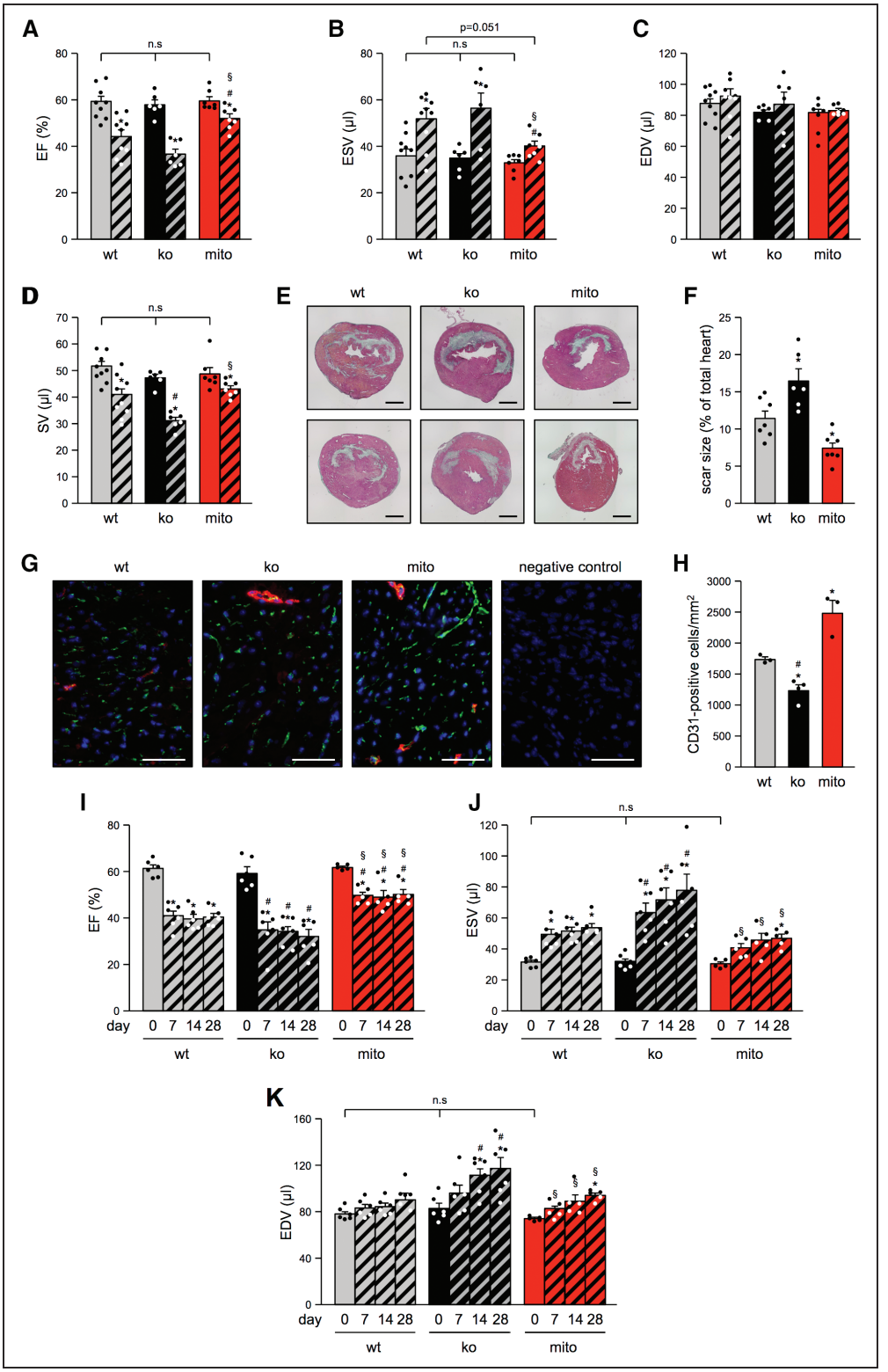

Figure 3. Mitochondrial TERT (telomerase reverse transcriptase) attenuates left ventricular dysfunction, reduces scar size, and improves vascularization after myocardial infarction.

A through **D**, Functional parameters of the heart were measured by echocardiography in wild-type (wt), TERT-deficient (ko), and mitoTERT (mito) animals before (baseline, filled bars) and 7 days after (hatched bars) infarction (data are mean±SEM, n=6–9 per group [wt: 9; ko: 6; mito: 7], $^{*}P<0.05$ vs baseline same genotype, 1-way ANOVA for repeated measurements with post hoc Tukey least significant difference test, $^{\#}P<0.05$ vs wt day 7, $^{\S}P<0.05$ vs ko day 7, n.s. indicates not significant, 1-way ANOVA with post hoc Tukey LSD test). **A**, Ejection fraction (EF). **B**, End-systolic volume (ESV). **C**, End-diastolic volume (EDV). **D**, Stroke volume (SV). **E** and **F**, Transverse cardiac sections were stained with Masson trichrome. **E**, Representative sections (scale bar=1 mm). **F**, Scar size (data are mean±SEM, n=6–7 per group (*Continued*)

Figure 3 Continued. [wt, mito: 7; ko: 6], *P<0.05 vs wt, 1-way ANOVA with post hoc Tukey least significant difference test). **G** and **H**, Transverse cardiac sections from the border zone were stained for CD31 (green) and α smooth muscle actin (αSMA; red) to visualize blood vessels, nuclei were counterstained with 4',6-diamidino-2-phenylindole (DAPI; blue). **G**, Representative sections (scale bar=50 μm). **H**, CD-31–positive cells/mm^2 (data are mean±SEM, n=3–4 per group [wt, mito: 3; ko: 4], *P<0.05 vs wt, #P<0.05 vs mito, 1-way ANOVA with post hoc Tukey LSD test). **I** through **K**, Functional parameters of the heart were measured by echocardiography in wild-type (wt), TERT-deficient (ko), and mitoTERT (mito) animals before (baseline, day 0, filled bars) and 7, 14, and 28 days after (hatched bars) infarction (data are mean±SEM, n=5–6 per group [wt, ko: 6; mito: 5], *P<0.05 vs baseline same genotype, n.s. indicates not significant, 1-way ANOVA for repeated measurements with post hoc Tukey LSD test, #P<0.05 vs wt same time point, §P<0.05 vs ko same time point, one-way ANOVA with post hoc Tukey LSD test). **I**, Ejection fraction (EF). **J**, End-systolic volume (ESV). **K**, End-diastolic volume (EDV).

TERT and nucTERT in endothelial cells (Figure S10). Because we found no differences in mtDNA content in mice, we also determined the mtDNA content in human cells. Similar to the results in mice, mtDNA content was unchanged (Figure 4G). Migratory capacity depends not only on intact mitochondria[17,22] but also on nitric oxide produced by endothelial nitric oxide synthase (eNOS). Therefore, we next investigated the phosphorylation of eNOS on serine 1177 as a surrogate marker for its activation. Overexpression of untargeted TERT increased phosphorylation of eNOS compared with cells transfected with an empty vector or an expression vector for TERT targeted to the nucleus, and mitochondrial TERT enhanced phosphorylation even further (Figure 4H and 4I, and Figure S11).

Increased Mitochondrial TERT Reduces Prohibitin Levels and Thereby Improves the Stoichiometry of Complex I Matrix Arm to Membrane Subunits, Leading to Increased Complex I Activity of the Respiratory Chain

Having demonstrated that mitochondrial TERT, but not nuclear TERT, is required for mitochondrial complex I respiration, we performed a proteome analysis of heart mitochondria from wild-type, TERT-deficient, and mitoTERT mice to get mechanistic insights. Therefore, differences in the abundance of particular mitochondrial proteins were examined by 2-dimensional gel electrophoresis. The spot showing the most prominent disparity between the genotypes was further analyzed by tandem mass spectrometry and identified as prohibitin. Compared with heart mitochondria from wild-type animals, prohibitin levels were higher in TERT-deficient mice but lower in mitoTERT animals (Figure 5A). Excessive prohibitin has been demonstrated to disturb the stoichiometry between matrix arm and membrane subunits of complex I as shown by a relative increase in matrix arm proteins, resulting in reduced complex I activity.[23] The differences in mitochondrial prohibitin levels, therefore, provide a first explanation for the differences in complex I respiration observed in wild-type, TERT-deficient, mitoTERT, and nucTERT mice presented in Figure 1B.

We have also shown that mitochondrial TERT is critical for myofibroblast differentiation, and there have been hints that this process is dependent on mitochondrial respiration.[24] Thus, it is possible that the interconnection between mitochondrial TERT, prohibitin, and complex I activity also exists in cardiac fibroblasts and plays a role in myofibroblast differentiation. Therefore, we first determined whether myofibroblast differentiation of cardiac fibroblasts is dependent on complex I activity of the respiratory chain. To this end, cardiac fibroblasts from wild-type animals were incubated with the complex I inhibitor rotenone, and myofibroblast differentiation induced by TGFβ1 was measured. Rotenone abrogated TGFβ1-induced formation of the typical myofibroblast structure (Figure 5B) and αSMA upregulation (Figure 5C and 5D and Figure S12). Moreover, a survey of prohibitin in cardiac fibroblasts isolated from the 4 different mouse genotypes revealed the highest levels in TERT-deficient and nucTERT cells and the lowest level in mitoTERT fibroblasts (Figure 5E and Figure S13). Based on this observation, we measured the levels of 2 complex I matrix arm subunits, namely NDUFS3, NDUFV2, and the 2 membrane subunits NDUFA9 and NDUFB9, and calculated the ratios between these different subunits, which determines complex I activity (Figure 1B). TERT deficiency led to an increase in matrix arm proteins relative to membrane subunits of complex I. The same results were observed in nucTERT fibroblasts. This disturbance was not only blunted in mitoTERT cells but was also further improved over wild-type cells (Figure 5F and 5G and Figure S14).

Mitochondrial TERT Levels in Human Right Atrial Tissue Are Increased by Remote Ischemic Preconditioning

Having shown that mitochondrial TERT improves the outcomes after myocardial infarction, we searched for strategies that could confer cardioprotection via mitochondrial TERT. One such strategy might be RIPC. The cardioprotective effect of RIPC was shown in a recent study with patients who had undergone coronary artery bypass grafting surgery.[11] To investigate whether RIPC has an effect on TERT localization, we used residual mitochondria from right atrial appendages of 7 patients receiving RIPC and 5 patients receiving placebo from this study (Table S1). Human right atrial appendages provide a unique opportunity to investigate cardioprotective signaling in human myocardium. However, data obtained from right atrial tissue cannot simply be extrapolated to left ventricular tissue. Consistent with their different functions, they also have differences in their proteomes, with mitochondrial proteins, for example,

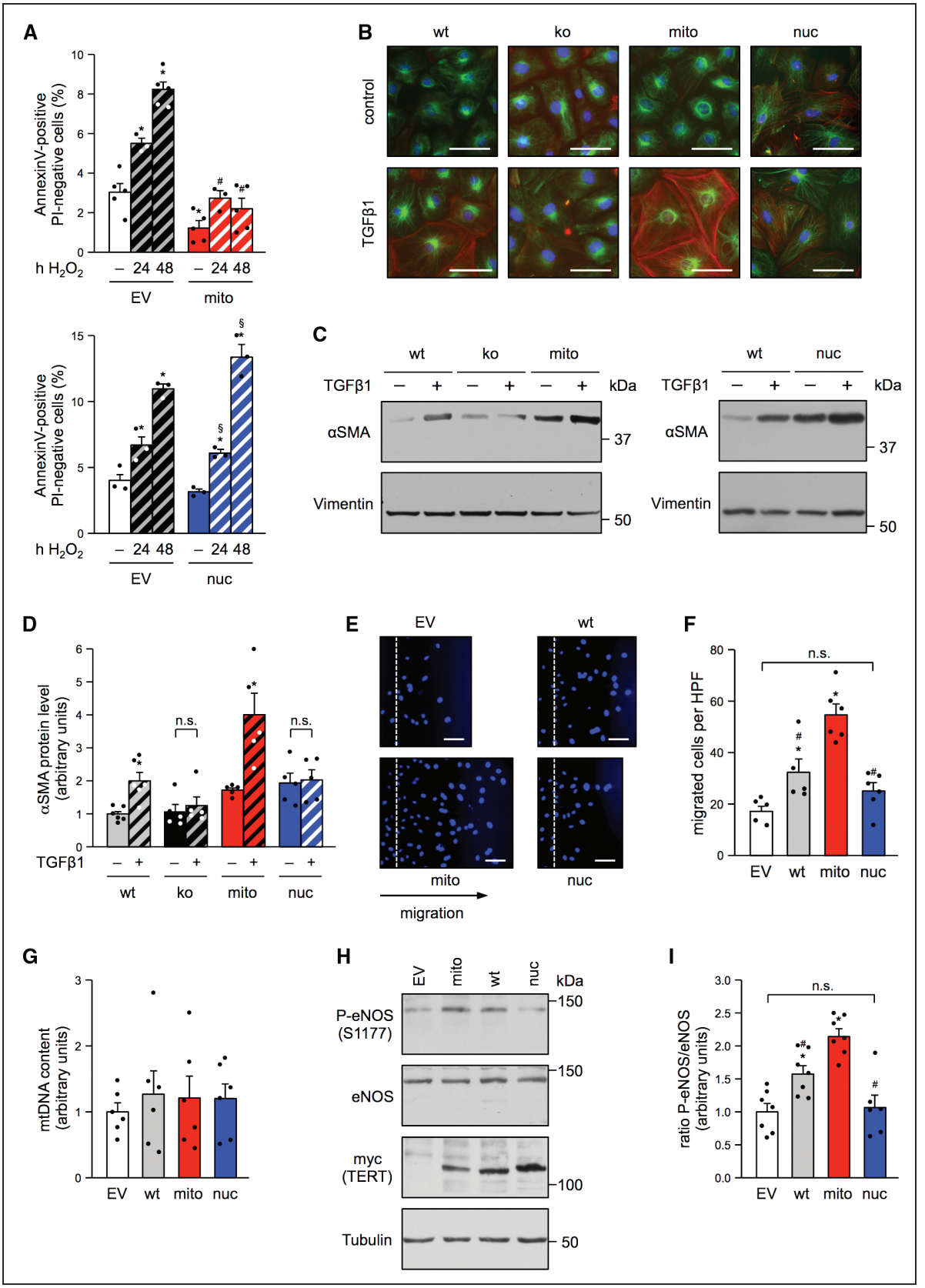

Figure 4. Mitochondrial TERT (telomerase reverse transcriptase) improves functional parameters in different cell types.
A, HL-1 cells were transduced with lentiviral expression vectors for mitochondrially (mito) or nuclear (nuc) targeted TERT or an empty vector (EV) as control. Apoptosis was induced by incubation with 500 µmol/L H_2O_2 for 24 and 48 hours and measured as annexin V–positive/propidium iodide (PI)–negative cells by flow cytometry (data are mean±SEM, n=3–5, **P*<0.05 vs EV/untreated, #*P*<0.05 vs EV/same (*Continued*)

Figure 4 Continued. treatment time, §$P<0.05$ vs same transduction/untreated, 1-way ANOVA with post hoc Tukey least significant difference test). **B** through **D**, Cardiac fibroblasts from wild-type (wt), TERT-deficient (ko), mitoTERT (mito), and nucTERT (nuc) mice were treated with TGFβ1 (transforming growth factor β1) or left untreated (−/control). α smooth muscle actin (αSMA) was detected by immunostaining and immunoblot. **B**, Representative immunostainings (red: αSMA; green: vimentin; blue: 4′,6-diamidino-2-phenylindole [DAPI]; scale bar=100 µm). **C**, Representative immunoblots; vimentin served as loading control. **D**, Semiquantitative analysis of αSMA normalized to vimentin (data are mean±SEM, n=5–6, *$P<0.05$ vs untreated same genotype, n.s.=not significant, Kruskal-Wallis test with post hoc Mann-Whitney test). **E** through **I**, Primary human endothelial cells were transfected with expression vectors for untargeted TERT (wt), mitochondrially (mito) or nuclear (nuc) targeted TERT, or an empty vector (EV) as control. **E** and **F**, Migratory capacity was measured in a scratch-wound assay. **E**, Representative DAPI staining (scale bar=100 µm). **F**, Migrated cells per high-power field (HPF; data are mean±SEM, n=5–6, *$P<0.05$ vs EV, #$P<0.05$ vs mito, n.s.=not significant, 1-way ANOVA with post hoc Tukey least significant difference test). **G**, Semiquantitative analysis of mitochondrial DNA (mtDNA) content (data are mean±SEM, n=6, not significant, 1-way ANOVA with post hoc Tukey least significant difference test). **H** and **I**, Phosphorylation of endothelial nitric oxide synthase (eNOS) on serine 1177 (P-eNOS(S1177)) and the total levels of eNOS were determined by immunoblot; tubulin served as loading control, and expression of TERT was verified with an anti-myc antibody (myc(TERT)). **H**, Representative immunoblots. **I**, Semiquantitative analysis of phosphorylated eNOS normalized to eNOS (data are mean±SEM, n=6–7, *$P<0.05$ vs EV, #$P<0.05$ vs mitoTERT, n.s.=not significant, 1-way ANOVA with post hoc Tukey least significant difference test).

being more abundant in ventricles than in atrial tissue.[25] Nevertheless, the cardioprotective effect of RIPC in this small subgroup was evident from the serum TnI/TnT (troponin I/troponin T) concentration area under the curve over 72 hours (RIPC, 161±11; placebo, 414±48; TnI/TnT of 99th reference percentile × 72h × 1000, $P<0.05$). Immunoblot analysis clearly demonstrated an increase in mitochondrial TERT in patients subjected to RIPC compared with placebo controls (Figure 6A and 6B, and Figure S15).

Effects of the Telomerase Activator TA-65 on Mitochondrial TERT, Endothelial Cell Migration, and Myofibroblast Differentiation

As an alternative strategy, which might be useful in a pharmacological setting, we tested the commercially available telomerase activator TA-65, a small molecule from *Astragalus membranaceus*. In healthy human subjects, TA-65 had not shown adverse effects when given over a 1-year period.[26] Therefore, we tested whether TA-65 affects mitochondrial TERT, endothelial cell functionality, and myofibroblast differentiation. First, we used TA-65 in TERT-deficient fibroblasts in the setting of myofibroblast differentiation to assess whether this compound has effects not dependent on TERT. However, TA-65 alone or in combination with TGFβ1 did not induce upregulation of αSMA or a phenotypic change (Figure S16). This inability to override the myofibroblast differentiation block, which is attributable to TERT deficiency, clearly indicates also that the TA-65 effects depend on TERT. Next, we treated primary human endothelial cells with TA-65 for 24 hours and isolated nuclear and mitochondrial fractions. In these fractions, we measured TERT activity as a surrogate marker for protein amount and found an increase in the mitochondrial fraction but not the nuclear fraction (Figure 6C). Along the same lines, immunostainings of endothelial cells demonstrated an increase in mitochondrial TERT levels as evident by the enhanced colocalization of TERT with the mitochondrial marker TIM23 (translocase of inner mitochondrial membrane 23) after TA-65 treatment (Figure 6D). This further supports the notion that TA-65 most likely affects mitochondrial TERT, at least in this cell type. To assess whether this increase in mitochondrial TERT is mirrored in cellular functions improved by mitochondrial TERT, we measured the migratory capacity of endothelial cells. TA-65 improved migration in a dose-dependent manner (Figure 6E and 6F). Having shown these TA-65 effects in endothelial cells, we next tested whether TA-65 also affects myofibroblast differentiation. TA-65 did not show any basal effects on fibroblasts but led to a significant increase in αSMA protein levels compared with TGFβ1 when coincubated with this cytokine (Figure 6G–6I and Figure S17). This enhanced upregulation of αSMA was comparable with the one observed in TGFβ1-treated cardiac fibroblasts from mitoTERT mice (Figure 4B–4D). Moreover, the cells coincubated with TA-65 and TGFβ1 displayed a more pronounced myofibroblast structure than fibroblasts treated with TGFβ1 alone (Figure 6G).

DISCUSSION

The protective role of TERT in the cardiovascular system has been demonstrated in several studies (for review, see Zurek et al[1]). However, after the discovery that the same protein is not only localized in the nucleus but also in the mitochondria, the tools were missing to distinguish between the functions of nuclear and mitochondrial TERT. To address this problem, we generated unique mice with TERT exclusively localized in the nucleus or the mitochondria. We have chosen to test the role of the localization of TERT in acute ischemia/reperfusion injury, because mitochondrial function is critical for cardioprotection.[27,28] Mitochondrial TERT, but not nuclear TERT, reversed the detrimental effects of TERT deficiency on infarct size and left ventricular functional recovery after myocardial ischemia/reperfusion. After myocardial infarction, myofibroblasts are needed to structurally stabilize the necrotic area,[21] and their differentiation depends on mitochondrial respiration,[24] which we now also have shown for cardiac fibroblasts. TERT deficiency impaired the differentiation of cardiac fibroblasts into myofibroblasts, whereas mitochondrial TERT stimulated this differentiation. In

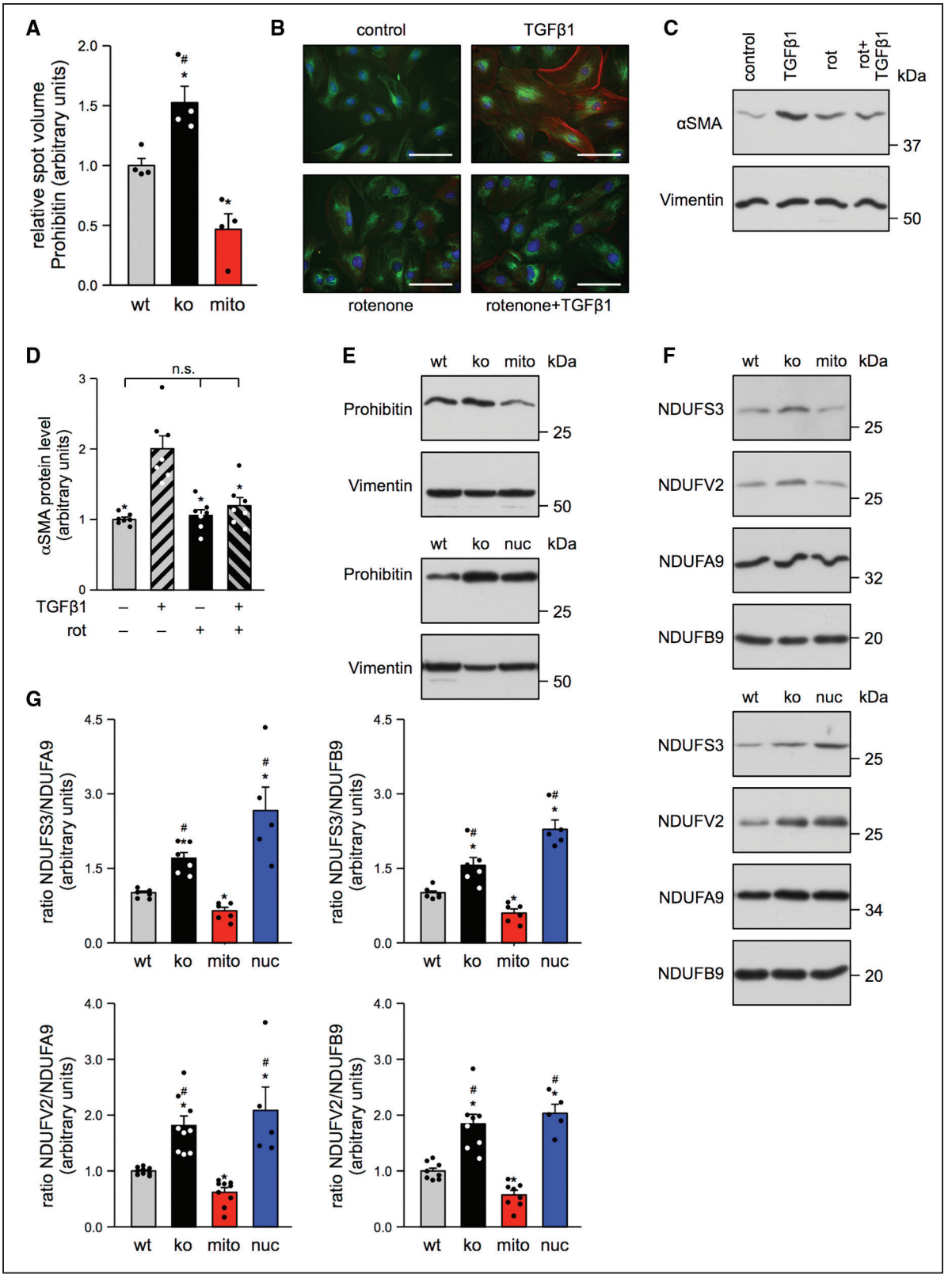

Figure 5. Mitochondrial TERT (telomerase reverse transcriptase) improves complex I subunit composition.
A, Proteins from the cardiac mitochondria used for O_2-consumption measurements in Figure 1B were resolved by 2-dimensional gel electrophoresis, and mitochondrial prohibitin levels were determined by spot volume measurement (data are mean±SEM, n=4, *P<0.05 vs wt, #P<0.05 vs mito, 1-way ANOVA with post hoc Tukey least significant difference test). **B** through **D**, Cardiac fibroblasts from wild-type mice were treated with TGFβ1 (transforming growth factor β1), 200 nmol/L rotenone (rot), or a combination of both. α smooth muscle actin (αSMA) was detected by immunostaining and immunoblot. **B**, Representative immunostainings (*Continued*)

Figure 5 Continued. (red: αSMA; green: vimentin; blue: 4′,6-diamidino-2-phenylindole [DAPI]; scale bar=100 μm). **C**, Representative immunoblot; vimentin served as loading control. **D**, Semiquantitative analysis of αSMA normalized to vimentin (data are mean±SEM, n=7, **P*<0.05 vs TGFβ1, n.s.=not significant, Kruskal-Wallis test with post hoc Mann-Whitney test). **E** through **G**, Lysates from cardiac fibroblasts from wild-type (wt), TERT-deficient (ko), mitoTERT (mito), and nucTERT (nuc) mice were used for immunoblotting. **E**, Representative immunoblots for prohibitin; vimentin served as loading control. **F** and **G**, Complex I matrix arm (NDUFS3, NDUFV2) and membrane (NDUFA9, NDUFB9) subunits were detected by immunoblot. **F**, Representative immunoblots. **G**, Semiquantitative analyses of matrix arm subunit to membrane subunit ratios (data are mean±SEM, n=5–9, **P*<0.05 vs wt, #*P*<0.05 vs mito, Kruskal-Wallis test with post hoc Mann-Whitney test).

fact, cardiac mitochondria from mitoTERT mice had increased state 4 and state 3 respiration, suggesting that mitochondrial TERT not only improved mitochondrial function in cardiomyocytes but also in fibroblasts. Along the same line, mitochondrial function is indispensable for endothelial cell migration,[22] which in turn is needed for angiogenesis in the infarcted myocardium. Mitochondrial TERT improved vascularization in the border zone of the infarcted area and migratory capacity of endothelial cells and increased phosphorylation of eNOS on serine 1177, an indicator for activation of the enzyme, as well. The latter observation supports the notion that nonnuclear, and thus, possibly mitochondrial TERT, is critical for flow-mediated dilation.[29] Apart from and in addition to endothelial migration, proliferation of endothelial cells and fibroblasts is critical to healing of the infarcted myocardium. Injection of an adeno-associated virus serotype 9 expressing TERT increased Ki-67–positive cells after experimental myocardial infarction.[3] However, it was not clear whether nuclear or mitochondrial TERT was responsible for the proliferative effects and whether mitochondria might have also been affected in a positive way.

According to our study, it is now indisputable that the major 3 cell types of the heart, cardiomyocytes, fibroblasts, and endothelial cells, require intact mitochondria for proper functionality in the case of injury. Increased mitochondrial TERT enhances mitochondrial functionality in all 3 cell types by improving complex I activity of the respiratory chain. Mechanistically, mitochondrial TERT prevents excessive accumulation of prohibitin and a shift in the ratio between matrix arm and membrane subunits of complex I. This improved subunit composition of complex I explains the enhanced state 4 and state 3 respiration observed in heart mitochondria of mitoTERT mice. This is in accordance with findings of Miwa et al[23] who demonstrated in several aging models that the reduced functionality of mitochondria during the process of aging is attributable to excessive prohibitin and disturbance of the balance between matrix arm and membrane proteins, leading to reduced complex I activity and increased ROS formation. Moreover, it has also been shown that mitochondrial TERT and not nuclear TERT protected cancer cells from damage by reducing ROS.[8] Of note, the mortality within the first 2 days after myocardial ischemia/reperfusion was higher in nucTERT than in TERT-deficient animals. On the basis of our data, it is most likely that enhanced ROS formation, and potentially ROS sensitivity, in nucTERT mice may contribute to this effect, because we observed trends in (1) even further elevated levels of complex I matrix arm subunits in the nucTERT mice compared with TERT-deficient animals (ratio S3/A9, *P*=0.111 and ratio S3/B9, *P*=0.09) and (2) increased ROS-mediated apoptosis (48-hour H_2O_2 treatment empty vector versus nucTERT, *P*=0.072). In combination with the reduced mitochondrial functionality, this could be detrimental in the case of an insult. To what extent this mediates arrhythmias, a frequent complication in humans, needs to be further investigated.

Aging is a major risk factor for the development of cardiovascular diseases. Furthermore, ROS levels increase during the aging process, and we have previously shown that oxidative stress leads to a downregulation of mitochondrial TERT.[7] Thus, it is tempting to speculate that the loss of mitochondrial functionality in the aging heart is in part attributable to an increase in prohibitin levels as a consequence of the loss of mitochondrial TERT.

Using our newly created mitoTERT mice, we have clearly demonstrated cardioprotective functions for mitochondrial TERT. In these mice, TERT expression is higher than in wild-type animals and, moreover, all the TERT protein is localized in the mitochondria. This might explain that the outcomes after myocardial infarction are improved even when compared with wild-type mice. Conversely, these results suggest that increasing mitochondrial TERT might be beneficial and, thus, seems to be a reasonable approach to develop new therapeutic concepts in acute myocardial infarction and ischemic conditioning.[30] This view is strongly supported by our observation that RIPC, a cardioprotective maneuver, elevates the levels of TERT in mitochondria of right atrial tissue of patients undergoing coronary artery bypass grafting surgery; however, a causal role for mitochondrial TERT in the protection by RIPC in humans remains to be proven. The commercially available telomerase activator TA-65 could provide another, more pharmacological therapeutic option. This compound has been given over a 1-year period to healthy human subjects and did not show any adverse effects in estimated 7000 person-years of use.[26,31,32] Our data presented here provide the first evidence for the notion that TA-65 could be of potential interest as a therapeutic component in ischemia/reperfusion injury of the heart, because it elevated mitochondrial rather than nuclear TERT and improved endothelial functionality and the ability of cardiac fibroblasts to differentiate into myofibroblasts. In this regard, the results from the TACTIC trial (Telomerase Activator to Reverse Immunosenescence in Acute Coronary Syn-

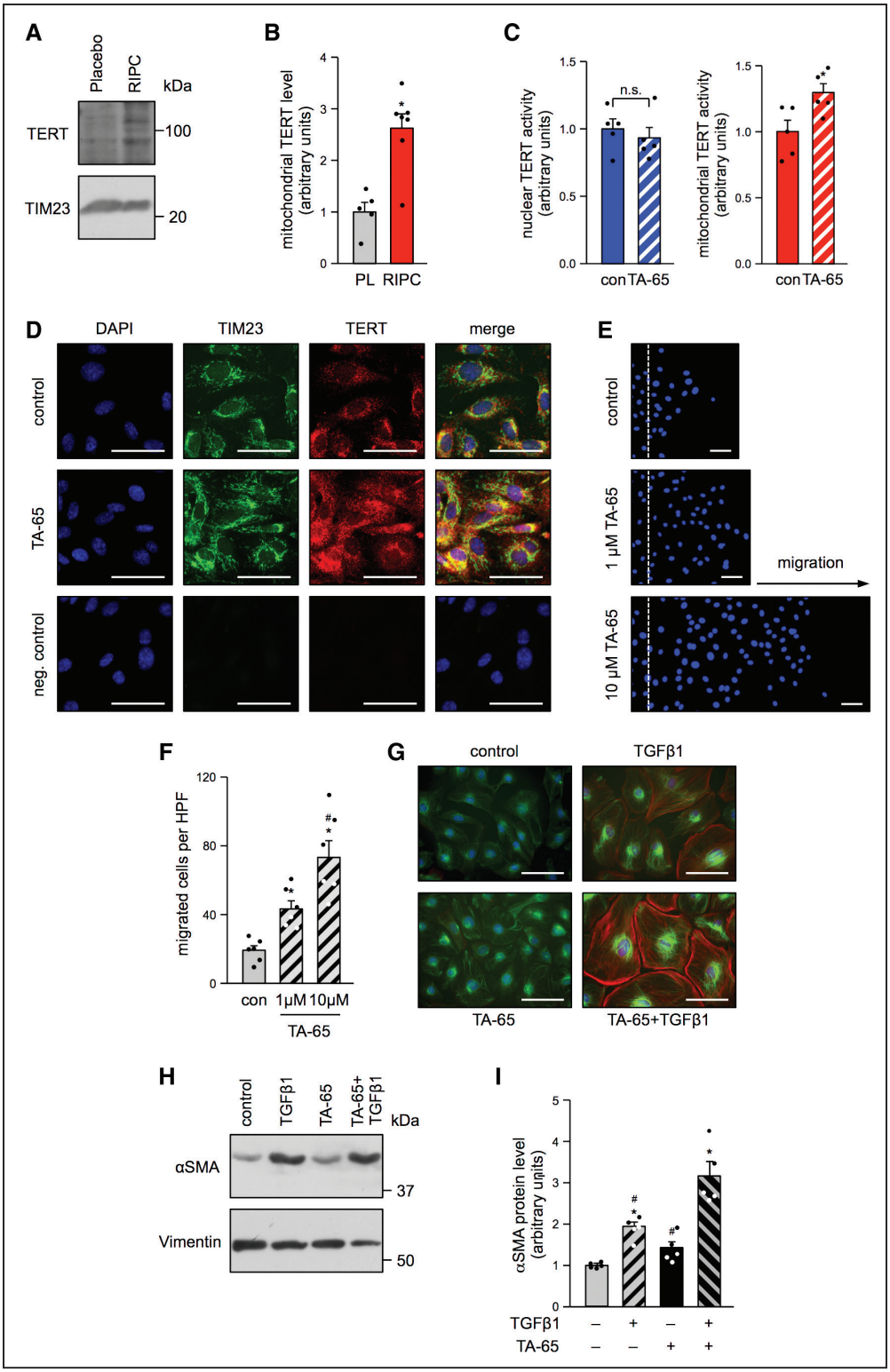

Figure 6. Remote ischemic preconditioning and the telomerase activator TA-65 increase TERT (telomerase reverse transcriptase) in the mitochondria.

A and **B**, Mitochondria were isolated from the right atrial tissue of patients undergoing coronary artery bypass grafting without (Placebo, PL) and with remote ischemic preconditioning (RIPC). Mitochondrial TERT was detected by immunoblot; TIM23 (translocase of inner mitochondrial membrane 23) served as loading control. **A**, Representative immunoblots. **B**, Semiquantitative analysis of TERT normalized to TIM23 (data are mean±SEM, n=5–7, **P*<0.05 vs PL, 2-sided unpaired Student *t* test). **C** through **F**, Human primary endothelial cells were treated for 24 hours with 10 µmol/L TA-65 or dimethyl sulfoxide as solvent control (con). **C**, TERT activity was determined in nuclear and mitochondrial fractions (data are mean±SEM, n=5, **P*<0.05 vs control, 2-sided unpaired Student *t* test). **D**, Cells were fixed and stained with antibodies directed against TIM23 (green) and TERT (red) and appropriate fluorescence-labeled secondary antibodies; (*Continued*)

Figure 6 Continued. nuclei were counterstained with 4′,6-diamidino-2-phenylindole (DAPI; blue). In the negative control, the primary antibodies were omitted; the merge is an overlay of all fluorescence channels. **E** and **F**, Migratory capacity was measured in a scratch-wound assay with TA-65 concentrations as indicated. **E**, Representative DAPI staining (scale bar=100 µm). **F**, Migrated cells per high-power field (HPF; data are mean±SEM, n=6, **P*<0.05 vs control, #*P*<0.05 vs 1 µmol/L, 1-way ANOVA with post hoc Tukey least significant difference test). **G** through **I**, Cardiac fibroblasts from wild-type mice were treated with TGFβ1 (transforming growth factor β1), 1 µmol/L TA-65, or a combination of both. α smooth muscle actin (αSMA) was detected by immunostaining and immunoblot. **G**, Representative immunostainings (red: αSMA; green: vimentin; blue: DAPI). **H**, Representative immunoblots; vimentin served as loading control. **I**, Semiquantitative analysis of αSMA normalized to vimentin (data are mean±SEM, n=5, **P*<0.05 vs control, #*P*<0.05 vs TA-65+TGFβ1, 1-way ANOVA with post hoc Tukey least significant difference test).

drome), in which TA-65 is used in patients with acute coronary syndrome (European Union Clinical Trials Register 2017-002876-26),[33] will be of great interest because it will reveal information about potential protective effects of this plant compound in humans.

Aside from its cardioprotective role, a concern relates to the potential tumor development with increased TERT. In fact, nearly all tumors are TERT positive, most likely because of the ability of nuclear TERT to promote cell proliferation by its canonical function of preventing telomere erosion and thus providing tumor cells with the ability to evade senescence. However, increasing mitochondrial TERT does not necessarily seem to result in tumor induction, because the mitoTERT mice are phenotypically normal and do not show obvious signs of hyperproliferative diseases, at least during the first 9 months of their life.

In conclusion, increased mitochondrial TERT exerts cardioprotection in mice and is associated with cardioprotection in patients. Mitochondrial function, which is enhanced by mitochondrial TERT, is critical for cardiomyocytes, fibroblasts, and endothelial cells to support their functions in acute myocardial ischemia/reperfusion.

Mechanistically, we demonstrated that mitochondrial TERT, but not nuclear TERT, improves complex I activity by balancing the ratio of matrix arm to membrane subunits of complex I of the mitochondrial electron transport chain, which is required for its proper functionality. Future studies aimed at deciphering the underlying molecular mechanisms should reveal details of how mitochondrial TERT affects the levels of prohibitin and complex I components and thereby improves mitochondrial respiration. Because of the striking similarities observed in whole hearts and cardiac fibroblasts, such mechanistic studies could be performed in these isolated cells from the different mouse genotypes used here, because they are amenable to genetic and pharmacological manipulations.

Last, an increase in mitochondrial TERT levels could be a novel approach for cardioprotective therapy, which could possibly be implemented by the intake of TA-65.

ARTICLE INFORMATION

Received October 2, 2020; accepted October 1, 2021.

Affiliations

Environmentally-induced Cardiovascular Degeneration, Clinical Chemistry and Laboratory Diagnostics (N.A.-A., P.J., C.G., M.Z., J.R., N.D.-R., J.G., F.v.A., O.E., J.A., J.H.), Institute for Cardiovascular Physiology (A.H., A.G.), Institute for Pharmacology and Clinical Pharmacology (F.B., M.G.), Medical Faculty, University Hospital and Heinrich-Heine University, Düsseldorf, Germany. IUF-Leibniz Research Institute for Environmental Medicine, Düsseldorf, Germany (C.G., N.D.-R., S.M., J.G., F.v.A., O.E., K.U., J.A.). Department of Thoracic and Cardiovascular Surgery, West German Heart Center, University of Duisburg-Essen, Essen, Germany (M.T., M.K.). Institute for Pathophysiology, West German Heart and Vascular Center, University Hospital Essen, University of Duisburg-Essen, Germany (N.G., P.K., G.H.).

Sources of Funding

This work was supported by grants from the Deutsche Forschungsgemeinschaft: CRC1116 A04 (to Drs Haendeler and Altschmied), B10 (to Dr Grandoch), A06 (to Dr Gödecke), B08 (to Drs Heusch and Kleinbongard); AL288/5-1, IRTG1902 P1 (to Dr Altschmied); IRTG1902 P2, HA2868/10-1, 10-2, HA2868/11-1, HA2868/14-1 (to Dr Haendeler). M. Zurek, J. Rosen, and J. Greulich held IRTG1902 fellowships. TA-65 was from T.A. Sciences Inc.

Disclosures

None.

Supplemental Material

Supplemental Methods
Table S1
Figures S1–S17
References 34–43

REFERENCES

1. Zurek M, Altschmied J, Kohlgrüber S, Ale-Agha N, Haendeler J. Role of telomerase in the cardiovascular system. *Genes (Basel)*. 2016;7:E29. doi: 10.3390/genes7060029
2. Oh H, Taffet GE, Youker KA, Entman ML, Overbeek PA, Michael LH, Schneider MD. Telomerase reverse transcriptase promotes cardiac muscle cell proliferation, hypertrophy, and survival. *Proc Natl Acad Sci USA*. 2001;98:10308–10313. doi: 10.1073/pnas.191169098
3. Bär C, Bernardes de Jesus B, Serrano R, Tejera A, Ayuso E, Jimenez V, Formentini I, Bobadilla M, Mizrahi J, de Martino A, et al. Telomerase expression confers cardioprotection in the adult mouse heart after acute myocardial infarction. *Nat Commun*. 2014;5:5863. doi: 10.1038/ncomms6863
4. Haendeler J, Dröse S, Büchner N, Jakob S, Altschmied J, Goy C, Spyridopoulos I, Zeiher AM, Brandt U, Dimmeler S. Mitochondrial telomerase reverse transcriptase binds to and protects mitochondrial DNA and function from damage. *Arterioscler Thromb Vasc Biol*. 2009;29:929–935. doi: 10.1161/ATVBAHA.109.185546
5. Ahmed S, Passos JF, Birket MJ, Beckmann T, Brings S, Peters H, Birch-Machin MA, von Zglinicki T, Saretzki G. Telomerase does not counteract telomere shortening but protects mitochondrial function under oxidative stress. *J Cell Sci*. 2008;121(pt 7):1046–1053. doi: 10.1242/jcs.019372
6. Sharma NK, Reyes A, Green P, Caron MJ, Bonini MG, Gordon DM, Holt IJ, Santos JH. Human telomerase acts as a hTR-independent reverse transcriptase in mitochondria. *Nucleic Acids Res*. 2012;40:712–725. doi: 10.1093/nar/gkr758
7. Büchner N, Zschauer TC, Lukosz M, Altschmied J, Haendeler J. Down-regulation of mitochondrial telomerase reverse transcriptase induced by H_2O_2 is Src kinase dependent. *Exp Gerontol*. 2010;45:558–562. doi: 10.1016/j.exger.2010.03.003
8. Singhapol C, Pal D, Czapiewski R, Porika M, Nelson G, Saretzki GC. Mitochondrial telomerase protects cancer cells from nuclear DNA damage and apoptosis. *PLoS One*. 2013;8:e52989. doi: 10.1371/journal.pone.0052989
9. Heusch G. Myocardial ischaemia-reperfusion injury and cardioprotection in perspective. *Nat Rev Cardiol*. 2020;17:773–789. doi: 10.1038/s41569-020-0403-y

10. Boengler K, Lochnit G, Schulz R. Mitochondria "THE" target of myocardial conditioning. *Am J Physiol Heart Circ Physiol.* 2018;315:H1215–H1231. doi: 10.1152/ajpheart.00124.2018
11. Kleinbongard P, Gedik N, Kirca M, Stoian L, Frey U, Zandi A, Thielmann M, Jakob H, Peters J, Kamler M, et al. Mitochondrial and contractile function of human right atrial tissue in response to remote ischemic conditioning. *J Am Heart Assoc.* 2018;7:e009540. doi: 10.1161/JAHA.118.009540
12. Chiang YJ, Hemann MT, Hathcock KS, Tessarollo L, Feigenbaum L, Hahn WC, Hodes RJ. Expression of telomerase RNA template, but not telomerase reverse transcriptase, is limiting for telomere length maintenance in vivo. *Mol Cell Biol.* 2004;24:7024–7031. doi: 10.1128/MCB.24.16.7024-7031.2004
13. Huang TT, Naeemuddin M, Elchuri S, Yamaguchi M, Kozy HM, Carlson EJ, Epstein CJ. Genetic modifiers of the phenotype of mice deficient in mitochondrial superoxide dismutase. *Hum Mol Genet.* 2006;15:1187–1194. doi: 10.1093/hmg/ddl034
14. Soriano P. Generalized lacZ expression with the ROSA26 Cre reporter strain. *Nat Genet.* 1999;21:70–71. doi: 10.1038/5007
15. Heinen A, Raupach A, Behmenburg F, Hölscher N, Flögel U, Kelm M, Kaisers W, Nederlof R, Huhn R, Gödecke A. Echocardiographic analysis of cardiac function after infarction in mice: validation of single-plane long-axis view measurements and the bi-plane Simpson method. *Ultrasound Med Biol.* 2018;44:1544–1555. doi: 10.1016/j.ultrasmedbio.2018.03.020
16. Gorressen S, Stern M, van de Sandt AM, Cortese-Krott MM, Ohlig J, Rassaf T, Gödecke A, Fischer JW, Heusch G, Merx MW, et al. Circulating NOS3 modulates left ventricular remodeling following reperfused myocardial infarction. *PLoS One.* 2015;10:e0120961. doi: 10.1371/journal.pone.0120961
17. Ale-Agha N, Goy C, Jakobs P, Spyridopoulos I, Gonnissen S, Dyballa-Rukes N, Aufenvenne K, von Ameln F, Zurek M, Spannbrucker T, et al. CDKN1B/p27 is localized in mitochondria and improves respiration-dependent processes in the cardiovascular system-new mode of action for caffeine. *PLoS Biol.* 2018;16:e2004408. doi: 10.1371/journal.pbio.2004408
18. Claycomb WC, Lanson NA Jr, Stallworth BS, Egeland DB, Delcarpio JB, Bahinski A, Izzo NJ Jr. HL-1 cells: a cardiac muscle cell line that contracts and retains phenotypic characteristics of the adult cardiomyocyte. *Proc Natl Acad Sci U S A.* 1998;95:2979–2984. doi: 10.1073/pnas.95.6.2979
19. Wan T, Weir EJ, Johnson M, Korolchuk VI, Saretzki GC. Increased telomerase improves motor function and alpha-synuclein pathology in a transgenic mouse model of Parkinson's disease associated with enhanced autophagy. *Prog Neurobiol.* 2021;199:101953. doi: 10.1016/j.pneurobio.2020.101953
20. Ronchi JA, Figueira TR, Ravagnani FG, Oliveira HC, Vercesi AE, Castilho RF. A spontaneous mutation in the nicotinamide nucleotide transhydrogenase gene of C57BL/6J mice results in mitochondrial redox abnormalities. *Free Radic Biol Med.* 2013;63:446–456. doi: 10.1016/j.freeradbiomed.2013.05.049
21. Fu X, Khalil H, Kanisicak O, Boyer JG, Vagnozzi RJ, Maliken BD, Sargent MA, Prasad V, Valiente-Alandi I, Blaxall BC, et al. Specialized fibroblast differentiated states underlie scar formation in the infarcted mouse heart. *J Clin Invest.* 2018;128:2127–2143. doi: 10.1172/JCI98215
22. Spyridopoulos I, Fichtlscherer S, Popp R, Toennes SW, Fisslthaler B, Trepels T, Zernecke A, Liehn EA, Weber C, Zeiher AM, et al. Caffeine enhances endothelial repair by an AMPK-dependent mechanism. *Arterioscler Thromb Vasc Biol.* 2008;28:1967–1974. doi: 10.1161/ATVBAHA.108.174060
23. Miwa S, Jow H, Baty K, Johnson A, Czapiewski R, Saretzki G, Treumann A, von Zglinicki T. Low abundance of the matrix arm of complex I in mitochondria predicts longevity in mice. *Nat Commun.* 2014;5:3837. doi: 10.1038/ncomms4837
24. Negmadjanov U, Godic Z, Rizvi F, Emelyanova L, Ross G, Richards J, Holmuhamedov EL, Jahangir A. TGF-β1-mediated differentiation of fibroblasts is associated with increased mitochondrial content and cellular respiration. *PLoS One.* 2015;10:e0123046. doi: 10.1371/journal.pone.0123046
25. Doll S, Dreßen M, Geyer PE, Itzhak DN, Braun C, Doppler SA, Meier F, Deutsch MA, Lahm H, Lange R, et al. Region and cell-type resolved quantitative proteomic map of the human heart. *Nat Commun.* 2017;8:1469. doi: 10.1038/s41467-017-01747-2
26. Harley CB, Liu W, Flom PL, Raffaele JM. A natural product telomerase activator as part of a health maintenance program: metabolic and cardiovascular response. *Rejuvenation Res.* 2013;16:386–395. doi: 10.1089/rej.2013.1430
27. Siasos G, Tsigkou V, Kosmopoulos M, Theodosiadis D, Simantiris S, Tagkou NM, Tsimpiktsioglou A, Stampouloglou PK, Oikonomou E, Mourouzis K, et al. Mitochondria and cardiovascular diseases-from pathophysiology to treatment. *Ann Transl Med.* 2018;6:256. doi: 10.21037/atm.2018.06.21
28. Heusch G. Molecular basis of cardioprotection: signal transduction in ischemic pre-, post-, and remote conditioning. *Circ Res.* 2015;116:674–699. doi: 10.1161/CIRCRESAHA.116.305348
29. Beyer AM, Freed JK, Durand MJ, Riedel M, Ait-Aissa K, Green P, Hockenberry JC, Morgan RG, Donato AJ, Peleg R, et al. Critical role for telomerase in the mechanism of flow-mediated dilation in the human microcirculation. *Circ Res.Circ Res.* 2016;118:856–866. doi: 10.1161/CIRCRESAHA.115.307918
30. Hausenloy DJ, Barrabes JA, Bøtker HE, Davidson SM, Di Lisa F, Downey J, Engstrom T, Ferdinandy P, Carbrera-Fuentes HA, Heusch G, et al. Ischaemic conditioning and targeting reperfusion injury: a 30 year voyage of discovery. *Basic Res Cardiol.* 2016;111:70. doi: 10.1007/s00395-016-0588-8
31. Harley CB, Liu W, Blasco M, Vera E, Andrews WH, Briggs LA, Raffaele JM. A natural product telomerase activator as part of a health maintenance program. *Rejuvenation Res.* 2011;14:45–56. doi: 10.1089/rej.2010.1085
32. Salvador L, Singaravelu G, Harley CB, Flom P, Suram A, Raffaele JM. A natural product telomerase activator lengthens telomeres in humans: a randomized, double blind, and placebo controlled study. *Rejuvenation Res.* 2016;19:478–484. doi: 10.1089/rej.2015.1793
33. Maier R, Bawamia B, Bennaceur K, Dunn S, Marsay L, Amoah R, Kasim A, Filby A, Austin D, Hancock H, et al. Telomerase activation to reverse immunosenescence in elderly patients with acute coronary syndrome: protocol for a randomized pilot trial. *JMIR Res Protoc.* 2020;9:e19456. doi: 10.2196/19456
34. Rizzuto R, Simpson AW, Brini M, Pozzan T. Rapid changes of mitochondrial Ca2+ revealed by specifically targeted recombinant aequorin. *Nature.* 1992;358:325–327. doi: 10.1038/358325a0
35. Fischer-Fantuzzi L, Vesco C. Cell-dependent efficiency of reiterated nuclear signals in a mutant simian virus 40 oncoprotein targeted to the nucleus. *Mol Cell Biol.* 1988;8:5495–5503. doi: 10.1128/mcb.8.12.5495-5503.1988
36. Yuan X, Ishibashi S, Hatakeyama S, Saito M, Nakayama J, Nikaido R, Haruyama T, Watanabe Y, Iwata H, Iida M, et al. Presence of telomeric G-strand tails in the telomerase catalytic subunit TERT knockout mice. *Genes Cells.* 1999;4:563–572. doi: 10.1046/j.1365-2443.1999.00284.x
37. Grandoch M, Feldmann K, Göthert JR, Dick LS, Homann S, Klatt C, Bayer JK, Waldheim JN, Rabausch B, Nagy N, et al. Deficiency in lymphotoxin β receptor protects from atherosclerosis in apoE-deficient mice. *Circ Res.* 2015;116:e57–e68. doi: 10.1161/CIRCRESAHA.116.305723
38. Bøtker HE, Hausenloy D, Andreadou I, Antonucci S, Boengler K, Davidson SM, Deshwal S, Devaux Y, Di Lisa F, Di Sante M, et al. Practical guidelines for rigor and reproducibility in preclinical and clinical studies on cardioprotection. *Basic Res Cardiol.* 2018;113:39. doi: 10.1007/s00395-018-0696-8
39. Schneider CA, Rasband WS, Eliceiri KW. NIH Image to ImageJ: 25 years of image analysis. *Nat Methods.* 2012;9:671–675. doi: 10.1038/nmeth.2089
40. Dyballa N, Metzger S. Fast and sensitive colloidal coomassie G-250 staining for proteins in polyacrylamide gels. *J Vis Exp.* 2009;3:1431 doi: 10.3791/1431
41. Dyballa-Rukes N, Schuh C, Vogt H, Toma O, Schlack WS, Weber NC, Metzger S. In vivo desflurane preconditioning evokes dynamic alterations of metabolic proteins in the heart–proteomic insights strengthen the link between bioenergetics and cardioprotection. *Cell Physiol Biochem.* 2014;33:967–981. doi: 10.1159/000358668
42. Callicott RJ, Womack JE. Real-time PCR assay for measurement of mouse telomeres. *Comp Med.* 2006;56:17–22.
43. Faul F, Erdfelder E, Lang AG, Buchner A. G*Power 3: a flexible statistical power analysis program for the social, behavioral, and biomedical sciences. *Behav Res Methods.* 2007;39:175–191. doi: 10.3758/bf03193146

SUPPLEMENTAL MATERIAL

Methods

Generation of mitoTERT and nucTERT mice

For organelle-specific targeting the human TERT coding sequence was fused to an N-terminal mitochondrial targeting sequence from the subunit VIII of human cytochrome c oxidase[34] or a C-terminal trimeric nuclear localization sequence from the simian virus 40 large T antigen[35]. In addition, both constructs contained a C-terminal myc-epitope tag. To ensure ubiquitous, low level expression, the coding sequences for these proteins were fused to a splice acceptor and placed under the transcriptional control of the ROSA26 promoter[14] by homologous recombination in mouse embryonic stem cells. Upstream of the mito/nucTERT cassettes the targeting constructs contained a stop cassette with the neomycin resistance gene preceded by a splice acceptor and flanked by two loxP sites. The neomycin resistance gene also served as a selective marker for positive selection of embryonic stem cells. As a negative selection marker the herpes simplex virus Thymidine Kinase gene was used, which was placed outside the homology arms used for homologous recombination. Gene targeting was performed in C57BL/6N Tac embryonic stem cells and cell clones were selected with G418 and Gancyclovir. Homologous recombination was validated by southern blot analysis and two ES cell clones each for mitoTERT and nucTERT were used for the generation of chimeric animals. Four mitoTERT and two nucTERT mice with >50% chimerism were bred with B6.ROSA Cre-deleter mice to generate constitutive mitoTERT and nucTERT knockin founders, which were subsequently crossed with C57BL/6N Tac individuals to obtain stable mouse lines carrying a single mitoTERT or nucTERT allele.

Animals carrying a single mitoTERT or nucTERT allele were mated with heterozygous TERT-deficient C57BL/6N mice to generate double-heterozygous offspring. These double-heterozygous mice were intercrossed to obtain animals carrying the mitoTERT or nucTERT

allele on an otherwise TERT-deficient genetic background as well as wildtype and TERT-deficient littermates (supplemental Figure IA). To generate more experimental mice, an additional, alternative breeding strategy was chosen, which instead of littermates yields genetically closely related experimental animals, i.e. cousins (supplemental Figure IB). This strategy is based on the use of siblings from the double heterozygous intercrosses as founders for two parallel breeding lines each for mitoTERT and nucTERT, respectively. In one of these lines both founders are homozygous for the mitoTERT or nucTERT allele and heterozygous for TERT-deficiency. This intercross yields progeny, of which 25% is deficient for endogenous TERT and positive for mitoTERT or nucTERT. The founders of the second, parallel breeding line do not carry the mitoTERT or nucTERT knockin in the ROSA26 locus, but are also heterozygous for TERT-deficiency. This cross yields wildtype and TERT-deficient mice, both with a frequency of 25%. These breeding strategies were chosen to avoid telomere erosion as a result of TERT-deficiency, which is not detectable in first generation TERT knockout mice[36]. Moreover, first generation TERT-deficient mice do not display any phenotypical differences or differences in cardiac functions compared to wildtype littermates[36].

Genotyping of mice

DNA was isolated from tail clips or ear punches using the DirectPCR Lysis Reagent (Mouse Tail) (Viagen Biotech, Los Angeles, USA) according to manufacturer's specifications. Genotyping was performed with multiplex PCRs and the reaction products were resolved on agarose gels. To identify the NNT mutation[13] amplifications were performed for 35 cycles with an annealing temperature of 55°C and an extension time of 60 seconds using the primers Exon6_L1, Exon6_L4 and Exon12_L1; the wild-type allele yields a product of 1011 bp, the allele carrying the deletion a product of 547 bp. The primers oIMR3739, oIMR3740 and oIMR3741 were used to screen for TERT-deficiency. The wildtype allele yields a fragment of approximately 150 bp, the knockout allele a fragment of approximately 420 bp. The presence of mitoTERT or nucTERT was detected with the primer combination

ROSA26 for1, ROSA26 rev1, hTERT Ex15 for1 and myc-tag rev2, which yields a 214 bp fragment for mitoTERT and 298 bp for nucTERT, while the unaltered ROSA26 locus produces a fragment of 503 bp. The TERT as well as the mitoTERT and nucTERT PCRs were performed for 35 cycles with an annealing temperature of 60°C and an extension time of 30 seconds. The primer sequences are as follows:

Exon6_L1	5'-CAATTCTGCCAACAACTGGA-3'
Exon6_L4	5'-TCCCCTCCCTTCCATTTAGT-3'
Exon12_L1	5'-GTAGGGCCAACTGTTTCTGC-3'
oIMR3739	5'-CCCCAGGCGCCGCACAAAGG-3'
oIMR3740	5'-GGTCCTGGCTGTTTTCTAAG-3'
oIMR3741	5'-CTGGATTCATCGACTGTGGC-3'
ROSA26 for1	5'-TGCTGCCTCCTGGCTTCTGA-3'
ROSA26 rev1	5'-GATAAGGCTGCAGAAGGAGCGG-3'
hTERT Ex15 for1	5'-GCCACCAAGCATTCCTGCTC-3'
myc-tag rev2	5'-TCCTCTTCTGAGATGAGTTTTTGTTC-3'

Preparation of mouse heart mitochondria

Mice were sacrificed by exsanguination under deep anesthesia using ketamine/xylazine (12/1.6 mg/kg body weight)**.** Hearts were explanted after perfusion with phosphate-buffered saline (PBS). After removal of residual PBS on Whatman paper (Merck KGaA, Darmstadt, Germany), hearts were cut into 1-2 mm pieces. Pieces were collected in 10 ml washing buffer (0.3 M sucrose, 10 mM HEPES pH 7.2, 0.2 mM EDTA), 250 µl Trypsin (bovine pancreas type I, Sigma-Aldrich/Merck KGaA, Darmstadt, Germany) of a 2.5 mg/ml stock solution were added, and minced tissue was further homogenized with a Ultra Turrax (3 x 5 seconds) (IKA-TIO Basic, Staufen, Germany). After constant stirring for 15 min, 5 ml of mitochondria isolation buffer (20 mM HEPES, pH 7.4, 10 mM KCl, 5 mM $MgCl_2$, 1 mM EDTA, 1 mM EGTA, 250 mM sucrose) containing 3.25 mg Trypsin inhibitor (*Glycine max*, Sigma-Aldrich/Merck KGaA, Darmstadt, Germany) were added. Samples were centrifuged for 10

min at 900 g and 4°C. The resulting supernatant was transferred to a fresh Eppendorf tube and centrifuged again for 15 min at 10.000 g and 4°C. After centrifugation, the supernatant was discarded, and the pellet was rinsed twice with fresh mitochondrial isolation buffer to remove the fluffy white outer rim layer. The resulting brown pellet containing intact mitochondria was resuspended in mitochondria isolation buffer. Mitochondria were used for Oxygraph measurements.

Preparation of nuclear fractions from mouse hearts and isolated heart fibroblasts

For the heart fractionation, the resulting pellets - after trypsin digestion in mitochondrial isolation buffer (see above) - were lysed and fractionated using the NE-PER^{TM} Nuclear and Cytoplasmic Extraction Reagent according to manufacturer's protocol (Life Technologies, Darmstadt, Germany). For heart fibroblasts, cells were scraped off the plates. Samples were centrifuged for 10 min at 900 g and 4°C. Resulting pellets were lysed and fractionated using the NE-PER^{TM} Nuclear and Cytoplasmic Extraction Reagent according to manufacturer's protocol (Life Technologies, Darmstadt, Germany).

Respiration of mouse heart mitochondria

The rate of mitochondrial respiration was monitored at 25°C using an Oxygraph-*2k* system (Oroboros, Innsbruck, Austria) equipped with two chambers and DatLab software [4]. In detail, 200-300 µg mitochondria were added to 2 ml of a buffer containing 200 mM sucrose, 10 mM potassium phosphate, 10 mM Tris-HCl, 10 mM $MgSO_4$, and 2 mM EDTA, pH 7.0, and respiration was measured. Oxygen consumption was measured after the addition of the NADH-generating substrates malate (0.5 mM) and glutamate (0.5 mM). Then, ADP (0.15 mM) was added. To inhibit complex I activity, rotenone was added to a final concentration of 100 nM. Then, succinate (10 mM) was added, and complex II dependent respiration was determined. Finally, KCN (2 mM) was added to inhibit complex IV activity. For each preparation a second set of measurements was performed in a cross-over design, by switching the mitochondria in the electrode chambers of the Oxygraph-*2k* system.

Myocardial ischemia and reperfusion

Male mice (6-8 months) underwent 45 min of coronary occlusion followed by reperfusion. Animals were anesthetized by mask inhalation of isoflurane 2.5% (v/v) and a mixture of oxygen and room air. After endotracheal intubation, mice were connected to a rodent ventilator (MiniVent Model 845, Hugo Sachs Elektronik, March-Hugstetten, Germany) and ventilated with a volume of 200-220 µl at a rate of 140-160 strokes/min, with a mixture of two thirds air, one third oxygen and isoflurane 2.0-2.5% (v/v) (Forene®, Abbott GmbH, Germany). Then mice were placed in supine position on a heating plate to maintain body temperature at 37.5°C throughout surgery. After a left lateral thoracotomy, the pericardium was opened, a 7-0 surgical suture was passed underneath the left anterior descending coronary artery, and both ends of the applied suture were threaded through a propylene tube to form a snare. Myocardial ischemia was achieved by tightening the snare, and coronary occlusion was verified by ST-elevation on the ECG (PowerLab/8SP, ADInstruments Pty Ltd., Castle Hill, Australia). The chest wall was covered with a piece of moistened gauze to prevent desiccation. After 45 min of ischemia, reperfusion was started by opening the snare. The suture was left in the subcutaneous tissue. The chest was closed with by using 6-0 suture, and after closing the skin, anesthesia was terminated. After mice regained spontaneous breathing, they were extubated and allowed to breath 100% O_2 through the mask until they started moving.

Echocardiography

Echocardiography was performed under mask anesthesia by an inhaled mixture of 2% (v/v) isoflurane and 100% oxygen using a 30 MHz linear-array transducer with a digital ultrasound system (Vevo 2100 Imaging System, Visual Sonics, Toronto, Canada). Body temperature was kept at 37°C using a heating pad. Images were acquired from parasternal long axis view and three orthogonal short axis views (basal, mid-ventricular and apical level). Left ventricular end-diastolic volume and end-systolic volume were calculated by the bi-plane

Simpson's method from B-mode parasternal and three short axis views. Ejection fraction was calculated.

Flow cytometry

Flow cytometry analyses of circulating immune cells in the blood were performed as described previously[37]. Briefly, red blood cells were lysed using a hypotonic ammonium chloride solution and stained with the following antibodies: CD11b-PE (M1/70; BD Pharmingen (BD Bioscience)), CD11c-PECy7 (N418), CD45-AlexaFluor®700 (30-F11), Ly-6C-AlexaFluor®488 (HK1.4), and Ly-6G-PacificBlue™ (1A8) all purchased from Biolegend (San Diego, CA, USA), and CD115-APC (AFS98; eBioscience, San Diego, CA, USA). Dead cells, debris, and doublets were excluded by forward scatter and side scatter. Absolute cell concentrations were determined with Flow-Count™ Fluorospheres (Beckman Coulter Inc., Krefeld, Germany). All measurements were performed on a Gallios Flow Cytometer (Beckman Coulter Inc) and analysed using FlowJo 10.7.1 software (Becton Dickinson, Heidelberg, Germany).

Intraperitoneal glucose tolerance test (GTT)

After undergoing starvation for 6 hours, mice were injected with 1 g/kg BW glucose. Blood glucose concentration was assessed before (fasting blood glucose) and 5, 15, 30, 60 and 120 minutes post injection post injection of glucose bolus using a StatStrip Glucometer (Nova Biomedical, Waltham, MA, USA).

Infarct size

After 48 hours of reperfusion, animals were sacrificed by cervical dislocation and hearts were explanted for infarct size analysis. Infarct size and area at risk (AAR) were determined by Evans Blue (Sigma-Aldrich/Merck KGaA, Darmstadt, Germany) and 2,3,5-triphenyltetrazolium chloride (TTC) (Sigma-Aldrich/Merck KGaA, Darmstadt, Germany) staining)[38]. The removed heart with the suture left in place was perfused with ice-cold normal saline via (0.9% NaCl) to wash out the intravascular blood. Subsequently the coronary artery was re-occluded with the suture left in place and the remainder of the myocardium was

perfused through the aortic root with 0.2% Evans blue in normal saline. Intravascular Evans blue was then washed out by perfusion with normal saline. Finally, the heart was frozen, and cut into approximately 2 mm transverse slices, from apex to base. The slices were stained with 0.75% triphenyltetrazolium chloride (TTC) solution (pH 7.4) for 15 minutes at 37°C and fixed in 4% formalin solution for 2-4 hours at room temperature. Images of the sections were taken with a Leica microscope and software LAS V4,7. The Infarct size and area at risk and the left ventricle (LV) were determined by planimetry using SigmaScan Pro5 (SPSS Science Software, Chicago, USA).

Masson's trichrome, Collagen I, CD31, and myc-tag staining in heart cryosections

To analyze fibrotic tissue another subset of mice were sacrificed by cervical dislocation 7 days post MI, their hearts were explanted, embedded in OCT (Tissue-Tek, 4583) and snap frozen at -40°C in isopentane/dry ice. Heart cryosections (4µm) were stained with Masson's trichrome (Morphisto, 11092) as described previously. Briefly, sections were incubated in Bouin’s solution (Sigma-Aldrich/Merck KGaA, Darmstadt, Germany) 15 min at RT and washed 5 min under running tap water. Afterwards sections were incubated with hematoxylin (Masson, 11717) to stain the nucleus. The sections were rinsed again for 10 min with running water and stained for 2 min with acid fuchsin-ponceau solution (Goldener I, 10366). After brief rinse with aqua dest., sections were stained for 2 min with phosphomolybdic acid-Orange G solution (11195) and after brief rinse they were incubated in Lightgreen solution (Goldener III,110267) for 20 min. The sections were rinsed again with running tap water and then placed in 1% acetic acid for 1min. Sections were rinsed, dehydrated through alcohol, cleared in xylene (2 x 5 min), and mounted with Entellan (Merck Millipore, Merck KGaA, Darmstadt, Germany). Images of the sections were taken with a fluorescence microscope Keyence BZ 9000, using 4x objective and the merge function (Keyence, Neu Isenburg, Germany). Cytoplasm and muscle fibers appear red; collagen and nuclei appear light blue. Other of those sections were incubated with an Alexa-Fluor 594 conjugated antibody against αSMA (clone 1A4, Abcam, Berlin, Germany, 1:50) and an antibody against CD31 (Abcam,

Berlin, Germany, 1:50) or with an antibody against Collagen I (Sigma-Aldrich/Merck KGaA, Darmstadt, Germany, 1:100). Then an Alexa Fluor Plus 488 anti-mouse secondary antibody (Thermo Fisher Scientific, Dreieich, Germany, 1:200) or an Alexa Fluor 594 anti-rabbit secondary antibody (Thermo Fisher Scientific, Dreieich, Germany, 1:200) was used, respectively. Other of those sections were incubated with an Alexa-Fluor 594 conjugated antibody against the myc-tag (Santa Cruz Biotechnology, Heidelberg, Germany, 1:50) and an antibody against TIM23 (clone 23, BD Biosciences, Heidelberg, Germany, 1:200) at 4°C overnight and an Alexa 488 anti-mouse secondary antibody was used (Thermo Fisher Scientific, Dreieich, Germany, 1:200, 1 hour, room temperature). Nuclei were stained with DAPI. Images of the sections were taken with a fluorescence microscope using 400x magnification. CD31 positive cells per mm^2 were calculated using the software program ImageJ 1.42q[39].

Study procedure patients

Anesthesia was induced with sufentanil (1 µg/kg), etomidate (0.3 mg/kg), and rocuronium (0.6 mg/kg) and maintained with isoflurane (0.6–1.0% end-tidal) and sufentanil, as required. The RIPC protocol consisted of 3 cycles of 5-minute left upper arm ischemia (by inflation of a blood pressure cuff to 200 mm Hg)/5 min reperfusion (cuff deflated). Data were compared to placebo (cuff left deflated for 30 minutes). CABG was performed using median sternotomy, mild systemic hypothermia (>32°C), and antegrade cold crystalloid Bretschneider (Köhler Chemie GmbH, Bensheim, Germany) cardioplegia, with additional topical cooling and single aortic cross-clamping for all distal anastomoses.

Sampling of right atrial appendages

Right atrial appendages were obtained at the onset of the cardiopulmonary bypass procedure 10 to 15 minutes after the last RIPC cycle or placebo, respectively, from the cannulation site (right atrium), placed in cardioplegic buffer (mmol/L: 100 NaCl, 10 KCl, 5 $MgSO_4 \cdot 7H_2O$, 1.2 KH_2PO_4, 50 taurine, 5 MOPS, and 22 glucose) and immediately transported to the laboratory and mitochondria were isolated.

Cardiomyocyte cell line HL-1

The murine cardiomyocyte cell line HL-1[18] was a gift from W.C. Claycomb and was cultivated in Claycomb medium supplemented with 1% penicillin/streptomycin, 100 µM norepinephrine, 2 mM L-glutamine (all Sigma-Aldrich, Merck KGaA, Darmstadt, Germany) and 10% fetal bovine serum for as many passages as the cells showed contractile activity in the culture dish in a humidified incubator at 37°C in an atmosphere containing 5% CO_2.

Lentiviral production and transduction

VSV-G pseudotyped lentiviral particles were generated as described[17]. HL-1 cells were transduced with a multiplicity of infection of approximately 20. The day after transduction the cells were washed three times, the medium replaced, and cells treated with H_2O_2 for 24 h and 48 h.

Cardiac fibroblasts and induction of myofibroblast differentiation

Cardiac fibroblasts were isolated, as described previously[17]. They were cultivated in DMEM GlutaMAX™ supplemented with 1% penicillin/streptomycin (both Thermo Fisher Scientific, Dreieich, Germany) and 10% fetal bovine serum in a humidified incubator at 37°C in an atmosphere containing 5% CO_2. For the induction of myofibroblast differentiation, the cells were grown for 24h in DMEM GlutaMAX™/1% fetal bovine serum/1% penicillin/streptomycin before recombinant human transforming growth factor β 1 (TGFβ1; 2 ng/ml) (PeproTech GmbH, Hamburg, Germany) was added for another 48h.

Isolation of lung fibroblasts

Mice were sacrificed by cervical dislocation, the lungs were excised and all fat removed with a scalpel. Lungs were placed in a culture dish with room temperature Phosphate Buffered Saline (Thermo Fisher Scientific, Dreieich, Germany) supplemented with 1% penicillin/streptomycin (Thermo Fisher Scientific, Dreieich, Germany) and 2 mM $CaCl_2$ ($PBS^{(++)}$) and the blood was squeezed out with tweezers. After transfer to a new culture dish with $PBS^{(++)}$, lungs were chopped into small pieces. The pieces were distributed into two 2 ml eppendorf tubes each containing 1 ml of a freshly prepared, ice-cold collagenase solution (1

U/ml Collagenase NB 8 Broad Range (Serva, Heidelberg, Germany) in $PBS^{(++)}$, filter sterilized) and incubated for 15 minutes at 37°C with gentle mixing every 5 minutes. The cell-containing supernatants were transferred to 2 ml eppendorf tubes containing DMEM GlutaMAX™ (Thermo Fisher Scientific, Dreieich, Germany) supplemented with 20% fetal bovine serum (Thermo Fisher Scientific, Dreieich, Germany) and 1% penicillin/streptomycin to stop the collagenase reaction. After centrifugation for 5 minutes at 400 g at 4°C, the pelleted cells were resuspended in 1 ml DMEM GlutaMAX™/20% fetal bovine serum/1% penicillin/streptomycin and placed on ice. In parallel, the remainder of the lung pieces was digested again with collagenase under identical conditions. The collagenase digestions were repeated until no more pieces were visible. Finally, all cells were pooled, plated onto a 10 cm culture dish and placed in humidified tissue culture incubator at 37°C in an atmosphere containing 5% CO_2. After 2 hours all non-adherent cells were carefully aspirated off. Attached cells were washed twice with DMEM GlutaMAX™/10% fetal bovine serum/1% penicillin/streptomycin and from then on grown in this medium.

Endothelial cells

Primary human endothelial cells were obtained from Lonza (Cologne, Germany) and cultured in endothelial basal medium supplemented with 1 µg/ml hydrocortisone, 12 µg/ml bovine brain extract, 50 µg/ml gentamicin, 50 ng/ml amphotericin B, 10 ng/ml epidermal growth factor (Lonza, Cologne, Germany), and 10% fetal bovine serum until the second or third passage in a humidified incubator at 37°C in an atmosphere containing 5% CO_2.

Scratch wound assay of endothelial cells

For detection of cell migration, wounds were created by scraping confluent cell monolayers with a sterile disposable rubber policeman. Nuclei were stained with DAPI and the cells, which had invaded the wound from the trace line, were automatically counted using the particle analysis feature of ImageJ 1.42q[39] after watershed separation of overlapping nuclei using an Axiovert 100 microscope, magnification 200 (Zeiss, Jena, Germany).

Immunostaining

A direct immunostaining of αSMA and Vimentin was performed in mouse cardiac fibroblasts. Cells were fixed and permeabilized as described above. An Alexa-Fluor 594 conjugated antibody against αSMA (clone 1A4, Abcam, Berlin, Germany, 1:100) and an Alexa-Fluor 488 conjugated anti-Vimentin antibody (clone D21H3, Cell Signaling Technologies, Frankfurt, Germany, 1:100) were incubated at 4°C overnight. Mouse cardiac or lung fibroblasts isolated from mitoTERT and nucTERT mice were incubated with an Alexa-Fluor 594 conjugated antibody against the myc-tag (Santa Cruz Biotechnology, Heidelberg, Germany, 1:50) and an antibody against TIM23 (clone 23, BD Biosciences, Heidelberg, Germany, 1:200) at 4°C overnight and an Alexa 488 anti-mouse secondary antibody was used (Thermo Fisher Scientific, Dreieich, Germany, 1:200, 1 hour, room temperature). Nuclei were stained with DAPI. In addition, the mouse cardiac or lung fibroblasts isolated from mitoTERT and nucTERT mice were stained with an antibody against the myc-tag (rabbit polyclonal, ab9106, Abcam, Berlin, Germany, 1:200) and an antibody against TIM23 (clone 23, BD Biosciences, Heidelberg, Germany, 1:200) at 4°C overnight and Alexa 594 anti-rabbit secondary antibody (Thermo Fisher Scientific, Dreieich, Germany, 1:200, 1 hour, room temperature) and Alexa 488 anti-mouse secondary antibody (Thermo Fisher Scientific, Dreieich, Germany, 1:200, 1 hour, room temperature) were used. Nuclei were stained with DAPI. Fixed and permeabilized human endothelial cells were incubated with an antibody against TERT (polyclonal, 600-401-252, Rockland, Limerick, USA, 1:50) or an antibody against the myc-tag (rabbit clone 71D10, Cell Signaling Technologies, Frankfurt, Germany, 1:50) at 4°C overnight and a Rhodamine Red-X-conjugated Fab fragment anti-rabbit was used as secondary antibody (Jackson ImmunoResearch, Ely, UK, 1:300, 1 hour, room temperature). Afterwards, cells were incubated with a mouse anti-TIM23 antibody (clone 23, BD Biosciences, Heidelberg, Germany, 1:200) at 4°C overnight and an Alexa 488 anti-mouse secondary antibody was used (Thermo Fisher Scientific, Dreieich, Germany, 1:200, 1 hour, room temperature). Nuclei were stained with DAPI.

SDS-PAGE and immunoblotting

Electrophoretic separation of proteins with sodium dodecyl sulfate polyacrylamide gel electrophoresis (SDS-PAGE) and blotting onto polyvinylidene difluoride membranes was performed according to standard methods. Detection of the different proteins was performed with antibodies directed against TERT (polyclonal, 600-401-252, Rockland, Limerick, USA, 1:500), TIM23 (clone 23, BD Biosciences, Heidelberg, Germany, 1:2000), α-Tubulin (clone DM1A, Sigma Aldrich, 1:50000), myc-tag (rabbit clone 71D10 or mouse clone 9B11, Cell Signaling Technologies, Frankfurt, Germany, 1:500), Vimentin (clone EPR3776, Abcam, Berlin, Germany, 1:12000), αSMA (polyclonal, ab5694, Abcam, Berlin, Germany, 1:6000), eNOS (polyclonal, ab5589, Abcam, Berlin, Germany, 1:500), phospho-eNOS (S1177) (polyclonal, Cell Signaling Technologies, Frankfurt, Germany, 1:500), NDUFS3 (clone 3F9DD2, Abcam, Berlin, Germany, 1:500), NDUFV2 (polyclonal, 15301-1-AP, Proteintech Germany GMBH, Leon-Rot, Germany, 1:1000), NDUFA9 (clone 20C11B11B11, Abcam, Berlin, Germany, 1:1000), NDUFB9 (clone EPR15955-78, Abcam, Berlin, Germany, 1:2000), Prohibitin (polyclonal, ab28172, Abcam, Berlin, Germany, 1:4000). After protein transfer, membranes were incubated with primary antibodies overnight at 4°C before they were washed and incubated with secondary antibodies (anti-mouse IgG, HRP-linked whole antibody from sheep, NA931V, GE Healthcare Life Sciences, Freiburg, Germany, anti-rabbit IgG, HRP-linked whole antibody from donkey, NA934V, GE Healthcare Life Sciences, Freiburg, Germany) according to standard procedures. Detection was performed by enhanced chemiluminescence using the ECL reagent (GE Healthcare Life Sciences, Freiburg, Germany) and standard X-ray films. Semi-quantitative analyses were performed on scanned X-ray films using ImageJ 1.42q[39].

Two-dimensional (2D) gel electrophoresis and protein identification by mass spectrometry

Cardiac mitochondria (150 µg) were resuspended in rehydration buffer (7 M urea, 2 M thiourea, 2 % (v/v) CHAPS, 40 mM DTT and 0.2 % (v/v) Bio-Lyte 3/10 Ampholyte (BioRad, Hercules, CA, USA)) for at least 2 hours to ensure complete solubilization and denaturation.

Protein samples were applied to pH 3-10NL ReadyStrip IPG strips (BioRad) overnight by in-gel rehydration. Isoelectric focusing was performed using the PROTEAN IEF Cell (BioRad) with a maximum current of 50 µA per strip at 20 °C using a program of progressively increasing voltage (300 V for 0:30 h (linear ramp), 300 V for 3:30 h (rapid ramp), 1000 V for 1:30 h (slow ramp), 5000 V for 1:30 h (linear ramp), 5000 V for 1:30 h (rapid ramp)). Every focused IPG strip was stored at -20 °C until equilibration and application to SDS-PAGE. The IPG strips were subjected to reduction and alkylation using 1 % (w/v) DTT and 2.5 % (w/v) iodoacetamide in 2.5 ml equilibration solution (6 M urea, 50 mM Tris-HCl (pH 8.8), 30 % (v/v) glycerol and 2 % (w/v) SDS) per strip. Following equilibration, the IPG strips were rinsed with Milli-Q water, and finally dipped in electrophoresis buffer (25 mM Tris base, 192 mM glycine, 0.1% (w/v) SDS in Milli-Q water). For second dimension separation, the Mini-PROTEAN Tetra system, (BioRad) was used. The equilibrated IPG strips were placed upright on the top of self-made 11 % SDS-PAGE resolving gels and covered with heated (75°C) agarose-sealing solution (0.5% (w/v) agarose in electrophoresis buffer). Proteins were separated for ~ 2.5 hours, starting at 50 V for 30 minutes followed by 150 V until the dye front reached the bottom of the gel. Afterwards, the colloidal Coomassie G-250 staining protocol was used to visualize the proteins[40]. For comparative proteome analyses, the Coomassie stained gels were digitized using a flatbed image scanner with a resolution of 600 dpi. Image analysis was performed with the Delta2D software (version 4.3, Decodon, Greifswald. Germany). Protein spots with normalized volume ratios between 0.5 and 2 among the genotypes were calculated by mean±RSD, and variations in protein expression were considered significant by statistical analysis using Student's t-Test (p-values <0.05).

Protein spots of interest were manually excised from Coomassie stained gels and completely destained with 40 % (v/v) ethanol and 2 % (v/v) phosphoric acid. In-gel tryptic digestion was carried out using 0.1 µg/µl sequencing grade modified trypsin (Promega, Madison, USA) in 25 mM ammonium bicarbonate (pH 8.0) for 12 - 16 hours at 37°C under continuous agitation like described before[41]. The extracted peptides were dried in a vacuum centrifuge (Eppendorf, Hamburg, Germany) and stored at -20°C until analysis by mass spectrometry

(MS). Prior to MS analyses, the tryptic peptides were desalted using C18 StageTips (Thermo Fisher Scientific, Dreieich, Germany) and eluted in 60 % (v/v) methanol and 5 % (v/v) formic acid. Differentially expressed proteins were analyzed on an electrospray hybrid mass spectrometer (Q-STAR XL, Applied Biosystems, Darmstadt, Germany) equipped with an offline nanospray source (Proxeon, Odense, Denmark). Full MS scans from 350 to 1500 m/z were recorded and at least five peptides per sample were further fragmented by collision-induced dissociation using Analyst QS software (version 1.1, Applied Biosystems). Subsequent MS/MS centroid peak lists were generated using the Mascot.dll script (version 1.6b27) and uploaded to the Mascot MS/MS Ions Search on the Matrix Science public Web site (Matrix Science, London, United Kingdom). Peptide mapping was performed against the National Center for Biotechnology Information data base (NCBIprot 20171205 (139213787 sequences; 51013024959 residues)) with the taxonomy limited to *Mus musculus* (house mouse) (175572 sequences). The algorithm was set to following parameters: protease: trypsin; missed cleavages: 1; variable modifications: carbamidomethyl (C) and oxidation (M); peptide tolerance: ± 1.2 Da; MS/MS tolerance: ± 0.6 Da. In general, Mascot searches are scored using the MOWSE algorithm. Here, the given probability value was used as indicator for a proposed protein, but manual *de novo* sequencing and alignment by the use of GPMAW (version 9.12, Lighthouse Data, Odense, Denmark) was applied to confirm the amino acid sequence suggested by Mascot. The criteria used to accept protein identification included the extent of sequence coverage (> 12 %), the number of peptides matched (minimum of five) and the mass accuracy.

RNA isolation

RNA was isolated from mouse ear punch biopsies using TRIzol reagent (Thermo Fisher Scientific, Dreieich, Germany) according to the manufacturer`s instructions and subjected to a second purification step using RNeasy columns (Qiagen, Hilden Germany). RNA concentrations were determined photometrically using a Nanodrop microvolume spectro-photometer (Thermo Fisher Scientific, Dreieich, Germany).

Real-time PCR analysis of TERT transcript levels

Total RNA was reversed transcribed using QuantiTect Reverse Transcription kit (Qiagen, Hilden Germany) according to the manufacturer`s instructions. Relative TERT transcript levels were determined by semi-quantitative real-time PCR using the primers hmTERT for1 and hmTERT rev2, which recognize the cDNAs derived from the transcripts of the endogenous murine TERT gene as well as of the human mitoTERT and nucTERT transgenes in the ROSA26 locus. The transcript for the ribosomal protein L32 (RPL32) served as reference and was detected with the primers hmRPL32 Ex02 for1 and hmRPL32 Ex03 rev1. The PCR reactions were done in a Rotor-Gene Q instrument (Qiagen, Hilden, Germany) using the SYBR Green qPCR Mastermix (Bimake, Munich, Germany). Relative expression was calculated as $2^{-\Delta Ct\ (Ct\ TERT - Ct\ RPL32)}$. The primer sequences are as follows:

hmTERT for1	5'-CATGGAGAACAAGCTGTTTGC-3'
hmTERT rev2	5'-CTGGAGGCTGTTCACCTGC-3'
hmRPL32 Ex02 for1	5'-GTGAAGCCCAAGATCGTCAA-3'
hmRPL32 Ex03 rev1	5'-TTGTTGCACATCAGCAGCAC-3'

Real-time PCR analysis of mitochondrial DNA levels

Murine DNA was isolated from tail clips using the DirectPCR Lysis Reagent (Mouse Tail) (Viagen Biotech, Los Angeles, USA) and subjected to s second purification step using the QIAamp DNA mini and blood mini kit (Qiagen, Hilden, Germany). DNA from human endothelial cells was isolated with the QIAamp DNA mini and blood mini kit (Qiagen, Hilden, Germany). DNA concentrations were determined photometrically using a Nanodrop microvolume spectrophotometer (Thermo Fisher Scientific, Dreieich, Germany) and 20 ng were used for real time PCRs. Relative mtDNA levels were determined by semi-quantitative real-time PCR using the primer combinations m12S for1/m12S rev1 for murine mitochondrial DNA (mtDNA) and hDloop for2/hDloop rev1 for human mtDNA. The single copy nuclear genes for murine Nicotinamide Nucleotide Transhydrogenase (NNT) and human Nucleoredoxin (NXN) served as references and were detected with the primers mNNT Ex10

for1/mNNT Ex10 rev1 and hNXN Ex08 for1/ hNXN Ex08 rev1, respectively. The PCR reactions were done in a Rotor-Gene Q instrument (Qiagen, Hilden, Germany) using the SYBR Green qPCR Mastermix (Bimake, Munich, Germany). Relative mtDNA content for both species was calculated as $2^{-\Delta Ct\ (Ct\ mtDNA\ –\ Ct\ nuclear\ reference\ gene)}$. The primer sequences are as follows:

m12S for1	5'-TGCAAACCTCCATAGACCGGTGT-3'
m12S rev1	5'-TTAATCGTATGACCGCGGTGGCT-3'
hDloop for2	5'-AGCCACTTTCCACACAGACATCAT-3'
hDloop rev1	5'- ATCTGGTTAGGCTGGTGTTAGGGT -3'
mNNT Ex10 for1	5'-GCGGATCCAGATTTCCGACT-3'
mNNT Ex10 rev1	5'-TGACTCCGCCGATGTAAGTG-3'
hNXN Ex08 for1	5'-CCACTCTTGTGTTCTCAGGCAGG-3'
hNXN Ex08 rev1	5'-CGTGGGAGCTGTTTGTATGATATGAACC-3'

Measurement of average relative telomere length

Murine DNA was isolated from tail clips and further purified as described under *Real-time PCR analysis of mitochondrial DNA levels*. Average relative telomere length was determined by semi-quantitative real-time PCR as described by Callicott and Womack[42] with the identical telomere repeat primers. The Nicotinamide Nucleotide Transhydrogenase (NNT) gene served as nuclear reference gene and amplification was performed with the primers used to determine mitochondrial DNA levels. The PCR reactions were done in a Rotor-Gene Q instrument (Qiagen, Hilden, Germany) using the SYBR Green qPCR Mastermix (Bimake, Munich, Germany). Average relative telomere length was calculated as $2^{-\Delta Ct\ (Ct\ telomere\ repeat\ –\ Ct\ nuclear\ reference\ gene)}$.

Statistics

The number of experiments (n) given in the figure legends represents independent biological replicates, the data shown are mean ± SEM. Normal distribution for all data sets was confirmed by Shapiro-Wilk test; homogeneity of variances (from means) between groups was

verified by Levene's test. Pairwise comparisons were performed with two-sided, unpaired Student's t-tests on raw data. Multiple comparisons were performed using one-way ANOVA with post-hoc Tukey LSD test or one-way ANOVA for repeated measurements with post-hoc Tukey LSD test when the same animals were followed over time. In case of not normal distribution, one-way ANOVA Kruskal-Wallis test with post-hoc Man-Whitney test was used. Sample sizes for experiments, which were based on the respective statistical tests for data analyses, were calculated employing G*Power version 3.1.9.2[43]. Effect strength for this power calculation was taken from our earlier studies[4]. Significance level (α-error) and sensitivity (β-error) were set to 0.05 and 0.95, respectively.

Table S1

Patient demographics and intraoperative characteristics			
	RIPC (n=7)	**placebo (n=5)**	**p-value**
demographics			
age [years]	68.0 ± 3.4	66.2 ± 4.2	0.738
sex [male]	5	4	1.000
body weight [kg]	91.4 ± 9.1	79.4 ± 7.1	0.356
risk factors and co-morbidities			
diabetes mellitus	2	0	0.470
hypertension	7	5	1.000
hyperlipidemia	1	3	0.222
peripheral vessel disease	0	0	1.000
COPD	1	0	1.000
renal disease [creatinine >200 µmol/L]	1	0	1.000
cardiac status			
angina CCS III-IV	2	3	0.242
previous myocardial infarction	2	0	0.491
left ventricular ejection fraction [%]	45.5 ± 6.5	54.4 ± 4.3	0.304
medication			
aspirin	7	3	0.364
clopidogrel	1	0	1.000
β-blockers	5	4	1.000
statins	6	4	1.000
ACE inhibitors or ARBs	6	3	0.523
risk scores			
logistic EuroSCORE [%]	4.1 ± 1.0	3.2 ± 1.0	0.602
EuroSCORE II [%]	2.5 ± 0.5	2.3 ± 0.7	0.832
intraoperative characteristics			
time from end of RIPC/placebo to cardiopulmonary bypass [min]	69.6 ± 13.5	71.5 ± 7.0	0.912
time from end of RIPC/placebo to reperfusion [min]	120.2 ± 15.8	144.3 ± 10.5	0.271
aortic cross-clamp duration [min]	61.7 ± 12.8	68.8 ± 9.5	0.690
cardioplegia [mL]	1628 ± 64	1540 ± 108	0.470
reperfusion time [min]	30.2 ± 7.2	29.0 ± 10.4	0.925
number of bypass grafts	3.6 ± 0.3	2.2 ± 1.2	0.223

Data are mean ± standard error of the mean or number. Patient demographics and intraoperative characteristics were compared using unpaired Student's t-test (continuous data) and 2-tailed Fisher's exact test (categorical data). Chronic obstructive pulmonary disease (COPD), Canadian cardiovascular society score (CCS), angiotensin-converting enzyme (ACE), angiotensin-II-receptor blockers (ARBs), European system for cardiac operative risk evaluation (EuroSCORE), remote ischemic preconditioning (RIPC). Reperfusion time: time from release of aortic cross-clamp to end of cardiopulmonary bypass.

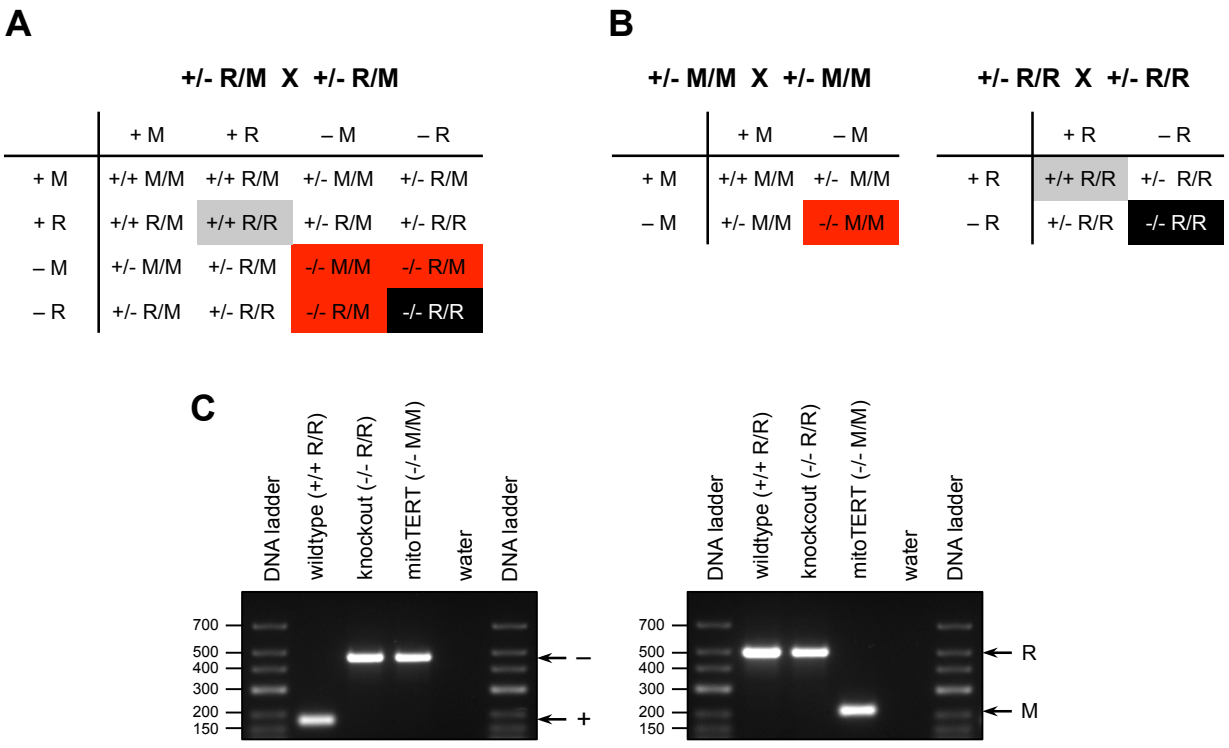

Figure S1: Breeding strategies and genotyping exemplified for mitoTERT mice. (A, B) First, animals with a single mitoTERT allele (M) and an unaltered ROSA26 locus (R) on a TERT-proficient background (+/+ R/M) were bred to heterozygous TERT-deficient animals carrying the intact ROSA26 gene (+/- R/R) to obtain double heterozygous animals (+/- R/M), which were then used for further breeding. Experimental animals were generated by double heterozygous intercross of (+/- R/M) animals or - to generate larger numbers of mice with maximal genetic relatedness - an alternative breeding strategy, which yields cousins. (A) Double-heterozygous intercross. The use of two double-heterozygous (+/- R/M) breeders yields offspring of the desired genotypes (wildtype: +/+ R/R, gray; TERT knockout: -/- R/R, black; homo- or heterozygous mitoTERT on an otherwise TERT-deficient background: -/- R/M or -/- M/M, red) at low frequency. (B) Alternative breeding strategy yielding cousins. Here, offspring from the double heterozygous crosses, carrying either two mitoTERT alleles on a heterozygous TERT-deficient background (+/- M/M) (left) or siblings with two unaltered ROSA26 loci, but also heterozygous for TERT-deficiency (+/- R/R) (right) were mated with animals of the same genotype to generate the experimental animals. (C) Exemplary genotyping. DNA prepared from tail clips was used in two separate amplification reactions for (i) the TERT locus on chromosome 13 (left) and (ii) the mitoTERT allele in the ROSA26 locus on chromosome 6 (right); control reactions contained water instead of DNA. Reaction products were resolved on agarose gels along with a DNA ladder; the fragment sizes of this ladder are given in bp. The different alleles yield the following amplification products: TERT wildtype (+) approximately 150 bp, TERT knockout (-) approximately 420 bp, mitoTERT (M) 214 bp and the unaltered ROSA26 locus (R) 503 bp.

The same breeding strategies were use to generate nucTERT animals and genotyping was performed with the identical primers, with which the nucTERT allele yields an amplification product of 298 bp.

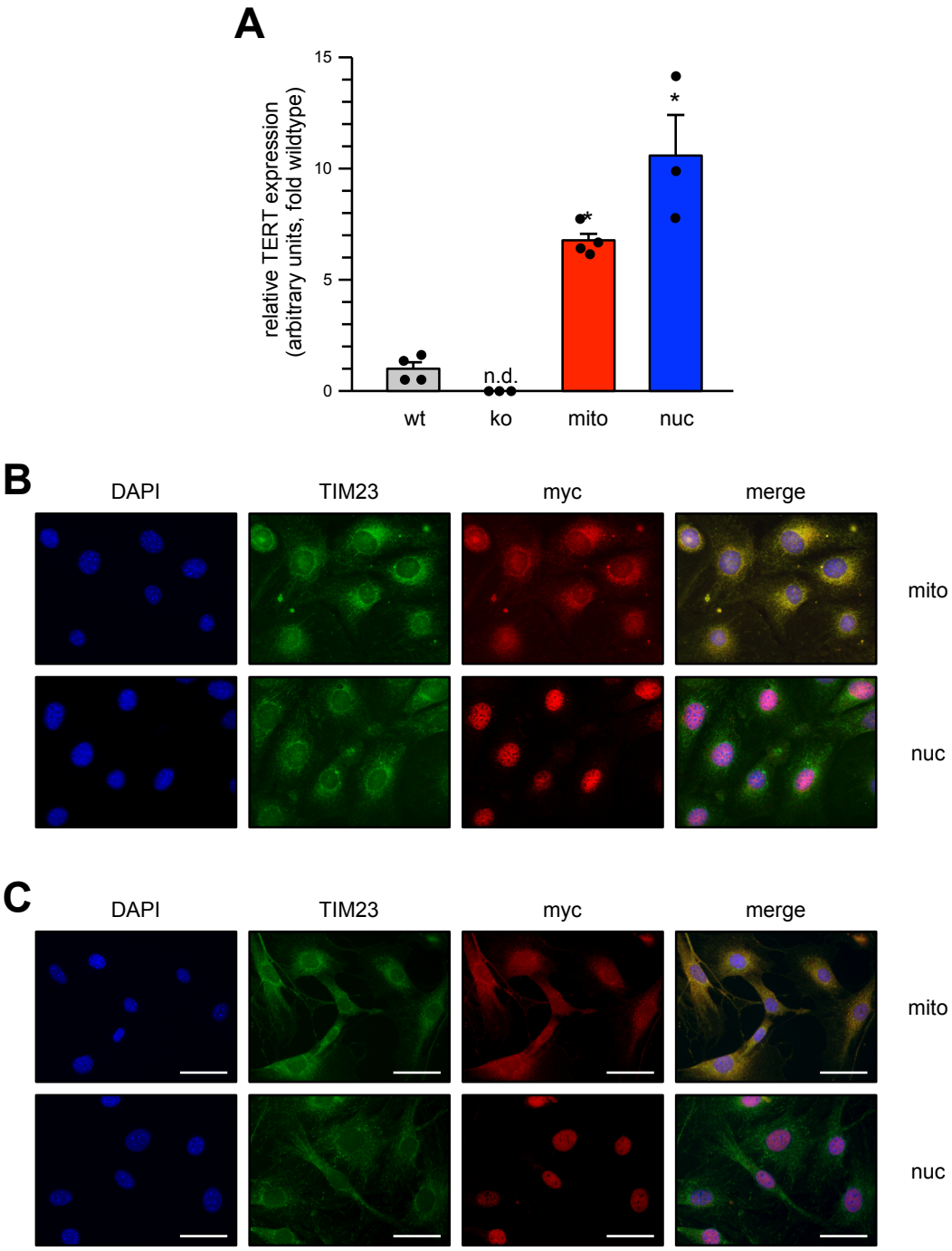

Figure S2: TERT expression in wildtype, knockout, mitoTERT and nucTERT mice and localization of organelle-targeted TERT. (A) RNAs were isolated from earclips of wildtype (wt), TERT-deficient (ko), mitoTERT (mito) and nucTERT (nuc) mice and reverse transcribed. The cDNAs were used in semi-quantitative real time PCRs. To obtain comparable data for the endogenous TERT transcript in the wildtype animals and the human transgene in the mitoTERT and nucTERT animals, primers were designed, which detect both the murine and human sequences. Control reactions were performed with cDNAs synthesized in the absence of reverse transcriptase, the RPL32 transcript served as reference. Relative expression was calculated with the ΔC_t method and is shown relative to wildtype mice (data are mean±SEM, n=3-4 per group [wt, mito: 4, ko, nuc: 3], *p<0.05 vs wt, n.d.=not detectable, one-way ANOVA with post-hoc Tukey LSD test). (B, C) Cardiac and lung fibroblasts were isolated from mitoTERT (mito) and nucTERT (nuc) mice and stained with antibodies against TIM23 and the myc tag, nuclei were counterstained with DAPI, merge is an overlay of all fluores-cence channels (scale bar=50 µm). The lack of a fluorescence signal in the respective other com-partment demonstrates specificity of the myc staining. (B) Cardiac fibroblasts. (C) Lung fibro-blasts.

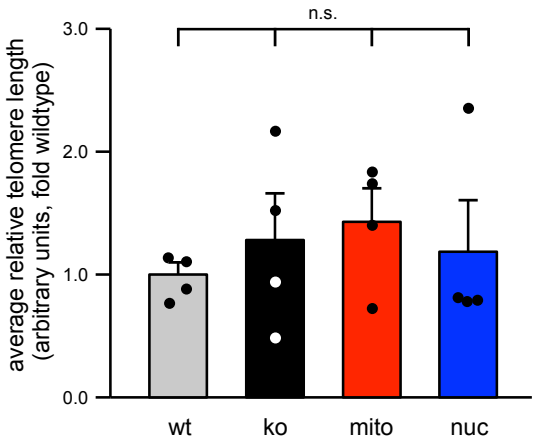

Figure S3: Mitochondrial and nuclear TERT do not affect average telomere length. DNAs were isolated from tail clips of wildtype (wt), TERT-deficient (ko), mitoTERT (mito) and nucTERT (nuc) animals and used as templates in semi-quantitative real time PCRs, the single copy nuclear NNT gene served as reference. Average relative telomere length was calculated with the ΔC_t method and is shown relative to wildtype mice (data are mean±SEM, n=4 per group, n.s.=not significant, one-way ANOVA with post-hoc Tukey LSD test).

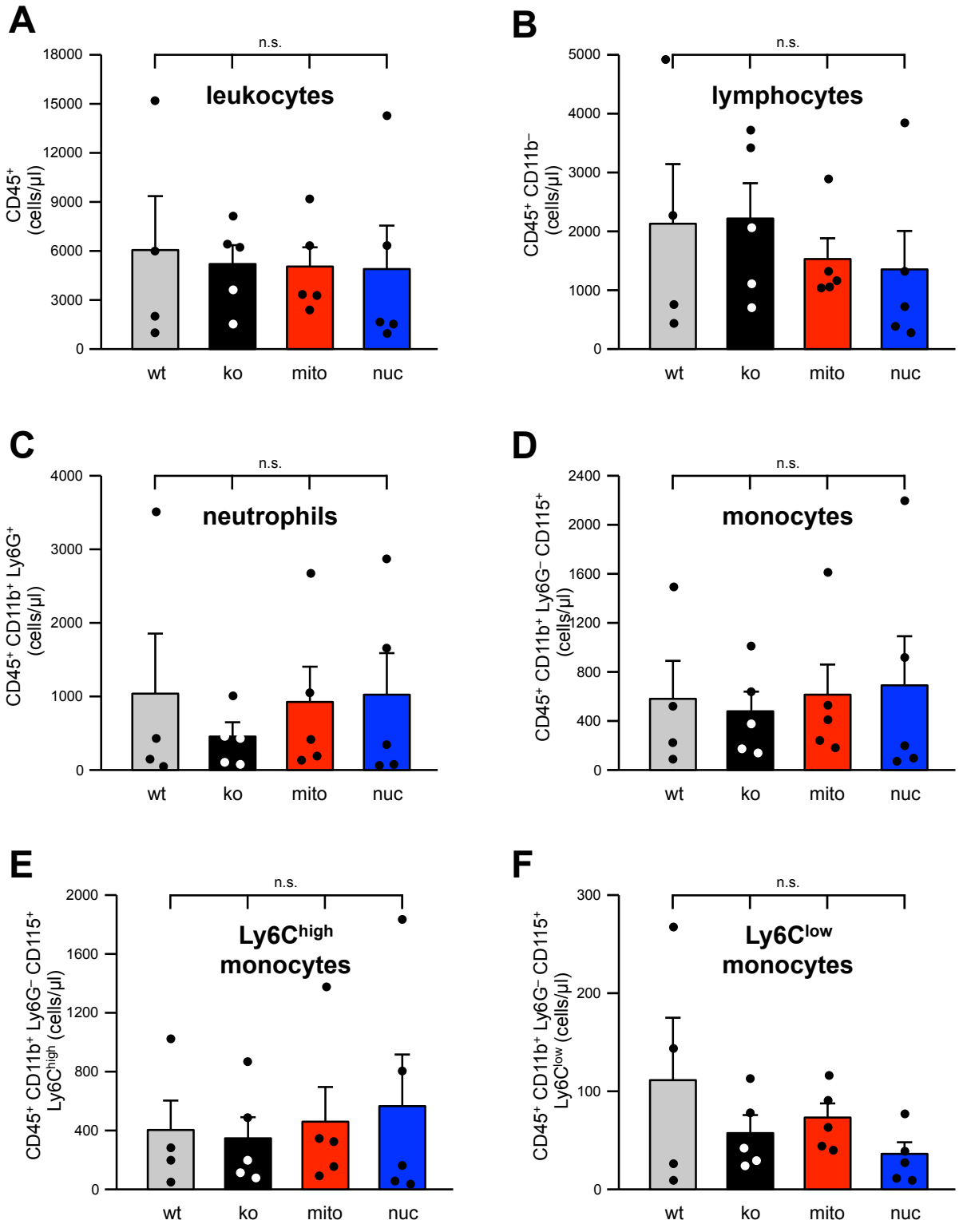

Figure S4: Mitochondrial and nuclear TERT do not affect circulating immune cells. (A-F) Immune cell composition in the blood of wildtype (wt), TERT-deficient (ko), mitoTERT (mito) and nucTERT (nuc) mice was analyzed by flow cytometry (data are mean±SEM, n=4-5 per group [wt: 4, ko, mito, nuc: 5], n.s.=not significant, one-way ANOVA with post-hoc Tukey LSD test). (A) Leukocytes. (B) Lymphocytes. (C) Neutrophils. (D) Monocytes. (E) Ly6C^{high} monocytes. (F) Ly6C^{low} monocytes.

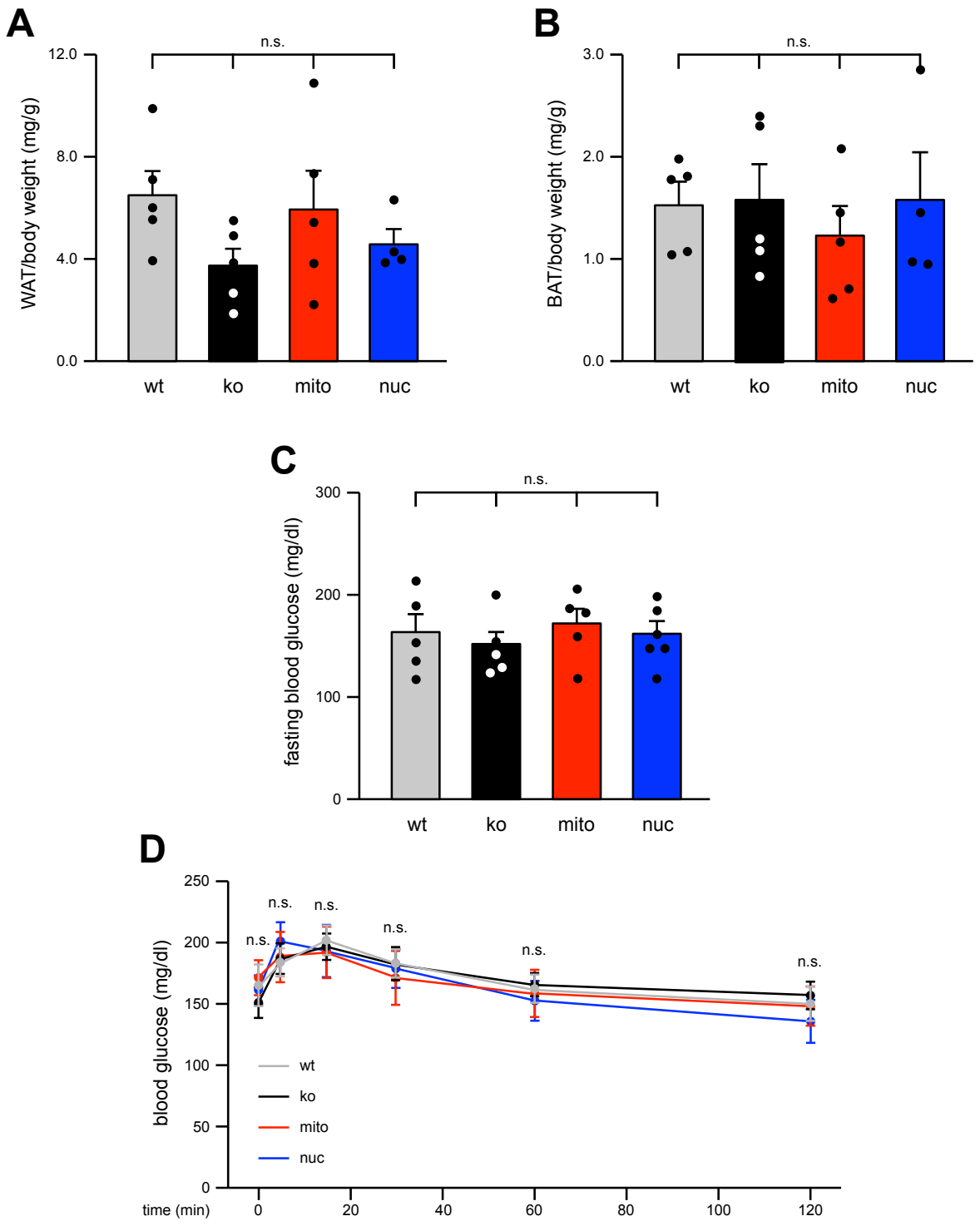

Figure S5: Mitochondrial and nuclear TERT do not affect adipose tissue deposits and blood glucose levels. (A, B) Wildtype (wt), TERT-deficient (ko), mitoTERT (mito) and nucTERT (nuc) mice were used to determine white and brown adipose tissue weight (data are mean±SEM, n=4-5 per group [wt, ko, mito: 5, nuc: 4], n.s.=not significant, one-way ANOVA with post-hoc Tukey LSD test). (A) White adipose tissue weight per body-weight. (B) Brown adipose tissue weight per bodyweight. (C, D) Wildtype (wt), TERT-deficient (ko), mitoTERT (mito) and nucTERT (nuc) mice were used for fasting blood glucose measurements and glucose tolerance tests (data are mean±SEM, n=5-6 per group [wt, ko, mito: 5, nuc: 6], n.s.=not significant, one-way ANOVA with post-hoc Tukey LSD test). (C) Blood glucose levels after 6 h of fasting. (D) Intraperitoneal glucose tolerance test.

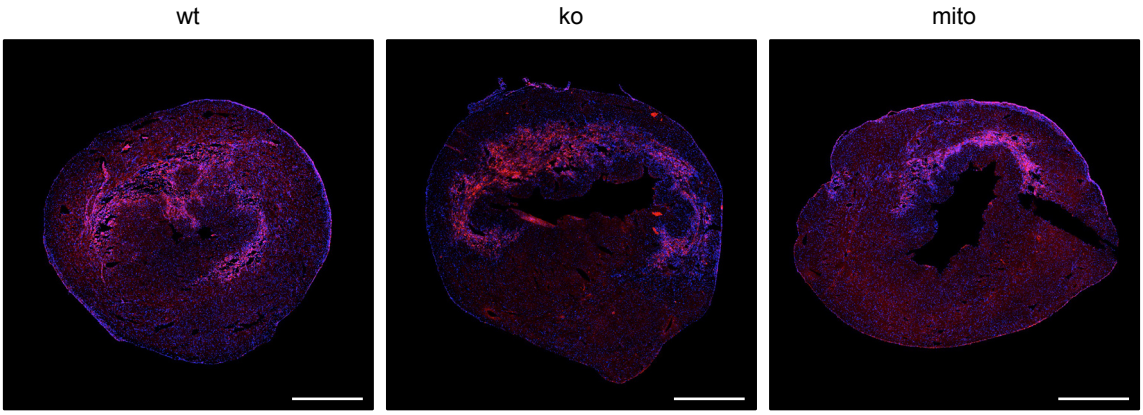

Figure S6: Mitochondrial TERT reduces scar formation 7 days after myocardial infarction. Myocardial ischemia reperfusion injury was induced in wildtype (wt), TERT-deficient (ko), and mitoTERT (mito) animals. 7 days after infarction, transverse cardiac sections adjacent to the ones shown in figure 3E were stained for Collagen I, nuclei were counterstained with DAPI. Representative sections, Collagen I staining is shown in red, nuclei in blue (scale bar=1 mm).

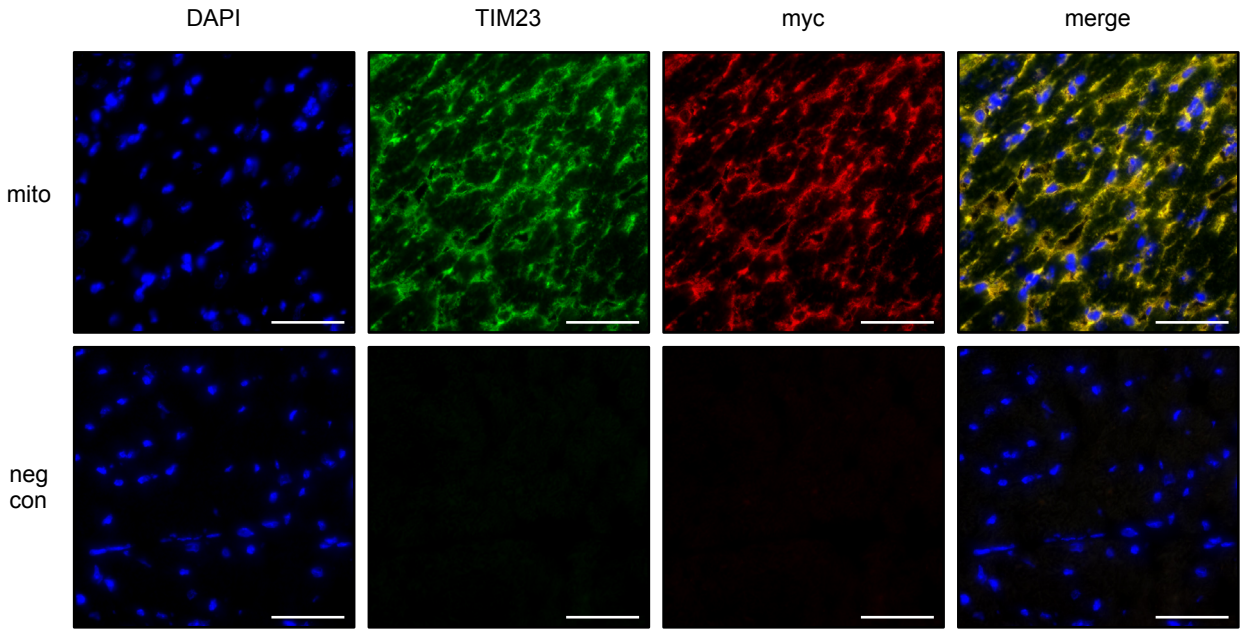

Figure S7: Mitochondrial TERT is present in heart mitochondria of mitoTERT mice 7 days after myocardial infarction. 7 days after infarction in a mitoTERT animal (mito), a transverse cardiac section was stained for mitochondrially targeted TERT expressed from the knockin into the ROSA26 locus using an anti-myc antibody. Mitochondria were visualized with an anti-TIM23 antibody and nuclei were counterstained with DAPI. In the negative control (neg con), which is a section from the same heart, the primary antibodies were omitted. Representative sections, TIM23 staining is shown in green, TERT-myc in red, nuclei in blue (scale bar=50 µm).

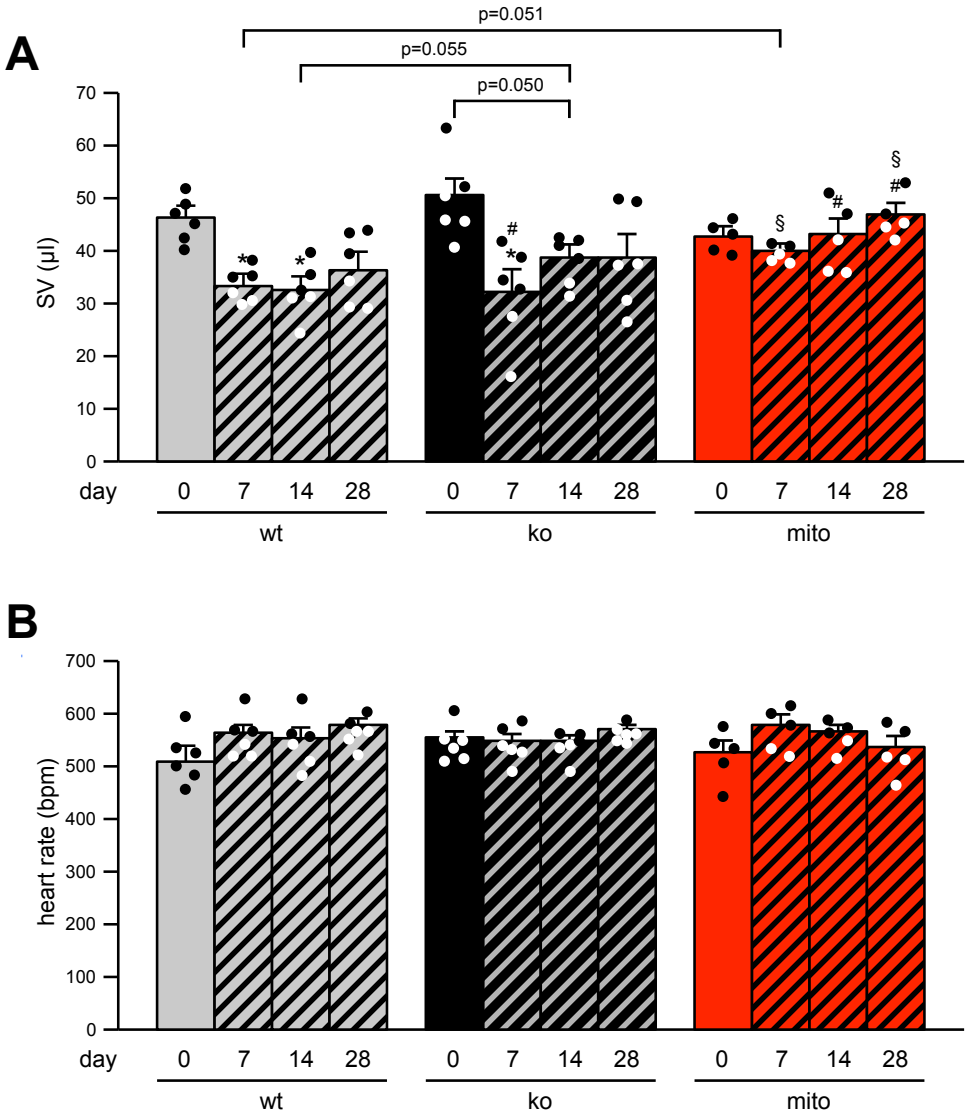

Figure S8: Stroke volume and heart rates at baseline and 7, 14 and 28 days after ischemia/reperfusion injury. Functional parameters of the heart were measured by echocardiography in wildtype (wt), TERT-deficient (ko) and mitoTERT (mito) animals before (baseline, day 0, filled bars) and 7, 14 and 28 days after infarction (hatched bars) (data are mean±SEM, n=5-6 per group [wt, ko: 6, mito: 5], *p<0.05 vs baseline same genotype, one-way ANOVA for repeated measurements with post-hoc Tukey LSD test, #p<0.05 vs wt same timepoint, §p<0.05 vs ko same timepoint, one-way ANOVA with post-hoc Tukey LSD test). (A) Stroke volume (SV). (B) Heart rate – no significant differences.

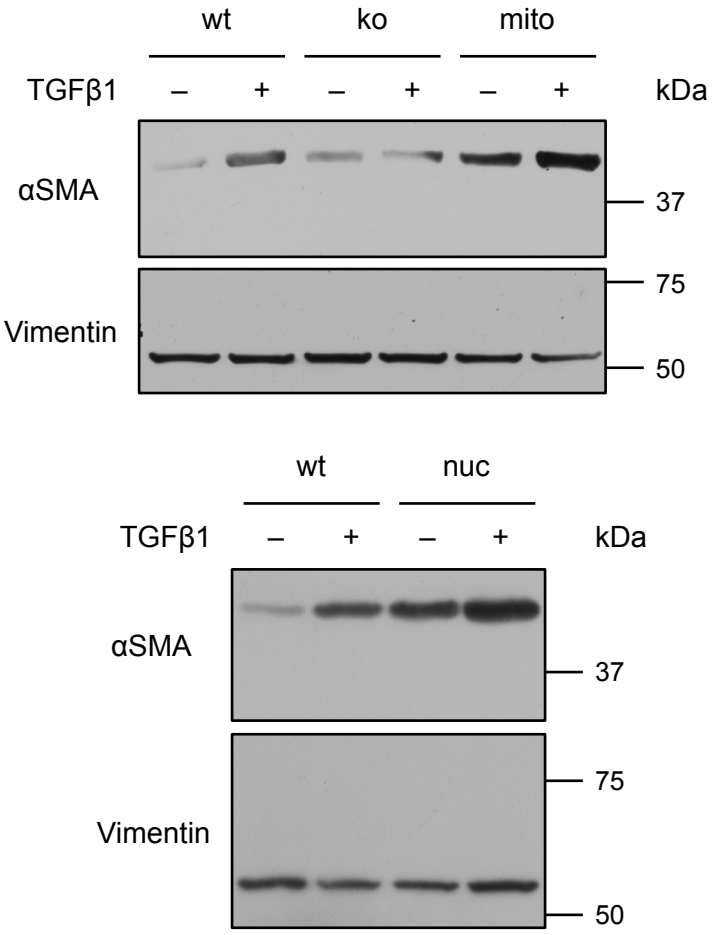

Figure S9: Original blots Figure 4C. The molecular weights of the marker proteins are shown to the right of the blots.

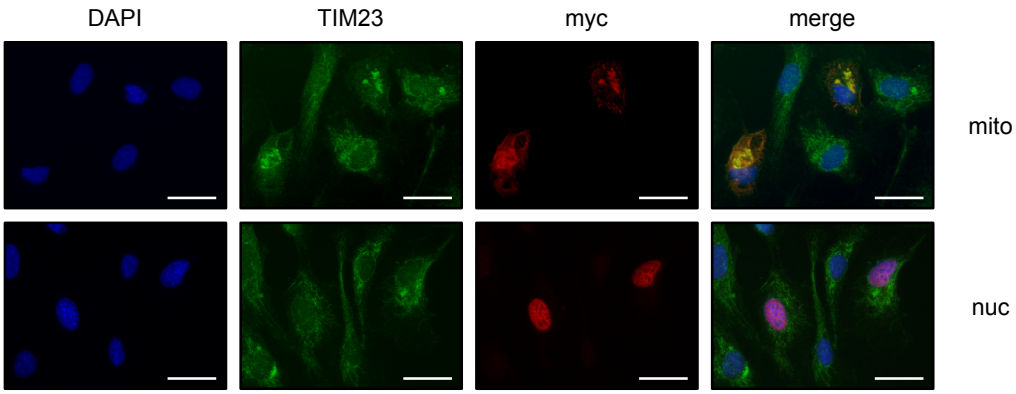

Figure S10: Organelle-specific targeting of TERT in endothelial cells. Primary human endo-thelial cells were transfected with expression vectors for mitochondrially (mito) and nuclear (nuc) targeted TERT, respectively. The cells were stained with antibodies against TIM23 and the myc tag, nuclei were counterstained with DAPI, merge is an overlay of all fluorescence channels (scale bar=20 µm). The lack of a fluorescence signal in the respective other com-partment demonstrates specificity of the myc staining.

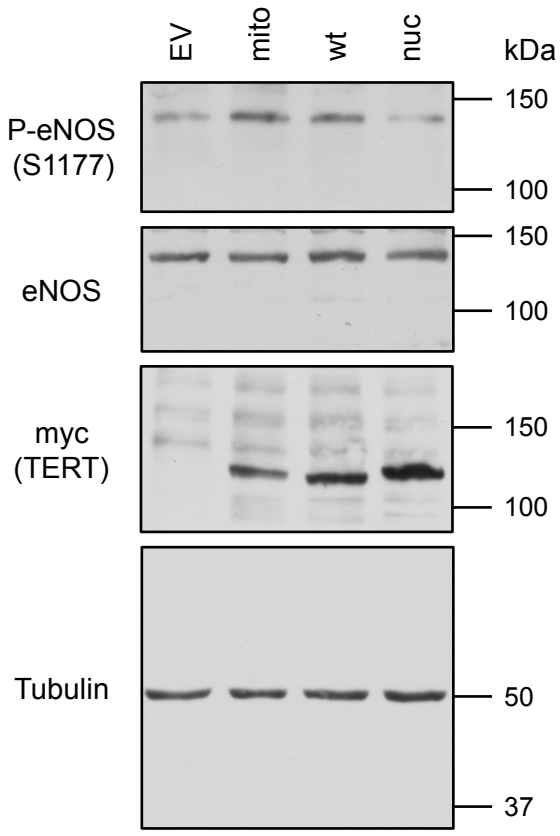

Figure S11: Original blots Figure 4H. The molecular weights of the marker proteins are shown to the right of the blots.

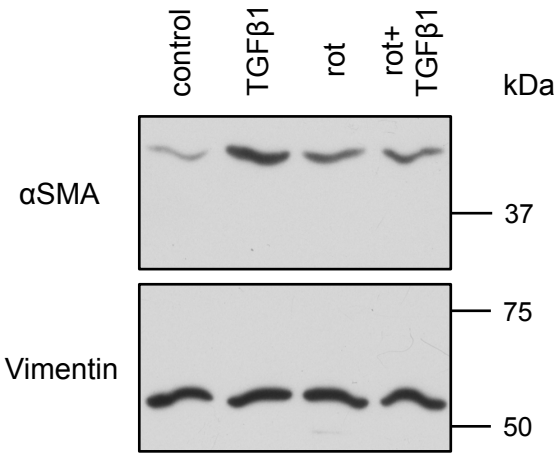

Figure S12: Original blots Figure 5C. The molecular weights of the marker proteins are shown to the right of the blots.

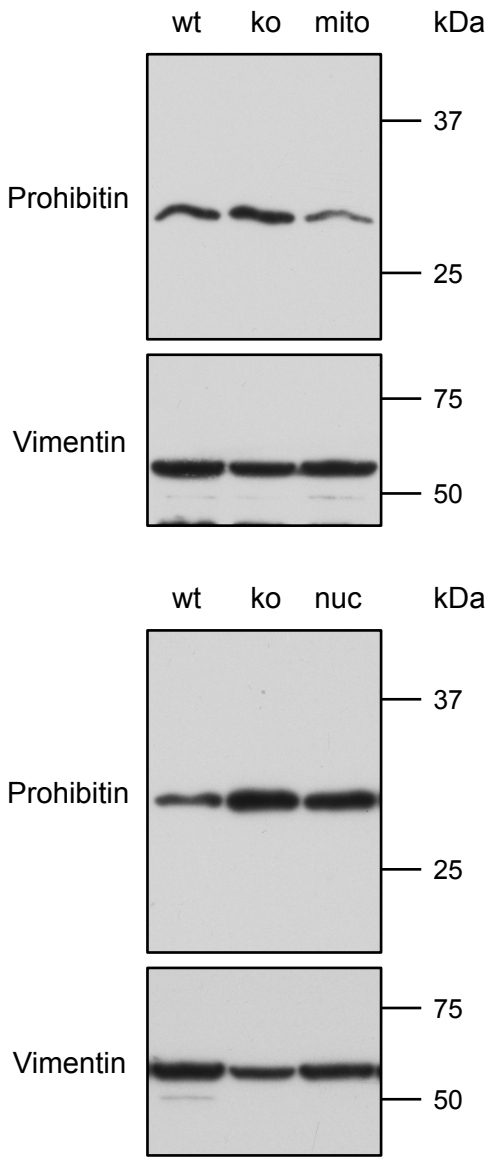

Figure S13: Original blots Figure 5E. The molecular weights of the marker proteins are shown to the right of the blots.

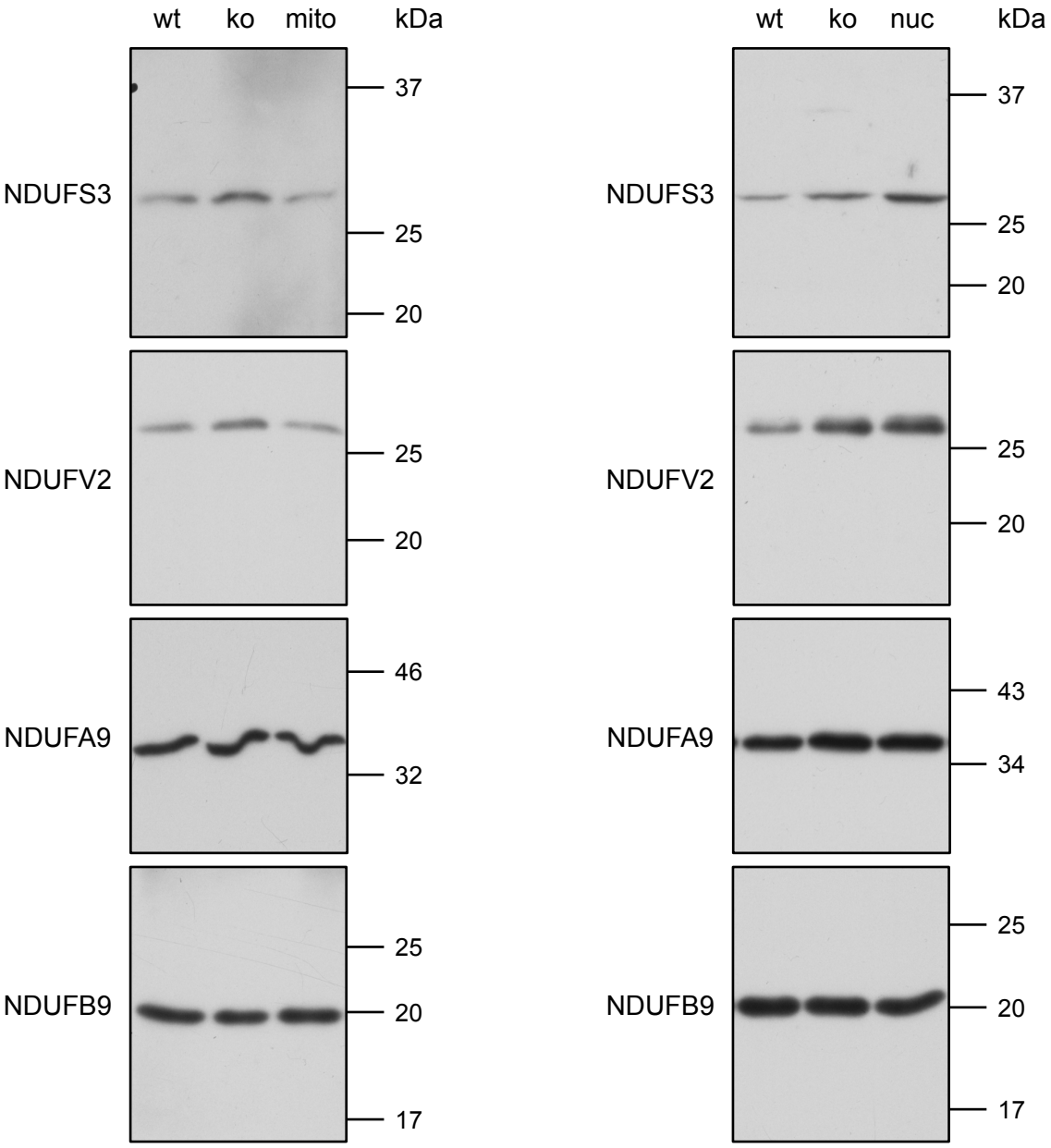

Figure S14: Original blots Figure 5F. The molecular weights of the marker proteins are shown to the right of the blots.

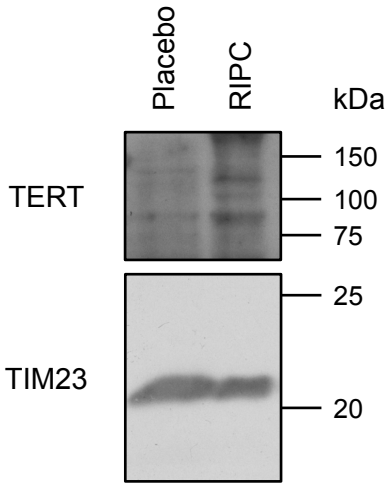

Figure S15: Original blots Figure 6A. The molecular weights of the marker proteins are shown to the right of the blots.

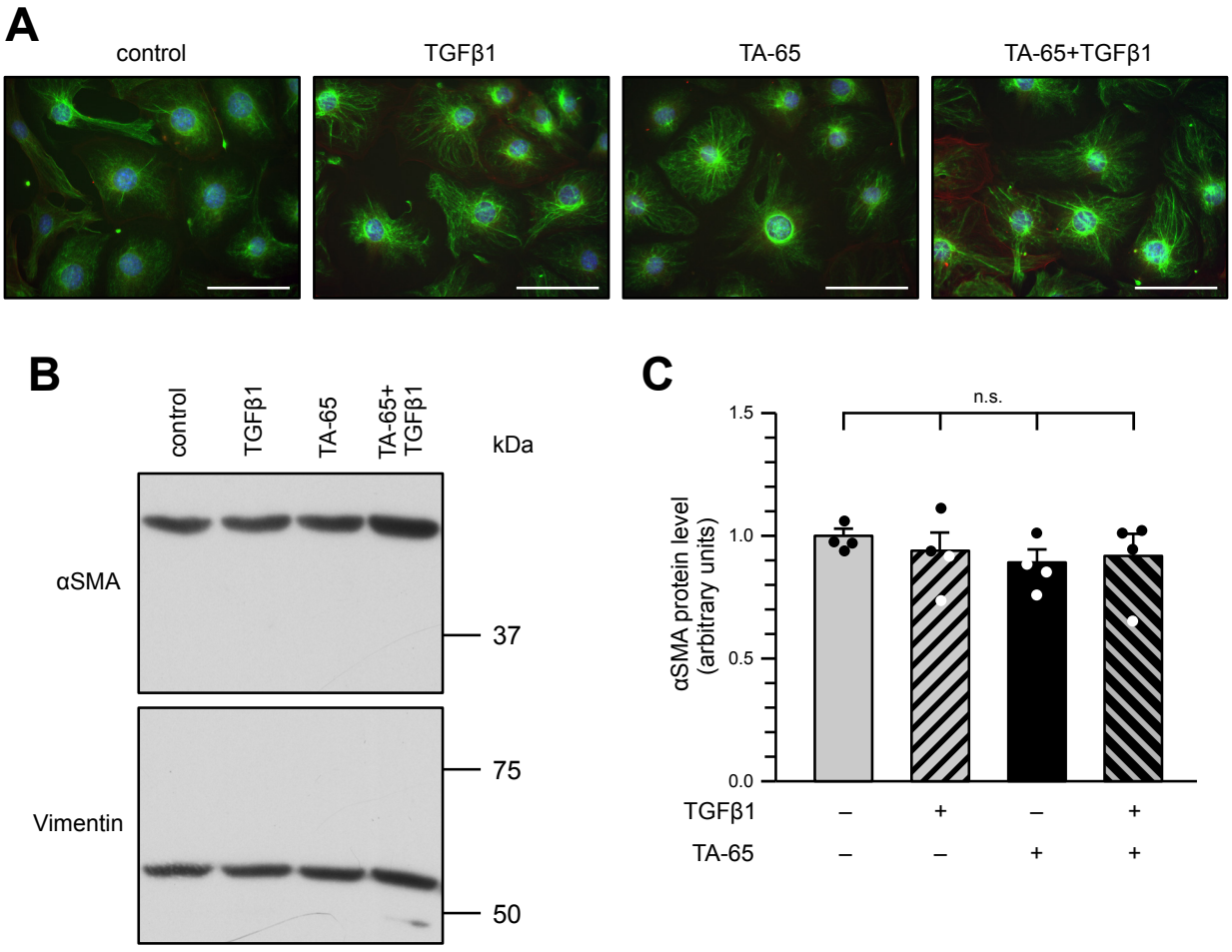

Figure S16: TA-65 cannot override the myofibroblast differentiation block of TERT-deficient cardiac fibroblasts. Cardiac fibroblasts from TERT-deficient mice were treated with TGFβ1, 1 μM TA-65 or a combination of both. Alpha Smooth Muscle Actin (αSMA) was detected by immunostaining and immunoblot. (A) Representative immunostainings (red: αSMA, green: Vimentin, blue: DAPI, scale bar=100μm). (B) Representative immunoblots, Vimentin served as loading control. (C) Semi-quantitative analysis of αSMA normalized to Vimentin (data are mean±SEM, n=4, n.s.=not significant, one-way ANOVA with post-hoc Tukey LSD test).

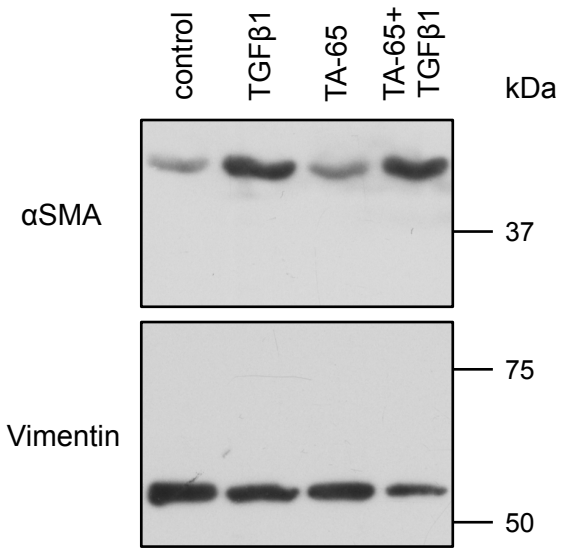

Figure S17: Original blots Figure 6H. The molecular weights of the marker proteins are shown to the right of the blots.

Macrophage acetyl-CoA carboxylase regulates acute inflammation through control of glucose and lipid metabolism

Yeudall S, Upchurch CM, Seegren PV, Pavelec CM, **Greulich J**, Lemke MC, Harris TE, Desai BN, Hoehn KL, Leitinger N

Science Advances. 2022; 8, eabq1984

Publikation III

Beteiligung der Autoren:

Yeudall S: Erstautor, war an der Planung und Durchführung aller Versuche beteiligt, führte die Datenanalyse durch und war am Entwurf des Manuskripts beteiligt; erstellte Abbildungen.

Upchurch CM: Führte Lipidomics und targeted massenspektrometrische Analysen von Lipiden durch und analysierte die Daten.

Seegren PV: Führte bakterielle killing assays durch, half bei Tierversuchen zur Untersuchung der bakteriellen Peritonitis, und führte FACS-Analysen durch.

Pavelec CM: Führte metabolische Messungen an Makrophagen mittels Seahorse-Analyzer durch und analysierte die Daten.

Greulich J: Führte Organentnahmen, RNA-Isolierungen und PCR-Analysen durch.

Lemke MC: Führte Acetylierungs assays durch und analysierte Daten.

Harris TE: War an der Planung zu den Acetylierungsversuchen beteiligt, und stellte Reagenzien zur Verfügung.

Desai BN: War an der Planung der bakteriellen killing assays und Tierversuchen zur Untersuchung der bakteriellen Peritonitis, und FACS-Analysen beteiligt.

Hoehn KL: Stellte die ACC-flox Mäuse zur Verfügung.

Leitinger N: Seniorautor, konzipierte die Studie, war an der Versuchsplanung beteiligt, finalisierte das Manuskript.

IMMUNOLOGY

Macrophage acetyl-CoA carboxylase regulates acute inflammation through control of glucose and lipid metabolism

Scott Yeudall[1], Clint M. Upchurch[1], Philip V. Seegren[1], Caitlin M. Pavelec[1,2], Jan Greulich[3], Michael C. Lemke[1], Thurl E. Harris[1], Bimal N. Desai[1], Kyle L. Hoehn[1,4], Norbert Leitinger[1,2]*

Acetyl-CoA carboxylase (ACC) regulates lipid synthesis; however, its role in inflammatory regulation in macrophages remains unclear. We generated mice that are deficient in both ACC isoforms in myeloid cells. ACC deficiency altered the lipidomic, transcriptomic, and bioenergetic profile of bone marrow–derived macrophages, resulting in a blunted response to proinflammatory stimulation. In response to lipopolysaccharide (LPS), ACC is required for the early metabolic switch to glycolysis and remodeling of the macrophage lipidome. ACC deficiency also resulted in impaired macrophage innate immune functions, including bacterial clearance. Myeloid-specific deletion or pharmacological inhibition of ACC in mice attenuated LPS-induced expression of proinflammatory cytokines interleukin-6 (IL-6) and IL-1β, while pharmacological inhibition of ACC increased susceptibility to bacterial peritonitis in wild-type mice. Together, we identify a critical role for ACC in metabolic regulation of the innate immune response in macrophages, and thus a clinically relevant, unexpected consequence of pharmacological ACC inhibition.

INTRODUCTION

Stimulus-dependent metabolic reprogramming is a hallmark of phenotypic polarization of immune cell types including macrophages (*1*). In response to Toll-like receptor (TLR)–activating pathogen-derived danger signals such as lipopolysaccharide (LPS), M1 macrophages rapidly switch to aerobic glycolysis for adenosine triphosphate (ATP) production and increase glucose uptake, and blockade of either of these processes is sufficient to inhibit the inflammatory response (*2*, *3*). Conversely, alternative activation (M2) of macrophages with stimuli such as interleukin-4 (IL-4) demonstrates a reliance on oxidation of fatty acids to fuel increased oxidative phosphorylation (*4*, *5*). Moreover, exposure of macrophages to redox-modulatory stimuli such as lipid oxidation products (Mox) or cell-free heme (Mhem) results in increased flux through the pentose phosphate pathway and production of NADPH [reduced form of nicotinamide adenine dinucleotide phosphate ($NADP^+$)] and the reducing agent glutathione at the expense of glycolysis (*6*, *7*).

A defining hallmark of the inflammatory response in macrophages is the accumulation of intracellular lipids, which is dependent on activation of TLR signaling (*8*). Genetic ablation of fatty acid synthase (FAS) in macrophages blunts proinflammatory polarization, adipose tissue inflammation, and insulin resistance in response to high-fat feeding through perturbations in membrane composition and LPS-induced signaling (*9*), while pharmacologic inhibition of FAS dampens dendritic cell activation in response to LPS by blocking endoplasmic reticulum (ER) and Golgi expansion (*10*). In addition, loss of diacylglycerol acyltransferase (DGAT)–dependent triacylglycerol (TAG) production in macrophages attenuates LPS-induced inflammation, in part through alterations in prostaglandin production (*11*). Furthermore, activation of the sterol- and lipid-sensing transcription factors liver X receptor (LXR) and sterol regulatory element–binding protein 1 (SREBP1) is critical for the resolution of TLR-dependent inflammation (*12*, *13*).

Acetyl–coenzyme A (CoA) carboxylase (ACC) enzymes, which catalyze the conversion of acetyl-CoA to malonyl-CoA committing carbon to de novo fatty acid synthesis, are central regulators of lipid metabolism in the cell. Mammals encode two isoforms of ACC: ACC1 is a cytosolic enzyme that acts to generate the malonyl-CoA primarily as a substrate for the lipogenesis pathway, while the localized production of malonyl-CoA by ACC2 acts to inhibit acylcarnitine transport into the mitochondria via carnitine palmitoyltransferase 1 (CPT1) (*14*), thereby regulating β-oxidation of fatty acids (*15*). Although the two isoforms are thought to serve these distinct roles, they catalyze the same biochemical transformation and are regulated at the enzymatic level by similar mechanisms such as phosphorylation (*16*–*18*). Whole-animal deletion of ACC1 is lethal during development (*19*), whereas global ACC2 knockout mice are viable (*20*). Some studies of global ACC2 knockout mice demonstrated increased mitochondrial oxidation, lower fat stores, and increased insulin sensitivity (*21*, *22*), while in other studies ACC2 mutant mice had increased levels of fatty acid oxidation without changes in adiposity or energy balance (*23*). Previous studies have demonstrated that liver-specific deletion of only ACC1 can result in compensation by the ACC2 isoform (*24*). However, genetic deletion of both ACC1 and ACC2 resulted in increased cellular glucose metabolism in hepatocytes in vitro and increased hepatic lipid accumulation in vivo. Unexpectedly, ablation of ACC expression also caused a shift in the global profile of protein

[1]Department of Pharmacology, University of Virginia School of Medicine, Charlottesville, VA 22908, USA. [2]Robert M. Berne Cardiovascular Research Center, University of Virginia School of Medicine, Charlottesville, VA 22908, USA. [3]Environmentally-Induced Cardiovascular Degeneration, Clinical Chemistry and Laboratory Diagnostics, Medical Faculty, University Hospital and Heinrich-Heine University Düsseldorf, 40225 Düsseldorf, Germany. [4]School of Biotechnology and Biomolecular Sciences, University of New South Wales, Sydney, New South Wales 2052, Australia.
*Corresponding author. Email: nl2q@virginia.edu

acetylation, without significantly altering overall levels of acetyl-CoA (*25*). The role for ACC enzymes in immune cells, however, remains less clear: Individual deletion of ACC1 or ACC2 in the myeloid lineage had minimal impact on the inflammatory response to mycobacterial infection (*26*). However, the consequences of ACC1/ACC2 double deletion, which eliminates potential for compensatory enzymatic activity, on myeloid cell function have not been assessed.

Here, we examined the impact of ACC deficiency on macrophage phenotypic and metabolic polarization during the inflammatory response. Using mice with a myeloid-specific deletion of both ACC isoforms, we demonstrate that ACC knockdown attenuates the LPS-induced macrophage activation through perturbation of cellular glucose and lipid metabolism to blunt inflammatory cytokine induction and impair macrophage effector functions. These findings identify a critical role for ACC enzymes at the nexus of metabolism, lipid synthesis, and cellular function in macrophages and discover that attenuation of the macrophage inflammatory response is an unexpected consequence of ACC inhibition.

RESULTS

ACC knockdown shifts macrophages to a hyperglycolytic bioenergetic state

To assess the role of ACC in the macrophage inflammatory response, we crossed mice expressing Cre recombinase under the control of the myeloid-specific *LysM* promoter (*27*) with mice expressing loxP-flanked alleles of both *Acaca* (encoding ACC1) and *Acacb* (encoding ACC2) (*25*) to generate mice with a myeloid-specific knockdown of ACC1 and ACC2 (hereafter ACC$^{\Delta LysM}$) (Fig. 1A and fig. S1A). We confirmed significantly decreased mRNA expression of *Acaca* and *Acacb* (Fig. 1B) and decreased ACC protein levels (Fig. 1C) in bone marrow–derived macrophages (BMDMs) isolated from ACC$^{\Delta LysM}$ mice. The degree of knockdown was in accordance with previous studies using LysM Cre to deplete the related metabolic enzyme ATP citrate lyase (ACLY) (*28*). ACC$^{\Delta LysM}$ mice grew and developed normally, and we observed no difference in total body mass or fat mass in male or female mice as compared to littermate flox controls (fig. S1, B and C).

To examine the impact of decreased ACC levels on macrophages, we first assessed baseline transcriptional and metabolic profiles in vitro. Comparison of unstimulated ACC$^{\Delta LysM}$ and control BMDMs using mass spectrometry–based lipidomics (Fig. 1D) revealed expected changes in the lipidome of ACC-deficient macrophages, with 52 species increased in abundance and 24 species decreased in abundance in ACC$^{\Delta LysM}$ (Fig. 1D, insets). We then examined whether loss of ACC has any impact on the transcriptional profile of macrophages at baseline. RNA sequencing (RNA-seq) analysis of BMDMs from control or ACC$^{\Delta LysM}$ mice revealed changes in metabolic pathways and lipid metabolism (Fig. 1E). Gene Ontology (GO) analysis identified enrichment of processes including "cholesterol biosynthetic process," "sterol biosynthetic process," and "phospholipid biosynthetic process" in ACC-deficient BMDMs (fig. S1D), which also demonstrated slightly higher levels of FASN protein compared with flox controls (fig. S1E).

Further analysis of gene expression in other metabolic pathways demonstrated alterations in glycolysis and glucose metabolism (Fig. 1E and fig. S1F), which we confirmed by qualitative polymerase chain reaction (qPCR) for a subset of genes (fig. S1G). We therefore assessed the metabolic status of ACC$^{\Delta LysM}$ macrophages using extracellular flux analysis. We found that BMDMs isolated from ACC$^{\Delta LysM}$ mice have increased rates of extracellular acidification than control macrophages (Fig. 1F), which corresponded to an increase in both basal glycolytic rate (Fig. 1G) and oligomycin-stressed glycolytic rate (Fig. 1H). Glucose utilization, as assessed by 2NDB-glucose uptake (Fig. 1I) and accumulation of extracellular lactate (Fig. 1J), was also significantly increased in BMDMs isolated from ACC$^{\Delta LysM}$ mice. On the other hand, analysis of mitochondrial function in ACC$^{\Delta LysM}$ BMDMs demonstrated a nonsignificant trend to increased basal and maximal oxygen consumption rate (OCR) (fig. S1, H to J). Together, these data demonstrate that loss of ACC, in addition to lipogenesis, affects cellular metabolism, shifting macrophages to a hyperenergetic, hyperglycolytic phenotype at baseline (Fig. 1K), which may affect innate effector functions of macrophages after stimulation.

Loss of ACC impairs proinflammatory macrophage activation in vitro

When we used RNA-seq analysis to assess the impact of LPS stimulation on ACC isoform expression, we found that treatment for 6 hours with LPS increased expression of both *Acaca* and *Acacb* (fig. S2A). This was associated with a trend toward increased ACC protein in LPS-treated BMDMs (fig. S2B). We therefore assessed the ability of BMDMs from ACC$^{\Delta LysM}$ mice to polarize in response to proinflammatory stimuli in vitro (Fig. 2A). We found that, compared to flox controls, induction of the proinflammatory genes *Il6*, *Il1b*, *Nos2*, *Il12a*, and *Il12b* was attenuated in ACC$^{\Delta LysM}$ BMDMs after treatment with LPS (Fig. 2B). We also observed a small but significant attenuation of LPS-induced expression of the inflammatory surface marker *Cd80*, but not *Cd86*, in response to LPS (fig. S2C). Furthermore, ACC$^{\Delta LysM}$ BMDMs treated with LPS secreted significantly less IL-6 protein into the supernatant (Fig. 2C). ACC$^{\Delta LysM}$ BMDMs also demonstrated deficiencies in proteasome-dependent cytokine production, because they released less IL-1β in response to LPS priming followed by NLRP3 activation through exposure to cholesterol crystals (*29*, *30*) (Fig. 2D). To extend our findings to human macrophages, we first assessed the impact of inflammatory stimulation on *ACC* isoform expression in human monocyte-derived macrophages (hMDMs). We observed no changes in *ACACA* or *ACACB* expression (fig. S3A) or ACC protein (fig. S3B) at 6 hours in response to LPS, while at 18 hours LPS induced a significant increase in *ACACB* expression (fig. S3C). We treated hMDMs with the pharmacological ACC inhibitor firsocostat to assess the role of ACC in the LPS response of human macrophages. Compared to vehicle-treated controls, hMDMs treated with firsocostat had significantly decreased expression of *IL6* and *IL1B* after stimulation with LPS for 6 hours (Fig. 2E), suggesting a similar role for ACC in the inflammatory response in both mouse and human macrophages. The blunted inflammatory response in ACC$^{\Delta LysM}$ BMDMs could also be extended to Gram-positive (TLR2)–dependent activation of the proinflammatory response, as stimulation with lipoteichoic acid (LTA), a TLR2 ligand derived from the Gram-positive bacterium *Staphylococcus aureus*, also demonstrated significantly decreased expression of *Il1b*, *Il6*, and *Nos2* in BMDMs from ACC$^{\Delta LysM}$ mice (Fig. 2F). We did not observe differences in the induction of surface markers *Cd80* and *Cd86* (fig. S2D). Furthermore, ACC$^{\Delta LysM}$ macrophages stimulated with LTA secreted

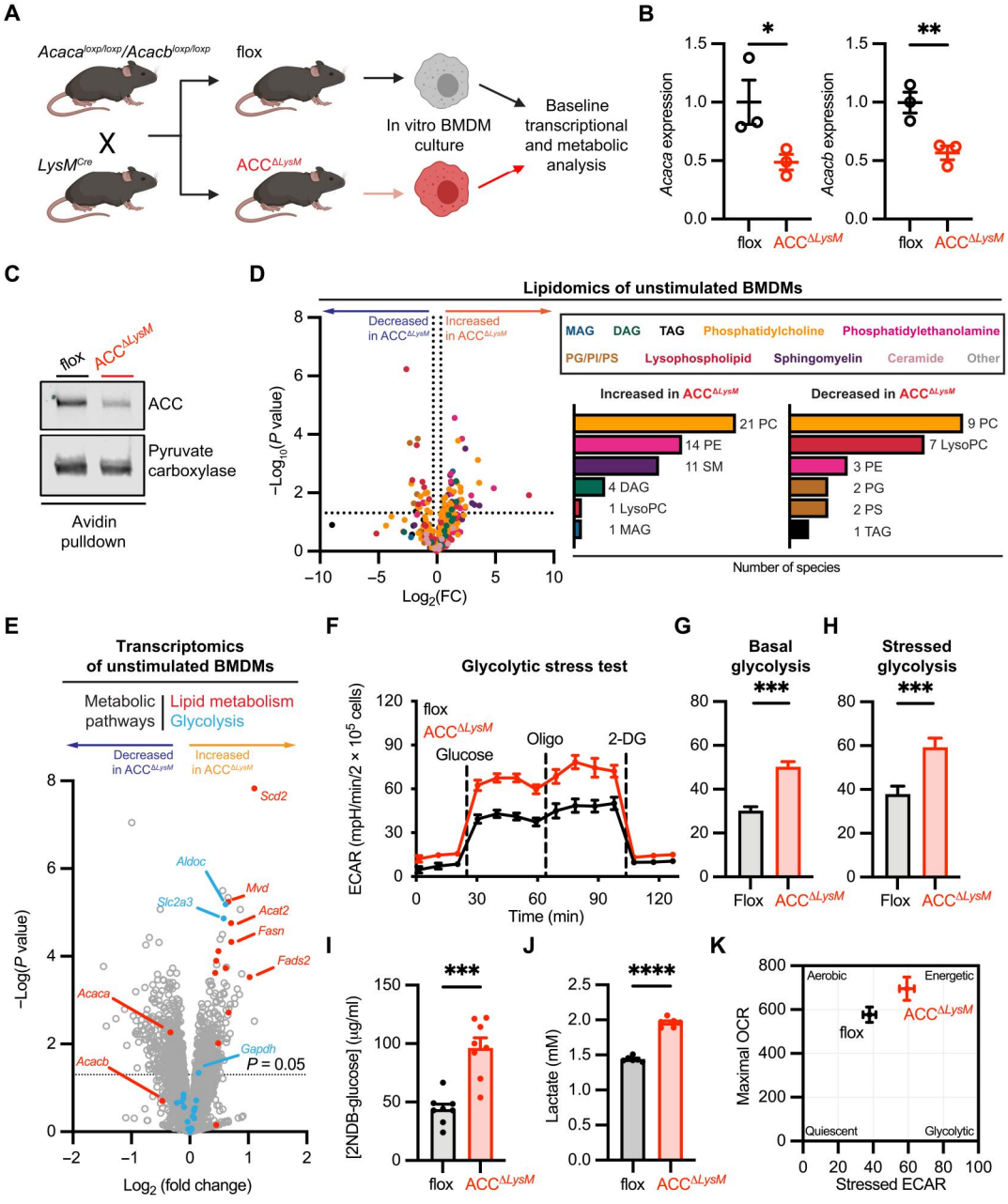

Fig. 1. Deletion of ACC shifts macrophage metabolism to hyperenergetic, glycolytic state. (**A**) Mice carrying loxP-flanked alleles of *Acaca* and *Acacb* were crossed with *LysM*^{Cre} mice to generate mice with a myeloid-specific deletion of ACC (ACC$^{\Delta LysM}$). (**B**) Relative mRNA levels of *Acaca* and *Acacb* in BMDMs from flox or ACC$^{\Delta LysM}$ mice ($n = 3$). (**C**) Representative immunoblot of ACC after avidin pulldown of biotin-containing proteins from flox or ACC$^{\Delta LysM}$ BMDMs. Pyruvate carboxylase was used as a loading control. (**D**) Relative levels of lipid species in unstimulated BMDMs from flox and ACC$^{\Delta LysM}$ mice. Left: Number of lipids increased [fold change (FC) > 1.25] in unstimulated BMDMs from ACC$^{\Delta LysM}$ mice. Right: Number of lipids decreased (fold change < 1.25) in BMDMs from ACC$^{\Delta LysM}$ mice ($n = 6$). TAG, triacylglycerol; PE, phosphatidylethanolamine; PC, phosphatidylcholine; MAG, monoacylglycerol; SM, sphingomyelin; PS, phosphatidylserine; PI, phosphatidylinositol; LysoPC, lysophosphatidylcholine; DAG, diacylglycerol. (**E**) Volcano plot of RNA-seq from unstimulated flox or ACC$^{\Delta LysM}$ BMDMs ($n = 4$). (**F**) Glycolytic stress test of flox or ACC$^{\Delta LysM}$ BMDMs ($n = 5$). 2-DG, 2-deoxyglucose. (**G**) Basal glycolytic rate of flox or ACC$^{\Delta LysM}$ BMDMs ($n = 5$). (**H**) Stressed glycolytic rate of flox or ACC$^{\Delta LysM}$ BMDMs ($n = 5$). (**I**) Six-hour 2NDB-glucose uptake in flox or ACC$^{\Delta LysM}$ BMDMs ($n = 8$). (**J**) Lactate levels in supernatant of unstimulated flox or ACC$^{\Delta LysM}$ BMDMs after 6 hours ($n = 6$). (**K**) Bioenergetics phenogram reveals a shift to a more energetic phenotype in ACC$^{\Delta LysM}$ BMDMs. Data are represented as means ± SEM. Significance determined by one-tailed Welch's *t* test (B and G to J) or two-tailed Student's *t* test (D). *$P < 0.05$, **$P < 0.01$, and ***$P < 0.001$. (A) Created using BioRender.com. See also fig. S1, related to Fig. 1.

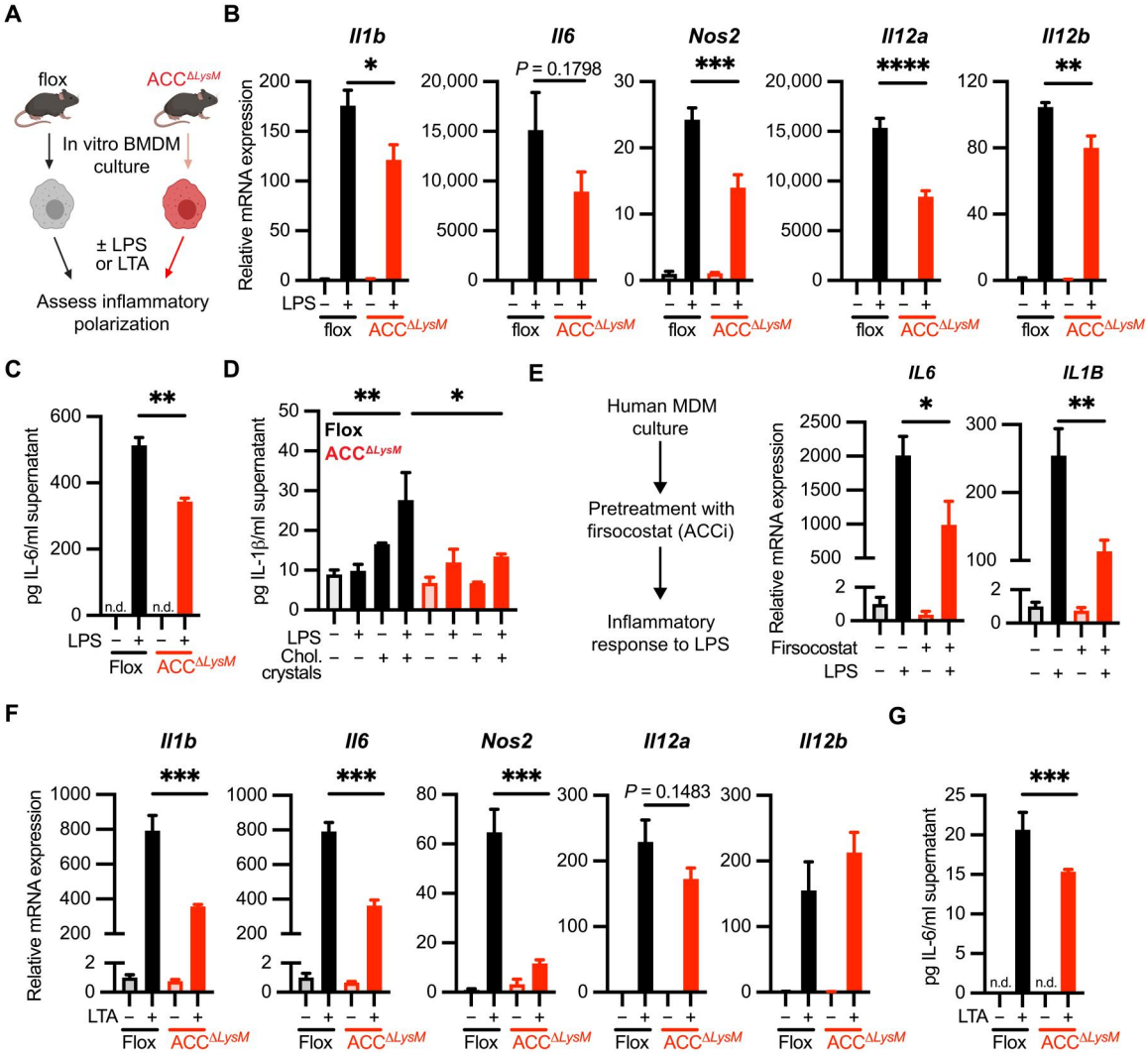

Fig. 2. ACC regulates TLR-induced macrophage polarization. (**A**) Schematic of M1 polarization of flox and ACC$^{\Delta LysM}$ BMDMs. (**B**) Relative mRNA expression of *Il1b*, *Il6*, *Nos2*, *Il12a*, and *Il12b* genes in flox or ACC$^{\Delta LysM}$ BMDMs stimulated for 6 hours with LPS (100 ng/ml) ($n = 4$). (**C**) Levels of IL-6 protein in supernatant of flox or ACC BMDMs stimulated with LPS for 18 hours ($n = 4$). n.d., not detected. (**D**) Levels of IL-1β protein in supernatant of flox or ACC BMDMs stimulated with LPS for 4 hours followed by cholesterol crystals for 18 hours ($n = 3$ to 4). (**E**) Relative mRNA expression of *IL1B* and *Il6* in human MDMs pretreated with the ACC inhibitor (ACCi) firsocostat (10 μM) before stimulation with LPS (100 ng/ml) for 6 hours ($n = 4$ replicates). (**F**) Relative mRNA expression of *Il1b*, *Il6*, *Nos2*, *Il12a*, and *Il12b* genes in flox or ACC$^{\Delta LysM}$ BMDMs stimulated for 6 hours with LTA (1 μg/ml) ($n = 4$). (**G**) Levels of IL-6 protein in supernatant of flox or ACC$^{\Delta LysM}$ BMDMs stimulated with LTA for 18 hours ($n = 4$). Data are represented as means ± SEM. Significance determined by one-way analysis of variance (ANOVA) (B and D to F) or one-tailed Welch's *t* test (C and G). *$P < 0.05$, **$P < 0.01$, ***$P < 0.001$, and ****$P < 0.0001$. (A) Created using BioRender.com. See also figs. S2 and S3, related to Fig. 2.

significantly lower levels of IL-6 into the supernatant compared with BMDMs from flox controls (Fig. 2G).

To assess whether this defect in inflammatory polarization was due to an alteration in intracellular signaling, we assessed activation of the extracellular signal–regulated kinase (ERK) and nuclear factor κB (NFκB) pathways, which are induced downstream of TLRs and required for the inflammatory response (*31*, *32*). In response to LPS stimulation, BMDMs from ACC$^{\Delta LysM}$ mice showed similar levels of phosphorylated ERK1/2 at T202/Y204 as flox controls (fig. S2E). This was also the case with phosphorylation of p65 NFκB at the activating S536 (fig. S2F). LPS stimulation also induced similar levels of p65 NFκB nuclear translocation in flox and ACC$^{\Delta LysM}$ BMDMs (fig. S2G). These data suggest that the blunted inflammatory response in ACC-deficient macrophages was not due to a defect in TLR-activated intracellular signaling.

ACC-deficient macrophages have an impaired transcriptional response to LPS in vitro

To investigate the mechanisms underlying the attenuation of LPS-induced inflammation, we profiled the transcriptional landscape of control ACC$^{\Delta LysM}$ BMDMs that were stimulated for 6 hours with LPS using RNA-seq (Fig. 3A). Differential gene expression analysis of LPS-stimulated flox and ACC$^{\Delta LysM}$ BMDMs identified more than 8000 genes regulated in response to LPS, with 166 uniquely up-regulated and 261 uniquely down-regulated transcripts in ACC$^{\Delta LysM}$ BMDMs (Fig. 3B). We used the Enrichr gene set enrichment tool

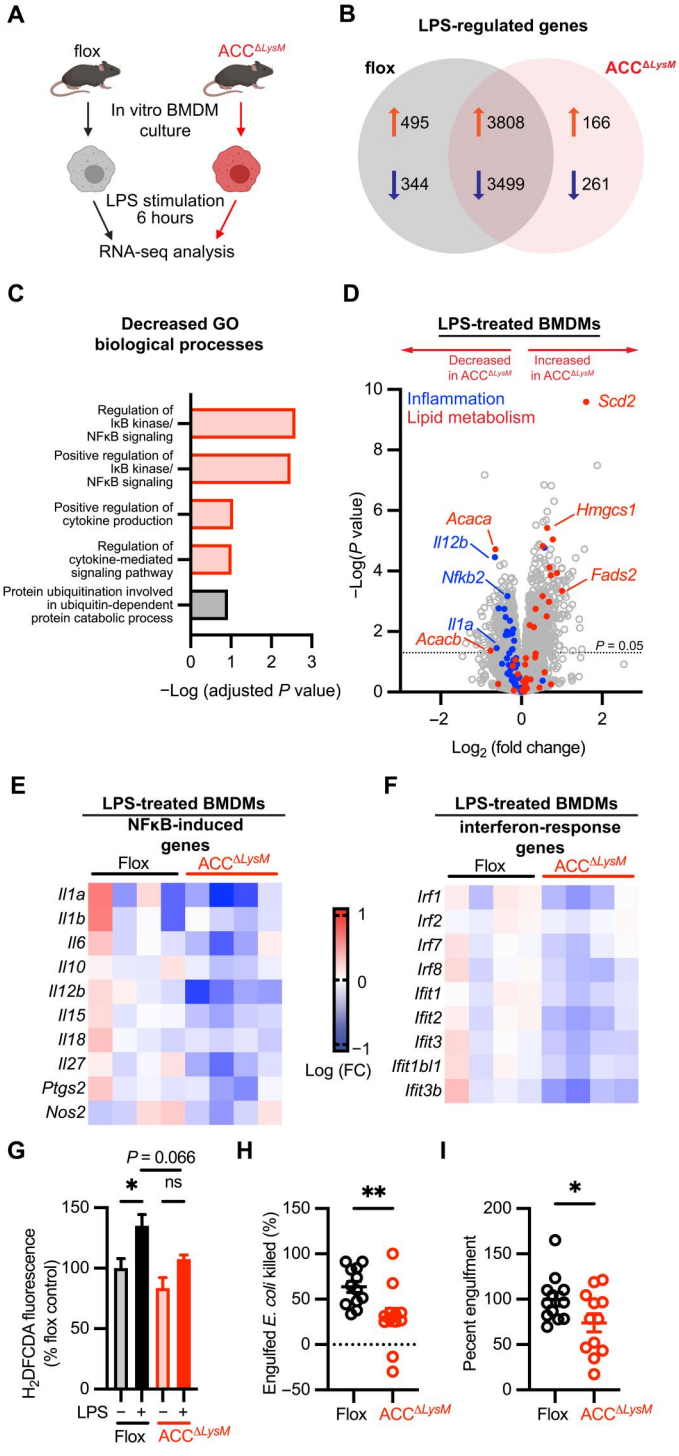

Fig. 3. ACC deficiency inhibits LPS-induced macrophage polarization and effector function. (**A**) Schematic showing experimental design of RNA-seq experiment from flox or ACC$^{\Delta LysM}$ BMDMs at baseline or after stimulation with LPS (100 ng/ml) for 6 hours. (**B**) Venn diagram showing number of genes uniquely regulated in flox or ACC$^{\Delta LysM}$ BMDMs stimulated with LPS and number of commonly regulated genes. (**C**) GO of genes with decreased expression [$-\log_2$ (fold change), $P < 0.05$)]. Processes related to inflammation highlighted in red. (**D**) Volcano plot showing relative gene expression of genes in LPS-stimulated ACC$^{\Delta LysM}$ BMDMs compared with LPS-stimulated flox controls. Blue circles represent genes related to the inflammatory response, and red circles represent lipid metabolism genes. (**E**) Heatmap showing relative expression of NFκB-induced genes in LPS-stimulated flox and ACC$^{\Delta LysM}$ BMDMs. (**F**) Heatmap showing relative expression of interferon-responsive genes in LPS-stimulated flox and ACC$^{\Delta LysM}$ BMDMs. (**G**) Relative H_2DFCDA fluorescence in flox or ACC$^{\Delta LysM}$ BMDMs stimulated with LPS for 6 hours ($n = 8$). ns, not significant. (**H**) Fraction of engulfed *E. coli* killed by BMDMs 2 hours after engulfment ($n = 12$). (**I**) Percent engulfment of *E. coli* by flox or ACC$^{\Delta LysM}$ BMDMs after 30 min ($n = 12$). Data are represented as means ± SEM. Significance determined by one-way ANOVA (G) or one-tailed Welch's *t* test (H and I). $^*P < 0.05$ and $^{**}P < 0.01$. (A) Created using BioRender.com.

(*33*, *34*) to assess the GO biological processes associated with down-regulated genes in LPS-stimulated ACC$^{\Delta LysM}$ BMDMs compared with LPS-stimulated flox BMDMs. Analysis of the significantly decreased genes identified pathways including "regulation of IκB kinase/NF-κB signaling," "positive regulation of IκB kinase/NF-κB signaling," "positive regulation of cytokine production," and "regulation of cytokine-mediated signaling pathway" among the decreased biological processes (Fig. 3C). Relative to LPS-stimulated flox control cells, BMDMs from ACC$^{\Delta LysM}$ mice showed an overall decrease in expression of genes associated with the inflammatory response, while genes related to lipid metabolism were significantly increased (*Scd2*, *Fads2*, and *Hmgcs1*) (Fig. 3D). Further analysis revealed a common trend in decreased expression of cytokines and other proinflammatory proteins induced in response to NFκB (Fig. 3E) and interferon-induced genes (Fig. 3F).

We then assessed the functional consequences of the impaired inflammatory response in ACC-deficient BMDMs. Generation of reactive oxygen species (ROS) is critical for pathogen destruction by macrophages (*35*). While LPS stimulation significantly increased levels of ROS in control BMDMs, the accumulation of ROS was blunted in ACC-deficient BMDMs (Fig. 3G). We then used an in vitro bacterial killing assay to assess whether deletion of ACC affects macrophage bactericidal capacity. Compared to control cells, ACC-deficient BMDMs killed a significantly lower percentage of engulfed *Escherichia coli* after 2 hours (Fig. 3H) and demonstrated significant defect in bacterial engulfment (Fig. 3I). Together, these data demonstrate that ACC is a central regulator of the transcriptional and functional aspects of the macrophage immune response.

ACC is dispensable for in vitro polarization in response to IL-4

To determine whether ACC plays a role in activation of macrophages to alternative stimuli, we examined IL-4–driven macrophage polarization in $ACC^{\Delta LysM}$ BMDMs (Fig. 4A). In contrast to LPS stimulation, treatment with IL-4 did not alter the expression of ACC isoforms in either mouse (fig. S4A) or human (fig. S3, A to D) macrophages. In response to IL-4 treatment, $ACC^{\Delta LysM}$ BMDMs showed no difference in the transcriptional up-regulation of the IL-4–responsive genes *Arg1*, *Chil3*, *Mrc1*, and *Retnla* compared to flox controls (Fig. 4B). This was associated with similar levels of the phosphorylation of signal transducer and activator of transcription 6 (STAT6) at tyrosine-641 and arginase, 6 hours after IL-4 stimulation (Fig. 4C and fig. S4B). The transition from the induction of inflammation to resolution has been proposed to involve phenotypic switching of highly plastic infiltrating macrophages. Therefore, we assessed the ability of M1-polarized $ACC^{\Delta LysM}$ BMDMs to repolarize in response to subsequent IL-4–induced M2 polarization (Fig. 4D). We found that $ACC^{\Delta LysM}$ macrophages, which had been previously stimulated with LPS for 24 hours, responded similarly to repolarization with IL-4 with respect to the up-regulation of *Arg1*, *Mrc1*, and *Retnla*, compared to BMDMs isolated from flox controls (Fig. 4D). Together, these data show that decreased ACC expression has neither an impact expression of typical IL-4–responsive genes nor does it affect repolarization from LPS-polarized macrophages, demonstrating that the defect in stimulus-induced gene expression observed in $ACC^{\Delta LysM}$ macrophages is specific for proinflammatory stimulation.

ACC is required for the TLR-induced switch to glycolysis in macrophages

The baseline perturbation of macrophage metabolism observed in $ACC^{\Delta LysM}$ BMDMs prompted us to investigate the impact of ACC knockdown on stimulation-dependent rewiring of macrophage metabolism. TLR stimulation results in a rapid reprogramming of macrophage metabolism, which is required for inflammatory gene transcription, cytokine production, and pathogen destruction (*2*, *3*, *36*). An increase in aerobic glycolysis and a concomitant decrease in oxidative phosphorylation are hallmarks of LPS-polarized macrophages (*3*). Our data show that ACC deficiency shifts macrophages to a hyperglycolytic bioenergetic state (Fig. 1). To assess the glycolytic rate of ACC-deficient BMDMs in response to the TLR4 ligand LPS, we measured extracellular acidification rate (ECAR) for 6 hours after LPS stimulation in control and $ACC^{\Delta LysM}$ macrophages.

Stimulation with LPS resulted in an increase in glycolytic rate within the first hour after treatment in BMDMs from flox control mice (early ΔLPS; Fig. 5A, left). However, the early LPS-dependent increase in glycolytic rate was less pronounced in ACC-deficient BMDMs (early ΔLPS; Fig. 5A, right), indicated by lower early LPS-induced change in ECAR compared with flox controls (Fig. 5B). Differences were less pronounced at 6 hours. To assess whether this defect in LPS-induced metabolic polarization was specific to the early increase in glycolysis, we polarized macrophages with LPS for 16 hours, a time point at which LPS induces suppression of mitochondrial oxidative phosphorylation, and assessed glycolytic rate, glucose uptake, and mitochondrial function (Fig. 5C). Glycolytic stress tests of BMDMs after 16 hours of stimulation with LPS revealed a significantly lower increase in stressed ECAR in ACC-deficient BMDMs (Fig. 5, D and E), and a similar response was seen after 16 hours of stimulation with the TLR2 ligand LTA (fig. S5, A and B). Furthermore, while stimulation with LPS increased glucose uptake in control BMDMs, there was no further increase in glucose uptake in response to LPS in ACC-deficient macrophages (Fig. 5F). Assessing the mechanism behind the differences in basal and LPS-induced glycolysis, we found that $ACC^{\Delta LysM}$ BMDMs had increased levels of cell surface–associated GLUT1 compared to flox controls, as assessed by cell surface biotinylation assay (fig. S5, C and D). However, while LPS increased the levels of GLUT1 associated with the cell surface in control macrophages, this response was not evident in $ACC^{\Delta LysM}$ BMDMs stimulated with LPS (fig. S5, C and D). Together, these data suggest that by increasing the baseline rate of glucose uptake, decreased levels of ACC in macrophages set an upper limit of glycolytic rate in response to LPS.

We then asked whether ACC played a role in other aspects of LPS-induced metabolic rewiring. Succinate dehydrogenase (SDH) activity, which has been reported to increase in response to LPS (*37*), was similar between control and $ACC^{\Delta LysM}$ BMDMs under both basal and LPS-stimulated conditions (fig. S5E). We also saw similar levels of reduced (fig. S5F) and oxidized NADPH (fig. S5G) and a similar increased $NADP^+$/NADPH ratio (fig. S5H) in response to LPS in control and $ACC^{\Delta LysM}$ BMDMs. We also assessed the impact of ACC knockdown on LPS-induced decrease in mitochondrial oxygen consumption by mitochondrial stress test (Fig. 5G). Compared to flox controls, BMDMs from $ACC^{\Delta LysM}$ mice demonstrated a similar decrease in maximal OCR in response to LPS treatment (Fig. 5H), suggesting that ACC is critical for the LPS-dependent switch to aerobic glycolysis, but not the later suppression of mitochondrial function. Transcriptional analysis of genes encoding tricarboxylic acid (TCA) cycle–related enzymes revealed modest increase in levels of *Idh1* (encoding isocitrate dehydrogenase) and *Pck2* (encoding mitochondrial phosphoenolpyruvate carboxykinase) 6 hours after LPS stimulation in BMDMs with decreased levels of ACC (fig. S5I), but overall expression levels of TCA enzymes were similar between control and $ACC^{\Delta LysM}$ BMDMs. Stimulation with LPS or LTA also induced increases in extracellular lactate levels in both flox and $ACC^{\Delta LysM}$ BMDMs (fig. S5J).

Stimulus-dependent metabolic rewiring is essential not only for proinflammatory polarization but also for alternative activation by IL-4 (*4*); therefore, we assessed whether loss of ACC plays a role in the increase of mitochondrial oxygen consumption in response to

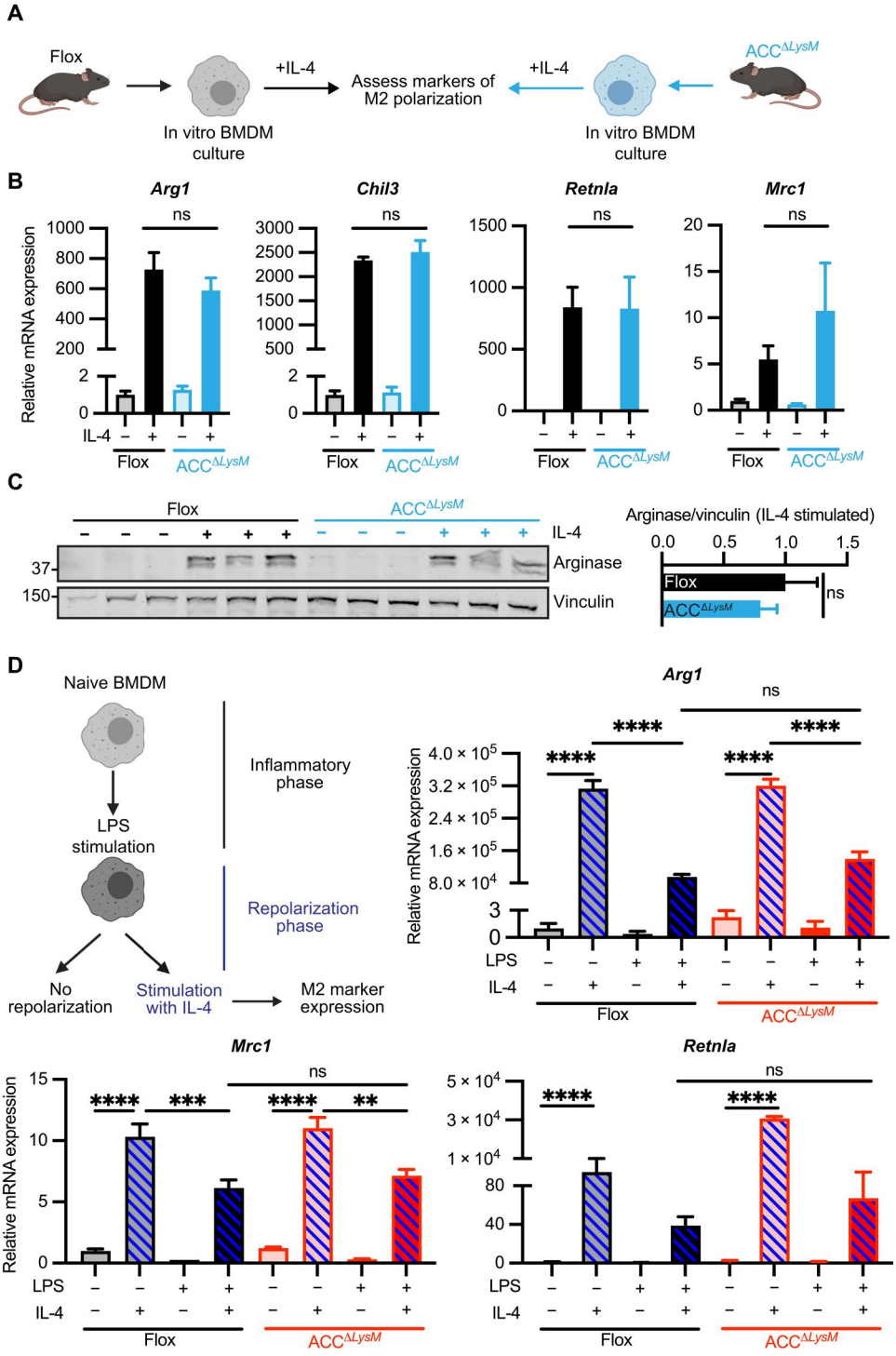

Fig. 4. ACC is dispensable for in vitro polarization in response to IL-4. (**A**) Schematic of M2 polarization of flox and ACC$^{\Delta LysM}$ BMDMs. (**B**) Relative mRNA expression of M2 marker genes *Arg1*, *Chil3*, *Mrc1*, and *Retnla* in flox or ACC$^{\Delta LysM}$ BMDMs stimulated with vehicle or IL-4 (10 ng/ml) for 6 hours ($n = 4$). (**C**) Whole-cell immunoblot analysis of arginase protein levels in flox or ACC$^{\Delta LysM}$ BMDMs stimulated with IL-4 (10 ng/ml) for 6 hours ($n = 3$ mice per group). Vinculin was used as a loading control. (**D**) Flox or ACC$^{\Delta LysM}$ BMDMs were polarized with LPS (100 ng/ml) for 24 hours before repolarization with IL-4 (10 ng/ml) for an additional 24 hours, and expression of *Arg1*, *Mrc1*, and *Retnla* was measured ($n = 4$). Data are represented as means ± SEM. Significance determined by one-way ANOVA (B and D) or one-tailed Welch's *t* test (C). $^{**}P < 0.01$. $^{***}P < 0.001$, and $^{****}P < 0.0001$. (A and D) Created using BioRender.com. See also figs. S3 and S4, related to Fig. 4.

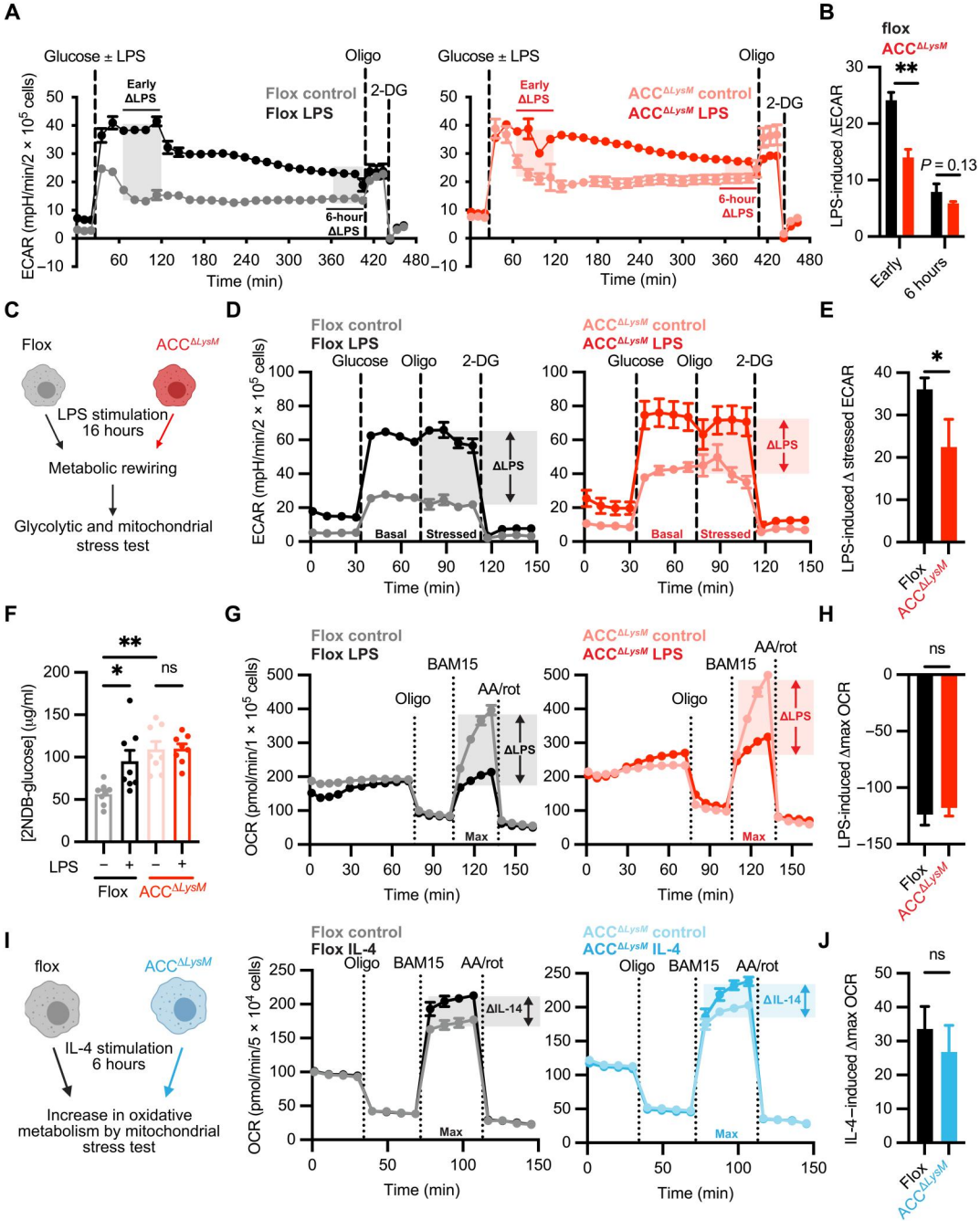

Fig. 5. ACC in macrophages regulates the TLR-induced increase in aerobic glycolysis. (**A**) BMDMs from flox or ACC$^{\Delta LysM}$ mice were stimulated with glucose ± LPS (100 ng/ml), and glycolytic rate was assessed by following ECAR for 6 hours before sequential stimulation with oligomycin and 2-deoxyglucose. The LPS-induced increase in ECAR approximately 30 min after LPS stimulation (early ΔECAR) and approximately 6 hours after LPS stimulation (6 hour ΔECAR) is represented with shaded areas ($n = 4$). (**B**) Quantification of LPS-induced ΔECAR in flox and ACC$^{\Delta LysM}$ BMDMs ($n = 4$). (**C**) Flox and ACC$^{\Delta LysM}$ BMDMs were stimulated with LPS for 16 hours before assessment of glycolytic rate, glucose uptake, and mitochondrial function. (**D**) Glycolytic stress test of flox or ACC$^{\Delta LysM}$ BMDMs after stimulation with LPS ($n = 5$). (**E**) Quantification of LPS-induced change in stressed ECAR in flox or ACC$^{\Delta LysM}$ BMDMs after 16 hours of stimulation with LPS ($n = 5$). (**F**) 2NDB-glucose uptake in flox or ACC$^{\Delta LysM}$ BMDMs stimulated with LPS ($n = 8$). (**G**) Flox or ACC$^{\Delta LysM}$ BMDMs were stimulated with LPS for 16 hours, and OCR was measured ($n = 5$ to 6). (**H**) LPS-induced change in maximal OCR in flox or ACC$^{\Delta LysM}$ BMDMs ($n = 5$ to 6). (**I**) Flox or ACC$^{\Delta LysM}$ BMDMs were stimulated with IL-4 for 6 hours before mitochondrial stress test ($n = 6$). (**J**) Quantification of IL-4–induced change in maximal OCR ($n = 6$). Data represented as means ± SEM. Significance determined by one-tailed Welch's t test (B, E, H, and J) or one-way ANOVA (F). *$P < 0.05$ and **$P < 0.01$. (C and I) Created using BioRender.com. See also fig. S5, related to Fig. 5.

IL-4 stimulation (Fig. 5I). In both flox and ACC$^{\Delta LysM}$ BMDMs, treatment with IL-4 resulted in an increase in maximum OCR (Fig. 5J), suggesting that loss of ACC does not impair the bioenergetic changes required for IL-4–dependent activation. Together, these data demonstrate that loss of ACC specifically impairs the early rewiring of glucose metabolism in response to proinflammatory stimulation, highlighting an unexpected role for ACC as a central regulator of metabolic control of macrophage inflammation.

ACC is required for LPS-induced modification of the macrophage lipidome

Activation of the de novo lipogenesis and cholesterol biosynthesis pathways is crucial for the inflammatory response to LPS (*8*, *9*, *38*, *39*). Given the role of ACC in lipid synthesis and based on our observation that loss of ACC blunts LPS-induced switch to glycolytic metabolism, we tested whether ACC is required for LPS-induced redistribution of lipid metabolism as well.

Using an unbiased liquid chromatography–mass spectrometry (LC-MS)–based lipidomics approach, we assessed the impact of ACC deficiency on macrophage lipid metabolism in response to LPS stimulation (Fig. 6A). We examined the role for ACC in LPS-induced modulation of lipid metabolism in the context of full culture medium supplementation, mirroring the conditions of our bioenergetics analyses. In comparison to unstimulated cells, LPS stimulation of BMDMs from control mice for 6 hours resulted in redistribution of lipid species across lipid classes (Fig. 6B, left), with 65 lipid species increased in abundance and 30 species decreased in abundance after LPS stimulation (|fold change| > 1.25; $P < 0.05$), representing changes in approximately 23% of total detected species (420). Strikingly, in comparison to control cells, LPS treatment resulted in regulation of only 36 total species (17 increased and 19 decreased) in ACC$^{\Delta LysM}$ BMDMs (Fig. 6B, right). Examination of the 65 species increased by LPS in control macrophages revealed that LPS-driven enrichment of phosphatidylcholine and phosphatidylethanolamine species was attenuated in ACC-deficient BMDMs (Fig. 6, C and D). We also observed attenuated accumulation of diacylglycerol, sphingomyelin, and ceramide species in ACC-deficient BMDMs treated with LPS (fig. S6, E and F).

LPS also stimulates the release of arachidonic acid from arachidonoyl-containing phospholipids by phospholipases, which is then converted to proinflammatory eicosanoids. Levels of the arachidonoyl-containing phospholipid 1-palmitoyl-2-arachidonoyl-*sn*-glycero-3-phosphocholine (16:0/20:4, PC/PAPC) were significantly decreased in control macrophages after LPS stimulation, while in ACC-deficient macrophages, levels of PAPC trended lower in response to LPS but did not reach statistical significance (Fig. 6E). We then considered how loss of ACC might affect other lipid metabolism–related processes stimulated by LPS. Acetyl-CoA is a common substrate for both de novo lipogenesis and cholesterol biosynthesis (Fig. 6F), and because expression levels of enzymes in the sterol biosynthesis pathway were increased in LPS-stimulated ACC$^{\Delta LysM}$ BMDMs (fig. S4, B and C), we assessed free cholesterol levels by LC-MS. Unstimulated ACC-deficient BMDMs showed a trend toward an increase in cholesterol levels compared with flox controls (Fig. 6G). However, while LPS treatment significantly increased cholesterol levels in control macrophages, we observed no changes in cholesterol levels in ACC$^{\Delta LysM}$ BMDMs upon LPS stimulation (Fig. 6G).

Transcriptional analysis using RNA-seq revealed that induction of genes associated with the de novo lipogenesis and cholesterol biosynthesis pathways was even more pronounced in LPS-stimulated ACC$^{\Delta LysM}$ BMDMs compared to flox controls (fig. S6, A and B). This was associated with slightly increased baseline expression levels of *Srebf1* and *Srebf2*, transcription factors that control lipid metabolism (fig. S6C). *Nr1h3* (encoding LXRα) and *Nr1h2* (encoding LXRβ) expression were similar between genotypes at baseline and similarly induced after LPS treatment (fig. S6C). We confirmed induction of genes involved in cholesterol synthesis by qPCR (fig. S6D). When we assessed accumulation of ^{14}C-labeled acetate into the lipid-soluble fraction of flox and ACC$^{\Delta LysM}$ macrophages, we observed a pattern suggestive of lower incorporation of labeled acetate in ACC$^{\Delta LysM}$ macrophages under control conditions after 6 hours (fig. S6G). However, when we first stimulated BMDMs with LPS for 4 hours before exposing them to ^{14}C-acetate for a 2-hour period, we found that the fold increase in ^{14}C-acetate incorporation rate induced by LPS was blunted in ACC$^{\Delta LysM}$ macrophages (fig. S6H). Both sterols and fatty acid–containing lipids partitioned into the lipid-soluble layer and can be made from acetate (Fig. 6F). Because ACC$^{\Delta LysM}$ macrophages demonstrate an up-regulation of genes involved in cholesterol synthesis (fig. S6, B and D), it is possible that, given that we observed a trend toward increased cholesterol sterol levels in ACC$^{\Delta LysM}$ macrophages (Fig. 6G), the effect of decreasing ACC levels is partially masked using this method, where all lipid-soluble species are measured together.

Together, these data reveal that rapid rewiring of the macrophage lipidome that occurs within 6 hours in response to LPS is dependent on ACC. Macrophages with decreased levels of ACC demonstrate profound deficiencies in lipidomic reprogramming, compensated by increased expression of lipogenic genes, which is critical for this component of the proinflammatory metabolic response.

Genetic or pharmacologic manipulation of ACC1 and ACC2 attenuates LPS-induced peritoneal inflammation but exacerbates bacterial peritonitis in mice

We then sought to examine whether decreased ACC affected the inflammatory response in vivo. To this end, we subjected mice to a model of LPS-induced systemic inflammation (*40*), in which onset of symptoms occurs between 6 and 24 hours and persists for 48 to 72 hours after LPS administration (Fig. 7A). ACC$^{\Delta LysM}$ mice responded significantly better to LPS-induced peritonitis, with an increased median survival time (68 hours), compared with flox control (56 hours) (Fig. 7B). The improved survival in response to LPS was associated with significantly lower levels of the proinflammatory cytokines IL-6 in the peritoneal lavage fluid (Fig. 7C) and IL-1β in the plasma (Fig. 6D) in ACC$^{\Delta LysM}$ mice 6 hours after LPS administration. Furthermore, analysis of mRNA of peritoneal exudate cells isolated 6 hours after LPS administration revealed trends of lower expression in proinflammatory genes *Il6*, *Il1b*, *Il12a*, *Il10*, and *Ifng* in cells isolated from ACC$^{\Delta LysM}$ mice compared with flox controls (Fig. 7E).

Pharmacological inhibitors of ACC are in clinical development for metabolic disorders including nonalcoholic steatohepatitis and several cancers (*41*–*43*). Given that ACC$^{\Delta LysM}$ mice showed an attenuated inflammatory response 6 hours after induction of LPS-induced peritonitis, we examined whether pharmacological inhibition of ACC would also blunt the response to LPS. To this end, we treated mice with the ACC inhibitor firsocostat (*41*) simultaneously

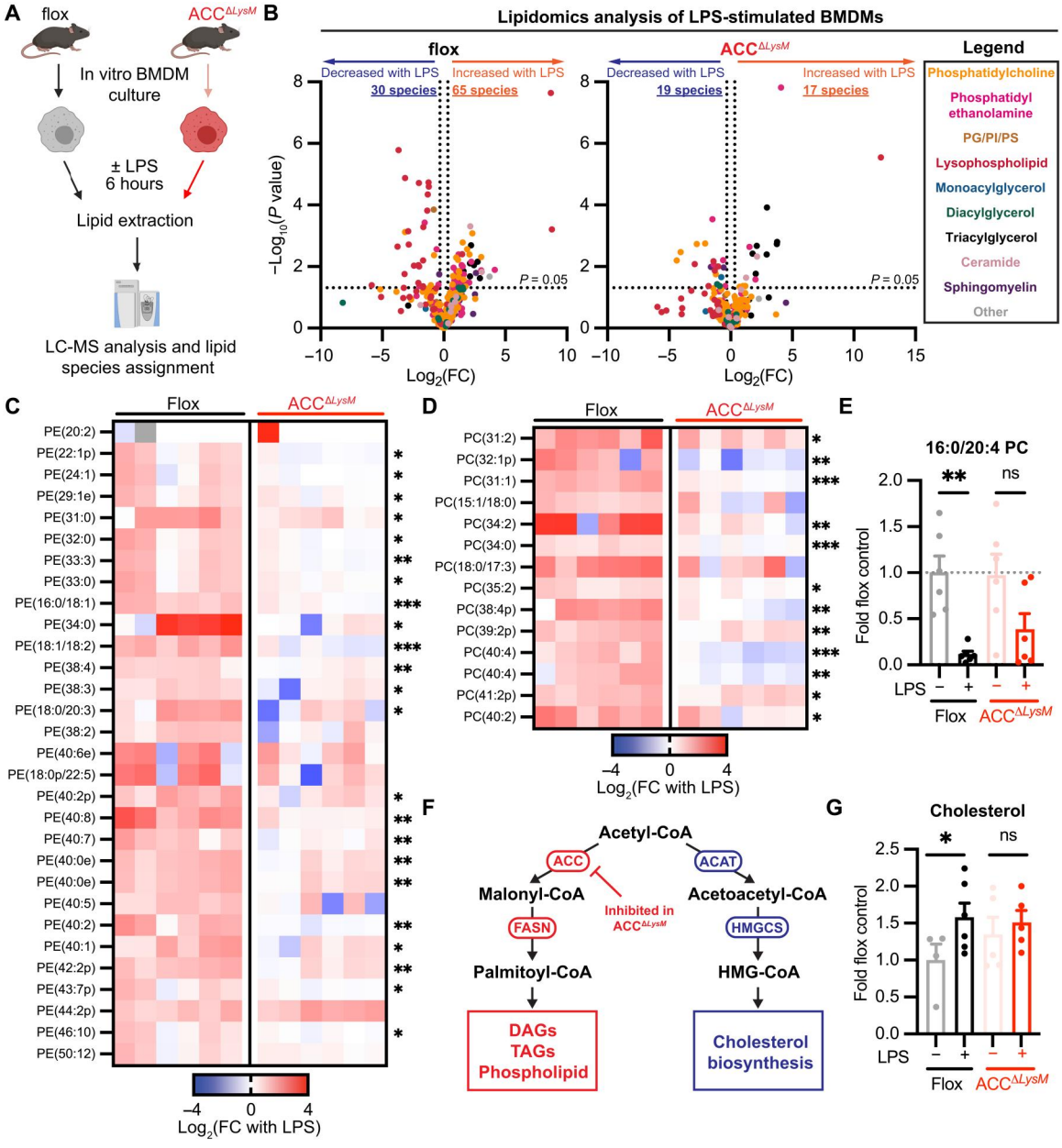

Fig. 6. ACC is required for LPS-induced rewiring of the macrophage lipidome. (**A**) Schematic of lipidomic analysis workflow from flox or ACC$^{\Delta LysM}$ BMDMs stimulated with LPS (100 ng/ml) for 6 hours. (**B**) Volcano plots representing fold change of lipid species abundance in flox or ACC$^{\Delta LysM}$ BMDMs stimulated with LPS (100 ng/ml) for 6 hours ($n = 6$). (**C**) Heatmap of significantly increased phosphatidylethanolamine (PE) species in LPS-stimulated flox and ACC$^{\Delta LysM}$ BMDMs, relative to respective unstimulated cells ($n = 6$). (**D**) Heatmap of significantly increased phosphatidylcholine (PC) species in LPS-stimulated flox and ACC$^{\Delta LysM}$ BMDMs relative to respective unstimulated cells ($n = 6$). (**E**) Levels of 16:0/20:4 phosphatidylcholine in flox or ACC$^{\Delta LysM}$ BMDMs stimulated with LPS (100 ng/ml) for 6 hours ($n = 6$). (**F**) Schematic showing fates of acetyl-CoA in the de novo lipogenesis and sterol biosynthesis pathways. (**G**) Levels of cholesterol in flox or ACC$^{\Delta LysM}$ BMDMs stimulated with LPS (100 ng/ml) for 6 hours ($n = 4$ to 6). Data are represented as means ± SEM (E and G). Significance determined by two-tailed Student's t test (C and D) or one-way ANOVA (E and G). *$P < 0.05$, **$P < 0.01$, and ***$P < 0.001$. (A) Created using BioRender.com. See also fig. S6, related to Fig. 6.

with the administration of LPS (Fig. 7F). Mice treated with firsocostat had significantly lower levels of IL-6 and IL-1β in the peritoneal lavage fluid (Fig. 7G) and lower levels of IL-1β in the plasma (Fig. 7H) at 6 hours after LPS administration compared with mice that received vehicle treatment. Furthermore, gene expression analysis of peritoneal exudate cells 6 hours after LPS injection revealed that transcript levels of cytokines including *Il6*, *Il18*, *Il12a*, and *Il12b* were significantly decreased or trending toward decreased in mice treated with firsocostat (Fig. 6I). We then assessed the impact of ACC inhibition in a clinically relevant model of bacterial peritonitis, where both activation of the inflammatory response and control of pathogen growth affect outcomes. We pretreated wild-type mice with firsocostat for 1 hour before intraperitoneal inoculation with *E. coli* O18ac:K1:H7 [approximately 9×10^6 colony-forming units

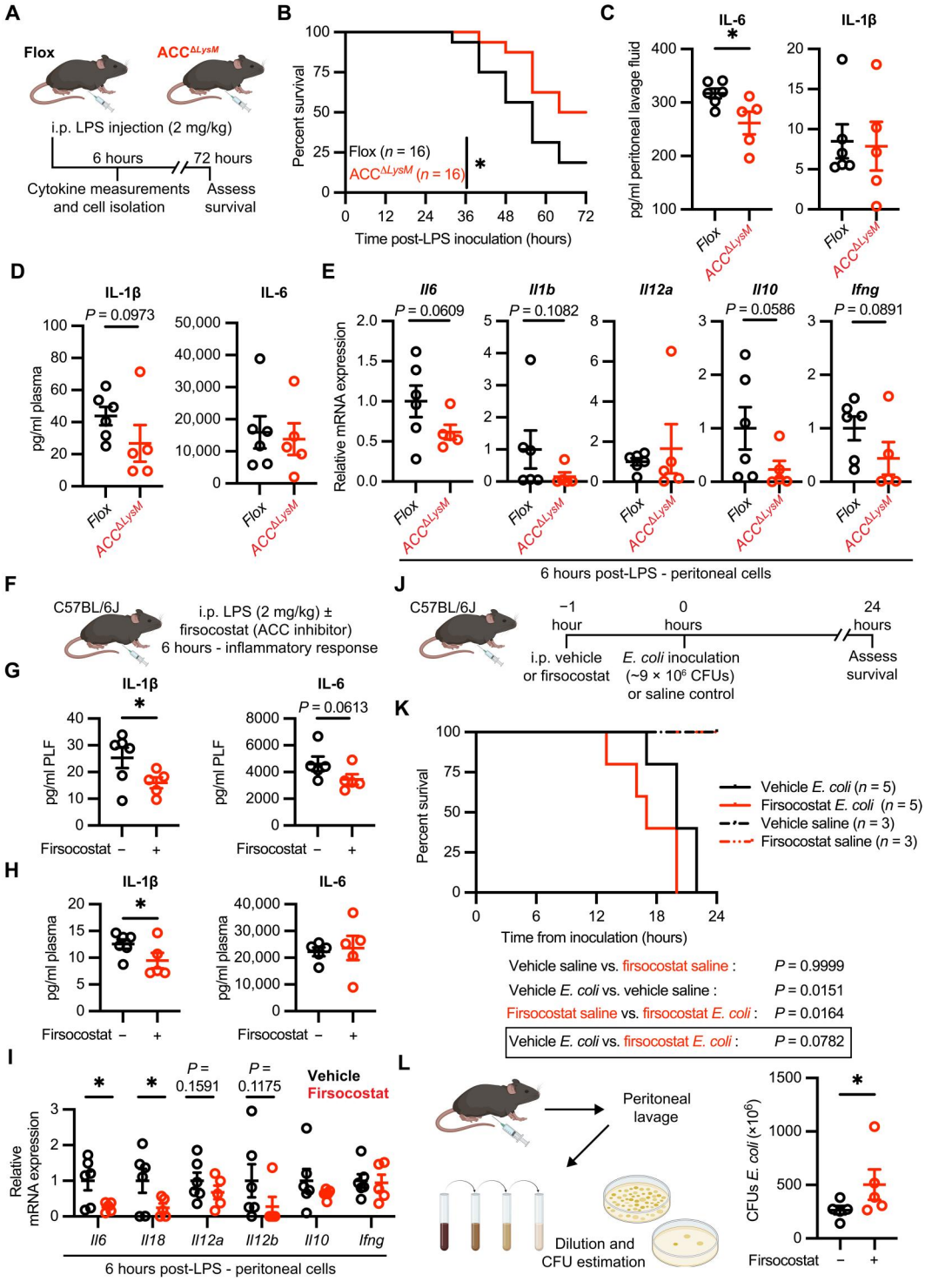

Fig. 7. Genetic or pharmacologic manipulation of ACC1 and ACC2 attenuates LPS-induced peritoneal inflammation but exacerbates bacterial peritonitis in mice. (**A**) Experimental schematic of LPS-induced model of systemic inflammation. (**B**) Survival curves of male flox or ACC$^{\Delta LysM}$ mice after intraperitoneal LPS administration (n = 16). (**C**) Peritoneal lavage cytokine levels 6 hours after LPS administration (n = 5 to 6). (**D**) Plasma cytokine levels 6 hours after LPS administration (n = 5 to 6). (**E**) Relative mRNA levels in peritoneal cells from flox or ACC$^{\Delta LysM}$ mice 6 hours after LPS (n = 5 to 6). (**F**) C57BL/6J mice were injected with LPS (2 mg/kg) and either DMSO control or firsocostat (25 mg/kg), and cytokines and peritoneal cell mRNA expression were measured at 6 hours. (**G**) Peritoneal lavage cytokine levels 6 hours after LPS (n = 5 to 6). (**H**) Plasma cytokine levels 6 hours after LPS (n = 5 to 6). (**I**) Relative mRNA levels in peritoneal cells isolated 6 hours after LPS administration (n = 5 to 6). For (G) to (I), one outlier in the firsocostat treatment group was removed (ROUT Q = 1%). (**J**) C57BL/6J mice were pretreated with firsocostat (25 mg/kg) before *E. coli* inoculation [~9 × 10^6 colony-forming units (CFUs) per mouse] or saline. (**K**) Survival of mice pretreated with control or firsocostat before *E. coli* inoculation or saline (saline, n = 3; *E. coli*, n = 5). (**L**) Peritoneal lavage of inoculated mice was serially diluted, and bacterial CFUs were estimated (n = 5). Data represented as means ± SEM. Significance determined by one-tailed Welch's t test (C to E and G to I), Mantel-Cox test (B and K), or one-tailed Mann-Whitney test (L). *P < 0.05 and **P < 0.01. (A, F, J, and L) Created using BioRender.com.

(CFUs) per mouse] or saline control and assessed survival (Fig. 7J). In the *E. coli* treatment group, mice treated with firsocostat had a shorter median survival time (17 hours) compared to controls (20 hours) (Fig. 7K). When we analyzed the bacterial burden in the peritoneal cavities of inoculated mice, we found that mice treated with firsocostat had significantly higher levels of *E. coli* in the peritoneal lavage compared to vehicle controls (Fig. 7L). Together, these data demonstrate that myeloid-specific deficiency or pharmacologic inhibition of ACC blunts the inflammatory response to LPS and innate immune functions of macrophages in vivo.

DISCUSSION

In response to insults such as infection or tissue damage, immune cells including macrophages must rapidly adapt their intracellular metabolism to mount an effective inflammatory response (*1*, *44*, *45*). Regulation of lipid metabolism is essential for both induction and resolution of the inflammatory response (*9*, *12*, *38*). A role for ACC, the committed step of de novo lipogenesis, has been implicated in regulation of some immune cell subtypes (*26*, *46*, *47*), but its role in myeloid cells remains unexplored. We generated a mouse model with a myeloid-specific knockdown of both ACC1 and ACC2 ($ACC^{\Delta LysM}$) and used transcriptional, functional, bioenergetics, and lipidomics approaches to assess the impact of decreased ACC levels on macrophage activation. We found that genetic knockdown or pharmacological inhibition of ACC attenuates LPS-induced inflammation in vivo, with reduced levels of proinflammatory cytokines 6 hours after induction of inflammation.

Our data show that decreased levels of ACC switch macrophages to a hyperglycolytic metabolism, with increased basal ECAR and glucose uptake. This mirrors the phenotype of isolated hepatocytes from liver-specific ACC1/ACC2 knockout mice, which demonstrated increased rates of glucose oxidation (*25*), and suggests a cell type–independent effect of ACC knockdown on regulation of glycolysis. Mechanistically, we identified a baseline increase in GLUT1 at the cell surface in $ACC^{\Delta LysM}$ macrophages, which, unlike flox controls, is not further increased upon LPS stimulation. In other cell types, GLUT1 trafficking to the plasma membrane has been shown to be related to cellular lipid metabolism. In adipocytes, glucose consumption via GLUT1 is related to association of GLUT1 with lipid rafts (*48*), which is enhanced in settings of glucose deprivation. In endothelial cells, the activity of vascular endothelial growth factor–B (VEGF-B) decreases cholesterol localization to the plasma membrane, which impairs GLUT1-dependent glucose metabolism (*49*). The importance of cholesterol for GLUT1 activity at the cell surface has also been demonstrated in multiple human cell types, as decreasing cholesterol levels by statin treatment decreased GLUT1 membrane localization (*50*, *51*). Here, we show that ACC knockdown in macrophages increases expression of cholesterol biosynthesis genes, with higher basal levels of cholesterol, which is not further increased in response to LPS stimulation, which may explain both the basal increase in GLUT1 membrane localization and the differences in glucose uptake and glycolytic rate in response to LPS.

We also observed baseline up-regulation of lipid synthesis pathway genes in ACC-deficient macrophages, demonstrating that the deletion of ACC upsets the baseline metabolic set point of macrophages. As discussed above, our findings of both increased basal glycolytic rate while reaching the same maximal glycolytic rate suggest that there is limited metabolic flexibility in macrophages with decreased levels of ACC. Because flexibility to increase glycolytic flux is essential for polarization of macrophages in response to inflammatory stimuli, the reduced flexibility of $ACC^{\Delta LysM}$ macrophages may be one contributing factor to the blunted inflammatory response we observed. However, other alterations in metabolism induced by LPS, such as suppression of mitochondrial oxygen consumption, changes in TCA cycle–associated gene expression, and increased SDH activity, were unaffected by ACC knockdown. Together, these findings demonstrate that, by shifting the bioenergetic set point to a hyperglycolytic state, decreased levels of ACC reduce the capacity of macrophages to enhance glycolytic rate in response to TLR activation, which results in attenuation of the inflammatory response.

Stimulus-induced metabolic reprogramming in macrophages is not limited to proinflammatory polarization: Enhancement of lipolysis and mitochondrial oxygen consumption is required for alternative "M2" activation (*4*, *52*), while polarization of macrophages to the redox-responsive "Mox" phenotype reroutes glucose consumption into the pentose phosphate pathway for NADPH production (*6*, *7*). However, we found that the IL-4–induced metabolic and transcriptional responses we evaluated were largely unaffected by ACC deletion, demonstrating that ACC deficiency impairs signal-specific macrophage polarization through selective perturbations in cellular metabolism.

In vitro, BMDMs from $ACC^{\Delta LysM}$ mice demonstrated an attenuated transcriptional response to polarization with inflammatory stimuli, which resulted in decreased secretion of proinflammatory cytokines and impaired proinflammatory effector function, including ROS production, bacterial engulfment, and pathogen killing. Recent work has demonstrated that the early LPS-stimulated induction of glycolysis activates ACLY, which uses citrate to generate acetyl-CoA for histone acetylation (*36*). The pharmacological inhibition of ACLY attenuated the LPS-induced inflammatory response in vitro and in an in vivo model of LPS endotoxemia (*36*); conversely, myeloid-specific deletion of ACLY resulted in a hyperresponsiveness to LPS in vitro (*28*) but had minimal impact in models of acute or chronic inflammation (*53*). We demonstrate here that either genetic deficiency or pharmacological inhibition of ACC attenuates LPS-induced inflammation in vivo.

Macrophages from $ACC^{\Delta LysM}$ mice demonstrated a profound defect in reconfiguration of cellular lipid metabolism in response to LPS stimulation. Together with the observation that $ACC^{\Delta LysM}$ BMDMs demonstrate attenuated expression of proinflammatory cytokines, our findings support previous studies that have demonstrated the link between control of lipid metabolism in macrophages and the inflammatory response (*9*, *11*). In addition, recent work demonstrated that *Drosophila* reroute lipid metabolism toward phospholipid synthesis in response to bacterial infection or genetic activation of the Toll signaling pathway, which facilitates ER expansion and antimicrobial peptide secretion (*54*). Furthermore, SREBP-dependent lipid synthesis is required for macrophage phagocytosis after TLR4 activation (*55*), and here, we find that $ACC^{\Delta LysM}$ macrophages have both blunted phospholipid accumulation in response to LPS and an attenuated capacity for bacterial engulfment.

Given its key role in the de novo synthesis of fatty acids, inhibition of ACC has become an attractive pharmacological target for nonalcoholic fatty liver disease (*41*, *42*, *56*, *57*). Furthermore, ACC inhibitors are under investigation for treatment of solid malignancies including hepatocellular carcinoma (*58*) and non–small cell lung cancer (*43*). Our findings that (i) treatment with an ACC inhibitor attenuates inflammatory responses in vivo and (ii) macrophages with decreased levels of ACC have a defect in pathogen killing in vitro suggest that attenuation of the immune response is a consequence of inhibition of ACC activity. Furthermore, our observation that treatment with a pharmacological inhibitor of ACC worsened outcomes in a model of peritoneal infection identified a role for ACC in in vivo pathogen control. The role of ACC in control of macrophage function that we identified could potentially be harnessed therapeutically in cases of hyperinflammation, such as seen

in patients with sepsis. However, our findings also point toward decreased bacterial killing as a potential unwanted side effect of pharmacological ACC inhibition in the context of metabolic disease or cancer. Previous studies in patients with sepsis have long demonstrated an impact of whole-body lipid metabolism on recovery outcomes (*59*, *60*). Recent studies have shown that metabolic processes including "fatty acid biosynthesis" are associated with nonresponse to therapy in sepsis (*61*), while metabolomics analysis identified a key role for lipid metabolites in stratifying outcomes in septic shock patients (*62*). Furthermore, expression of the lipid-responsive transcription actor peroxisome proliferator–activated receptor α (PPARα) is decreased in patients with sepsis, and decreased PPARα is associated with increased bacterial burden and mortality in a rodent sepsis model (*63*). Our findings further elucidate the role of de novo lipid synthesis in both the hyperinflammatory and bacterial clearance components of systemic infection.

In our genetic model of ACC deficiency, we observed an incomplete deletion of ACC isoforms in our in vitro macrophage culture; nevertheless, we observed significant perturbations in glucose and lipid metabolism at baseline and response to LPS in macrophages with decreased levels of ACC. The partial knockdown of ACC that we observed in our model corresponded to a partial decrease in carbon flux through lipid synthesis pathways, to which both de novo lipogenesis (which ACC knockdown would partially impair) and cholesterol biosynthesis (which is up-regulated in our model) can contribute, which may mask some of the effect in this assay. Nevertheless, we still identified major deficits in LPS-induced increases in multiple lipid species, in particular phospholipid species that contribute to key macrophage functions, including cytokine secretion and bacterial killing, which were impaired in $ACC^{\Delta LysM}$ macrophages. In this study, we limited most of our metabolic and lipidomic analysis to the first 6 hours after LPS stimulation. Multiple studies have demonstrated that LPS-induced alterations in lipid metabolism evolve during the course of the inflammatory response (*8*, *9*, *13*). Our observation that knockdown of ACC results in a basal increase in glycolysis through both changes in glycolytic gene expression and cell surface association of GLUT1 identifies a novel link between perturbation of the de novo lipogenesis pathway and the metabolic component of inflammatory macrophage polarization. Future studies might evaluate the role of ACC in other aspects of macrophage metabolic responses during distinct stages of initiation and resolution of inflammation. We observed a pattern of decreased gene expression of key inflammatory mediators including *Il1b*, *Il6*, *Il12*, and *Il10*, as well as changes in IL-6 and IL-1β levels, 6 hours after induction of inflammation with LPS in vivo. While we focused our analyses to the initial response to inflammation, future studies analyzing the impact of ACC knockdown at later stages of infection and pharmacological ACC inhibition after the initial inflammatory phase would serve to further elucidate the role of this metabolic regulator during all aspects of the induction and resolution of the inflammatory response.

In conclusion, we identified an unexpected role for ACC in linking metabolic reprogramming and activation of inflammatory responses in macrophages. Using genetic and pharmacological approaches in vivo, as well as bioenergetics, lipidomics, and transcriptional methods in vitro, we found that loss of ACC shifts macrophages to a hyperglycolytic metabolism while limiting the capacity to enhance glucose utilization and blocking lipid accumulation in response to TLR stimulation. ACC knockdown blunted proinflammatory gene transcription, which impaired macrophage cytokine secretion, phagocytosis, and pathogen destruction. These findings identify a role for ACC in regulation of the inflammatory response and underscore the links between control of cellular metabolism and stimulus-dependent macrophage polarization.

METHODS

Experimental design

The purpose of this study was to assess the role of ACC in the macrophage acute inflammatory response and the impact of ACC deficiency on macrophage polarization in vitro and the inflammatory response in vivo. For in vitro experiments, BMDMs from age- and sex-matched flox control and $ACC^{\Delta LysM}$ mice were cultured as described below and used for experiments. In vitro experiments were performed using biological replicates of primary cells derived from multiple mice or repeated at least twice, with representative results (technical replicates) presented. Experiments in hMDMs were performed in technical triplicate or quadruplicate as listed in figure legends. In vivo experiments for the LPS-induced peritonitis model used age- and sex-matched flox control and $ACC^{\Delta LysM}$ mice, and for survival experiments, experimenters assessing the clinical score and overall survival were blinded to genotype before the end of the experiment. Sample sizes for in vivo experiments were based on previous publications from our group using this model of LPS-induced endotoxemia (*40*, *64*), and animals from multiple independent litters were used for experiments. Mice were randomized by weight to treatment groups for experiments using wild-type mice where appropriate. Humane end points for in vivo experiments were predefined as described below and approved by the University of Virginia Animal Care and Use Committee. No other components were prespecified.

Mice

C57BL/6J mice (stock 000664) were purchased from The Jackson Laboratory (Bar Harbor, ME). Myeloid-specific ACC1/ACC2-deficient mice were generated by crossing $Acaca^{loxP/loxP}$ $Acacb^{loxP/loxP}$ (ACC1/ACC2 floxed) mice (*25*) with B6.129P2-$Lyz2^{tm1(cre)Ifo}$/J (LysM Cre) mice (*27*) obtained from The Jackson Laboratory (stock 004781). Mice were backcrossed to give mice homozygous for the *Acaca* and *Acacb* floxed alleles with the LysM Cre. For breeding, mice hemizygous for the LysM Cre transgene were crossed with *Acaca*/*Acacb* floxed mice to give littermates of $Acaca^{loxP/loxP}$ $Acacb^{loxP/loxP}$ $LysM^{wt/wt}$ (flox) and $Acaca^{loxP/loxP}$ $Acacb^{loxP/loxP}$ $LysM^{cre/wt}$ ($ACC^{\Delta LysM}$) mice. Unless otherwise stated, animals were maintained in the University of Virginia Center for Comparative Medicine in a pathogen-free animal facility with ad libitum access to food (standard rodent chow, Teklad) and water and a 12-hour light/12-hour dark cycle. All animal experiments were approved by the University of Virginia Animal Care and Use Committee (protocol #3444). The genomic DNA was isolated from tail clip biopsies by proteinase K (Bioline) digestion in DirectPCR tail lysis reagent (Viagen Biotech). Genotype was confirmed by PCR analysis of genomic DNA using Apex Taq Master Mix (Genesee Scientific) with primers as previously described. Age- and sex-matched littermate controls were used for experiments.

Endotoxemia model

Ten- to 14-week-old male mice were injected with LPS (2 mg/kg; Ultrapure LPS from *E. coli*, InvivoGen) in sterile saline by intraperitoneal injection, and body mass and rectal temperature were recorded by an observer blinded to the experimental conditions. For ACC inhibitor administration, dimethyl sulfoxide (DMSO) vehicle or firsocostat (Selleck Chemicals) was administered via intraperitoneal injection just before administration of LPS. Clinical symptoms were assessed using a scoring scale as previously described (*64*). At the times indicated, mice were euthanized by carbon dioxide inhalation and cardiac puncture, and lavage and tissues were collected for further analysis. For survival analysis, mice were monitored for weight loss, symptom severity, and survival every 8 hours for 72 hours. Mice found dead/moribund or reaching predetermined humane end points were euthanized.

E. coli peritonitis model

E. coli O18ac:K1:H7 [American Type Culture Collection (ATCC) 700973] bacterial culture was obtained from ATCC and reconstituted in LB growth medium. For peritonitis model, bacteria were subcultured in LB growth medium and collected in the logarithmic growth phase. Bacteria were pelleted and washed three times with sterile saline, and CFUs were estimated on the basis of optical density at 600 nm. Culture was serially diluted in sterile saline to a concentration of approximately 10^8 CFUs/ml. An aliquot of inoculum was plated on LB agar plates to determine the final concentration. After pretreatment with vehicle or firsocostat for 1 hour, male C57BL/6J mice were inoculated with 100 μl of solution (approximately 10^7 CFUs) or saline control and monitored for survival and humane end points. When mice reached humane end-point criteria or at the end of the experiment, peritoneal cavities were lavaged with 5 ml of sterile saline, which was serially diluted and plated on LB agar plates to estimate final CFU counts from *E. coli*–inoculated animals.

BMDM culture

BMDMs were cultured as described previously (*7*). Briefly, bone marrow was isolated from the hindlimbs of mice and incubated with 0.83% (w/v) ammonium chloride for 5 min to lyse erythroid progenitors. Bone marrow cells were cultured in RPMI 1640 medium (Gibco) supplemented with 10% heat-inactivated fetal bovine serum (FBS) (Atlanta Biologicals), 2% Hepes (Gibco), 2% antibiotic-antimycotic (Gibco), and 10% L929-conditioned medium (L929 cells obtained from ATCC). Cells were cultured for 7 days, with medium changes every 3 to 4 days, before cells were switched to a medium lacking L929-conditioned medium. Cells were detached from petri dishes by brief incubation with 0.25% trypsin-EDTA (Gibco) and plated for analysis.

hMDM culture

hMDMs were cultured from human peripheral blood mononuclear cells (PBMCs) enriched from buffy coats obtained from the Program for Non-Transfusable Material for In-Vitro Use of the American Red Cross (Columbus, OH). Buffy coat diluted 1:1 with sterile phosphate-buffered saline (PBS) was cleared of erythrocytes by differential centrifugation over Ficoll Paque Plus (GE Healthcare) using SepMate tubes (STEMCELL Technologies). Enriched PBMCs were pelleted by centrifugation at 300*g*, washed twice in sterile PBS, and resuspended for counting. Cells were resuspended in monocyte attachment medium (PromoCell) following the manufacturer's instructions and allowed to adhere for 90 min. After two washes with monocyte attachment medium, adherent cells were cultured in RPMI 1640 (Gibco) supplemented with 2% Hepes (Gibco), 2% antibiotic-antimycotic (Gibco), 10% heat-inactivated FBS (Atlanta Biologicals), and recombinant human macrophage colony-stimulating factor (20 ng/ml; PeproTech) for 6 days. After 6 days, adherent monocyte-derived macrophages were detached using trypsin, counted, and plated for analysis.

Peritoneal lavage and cell isolation

Cells were isolated from the peritoneal cavities of mice 6 or 24 hours after LPS inoculation. After confirmation of euthanasia, 5 ml of ice-cold sterile PBS with 5 mM EDTA was instilled in the peritoneal cavity, and the peritoneum was gently massaged to dislodge resident and infiltrating cells. Lavage fluid was recovered, and peritoneal cells were pelleted by centrifugation at 400*g* for 5 min. Supernatant lavage fluid was stored at −80°C, and cells were incubated in ACK lysis buffer to lyse erythrocytes. Cells were collected by centrifugation and resuspended in TRIzol (Invitrogen) before analysis.

RNA sequencing

BMDMs (1×10^7 cells) were plated on 10-cm petri dishes and allowed to adhere overnight. After 6-hour treatment with control or LPS (100 ng/ml), cells were washed once in ice-cold PBS, collected by centrifugation at 500*g* for 5 min, and lysed in RLT buffer (QIAGEN) before extraction of total RNA with the RNeasy Mini Kit (QIAGEN) and elution into nuclease-free water (Invitrogen). RNA concentration and purity were assessed on a NanoDrop 2000 spectrophotometer (Thermo Fisher Scientific). Library preparation and sequencing were performed by GENEWIZ (South Plainfield, NJ). Sample integrity was assessed on Agilent TapeStation before library preparation. One hundred fifty–base pair paired-end sequencing was performed using the Illumina HiSeq platform following the manufacturer's instructions. Sequencing data were converted to Fastq files and demultiplexed. FastQC was used to check for read quality, trimmed reads were aligned to the mouse reference genome using STAR (*65*), and FeatureCounts (*66*) was used to tabulate reads across each gene. Gene expression analysis was performed using the edgeR workflow (*67*). Pathway, ontology, and related analyses of differentially expressed gene lists were performed using Enrichr (*33*, *34*).

RNA isolation and quantitative reverse transcription PCR

RNA was isolated from approximately 4×10^5 BMDMs lysed in RLT lysis buffer or from tissues homogenized in TRIzol using the RNeasy Mini Kit (QIAGEN) according to the manufacturer's instructions. RNA was quantified using a NanoDrop spectrophotometer (Thermo Fisher Scientific), and complementary DNA (cDNA) libraries were generated using the iScript cDNA Synthesis Kit (Bio-Rad). Quantitative reverse transcription PCR was performed using SensiMix SYBR Green reagent (Bioline) and primer pairs for genes of interest on a CFX Connect real-time PCR instrument (Bio-Rad). Relative gene expression was determined using *B2m* or *Hprt* as a housekeeping gene. Primer sequences were verified against genes of interest using the National Center for Biotechnology Information (NCBI) Primer-BLAST.

Immunoblot analysis

Approximately 2×10^6 BMDMs were lysed on ice into radioimmunoprecipitation assay (RIPA) buffer containing cOmplete Mini Protease Inhibitor (Roche), phosphatase inhibitor cocktails (Sigma-Aldrich), 5 μM trichostatin A, and 10 mM nicotinamide (deacetylase inhibitors) and cleared by centrifugation at 20,000*g*. The protein content in cleared supernatants was estimated by bicinchoninic acid (BCA) assay (Pierce), and 10 to 50 μg of protein were denatured in Laemmli buffer, separated on a 6 to 15% gel by SDS–polyacrylamide gel electrophoresis, and transferred to nitrocellulose membranes. Membranes were blocked in 5% bovine serum albumin in tris-buffered saline (TBS) and stained overnight at 4°C with primary antibodies. Membranes were washed in TBS with 0.1% Tween 20 and stained with IRDye-conjugated secondary antibodies (1:10,000; LI-COR Biosciences), and protein was visualized on an Odyssey Imager (LI-COR Biosciences).

For histone immunoblotting, approximately 4×10^6 to 5×10^6 BMDMs were lysed in extraction buffer [PBS with 0.5% (v/v) Triton X-100, 2 mM phenylmethylsulfonyl fluoride (PMSF), and 0.02% (w/v) NaN_3 supplemented with protease, phosphatase, and deacetylase inhibitors as above] on ice for 10 min, and nuclei were pelleted by centrifugation at 6500*g* for 10 min. Nuclei were resuspended in 100 μl of acid extraction buffer (0.2 M HCl in H_2O with protease, phosphatase, and deacetylase inhibitors), and histones were extracted at 4°C overnight. Samples were neutralized by addition of 2 M NaOH in H_2O and cleared by centrifugation at 6500*g* for 10 min. The protein content of supernatants (containing extracted histones) was estimated by BCA assay, and 2 to 10 μg of samples were assayed by immunoblot.

Avidin pulldown of biotin-containing proteins was done as previously described (*25*). Briefly, BMDMs were lysed in RIPA buffer containing cOmplete Mini Protease Inhibitor (Roche), phosphatase inhibitor cocktails (Sigma-Aldrich), 5 μM trichostatin A, and 10 mM nicotinamide (deacetylase inhibitors) and cleared by centrifugation at 20,000*g*. Protein content in cleared supernatants was estimated by BCA assay (Pierce), and approximately 300 μg of total protein was incubated with streptavidin-conjugated agarose (Strep-Tactin Superflow Plus, QIAGEN) overnight to enrich biotin-containing proteins. Beads were pelleted by centrifugation at 2000*g*, washed two times in RIPA buffer, and heated to 60°C for 15 min in Laemmli buffer, and samples were assayed by immunoblot.

For preparation of nuclear and cytoplasmic extracts, the protocol of Schreiber *et al.* (*68*) was followed with minor modifications. Briefly, approximately 1×10^7 BMDMs were plated on 10-cm petri dishes and allowed to adhere overnight. After treatments as indicated, cells were scraped into sterile, ice-cold PBS and pelleted by centrifugation for 5 min at 400*g*. PBS was removed, and the cell pellet was resuspended in cytoplasmic lysis buffer [10 mM Hepes (pH 7.9), 10 mM KCl, 0.1 mM EDTA, 0.1 mM EGTA, 1 mM dithiothreitol (DTT), and 0.5 mM PMSF supplemented with protease, phosphatase, and deacetylase inhibitors as described above]. Samples were allowed to swell on ice for 15 min before the addition of NP-40 (10% in water) at $^1/_{16}$ the total volume and disruption by vortexing for 10 s. Samples were centrifuged at 6600*g* for 5 min, and the supernatant was retained as the cytoplasmic fraction. Pelleted nuclei were resuspended in nuclear buffer [20 mM Hepes (pH 7.9), 400 mM NaCl, 1 mM EDTA, 1 mM EGTA, 1 mM DTT, and 1 mM PMSF supplemented with protease, phosphatase, and deacetylase inhibitors as described above] at one-fourth the volume of cytoplasmic buffer and mixed at 1100 rpm in a tube shaker at 4°C for 15 min. The insoluble material was pelleted by centrifugation at 6600*g* for 10 min, and supernatants were retained as nuclear extract. Cytoplasmic and nuclear extracts were frozen at −80°C before use, and the protein content was estimated using the method of Bradford (*69*). Samples (10 to 25 μg) were assayed by immunoblot.

For cell surface biotinylation enrichment of surface-associated proteins, approximately 10^7 BMDMs were seeded on 10-cm petri dishes and allowed to adhere overnight. After stimulation with control or LPS for 6 hours, cells were washed with ice-cold PBS before incubation with a solution of Pierce EZ-Link Sulfo-NHS-LC-Biotin (Thermo Fisher Scientific) in PBS at 4°C for 1 hour with rocking. Biotin was quenched with the addition of 100 mM glycine in PBS before cells were washed in PBS and lysed into RIPA buffer with protease and phosphatase inhibitors. DNA was sheared by brief sonication before protein concentration was estimated using BCA assay. An aliquot of each sample was lysed in Laemmli buffer as an input control before 400 μg of each sample was incubated with streptavidin-conjugated agarose (Strep-Tactin Superflow Plus, QIAGEN) overnight. Samples were pelleted by gentle centrifugation, washed twice with fresh RIPA buffer, and eluted into 2× Laemmli buffer at 60°C for 15 min before analysis by immunoblot.

Antibodies

Antibodies used were the following: anti-ACC (1:500; C83B10, Cell Signaling Technology, 3676), anti–β-actin (1:1000; LI-COR Biosciences, 926-42210), anti-NFκB p65 (1:500; Cell Signaling Technology, 8242), anti–phospho-NFκB p65 (S536) (1:500; Cell Signaling Technology, 3033), anti-ERK p42/p44 (1:1000; Cell Signaling Technology, 4696), anti–phospho-ERK p42/p44 (T202/Y204) (1:1000; Cell Signaling Technology, 4377), anti–glyceraldehyde-3-phosphate dehydrogenase (GAPDH) (1:1000; Cell Signaling Technology, 5174), anti–phospho-STAT6 (Y641) (1:1000; Cell Signaling Technology, 9361), anti-STAT6 (1:1000; Cell Signaling Technology, 9362), anti-vinculin (1:1000; Cell Signaling Technology, 13901), anti-FASN (1:1000; Cell Signaling Technology, 3180), anti-arginase (1:500; Santa Cruz Biotechnology, sc-18351), anti–acetyl-H3 (K27) (1:500; Active Motif, 39133), anti-H3 (1:5000; Abcam, ab1791), rodent OXPHOS antibody cocktail (1:250; Abcam, ab110413), and anti-GLUT1 (1:1000; Novus Biologicals, NB110-39113).

Extracellular flux analysis

Extracellular flux analysis was performed as previously described (*7*). Briefly, BMDMs were seeded into a 24-well or 96-well XF culture plate (Agilent Technologies) and allowed to adhere overnight. To assess glycolytic capacity, cells were subjected to a glycolytic stress test, which measures the ECAR as established previously. At the end of the experimental treatment, cells were switched to unbuffered, glucose-free Dulbecco's modified Eagle's medium (DMEM) (Sigma-Aldrich, D5030) supplemented with 143 mM NaCl (Sigma-Aldrich) and 2 mM L-glutamine (Gibco) (pH 7.35) at 37°C. After basal ECAR measurements, glucose (20 mM), oligomycin (1 μM), and 2-deoxyglucose (80 mM) were sequentially injected every four measurements and ECAR was recorded. Basal glycolysis was measured by subtracting the average of the post–2-deoxyglucose measurements from the average of the post-glucose

measurements. Glycolytic capacity was calculated by subtracting the average of the post–2-deoxyglucose measurements from the average of the post-oligomycin measurements. For modified glycolytic stress test, glucose was co-injected with or without LPS (100 ng/ml) and ECAR followed for 6 hours before injection of oligomycin and 2-deoxyglucose.

To assess mitochondrial function, cells were subjected to a mitochondrial stress test as previously described (*7*). Briefly, at the end of the experiment, the medium was changed to DMEM with pyruvate (pH 7.35 at 37°C; 12800017, Thermo Fisher Scientific) and cells were equilibrated for 30 min. After basal OCR measurements, compounds to modulate cellular respiratory function [1 μM oligomycin (to inhibit ATP synthase), 2 μM BAM15 (to cause mitochondrial uncoupling), 1 μM antimycin A, and 100 nM rotenone (to inhibit mitochondrial respiration)] were injected into the plate, and OCR was recorded for three to four measurements between injections. Basal respiration was calculated by subtracting the average of the post–antimycin A and rotenone measurements from the average of the first three measurements. The maximum respiratory capacity was calculated by subtracting the average of the post–antimycin A and rotenone measurements from the average of the post-BAM15 measurements. The reserve capacity was calculated by subtracting the average of the basal measurements from the average of the post-BAM15 measurements.

Cytokine measurements

Cytokine concentrations were quantified by enzyme-linked immunosorbent assay (ELISA). For in vitro experiments, 4×10^5 BMDMs were seeded in 24-well plates and allowed to adhere overnight before experimental treatment. At the end of the experiment, the supernatant medium was collected and stored at −80°C for further analysis. For in vivo experiments, the peritoneal lavage supernatant or plasma was collected and stored at −80°C for further analysis. Cytokine concentrations were determined using commercial ELISA kits (Invitrogen) against IL-6 and IL-1β according to the manufacturer's instructions, and absorbance was recorded on a Synergy HTX plate reader (BioTek Instruments).

Cell-based glucose uptake assay

BMDMs were plated at 5×10^4 per well in a black, clear-bottom 96-well plate and allowed to adhere overnight. After stimulation as indicated, the uptake of the fluorescent glucose analog 2-NDBG in glucose-free RPMI 1640 (11879020, Gibco) was assessed by fluorescence according to the manufacturer's instructions (Glucose Uptake Cell-Based Assay Kit, Cayman Chemical).

H_2DFCDA ROS assay

BMDMs were plated at 5×10^4 per well in a black, clear-bottom 96-well plate and allowed to adhere overnight. After LPS stimulation, cells were incubated with 2',7'-dichlorodihydrofluorescein diacetate (H_2DFCDA) for 30 min before fluorescence measurement according to the manufacturer's instructions (ROS Assay Kit, BioVision). Fluorescence values were corrected for background (unstained cells) and represented as percent of unstimulated flox control.

Lactate assay

Lactate concentration was determined from supernatants of cells unstimulated or after 6 hours of stimulation with LPS or LTA. Lactate concentration in serum-free supernatants was determined using the BioVision Colorimetric/Fluorometric Lactate Assay Kit (K607) according to the manufacturer's instructions.

SDH activity assay

BMDMs (~1×10^7) were stimulated with vehicle or LPS for 6 hours; cells were scraped into SDH assay buffer supplemented with protease, phosphatase, and deacetylase inhibitors; and samples were cleared by centrifugation at 20,000*g* for 15 min. SDH activity of cleared supernatants was determined according to the manufacturer's instructions (SDH Activity Assay Kit, Sigma-Aldrich) and normalized to protein concentration as determined by BCA assay.

NADPH assay

BMDMs (2×10^6) were plated in six-well plates and allowed to adhere overnight. After stimulation with LPS, cells were washed with PBS and lysed into 150 μl of PBS and 150 μl of bicarbonate lysis buffer (100 mM sodium carbonate, 20 mM sodium bicarbonate, 10 mM nicotinamide, and 0.05% Triton X-100). Samples were digested in acidic or basic solution to allow for measurement of $NADP^+$ or NADPH. After neutralization, levels of oxidized or reduced NADPH were measured with the NADP/NADPH-Glo Assay (Promega) and luminescence was measured on a Synergy HTX plate reader (BioTek Instruments).

Bacterial killing assay

BMDMs (2×10^5) were seeded in 24-well plates and allowed to adhere overnight. *E. coli* was grown overnight in LB, and OD_{600} (optical density at 600 nm) was used to determine bacterial counts. On the day of the experiment, *E. coli* was washed in RPMI 1640 supplemented with 10% FBS and plated on BMDMs at a multiplicity of infection of 1. Plates were spun at 500*g* for 5 min to facilitate bacterial engulfment. Plates were placed in incubator (37°C, 5% CO_2) for 30 min. After 30 min, BMDMs were washed three times in RPMI 1640 supplemented with gentamicin (50 μg/ml; Gibco) to remove non-engulfed bacteria. One plate of cells was harvested at 30-min time point and lysed in sterile distilled H_2O for 30 min before being serially diluted and plated on LB agar plates for T0 CFUs. The second, T2 plate, was placed back into the incubator for 2 hours in RPMI 1640 supplemented with 10% FBS and gentamicin (50 μg/ml). After 2 hours, T2 plates were lysed and plated in the same method as T0 plates. Percent killing was calculated from CFUs using the formula [(T0 − T2)/T0]*100.

LC-MS lipidomics

BMDMs were plated on 10-cm petri dishes and allowed to adhere overnight. Cells were treated with control medium or medium containing LPS (100 ng/ml) for 6 hours before cells were washed, scraped into PBS, and counted. Approximately 2.5×10^6 cells were lysed in high-performance LC (HPLC)–grade water (Sigma-Aldrich) and spiked with deuterated lipid standards (SPLASH LIPIDOMIX, Avanti Polar Lipids) before modified Bligh-Dyer extraction. Lipids were extracted in a 1:1:1 ratio of water/methanol/chloroform in glass culture tubes, which was homogenized by vortexing, before centrifugation at 800*g* for 10 min to accelerate phase separation. The organic phase was removed, and extraction was performed twice more for a total of three extractions. Combined organic phases were dried under nitrogen gas and resuspended in 100 μl of HPLC-grade methanol before LC-MS analysis.

LC-MS analysis was performed on a Q Exactive Orbitrap high-resolution mass spectrometer (Thermo Fisher Scientific) coupled to a Vanquish UHPLC system essentially as previously described (*70*). Samples (10 μl) were separated by reverse phase on a 100 mm × 4.6 mm C18 column (5 μm, 120 Å; Thermo Fisher Scientific, Acclaim 120) using a two-phase solvent system consisting of mobile phase A (50% acetonitrile, 50% water, and 0.1% formic acid with 10 mM ammonium formate) and mobile phase B (88% isopropanol, 10% acetonitrile, 2% water, and 0.02% formic acid with 2 mM ammonium formate) at 400 μl/min using the following gradient: 0 to 4 min, 30 to 60% B; 4 to 10 min, 60 to 80% B; 10 to 15 min, 80 to 90% B; 15 to 24 min, 90 to 100% B; 24 to 27 min, 100% B; 27 to 27.1 min, 100 to 30% B; and 27.1 to 31 min, 30% B. Mass spectra were collected in positive ionization mode using a Top5 Full MS data-dependent MS/MS (ddMS^2) method with the following settings: full MS settings: resolution of 35,000, automatic gain control (AGC) target of 1×10^5, maximum injection time (IT) of 128 ms, and scan range of 200 to 1500 mass/charge ratio (m/z); ddMS^2 settings: resolution of 17,500, AGC target of 2×10^5, maximum IT of 64 ms, loop count of 5, and normalized collision energy of 40. Data analysis and assignment of lipid species were performed using LipidSearch 4.1.16 (Thermo Fisher Scientific) with the following settings: search—database: Q Exactive, precursor tolerance of 5.0 parts per million (ppm), and product tolerance of 8.0 ppm; alignment—alignment method, mean and retention time tolerance, 0.25 min.

Cholesterol measurements

Cholesterol was measured using LC-MS on a Q Exactive Orbitrap high-resolution mass spectrometer (Thermo Fisher Scientific) coupled to a Vanquish UHPLC system. Samples spiked with SPLASH LIPIDOMIX (containing cholesterol-*d7*) extracted as described for lipidomics were analyzed by reversed-phase separation on a 100 mm × 4.6 mm, 5 μm, C18 column (Kinetex, Phenomenex) consisting of mobile phase A (85% methanol, 15% water, and 5 mM ammonium acetate) and mobile phase B (100% methanol and 5 mM ammonium acetate) at a flow rate of 200 μl/min using the following gradient as previously described (*71*): 2 min, 50% B; 2 to 5 min, 50 to 100% B; 5 to 18 min, 100% B; 18 to 22 min, 100 to 0% B; 22 to 27 min, 0% B; 27 to 28 min, 0 to 50% B; and 28 to 35 min, 50% B. Mass spectra were collected in positive ionization mode using parallel reaction monitoring with an inclusion list for cholesterol and the deuterated cholesterol-*d7* standard. Data were analyzed using the Xcalibur Quan Browser, abundance was corrected for extraction efficiency using recovery of cholesterol-*d7*, and data were presented relative to flox control condition.

^{14}C-acetate incorporation

BMDMs (approximately 2×10^6 per plate) were seeded on petri dishes and allowed to adhere overnight. Serum-free RPMI 1640 was spiked with [1,2-^{14}C]sodium acetate (PerkinElmer, NEC553050UC) to a final concentration of 1 μCi/ml with or without LPS (100 ng/ml) and incubated at 37°C for 6 hours. At the end of the experiment, medium was aspirated and cells were washed twice with ice-cold PBS and scraped into lysis buffer (PBS + 0.1% Triton X-100 with protease inhibitors and 0.5 mM DTT). Lysates (200 μl) were extracted with 0.5 ml of acidified methanol, 0.25 ml of chloroform, and 0.25 ml of 200 mM NaCl, and the remaining sample was saved for estimation of protein concentration. After vortexing, phase separation was accelerated by centrifugation at 1000*g* for 2 min. Incorporation of ^{14}C-labeled acetate into the lipid-soluble fraction was determined by scintillation counting and normalized to protein content of samples.

Statistical analysis

Statistical analysis was performed using Prism 9 (GraphPad Software). Comparisons between two groups were conducted by Welch's or Student's *t* test or Mann-Whitney test, while comparisons of more than two groups were made by one-way analysis of variance (ANOVA) with post hoc testing of differences between individual groups, where appropriate. Statistical details are provided in individual figure legends. Outliers were assessed using the ROUT outlier test in Prism 9 ($Q = 5\%$) and excluded from analysis. Data are represented as means ± SEM.

Study approval

All animal studies described were approved by the Animal Care and Use Committee of the University of Virginia, under protocol number 3444. The use of anonymized human buffy coat for hMDM isolation was approved by agreement with the Institutional Review Board of the American Red Cross (Columbus, OH).

Supplementary Materials

This PDF file includes:

Figs. S1 to S6
Table S1
Data S2. Uncropped_Gels_Blots: Summary PDF of uncropped gels and blots.

Other Supplementary Material for this manuscript includes the following:

Data S1 and S3

View/request a protocol for this paper from *Bio-protocol*.

REFERENCES AND NOTES

1. L. A. J. O'Neill, R. J. Kishton, J. Rathmell, A guide to immunometabolism for immunologists. *Nat. Rev. Immunol.* **16**, 553–565 (2016).
2. A. J. Freemerman, L. Zhao, A. K. Pingili, B. Teng, A. J. Cozzo, A. M. Fuller, A. R. Johnson, J. J. Milner, M. F. Lim, J. A. Galanko, M. A. Beck, J. E. Bear, J. D. Rotty, L. Bezavada, H. S. Smallwood, M. A. Puchowicz, J. Liu, J. W. Locasale, D. P. Lee, B. J. Bennett, E. D. Abel, J. C. Rathmell, L. Makowski, Myeloid *Slc2a1*-deficient murine model revealed macrophage activation and metabolic phenotype are fueled by GLUT1. *J. Immunol.* **202**, 1265–1286 (2019).
3. G. M. Tannahill, A. M. Curtis, J. Adamik, E. M. Palsson-McDermott, A. F. McGettrick, G. Goel, C. Frezza, N. J. Bernard, B. Kelly, N. H. Foley, L. Zheng, A. Gardet, Z. Tong, S. S. Jany, S. C. Corr, M. Haneklaus, B. E. Caffrey, K. Pierce, S. Walmsley, F. C. Beasley, E. Cummins, V. Nizet, M. Whyte, C. T. Taylor, H. Lin, S. L. Masters, E. Gottlieb, V. P. Kelly, C. Clish, P. E. Auron, R. J. Xavier, L. A. J. O'Neill, Succinate is an inflammatory signal that induces IL-1β through HIF-1α. *Nature* **496**, 238–242 (2013).
4. S. C.-C. Huang, B. Everts, Y. Ivanova, D. O'Sullivan, M. Nascimento, A. M. Smith, W. Beatty, L. Love-Gregory, W. Y. Lam, C. M. O'Neill, C. Yan, H. Du, N. A. Abumrad, J. F. Urban Jr., M. N. Artyomov, E. L. Pearce, E. J. Pearce, Cell-intrinsic lysosomal lipolysis is essential for alternative activation of macrophages. *Nat. Immunol.* **15**, 846–855 (2014).
5. D. Vats, L. Mukundan, J. I. Odegaard, L. Zhang, K. L. Smith, C. R. Morel, D. R. Greaves, P. J. Murray, A. Chawla, Oxidative metabolism and PGC-1β attenuate macrophage-mediated inflammation. *Cell Metab.* **4**, 13–24 (2006).
6. G. F. P. Bories, S. Yeudall, V. Serbulea, T. E. Fox, B. E. Isakson, N. Leitinger, Macrophage metabolic adaptation to heme detoxification involves CO-dependent activation of the pentose phosphate pathway. *Blood* **136**, 1535–1548 (2020).
7. V. Serbulea, C. M. Upchurch, K. W. Ahern, G. Bories, P. Voigt, D. E. DeWeese, A. K. Meher, T. E. Harris, N. Leitinger, Macrophages sensing oxidized DAMPs reprogram their metabolism to support redox homeostasis and inflammation through a TLR2-Syk-ceramide dependent mechanism. *Mol. Metab.* **7**, 23–34 (2018).

8. W.-Y. Hsieh, Q. D. Zhou, A. G. York, K. J. Williams, P. O. Scumpia, E. B. Kronenberger, X. P. Hoi, B. Su, X. Chi, V. L. Bui, E. Khialeeva, A. Kaplan, Y. M. Son, A. S. Divakaruni, J. Sun, S. T. Smale, R. A. Flavell, S. J. Bensinger, Toll-like receptors induce signal-specific reprogramming of the macrophage lipidome. *Cell Metab.* **32**, 128–143.e5 (2020).
9. X. Wei, H. Song, L. Yin, M. G. Rizzo, R. Sidhu, D. F. Covey, D. S. Ory, C. F. Semenkovich, Fatty acid synthesis configures the plasma membrane for inflammation in diabetes. *Nature* **539**, 294–298 (2016).
10. B. Everts, E. Amiel, S. C.-C. Huang, A. M. Smith, C.-H. Chang, W. Y. Lam, V. Redmann, T. C. Freitas, J. Blagih, G. J. W. van der Windt, M. N. Artyomov, R. G. Jones, E. L. Pearce, E. J. Pearce, TLR-driven early glycolytic reprogramming via the kinases TBK1-IKKε supports the anabolic demands of dendritic cell activation. *Nat. Immunol.* **15**, 323–332 (2014).
11. A. Castoldi, L. B. Monteiro, N. van Teijlingen Bakker, D. E. Sanin, N. Rana, M. Corrado, A. M. Cameron, F. Hässler, M. Matsushita, G. Caputa, R. I. Klein Geltink, J. Büscher, J. Edwards-Hicks, E. L. Pearce, E. J. Pearce, Triacylglycerol synthesis enhances macrophage inflammatory function. *Nat. Commun.* **11**, 4107 (2020).
12. S. R. Liebergall, J. Angdisen, S. H. Chan, Y. Chang, T. F. Osborne, A. F. Koeppel, S. D. Turner, I. G. Schulman, Inflammation triggers liver X receptor-dependent lipogenesis. *Mol. Cell Biol.* **40**, e00364-19 (2020).
13. Y. Oishi, N. J. Spann, V. M. Link, E. D. Muse, T. Strid, C. Edillor, M. J. Kolar, T. Matsuzaka, S. Hayakawa, J. Tao, M. U. Kaikkonen, A. F. Carlin, M. T. Lam, I. Manabe, H. Shimano, A. Saghatelian, C. K. Glass, srebp1 contributes to resolution of pro-inflammatory TLR4 signaling by reprogramming fatty acid metabolism. *Cell Metab.* **25**, 412–427 (2017).
14. J. D. McGarry, G. F. Leatherman, D. W. Foster, Carnitine palmitoyltransferase I. The site of inhibition of hepatic fatty acid oxidation by malonyl-CoA. *J. Biol. Chem.* **253**, 4128–4136 (1978).
15. J. D. McGarry, G. P. Mannaerts, D. W. Foster, A possible role for malonyl-CoA in the regulation of hepatic fatty acid oxidation and ketogenesis. *J. Clin. Invest.* **60**, 265–270 (1977).
16. S. P. Davies, A. T. R. Sim, D. G. Hardie, Location and function of three sites phosphorylated on rat acetyl-CoA carboxylase by the AMP-activated protein kinase. *Eur. J. Biochem.* **187**, 183–190 (1990).
17. J. R. B. Dyck, N. Kudo, A. J. Barr, S. P. Davies, D. G. Hardie, G. D. Lopaschuk, Phosphorylation control of cardiac acetyl-CoA carboxylase by cAMP-dependent protein kinase and 5′-AMP activated protein kinase. *Eur. J. Biochem.* **262**, 184–190 (1999).
18. J. Ha, S. Daniel, S. S. Broyles, K. H. Kim, Critical phosphorylation sites for acetyl-CoA carboxylase activity. *J. Biol. Chem.* **269**, 22162–22168 (1994).
19. L. Abu-Elheiga, M. M. Matzuk, P. Kordari, W. Oh, T. Shaikenov, Z. Gu, S. J. Wakil, Mutant mice lacking acetyl-CoA carboxylase 1 are embryonically lethal. *Proc. Natl. Acad. Sci. U.S.A.* **102**, 12011–12016 (2005).
20. D. P. Olson, T. Pulinilkunnil, G. W. Cline, G. I. Shulman, B. B. Lowell, Gene knockout of Acc2 has little effect on body weight, fat mass, or food intake. *Proc. Natl. Acad. Sci. U.S.A.* **107**, 7598–7603 (2010).
21. L. Abu-Elheiga, M. M. Matzuk, K. A. Abo-Hashema, S. J. Wakil, Continuous fatty acid oxidation and reduced fat storage in mice lacking acetyl-CoA carboxylase 2. *Science* **291**, 2613–2616 (2001).
22. C. S. Choi, D. B. Savage, L. Abu-Elheiga, Z.-X. Liu, S. Kim, A. Kulkarni, A. Distefano, Y.-J. Hwang, R. M. Reznick, R. Codella, D. Zhang, G. W. Cline, S. J. Wakil, G. I. Shulman, Continuous fat oxidation in acetyl–CoA carboxylase 2 knockout mice increases total energy expenditure, reduces fat mass, and improves insulin sensitivity. *Proc. Natl. Acad. Sci. U.S.A.* **104**, 16480–16485 (2007).
23. K. Hoehn, N. Turner, M. Swarbrick, D. Wilks, E. Preston, P. Yuwei, H. Joshi, S. Furler, M. Larance, B. Hegarty, S. Leslie, R. Pickford, A. Hoy, E. Kraegen, D. James, G. Cooney, Acute or chronic upregulation of mitochondrial fatty acid oxidation has no net effect on whole-body energy expenditure or adiposity. *Cell Metab.* **11**, 70–76 (2010).
24. N. Harada, Z. Oda, Y. Hara, K. Fujinami, M. Okawa, K. Ohbuchi, M. Yonemoto, Y. Ikeda, K. Ohwaki, K. Aragane, Y. Tamai, J. Kusunoki, Hepatic de novo lipogenesis is present in liver-specific ACC1-deficient mice. *Mol. Cell. Biol.* **27**, 1881–1888 (2007).
25. J. D. Y. Chow, R. T. Lawrence, M. E. Healy, J. E. Dominy, J. A. Liao, D. S. Breen, F. L. Byrne, B. M. Kenwood, C. Lackner, S. Okutsu, V. R. Mas, S. H. Caldwell, J. L. Tomsig, G. J. Cooney, P. B. Puigserver, N. Turner, D. E. James, J. Villén, K. L. Hoehn, Genetic inhibition of hepatic acetyl-CoA carboxylase activity increases liver fat and alters global protein acetylation. *Mol. Metab.* **3**, 419–431 (2014).
26. P. Stüve, L. Minarrieta, H. Erdmann, C. Arnold-Schrauf, M. Swallow, M. Guderian, F. Krull, A. Hölscher, P. Ghorbani, J. Behrends, W.-R. Abraham, C. Hölscher, T. D. Sparwasser, L. Berod, *De Novo* fatty acid synthesis during mycobacterial infection is a prerequisite for the function of highly proliferative T cells, but not for dendritic cells or macrophages. *Front. Immunol.* **9**, 495 (2018).
27. B. E. Clausen, C. Burkhardt, W. Reith, R. Renkawitz, I. Förster, Conditional gene targeting in macrophages and granulocytes using LysMcre mice. *Transgenic Res.* **8**, 265–277 (1999).
28. J. Baardman, S. G. S. Verberk, S. van der Velden, M. J. J. Gijbels, C. P. P. A. van Roomen, J. C. Sluimer, J. Y. Broos, G. R. Griffith, K. H. M. Prange, M. van Weeghel, S. Lakbir, D. Molenaar, E. Meinster, A. E. Neele, G. Kooij, H. E. de Vries, E. Lutgens, K. E. Wellen, M. P. J. de Winther, J. Van den Bossche, Macrophage ATP citrate lyase deficiency stabilizes atherosclerotic plaques. *Nat. Commun.* **11**, 6296 (2020).
29. P. Duewell, H. Kono, K. J. Rayner, C. M. Sirois, G. Vladimer, F. G. Bauernfeind, G. S. Abela, L. Franchi, G. Nuñez, M. Schnurr, T. Espevik, E. Lien, K. A. Fitzgerald, K. L. Rock, K. J. Moore, S. D. Wright, V. Hornung, E. Latz, NLRP3 inflammasomes are required for atherogenesis and activated by cholesterol crystals. *Nature* **464**, 1357–1361 (2010).
30. E. O. Samstad, N. Niyonzima, S. Nymo, M. H. Aune, L. Ryan, S. S. Bakke, K. T. Lappegård, O.-L. Brekke, J. D. Lambris, J. K. Damås, E. Latz, T. E. Mollnes, T. Espevik, Cholesterol crystals induce complement-dependent inflammasome activation and cytokine release. *J. Immunol.* **192**, 2837–2845 (2014).
31. H. Sakurai, H. Chiba, H. Miyoshi, T. Sugita, W. Toriumi, IκB kinases phosphorylate NF-κB p65 subunit on serine 536 in the transactivation domain. *J. Biol. Chem.* **274**, 30353–30356 (1999).
32. M. Arditi, J. Zhou, M. Torres, D. L. Durden, M. Stins, K. S. Kim, Lipopolysaccharide stimulates the tyrosine phosphorylation of mitogen-activated protein kinases p44, p42, and p41 in vascular endothelial cells in a soluble CD14-dependent manner. Role of protein tyrosine phosphorylation in lipopolysaccharide-induced stimulation of endothelial cells. *J. Immunol.* **155**, 3994–4003 (1995).
33. E. Y. Chen, C. M. Tan, Y. Kou, Q. Duan, Z. Wang, G. V. Meirelles, N. R. Clark, A. Ma'ayan, Enrichr: Interactive and collaborative HTML5 gene list enrichment analysis tool. *BMC Bioinformatics* **14**, 128 (2013).
34. M. V. Kuleshov, M. R. Jones, A. D. Rouillard, N. F. Fernandez, Q. Duan, Z. Wang, S. Koplev, S. L. Jenkins, K. M. Jagodnik, A. Lachmann, M. G. McDermott, C. D. Monteiro, G. W. Gundersen, A. Ma'ayan, Enrichr: A comprehensive gene set enrichment analysis web server 2016 update. *Nucleic Acids Res.* **44**, W90–W97 (2016).
35. J. D. Lambeth, NOX enzymes and the biology of reactive oxygen. *Nat. Rev. Immunol.* **4**, 181–189 (2004).
36. M. A. Lauterbach, J. E. Hanke, M. Serefidou, M. S. J. Mangan, C.-C. Kolbe, T. Hess, M. Rothe, R. Kaiser, F. Hoss, J. Gehlen, G. Engels, M. Kreutzenbeck, S. V. Schmidt, A. Christ, A. Imhof, K. Hiller, E. Latz, Toll-like receptor signaling rewires macrophage metabolism and promotes histone acetylation via ATP-citrate lyase. *Immunity* **51**, 997–1011.e7 (2019).
37. E. L. Mills, B. Kelly, A. Logan, A. S. H. Costa, M. Varma, C. E. Bryant, P. Tourlomousis, J. H. M. Däbritz, E. Gottlieb, I. Latorre, S. C. Corr, G. McManus, D. Ryan, H. T. Jacobs, M. Szibor, R. J. Xavier, T. Braun, C. Frezza, M. P. Murphy, L. A. O'Neill, Succinate dehydrogenase supports metabolic repurposing of mitochondria to drive inflammatory macrophages. *Cell* **167**, 457–470.e13 (2016).
38. R. G. Carroll, Z. Zasłona, S. Galván-Peña, E. L. Koppe, D. C. Sévin, S. Angiari, M. Triantafilou, K. Triantafilou, L. K. Modis, L. A. O'Neill, An unexpected link between fatty acid synthase and cholesterol synthesis in proinflammatory macrophage activation. *J. Biol. Chem.* **293**, 5509–5521 (2018).
39. Y.-C. Kim, S. E. Lee, S. K. Kim, H.-D. Jang, I. Hwang, S. Jin, E.-B. Hong, K.-S. Jang, H.-S. Kim, Toll-like receptor mediated inflammation requires FASN-dependent MYD88 palmitoylation. *Nat. Chem. Biol.* **15**, 907–916 (2019).
40. A. Kadl, J. Pontiller, M. Exner, N. Leitinger, Single bolus injection of bilirubin improves the clinical outcome in a mouse model of endotoxemia. *Shock* **28**, 582–588 (2007).
41. G. Harriman, J. Greenwood, S. Bhat, X. Huang, R. Wang, D. Paul, L. Tong, A. K. Saha, W. F. Westlin, R. Kapeller, H. J. Harwood Jr., Acetyl-CoA carboxylase inhibition by ND-630 reduces hepatic steatosis, improves insulin sensitivity, and modulates dyslipidemia in rats. *Proc. Natl. Acad.Sci. U.S.A.* **113**, E1796–E1805 (2016).
42. R. Loomba, M. Noureddin, K. V. Kowdley, A. Kohli, A. Sheikh, G. Neff, B. R. Bhandari, N. Gunn, S. H. Caldwell, Z. Goodman, I. Wapinski, M. Resnick, A. H. Beck, D. Ding, C. Jia, J.-C. Chuang, R. S. Huss, C. Chung, G. M. Subramanian, R. P. Myers, K. Patel, B. B. Borg, R. Ghalib, H. Kabler, J. Poulos, Z. Younes, M. Elkhashab, T. Hassanein, R. Iyer, P. Ruane, M. L. Shiffman, S. Strasser, V. W.-S. Wong, N. Alkhouri; ATLAS Investigators, Combination therapies including Cilofexor and Firsocostat for bridging fibrosis and cirrhosis attributable to NASH. *Hepatology* **73**, 625–643 (2021).
43. R. U. Svensson, S. J. Parker, L. J. Eichner, M. J. Kolar, M. Wallace, S. N. Brun, P. S. Lombardo, J. L. Van Nostrand, A. Hutchins, L. Vera, L. Gerken, J. Greenwood, S. Bhat, G. Harriman, W. F. Westlin, H. J. Harwood, A. Saghatelian, R. Kapeller, C. M. Metallo, R. J. Shaw, Inhibition of acetyl-CoA carboxylase suppresses fatty acid synthesis and tumor growth of non-small cell lung cancer in preclinical models. *Nat. Med.* **22**, 1108–1119 (2016).
44. L. A. J. O'Neill, E. J. Pearce, Immunometabolism governs dendritic cell and macrophage function. *J. Exp. Med.* **213**, 15–23 (2016).
45. J. Van den Bossche, L. A. O'Neill, D. Menon, Macrophage immunometabolism: Where are we (going)? *Trends Immunol.* **38**, 395–406 (2017).
46. Y. Endo, A. Onodera, K. Obata-Ninomiya, R. Koyama-Nasu, H. K. Asou, T. Ito, T. Yamamoto, T. Kanno, T. Nakajima, K. Ishiwata, H. Kanuka, D. J. Tumes, T. Nakayama, ACC1 determines

memory potential of individual CD4$^+$ T cells by regulating de novo fatty acid biosynthesis. *Nat. Metab.* **1**, 261–275 (2019).
47. J. Lee, M. C. Walsh, K. L. Hoehn, D. E. James, E. J. Wherry, Y. Choi, Regulator of fatty acid metabolism, acetyl coenzyme A carboxylase 1, controls T cell immunity. *J. Immunol.* **192**, 3190–3199 (2014).
48. A. Kumar, Y.-P. Xiao, P. J. Laipis, B. S. Fletcher, S. C. Frost, Glucose deprivation enhances targeting of GLUT1 to lipid rafts in 3T3-L1 adipocytes. *Am. J. Physiol. Endocrinol. Metab.* **286**, E568–E576 (2004).
49. C. Moessinger, I. Nilsson, L. Muhl, M. Zeitelhofer, B. Heller Sahlgren, J. Skogsberg, U. Eriksson, VEGF-B signaling impairs endothelial glucose transcytosis by decreasing membrane cholesterol content. *EMBO Rep.* **21**, e49343 (2020).
50. A. Malenda, A. Skrobanska, T. Issat, M. Winiarska, J. Bil, B. Oleszczak, M. Sinski, M. Firczuk, J. M. Bujnicki, J. Chlebowska, A. D. Staruch, E. Glodkowska-Mrowka, J. Kunikowska, L. Krolicki, L. Szablewski, Z. Gaciong, K. Koziak, M. Jakobisiak, J. Golab, D. A. Nowis, Statins impair glucose uptake in tumor cells. *Neoplasia* **14**, 311–323 (2012).
51. D. Nowis, A. Malenda, K. Furs, B. Oleszczak, R. Sadowski, J. Chlebowska, M. Firczuk, J. M. Bujnicki, A. D. Staruch, R. Zagozdzon, E. Glodkowska-Mrowka, L. Szablewski, J. Golab, Statins impair glucose uptake in human cells. *BMJ Open Diabetes Res. Care* **2**, e000017 (2014).
52. M. Faas, N. Ipseiz, J. Ackermann, S. Culemann, A. Grüneboom, F. Schröder, T. Rothe, C. Scholtysek, M. Eberhardt, M. Böttcher, P. Kirchner, C. Stoll, A. Ekici, M. Fuchs, M. Kunz, B. Weigmann, S. Wirtz, R. Lang, J. Hofmann, J. Vera, D. Voehringer, A. Michelucci, D. Mougiakakos, S. Uderhardt, G. Schett, G. Krönke, IL-33-induced metabolic reprogramming controls the differentiation of alternatively activated macrophages and the resolution of inflammation. *Immunity* **54**, 531–2546.e5 (2021).
53. S. G. S. Verberk, H. J. P. van der Zande, J. Baardman, K. E. de Goede, K. J. Harber, E. D. Keuning, J. M. Lambooij, F. Otto, A. Zawistowska-Deniziak, H. E. de Vries, M. P. J. de Winther, B. Guigas, J. Van den Bossche, Myeloid ATP Citrate Lyase regulates macrophage inflammatory responses *in vitro* without altering inflammatory disease outcomes. *Front. Immunol.* **12**, 669920 (2021).
54. B. A. Martínez, R. G. Hoyle, S. Yeudall, M. E. Granade, T. E. Harris, J. D. Castle, N. Leitinger, M. L. Bland, Innate immune signaling in Drosophila shifts anabolic lipid metabolism from triglyceride storage to phospholipid synthesis to support immune function. *PLOS Genet.* **16**, e1009192 (2020).
55. J.-H. Lee, P. Phelan, M. Shin, B.-C. Oh, X. Han, S.-S. Im, T. F. Osborne, SREBP-1a–stimulated lipid synthesis is required for macrophage phagocytosis downstream of TLR4-directed mTORC1. *Proc. Natl. Acad. Sci. U. S. A.* **115**, E12228–E12234 (2018).
56. E. J. Lawitz, A. Coste, F. Poordad, N. Alkhouri, N. Loo, B. J. McColgan, J. M. Tarrant, T. Nguyen, L. Han, C. Chung, A. S. Ray, J. G. McHutchison, G. M. Subramanian, R. P. Myers, M. S. Middleton, C. Sirlin, R. Loomba, E. Nyangau, M. Fitch, K. Li, M. Hellerstein, Acetyl-CoA Carboxylase inhibitor GS-0976 for 12 weeks reduces Hepatic De Novo Lipogenesis and Steatosis in patients with nonalcoholic Steatohepatitis. *Clin. Gastroenterol. Hepatol.* **16**, 1983–1991.e3 (2018).
57. R. Loomba, Z. Kayali, M. Noureddin, P. Ruane, E. J. Lawitz, M. Bennett, L. Wang, E. Harting, J. M. Tarrant, B. J. McColgan, C. Chung, A. S. Ray, G. M. Subramanian, R. P. Myers, M. S. Middleton, M. Lai, M. Charlton, S. A. Harrison, GS-0976 reduces hepatic steatosis and fibrosis markers in patients with nonalcoholic fatty liver disease. *Gastroenterology* **155**, 1463–1473.e6 (2018).
58. J. S. V. Lally, S. Ghoshal, D. K. DePeralta, O. Moaven, L. Wei, R. Masia, D. J. Erstad, N. Fujiwara, V. Leong, V. P. Houde, A. E. Anagnostopoulos, A. Wang, L. A. Broadfield, R. J. Ford, R. A. Foster, J. Bates, H. Sun, T. Wang, H. Liu, A. S. Ray, A. K. Saha, J. Greenwood, S. Bhat, G. Harriman, W. Miao, J. L. Rocnik, W. F. Westlin, P. Muti, T. Tsakiridis, H. J. Harwood, R. Kapeller, Y. Hoshida, K. K. Tanabe, G. R. Steinberg, B. C. Fuchs, Inhibition of acetyl-CoA carboxylase by phosphorylation or the inhibitor ND-654 suppresses lipogenesis and hepatocellular carcinoma. *Cell Metab.* **29**, 174–182.e5 (2019).
59. D. A. Hofmaenner, A. Kleyman, A. Press, M. Bauer, M. Singer, The many roles of cholesterol in sepsis: A review. *Am. J. Respir. Crit. Care Med.* **205**, 388–396 (2022).
60. S. Tanaka, D. Couret, A. Tran-Dinh, J. Duranteau, P. Montravers, A. Schwendeman, O. Meilhac, High-density lipoproteins during sepsis: From bench to bedside. *Crit. Care* **24**, 134 (2020).
61. M. Barcella, B. Bollen Pinto, D. Braga, F. D'Avila, F. Tagliaferri, M.-A. Cazalis, G. Monneret, A. Herpain, K. Bendjelid, C. Barlassina, Identification of a transcriptome profile associated with improvement of organ function in septic shock patients after early supportive therapy. *Crit. Care* **22**, 312 (2018).
62. A. Cambiaghi, B. B. Pinto, L. Brunelli, F. Falcetta, F. Aletti, K. Bendjelid, R. Pastorelli, M. Ferrario, Characterization of a metabolomic profile associated with responsiveness to therapy in the acute phase of septic shock. *Sci. Rep.* **7**, 9748 (2017).
63. S. W. Standage, C. C. Caldwell, B. Zingarelli, H. R. Wong, Reduced peroxisome proliferator-activated receptor α expression is associated with decreased survival and increased tissue bacterial load in sepsis. *Shock* **37**, 164–169 (2012).
64. S. E. Adamson, R. Griffiths, R. Moravec, S. Senthivinayagam, G. Montgomery, W. Chen, J. Han, P. R. Sharma, G. R. Mullins, S. A. Gorski, J. A. Cooper, A. Kadl, K. Enfield, T. J. Braciale, T. E. Harris, N. Leitinger, Disabled homolog 2 controls macrophage phenotypic polarization and adipose tissue inflammation. *J. Clin. Investig.* **126**, 1311–1322 (2016).
65. A. Dobin, C. A. Davis, F. Schlesinger, J. Drenkow, C. Zaleski, S. Jha, P. Batut, M. Chaisson, T. R. Gingeras, STAR: Ultrafast universal RNA-seq aligner. *Bioinformatics* **29**, 15–21 (2013).
66. Y. Liao, G. K. Smyth, W. Shi, featureCounts: An efficient general purpose program for assigning sequence reads to genomic features. *Bioinformatics* **30**, 923–930 (2014).
67. M. D. Robinson, D. J. McCarthy, G. K. Smyth, edgeR: A Bioconductor package for differential expression analysis of digital gene expression data. *Bioinformatics* **26**, 139–140 (2010).
68. E. Schreiber, P. Matthias, M. M. Müller, W. Schaffner, Rapid detection of octamer binding proteins with 'mini-extracts', prepared from a small number of cells. *Nucleic Acids Res.* **17**, 6419 (1989).
69. M. M. Bradford, A rapid and sensitive method for the quantitation of microgram quantities of protein utilizing the principle of protein-dye binding. *Anal. Biochem.* **72**, 248–254 (1976).
70. C. M. Upchurch, S. Yeudall, C. M. Pavelec, D. Merk, J. Greulich, M. Manjegowda, S. S. Raghavan, I. M. Bochkis, M. M. Scott, E. Perez-Reyes, N. Leitinger, Targeting oxidized phospholipids by AAV-based gene therapy in mice with established hepatic steatosis prevents progression to fibrosis. *Sci. Adv.* **8**, eabn0050 (2022).
71. J. G. McDonald, B. M. Thompson, E. C. McCrum, D. W. Russell, Extraction and analysis of sterols in biological matrices by high performance liquid chromatography electrospray ionization mass spectrometry, in *Methods in Enzymology*, J. Jesz, Ed. (Academic Press, 2007), vol. 432, pp. 145–170.

Acknowledgments: We thank S. Hargett, A. Meher, and S. Sahu for assistance with *Acaca/Acacb* flox mice; J. Katz and C. Dhanireddy for technical support; and T. Harris, K. Lynch, M. Bland, B. Isakson, and the members of the Leitinger laboratory for discussions. **Funding:** This work was supported by NIH grants P01 HL120840 (to N.L.), R01 AI155808 (to B.N.D.), R01 GM108989 (to B.N.D.), R01 DK101803 (to K.L.H.), F30 HL154554-01 (to S.Y.), T32 GM007267 (to S.Y.), T32 GM007055 (to S.Y., C.M.U., P.V.S., and M.C.L.), T32 HL007284 (to C.M.P.), and R01 GM136900 (to T.E.H.) and Deutsche Forschungsgemeinschaft IRTG 1902-1 (to J.G.). **Author contributions:** S.Y. conceived the project, designed and conducted experiments, analyzed data, and wrote the manuscript. C.M.U. and P.V.S. designed and conducted experiments and analyzed data. C.M.P. J.G., and M.C.L. conducted experiments. B.N.D. and T.E.H. acquired funding. K.L.H. contributed unique reagents. N.L. conceived the project, designed experiments, acquired funding, analyzed data, and wrote the manuscript. All authors read and approved the final version of this manuscript. **Competing interests:** K.L.H. has commercial interests in Continuum Biosciences and Life Biosciences, which are not related to ACC enzymes relevant in this manuscript. The other authors declare that they have no competing interests. **Data and materials availability:** Sequencing data reported in this paper are deposited in the NCBI Gene Expression Omnibus (GEO) under accession number GSE193294. All data needed to evaluate the conclusions in the paper are present in the paper and/or the Supplementary Materials. Graphics are prepared using BioRender (https://app.biorender.com). The ACC1/ACC1 floxed mice are used under a materials transfer agreement with the Garvan Institute of Medical Research (Sydney, NSW, Australia). These mice can be provided by K.L.H. upon completion of a materials transfer agreement with the Garvan Institute. Requests for the ACC1/ACC2 floxed mice should be submitted to K.L.H. (k.hoehn@unsw.edu.au).

Submitted 26 March 2022
Accepted 27 October 2022
Published 23 November 2022
10.1126/sciadv.abq1984

Science Advances
AAAS

Supplementary Materials for

Macrophage acetyl-CoA carboxylase regulates acute inflammation through control of glucose and lipid metabolism

Scott Yeudall *et al.*

Corresponding author: Norbert Leitinger, nl2q@virginia.edu

Sci. Adv. **8**, eabq1984 (2022)
DOI: 10.1126/sciadv.abq1984

The PDF file includes:

Other Supplementary Material for this manuscript includes the following:

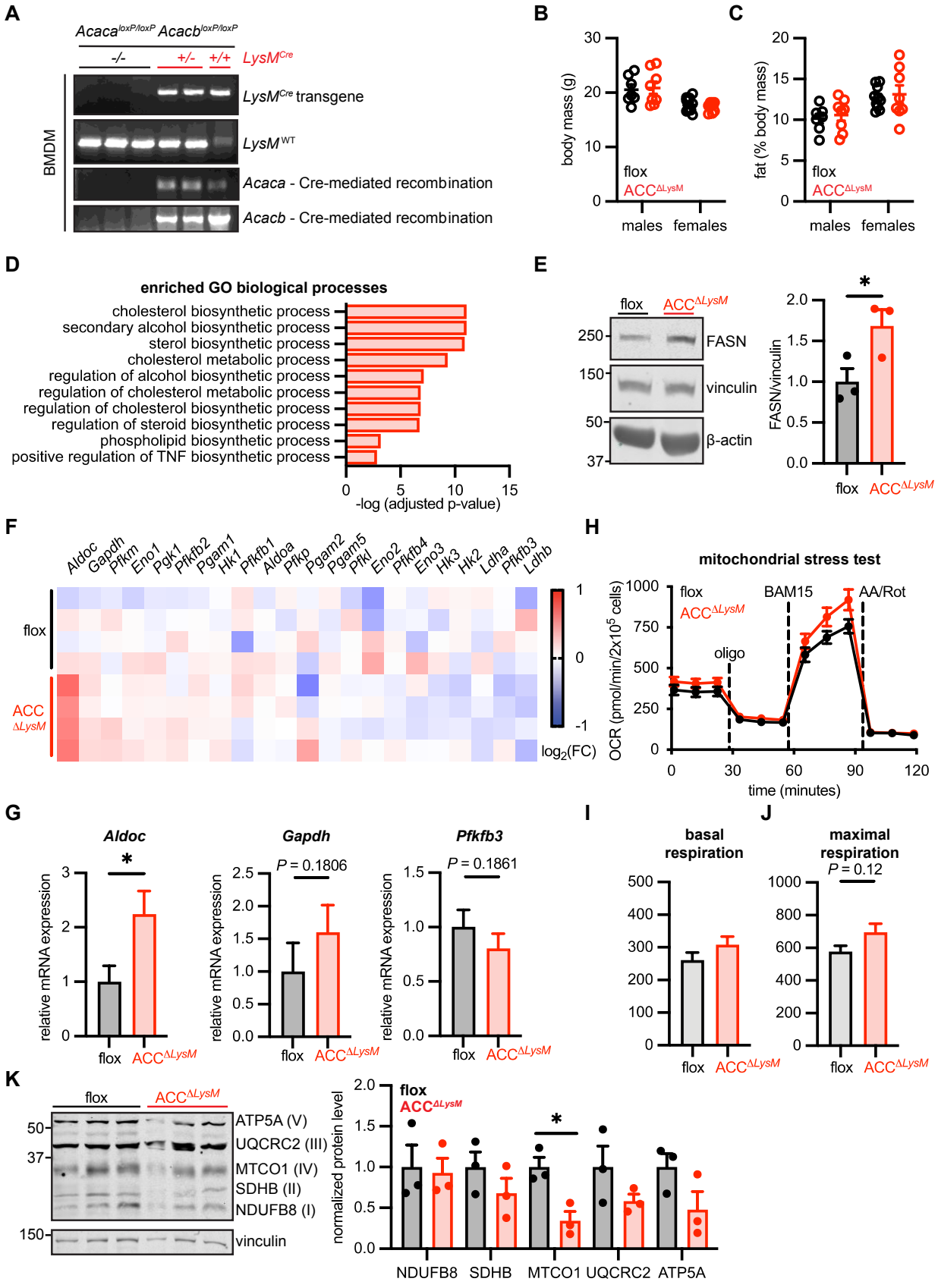
A
Acaca loxP/loxP Acacb loxP/loxP
-/-
+/-
+/+
LysM Cre
BMDM
LysM Cre transgene
LysM WT
Acaca - Cre-mediated recombination
Acacb - Cre-mediated recombination
B
body mass (g)
flox
ACC ΔLysM
males
females
C
fat (% body mass)
flox
ACC ΔLysM
males
females
D
enriched GO biological processes
cholesterol biosynthetic process
secondary alcohol biosynthetic process
sterol biosynthetic process
cholesterol metabolic process
regulation of alcohol biosynthetic process
regulation of cholesterol metabolic process
regulation of cholesterol biosynthetic process
regulation of steroid biosynthetic process
phospholipid biosynthetic process
positive regulation of TNF biosynthetic process
-log (adjusted p-value)
E
flox
ACC ΔLysM
FASN
vinculin
β-actin
FASN/vinculin
F
Aldoc Gapdh Pfkm Eno1 Pgk1 Pfkfb2 Pgam1 Hk1 Pfkfb1 Aldoa Pfkp Pgam2 Pgam5 Pfkl Eno2 Pfkfb4 Eno3 Hk3 Hk2 Ldha Pfkfb3 Ldhb
flox
ACC ΔLysM
log2(FC)
G
Aldoc
Gapdh
Pfkfb3
P = 0.1806
P = 0.1861
relative mRNA expression
H
mitochondrial stress test
flox
ACC ΔLysM
oligo
BAM15
AA/Rot
OCR (pmol/min/2x10^5 cells)
time (minutes)
I
basal respiration
J
maximal respiration
P = 0.12
K
ATP5A (V)
UQCRC2 (III)
MTCO1 (IV)
SDHB (II)
NDUFB8 (I)
vinculin
normalized protein level
NDUFB8
SDHB
MTCO1
UQCRC2
ATP5A

Supplementary Figure 1, related to Figure 1.

A. Representative genotyping of BMDM samples from flox or ACC$^{\Delta LysM}$ mice.

B. Body mass of flox and ACC$^{\Delta LysM}$ mice at 8 weeks of age (male flox, n = 7; male ACC$^{\Delta LysM}$, n = 8; female flox, n = 10; female ACC$^{\Delta LysM}$, n = 8).

C. Fat as percentage of total body mass in flox and ACC$^{\Delta LysM}$ mice at 8 weeks of age (male flox, n = 7; male ACC$^{\Delta LysM}$, n = 8; female flox, n = 10; female ACC$^{\Delta LysM}$, n = 8).

D. Enriched GO Biological Processes from unstimulated ACC$^{\Delta LysM}$ BMDMs.

E. Representative immunoblot analysis and quantification of fatty acid synthase (FASN) in unstimulated BMDMs from flox or ACC$^{\Delta LysM}$ mice (n = 3 mice per group). Vinculin and β-actin were used as loading controls.

F. Heatmap showing fold expression of glycolytic enzyme genes in unstimulated flox and ACC$^{\Delta LysM}$ BMDMs (n = 4).

G. Expression of glycolytic genes *Aldoc, Gapdh,* and *Pfkfb3* in unstimulated flox or ACC$^{\Delta LysM}$ BMDMs (n = 4).

H. Mitochondrial stress test (MST) of BMDMs from flox or ACC$^{\Delta LysM}$ mice (n = 4).

I. Basal respiration (calculated as average basal OCR – average post-AA/rot OCR) of flox or ACC$^{\Delta LysM}$ BMDMs (n = 4).

J. Maximal respiration (calculated as average post-BAM15 OCR – average post-AA/rot OCR) of flox or ACC$^{\Delta LysM}$ BMDMs (n = 4).

K. Immunoblot analysis of mitochondrial oxidative phosphorylation complexes (n = 3 mice per group). Vinculin was used as loading control.

Data are represented as mean±SEM. Significance determined by one-tailed Welch's t-test (B, C, E, G, I, J, K). * $P < 0.05$.

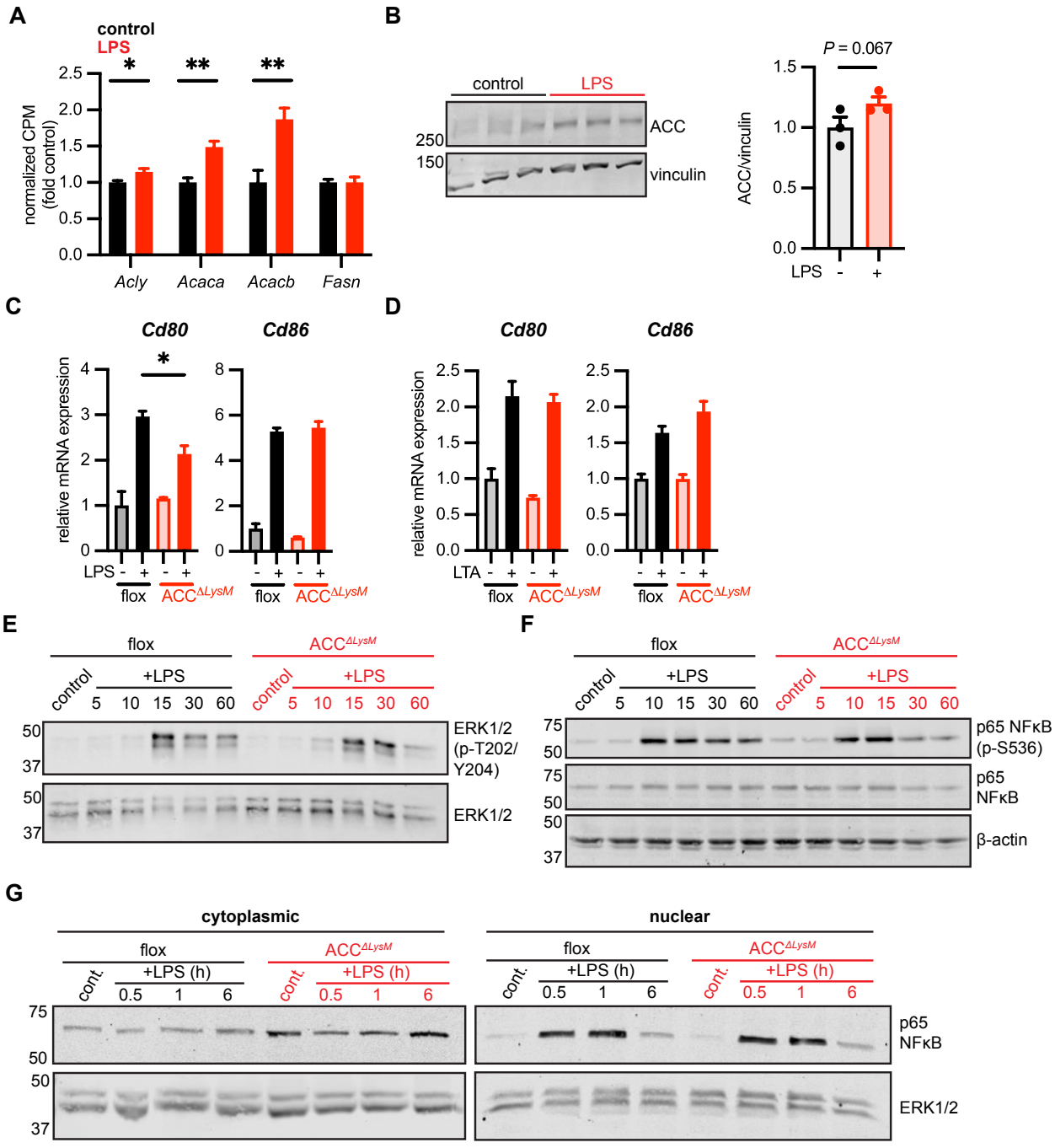

Supplementary Figure 2, related to Figure 2.

A. Normalized gene expression (normalized counts per million) of *Acly, Acaca, Acacb,* and *Fasn* of BMDMs treated with control or LPS (100ng/mL) for 6 hours (n = 4).

B. Immunoblot and semi-quantification of ACC in BMDMs treated with LPS (100ng/mL) for 6 hours (n = 3). Vinculin was used as a loading control.

C. Relative mRNA expression of *Cd80* and *Cd86* in flox or ACC$^{\Delta LysM}$ BMDMs treated with LPS (100ng/mL) for 6 hours (n = 4).

D. Relative mRNA expression of *Cd80* and *Cd86* in flox or ACC$^{\Delta LysM}$ BMDMs treated with LTA (1μg/ml) for 6 hours (n = 4).
E. Immunoblot of ERK1/2 phosphorylation at T202/Y204 in flox or ACC$^{\Delta LysM}$ BMDMs unstimulated or after LPS stimulation (100ng/ml) for 5-60 minutes. Representative of two independent experiments.
F. Immunoblot of p65 NF-κB phosphorylation at S536 in flox or ACC$^{\Delta LysM}$ BMDMs unstimulated or after LPS stimulation (100ng/ml) for 5-60 minutes. Representative of two independent experiments. β-actin was used as a loading control.
G. Immunoblot of total p65 NF-κB in cytoplasmic or nuclear extracts from flox or ACC$^{\Delta LysM}$ BMDMs unstimulated or after LPS stimulation (100ng/ml) for 0.5, 1, or 6 hours. Representative of two independent experiments. ERK1/2 was used as a loading control.
Data are represented as mean ± SEM. Significance determined by one-tailed Welch's t-test (A, B) or One-Way ANOVA (C,D) . * $P < 0.05$, ** $P < 0.01$.

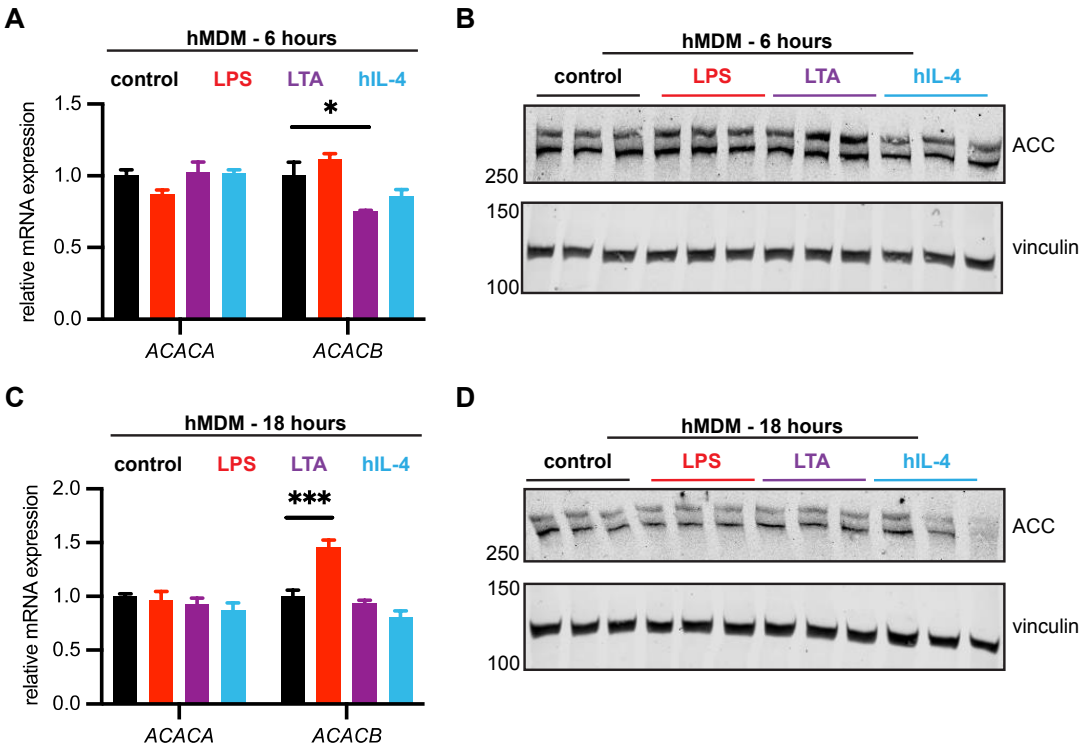

Supplementary Figure 3, related to Figures 2 and 4.

A. Relative mRNA expression of *ACACA* and *ACACB* in human MDMs treated with LPS (100ng/mL), LTA (1µg/ml) or hIL-4 (10ng/mL) for 6 hours (n = 4).

B. Immunoblot of ACC in human MDMs treated with LPS (100ng/mL), LTA (1µg/ml) or hIL-4 (10ng/mL) for 6 hours (n = 3). Vinculin was used as a loading control.

C. Relative mRNA expression of *ACACA* and *ACACB* in human MDMs treated with LPS (100ng/mL), LTA (1µg/ml) or hIL-4 (10ng/mL) for 18 hours (n = 4).

D. Immunoblot of ACC in human MDMs treated with LPS (100ng/mL), LTA (1µg/ml) or hIL-4 (10ng/mL) for 18 hours (n = 3). Vinculin was used as a loading control.

Data are represented as mean±SEM. Significance determined by One-Way ANOVA (A, C). * $P < 0.05$, *** $P < 0.001$.

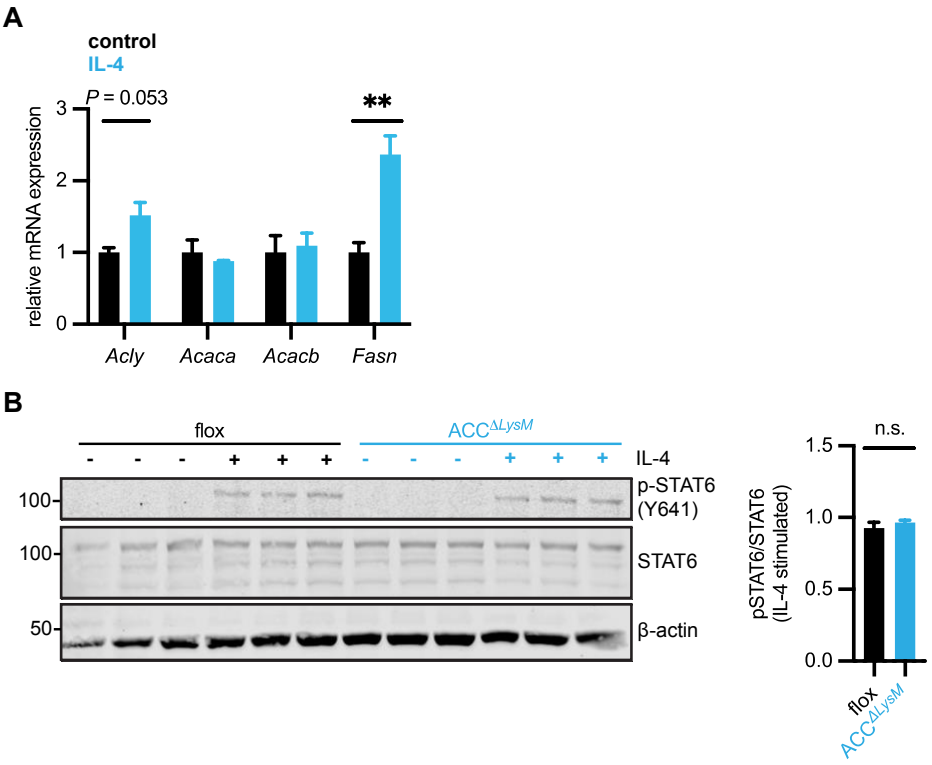

Supplementary Figure 4, related to Figure 4

A. Relative mRNA expression of *Acly, Acaca, Acacb,* and *Fasn* in BMDMs stimulated with IL-4 (10ng/mL) for 6 hours (n = 4).

B. Whole-cell immunoblot analysis of STAT6 phosphorylation at Y64 in flox or ACC$^{\Delta LysM}$ BMDMs stimulated with IL-4 (10ng/ml) for 6 hours (n = 3 mice per group). B-actin was used as a loading control.

Data are represented as mean±SEM. Significance determined by one-tailed Welch's t-test (A, B).
** $P < 0.01$

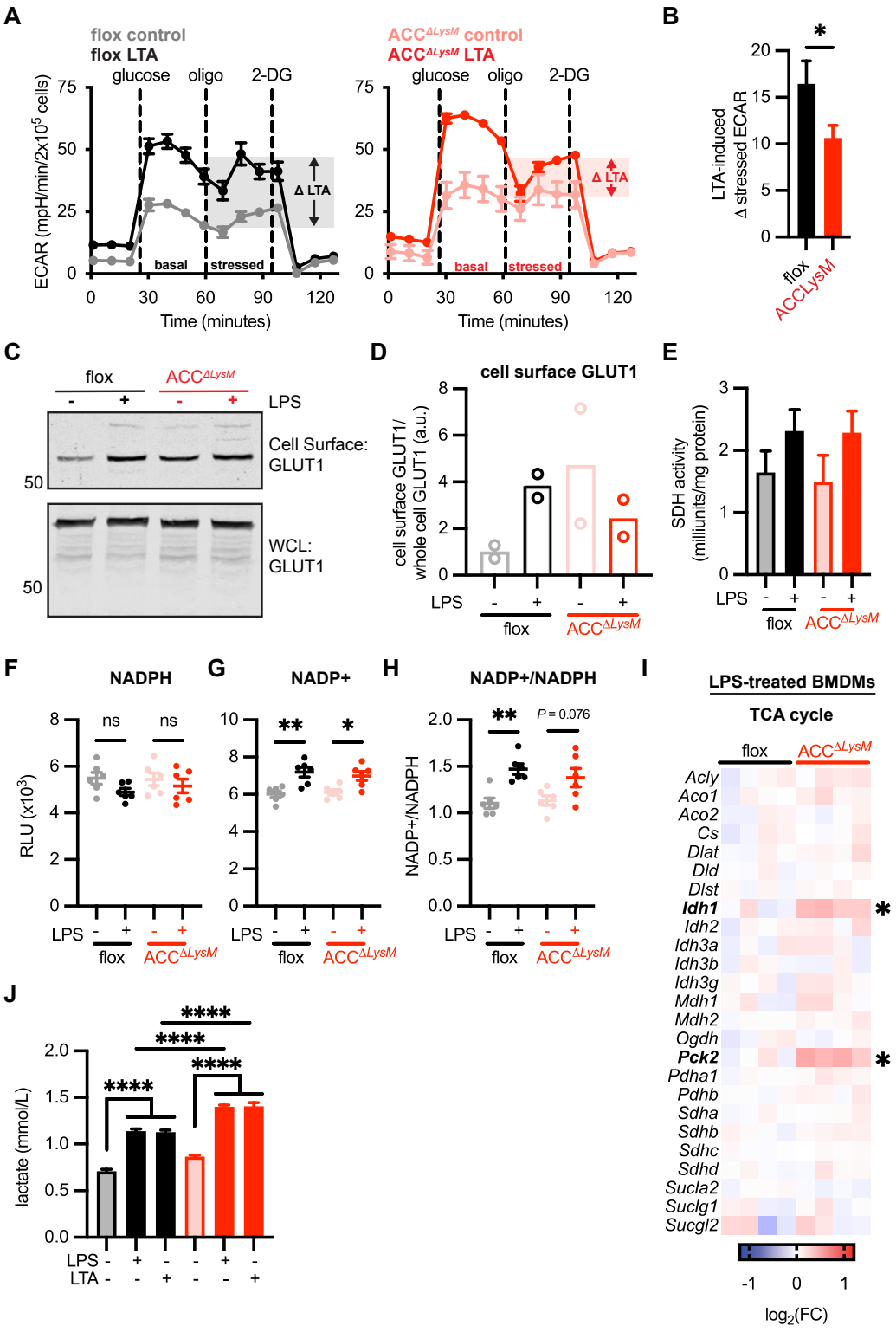

Supplementary Figure 5, Related to Figure 5

A. Glycolytic stress test of flox (black, left) or ACC$^{\Delta LysM}$ (red, right) BMDMs after stimulation with LTA for 16 hours. Shaded areas represent the LT+LTA-induced increase in stressed (post-oligomycin) ECAR (n = 5).

B. Quantification of LTA-induced change in stressed ECAR in flox or ACC$^{\Delta LysM}$ BMDMs after 16-hour stimulation with LPS (n = 5).
C. Representative immunoblot and **D.** semi-quantification of cell-surface and whole cell GLUT1 of flox or ACC$^{\Delta LysM}$ BMDMs treated with LPS for 6 hours subjected to cell-surface biotinylation protocol (n = 2 biological replicates).
D. Succinate dehydrogenase activity of flox or ACC$^{\Delta LysM}$ BMDMs treated with LPS for 6 hours (n = 6).
F. NADPH and **G.** NADP+ levels in BMDMs from flox or ACC$^{\Delta LysM}$ BMDMs treated with LPS for 6 hours (n = 6).
H. NADP+/NADPH ratio in BMDMs from flox or ACC$^{\Delta LysM}$ BMDMs treated with LPS for 6 hours (n = 6).
I. Heat map of relative expression of genes related to the tricarboxylic acid (TCA) cycle in LPS-treated flox and ACC$^{\Delta LysM}$ BMDMs (n = 4).
J. Supernatant lactate of flox or ACC$^{\Delta LysM}$ BMDMs unstimulated or after 6 hours of LPS or LTA stimulation (n = 6).
Data are represented as mean±SEM. Significance determined by One-Way ANOVA (C, E, G, H, J) or one-tailed Welch's t-test (B,I) or. * $P < 0.05$, ** $P < 0.01$, **** $P < 0.0001$.

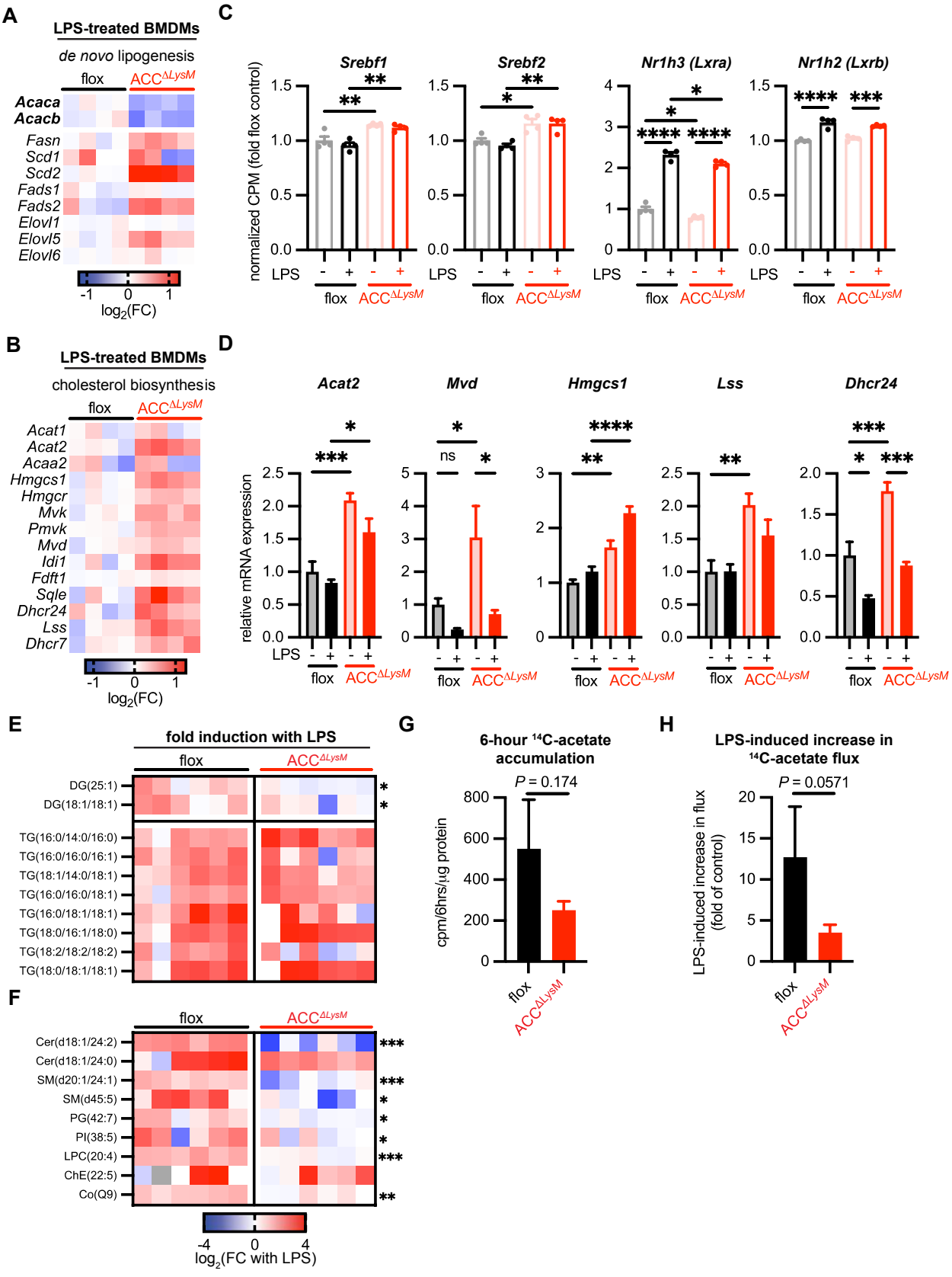
A
LPS-treated BMDMs
de novo lipogenesis
flox
ACC^ΔLysM
Acaca
Acacb
Fasn
Scd1
Scd2
Fads1
Fads2
Elovl1
Elovl5
Elovl6
-1 0 1
log2(FC)
B
LPS-treated BMDMs
cholesterol biosynthesis
Acat1
Acat2
Acaa2
Hmgcs1
Hmgcr
Mvk
Pmvk
Mvd
Idi1
Fdft1
Sqle
Dhcr24
Lss
Dhcr7
C
Srebf1
Srebf2
Nr1h3 (Lxra)
Nr1h2 (Lxrb)
normalized CPM (fold flox control)
LPS
D
Acat2
Mvd
Hmgcs1
Lss
Dhcr24
relative mRNA expression
ns
E
fold induction with LPS
DG(25:1)
DG(18:1/18:1)
TG(16:0/14:0/16:0)
TG(16:0/16:0/16:1)
TG(18:1/14:0/18:1)
TG(16:0/16:0/18:1)
TG(16:0/18:1/18:1)
TG(18:0/16:1/18:0)
TG(18:2/18:2/18:2)
TG(18:0/18:1/18:1)
F
Cer(d18:1/24:2)
Cer(d18:1/24:0)
SM(d20:1/24:1)
SM(d45:5)
PG(42:7)
PI(38:5)
LPC(20:4)
ChE(22:5)
Co(Q9)
-4 0 4
log2(FC with LPS)
G
6-hour 14C-acetate accumulation
P = 0.174
cpm/6hrs/μg protein
H
LPS-induced increase in 14C-acetate flux
P = 0.0571
LPS-induced increase in flux (fold of control)

Supplementary Figure 6, related to Figure 6.

A. Heat map of relative expression of genes in the *de novo* lipogenesis pathway in LPS-treated flox and ACC$^{\Delta LysM}$ BMDMs (n = 4).

B. Heat map of relative expression of genes in the cholesterol biosynthesis pathway in LPS-treated flox and ACC$^{\Delta LysM}$ BMDMs (n = 4).

C. Relative expression of transcription factor genes *Srebf1*, *Srebf2*, *N21h3*, and *Nr1h2* in flox and ACC$^{\Delta LysM}$ BMDMs after control and LPS stimulation (n = 4).

D. Expression of cholesterol pathway genes from in flox and ACC$^{\Delta LysM}$ BMDMs after control and LPS stimulation was confirmed by qPCR (n = 4).

E. Heat map of significantly increased diacylglycerol (DAG) and triacylglycerol (TAG) species in LPS-stimulated flox and ACC$^{\Delta LysM}$ BMDMs, relative to respective unstimulated cells (n = 6).

F. Heat map of significantly increased ceramide, sphingomyelin, and other lipid species in LPS-stimulated flox and ACC$^{\Delta LysM}$ BMDMs, relative to respective unstimulated cells (n = 6).

G. Accumulation of ^{14}C-acetate signal in the lipid-soluble fraction of flox or ACC$^{\Delta LysM}$ BMDMs after 6 hours (n = 4).

H. BMDMs were stimulated with control or LPS (100ng/ml) for 4 hours, before corresponding media containing ^{14}C-acetate was added for 2 hours. Fold increase in ^{14}C-actetate flux into lipid-soluble fraction was determined (flox, n = 3; ACC$^{\Delta LysM}$, n = 4)

Significance determined by two-tailed Student's t-test (E,F), one-tailed Mann-Whitney test (G,H) or One-Way ANOVA (C,D). * $P < 0.05$, ** $P < 0.01$, *** $P < 0.001$, **** $P < 0.0001$

Supplementary Table 1. Primer Sequences for RT-qPCR

Gene	Forward Primer	Reverse Primer	Source
Mus musculus			
Acaca	GTCTGCTGGGAAGTTAATCCAG	TCCTGCAGCTCTAGCAGAGG	(*25*)
Acacb	ACAGAGATTTCACCGTCGCGT	CGCAGCGATGCCATTGT	(*25*)
Il6	ACAACGATGATGCACTTGCAG	GCATTGGAAATTCGGGTAGGAA	(*62*)
Il1b	CAAAATACCTGTGGCCTTGG	TACCAGTTGGGGAACTCTGC	(*7*)
Il18	GACTCTTGCGTCAACTTCAAGG	CAGGCTGTCTTTTGTCAACGA	Primer Bank
Arg1	AAGACAGCAGAGGAGGTGAAGAG	TGGGAGGAGAAGGCGTTTGC	(*7*)
Chil3	CTTCCACAGGAGCAGGAATC	GCTCCATGGTCCTTCCAGTA	(*6*)
Ifng			
Nos2	CCTGGTACGGGCATTGCT	GCTCATGCCTCCTT	(*7*)
B2m	ATTCACCCCCACTGAGACTG	TGCTATTTCTTTCTGCGTGC	(*6*)
Hprt	TGAAGTACTCATTATAGTCAAGGGCA	CTGGTGAAAAGGACCTCTCG	(*29*)
Mrc1			Primer Bank
Retnla	CCAATCCAGCTAACTATCCCTCC	CCAGTCAACGAGTAAGCACAG	Primer Bank
Il12a	CTGTGCCTTGGTAGCATCTATG	GCAGAGTCTCGCCATTATGATTC	Primer Bank
Il12b	TGGTTTGCCATCGTTTTGCTG	ACAGGTGAGGTTCACTGTTTCT	Primer Bank
Aldoc	TCTCTCTTGGGATCAGGGGG	CAGGTGAACCCTTCCTCCAC	(*6*)
Gapdh	TGAAGGGTGGAGCCAAAAGG	ACTTGGCAGGTTTCTCCAGG	(*6*)
Pfkfb3	AACGGATGTCTCCCGGTTTC	TGGTATGGAGGCTGCTCTCT	Primer Bank
Acly	TGATGGGAGAAGTTGGGAAG	ATCAGCTCGGGACTCAGAAA	Primer Bank
Fasn	GGAGGTGGTGATAGCCGGTAT	TGGGTAATCCATAGAGCCCAG	Primer Bank
Acat2	CCCGTGGTCATCGTCTCAG	GGACAGGGCACCATTGAAGG	Primer Bank
Mvd	ATGGCCTCAGAAAAGCCTCAG	TGGTCGTTTTTAGCTGGTCCT	Primer Bank
Hmgcs1	AACTGGTGCAGAAATCTCTAGC	GGTTGAATAGCTCAGAACTAGCC	Primer Bank
Lss	TCGTGGGGGACCCTATAAAAC	CGTCCTCCGCTTGATAATAAGTC	Primer Bank
Dhcr24	CTCTGGGTGCGAGTGAAGG	TTCCCGGACCTGTTTCTGGAT	Primer Bank
Cd80	GCTGTGTCGTTCAAAAGAAGGA	TGGGAAATTGTCGTATTGATGCC	Primer Bank
Cd86	GAGCTGGTAGTATTTTGGCAGG	GGCCCAGGTACTTGGCATT	Primer Bank
Il10	ACTACCAAAGCCACAAGGCA	TGGCAACCCAAGTAACCCTTA	(*6*)
Homo sapiens			
ACACA	CATGCGGTCTATCCGTAGGTG	GTGTGACCATGACAACGAATCT	Primer Bank
ACACB	AGAAGACAAGAAGCAGGCAAAC	GTAGACTCACGAGATGAGCCA	Primer Bank
IL6	ACTCACCTCTTCAGAACGAATTG	CCATCTTTGGAAGGTTCAGGTTG	Primer Bank

IL1B	AGCTACGAATCTCCGACCAC	CGTTATCCCATGTGTCGAAGAA	Primer Bank
RPS18	GCGGCGGAAAATAGCCTTTG	GATCACACGTTCCACCTCATC	Primer Bank

Data S1. Lipidomics_Data

Summary data for lipidomics experiment from unstimulated or LPS-treated flox and ACC$^{\Delta LysM}$ BMDMs.

Data S3. Source_Data_File

Source Data for figures.

Data S2. Uncropped_Gels_Blots: Summary PDF of uncropped gels and blots.

Macrophage acetyl-CoA carboxylase regulates acute inflammation through control of glucose and lipid metabolism

Scott Yeudall[1], Clint M Upchurch[1], Philip V Seegren[1], Caitlin M Pavelec[1,2], Jan Greulich[3], Michael C Lemke[1], Thurl E Harris[1], Bimal N Desai[1], Kyle L Hoehn[1,4], and Norbert Leitinger[1,2]

[1] Department of Pharmacology,
[2] Robert M Berne Cardiovascular Research Center,
University of Virginia School of Medicine, Charlottesville, Virginia 22908

[3]Environmentally-Induced Cardiovascular Degeneration, Clinical Chemistry and Laboratory Diagnostics, Medical Faculty, University Hospital and Heinrich-Heine University Düsseldorf, 40225 Düsseldorf, Germany

[4]School of Biotechnology and Biomolecular Sciences,
University of New South Wales, Sydney, Australia 2052.

Uncropped blots and gels

Full unedited blots for Figure 1C

MW

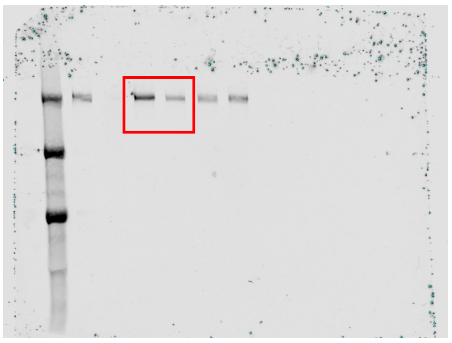

← pan-ACC (CST #3676, C83B10)

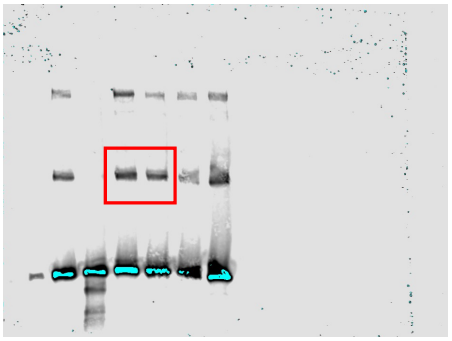

IRDye-800CW conjugated streptavidin (Licor # 926-32230)

← IR800-conjugated avidin (for biotinylated proteins) for pyruvate carboxylase

← IR800-conjugated avidin (for biotinylated proteins) for propionyl-coA carboxylase (blue indicates saturation of detection on Licor instrument)

Samples after streptavidin pulldown of cell lysates – lanes alternate flox and ACC$^{\Delta LysM}$ BMDMs. Lanes 3 and 4 are shown in figure 1C.

Full unedited blots for Figure 4C

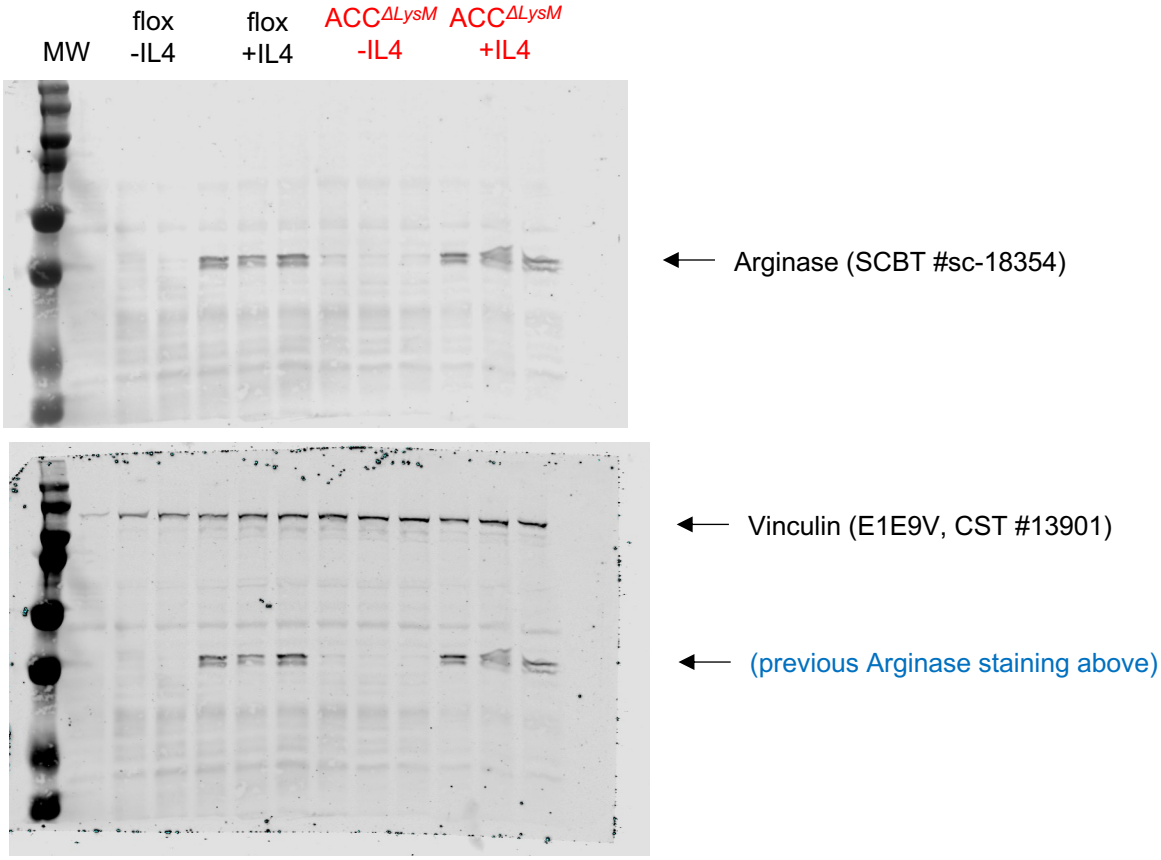

Full unedited blots for Supplementary Figure 1E

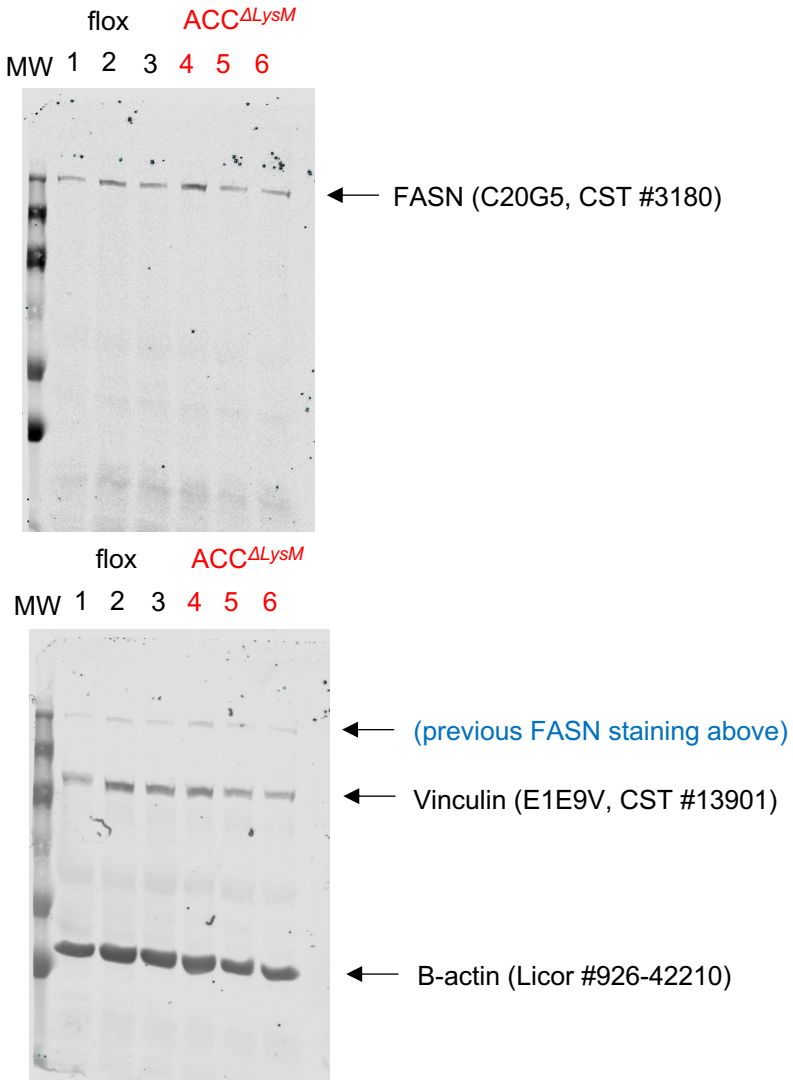

Lanes 3 and 4 displayed in Supplementary Figure 1E

Full unedited blots for Supplementary Figure 1K

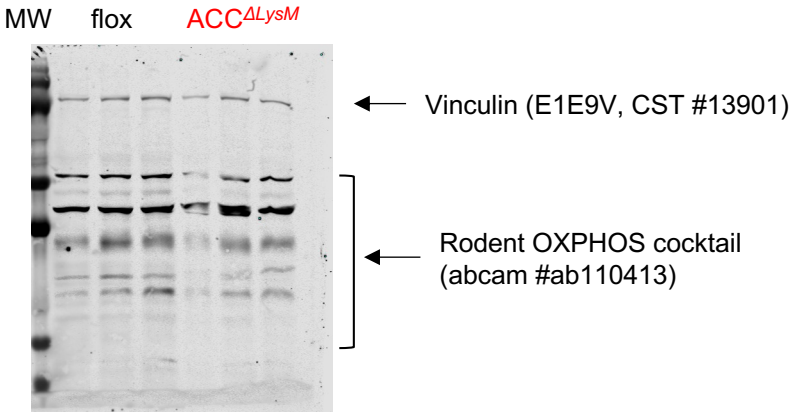

Full unedited blots for Supplementary Figure 2B

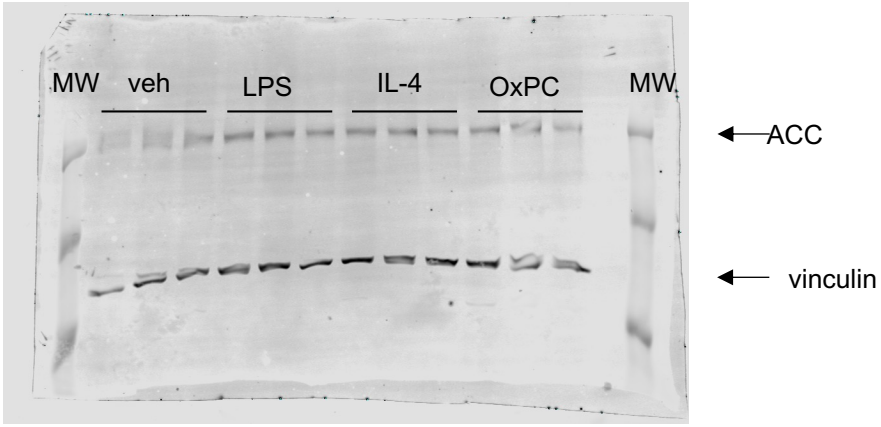

Full unedited blots for Supplementary Figure 2E

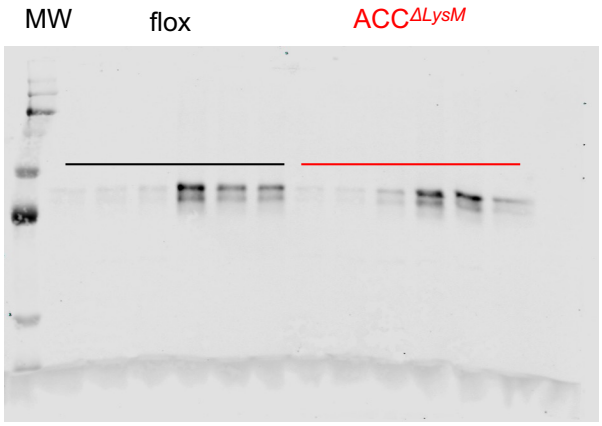

← p-ERK1/2 (T202/Y204) (CST #9101)

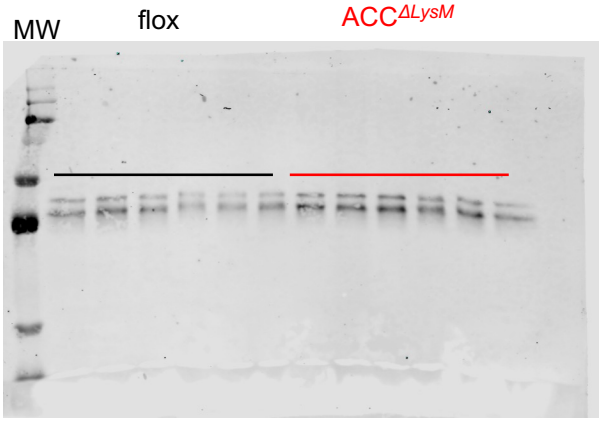

← ERK1/2 (L34F12, CST #4696)

Full unedited blots for Supplementary Figure 2F

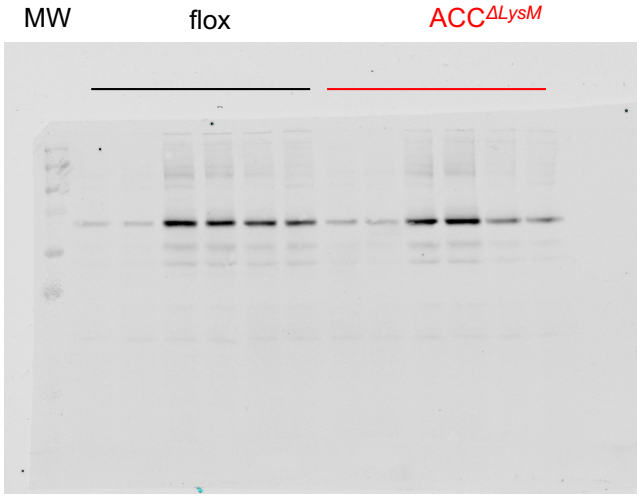

← p-p65 NFκB (S536) (93H1, CST #3033)

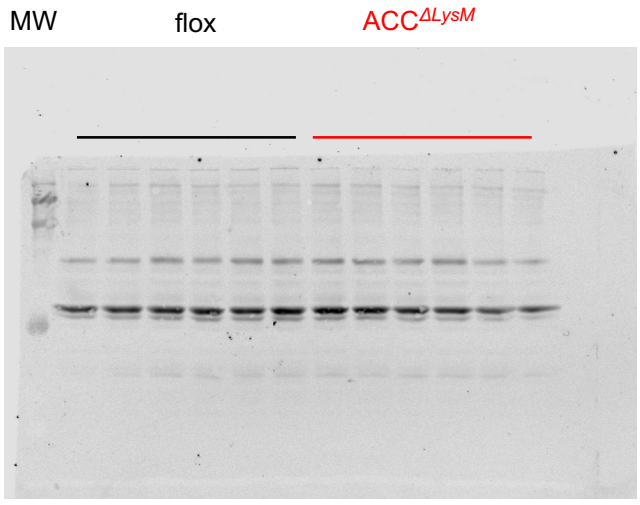

← p65 NFκB (D14E12, CST #8242)

← B-actin (Licor #926-42210)

Full unedited blots for Supplementary Figure 2G

cytoplasmic

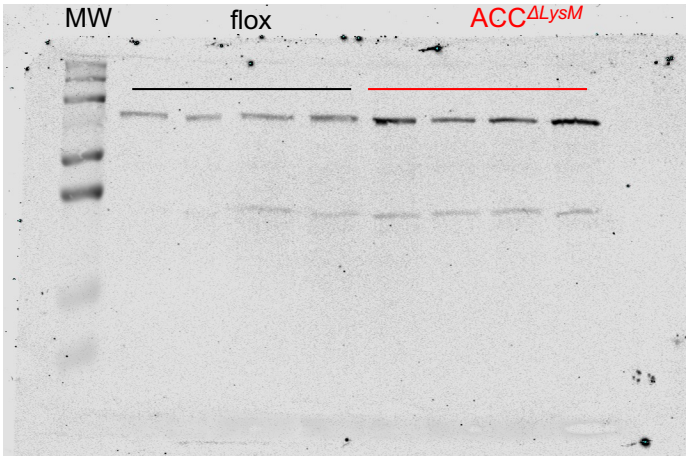

← p65 NFκB (D14E12, CST #8242)

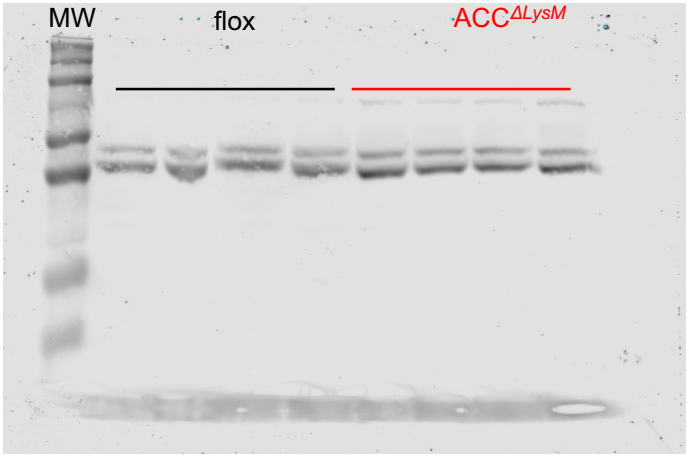

← ERK1/2 (L34F12, CST #4696)

Full unedited blots for Supplementary Figure 2G

nuclear

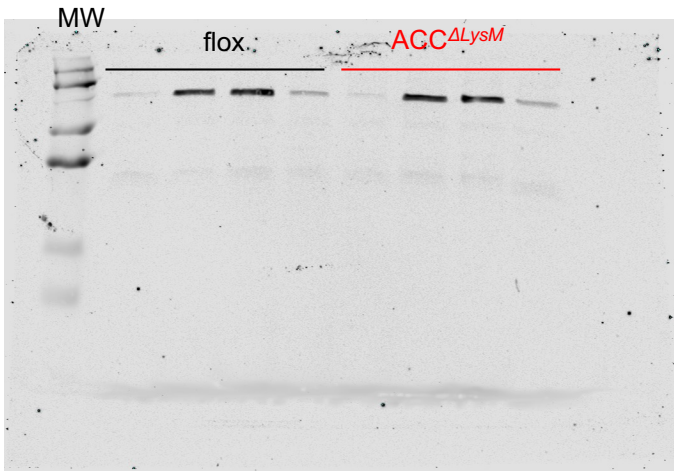

←p65 NFκB (D14E12, CST #8242)

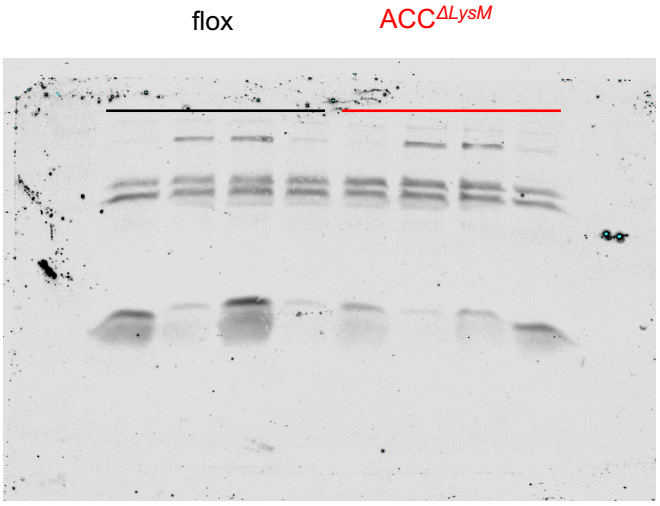

← ERK1/2 (L34F12, CST #4696)

Full unedited blots for Supplementary Figure 3B

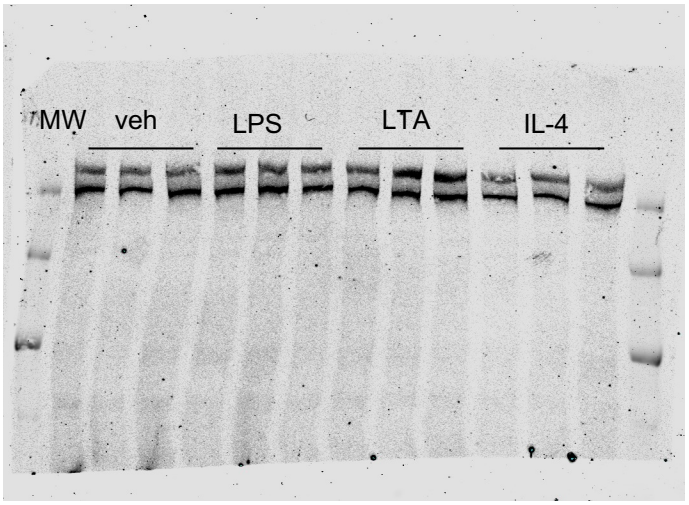

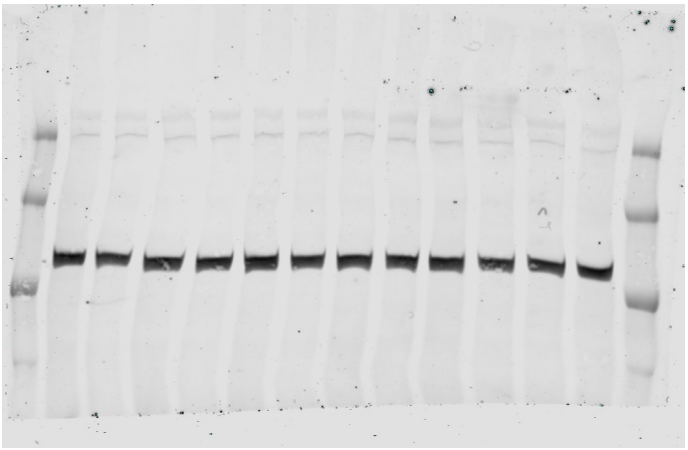

Full unedited blots for Supplementary Figure 3D

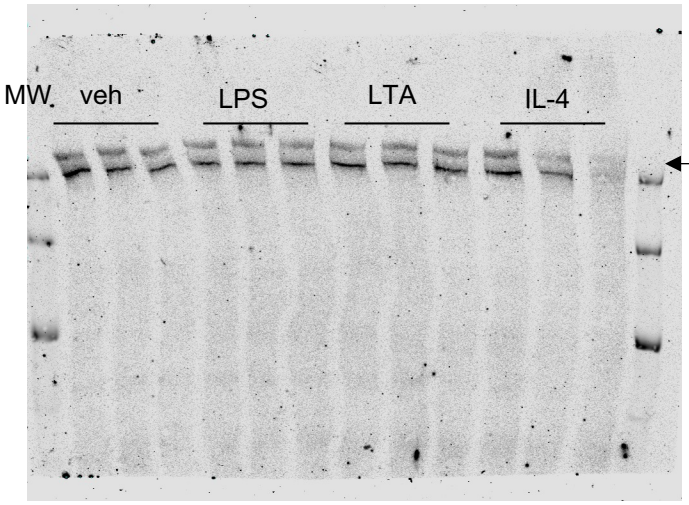

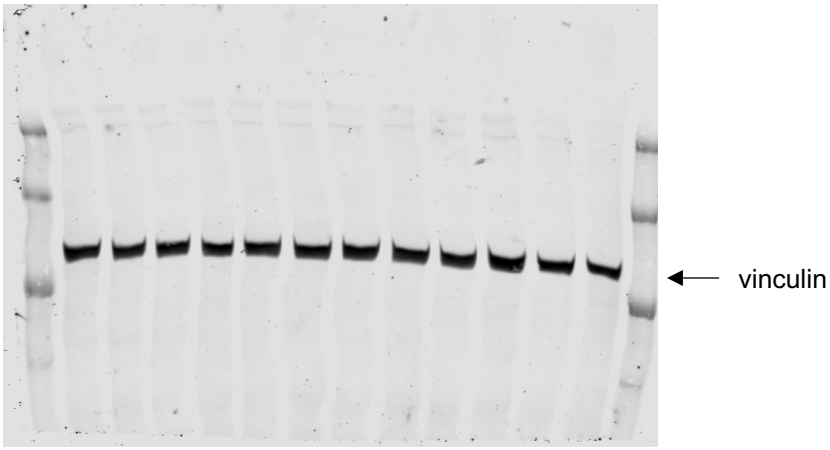

Full unedited blots for Figure S4B

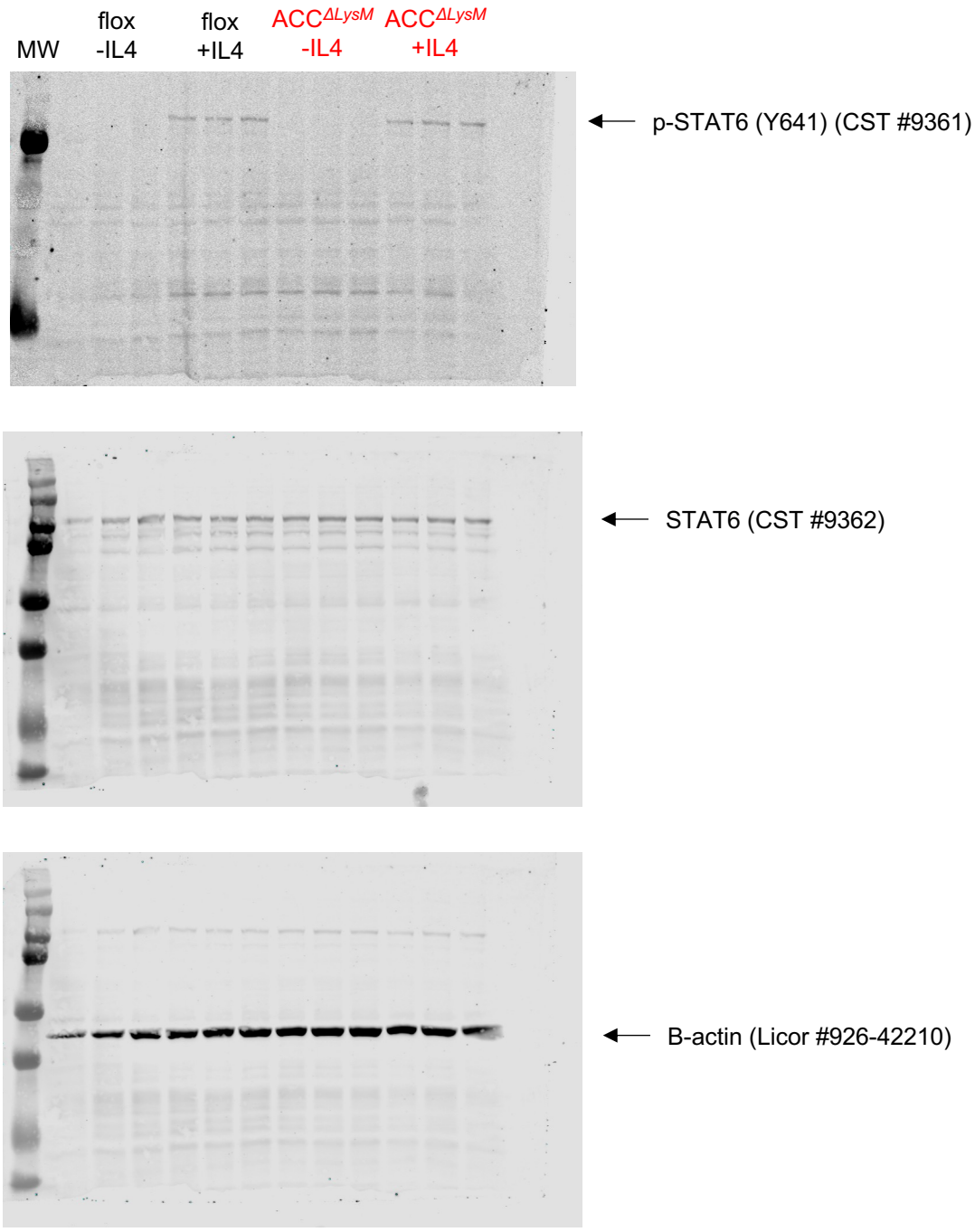

Full unedited blots for Figure S5C

Cell-surface biotin pulldown

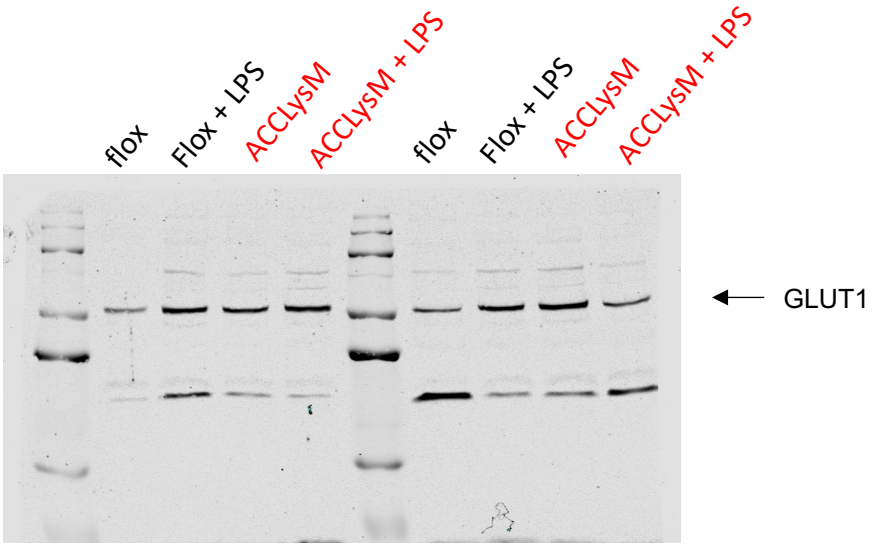

Input: whole cell lysate

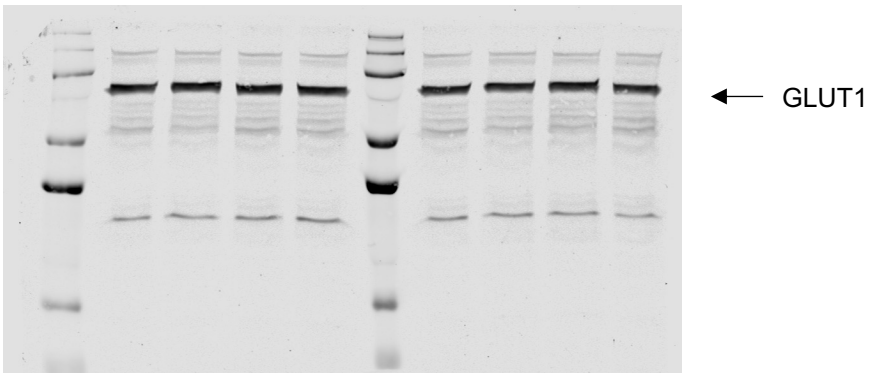

Full unedited gels for Supplementary Figure 1A – DNA gels

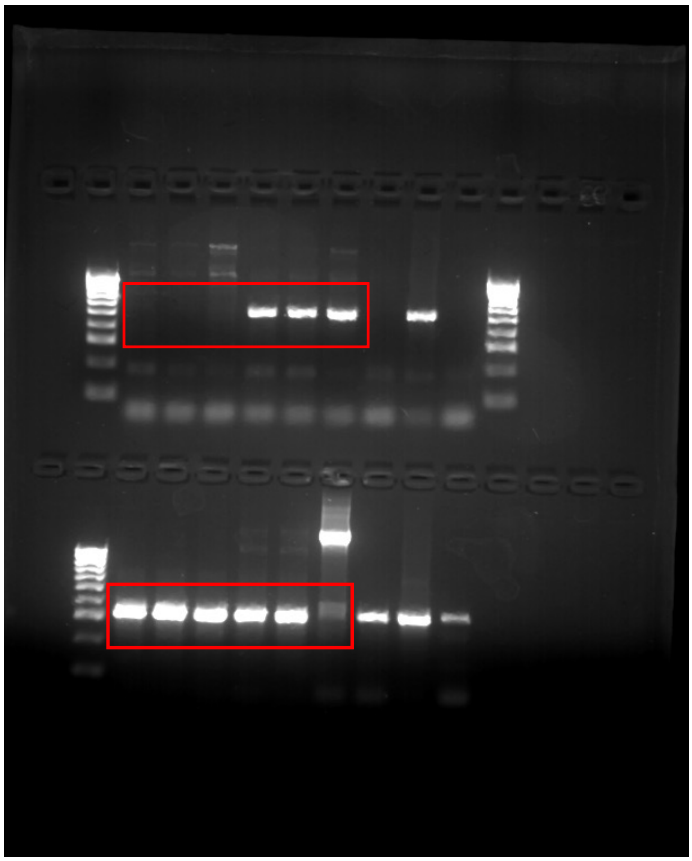

← LysM Cre transgene

← LysM WT gene

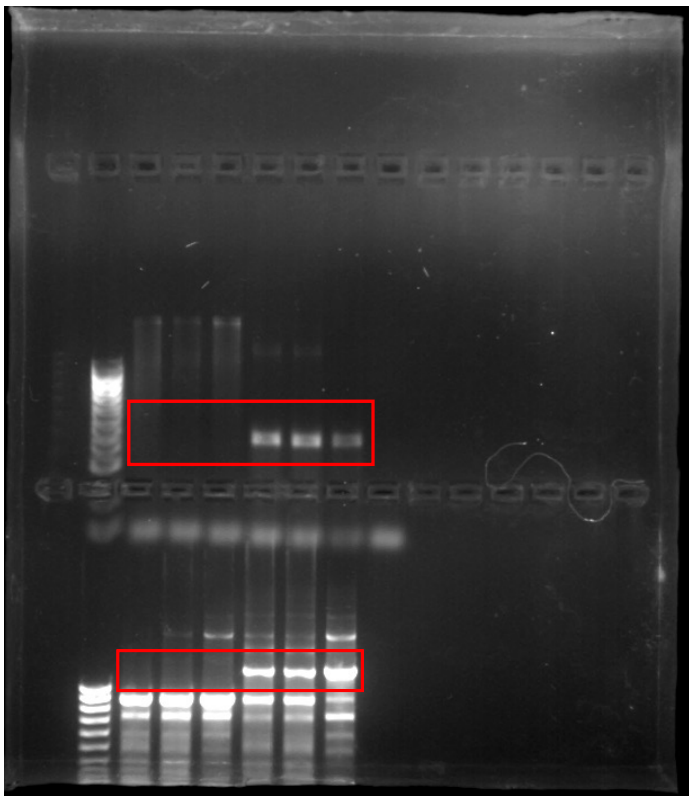

← *Acaca* – cre-mediated recombination

← *Acacb* – cre-mediated recombination

Selenoprotein T Protects Endothelial Cells against Lipopolysaccharide-Induced Activation and Apoptosis

Merk D*, Ptok J*, Jakobs P*, von Ameln F, **Greulich J**, Kluge P, Semperowitsch K, Eckermann O, Schaal H, Ale-Agha N[#], Altschmied J[#], Haendeler J[#]

Antioxidants. 2021; 10, 1427

*gleichberechtigte Erstautoren, [#]gleichberechtigete Seniorautoren

Publikation IV

Beteiligung der Autoren:

Merk D: Erstautor, war an der Planung und Durchführung der Versuche beteiligt, führte die Datenanalyse durch und war zudem am Entwurf des Manuskripts beteiligt.

Ptok J: Erstautor, war an der Planung und Durchführung der RNAseq Analysen beteiligt, führte die bioinformatische Datenanalyse durch und war zudem am Entwurf des Manuskripts beteiligt.

Jakobs P: Erstautor, war an der Planung und Durchführung der Versuche beteiligt, führte die Datenanalyse durch und war zudem am Entwurf des Manuskripts beteiligt.

von Ameln F: Führte real-time PCR-Analysen durch.

Greulich J: Führte Immunoblots durch.

Kluge P: Führte real-time PCR-Analysen durch.

Semperowitsch K: Führte lentivirale Transduktionen und RNA-Isolierungen durch.

Eckermann O: Führte Produktion und Titration lentiviraler Partikel durch.

Schaal H: Betreute die RNAseq Analysen und die bioinformatische Auswertung.

Ale-Agha N: Seniorautorin, war an der Konzeption der Studie federführend beteiligt, war an der Versuchsplanung beteiligt, schrieb und finalisierte das Manuskript.

Altschmied J: Seniorautor, war an der Konzeption der Studie federführend beteiligt, war an der Versuchsplanung beteiligt, schrieb und finalisierte das Manuskript.

Haendeler J: Seniorautorin, konzipierte die Studie, war an der Versuchsplanung beteiligt, schrieb und finalisierte das Manuskript.

antioxidants

MDPI

Article

Selenoprotein T Protects Endothelial Cells against Lipopolysaccharide-Induced Activation and Apoptosis

Dennis Merk [1,†], Johannes Ptok [2,†], Philipp Jakobs [1,†], Florian von Ameln [3], Jan Greulich [3], Pia Kluge [1], Kathrin Semperowitsch [1], Olaf Eckermann [1,3], Heiner Schaal [2], Niloofar Ale-Agha [1,*], Joachim Altschmied [1,3,*] and Judith Haendeler [1,*]

1 Environmentally-Induced Cardiovascular Degeneration, Clinical Chemistry and Laboratory Diagnostics, Medical Faculty, University Hospital and Heinrich-Heine University Düsseldorf, 40225 Düsseldorf, Germany; dennis.merk@hhu.de (D.M.); philipp.jakobs@hhu.de (P.J.); pia.kluge@uni-potsdam.de (P.K.); semperina@gmail.com (K.S.); olaf.eckermann@hhu.de (O.E.)

2 Institute for Virology, Medical Faculty, University Hospital and Heinrich-Heine University Düsseldorf, 40225 Düsseldorf, Germany; Johannes.ptok@hhu.de (J.P.); schaal@uni-duesseldorf.de (H.S.)

3 Environmentally-Induced Cardiovascular Degeneration, Clinical Chemistry and Laboratory Diagnostics, Medical Faculty, University Hospital and Heinrich-Heine University Düsseldorf, Germany and IUF-Leibniz Research Institute for Environmental Medicine, 40225 Düsseldorf, Germany; florian.ameln@hhu.de (F.v.A.); jan.greulich@hhu.de (J.G.)

* Correspondence: aleagha@hhu.de (N.A.-A.); joalt001@hhu.de (J.A.); juhae001@hhu.de (J.H.); Tel.: +49-211-3389-291 (N.A.-A. & J.A. & J.H.); Fax: +49-211-3389-331 (N.A.-A. & J.A. & J.H.)

† D.M., J.P. and P.J. contributed equally to the work.

Citation: Merk, D.; Ptok, J.; Jakobs, P.; von Ameln, F.; Greulich, J.; Kluge, P.; Semperowitsch, K.; Eckermann, O.; Schaal, H.; Ale-Agha, N.; et al. Selenoprotein T Protects Endothelial Cells against Lipopolysaccharide-Induced Activation and Apoptosis. *Antioxidants* **2021**, *10*, 1427. https://doi.org/10.3390/antiox10091427

Academic Editor: Stanley Omaye

Received: 17 August 2021
Accepted: 3 September 2021
Published: 7 September 2021

Abstract: Sepsis is an exaggerated immune response upon infection with lipopolysaccharide (LPS) as the main causative agent. LPS-induced activation and apoptosis of endothelial cells (EC) can lead to organ dysfunction and finally organ failure. We previously demonstrated that the first twenty amino acids of the Apurinic/Apyrimidinic Endodeoxyribonuclease 1 (APEX1) are sufficient to inhibit EC apoptosis. To identify genes whose regulation by LPS is affected by this N-terminal APEX1 peptide, EC were transduced with an expression vector for the APEX1 peptide or an empty control vector and treated with LPS. Following RNA deep sequencing, genes upregulated in LPS-treated EC expressing the APEX1 peptide were identified bioinformatically. Selected candidates were validated by semi-quantitative real time PCR, a promising one was Selenoprotein T (SELENOT). For functional analyses, an expression vector for SELENOT was generated. To study the effect of SELENOT expression on LPS-induced EC activation and apoptosis, the SELENOT vector was transfected in EC. Immunostaining showed that SELENOT was expressed and localized in the ER. EC transfected with the SELENOT plasmid showed no activation and reduced apoptosis induced by LPS. SELENOT as well as APEX1(1-20) can protect EC against activation and apoptosis and could provide new therapeutic approaches in the treatment of sepsis.

Keywords: APEX1(1-20); Selenoprotein T; lipopolysaccharide; endothelial cell activation; apoptosis

1. Introduction

Sepsis can best be described as an overwhelming inflammatory condition, in which the body responds to an infection in a hyperactive, dysregulated way, which in turn results in life-threatening organ dysfunction and eventually septic shock. According to an estimate of the World Health Organization (WHO), sepsis affects more than 48 million people every year, potentially leading to 11 million deaths [1]. The basis for the pathophysiological responses in the context of sepsis is multifactorial. Therefore, except for the introduction of vasopressor agents 40 years ago, no new therapeutic principle for the treatment of sepsis has been developed until today.

Lipopolysaccharide (LPS) is an outer membrane component of Gram-negative bacteria. Most bacterial LPS molecules are thermostable and generate a pro-inflammatory stimulus

for the immune system in humans. LPS is a serologically reactive bacterial toxin, and 1 to 2 mg in the bloodstream can be lethal. LPS can enter the bloodstream through intestinal absorption of the LPS produced by gut bacteria. Moreover, gut lesions and diet rich in lipids boost the transport across membranes into the systemic circulation [2]. Therefore, at the cellular level, endothelial cells (EC) are directly affected by LPS, which triggers their activation and ultimately apoptosis, leading to vascular leakage. Thus, it is undisputable that the loss of endothelial cell integrity is a mainstay of septic shock [3]. Hence, therapies that could prevent endothelial cell leakage or even restore endothelial cell integrity would be of tremendous value for patients and would address medical needs. EC with LPS affect the endothelial transcriptome by regulating the levels of numerous transcripts, not only of protein coding RNAs, but also of non-coding RNAs such as microRNAs and long non-coding RNAs [4,5]. Having pointed this out, it is a mystery to us that we failed to find any RNA deep sequencing data on LPS-induced transcriptome changes in the endothelium in the established databases such as the Gene expression omnibus (GEO), the European nucleotide archive (ENA), Short Sequence Archive (SRA) or ArrayExpress. However, such an in-depth transcriptome profiling combined with pathway analyses could provide novel targets for the development of new therapeutic principles for the treatment of sepsis, especially for protecting the endothelium. Therefore, one aim of this study was to perform a deep sequencing analysis in LPS-treated primary EC.

Moreover, we have recently shown that the first 20 amino acids of the Apurinic/Apyrimidinic Endodeoxyribonuclease 1 (APEX1) are sufficient to inhibit H_2O_2-induced apoptosis [6]. As the underlying molecular mechanisms initiating apoptosis are independent of the trigger, we hypothesized that this N-terminal APEX1 peptide, APEX1(1-20), could also interfere with LPS-induced apoptosis. Therefore, we included cells expressing the APEX1(1-20) in our deep sequencing analysis to find potential therapeutic targets for sepsis, possibly regulated by this peptide.

2. Materials and Methods

2.1. Cultivation of Primary Human Endothelial Cells and HEK293

Primary human endothelial cells (EC) were obtained from LONZA (Cologne, Germany) and cultured as previously described [7]. In detail, EC were cultured in endothelial basal medium supplemented with 1 µg/mL hydrocortisone, 12 µg/mL bovine brain extract, 50 µg/mL gentamicin, 50 ng/mL amphotericin B, 10 ng/mL epidermal growth factor (LONZA, Cologne, Germany) and 10% fetal bovine serum until the third passage. After detachment with trypsin, cells were grown for at least 20 h. All experiments were performed with EC in passage 3. HEK293 were cultured in DMEM GlutaMAX™ supplemented with 10% heat-inactivated fetal bovine serum and 1% penicillin/streptomycin and then used for the production of lentiviruses.

2.2. Lentiviral Production and Transduction of EC

Generation of VSV-G pseudotyped lentiviral particles and transduction of EC were performed as previously described [8]. Lentiviral titers were determined with the QuickTiter™ Lentivirus Titer kit (Lentivirus-Associated HIV p24) (Biocat, Heidelberg, Germany). EC were transduced with a multiplicity of infection of approximately 20. The day after transduction the cells were washed three times, the medium replaced, and cells cultivated for another day before they were treated with 150 ng/mL LPS for 18 h.

2.3. Isolation of Total Cellular RNA

Cells were lysed using TRIzol® (Thermo Fisher Scientific, Dreieich, Germany) and RNA was isolated according to the manufacturer's instructions. RNAs were subjected to a second purification step using the RNeasy® Mini kit (Qiagen, Hilden, Germany). RNA concentrations were measured using a NanoDrop™ 2000c (Thermo Fisher Scientific, Dreieich, Germany), and RNA integrity and purity were determined by agarose gel electrophoresis.

2.4. RNA Sequencing and Bioinformatic Analysis

RNA sequencing data were obtained from quadruplicate total RNA samples. Total RNAs used for transcriptome analyses were quantified using the Qubit™ RNA HS Assay kit (Thermo Fisher Scientific, Dreieich, Germany) and quality was determined by capillary electrophoresis using the FragmentAnalyzer and the Total RNA Standard Sensitivity Assay (Agilent Technologies, Santa Clara, CA, USA). All samples in this study showed highest RNA Quality Numbers (RQN 10.0). Library construction and sequencing were performed at the Genomics and Transcriptomics Laboratory at the Biological Medical Research Centre (BMFZ) of the Heinrich-Heine University Düsseldorf. Library preparation was performed according to the manufacturer's protocol using the TruSeq Stranded mRNA Assay kit (Illumina, San Diego, CA, USA). Briefly, 500 ng total RNA was used for mRNA capturing, fragmentation, synthesis of cDNA, adapter ligation and library amplification. Bead purified libraries were normalized and finally sequenced on the HiSeq 3000 system (Illumina San Diego, CA, USA) with a read setup of 1 × 150 bp. The bcl2fastq2 (version 2.17.1.4) tool was used to convert the bcl files to fastq files as well for adapter trimming and demultiplexing. GC-content, base-calling quality, adapter content and read length were measured using the tool FASTQC by Andrews (http://www.bioinformatics.babraham.ac.uk/projects/fastqc/ accessed on 17 August 2021) and MultiQC [9]. Reads were then trimmed or discarded based on their base calling quality and adapter content with Trimmomatic version 0.36 [10]. Subsequently, with the help of the SortMeRNA algorithm version 2.1b [11], the extent of rRNA depletion was measured by mapping the reads to rRNA databases. For alignment and the following analyses, the human genomic reference sequence (GRCh38) and annotation data (release 101) were downloaded from Ensembl [12] and BioMart [13]. For splice site usage analysis, the reads were then aligned to the human reference genome using the two-pass mapping protocol of the STAR aligner (2.5.4b) [14]. With help of the SAMtools software package [15], uniquely mapped reads were selected for creation of a gap table, listing the coordinates of every gap found in the alignment of the reads and the number of overlapping reads. For DGE analysis with the R package DESeq2 version 1.18.1 [16], count matrices were generated using the software salmon version 0.9.1 [17]. Significantly enriched gene sets were calculated, using the R package GOseq [18]. Scripts used for this work are publicly available at https://github.com/caggtaagtat/SELENOT (accessed on 17 August 2021). FASTQ file preparation and alignment were accomplished using custom BASH shell scripts in the environment of the High Performing Cluster of the Heinrich-Heine University Düsseldorf.

2.5. cDNA Synthesis

Total cellular RNA was reverse transcribed using the QuantiTect Reverse Transcription kit (Qiagen, Hilden Germany) according to the manufacturer's instructions.

2.6. Polymerase Chain Reaction (PCR)

Endpoint PCRs were performed with MyTaq™ HS DNA Polymerase (Biocat, Heidelberg, Germany) according to manufacturer's recommendations in a Bio-Rad T100 Thermal Cycler (Bio-Rad, Feldkirchen Germany). Reaction products were resolved on standard agarose gels.

Relative transcript levels were determined by semi-quantitative real-time PCR using cDNA as a template and the primaQUANT 2x qPCR-SYBR-Green-MasterMix (Steinbrenner, Wiesenbach, Germany), the transcript for the ribosomal protein L32 (RPL32), served as a reference. The PCR reactions were performed in a Rotor-Gene Q instrument (Qiagen, Hilden, Germany). Relative expression was calculated by the ΔC_t method [19].

The sequences of all primer used for PCR are listed in Supplementary Table S1.

2.7. Plasmids

A lentiviral expression vector for the first twenty amino acids of APEX1 was constructed by transferring the coding sequence for APEX1(1-20) with a C-terminal myc-tag

from the previously published expression vector [6] into a lentiviral transfer vector, in which the transgene is expressed under the transcriptional control of the cytomegalovirus immediate early promoter/enhancer [8]. To generate an expression vector for human SELENOT with an N-terminal FLAG-tag, the SELENOT coding sequence together with the first 179 bp of the 3′-untranslated region of the human SELENOT gene containing the selenocysteine insertion sequence were amplified from a human EC cDNA using Q5® High-Fidelity DNA Polymerase (New England Biolabs, Frankfurt, Germany). This fragment was inserted into pFLAG-CMV-2 (Sigma-Aldrich, Deisenhofen, Germany) opened with Not I and Xba I using the Gibson Assembly® Cloning kit (New England Biolabs, Frankfurt, Germany) according to the manufacturer's protocol. The construct was verified by DNA sequencing. Cloning details and the complete plasmid sequence are available upon request.

2.8. Transient Transfection of EC

Transient transfections of EC with plasmid DNA were performed using Superfect (Qiagen, Hilden, Germany) as previously described [20,21]. In detail, EC were transfected on 6 cm culture dishes with 3 µg plasmid DNA and 22.5 µL Superfect, or in 6-well plates with 1.2 µg plasmid DNA and 12 µL Superfect per well.

2.9. Immunostaining of EC

EC were fixed and permeabilized as described previously [7]. Afterwards, cells were incubated with an anti-FLAG-tag antibody (1:100, DYKDDDDK Tag Antibody (clone 8H8L17), Abfinity™, Cat. No. 701629, Invitrogen, Darmstadt, Germany). As secondary antibody, a goat anti-rabbit highly cross-adsorbed antibody coupled to Alexa Fluor 594 (1:500, Cat. No. A-11012, Invitrogen, Darmstadt, Germany) was used. For ICAM1 staining, an Alexa Fluor 488-coupled primary antibody (1:50, ICAM1/CD54 (15.2), Cat. No. SC-107 AF488, Santa Cruz Biotechnology, Heidelberg, Germany) was used. The endoplasmic reticulum (ER) was stained with an anti-Calnexin (clone C5C9) Alexa Fluor 488-conjugate (1:25, Cat. No. 38552, Cell Signaling, Technology, Frankfurt, Germany). Nuclei were counterstained with 4′,6-diamidino-2-phenylindole (DAPI) (100 ng/mL, Sigma-Aldrich, Deisenhofen, Germany). Images were taken using Zeiss microscopes (Axio Observer D1 or Axio Imager M2, magnification 400-fold, oil).

2.10. Immunoblotting

Cells were detached from the culture surface with a rubber policeman, centrifuged at 800× *g*, resuspended in radioimmunoprecipitation assay (RIPA) buffer (50 mM Tris-HCl pH 8.0, 150 mM NaCl, 1% (*v*/*v*) IGEPAL®-CA630, 0.1% (*w*/*v*) SDS and 0.5% (*w*/*v*) Na-Deoxycholate) supplemented with 1/100 volume of a protease inhibitor cocktail (Bimake, Munich, Germany) and lysed for 30 min on ice. The lysates were centrifuged at 18,000× *g* and 4 °C for 15 min and the supernatant was transferred to a fresh tube. Lysate proteins were separated by sodium-dodecyl-sulfate polyacrylamide gel electrophoresis according to standard procedures and transferred onto polyvinylidene difluoride membranes. After blocking with 5% milk powder in TBS (200 mM Tris-HCl pH 8.0, 300 mM NaCl, 100 mM KCl) with 0.1% (*v*/*v*) Tween-20 for 1 h at room temperature, membranes were incubated with an antibody directed against Caspase 3 (1:300 for detection of cleaved Caspase 3, 1:500 for uncleaved Caspase 3, Cat. No. 9662, Cell Signaling Technology, Frankfurt, Germany) and an anti α-Tubulin antibody (clone (DM1A), 1:50,000, Cat. No. T9026, Sigma-Aldrich, Deisenhofen, Germany). Antibodies were incubated overnight at 4 °C. The following day, membranes were incubated with secondary antibodies coupled to horseradish peroxidase (ECL™ Anti-Rabbit or Anti-Mouse IgG, Horseradish Peroxidase linked whole antibody (from sheep), 1:5000; Cat. Nos. NA934V and NA931V, GE healthcare, Solingen, Germany). Detection was performed using ECL substrate (GE healthcare, Solingen, Germany) and X-ray films. Semi-quantitative analyses were performed on scanned X-ray films using Fiji [22].

2.11. Statistics

The number of experiments (n) given in the figure legends represents independent biological replicates, the data shown are mean ± SEM. Normal distribution for all data sets was confirmed by a Shapiro–Wilk test; homogeneity of variances (from means) between groups was verified by Levene's test. Multiple comparisons were performed using one-way ANOVA with post-hoc Tukey LSD test.

3. Results

3.1. APEX1(1-20) Induces Specific Transcriptome Changes in EC in Response to LPS

To identify APEX1(1-20)-mediated transcriptome differences in the response of EC to LPS we performed RNA deep sequencing. For this purpose, primary human EC were transduced with either a lentiviral vector leading to moderate expression of APEX1(1-20) or an empty vector, respectively. Cells were then treated with 150 ng/mL active LPS or detoxified LPS as control. RNA from these cells was used for RNA deep sequencing and analyzed for differential gene expression (DGE). To identify APEX1(1-20)-specific transcriptome changes in response to LPS, we analyzed which genes were specifically regulated by LPS in the APEX1(1-20) expressing cells, but not in the cells transduced with the empty vector.

PCA analysis revealed that all samples from the cells treated with detoxified LPS cluster together, no matter whether the cells expressed APEX1(1-20) or not. The same held true for the LPS-treated cells (Supplementary Figure S1), showing a clear effect of LPS on the cellular transcriptome.

DGE analysis revealed that the APEX1(1-20) transcript derived from the expression vector was only detectable in the cells transduced with this vector, but not in the cells transduced with the empty vector. More importantly, expression of APEX1(1-20) alone did not appear to affect the overall transcriptome as changes in the expression of only a very small number of genes were observed (Supplementary Table S2).

In addition to the DGE analysis, we performed a gene set enrichment analysis (GSEA) focusing on genes that were significantly regulated by LPS exclusively in either the cells transduced with the empty vector or the cells expressing APEX1(1-20). As expected, cells transduced with the empty vector showed a significant enrichment of upregulated genes belonging to gene ontology (GO) terms related to immune responses including the response to bacteria and tumor necrosis factor signaling (Supplementary Table S3). Interestingly, we did not observe these changes in the presence of APEX1(1-20), and, moreover, genes belonging to the GO term cellular response to tumor necrosis factor were significantly downregulated in LPS-treated cells expressing the APEX1 peptide (Supplementary Table S4). These data support the assumption that APEX1(1-20) might provide protection against endothelial cell activation and apoptosis via alteration of the transcriptional responses to LPS treatment.

In the DGE analysis, we found that after LPS treatment, 323 genes were significantly upregulated in cells transduced with the empty vector and 280 were downregulated. In contrast, in the cells expressing APEX1(1-20), only 177 genes were upregulated by LPS and 139 genes were downregulated (Figure 1A,B and Supplementary Tables S5 and S6). Thus, the expression of only roughly half as many genes appeared to be affected by the presence of APEX1(1-20).

Notably, we observed clearly different LPS responses in cells expressing APEX1(1-20) when compared to cells transduced with the empty vector (Figure 1C–F and Supplementary Tables S7–S10).

For functional studies, we focused on genes whose expression is upregulated by LPS only in cells expressing the small APEX1 peptide as the corresponding proteins might evoke APEX1(1-20)-dependent protective effects in EC, which could be of interest in a therapeutic setting.

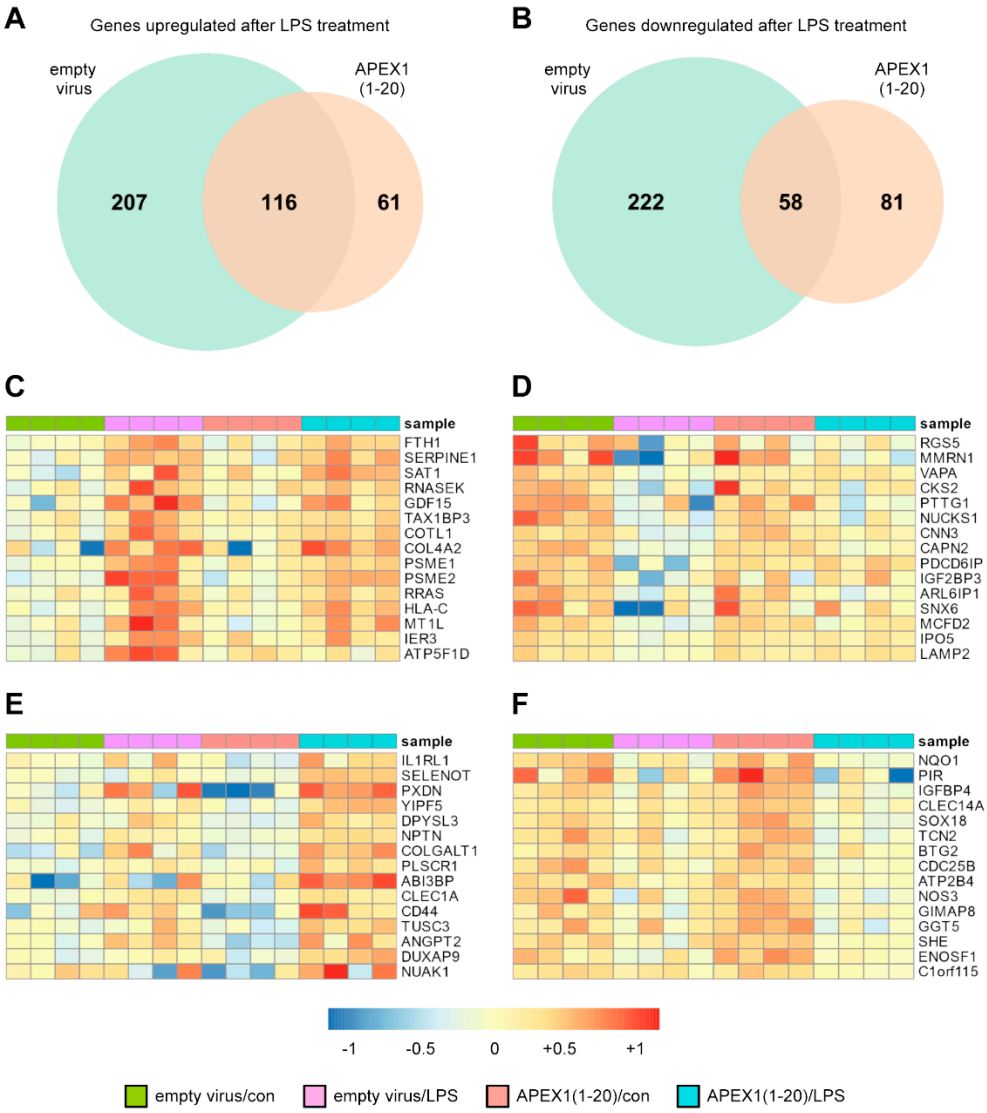

Figure 1. APEX1(1-20) induces specific transcriptome changes in EC in response to LPS. (**A**–**F**) EC were transduced with a lentiviral expression vector for APEX1(1-20) or an empty virus and treated with 150 ng/mL detoxified (con) or active LPS (LPS) for 18 h. RNAs from the transduced cells were subjected to RNA deep sequencing. Differential gene expression was calculated using the R package DESeq2. Wald test from DESeq2 was used to calculate the significance of the change in the expression. (**A**,**B**) Venn-diagrams for genes upregulated (**A**) or downregulated (**B**) after LPS treatment of empty virus transduced cells and cells expressing APEX1(1-20). (**C**–**F**) Heatmaps of genes significantly differentially expressed upon LPS treatment of cells transduced with the empty virus or cells expressing APEX1(1-20). Shown are the 15 top ranked genes from Supplementary Tables S7–S10. The color depicts the normalized expression relative to the respective mean in all samples. (**C**) Genes uniquely upregulated after LPS treatment of empty virus transduced cells. (**D**) Genes uniquely downregulated after LPS treatment of empty virus transduced cells. (**E**) Genes uniquely upregulated after LPS treatment of APEX1(1-20) expressing cells. (**F**) Genes uniquely downregulated after LPS treatment of APEX1(1-20) expressing cells.

3.2. Expression of PXDN and SELENOT Is Specifically Upregulated after LPS Treatment of EC Expressing APEX1(1-20)

As a prerequisite for functional studies, we first validated the regulation of the top-ranked candidates, which, according to the RNA sequencing data, should be expressed to levels allowing reliable detection and quantification.

IL1RL encodes an Interleukin 1 Receptor-like protein, which belongs to a family of ten distinct but structurally related receptors. These proteins serve either as ligand binding or accessory chains and some act as signaling inhibitors. Moreover, two members of this family are orphan receptors [23]. Therefore, IL1RL1 is part of a complex signaling network and one could easily envision that—due to this redundancy—interference with this network might be compensated or evoke unwanted side effects.

Peroxidasin (PXDN), originally described as Vascular Peroxidase 1, is a heme-containing peroxidase, which shows highest expression in the heart and the vascular wall [24]. The protein is rapidly secreted [25] and required for formation of the vascular basement membrane by reinforcing fibrillar network assembly in the extracellular matrix through formation of sulfilimine bonds [26]. It has recently been shown that PXDN promotes angiogenesis [27] and, furthermore, is essential for endothelial cell survival [28].

Selenoprotein T (SELENOT) is a member of the selenoprotein family, whose members are characterized by containing one or more selenocysteine residues, frequently in enzymatically active sites [29]. SELENOT is the most highly conserved selenoprotein throughout evolution [30], suggestive of an essential function, which is underscored by the early embryonic lethality of mice in which the *selenot* gene is constitutively disrupted [31]. SELENOT is one of 7 out of 25 human selenoproteins localized to the ER [32]. The expression of SELENOT, like all other selenoproteins, depends on dietary selenium as shown by a reduced expression in chicken stomach after 55 days on a selenium-deficient diet. Moreover, this regimen resulted in stress injuries [33]. In addition, SELENOT protects kidney cells against cisplatin-induced apoptosis [34]. These observations go along with the notion that ER-resident selenoproteins are critical in cellular stress responses [35].

For the reasons explained above, we did not follow up on IL1RL, but validated the regulation of PXDN and SELENOT by semi-quantitative real-time PCR (Figure 2).

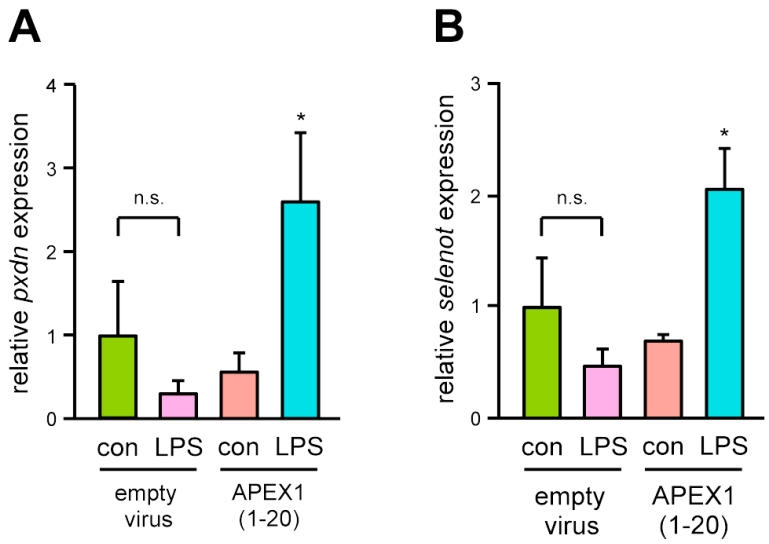

Figure 2. LPS induces upregulation of PXDN and SELENOT expression specifically in EC expressing APEX1(1-20). Transcript levels of PXDN (**A**) and SELENOT (**B**) in EC transduced with an empty virus or the expression vector for APEX1(1-20) and treated with 150 ng/mL detoxified (con) or active LPS (LPS) for 18 h were analyzed by semi-quantitative real-time PCR; RPL32 served as reference (data are mean ± SEM, $n = 4$, * $p < 0.05$ vs. APEX1(1-20)/con, n.s. = not significant, one-way ANOVA with post-hoc Tukey LSD test).

The real-time PCR analysis corroborated the deep sequencing data as for both genes, an upregulation of the transcript level by LPS was only observed in the cells expressing APEX1(1-20). Although PXDN has already been characterized with respect to protective functions in EC [28], these data provide independent proof for the validity of the experi-

mental approach. The second protein, SELENOT, for which no functions in endothelial activation and apoptosis have been described so far, was chosen for functional analyses.

3.3. Generation of a SELENOT Expression Vector and Intracellular Localization of the Overexpressed Protein

To study the impact of SELENOT on endothelial cell functions affected by LPS, we generated an expression vector, which contained a FLAG-epitope tag allowing the identification of the overexpressed protein. For the generation of this expression vector, an aspect unique to selenoproteins had to be taken into account. Selenocysteine (Sec) residues in selenoproteins are not the product of a post-translational modification, but are rather incorporated already during translation by using one of the translation termination codons, namely UGA, for binding of the selenocysteine tRNA ($tRNA^{Sec}$) to the mRNA. This translational recoding of the UGA codon involves a so-called selenocysteine insertion sequence (SECIS) in the 3′-untranslated region (UTR) of the transcript. The SECIS, which is not highly conserved on the sequence level, forms a stem-loop structure that is required for recruitment of the $tRNA^{Sec}$ to the UGA codon [36]. Consequently, the lack of a SECIS leads to premature translation termination, when the ribosome encounters the first UGA within the open reading frame. Therefore, we included—besides the SELENOT open reading frame—a portion of the SELENOT 3′-UTR including the SECIS in the expression vector.

We first analyzed the expression of FLAG-SELENOT after transient transfection of EC on the RNA level by reverse transcriptase PCR (Figure 3A). We then determined the intracellular localization of the overexpressed FLAG-SELENOT protein by immunofluorescence. As demonstrated by colocalization with the ER-resident protein Calnexin (Figure 3B), FLAG-SELENOT was localized in the ER.

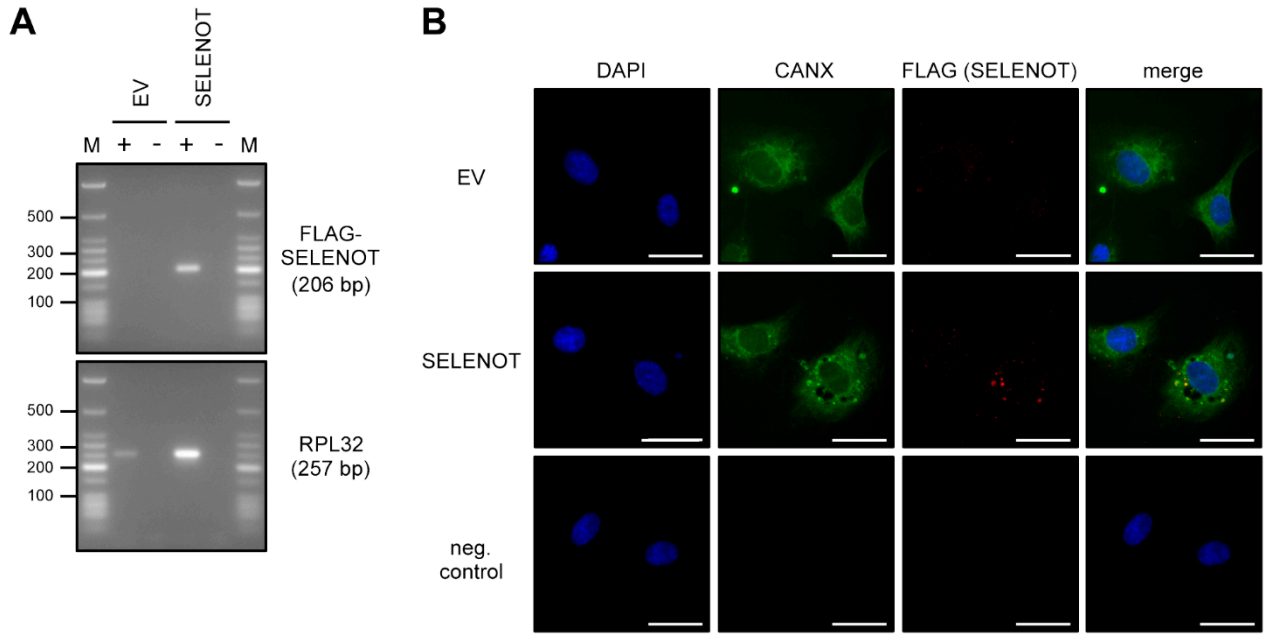

Figure 3. Overexpressed SELENOT is localized in the ER. (**A**,**B**) EC were transfected with the FLAG-SELENOT expression vector (SELENOT) or an empty vector (EV). Expression and localization of exogenously expressed SELENOT was verified on the RNA (**A**) and protein (**B**) level. (**A**) Expression of SELENOT was analyzed by reverse transcription polymerase chain reaction (RT-PCR). Therefore, RNA was isolated from the transfected cells and cDNA was synthesized in the presence (+) or absence (−) of reverse transcriptase. Amplification was performed with primers specifically detecting the FLAG-SELENOT fusion transcript, the housekeeping gene RPL32 served as control. Amplification products were resolved by agarose gel electrophoresis, the expected fragment sizes are specified, numbers on the left indicate selected DNA size markers (M). (**B**) Localization of FLAG-SELENOT was examined by immunostaining and fluorescence microscopy. Cells were stained with an antibody directed against Calnexin (CANX), a marker for the ER (green) and an anti-FLAG antibody (red). Nuclei were counterstained with DAPI (blue); merge is the overlay of all channels (scale bar = 30 µm).

3.4. SELENOT Overexpression Inhibits LPS-Induced Endothelial Cell Activation

Having demonstrated that FLAG-SELENOT is localized in the ER, we next investigated the effect of SELENOT on LPS-induced endothelial cell activation. Therefore, FLAG-SELENOT was expressed in EC as before. After treatment with 150 ng/mL LPS for 18 h, ICAM1—a marker for endothelial cell activation—was detected. As expected, LPS upregulated ICAM1 protein levels in empty vector transfected EC. This upregulation was completely inhibited in cells, in which SELENOT is overexpressed (Figure 4).

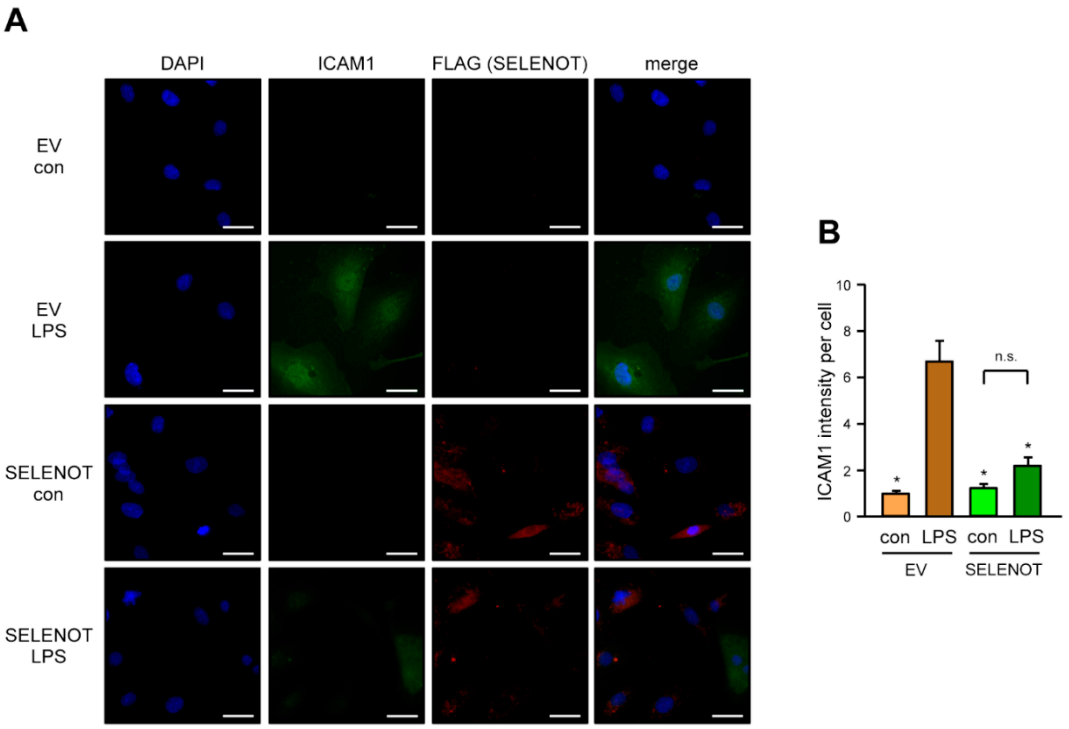

Figure 4. SELENOT suppresses LPS-induced upregulation of ICAM1. (**A**,**B**) EC were transfected with the FLAG-SELENOT expression vector (SELENOT) or an empty vector (EV) and treated with 150 ng/mL detoxified (con) or active LPS (LPS) for 18 h. FLAG-SELENOT and ICAM1 were detected by immunofluorescence. Cells were stained with an antibody directed ICAM1 (green) and an anti-FLAG antibody (red). Nuclei were counterstained with DAPI (blue); merge is the overlay of all channels. (**A**) Representative immunostaining (scale bar = 30 µm). (**B**) Quantitation of ICAM1 levels. The intensity of the green fluorescence per cell was measured using Fiji; in the cells transfected with the SELENOT expression vector, only FLAG-SELENOT positive cells were included (data are mean ± SEM, $n = 4$, * $p < 0.05$ vs. EV/LPS, n.s. = not significant, one-way ANOVA with post-hoc Tukey LSD test).

3.5. SELENOT Overexpression Inhibits LPS-Induced Endothelial Cell Apoptosis

Besides endothelial cell activation, LPS also induces apoptosis of EC [37]. Therefore, we determined Caspase 3 cleavage as a marker for apoptosis in EC. As for ICAM1, LPS increased Caspase 3 cleavage in cells not expressing SELENOT. On the contrary, overexpression of SELENOT completely blunted apoptosis induction by LPS (Figure 5).

In conclusion, SELENOT, which is upregulated by LPS in EC expressing APEX1(1-20), seems to be an important mediator of the protective effects of APEX1(1-20) and could thus be of interest as an adjuvant therapeutic agent in endotoxemia.

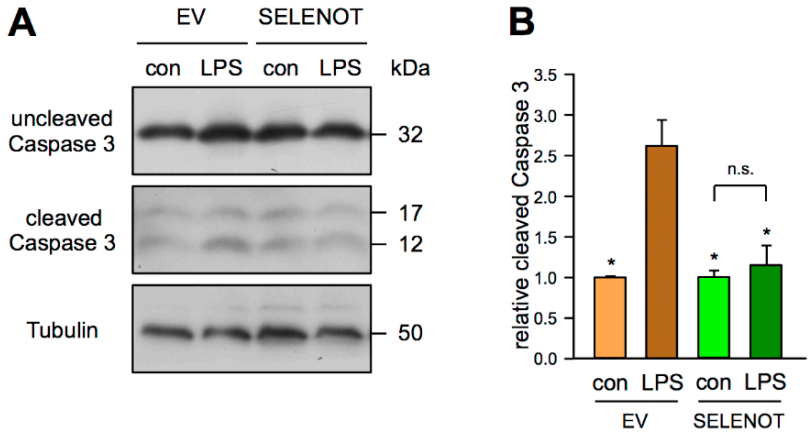

Figure 5. SELENOT suppresses apoptosis induction by LPS. (**A**,**B**) EC were transfected with the FLAG-SELENOT expression vector (SELENOT) or an empty vector (EV) and treated with 150 ng/mL detoxified (con) or active LPS (LPS) for 18 h. Uncleaved and cleaved Caspase 3 were detected by immunoblot, Tubulin served as loading control. (**A**) Representative immunoblot. (**B**) Semi-quantitative analysis of relative amounts of cleaved Caspase 3 (data are mean ± SEM, $n = 4$, * $p < 0.05$ vs. EV/LPS, n.s. = not significant, one-way ANOVA with post-hoc Tukey LSD test).

4. Discussion

The major findings of the present study are the first RNA deep sequencing analysis of LPS-induced changes in primary human EC and the identification of a protective role of APEX1(1-20) and SELENOT in LPS-induced endothelial cell activation and apoptosis.

With respect to the possibility of using an APEX1(1-20) peptide or a related small molecule as a therapeutic agent, it has to be noted that APEX1(1-20) does not change the transcriptome when compared to empty virus transduced cells. Thus, there is no evidence of potential side effects induced by APEX1(1-20) in the endothelium. As expected, LPS treatment induced typical pathways known in sepsis. Those upregulated genes upon LPS treatment in cells not expressing APEX1(1-20) are found, for example, under the GO terms cellular response to tumor necrosis factor, tumor necrosis factor-mediated signaling pathway, and plasma membrane (Supplementary Table S3). It has been known for years that tumor necrosis factor induces endothelial cell activation [38] and apoptosis [39]. Therefore, activation of those pathways is a typical answer of the endothelium to LPS, which in turn leads to loss of endothelial integrity and barrier function. Loss of endothelial cell integrity is a mainstay of septic shock [3], because LPS can enter the systemic circulation destroy endothelial cell integrity, thereby leading to multiple organ failure. Thus, an additional therapy protecting the integrity of the endothelium would be of tremendous interest. Interestingly, APEX1(1-20) leads to reduced responses of the tumor necrosis factor pathways (Supplementary Table S4). Hence, APEX1(1-20) or its downstream targets could be of interest as potential therapeutic options. Therefore, we specifically focused on those targets induced by APEX1(1-20) in the presence of LPS in EC to identify potential candidates. Indeed, we found SELENOT to be upregulated upon APEX1(1-20).

SELENOT is an ER-resident selenoprotein, which is associated with the ER membrane and required to maintain ER redox homeostasis. It is needed to cope with intracellular stress conditions and is one of the most important selenoproteins [30].

As mentioned before, the expression of all selenoproteins depends on selenium. However, there seems to be a hierarchy in the sensitivity of different selenoproteins with respect to selenium levels and SELENOT seems to respond more avidly to selenium depletion than several other proteins of this family [40]. It has been estimated that up to one in seven people worldwide have a low dietary selenium intake [41] and it is clear that proper endothelial functionality depends on an adequate selenium supply [42]. Even more interesting is the observation that selenium serum levels are dramatically reduced in critically ill patients with sepsis [43]. Therefore, selenium supplementation seems to be an obvious

supplementary treatment option for sepsis and possibly the protection of the endothelium in this disease. In this context, it is interesting to note that selenium pretreatment or supplementation alleviates some of the deleterious effects of LPS. In the murine macrophage cell line RAW264.7, LPS induced immunological stress as shown by the upregulation of multiple inflammation-related genes. This was accompanied by a reduction in the relative *selenot* mRNA level. Pretreatment with selenium partially rescued this downregulation and had only a very modest effect on the expression of the inflammation-related genes [44]. In mice, LPS-induced myocardial dysfunction, oxidative stress and apoptosis in the heart could be attenuated when the animals were put on a selenium-supplemented diet 2 weeks prior to LPS treatment [45]. Again, this pretreatment did not completely restore heart functionality or prevent oxidative stress and apoptosis induction evoked by LPS. Our experiments did not show a significant downregulation of *selenot* expression in LPS-treated EC, although there seems to be a trend in this direction. On the contrary, the cells expressing APEX1(1-20) showed an upregulation of *selenot* RNA levels of approximately threefold after LPS treatment. This clearly indicates that the small APEX1 peptide can convey a protective outcome, which is much stronger than the effects observed with selenium supplementation or pretreatment.

Up to now, the precise molecular functions of SELENOT have not been elucidated. Nevertheless, a peptide derived from SELENOT has already been used in animal models. Rocca et al. demonstrated that this SELENOT-derived peptide—including the active catalytic site corresponding to the sequence FQICVSUGYR—applied after ischemia and prior to reperfusion is able to protect the heart from ischemia/reperfusion injury. This protection was attributed to a reduction in oxidative stress and inhibition of apoptosis [46]. This is in accordance with our study presented here, in which we demonstrate that SELENOT completely inhibited LPS-induced activation and apoptosis in human primary EC.

The same peptide was applied in a cell-permeable form in a mouse model for Parkinson's disease, where it protected dopaminergic neurons. This effect was also associated with reduced oxidative stress and Caspase 3 activity [47].

Based on the protective effects of this SELENOT peptide in such different organs as the brain and the heart, it is conceivable that it could exert its protective functions also in the vasculature in the setting of sepsis.

Given the high numbers of patients and the up to 11 million deaths per year due to sepsis, a protection of the endothelium as an additional additive therapy could be of tremendous importance. The metabolic response to sepsis entails the rapid breakdown of intracellular reserves of proteins, carbohydrates and fat. This is accompanied by an increase in ER stress. An increase in SELENOT or application of a peptide could dampen this stress and maintain the ER homeostasis, counteracting the overshooting responses of the body to sepsis.

5. Conclusions

In conclusion, our data presented here suggest that APEX1(1-20) and SELENOT are promising therapeutic options for the treatment of sepsis to protect the endothelium and thus, to prevent endothelial cell leakage or even to restore endothelial cell integrity. This would be of tremendous value for patients and would potentially lower the numbers of septic shock, multiple organ failure and deaths.

Supplementary Materials: The following are available online at https://www.mdpi.com/article/10.3390/antiox10091427/s1, Figure S1: Principal component analysis, Table S1: Primer pairs used for endpoint PCR and semi-quantitative real-time PCR. Primer pairs used for endpoint PCR and semi-quantitative real-time PCR, Table S2: Differential gene expression analysis for genes regulated byexpression of APEX1(1-20), Table S3: Overrepresented GO terms in genes upregulated by LPS exclusively in cells not expressing APEX1(1-20), Table S4: Overrepresented GO terms in genes downregulated by LPS exclusively in cells expressing APEX1(1-20), Table S5: Differentially expressed genes upon LPS treatment of cells not expressing APEX1(1-20), Table S6: Differentially expressed genes upon LPS treatment of cells expressing APEX1(1-20), Table S7: Genes upregulated by LPS exclusively

in cells that do not express APEX1(1-20), Table S8: Genes downregulated by LPS exclusively in cells that do not express APEX1(1-20), Table S9: Genes upregulated by LPS exclusively in cells that express APEX1(1-20), Table S10: Genes downregulated by LPS exclusively in cells that express APEX1(1-20).

Author Contributions: Conceptualization, H.S., N.A.-A., J.A. and J.H.; Data curation, H.S., N.A.-A., J.A. and J.H.; Formal analysis, D.M., J.P., P.J. and P.K.; Funding acquisition, H.S. and J.A.; Investigation, D.M., J.P., P.J., F.v.A., J.G., P.K., K.S., O.E. and N.A.-A.; Methodology, D.M., J.P., P.J. and P.K.; Project administration, H.S., J.A. and J.H.; Resources, H.S., J.A. and J.H.; Supervision, P.J., H.S., N.A.-A., J.A. and J.H.; Validation, D.M., J.P., P.J. and P.K.; Visualization, D.M., J.P. and N.A.-A.; Writing—original draft, D.M. and J.P.; Writing—review and editing, H.S., N.A.-A., J.A. and J.H. All authors have read and agreed to the published version of the manuscript.

Funding: This research was funded by the Deutsche Forschungsgemeinschaft (DFG), IRTG1902-1 and IRTG1902-2 to J.A. and J.H. D.M., J.G. and K.S. are stipend holders of the IRTG1902. This research was also in part funded by Bayer Grant4Target (2019-08-2427) to J.H. and by intramural funding (9772727) of the University Hospital of the Heinrich-Heine University to H.S. and J.H.

Institutional Review Board Statement: Not applicable.

Informed Consent Statement: Not applicable.

Data Availability Statement: Data are contained within the article. The RNA sequencing data used to support the findings of this study have been deposited at ArrayExpress under accession number E-MTAB-10936 (https://www.ebi.ac.uk/arrayexpress/09/2021, accessed on 17 August 2021).

Acknowledgments: Computational support and infrastructure were provided by the Center for Information and Media Technology (ZIM) at the Heinrich-Heine University Düsseldorf.

Conflicts of Interest: The authors declare no conflict of interest.

References

1. Rudd, K.E.; Johnson, S.C.; Agesa, K.M.; Shackelford, K.A.; Tsoi, D.; Kievlan, D.R.; Colombara, D.V.; Ikuta, K.S.; Kissoon, N.; Finfer, S.; et al. Global, regional, and national sepsis incidence and mortality, 1990–2017: Analysis for the Global Burden of Disease Study. *Lancet* **2020**, *395*, 200–211. [CrossRef]
2. Boutagy, N.E.; McMillan, R.P.; Frisard, M.I.; Hulver, M.W. Metabolic endotoxemia with obesity: Is it real and is it relevant? *Biochimie* **2016**, *124*, 11–20. [CrossRef]
3. Joffre, J.; Hellman, J.; Ince, C.; Ait-Oufella, H. Endothelial Responses in Sepsis. *Am. J. Respir. Crit. Care Med.* **2020**, *202*, 361–370. [CrossRef]
4. Zhao, B.; Bowden, R.A.; Stavchansky, S.A.; Bowman, P.D. Human endothelial cell response to gram-negative lipopolysaccharide assessed with cDNA microarrays. *Am. J. Physiol. Cell Physiol.* **2001**, *281*, C1587–C1595. [CrossRef]
5. Ho, J.; Chan, H.; Wong, S.H.; Wang, M.H.; Yu, J.; Xiao, Z.; Liu, X.; Choi, G.; Leung, C.C.; Wong, W.T.; et al. The involvement of regulatory non-coding RNAs in sepsis: A systematic review. *Crit. Care* **2016**, *20*, 383. [CrossRef]
6. Dyballa-Rukes, N.; Jakobs, P.; Eckers, A.; Ale-Agha, N.; Serbulea, V.; Aufenvenne, K.; Zschauer, T.C.; Rabanter, L.L.; Jakob, S.; von Ameln, F.; et al. The Anti-Apoptotic Properties of APEX1 in the Endothelium Require the First 20 Amino Acids and Converge on Thioredoxin-1. *Antioxid. Redox Signal.* **2017**, *26*, 616–629. [CrossRef]
7. Ale-Agha, N.; Goy, C.; Jakobs, P.; Spyridopoulos, I.; Gonnissen, S.; Dyballa-Rukes, N.; Aufenvenne, K.; von Ameln, F.; Zurek, M.; Spannbrucker, T.; et al. CDKN1B/p27 is localized in mitochondria and improves respiration-dependent processes in the cardiovascular system-New mode of action for caffeine. *PLoS Biol.* **2018**, *16*, e2004408. [CrossRef]
8. Goy, C.; Czypiorski, P.; Altschmied, J.; Jakob, S.; Rabanter, L.L.; Brewer, A.C.; Ale-Agha, N.; Dyballa-Rukes, N.; Shah, A.M.; Haendeler, J. The imbalanced redox status in senescent endothelial cells is due to dysregulated Thioredoxin-1 and NADPH oxidase 4. *Exp. Gerontol.* **2014**, *56*, 45–52. [CrossRef]
9. Ewels, P.; Magnusson, M.; Lundin, S.; Käller, M. MultiQC: Summarize analysis results for multiple tools and samples in a single report. *Bioinformatics* **2016**, *32*, 3047–3048. [CrossRef]
10. Bolger, A.M.; Lohse, M.; Usadel, B. Trimmomatic: A flexible trimmer for Illumina sequence data. *Bioinformatics* **2014**, *30*, 2114–2120. [CrossRef]
11. Kopylova, E.; Noé, L.; Touzet, H. SortMeRNA: Fast and accurate filtering of ribosomal RNAs in metatranscriptomic data. *Bioinformatics* **2012**, *28*, 3211–3217. [CrossRef]
12. Yates, A.D.; Achuthan, P.; Akanni, W.; Allen, J.; Allen, J.; Alvarez-Jarreta, J.; Amode, M.R.; Armean, I.M.; Azov, A.G.; Bennett, R.; et al. Ensembl 2020. *Nucleic Acids Res.* **2020**, *48*, D682–D688. [CrossRef]
13. Durinck, S.; Moreau, Y.; Kasprzyk, A.; Davis, S.; De Moor, B.; Brazma, A.; Huber, W. BioMart and Bioconductor: A powerful link between biological databases and microarray data analysis. *Bioinformatics* **2005**, *21*, 3439–3440. [CrossRef]

14. Dobin, A.; Davis, C.A.; Schlesinger, F.; Drenkow, J.; Zaleski, C.; Jha, S.; Batut, P.; Chaisson, M.; Gingeras, T.R. STAR: Ultrafast universal RNA-seq aligner. *Bioinformatics* **2013**, *29*, 15–21. [CrossRef]
15. Li, H.; Handsaker, B.; Wysoker, A.; Fennell, T.; Ruan, J.; Homer, N.; Marth, G.; Abecasis, G.; Durbin, R. The Sequence Alignment/Map format and SAMtools. *Bioinformatics* **2009**, *25*, 2078–2079. [CrossRef]
16. Love, M.I.; Huber, W.; Anders, S. Moderated estimation of fold change and dispersion for RNA-seq data with DESeq2. *Genome Biol.* **2014**, *15*, 550. [CrossRef]
17. Patro, R.; Duggal, G.; Love, M.I.; Irizarry, R.A.; Kingsford, C. Salmon provides fast and bias-aware quantification of transcript expression. *Nat. Methods* **2017**, *14*, 417–419. [CrossRef] [PubMed]
18. Young, M.D.; Wakefield, M.J.; Smyth, G.K.; Oshlack, A. Gene ontology analysis for RNA-seq: Accounting for selection bias. *Genome Biol.* **2010**, *11*, R14. [CrossRef]
19. Pfaffl, M.W. A new mathematical model for relative quantification in real-time RT-PCR. *Nucleic Acids Res.* **2001**, *29*, e45. [CrossRef]
20. Jakob, S.; Schroeder, P.; Lukosz, M.; Büchner, N.; Spyridopoulos, I.; Altschmied, J.; Haendeler, J. Nuclear protein tyrosine phosphatase Shp-2 is one important negative regulator of nuclear export of telomerase reverse transcriptase. *J. Biol. Chem.* **2008**, *283*, 33155–33161. [CrossRef]
21. Schroeder, P.; Popp, R.; Wiegand, B.; Altschmied, J.; Haendeler, J. Nuclear redox-signaling is essential for apoptosis inhibition in endothelial cells–important role for nuclear thioredoxin-1. *Arterioscler. Thromb. Vasc. Biol.* **2007**, *27*, 2325–2331. [CrossRef] [PubMed]
22. Schindelin, J.; Arganda-Carreras, I.; Frise, E.; Kaynig, V.; Longair, M.; Pietzsch, T.; Preibisch, S.; Rueden, C.; Saalfeld, S.; Schmid, B.; et al. Fiji: An open-source platform for biological-image analysis. *Nat. Methods* **2012**, *9*, 676–682. [CrossRef]
23. Boraschi, D.; Italiani, P.; Weil, S.; Martin, M.U. The family of the interleukin-1 receptors. *Immunol. Rev.* **2018**, *281*, 197–232. [CrossRef]
24. Cheng, G.; Salerno, J.C.; Cao, Z.; Pagano, P.J.; Lambeth, J.D. Identification and characterization of VPO1, a new animal heme-containing peroxidase. *Free Radic. Biol. Med.* **2008**, *45*, 1682–1694. [CrossRef] [PubMed]
25. Cheng, G.; Li, H.; Cao, Z.; Qiu, X.; McCormick, S.; Thannickal, V.J.; Nauseef, W.M. Vascular peroxidase-1 is rapidly secreted, circulates in plasma, and supports dityrosine cross-linking reactions. *Free Radic. Biol. Med.* **2011**, *51*, 1445–1453. [CrossRef]
26. Bhave, G.; Cummings, C.F.; Vanacore, R.M.; Kumagai-Cresse, C.; Ero-Tolliver, I.A.; Rafi, M.; Kang, J.S.; Pedchenko, V.; Fessler, L.I.; Fessler, J.H.; et al. Peroxidasin forms sulfilimine chemical bonds using hypohalous acids in tissue genesis. *Nat. Chem. Biol.* **2012**, *8*, 784–790. [CrossRef]
27. Medfai, H.; Khalil, A.; Rousseau, A.; Nuyens, V.; Paumann-Page, M.; Sevcnikar, B.; Furtmüller, P.G.; Obinger, C.; Moguilevsky, N.; Peulen, O.; et al. Human peroxidasin 1 promotes angiogenesis through ERK1/2, Akt, and FAK pathways. *Cardiovasc. Res.* **2019**, *115*, 463–475. [CrossRef]
28. Lee, S.W.; Kim, H.K.; Naidansuren, P.; Ham, K.A.; Choi, H.S.; Ahn, H.Y.; Kim, M.; Kang, D.H.; Kang, S.W.; Joe, Y.A. Peroxidasin is essential for endothelial cell survival and growth signaling by sulfilimine crosslink-dependent matrix assembly. *FASEB J.* **2020**, *34*, 10228–10241. [CrossRef]
29. Mariotti, M.; Ridge, P.G.; Zhang, Y.; Lobanov, A.V.; Pringle, T.H.; Guigo, R.; Hatfield, D.L.; Gladyshev, V.N. Composition and evolution of the vertebrate and mammalian selenoproteomes. *PLoS ONE* **2012**, *7*, e33066. [CrossRef]
30. Pothion, H.; Jehan, C.; Tostivint, H.; Cartier, D.; Bucharles, C.; Falluel-Morel, A.; Boukhzar, L.; Anouar, Y.; Lihrmann, I. Selenoprotein T: An Essential Oxidoreductase Serving as a Guardian of Endoplasmic Reticulum Homeostasis. *Antioxid. Redox Signal.* **2020**, *33*, 1257–1275. [CrossRef]
31. Boukhzar, L.; Hamieh, A.; Cartier, D.; Tanguy, Y.; Alsharif, I.; Castex, M.; Arabo, A.; El Hajji, S.; Bonnet, J.J.; Errami, M.; et al. Selenoprotein T Exerts an Essential Oxidoreductase Activity That Protects Dopaminergic Neurons in Mouse Models of Parkinson's Disease. *Antioxid. Redox Signal.* **2016**, *24*, 557–574. [CrossRef] [PubMed]
32. Pitts, M.W.; Hoffmann, P.R. Endoplasmic reticulum-resident selenoproteins as regulators of calcium signaling and homeostasis. *Cell Calcium* **2018**, *70*, 76–86. [CrossRef]
33. Huang, X.; Sun, B.; Zhang, J.; Gao, Y.; Li, G.; Chang, Y. Selenium Deficiency Induced Injury in Chicken Muscular Stomach by Downregulating Selenoproteins. *Biol. Trace Elem. Res.* **2017**, *179*, 277–283. [CrossRef] [PubMed]
34. Huang, J.; Bao, D.; Lei, C.T.; Tang, H.; Zhang, C.Y.; Su, H.; Zhang, C. Selenoprotein T protects against cisplatin-induced acute kidney injury through suppression of oxidative stress and apoptosis. *FASEB J.* **2020**, *34*, 11983–11996. [CrossRef]
35. Addinsall, A.B.; Wright, C.R.; Andrikopoulos, S.; van der Poel, C.; Stupka, N. Emerging roles of endoplasmic reticulum-resident selenoproteins in the regulation of cellular stress responses and the implications for metabolic disease. *Biochem. J.* **2018**, *475*, 1037–1057. [CrossRef]
36. Tujebajeva, R.M.; Copeland, P.R.; Xu, X.M.; Carlson, B.A.; Harney, J.W.; Driscoll, D.M.; Hatfield, D.L.; Berry, M.J. Decoding apparatus for eukaryotic selenocysteine insertion. *EMBO Rep.* **2000**, *1*, 158–163. [CrossRef]
37. Haendeler, J.; Messmer, U.K.; Brüne, B.; Neugebauer, E.; Dimmeler, S. Endotoxic shock leads to apoptosis in vivo and reduces Bcl-2. *Shock* **1996**, *6*, 405–409. [CrossRef]
38. Pober, J.S. Endothelial activation: Intracellular signaling pathways. *Arthritis Res. Ther.* **2002**, *4* (Suppl. 3), S109–S116. [CrossRef]
39. Dimmeler, S.; Haendeler, J.; Rippmann, V.; Nehls, M.; Zeiher, A.M. Shear stress inhibits apoptosis of human endothelial cells. *FEBS Lett.* **1996**, *399*, 71–74. [CrossRef]

40. Carlson, B.A.; Xu, X.M.; Gladyshev, V.N.; Hatfield, D.L. Selective rescue of selenoprotein expression in mice lacking a highly specialized methyl group in selenocysteine tRNA. *J. Biol. Chem.* **2005**, *280*, 5542–5548. [CrossRef]
41. Jones, G.D.; Droz, B.; Greve, P.; Gottschalk, P.; Poffet, D.; McGrath, S.P.; Seneviratne, S.I.; Smith, P.; Winkel, L.H. Selenium deficiency risk predicted to increase under future climate change. *Proc. Natl. Acad. Sci. USA* **2017**, *114*, 2848–2853. [CrossRef] [PubMed]
42. Lopes Junior, E.; Leite, H.P.; Konstantyner, T. Selenium and selenoproteins: From endothelial cytoprotection to clinical outcomes. *Transl. Res.* **2019**, *208*, 85–104. [CrossRef]
43. Mertens, K.; Lowes, D.A.; Webster, N.R.; Talib, J.; Hall, L.; Davies, M.J.; Beattie, J.H.; Galley, H.F. Low zinc and selenium concentrations in sepsis are associated with oxidative damage and inflammation. *Br. J. Anaesth.* **2015**, *114*, 990–999. [CrossRef]
44. Wang, L.; Jing, J.; Yan, H.; Tang, J.; Jia, G.; Liu, G.; Chen, X.; Tian, G.; Cai, J.; Shang, H.; et al. Selenium Pretreatment Alleviated LPS-Induced Immunological Stress Via Upregulation of Several Selenoprotein Encoding Genes in Murine RAW264.7 Cells. *Biol. Trace Elem. Res.* **2018**, *186*, 505–513. [CrossRef] [PubMed]
45. Wang, X.; Yang, B.; Cao, H.L.; Wang, R.Y.; Lu, Z.Y.; Chi, R.F.; Li, B. Selenium Supplementation Protects Against Lipopolysaccharide-Induced Heart Injury via Sting Pathway in Mice. *Biol. Trace Elem. Res.* **2021**, *199*, 1885–1892. [CrossRef] [PubMed]
46. Rocca, C.; Boukhzar, L.; Granieri, M.C.; Alsharif, I.; Mazza, R.; Lefranc, B.; Tota, B.; Leprince, J.; Cerra, M.C.; Anouar, Y.; et al. A selenoprotein T-derived peptide protects the heart against ischaemia/reperfusion injury through inhibition of apoptosis and oxidative stress. *Acta Physiol.* **2018**, *223*, e13067. [CrossRef] [PubMed]
47. Alsharif, I.; Boukhzar, L.; Lefranc, B.; Godefroy, D.; Aury-Landas, J.; Rego, J.D.; Rego, J.D.; Naudet, F.; Arabo, A.; Chagraoui, A.; et al. Cell-penetrating, antioxidant SELENOT mimetic protects dopaminergic neurons and ameliorates motor dysfunction in Parkinson's disease animal models. *Redox Biol.* **2021**, *40*, 101839. [CrossRef]

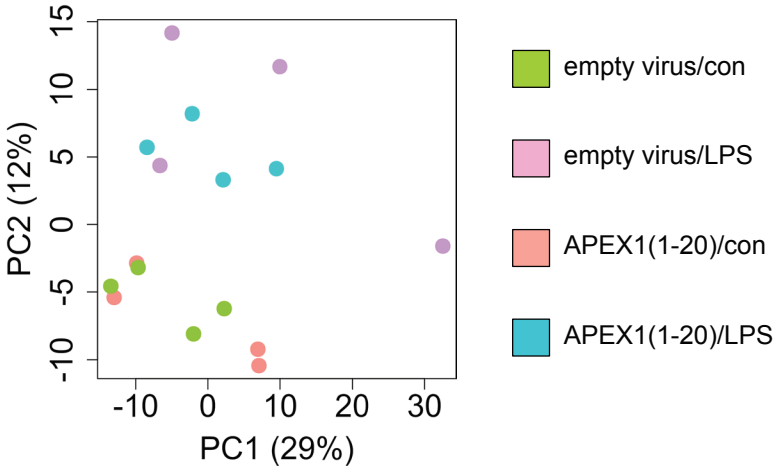

Supplementary figure S1: Principal component analysis. Endothelial cells were transduced with a lentiviral expression vector for APEX1(1-20) or an empty virus and treated with detoxified (con) or active LPS (LPS). and subjected to RNA deep sequencing.

Supplementary table S1: Primer pairs used for endpoint PCR and semi-quantitative real-time PCR.
Shown are the sequences of the primers in 5'→3' direction and the expected amplification products.

transcript	primer	sequence	amplification product
RPL32	hmRPL32 Ex02 for1	5'- GTGAAGCCCAAGATCGTCAA -3'	257 bp
	hmRPL32 Ex03 rev1	5'- TTGTTGCACATCAGCAGCAC -3'	
PXDN	hPXDN Ex20/21 for1	5'- CGGAAAATACCCAGTGTTGGGAG -3'	223 bp
	hPXDN Ex22 rev1	5'- TGGTGTTGTTGGCGTGAGATTC -3'	
SELENOT	hSELENOT Ex01 for	5'- GCGTGCCCAGCAAGAGATTA -3'	99bp
	hSELENOT Ex02 rev1	5'- ACTCCTCAAACACCCGCCTA -3'	
FLAG-SELENOT	FLAG for2	5'- CAAAGACGATGACGACAAGC -3'	206 bp
	hSELENOT Ex02 rev1	5'- ACTCCTCAAACACCCGCCTA -3'	

Supplementary Table S2: Differential gene expression analysis for genes regulated by expression of APEX1(1-20). DGE was calculated using the R package DESeq2 in samples of cells transduced with the lentivirus expressing APEX1(1-20) versus cells transduced with the empty virus both treated with detoxified LPS. The L2FC (Log 2-fold change) states the ave-rage difference in gene expression between the two cell populations. Positive L2FC values denote upregulation by APEX1(1-20) expression, negative values downregulation. Wald test from DESeq2 was used to calculate the significance of the change in the expression. The adjusted p-values take the number of tested genes into account, the threshold for the adjusted p-value was set to 0.05. APEX1(1-20)-myc represents the transcript originating from the APEX1(1-20) expression vector, which codes for a fusion between the APEX1 peptide and a myc epitope tag.

gene name	Ensembl gene ID	L2FC	p-value	adusted p-value
APEX1(1-20)-myc	NA	9,861	3,73E-40	2,92E-36
LRTOMT	ENSG00000184154	0,653	5,85E-11	3,06E-07
SRP9P1	ENSG00000180581	-26,509	5,11E-10	2,00E-06
AL358472.7	NA	21,631	2,86E-08	8,99E-05
CR354443.1	NA	-23,191	6,74E-08	1,51E-04
H3P6	ENSG00000235655	-22,915	6,69E-08	1,51E-04
KCNJ15	ENSG00000157551	-0,848	1,05E-06	2,06E-03
CAMSAP3	ENSG00000076826	1,139	7,29E-06	1,21E-02
GJA5	ENSG00000265107	0,484	7,73E-06	1,21E-02
GDF7	ENSG00000143869	0,397	9,76E-06	1,39E-02
CCL2	ENSG00000108691	0,324	1,80E-05	2,35E-02
HNRNPCP1	ENSG00000258900	17,502	4,12E-05	4,97E-02

Supplementary Table S3: Overrepresented GO terms in genes upregulated by LPS exclusively in cells not expressing APEX1(1-20). Gene set enrichment analysis (GSEA) was applied to genes from the DGE analysis, which were significantly upregulated by LPS exclusively in cells transduced with the empty virus GSEA was performed using R package goseq with a treshold on the adjusted p-values of 0.05. numDEInCat: number of differentially expressed genes belonging to the respective GO term; numInCat: number of genes related to the GO term.

GO ID	GO term	overrepresented p-value	adjusted p-value	numDEInCat	numInCat
GO:0005886	plasma membrane	8,50E-08	8,19E-05	101	2946
GO:0002479	antigen processing and presentation of exogenous peptide antigen via MHC class I, TAP-dependent	5,13E-06	2,95E-03	10	65
GO:0050852	T cell receptor signaling pathway	8,51E-06	4,63E-03	13	134
GO:0033209	tumor necrosis factor-mediated signaling pathway	9,82E-06	5,18E-03	12	102
GO:0019722	calcium-mediated signaling	1,05E-05	5,38E-03	8	49
GO:0002250	adaptive immune response	1,11E-05	5,45E-03	11	92
GO:0006959	humoral immune response	1,13E-05	5,45E-03	6	22
GO:0045766	positive regulation of angiogenesis	1,25E-05	5,86E-03	11	100
GO:0019955	cytokine binding	2,55E-05	1,16E-02	6	27
GO:0002486	antigen processing and presentation of endogenous peptide antigen via MHC class I via ER pathway, TAP-independent	3,90E-05	1,61E-02	3	3
GO:0046977	TAP binding	3,90E-05	1,61E-02	3	3
GO:0009395	phospholipid catabolic process	4,21E-05	1,69E-02	4	11
GO:0005604	basement membrane	4,36E-05	1,71E-02	8	71
GO:0016020	membrane	5,34E-05	2,00E-02	159	5600
GO:0016032	viral process	6,23E-05	2,29E-02	26	520
GO:0071356	cellular response to tumor necrosis factor	8,18E-05	2,87E-02	10	92
GO:1990111	spermatoproteasome complex	8,70E-05	2,99E-02	3	4
GO:0035455	response to interferon-alpha	9,63E-05	3,25E-02	4	10
GO:0010466	negative regulation of peptidase activity	1,07E-04	3,48E-02	7	46
GO:0030414	peptidase inhibitor activity	1,11E-04	3,49E-02	7	46
GO:0009617	response to bacterium	1,15E-04	3,49E-02	8	66
GO:0010951	negative regulation of endopeptidase activity	1,17E-04	3,49E-02	8	64
GO:0042270	protection from natural killer cell mediated cytotoxicity	1,18E-04	3,49E-02	3	4
GO:0001968	fibronectin binding	1,18E-04	3,49E-02	5	22
GO:0004867	serine-type endopeptidase inhibitor activity	1,40E-04	4,06E-02	6	37
GO:0019882	antigen processing and presentation	1,45E-04	4,15E-02	6	32

Supplementary Table S4: Overrepresented GO terms in genes downregulated by LPS exclusively in cells expressing APEX1(1-20). Gene set enrichment analysis (GSEA) was applied to genes from the DGE analysis, which were significantly downregulated by LPS exclusively in cells transduced with the lentivrus expressing APEX1(1-20). GSEA was performed using R package goseq with a treshold on the adjusted p-values of 0.05. numDEInCat: number of differentially expressed genes belonging to the respective GO term; numInCat: number of genes related to the GO term.

GO ID	GO term	overrepresented p-value	adjusted p-value	numDEInCat	numInCat
GO:0008217	regulation of blood pressure	4,11E-08	4,89E-04	7	38
GO:0005615	extracellular space	7,26E-08	4,89E-04	26	853
GO:0032355	response to estradiol	8,53E-08	4,89E-04	9	87
GO:0005576	extracellular region	2,65E-07	1,14E-03	32	1306
GO:0031994	insulin-like growth factor I binding	2,85E-06	9,81E-03	4	12
GO:0005887	integral component of plasma membrane	5,11E-06	1,46E-02	22	839
GO:0016324	apical plasma membrane	6,85E-06	1,56E-02	11	236
GO:0009612	response to mechanical stimulus	8,14E-06	1,56E-02	6	53
GO:0048247	lymphocyte chemotaxis	8,17E-06	1,56E-02	4	13
GO:0009986	cell surface	9,27E-06	1,59E-02	15	444
GO:0031526	brush border membrane	1,58E-05	2,46E-02	5	36
GO:0005113	patched binding	2,55E-05	3,37E-02	3	7
GO:0071356	cellular response to tumor necrosis factor	2,55E-05	3,37E-02	7	93
GO:0006874	cellular calcium ion homeostasis	3,35E-05	4,12E-02	6	69
GO:0002548	monocyte chemotaxis	4,05E-05	4,59E-02	4	20
GO:0031995	insulin-like growth factor II binding	4,27E-05	4,59E-02	3	8

Supplementary Table S5: Differentially expressed genes upon LPS treatment of cells not expressing APEX1(1-20). DGE calculated using the R package DESeq2 comparing samples of cells transduced with an empty virus and treated with active LPS versus treated with detoxified LPS. The L2FC (Log 2-fold change) states the average difference in gene expression between both treatments. Positive L2FC values denote upregulation by LPS treatment, negative values downregulation. Wald test from DESeq2 was used to calculate the significance of the change in the expression. The adjusted p-values take the number of tested genes into account, the threshold for the adjusted p-value was 0.05.

gene name	Ensembl gene ID	L2FC	p-value	adusted p-value
LAMC2	ENSG00000058085	2,175	1,73E-211	2,50E-207
EBI3	ENSG00000105246	2,426	1,30E-60	9,40E-57
CXCL6	ENSG00000124875	1,813	1,84E-58	8,86E-55
SOD2	ENSG00000112096	1,027	2,11E-57	7,64E-54
CCL2	ENSG00000108691	1,201	6,20E-57	1,79E-53
UBD	ENSG00000226898	2,737	4,26E-56	1,03E-52
CFB	ENSG00000242335	1,832	3,80E-54	7,85E-51
MMP10	ENSG00000166670	1,176	2,23E-52	4,04E-49
CTSS	ENSG00000163131	1,296	2,29E-41	3,69E-38
IL32	ENSG00000008517	1,326	5,27E-36	7,63E-33
CTSK	ENSG00000143387	1,404	1,42E-35	1,87E-32
POU2F2	ENSG00000028277	1,233	3,86E-35	4,65E-32
LTB	ENSG00000223448	1,341	2,37E-34	2,64E-31
S100A3	ENSG00000188015	2,189	1,39E-33	1,44E-30
IGFBP3	ENSG00000146674	-0,846	3,62E-31	3,49E-28
PAPLN	ENSG00000100767	1,617	2,35E-29	2,13E-26
HLA-B	ENSG00000206450	1,221	5,52E-25	4,70E-22
ISG20	ENSG00000172183	0,842	2,84E-24	2,29E-21
CXCL1	ENSG00000163739	1,075	6,17E-23	4,70E-20
CNTNAP1	ENSG00000108797	0,572	1,34E-22	9,73E-20
CXCL3	ENSG00000163734	0,929	2,43E-22	1,67E-19
PLA2G4C	ENSG00000105499	0,885	6,16E-22	4,05E-19
IFI27	ENSG00000275214	0,615	1,36E-21	8,58E-19
MX1	ENSG00000157601	1,110	1,53E-20	9,21E-18
ANO9	ENSG00000185101	4,656	2,14E-20	1,24E-17
CXCL5	ENSG00000163735	1,905	5,18E-20	2,88E-17
ICAM1	ENSG00000090339	0,723	1,24E-18	6,64E-16
PSMB9	ENSG00000243958	0,719	2,21E-16	1,14E-13
IL4I1	ENSG00000104951	0,729	1,24E-15	6,21E-13
CXCL2	ENSG00000081041	1,059	2,09E-14	1,01E-11
SLC7A2	ENSG00000003989	0,634	4,06E-14	1,89E-11
THSD4	ENSG00000187720	0,353	4,20E-14	1,90E-11
MAMDC2	ENSG00000278608	0,919	8,41E-14	3,69E-11
IFI6	ENSG00000126709	0,620	1,71E-13	7,28E-11
NEURL1B	ENSG00000214357	-0,767	1,85E-13	7,63E-11
TFPI2	ENSG00000105825	0,766	2,66E-13	1,07E-10
AC139530.2	NA	-30,000	9,87E-13	3,86E-10
TNFRSF9	ENSG00000049249	1,451	1,08E-12	4,10E-10
LAMP3	ENSG00000078081	0,608	4,93E-12	1,83E-09
UBE2L6	ENSG00000156587	0,403	1,16E-11	4,19E-09
OAS2	ENSG00000111335	1,100	2,43E-11	8,58E-09
PSMB8	ENSG00000230669	0,433	3,00E-11	1,03E-08
CCL20	ENSG00000115009	1,110	4,08E-11	1,37E-08
CYB5R2	ENSG00000166394	0,696	5,67E-11	1,86E-08
GPSM2	ENSG00000121957	-0,652	7,28E-11	2,34E-08

CTHRC1	ENSG00000164932	0,593	1,00E-10	3,15E-08
P2RX4	ENSG00000135124	0,371	1,44E-10	4,40E-08
TNC	ENSG00000041982	3,090	1,46E-10	4,40E-08
CXCL8	ENSG00000169429	0,851	1,77E-10	5,21E-08
STAP2	ENSG00000178078	0,498	2,27E-10	6,56E-08
CSF2	ENSG00000164400	1,656	3,48E-10	9,87E-08
ARHGDIG	ENSG00000242173	0,656	4,24E-10	1,17E-07
C2CD4A	ENSG00000198535	0,895	4,27E-10	1,17E-07
PRICKLE1	ENSG00000139174	-0,558	6,19E-10	1,66E-07
CAV1	ENSG00000105974	-0,380	7,33E-10	1,93E-07
CDKN3	ENSG00000100526	-0,614	8,83E-10	2,21E-07
KIF20A	ENSG00000112984	-0,583	8,86E-10	2,21E-07
METTL7A	ENSG00000185432	-0,478	8,64E-10	2,21E-07
CYP51A1	ENSG00000001630	-0,352	1,73E-09	4,24E-07
STARD10	ENSG00000214530	0,569	1,99E-09	4,79E-07
VWA1	ENSG00000179403	0,476	3,39E-09	8,05E-07
MX2	ENSG00000183486	2,548	3,69E-09	8,60E-07
APOL1	ENSG00000100342	0,388	5,39E-09	1,24E-06
TAPBP	ENSG00000206281	0,477	5,53E-09	1,25E-06
GP1BB	ENSG00000203618	-22,691	6,22E-09	1,38E-06
DHRS3	ENSG00000162496	0,429	6,82E-09	1,50E-06
CEBPD	ENSG00000221869	0,785	7,57E-09	1,63E-06
PLA1A	ENSG00000144837	1,472	7,81E-09	1,66E-06
WASF3	ENSG00000132970	-0,313	9,19E-09	1,93E-06
LYPD6	ENSG00000187123	0,469	1,20E-08	2,47E-06
CAPN2	ENSG00000162909	-0,289	1,47E-08	2,95E-06
HLA-A	ENSG00000227715	0,395	1,47E-08	2,95E-06
HMGCS1	ENSG00000112972	-0,427	1,83E-08	3,63E-06
BUB1	ENSG00000169679	-0,492	1,96E-08	3,83E-06
SELENOM	ENSG00000198832	0,545	1,98E-08	3,83E-06
F2RL1	ENSG00000164251	0,380	2,29E-08	4,36E-06
BST1	ENSG00000109743	0,394	2,56E-08	4,81E-06
PCK2	ENSG00000285241	0,426	2,61E-08	4,84E-06
TNFSF18	ENSG00000120337	-0,583	3,14E-08	5,75E-06
DENND2B	ENSG00000166444	0,984	3,20E-08	5,79E-06
AL451062.4	NA	-23,299	3,34E-08	5,98E-06
UBA7	ENSG00000182179	0,446	3,41E-08	6,02E-06
ALOX5AP	ENSG00000132965	1,587	3,68E-08	6,41E-06
DLGAP5	ENSG00000126787	-0,621	4,30E-08	7,41E-06
CRYBG1	ENSG00000112297	-0,333	4,95E-08	8,42E-06
PRSS12	ENSG00000164099	1,198	5,39E-08	9,07E-06
LIPG	ENSG00000101670	0,513	5,53E-08	9,19E-06
SLC15A3	ENSG00000110446	0,517	5,73E-08	9,43E-06
ICOSLG	ENSG00000160223	0,533	7,11E-08	1,16E-05
OAS1	ENSG00000089127	0,519	8,71E-08	1,40E-05
CCNB2	ENSG00000157456	-0,480	9,09E-08	1,45E-05
AL358472.7	NA	20,830	9,30E-08	1,46E-05
ACBD7	ENSG00000176244	-0,775	1,04E-07	1,62E-05
MEST	ENSG00000106484	-0,435	1,21E-07	1,86E-05
JAK3	ENSG00000105639	0,743	1,22E-07	1,86E-05
ALDH1A1	ENSG00000165092	-0,403	1,34E-07	2,02E-05
CRTAC1	ENSG00000095713	0,499	1,67E-07	2,49E-05
OCIAD2	ENSG00000145247	0,437	1,74E-07	2,56E-05

CD69	ENSG00000110848	0,949	1,88E-07	2,75E-05
MKI67	ENSG00000148773	-0,525	1,98E-07	2,87E-05
FSTL3	ENSG00000070404	0,444	2,37E-07	3,39E-05
ADAMTS18	ENSG00000140873	-0,551	2,60E-07	3,59E-05
CIT	ENSG00000122966	-0,468	2,53E-07	3,59E-05
TMEM120A	ENSG00000189077	0,427	2,59E-07	3,59E-05
TNFRSF4	ENSG00000186827	0,959	2,61E-07	3,59E-05
DHH	ENSG00000139549	-0,464	3,68E-07	5,02E-05
PRR11	ENSG00000068489	-0,326	3,87E-07	5,24E-05
SERPINA3	ENSG00000196136	2,440	4,12E-07	5,52E-05
KIF12	ENSG00000136883	0,697	6,16E-07	8,18E-05
PLCG2	ENSG00000197943	1,263	6,57E-07	8,65E-05
PSME2	ENSG00000284889	0,443	6,76E-07	8,81E-05
BDKRB2	ENSG00000168398	0,931	8,27E-07	1,07E-04
ACSS1	ENSG00000154930	0,279	8,67E-07	1,11E-04
MAP2K6	ENSG00000108984	-0,373	8,88E-07	1,13E-04
CCL15-CCL14	ENSG00000282521	-0,416	9,40E-07	1,18E-04
MMP19	ENSG00000123342	0,573	1,04E-06	1,29E-04
ACE	ENSG00000159640	-0,620	1,11E-06	1,37E-04
ZCCHC2	ENSG00000141664	-0,507	1,16E-06	1,42E-04
PAQR7	ENSG00000182749	0,277	1,18E-06	1,42E-04
RASA4B	ENSG00000170667	0,567	1,18E-06	1,42E-04
CCNB1	ENSG00000134057	-0,496	1,20E-06	1,43E-04
PLAAT4	ENSG00000133321	0,728	1,30E-06	1,54E-04
TAPBPL	ENSG00000139192	0,812	1,37E-06	1,61E-04
LYVE1	ENSG00000133800	-0,703	1,52E-06	1,78E-04
APOD	ENSG00000189058	0,469	1,76E-06	2,04E-04
ZC3H12A	ENSG00000163874	0,514	1,86E-06	2,14E-04
CEP55	ENSG00000138180	-0,538	1,94E-06	2,21E-04
ITGAV	ENSG00000138448	0,523	2,09E-06	2,37E-04
ARHGEF19	ENSG00000142632	0,356	2,35E-06	2,64E-04
MAP3K6	ENSG00000142733	0,371	2,50E-06	2,76E-04
SEMA3G	ENSG00000010319	0,417	2,49E-06	2,76E-04
POSTN	ENSG00000133110	-0,702	2,60E-06	2,85E-04
GXYLT2	ENSG00000172986	1,226	2,62E-06	2,85E-04
AC087632.2	NA	-1,660	3,01E-06	3,23E-04
ZDHHC13	ENSG00000177054	-0,297	3,01E-06	3,23E-04
NUCKS1	ENSG00000069275	-0,368	3,07E-06	3,27E-04
CKAP2	ENSG00000136108	-0,456	3,21E-06	3,39E-04
ALDH1A2	ENSG00000128918	-0,356	3,38E-06	3,55E-04
ZNF791	ENSG00000173875	-0,512	3,74E-06	3,90E-04
AKAP12	ENSG00000131016	0,272	4,09E-06	4,23E-04
MTMR10	ENSG00000277086	-0,375	4,67E-06	4,79E-04
AL109918.1	NA	-0,486	4,70E-06	4,80E-04
CERS1	ENSG00000223802	0,381	4,84E-06	4,90E-04
C11orf96	ENSG00000187479	0,453	5,27E-06	5,30E-04
PLCG1	ENSG00000124181	0,243	5,57E-06	5,56E-04
MYRIP	ENSG00000170011	-0,347	5,87E-06	5,81E-04
CXADR	ENSG00000154639	-0,411	6,06E-06	5,93E-04
RASA4	ENSG00000105808	0,440	6,03E-06	5,93E-04
INCENP	ENSG00000149503	-0,443	6,36E-06	6,18E-04
ELMOD1	ENSG00000110675	-0,476	6,88E-06	6,64E-04
KNL1	ENSG00000137812	-0,713	7,35E-06	6,93E-04

MSMP	ENSG00000215183	-0,370	7,33E-06	6,93E-04
SAMD14	ENSG00000167100	0,369	7,29E-06	6,93E-04
SDC4	ENSG00000124145	0,352	7,37E-06	6,93E-04
MCFD2	ENSG00000180398	-0,277	7,55E-06	7,05E-04
BST2	ENSG00000130303	0,315	7,71E-06	7,15E-04
MYZAP	ENSG00000263155	-0,413	8,20E-06	7,55E-04
CENPF	ENSG00000117724	-0,557	8,47E-06	7,76E-04
HMMR	ENSG00000072571	-0,747	8,70E-06	7,92E-04
TSPAN13	ENSG00000106537	0,390	9,00E-06	8,14E-04
ASAP1	ENSG00000153317	-0,339	9,46E-06	8,50E-04
PIGK	ENSG00000142892	-0,369	9,79E-06	8,75E-04
PRCP	ENSG00000137509	0,212	1,02E-05	9,10E-04
PDCD6IP	ENSG00000170248	-0,363	1,11E-05	9,81E-04
LRFN4	ENSG00000173621	0,375	1,13E-05	9,94E-04
ACAT2	ENSG00000120437	-0,299	1,15E-05	9,95E-04
FXYD6	ENSG00000137726	0,656	1,15E-05	9,95E-04
R3HDM1	ENSG00000048991	-0,468	1,16E-05	1,00E-03
TNFRSF14	ENSG00000273936	0,388	1,20E-05	1,03E-03
AC087721.2	NA	-0,375	1,31E-05	1,11E-03
KIT	ENSG00000157404	0,262	1,33E-05	1,13E-03
IL27RA	ENSG00000288185	0,362	1,36E-05	1,14E-03
NEK2	ENSG00000117650	-0,489	1,35E-05	1,14E-03
SYNJ2	ENSG00000078269	0,160	1,36E-05	1,14E-03
TMPO	ENSG00000120802	-0,320	1,40E-05	1,16E-03
DEPDC1B	ENSG00000035499	-0,341	1,45E-05	1,19E-03
SEMA7A	ENSG00000288455	0,515	1,46E-05	1,19E-03
IRF9	ENSG00000285048	0,498	1,55E-05	1,26E-03
MTMR11	ENSG00000014914	0,364	1,57E-05	1,27E-03
MGARP	ENSG00000137463	-0,476	1,62E-05	1,31E-03
KCNJ15	ENSG00000157551	-0,746	1,74E-05	1,39E-03
MGME1	ENSG00000125871	-0,250	1,79E-05	1,42E-03
BORA	ENSG00000136122	-0,605	1,87E-05	1,48E-03
CENPA	ENSG00000115163	-0,407	1,95E-05	1,53E-03
ERMP1	ENSG00000099219	-0,267	1,95E-05	1,53E-03
ITGB4	ENSG00000132470	-0,576	2,06E-05	1,61E-03
CBR3	ENSG00000159231	0,357	2,09E-05	1,62E-03
PPL	ENSG00000118898	-0,801	2,30E-05	1,77E-03
SPTLC1P1	ENSG00000230397	-0,705	2,49E-05	1,91E-03
HSPE1-MOB4	ENSG00000270757	-0,483	2,51E-05	1,91E-03
ASPM	ENSG00000066279	-0,784	2,55E-05	1,93E-03
COBLL1	ENSG00000082438	-0,381	2,60E-05	1,95E-03
ULBP2	ENSG00000131015	0,338	2,59E-05	1,95E-03
CX3CL1	ENSG00000006210	0,553	2,63E-05	1,96E-03
RAB14	ENSG00000119396	-0,247	2,72E-05	2,01E-03
TOP2A	ENSG00000131747	-0,435	2,73E-05	2,01E-03
AC091951.4	NA	2,510	3,21E-05	2,35E-03
DPP4	ENSG00000197635	-0,347	3,23E-05	2,35E-03
LAMB3	ENSG00000196878	0,446	3,26E-05	2,35E-03
NFKBIZ	ENSG00000144802	0,541	3,24E-05	2,35E-03
NUF2	ENSG00000143228	-0,646	3,24E-05	2,35E-03
ARL5A	ENSG00000162980	-0,701	3,35E-05	2,40E-03
ABCA8	ENSG00000141338	-0,677	3,54E-05	2,53E-03
DIAPH3	ENSG00000139734	-0,353	3,57E-05	2,53E-03

FAHD2CP	ENSG00000231584	0,381	3,69E-05	2,59E-03
FP565260.3	NA	0,391	3,68E-05	2,59E-03
PSMB10	ENSG00000205220	0,328	3,84E-05	2,68E-03
TMEM121	ENSG00000184986	0,381	3,87E-05	2,69E-03
IFITM1	ENSG00000185885	0,366	4,00E-05	2,77E-03
SYNJ1	ENSG00000159082	-0,312	4,26E-05	2,94E-03
EMCN	ENSG00000164035	-0,524	4,30E-05	2,95E-03
IFIT1	ENSG00000185745	0,820	4,33E-05	2,95E-03
CCL14	ENSG00000277236	-0,431	4,57E-05	3,11E-03
VAPA	ENSG00000101558	-0,205	4,75E-05	3,21E-03
ACKR4	ENSG00000129048	-0,562	4,85E-05	3,26E-03
HMGCR	ENSG00000113161	-0,321	4,93E-05	3,30E-03
APAF1	ENSG00000120868	-0,294	5,05E-05	3,35E-03
CLDN14	ENSG00000159261	0,877	5,05E-05	3,35E-03
FBXO32	ENSG00000156804	0,355	5,18E-05	3,42E-03
CSF3	ENSG00000108342	1,066	5,63E-05	3,71E-03
CENPE	ENSG00000138778	-0,750	5,78E-05	3,78E-03
CPLANE2	ENSG00000132881	0,390	5,88E-05	3,83E-03
CAMTA2	ENSG00000108509	0,290	6,00E-05	3,88E-03
SLC22A31	ENSG00000259803	0,695	6,00E-05	3,88E-03
IFI35	ENSG00000068079	0,380	6,14E-05	3,95E-03
ZNF365	ENSG00000138311	0,517	6,32E-05	4,05E-03
PSME1	ENSG00000284916	0,266	6,45E-05	4,11E-03
GDF15	ENSG00000130513	0,428	6,56E-05	4,16E-03
HIBCH	ENSG00000198130	-0,436	6,70E-05	4,24E-03
ACHE	ENSG00000087085	0,801	6,78E-05	4,26E-03
FTH1	ENSG00000167996	0,268	6,87E-05	4,30E-03
RPS6KL1	ENSG00000198208	0,352	6,97E-05	4,35E-03
PTK7	ENSG00000112655	0,269	7,23E-05	4,49E-03
TNFRSF6B	ENSG00000243509	0,338	7,31E-05	4,52E-03
C17orf107	ENSG00000205710	0,459	7,81E-05	4,81E-03
NECTIN3	ENSG00000177707	-0,470	8,03E-05	4,92E-03
RNASE1	ENSG00000129538	-0,276	8,27E-05	5,05E-03
AFF1	ENSG00000172493	-0,327	8,44E-05	5,05E-03
GLRX	ENSG00000173221	-0,240	8,45E-05	5,05E-03
GRASP	NA	0,197	8,45E-05	5,05E-03
LPCAT2	ENSG00000087253	-0,362	8,40E-05	5,05E-03
NFKBIA	ENSG00000100906	0,272	8,34E-05	5,05E-03
INSIG1	ENSG00000186480	-0,278	9,05E-05	5,37E-03
TMOD1	ENSG00000136842	0,496	9,02E-05	5,37E-03
B3GALT4	ENSG00000235155	0,398	9,28E-05	5,43E-03
CCNYL1	ENSG00000163249	-0,395	9,26E-05	5,43E-03
MFAP2	ENSG00000117122	0,276	9,30E-05	5,43E-03
SYNGR3	ENSG00000127561	0,367	9,20E-05	5,43E-03
HTR2B	ENSG00000135914	-0,426	9,46E-05	5,50E-03
ADAM12	ENSG00000148848	1,044	9,52E-05	5,51E-03
MEF2C	ENSG00000081189	-0,347	9,70E-05	5,59E-03
SAPCD2	ENSG00000186193	-0,377	9,74E-05	5,60E-03
MS4A6A	ENSG00000110077	0,466	9,89E-05	5,66E-03
PLTP	ENSG00000100979	0,355	9,95E-05	5,67E-03
CCNA2	ENSG00000145386	-0,400	1,01E-04	5,75E-03
DPP3	ENSG00000254986	0,281	1,02E-04	5,75E-03
P2RY6	ENSG00000171631	1,229	1,03E-04	5,79E-03

MAP6	ENSG00000171533	0,992	1,05E-04	5,88E-03
TCEAL7	ENSG00000182916	0,328	1,05E-04	5,88E-03
TGFBR3L	ENSG00000260001	0,467	1,12E-04	6,18E-03
TMEM132A	ENSG00000006118	0,351	1,11E-04	6,18E-03
WDFY3	ENSG00000163625	-0,381	1,12E-04	6,18E-03
EPSTI1	ENSG00000133106	0,802	1,13E-04	6,22E-03
RND1	ENSG00000172602	0,401	1,15E-04	6,28E-03
HLA-H	ENSG00000231904	0,356	1,15E-04	6,30E-03
MSMO1	ENSG00000052802	-0,536	1,16E-04	6,33E-03
RNMT	ENSG00000101654	-0,425	1,17E-04	6,33E-03
MPHOSPH9	ENSG00000051825	-0,464	1,19E-04	6,44E-03
RAB7B	ENSG00000276600	1,191	1,20E-04	6,46E-03
AMPH	ENSG00000078053	0,488	1,23E-04	6,61E-03
HAS2	ENSG00000170961	1,050	1,30E-04	6,88E-03
KIF4A	ENSG00000090889	-0,318	1,29E-04	6,88E-03
SNX22	ENSG00000157734	0,983	1,30E-04	6,88E-03
AQP1	ENSG00000240583	-1,028	1,33E-04	6,98E-03
H2AC6	ENSG00000180573	-0,697	1,33E-04	6,98E-03
CASP1	ENSG00000137752	0,488	1,34E-04	6,99E-03
COTL1	ENSG00000103187	0,280	1,35E-04	6,99E-03
GSDMD	ENSG00000278718	0,274	1,35E-04	6,99E-03
KIF14	ENSG00000118193	-0,564	1,35E-04	6,99E-03
QTRT2	ENSG00000151576	-0,279	1,34E-04	6,99E-03
EFCAB14	ENSG00000159658	-0,243	1,40E-04	7,20E-03
IER3	ENSG00000235030	0,270	1,40E-04	7,20E-03
RASD1	ENSG00000108551	0,316	1,49E-04	7,60E-03
AOX1	ENSG00000138356	0,614	1,55E-04	7,85E-03
FRY	ENSG00000073910	-0,171	1,55E-04	7,85E-03
NBPF10	ENSG00000271425	-0,326	1,55E-04	7,85E-03
STEAP1	ENSG00000164647	-0,346	1,56E-04	7,86E-03
SULT1B1	ENSG00000173597	-0,498	1,58E-04	7,96E-03
OIP5	ENSG00000104147	-0,352	1,61E-04	8,05E-03
ANKH	ENSG00000154122	0,290	1,63E-04	8,12E-03
TMEM54	ENSG00000121900	0,266	1,64E-04	8,15E-03
SLC1A4	ENSG00000115902	0,234	1,68E-04	8,33E-03
IL11	ENSG00000095752	0,997	1,69E-04	8,34E-03
CGNL1	ENSG00000128849	-0,198	1,73E-04	8,48E-03
NRG1	ENSG00000157168	-0,397	1,73E-04	8,48E-03
RBBP9	ENSG00000089050	-0,332	1,74E-04	8,48E-03
CKS2	ENSG00000123975	-0,336	1,83E-04	8,89E-03
HLA-C	ENSG00000206435	0,313	1,83E-04	8,89E-03
TNIP3	ENSG00000050730	1,038	1,84E-04	8,90E-03
ADAM32	ENSG00000275594	-1,239	1,85E-04	8,91E-03
MYO5A	ENSG00000197535	-0,276	1,85E-04	8,91E-03
ACER3	ENSG00000078124	-0,213	1,97E-04	9,46E-03
RELB	ENSG00000104856	0,353	2,00E-04	9,55E-03
GBP4	ENSG00000162654	0,310	2,02E-04	9,61E-03
RAB11FIP2	ENSG00000107560	-0,544	2,02E-04	9,61E-03
SURF1	ENSG00000280627	0,234	2,04E-04	9,64E-03
MYH10	ENSG00000133026	-0,217	2,09E-04	9,83E-03
PIMREG	ENSG00000129195	-0,446	2,09E-04	9,83E-03
IL1A	ENSG00000115008	0,507	2,18E-04	1,02E-02
GMPPA	ENSG00000144591	0,312	2,20E-04	1,03E-02

ARL6IP1	ENSG00000170540	-0,280	2,22E-04	1,03E-02
CNN3	ENSG00000117519	-0,234	2,24E-04	1,04E-02
GALNT18	ENSG00000110328	0,494	2,25E-04	1,04E-02
FNBP1	ENSG00000187239	-0,269	2,28E-04	1,05E-02
PARP10	ENSG00000178685	0,319	2,28E-04	1,05E-02
MLIP	ENSG00000146147	-0,301	2,45E-04	1,12E-02
TM4SF18	ENSG00000163762	-0,366	2,45E-04	1,12E-02
UBR4	ENSG00000127481	0,376	2,47E-04	1,12E-02
RMDN2	ENSG00000115841	-0,550	2,48E-04	1,13E-02
HOXB9	ENSG00000170689	0,395	2,52E-04	1,14E-02
ARSA	ENSG00000100299	0,292	2,55E-04	1,15E-02
SOCS3	ENSG00000184557	0,302	2,55E-04	1,15E-02
FBLN5	ENSG00000140092	0,404	2,58E-04	1,15E-02
TSPAN5	ENSG00000168785	-0,195	2,58E-04	1,15E-02
RSAD1	ENSG00000136444	0,197	2,64E-04	1,18E-02
ARHGAP11A	ENSG00000275568	-0,412	2,65E-04	1,18E-02
ATP5F1D	ENSG00000099624	0,341	2,66E-04	1,18E-02
NSD2	ENSG00000109685	-0,239	2,68E-04	1,18E-02
ISG15	ENSG00000187608	0,345	2,81E-04	1,23E-02
PBK	ENSG00000168078	-0,449	2,82E-04	1,23E-02
LATS2	ENSG00000150457	-0,211	2,83E-04	1,24E-02
AGRN	ENSG00000188157	0,368	2,93E-04	1,28E-02
TSSC4	ENSG00000184281	0,419	2,95E-04	1,28E-02
PMM1	ENSG00000100417	0,341	3,00E-04	1,30E-02
H2AC11	ENSG00000196787	-0,650	3,06E-04	1,32E-02
EML2	ENSG00000125746	0,311	3,14E-04	1,35E-02
PCDH1	ENSG00000156453	0,269	3,14E-04	1,35E-02
NCKAP5	ENSG00000176771	0,847	3,16E-04	1,35E-02
TSPAN11	ENSG00000110900	-0,360	3,21E-04	1,37E-02
CEP70	ENSG00000114107	-0,520	3,27E-04	1,39E-02
CKAP5	ENSG00000175216	-0,220	3,32E-04	1,40E-02
HSPB8	ENSG00000152137	0,347	3,31E-04	1,40E-02
AHNAK	ENSG00000124942	-0,388	3,34E-04	1,41E-02
CCM2L	ENSG00000101331	-0,325	3,38E-04	1,42E-02
DUSP4	ENSG00000120875	-0,269	3,41E-04	1,43E-02
SULT1E1	ENSG00000109193	-0,482	3,41E-04	1,43E-02
TCIRG1	ENSG00000110719	0,271	3,43E-04	1,43E-02
FXYD2	ENSG00000137731	0,734	3,45E-04	1,43E-02
UBN2	ENSG00000157741	-0,561	3,47E-04	1,44E-02
SPAG5	ENSG00000076382	-0,278	3,49E-04	1,44E-02
THBS2	ENSG00000186340	0,836	3,48E-04	1,44E-02
ZNF800	ENSG00000048405	-0,353	3,52E-04	1,45E-02
SGO2	ENSG00000163535	-0,656	3,64E-04	1,49E-02
GFPT2	ENSG00000131459	0,367	3,69E-04	1,51E-02
APLN	ENSG00000171388	-0,407	3,81E-04	1,55E-02
ARHGAP11B	ENSG00000274734	-0,429	3,86E-04	1,57E-02
JUNB	ENSG00000171223	0,259	3,87E-04	1,57E-02
BPGM	ENSG00000172331	0,259	3,89E-04	1,57E-02
CDH15	ENSG00000129910	0,509	3,90E-04	1,57E-02
MTMR7	ENSG00000003987	0,867	3,93E-04	1,58E-02
ST6GALNAC2	ENSG00000070731	0,756	3,98E-04	1,60E-02
AC241640.1	NA	-1,539	4,06E-04	1,62E-02
SFRP1	ENSG00000104332	-0,311	4,07E-04	1,62E-02

LIG1	ENSG00000105486	0,274	4,10E-04	1,63E-02
SLC7A7	ENSG00000155465	0,298	4,23E-04	1,68E-02
CXCR4	ENSG00000121966	0,237	4,25E-04	1,68E-02
GBGT1	ENSG00000148288	0,343	4,36E-04	1,72E-02
SESN3	ENSG00000149212	-0,641	4,37E-04	1,72E-02
MAPK1	ENSG00000100030	-0,294	4,38E-04	1,72E-02
AC079594.2	NA	-0,631	4,42E-04	1,73E-02
FMNL1	ENSG00000184922	0,395	4,45E-04	1,74E-02
HIVEP1	ENSG00000095951	-0,366	4,48E-04	1,74E-02
PLEKHN1	ENSG00000187583	0,492	4,49E-04	1,74E-02
RBL2	ENSG00000103479	-0,287	4,48E-04	1,74E-02
PTGS2	ENSG00000073756	0,553	4,55E-04	1,76E-02
WNK3	ENSG00000196632	-0,654	4,59E-04	1,77E-02
NMNAT2	ENSG00000157064	0,987	4,62E-04	1,77E-02
TMSB15A	ENSG00000158164	-0,521	4,64E-04	1,77E-02
WASF1	ENSG00000112290	-0,307	4,63E-04	1,77E-02
PTGES3L	ENSG00000267060	1,020	4,69E-04	1,79E-02
GMFG	ENSG00000130755	0,214	4,74E-04	1,80E-02
HP1BP3	ENSG00000127483	-0,314	4,79E-04	1,81E-02
SLC35C2	ENSG00000080189	0,269	4,88E-04	1,84E-02
SLC27A3	ENSG00000263163	0,380	4,93E-04	1,86E-02
CFAP69	ENSG00000105792	-0,585	4,96E-04	1,86E-02
ZBTB42	ENSG00000179627	0,284	4,98E-04	1,87E-02
CPAMD8	ENSG00000160111	0,499	5,08E-04	1,88E-02
MAP1LC3A	ENSG00000101460	0,328	5,06E-04	1,88E-02
MT1L	ENSG00000260549	0,355	5,05E-04	1,88E-02
SMAD5	ENSG00000113658	-0,472	5,07E-04	1,88E-02
SMG1P3	ENSG00000180747	-0,283	5,13E-04	1,90E-02
DAW1	ENSG00000123977	-0,338	5,15E-04	1,90E-02
SLC38A5	ENSG00000017483	0,391	5,18E-04	1,91E-02
ACBD4	ENSG00000181513	0,278	5,27E-04	1,93E-02
SUV39H2	ENSG00000152455	-0,517	5,28E-04	1,93E-02
CPA4	ENSG00000128510	-0,847	5,34E-04	1,94E-02
MROH6	ENSG00000277781	0,678	5,31E-04	1,94E-02
NFATC4	ENSG00000285485	0,371	5,35E-04	1,94E-02
TM7SF3	ENSG00000064115	-0,245	5,34E-04	1,94E-02
UPP1	ENSG00000183696	0,232	5,41E-04	1,96E-02
ADGRB2	ENSG00000121753	0,324	5,56E-04	2,01E-02
ATOH8	ENSG00000168874	0,364	5,61E-04	2,02E-02
KNSTRN	ENSG00000128944	-0,257	5,71E-04	2,04E-02
ODF3B	ENSG00000177989	0,753	5,69E-04	2,04E-02
SERPINB9	ENSG00000170542	0,176	5,69E-04	2,04E-02
PTP4A1	ENSG00000112245	-0,335	5,88E-04	2,09E-02
TMC6	ENSG00000141524	0,276	5,88E-04	2,09E-02
SPTA1	ENSG00000163554	-1,154	5,92E-04	2,10E-02
SENP1	ENSG00000079387	-0,270	5,95E-04	2,11E-02
PIK3CD	ENSG00000171608	0,296	6,11E-04	2,16E-02
SPHK1	ENSG00000176170	0,285	6,15E-04	2,16E-02
TSPAN8	ENSG00000127324	-0,637	6,15E-04	2,16E-02
CD34	ENSG00000174059	-0,226	6,22E-04	2,18E-02
PLAC8	ENSG00000145287	-0,413	6,26E-04	2,19E-02
E2F1	ENSG00000101412	0,419	6,32E-04	2,20E-02
AMOT	ENSG00000126016	-0,550	6,38E-04	2,22E-02

C2CD2	ENSG00000157617	-0,279	6,60E-04	2,28E-02
CST1	ENSG00000170373	0,592	6,60E-04	2,28E-02
SAT1	ENSG00000130066	0,334	6,60E-04	2,28E-02
EFNA2	ENSG00000099617	0,374	6,66E-04	2,30E-02
ANGEL2	ENSG00000174606	-0,371	6,77E-04	2,33E-02
MCM9	ENSG00000111877	-0,297	6,81E-04	2,33E-02
POLD1	ENSG00000062822	0,320	6,82E-04	2,33E-02
SH3TC2	ENSG00000169247	-0,555	6,88E-04	2,35E-02
PHACTR4	ENSG00000204138	-0,233	6,93E-04	2,36E-02
HNRNPLL	ENSG00000143889	-0,211	6,99E-04	2,37E-02
MYO5C	ENSG00000128833	-0,322	7,01E-04	2,37E-02
TREX1	ENSG00000213689	0,275	7,02E-04	2,37E-02
LPAR1	ENSG00000198121	-0,631	7,06E-04	2,38E-02
DNM1P47	ENSG00000259660	-0,477	7,12E-04	2,40E-02
ARHGAP17	ENSG00000288353	-0,465	7,24E-04	2,43E-02
FBXO15	ENSG00000141665	-1,172	7,23E-04	2,43E-02
MMRN1	ENSG00000138722	-0,492	7,26E-04	2,43E-02
TNFSF15	ENSG00000181634	0,218	7,37E-04	2,46E-02
OCLN	ENSG00000273814	-0,336	7,39E-04	2,46E-02
CDK19	ENSG00000155111	-0,377	7,45E-04	2,47E-02
GALT	ENSG00000213930	0,230	7,58E-04	2,51E-02
C2CD4B	ENSG00000205502	0,558	7,68E-04	2,54E-02
IFI44L	ENSG00000137959	0,720	7,78E-04	2,56E-02
CCDC28B	ENSG00000160050	0,254	7,83E-04	2,57E-02
ADM2	ENSG00000128165	0,487	7,92E-04	2,59E-02
GAS2L3	ENSG00000139354	-0,436	7,90E-04	2,59E-02
BATF3	ENSG00000123685	0,662	7,95E-04	2,60E-02
ARNTL	ENSG00000133794	-0,285	8,03E-04	2,61E-02
TPPP3	ENSG00000159713	0,496	8,03E-04	2,61E-02
IPO5	ENSG00000065150	-0,156	8,09E-04	2,63E-02
GPNMB	ENSG00000136235	-0,996	8,15E-04	2,64E-02
IL3RA	ENSG00000185291	0,238	8,30E-04	2,67E-02
PDE3A	ENSG00000172572	-0,239	8,29E-04	2,67E-02
SCUBE3	ENSG00000146197	-0,411	8,38E-04	2,69E-02
ADAMTS12	ENSG00000281690	-0,546	8,53E-04	2,74E-02
PIK3CG	ENSG00000105851	-0,918	8,54E-04	2,74E-02
THOC3	ENSG00000051596	-0,528	8,70E-04	2,78E-02
COL4A2	ENSG00000134871	0,432	8,84E-04	2,82E-02
BLOC1S3	ENSG00000189114	0,447	9,02E-04	2,87E-02
APOBEC3G	ENSG00000239713	0,249	9,11E-04	2,89E-02
DHX58	ENSG00000108771	0,330	9,19E-04	2,91E-02
SGO1	ENSG00000129810	-0,365	9,31E-04	2,94E-02
PIK3R3	ENSG00000117461	-0,301	9,33E-04	2,94E-02
MOBP	ENSG00000168314	0,777	9,37E-04	2,95E-02
RACGAP1	ENSG00000161800	-0,327	9,45E-04	2,97E-02
C19orf47	ENSG00000160392	0,357	9,56E-04	2,99E-02
DHCR7	ENSG00000172893	-0,348	9,60E-04	3,00E-02
FHL3	ENSG00000183386	0,276	9,60E-04	3,00E-02
MELTF	ENSG00000163975	0,373	9,63E-04	3,00E-02
CCNE1	ENSG00000105173	0,263	9,67E-04	3,00E-02
CFAP410	ENSG00000160226	0,304	9,90E-04	3,05E-02
LRRC3	ENSG00000160233	0,273	9,89E-04	3,05E-02
PTTG1	ENSG00000164611	-0,362	9,88E-04	3,05E-02

SLC26A4	ENSG00000091137	-0,719	9,91E-04	3,05E-02
NDE1	ENSG00000275911	-0,219	1,01E-03	3,10E-02
TNFRSF21	ENSG00000146072	0,172	1,01E-03	3,10E-02
MMP28	ENSG00000278843	-1,256	1,02E-03	3,11E-02
WASHC5	ENSG00000164961	-0,200	1,02E-03	3,11E-02
NUDT22	ENSG00000149761	0,284	1,03E-03	3,13E-02
SIPA1	ENSG00000213445	0,279	1,03E-03	3,13E-02
PPP3CA	ENSG00000138814	-0,232	1,04E-03	3,15E-02
MFSD3	ENSG00000167700	0,235	1,04E-03	3,15E-02
TYMP	ENSG00000025708	0,669	1,04E-03	3,16E-02
DNAH5	ENSG00000039139	0,375	1,05E-03	3,16E-02
AC005363.1	NA	6,479	1,06E-03	3,18E-02
IGF2BP3	ENSG00000136231	-0,313	1,06E-03	3,19E-02
FEM1B	ENSG00000169018	-0,299	1,07E-03	3,20E-02
RALB	ENSG00000144118	-0,165	1,07E-03	3,20E-02
ASPHD2	ENSG00000128203	0,209	1,08E-03	3,21E-02
GALNT12	ENSG00000119514	0,317	1,08E-03	3,21E-02
RPL23AP87	ENSG00000232938	2,313	1,08E-03	3,21E-02
COMMD3-BMI1	ENSG00000269897	-0,606	1,09E-03	3,22E-02
CDK20	ENSG00000156345	0,409	1,09E-03	3,22E-02
ACTL10	ENSG00000288649	0,358	1,11E-03	3,23E-02
AKT3	ENSG00000275199	-0,276	1,11E-03	3,23E-02
BEST1	ENSG00000167995	3,000	1,10E-03	3,23E-02
ITPKC	ENSG00000086544	0,230	1,11E-03	3,23E-02
LRG1	ENSG00000171236	0,915	1,10E-03	3,23E-02
TNRC18	ENSG00000182095	-0,235	1,10E-03	3,23E-02
VPS8	ENSG00000156931	-0,319	1,10E-03	3,23E-02
PRRC2B	ENSG00000288701	-0,252	1,11E-03	3,23E-02
CHST6	ENSG00000183196	0,461	1,14E-03	3,30E-02
CLDN10	ENSG00000134873	-0,387	1,16E-03	3,36E-02
ELK3	ENSG00000111145	-0,267	1,16E-03	3,36E-02
IGFBP1	ENSG00000146678	-0,548	1,16E-03	3,36E-02
TXNIP	ENSG00000265972	-0,485	1,16E-03	3,36E-02
GLCE	ENSG00000138604	-0,244	1,17E-03	3,37E-02
PLCD3	ENSG00000161714	-0,285	1,17E-03	3,37E-02
CHKB	ENSG00000100288	0,197	1,19E-03	3,40E-02
POLD4	ENSG00000175482	0,346	1,20E-03	3,42E-02
FCF1	ENSG00000119616	-0,213	1,21E-03	3,43E-02
SP110	ENSG00000135899	0,241	1,20E-03	3,43E-02
LGALS3BP	ENSG00000108679	0,620	1,21E-03	3,43E-02
OAS3	ENSG00000111331	0,322	1,23E-03	3,49E-02
PLEKHA4	ENSG00000105559	0,272	1,24E-03	3,51E-02
ASPHD1	ENSG00000174939	0,680	1,26E-03	3,55E-02
ITPRIPL1	ENSG00000198885	0,456	1,26E-03	3,55E-02
S1PR2	ENSG00000267534	0,346	1,26E-03	3,55E-02
SIRT3	ENSG00000142082	0,207	1,26E-03	3,55E-02
UBA6	ENSG00000033178	-0,346	1,27E-03	3,56E-02
AMDHD2	ENSG00000162066	0,275	1,27E-03	3,56E-02
AGFG1	ENSG00000173744	-0,166	1,29E-03	3,60E-02
DEPDC1	ENSG00000024526	-0,581	1,31E-03	3,66E-02
NCEH1	ENSG00000144959	-0,174	1,32E-03	3,69E-02
STEAP1B	ENSG00000105889	-0,254	1,33E-03	3,71E-02
RMND5A	ENSG00000153561	-0,187	1,35E-03	3,74E-02

APPBP2	ENSG00000062725	-0,365	1,36E-03	3,76E-02
MALL	ENSG00000144063	-0,226	1,36E-03	3,76E-02
MAP3K5	ENSG00000197442	-0,280	1,37E-03	3,78E-02
CCS	ENSG00000173992	0,222	1,38E-03	3,81E-02
SELP	ENSG00000174175	-0,676	1,39E-03	3,81E-02
P4HA2	ENSG00000072682	0,217	1,40E-03	3,84E-02
NUDT18	ENSG00000275074	0,274	1,41E-03	3,86E-02
DOCK4	ENSG00000128512	-0,288	1,43E-03	3,91E-02
SERPINE1	ENSG00000106366	0,263	1,43E-03	3,91E-02
CDC20	ENSG00000117399	-0,358	1,44E-03	3,91E-02
LAMP2	ENSG00000005893	-0,141	1,44E-03	3,91E-02
SAMHD1	ENSG00000101347	-0,369	1,45E-03	3,92E-02
FANCG	ENSG00000221829	0,345	1,45E-03	3,94E-02
KYNU	ENSG00000115919	0,782	1,46E-03	3,95E-02
RSC1A1	ENSG00000215695	-0,388	1,47E-03	3,96E-02
SNX6	ENSG00000129515	-0,454	1,47E-03	3,97E-02
DIS3L	ENSG00000166938	-0,276	1,48E-03	3,98E-02
FLI1	ENSG00000151702	-0,212	1,48E-03	3,98E-02
SMG1P1	ENSG00000237296	-0,304	1,50E-03	4,00E-02
C6orf136	ENSG00000224120	0,223	1,51E-03	4,04E-02
ANKRD55	ENSG00000164512	0,227	1,53E-03	4,07E-02
NUSAP1	ENSG00000137804	-0,257	1,54E-03	4,10E-02
MCTP2	ENSG00000140563	0,553	1,55E-03	4,12E-02
SMIM10	ENSG00000184785	-0,426	1,56E-03	4,12E-02
IRF7	ENSG00000276561	0,301	1,56E-03	4,14E-02
FBXW4	ENSG00000107829	0,228	1,57E-03	4,15E-02
PDXK	ENSG00000160209	0,284	1,60E-03	4,22E-02
SIK1B	ENSG00000275993	0,287	1,62E-03	4,26E-02
ALDH3A2	ENSG00000072210	-0,186	1,62E-03	4,27E-02
MICAL1	ENSG00000135596	0,209	1,63E-03	4,27E-02
RNASEK	ENSG00000219200	0,259	1,63E-03	4,27E-02
POGLUT3	ENSG00000178202	-0,247	1,64E-03	4,29E-02
PIF1	ENSG00000140451	-0,318	1,69E-03	4,39E-02
SQLE	ENSG00000104549	-0,304	1,69E-03	4,39E-02
AP000295.1	NA	-0,791	1,72E-03	4,42E-02
ARHGAP29	ENSG00000137962	-0,385	1,70E-03	4,42E-02
HSD3B7	ENSG00000099377	0,300	1,71E-03	4,42E-02
KAT2B	ENSG00000114166	-0,353	1,72E-03	4,42E-02
LZTFL1	ENSG00000163818	-0,296	1,71E-03	4,42E-02
PARPBP	ENSG00000185480	-0,421	1,72E-03	4,42E-02
RRAS	ENSG00000126458	0,247	1,72E-03	4,42E-02
TAX1BP3	ENSG00000213977	0,221	1,70E-03	4,42E-02
YAP1	ENSG00000137693	-0,249	1,73E-03	4,42E-02
CFLAR	ENSG00000003402	0,156	1,74E-03	4,44E-02
ZBTB21	ENSG00000173276	-0,333	1,74E-03	4,44E-02
NPAS2	ENSG00000170485	-0,270	1,75E-03	4,45E-02
SPIN2B	ENSG00000186787	-0,244	1,75E-03	4,45E-02
ARHGAP4	ENSG00000089820	0,214	1,77E-03	4,48E-02
GPD1L	ENSG00000152642	-0,209	1,77E-03	4,48E-02
MEF2A	ENSG00000068305	-0,344	1,79E-03	4,52E-02
RGS5	ENSG00000232995	-0,291	1,80E-03	4,54E-02
YPEL3	ENSG00000090238	0,217	1,80E-03	4,54E-02
PRRX1	ENSG00000116132	1,003	1,81E-03	4,54E-02

YIPF1	ENSG00000058799	0,223	1,84E-03	4,62E-02
PIEZO2	ENSG00000154864	-0,312	1,85E-03	4,64E-02
IL1R1	ENSG00000115594	-0,282	1,86E-03	4,65E-02
SAMD8	ENSG00000156671	-0,225	1,86E-03	4,66E-02
NUDT4B	ENSG00000177144	-0,160	1,89E-03	4,73E-02
SULF1	ENSG00000137573	-0,415	1,90E-03	4,73E-02
ADGRF3	ENSG00000173567	2,100	1,91E-03	4,75E-02
PGM2	ENSG00000169299	-0,220	1,91E-03	4,75E-02
MOV10	ENSG00000155363	0,221	1,93E-03	4,78E-02
C1S	ENSG00000182326	1,036	1,95E-03	4,83E-02
FAM114A1	ENSG00000197712	-0,168	1,96E-03	4,83E-02
KPNA1	ENSG00000114030	-0,182	1,96E-03	4,83E-02
SCLT1	ENSG00000151466	-0,365	1,98E-03	4,88E-02
MARCHF2	ENSG00000099785	0,189	1,99E-03	4,89E-02
CMKLR1	ENSG00000174600	-1,002	2,00E-03	4,91E-02
DARS2	ENSG00000117593	-0,281	2,01E-03	4,92E-02
B3GAT3	ENSG00000149541	0,247	2,02E-03	4,92E-02
CCDC190	ENSG00000185860	-0,264	2,02E-03	4,92E-02
CD109	ENSG00000156535	-0,318	2,02E-03	4,92E-02
SBNO2	ENSG00000278788	0,304	2,03E-03	4,92E-02
STYXL1	ENSG00000127952	0,217	2,01E-03	4,92E-02
CYSTM1	ENSG00000120306	0,205	2,04E-03	4,95E-02
VPS26A	ENSG00000122958	-0,298	2,05E-03	4,96E-02
PTK2	ENSG00000169398	-0,273	2,06E-03	4,98E-02
PRKAR2B	ENSG00000284096	-0,307	2,07E-03	4,99E-02
RBPMS2	ENSG00000166831	0,311	2,07E-03	4,99E-02
RGS4	ENSG00000117152	-0,258	2,08E-03	5,00E-02
TAP2	ENSG00000225967	0,212	2,08E-03	5,00E-02

Supplementary Table S6: Differentially expressed genes upon LPS treatment of cells expressing APEX1(1-20). DGE calculated using the R package DESeq2 comparing sam-ples of cells transduced with the lentivirus expressing APEX1(1-20) and treated with active LPS versus treated with detoxified LPS. The L2FC (Log 2-fold change) states the average difference in gene expression between both treatments. Positive L2FC values denote upregulation by LPS treatment, negative values downregulation. Wald test from DESeq2 was used to calculate the significance of the change in the expression. The adjusted p-values take the number of tested genes into account, the threshold for the adjusted p-value was 0.05.

gene name	Ensembl gene ID	L2FC	p-value	adusted p-value
LAMC2	ENSG00000058085	2,107	1,12E-198	1,76E-194
SOD2	ENSG00000112096	1,108	1,25E-66	9,84E-63
EBI3	ENSG00000105246	2,271	1,43E-53	7,47E-50
CXCL6	ENSG00000124875	1,655	1,16E-49	4,57E-46
MMP10	ENSG00000166670	1,106	1,31E-46	4,12E-43
CCL2	ENSG00000108691	1,060	7,21E-45	1,88E-41
CTSS	ENSG00000163131	1,287	6,43E-41	1,44E-37
CFB	ENSG00000242335	1,565	1,12E-40	2,21E-37
UBD	ENSG00000226898	2,203	9,00E-40	1,57E-36
CTSK	ENSG00000143387	1,417	1,61E-36	2,53E-33
POU2F2	ENSG00000028277	1,240	1,29E-35	1,83E-32
LTB	ENSG00000223448	1,169	9,43E-27	1,23E-23
IGFBP3	ENSG00000146674	-0,776	2,00E-26	2,42E-23
IL32	ENSG00000008517	1,115	5,74E-26	6,43E-23
CNTNAP1	ENSG00000108797	0,597	1,69E-24	1,77E-21
IFI27	ENSG00000275214	0,640	2,88E-23	2,82E-20
PAPLN	ENSG00000100767	1,408	9,10E-23	8,39E-20
ANO9	ENSG00000185101	4,416	3,91E-20	3,41E-17
ISG20	ENSG00000172183	0,752	1,23E-19	1,02E-16
S100A3	ENSG00000188015	1,601	7,48E-19	5,87E-16
CXCL1	ENSG00000163739	0,959	1,42E-18	1,06E-15
CXCL5	ENSG00000163735	1,745	1,40E-17	9,96E-15
METTL7A	ENSG00000185432	-0,636	3,12E-16	2,13E-13
AC091951.4	NA	4,960	5,48E-16	3,58E-13
THSD4	ENSG00000187720	0,378	6,63E-16	4,16E-13
NEURL1B	ENSG00000214357	-0,822	3,17E-15	1,91E-12
CXCL8	ENSG00000169429	1,039	6,64E-15	3,86E-12
MAMDC2	ENSG00000278608	0,926	2,34E-14	1,31E-11
CR354443.1	NA	32,453	2,78E-14	1,50E-11
CCL15-CCL14	ENSG00000282521	-0,637	6,52E-14	3,30E-11
FCF1P2	ENSG00000228638	-23,428	6,46E-14	3,30E-11
MX1	ENSG00000157601	0,881	1,11E-13	5,45E-11
SLC7A2	ENSG00000003989	0,614	2,48E-13	1,18E-10
H3P6	ENSG00000235655	30,910	2,90E-13	1,34E-10
PLA2G4C	ENSG00000105499	0,669	3,43E-13	1,54E-10
TBC1D3K	ENSG00000275153	-30,254	6,41E-13	2,79E-10
HLA-B	ENSG00000206450	0,830	2,21E-12	9,37E-10
AL451062.4	NA	-29,257	3,51E-12	1,45E-09
LYPD6	ENSG00000187123	0,545	2,51E-11	1,01E-08
ITGB4	ENSG00000132470	-0,899	3,01E-11	1,18E-08
AKAP12	ENSG00000131016	0,392	3,13E-11	1,20E-08
ACBD7	ENSG00000176244	-0,963	3,63E-11	1,34E-08
PXDN	ENSG00000130508	0,668	3,67E-11	1,34E-08
LAMP3	ENSG00000078081	0,580	3,98E-11	1,42E-08
IL4I1	ENSG00000104951	0,582	1,45E-10	5,05E-08

LIPG	ENSG00000101670	0,605	1,48E-10	5,05E-08
CTHRC1	ENSG00000164932	0,586	1,60E-10	5,34E-08
ICAM1	ENSG00000090339	0,518	2,53E-10	8,27E-08
ALOX5AP	ENSG00000132965	1,792	4,57E-10	1,46E-07
CD69	ENSG00000110848	1,109	8,28E-10	2,60E-07
CYB5R2	ENSG00000166394	0,651	9,12E-10	2,80E-07
KLF2	ENSG00000127528	-0,494	1,42E-09	4,28E-07
MMP19	ENSG00000123342	0,700	1,82E-09	5,29E-07
SRP9P1	ENSG00000180581	25,646	1,82E-09	5,29E-07
CD34	ENSG00000174059	-0,395	1,98E-09	5,66E-07
PSMB9	ENSG00000243958	0,523	2,11E-09	5,90E-07
CXCL2	ENSG00000081041	0,820	3,17E-09	8,72E-07
IFI6	ENSG00000126709	0,493	4,18E-09	1,13E-06
KIT	ENSG00000157404	0,351	5,37E-09	1,43E-06
PPL	ENSG00000118898	-1,098	6,56E-09	1,72E-06
TFPI2	ENSG00000105825	0,607	6,91E-09	1,78E-06
C2CD4A	ENSG00000198535	0,816	1,09E-08	2,76E-06
AP005018.2	NA	-23,882	1,38E-08	3,43E-06
CCL14	ENSG00000277236	-0,599	1,43E-08	3,51E-06
F2RL1	ENSG00000164251	0,378	2,81E-08	6,78E-06
RNASE1	ENSG00000129538	-0,388	3,16E-08	7,52E-06
ALDH1A1	ENSG00000165092	-0,420	3,70E-08	8,66E-06
NID2	ENSG00000087303	0,901	4,00E-08	9,23E-06
NFKBIZ	ENSG00000144802	0,715	4,07E-08	9,25E-06
P2RX4	ENSG00000135124	0,313	6,22E-08	1,39E-05
SOX18	ENSG00000203883	-0,314	7,70E-08	1,70E-05
AQP1	ENSG00000240583	-1,437	9,16E-08	2,00E-05
CCNE1	ENSG00000105173	0,424	1,00E-07	2,16E-05
CXCL3	ENSG00000163734	0,498	1,33E-07	2,81E-05
CCL20	ENSG00000115009	0,878	1,41E-07	2,94E-05
ITGAV	ENSG00000138448	0,580	1,45E-07	2,99E-05
ACE	ENSG00000159640	-0,668	1,56E-07	3,18E-05
LYVE1	ENSG00000133800	-0,766	1,64E-07	3,29E-05
TNFRSF9	ENSG00000049249	1,044	2,28E-07	4,53E-05
STAP2	ENSG00000178078	0,406	2,37E-07	4,65E-05
PRICKLE1	ENSG00000139174	-0,462	2,88E-07	5,57E-05
OAS3	ENSG00000111331	0,509	3,18E-07	6,08E-05
ANGPT2	ENSG00000091879	0,361	4,34E-07	8,20E-05
BST1	ENSG00000109743	0,352	5,75E-07	1,07E-04
IL1A	ENSG00000115008	0,680	6,75E-07	1,25E-04
MEST	ENSG00000106484	-0,406	7,83E-07	1,43E-04
CCM2L	ENSG00000101331	-0,448	8,16E-07	1,47E-04
IFIT1	ENSG00000185745	0,962	9,22E-07	1,64E-04
CRACR2B	ENSG00000177685	-0,419	9,45E-07	1,65E-04
OAS1	ENSG00000089127	0,474	9,42E-07	1,65E-04
INHBB	ENSG00000163083	-0,814	9,82E-07	1,69E-04
PAPPA2	ENSG00000116183	1,562	9,88E-07	1,69E-04
TXNIP	ENSG00000265972	-0,730	1,01E-06	1,70E-04
GJA4	ENSG00000187513	-0,568	1,05E-06	1,75E-04
IGFBP4	ENSG00000141753	-0,294	1,18E-06	1,95E-04
TNFSF15	ENSG00000181634	0,311	1,38E-06	2,25E-04
ADAMTS18	ENSG00000140873	-0,514	1,55E-06	2,50E-04
FRY	ENSG00000073910	-0,217	1,61E-06	2,58E-04

PLCD3	ENSG00000161714	-0,419	1,81E-06	2,87E-04
IL7R	ENSG00000168685	0,419	1,89E-06	2,96E-04
TNC	ENSG00000041982	2,315	1,99E-06	3,09E-04
SYNJ2	ENSG00000078269	0,174	2,09E-06	3,21E-04
MSMP	ENSG00000215183	-0,386	3,03E-06	4,62E-04
GMFG	ENSG00000130755	0,286	3,12E-06	4,70E-04
OCIAD2	ENSG00000145247	0,388	3,39E-06	5,07E-04
TMEM120A	ENSG00000189077	0,384	3,56E-06	5,27E-04
CSF2	ENSG00000164400	1,186	3,78E-06	5,54E-04
CREB5	ENSG00000146592	0,326	4,06E-06	5,89E-04
EPSTI1	ENSG00000133106	0,947	4,15E-06	5,93E-04
KIF20A	ENSG00000112984	-0,438	4,16E-06	5,93E-04
PRIM1	ENSG00000198056	0,506	4,50E-06	6,36E-04
TMEM184A	ENSG00000164855	1,991	4,78E-06	6,69E-04
OAS2	ENSG00000111335	0,745	5,53E-06	7,67E-04
CAV1	ENSG00000105974	-0,277	7,04E-06	9,64E-04
NRROS	ENSG00000174004	-0,303	7,06E-06	9,64E-04
TNIP3	ENSG00000050730	1,239	7,28E-06	9,85E-04
ADAMTS15	ENSG00000166106	-1,383	7,59E-06	1,02E-03
TAPBP	ENSG00000206281	0,364	8,63E-06	1,15E-03
ABCG2	ENSG00000118777	-0,578	9,42E-06	1,24E-03
NLRC3	ENSG00000167984	0,376	9,48E-06	1,24E-03
LRRC75A	ENSG00000181350	-0,393	1,00E-05	1,30E-03
PRSS12	ENSG00000164099	0,973	1,02E-05	1,32E-03
IFI44L	ENSG00000137959	0,935	1,18E-05	1,51E-03
EGLN3	ENSG00000129521	-1,171	1,28E-05	1,62E-03
TSPAN11	ENSG00000110900	-0,436	1,33E-05	1,67E-03
QPCT	ENSG00000115828	0,564	1,38E-05	1,72E-03
TNFRSF4	ENSG00000186827	0,805	1,41E-05	1,75E-03
COL1A2	ENSG00000164692	-0,415	1,53E-05	1,87E-03
CCNB2	ENSG00000157456	-0,387	1,64E-05	1,98E-03
EXO1	ENSG00000174371	0,511	1,64E-05	1,98E-03
CFLAR	ENSG00000003402	0,213	1,90E-05	2,27E-03
ZNF365	ENSG00000138311	0,547	2,07E-05	2,47E-03
ALDH1A2	ENSG00000128918	-0,324	2,29E-05	2,68E-03
GALNT18	ENSG00000110328	0,563	2,28E-05	2,68E-03
APLN	ENSG00000171388	-0,484	2,33E-05	2,71E-03
HMGCS1	ENSG00000112972	-0,321	2,41E-05	2,78E-03
ARHGDIG	ENSG00000242173	0,442	2,47E-05	2,83E-03
ZC3H12A	ENSG00000163874	0,454	2,53E-05	2,87E-03
ZNF467	ENSG00000181444	-0,453	3,02E-05	3,40E-03
SELENOT	ENSG00000198843	0,254	3,21E-05	3,59E-03
ACAT2	ENSG00000120437	-0,283	3,27E-05	3,61E-03
GPX3	ENSG00000211445	-0,573	3,27E-05	3,61E-03
GGT5	ENSG00000099998	-0,353	3,35E-05	3,66E-03
HLA-A	ENSG00000227715	0,289	3,36E-05	3,66E-03
SEMA7A	ENSG00000288455	0,486	3,81E-05	4,13E-03
YIPF5	ENSG00000145817	0,269	3,90E-05	4,19E-03
ASS1	ENSG00000130707	-0,446	4,11E-05	4,39E-03
MGARP	ENSG00000137463	-0,451	4,35E-05	4,61E-03
FP565260.3	NA	0,386	4,38E-05	4,61E-03
MALL	ENSG00000144063	-0,288	4,47E-05	4,67E-03
MRAP2	ENSG00000135324	-0,384	4,63E-05	4,81E-03

IL1RL1	ENSG00000115602	0,254	4,78E-05	4,90E-03
RAMP2	ENSG00000131477	-0,465	4,75E-05	4,90E-03
CD44	ENSG00000026508	0,503	5,20E-05	5,30E-03
LRTOMT	ENSG00000184154	-0,402	5,45E-05	5,51E-03
AC005520.3	NA	-1,051	5,60E-05	5,63E-03
CSF3	ENSG00000108342	1,064	5,92E-05	5,91E-03
FBXO32	ENSG00000156804	0,351	6,03E-05	5,99E-03
DHH	ENSG00000139549	-0,365	6,08E-05	5,99E-03
RALB	ENSG00000144118	-0,201	6,25E-05	6,13E-03
HPSE	ENSG00000173083	0,245	6,31E-05	6,15E-03
LGALS3BP	ENSG00000108679	0,760	6,40E-05	6,19E-03
TUSC3	ENSG00000104723	0,294	6,43E-05	6,19E-03
SH3BP1	ENSG00000100092	0,715	6,69E-05	6,40E-03
SMIM3	ENSG00000256235	-0,424	6,75E-05	6,42E-03
NPTN	ENSG00000156642	0,193	6,88E-05	6,51E-03
ABLIM2	ENSG00000163995	-1,741	8,11E-05	7,58E-03
MYRIP	ENSG00000170011	-0,301	8,15E-05	7,58E-03
TCF15	ENSG00000125878	-0,467	8,17E-05	7,58E-03
C4B	ENSG00000224639	-1,377	8,74E-05	7,99E-03
CASP1	ENSG00000137752	0,501	8,76E-05	7,99E-03
KIF12	ENSG00000136883	0,542	8,73E-05	7,99E-03
SERPINA3	ENSG00000196136	1,848	8,87E-05	8,05E-03
COLGALT1	ENSG00000130309	0,367	9,66E-05	8,71E-03
AFF3	ENSG00000144218	1,033	1,05E-04	9,24E-03
EIF3CL	ENSG00000205609	-0,720	1,04E-04	9,24E-03
ERMP1	ENSG00000099219	-0,243	1,04E-04	9,24E-03
HLA-H	ENSG00000231904	0,357	1,05E-04	9,24E-03
SPACA6	ENSG00000182310	-0,405	1,04E-04	9,24E-03
CCNB1	ENSG00000134057	-0,396	1,06E-04	9,27E-03
MYZAP	ENSG00000263155	-0,356	1,19E-04	1,03E-02
C20orf204	ENSG00000196421	-0,498	1,21E-04	1,04E-02
CGNL1	ENSG00000128849	-0,203	1,21E-04	1,04E-02
SLC6A15	ENSG00000072041	0,655	1,22E-04	1,04E-02
DHRS3	ENSG00000162496	0,284	1,24E-04	1,05E-02
OASL	ENSG00000135114	1,044	1,24E-04	1,05E-02
DNAH5	ENSG00000039139	0,437	1,26E-04	1,05E-02
FBLN2	ENSG00000163520	-0,677	1,26E-04	1,05E-02
AOX1	ENSG00000138356	0,620	1,39E-04	1,15E-02
ICOSLG	ENSG00000160223	0,377	1,40E-04	1,15E-02
LHX6	ENSG00000106852	-0,471	1,41E-04	1,15E-02
SLIT3	ENSG00000184347	0,552	1,42E-04	1,16E-02
AC019117.4	NA	8,471	1,44E-04	1,17E-02
MAP3K6	ENSG00000142733	0,299	1,49E-04	1,20E-02
ABI3BP	ENSG00000154175	0,365	1,52E-04	1,22E-02
KYNU	ENSG00000115919	0,927	1,53E-04	1,22E-02
SAPCD2	ENSG00000186193	-0,366	1,52E-04	1,22E-02
MTMR7	ENSG00000003987	0,923	1,53E-04	1,22E-02
GIMAP1	ENSG00000213203	-0,265	1,60E-04	1,26E-02
NQO1	ENSG00000181019	-0,281	1,60E-04	1,26E-02
CASKIN1	ENSG00000167971	-2,314	1,67E-04	1,30E-02
CA4	ENSG00000167434	-1,172	1,76E-04	1,37E-02
LY75-CD302	ENSG00000248672	0,547	1,79E-04	1,38E-02
AC244260.1	NA	8,622	1,92E-04	1,48E-02

CDH4	ENSG00000280641	-0,476	1,93E-04	1,48E-02
GALNT12	ENSG00000119514	0,363	1,95E-04	1,49E-02
PCK2	ENSG00000285241	0,283	2,15E-04	1,63E-02
ABCC2	ENSG00000023839	-0,663	2,17E-04	1,63E-02
CAMSAP3	ENSG00000076826	-0,935	2,17E-04	1,63E-02
GUCY1A1	ENSG00000164116	-0,911	2,21E-04	1,65E-02
MAP3K14	ENSG00000282637	-0,384	2,28E-04	1,70E-02
ALDH1L2	ENSG00000136010	0,311	2,30E-04	1,70E-02
IFI44	ENSG00000137965	0,499	2,32E-04	1,71E-02
BCAM	ENSG00000187244	-0,275	2,37E-04	1,74E-02
TCF7	ENSG00000081059	0,391	2,44E-04	1,78E-02
SCNN1B	ENSG00000168447	-2,117	2,45E-04	1,78E-02
CHRNA1	ENSG00000138435	0,426	2,48E-04	1,79E-02
PLAAT4	ENSG00000133321	0,548	2,56E-04	1,84E-02
CYP1A1	ENSG00000140465	-0,508	2,66E-04	1,91E-02
PRCP	ENSG00000137509	0,175	2,71E-04	1,93E-02
NOS3	ENSG00000164867	-0,330	2,80E-04	1,99E-02
CLEC14A	ENSG00000176435	-0,190	2,82E-04	1,99E-02
IFI35	ENSG00000068079	0,344	2,86E-04	2,01E-02
PTGS2	ENSG00000073756	0,572	2,92E-04	2,05E-02
POSTN	ENSG00000133110	-0,539	3,01E-04	2,10E-02
DUXAP9	ENSG00000225210	0,284	3,07E-04	2,13E-02
MYPN	ENSG00000138347	0,620	3,15E-04	2,17E-02
PIR	ENSG00000087842	-0,566	3,27E-04	2,25E-02
AK4	ENSG00000162433	0,170	3,35E-04	2,29E-02
IFT122	ENSG00000163913	-0,270	3,36E-04	2,29E-02
P2RY6	ENSG00000171631	1,128	3,53E-04	2,40E-02
DPYSL3	ENSG00000113657	0,257	3,60E-04	2,43E-02
ATP2B4	ENSG00000058668	-0,175	3,69E-04	2,48E-02
GK	ENSG00000198814	0,285	3,79E-04	2,52E-02
SELENOM	ENSG00000198832	0,345	3,78E-04	2,52E-02
ZNF219	ENSG00000165804	-0,385	3,80E-04	2,52E-02
PIEZO2	ENSG00000154864	-0,355	3,88E-04	2,57E-02
STC1	ENSG00000159167	-0,462	3,91E-04	2,58E-02
APOD	ENSG00000189058	0,347	4,06E-04	2,64E-02
ATAD2	ENSG00000156802	0,366	4,10E-04	2,64E-02
BUB1	ENSG00000169679	-0,310	4,11E-04	2,64E-02
GPNMB	ENSG00000136235	-1,050	4,09E-04	2,64E-02
NOS1	ENSG00000089250	-2,260	4,09E-04	2,64E-02
PCDH1	ENSG00000156453	0,264	4,06E-04	2,64E-02
DLL1	ENSG00000275555	-0,370	4,21E-04	2,69E-02
ENOSF1	ENSG00000132199	-0,301	4,25E-04	2,71E-02
TMOD1	ENSG00000136842	0,445	4,30E-04	2,72E-02
TSPAN8	ENSG00000127324	-0,646	4,30E-04	2,72E-02
CLEC3B	ENSG00000163815	-1,195	4,35E-04	2,74E-02
SLCO2A1	ENSG00000174640	-0,674	4,36E-04	2,74E-02
PLA2G5	ENSG00000127472	1,414	4,50E-04	2,80E-02
RASSF10	ENSG00000189431	-1,470	4,49E-04	2,80E-02
AMPD3	ENSG00000133805	0,780	4,55E-04	2,81E-02
LRP12	ENSG00000147650	0,252	4,54E-04	2,81E-02
CHAF1A	ENSG00000167670	0,466	4,61E-04	2,83E-02
PRRT2	ENSG00000167371	2,229	4,61E-04	2,83E-02
HSPB6	ENSG00000004776	-0,351	4,65E-04	2,83E-02

WNT9A	ENSG00000143816	-0,439	4,66E-04	2,83E-02
CACHD1	ENSG00000158966	0,277	4,80E-04	2,91E-02
GSTM2	ENSG00000213366	-0,342	4,84E-04	2,92E-02
CD36	ENSG00000135218	-0,760	4,87E-04	2,93E-02
TNFSF18	ENSG00000120337	-0,366	5,05E-04	3,02E-02
CST1	ENSG00000170373	0,610	5,07E-04	3,02E-02
KCNN4	ENSG00000104783	-0,792	5,12E-04	3,04E-02
SHE	ENSG00000169291	-0,219	5,15E-04	3,05E-02
DUSP4	ENSG00000120875	-0,261	5,23E-04	3,09E-02
CENPBD1	ENSG00000177946	0,199	5,36E-04	3,14E-02
TM7SF2	ENSG00000149809	-0,335	5,35E-04	3,14E-02
HSPB8	ENSG00000152137	0,334	5,44E-04	3,18E-02
IGFBP1	ENSG00000146678	-0,582	5,65E-04	3,27E-02
UBE2L6	ENSG00000156587	0,205	5,64E-04	3,27E-02
SYT7	ENSG00000011347	-0,953	5,70E-04	3,29E-02
SLC15A3	ENSG00000110446	0,327	5,73E-04	3,29E-02
ZFPM2	ENSG00000169946	0,369	5,92E-04	3,39E-02
CDC20	ENSG00000117399	-0,386	6,03E-04	3,44E-02
ANKRD44	ENSG00000065413	-0,767	6,07E-04	3,45E-02
NTSR1	ENSG00000101188	-0,347	6,10E-04	3,46E-02
DNAH11	ENSG00000105877	0,366	6,21E-04	3,50E-02
CLSPN	ENSG00000092853	0,378	6,31E-04	3,55E-02
FAM221A	ENSG00000188732	-0,310	6,40E-04	3,55E-02
PIK3R3	ENSG00000117461	-0,311	6,35E-04	3,55E-02
PLSCR1	ENSG00000188313	0,208	6,38E-04	3,55E-02
RTN4RL1	ENSG00000185924	-2,401	6,39E-04	3,55E-02
BDKRB2	ENSG00000168398	0,651	6,48E-04	3,55E-02
CDC25B	ENSG00000101224	-0,240	6,46E-04	3,55E-02
MOBP	ENSG00000168314	0,795	6,44E-04	3,55E-02
NFIA	ENSG00000162599	-0,403	6,63E-04	3,63E-02
GIMAP8	ENSG00000171115	-0,227	6,76E-04	3,68E-02
PARD6A	ENSG00000102981	-0,362	6,88E-04	3,74E-02
ADGRF3	ENSG00000173567	2,256	7,00E-04	3,78E-02
PSMB8	ENSG00000230669	0,220	7,14E-04	3,85E-02
CCL23	ENSG00000276114	-0,826	7,24E-04	3,88E-02
RASGRF2	ENSG00000113319	0,347	7,24E-04	3,88E-02
C1orf115	ENSG00000162817	-0,180	7,31E-04	3,90E-02
NUAK1	ENSG00000074590	0,442	7,38E-04	3,93E-02
AUNIP	ENSG00000127423	0,412	7,58E-04	4,00E-02
FSTL3	ENSG00000070404	0,289	7,58E-04	4,00E-02
ARSK	ENSG00000164291	0,211	7,70E-04	4,04E-02
MXD3	ENSG00000213347	-0,387	7,69E-04	4,04E-02
CLEC1A	ENSG00000150048	0,182	7,77E-04	4,06E-02
HTR2B	ENSG00000135914	-0,366	8,16E-04	4,25E-02
BTD	ENSG00000169814	-0,185	8,29E-04	4,29E-02
TCN2	ENSG00000185339	-0,295	8,26E-04	4,29E-02
TSPAN5	ENSG00000168785	-0,178	8,41E-04	4,34E-02
CIT	ENSG00000122966	-0,302	8,70E-04	4,48E-02
ZDHHC13	ENSG00000177054	-0,211	8,97E-04	4,60E-02
ACKR4	ENSG00000129048	-0,454	9,16E-04	4,63E-02
ARL14EPL	ENSG00000268223	-0,995	9,21E-04	4,63E-02
MATN2	ENSG00000132561	-0,529	9,21E-04	4,63E-02
PDE1C	ENSG00000154678	0,280	9,17E-04	4,63E-02

RGS2	ENSG00000116741	0,398	9,15E-04	4,63E-02
SULF1	ENSG00000137573	-0,443	9,12E-04	4,63E-02
CYP51A1	ENSG00000001630	-0,193	9,28E-04	4,65E-02
ARHGEF26	ENSG00000277101	0,351	9,35E-04	4,67E-02
TUBB2B	ENSG00000137285	0,445	9,73E-04	4,84E-02
BTG2	ENSG00000159388	-0,190	9,94E-04	4,93E-02

Supplementary Table S7: Genes upregulated by LPS exclusively in cells that do not express APEX1(1-20). To identify genes upregulated by LPS specifically in cells transduced with the empty virus, but not in cells expressing moderate levels of APEX1(1- 20), the results of the DGE analysis of both cells populations after treatment with detoxified (con) or active LPS (LPS) were combined. The L2FC (Log 2-fold change) states the average difference in gene expression between both treatments, positive values denote upregulation by LPS treatment. Wald test from DESeq2 was used to calculate the significance of the change in the expression. The adjusted p-values take the number of tested genes into account, the threshold for the adjusted p-value was 0.05. Mean expression levels per sample group are stated in transcripts per million (TPM), calculated during quasi-mapping with the tool salmon. The list is sorted by gene expression.

gene name	L2FC	adjusted p-value	mean TPM empty virus con	mean TPM empty virus LPS	mean TPM APEX1(1-20) con	mean TPM APEX1(1-20) LPS
FTH1	0,268	4,30E-03	4639,36	5565,16	4723,13	5429,98
SERPINE1	0,263	3,91E-02	2753,76	3306,84	2860,91	3352,05
SAT1	0,334	2,28E-02	372,10	468,58	420,02	491,31
RNASEK	0,259	4,27E-02	302,79	362,46	319,66	347,36
GDF15	0,428	4,16E-03	181,22	243,01	186,96	225,56
TAX1BP3	0,221	4,42E-02	166,16	193,15	174,50	184,39
COTL1	0,280	6,99E-03	165,55	200,62	173,08	192,33
COL4A2	0,432	2,82E-02	148,83	198,87	156,04	201,24
PSME1	0,266	4,11E-03	147,10	176,17	153,10	168,61
PSME2	0,443	8,81E-05	134,36	181,67	140,36	171,61
RRAS	0,247	4,42E-02	128,19	152,15	131,01	143,27
HLA-C	0,313	8,89E-03	120,68	149,68	127,87	149,23
MT1L	0,355	1,88E-02	119,01	151,73	116,61	144,39
IER3	0,270	7,20E-03	100,45	120,93	107,70	115,41
ATP5F1D	0,341	1,18E-02	92,26	116,67	100,23	97,38
MFAP2	0,276	5,43E-03	70,80	85,75	75,64	78,59
CYSTM1	0,205	4,95E-02	68,11	78,37	68,82	69,97
SPHK1	0,285	2,16E-02	64,57	78,63	65,73	71,53
PDXK	0,284	4,22E-02	63,89	77,58	69,04	72,86
STYXL1	0,217	4,92E-02	55,70	64,54	53,68	57,32
BPGM	0,259	1,57E-02	47,34	56,61	48,03	56,46
PLCG1	0,243	5,56E-04	46,66	55,06	50,10	50,59
NFKBIA	0,272	5,05E-03	44,13	53,19	48,70	53,45
P4HA2	0,217	3,84E-02	41,12	47,65	40,49	44,88
ISG15	0,345	1,23E-02	40,32	51,21	43,32	50,22
SERPINB9	0,176	2,04E-02	40,12	45,26	43,72	46,50
DPP3	0,281	5,75E-03	39,09	47,59	39,50	45,15
CXCR4	0,237	1,68E-02	37,57	44,12	36,06	41,30
TSPAN13	0,390	8,14E-04	36,14	47,46	38,66	43,40
BST2	0,315	7,15E-04	35,86	44,46	37,59	42,84
SIPA1	0,279	3,13E-02	32,32	39,17	34,52	35,80
TMEM132A	0,351	6,18E-03	31,27	39,93	34,67	35,67
POLD4	0,346	3,42E-02	28,60	36,48	29,78	31,91
UPP1	0,232	1,96E-02	28,15	32,94	27,23	31,38
GMPPA	0,312	1,03E-02	28,14	34,92	28,84	32,19
PSMB10	0,328	2,68E-03	27,59	34,55	28,71	32,02
YPEL3	0,217	4,54E-02	26,38	30,64	29,57	28,61
GSDMD	0,274	6,99E-03	25,96	31,39	27,55	29,02
FHL3	0,276	3,00E-02	25,68	31,13	27,18	29,16
PLTP	0,355	5,67E-03	25,47	32,76	27,27	31,30
MARCHF2	0,189	4,89E-02	23,89	27,20	26,73	24,84
TMEM54	0,266	8,15E-03	23,67	28,40	25,16	25,07
NUDT22	0,284	3,13E-02	22,84	27,79	24,16	24,80
TNFRSF21	0,172	3,10E-02	22,78	25,62	24,02	26,02
UBR4	0,376	1,12E-02	22,72	29,57	22,32	25,97

ANKH	0,290	8,12E-03	22,47	27,49	22,50	24,26
GRASP	0,197	5,05E-03	22,21	25,48	23,13	23,42
AGRN	0,368	1,28E-02	21,33	27,78	21,89	26,02
MOV10	0,221	4,78E-02	20,49	23,73	21,01	20,55
FBLN5	0,404	1,15E-02	19,17	25,33	21,56	26,50
TSSC4	0,419	1,28E-02	18,98	25,48	19,43	19,63
TCIRG1	0,271	1,43E-02	18,05	21,85	19,29	20,30
EML2	0,311	1,35E-02	17,59	21,82	19,57	18,49
SURF1	0,234	9,64E-03	17,51	20,53	18,53	18,21
RSAD1	0,197	1,18E-02	16,94	19,36	17,55	18,60
CCS	0,222	3,81E-02	16,90	19,69	17,92	17,70
GBGT1	0,343	1,72E-02	16,83	21,36	17,33	19,51
SLC35C2	0,269	1,84E-02	16,83	20,30	17,60	18,66
CHKB	0,197	3,40E-02	16,68	19,04	17,40	17,25
LIG1	0,274	1,63E-02	16,52	19,88	15,96	18,60
SDC4	0,352	6,93E-04	16,38	20,79	17,77	19,54
STARD10	0,569	4,79E-07	16,35	24,40	18,98	22,60
SLC38A5	0,391	1,91E-02	16,17	21,13	18,27	19,16
MAP1LC3A	0,328	1,88E-02	15,91	19,99	17,73	18,79
LRFN4	0,375	9,94E-04	15,46	19,96	17,12	17,34
APOL1	0,388	1,24E-06	14,89	19,46	17,09	18,97
CAMTA2	0,290	3,88E-03	14,70	17,96	13,71	15,09
CRTAC1	0,499	2,49E-05	14,63	20,56	15,89	19,72
YIPF1	0,223	4,62E-02	14,38	16,72	14,35	15,65
MICAL1	0,209	4,27E-02	14,02	16,23	14,04	15,16
TNFRSF6B	0,338	4,52E-03	13,87	17,58	14,85	15,80
JUNB	0,259	1,57E-02	13,62	16,41	14,14	15,42
SBNO2	0,304	4,92E-02	13,55	16,80	14,23	16,14
NFATC4	0,371	1,94E-02	13,55	17,33	16,04	14,90
C6orf136	0,223	4,04E-02	13,28	15,48	12,90	13,51
POLD1	0,320	2,33E-02	12,27	15,26	12,21	14,22
B3GAT3	0,247	4,92E-02	12,23	14,49	12,50	13,71
GALT	0,230	2,51E-02	12,15	14,22	13,09	13,54
PTK7	0,269	4,49E-03	12,13	14,54	12,75	13,40
CCDC28B	0,254	2,57E-02	11,16	13,29	11,61	12,56
TAP2	0,212	5,00E-02	10,59	12,21	10,79	11,33
TNFRSF14	0,388	1,03E-03	10,32	13,55	11,52	13,07
IFITM1	0,366	2,77E-03	10,28	13,27	11,68	13,46
TMC6	0,276	2,09E-02	9,99	12,12	10,48	11,78
CBR3	0,357	1,62E-03	9,82	12,53	10,15	11,75
FBXW4	0,228	4,15E-02	9,73	11,36	10,21	10,78
FANCG	0,345	3,94E-02	9,48	12,03	9,66	10,17
SLC7A7	0,298	1,68E-02	9,01	11,09	9,71	10,53
ITPKC	0,230	3,23E-02	8,88	10,40	9,02	9,99
MFSD3	0,235	3,15E-02	8,42	9,89	8,93	8,74
SP110	0,241	3,43E-02	8,34	9,85	8,64	9,84
IRF9	0,498	1,26E-03	8,34	11,68	8,74	10,84
SIRT3	0,207	3,55E-02	8,30	9,56	8,63	8,25
UBA7	0,446	6,02E-06	7,69	10,51	8,69	10,17
TREX1	0,275	2,37E-02	7,35	8,84	7,15	8,25
IL3RA	0,238	2,67E-02	7,32	8,63	8,49	8,64
PARP10	0,319	1,05E-02	7,31	9,12	7,17	8,69
SLC27A3	0,380	1,86E-02	7,02	9,15	7,23	8,06

ULBP2	0,338	1,95E-03	6,99	8,81	7,68	8,43
C19orf47	0,357	2,99E-02	6,93	8,83	7,20	8,14
ARHGAP4	0,214	4,48E-02	6,92	8,02	7,26	6,77
RELB	0,353	9,55E-03	6,79	8,68	7,33	7,87
MS4A6A	0,466	5,66E-03	6,75	9,31	6,92	8,42
LAMB3	0,446	2,35E-03	6,66	9,08	6,82	7,85
SOCS3	0,302	1,15E-02	6,29	7,77	6,34	7,05
AMDHD2	0,275	3,56E-02	6,18	7,50	6,51	7,01
ARSA	0,292	1,15E-02	6,12	7,50	6,64	7,17
TCEAL7	0,328	5,88E-03	6,06	7,61	7,03	7,48
PMM1	0,341	1,30E-02	5,47	6,91	5,80	6,62
RPS6KL1	0,352	4,35E-03	5,18	6,57	6,25	6,57
APOBEC3G	0,249	2,89E-02	5,17	6,13	5,50	6,00
SAMD14	0,369	6,93E-04	5,09	6,59	5,72	6,44
E2F1	0,419	2,20E-02	5,08	6,74	5,14	6,70
RND1	0,401	6,28E-03	4,89	6,53	5,96	7,31
MTMR11	0,364	1,27E-03	4,50	5,80	4,61	5,11
PLCG2	1,263	8,65E-05	4,47	10,93	6,94	9,00
GFPT2	0,367	1,51E-02	4,46	5,74	4,86	6,11
PAQR7	0,277	1,42E-04	4,36	5,28	4,58	4,75
BLOC1S3	0,447	2,87E-02	4,25	5,83	5,33	4,58
NUDT18	0,274	3,86E-02	4,17	5,03	4,43	4,75
RASD1	0,316	7,60E-03	4,10	5,11	4,04	4,80
ANKRD55	0,227	4,07E-02	3,96	4,62	4,03	4,54
CERS1	0,381	4,90E-04	3,71	4,83	3,84	4,15
PLEKHA4	0,272	3,51E-02	3,61	4,37	3,79	4,16
TAPBPL	0,812	1,61E-04	3,35	5,70	4,36	4,51
SLC1A4	0,234	8,33E-03	3,22	3,78	3,42	3,70
CPLANE2	0,390	3,83E-03	3,18	4,17	3,23	3,57
SEMA3G	0,417	2,76E-04	3,17	4,24	3,57	4,37
CFAP410	0,304	3,05E-02	3,16	3,91	3,60	3,41
GBP4	0,310	9,61E-03	3,06	3,80	3,21	3,55
ACBD4	0,278	1,93E-02	2,93	3,55	3,31	3,18
CEBPD	0,785	1,63E-06	2,89	5,00	3,62	4,84
ACSS1	0,279	1,11E-04	2,85	3,45	2,97	3,29
RASA4	0,440	5,93E-04	2,80	3,81	3,00	3,68
IL27RA	0,362	1,14E-03	2,67	3,43	2,87	3,38
AMPH	0,488	6,61E-03	2,65	3,70	3,11	4,11
IRF7	0,301	4,14E-02	2,59	3,20	2,64	3,21
ASPHD2	0,209	3,21E-02	2,57	2,97	2,85	3,03
DENND2B	0,984	5,79E-06	2,56	4,92	3,05	3,49
PIK3CD	0,296	2,16E-02	2,54	3,14	2,75	3,18
SIK1B	0,287	4,26E-02	2,53	3,07	2,62	2,94
TMEM121	0,381	2,69E-03	2,44	3,17	2,82	2,99
C2CD4B	0,558	2,54E-02	2,43	3,57	2,65	3,46
TYMP	0,669	3,16E-02	2,16	3,43	3,14	3,38
FAHD2CP	0,381	2,59E-03	2,10	2,73	2,39	2,42
DHX58	0,330	2,91E-02	2,01	2,53	2,18	2,56
C11orf96	0,453	5,30E-04	1,98	2,72	2,22	2,34
VWA1	0,476	8,05E-07	1,95	2,71	2,18	2,54
RBPMS2	0,311	4,99E-02	1,84	2,28	1,97	2,08
SYNGR3	0,367	5,43E-03	1,82	2,36	2,02	2,27
ATOH8	0,364	2,02E-02	1,80	2,32	1,95	2,21

ARHGEF19	0,356	2,64E-04	1,59	2,04	1,71	1,88
TGFBR3L	0,467	6,18E-03	1,51	2,09	1,60	1,69
LRRC3	0,273	3,05E-02	1,31	1,58	1,35	1,52
RASA4B	0,567	1,42E-04	1,29	1,90	1,43	1,79
ZBTB42	0,284	1,87E-02	1,28	1,55	1,37	1,51
HSD3B7	0,300	4,42E-02	1,21	1,50	1,34	1,44
ITPRIPL1	0,456	3,55E-02	1,08	1,48	1,41	1,49
B3GALT4	0,398	5,43E-03	0,99	1,30	1,03	1,16
CX3CL1	0,553	1,96E-03	0,93	1,37	1,30	1,38
FMNL1	0,395	1,74E-02	0,93	1,23	1,10	1,15
AC005363.1	6,479	3,18E-02	0,89	3,89	2,74	2,46
ASPHD1	0,680	3,55E-02	0,87	1,41	1,44	1,44
CPAMD8	0,499	1,88E-02	0,77	1,10	0,82	0,96
FXYD6	0,656	9,95E-04	0,75	1,19	0,96	1,14
ODF3B	0,753	2,04E-02	0,74	1,25	0,82	1,21
MROH6	0,678	1,94E-02	0,69	1,10	1,10	0,90
ADM2	0,487	2,59E-02	0,65	0,91	0,65	0,81
FXYD2	0,734	1,43E-02	0,63	1,04	0,67	0,79
BATF3	0,662	2,60E-02	0,63	0,99	0,73	0,85
SLC22A31	0,695	3,88E-03	0,58	0,93	0,79	0,87
MELTF	0,373	3,00E-02	0,55	0,71	0,61	0,69
PLEKHN1	0,492	1,74E-02	0,54	0,76	0,52	0,70
TPPP3	0,496	2,61E-02	0,54	0,75	0,51	0,70
CDK20	0,409	3,22E-02	0,53	0,71	0,58	0,63
ACTL10	0,358	3,23E-02	0,50	0,64	0,54	0,56
HOXB9	0,395	1,14E-02	0,49	0,65	0,48	0,58
ADGRB2	0,324	2,01E-02	0,47	0,59	0,50	0,57
MCTP2	0,553	4,12E-02	0,44	0,64	0,58	0,53
ST6GALNAC2	0,756	1,60E-02	0,37	0,63	0,46	0,53
CDH15	0,509	1,57E-02	0,36	0,52	0,40	0,51
EFNA2	0,374	2,30E-02	0,34	0,44	0,39	0,39
JAK3	0,743	1,86E-05	0,33	0,56	0,40	0,55
C17orf107	0,459	4,81E-03	0,32	0,43	0,35	0,44
S1PR2	0,346	3,55E-02	0,29	0,37	0,33	0,37
NCKAP5	0,847	1,35E-02	0,27	0,49	0,33	0,50
NMNAT2	0,987	1,77E-02	0,21	0,41	0,27	0,35
PRRX1	1,003	4,54E-02	0,18	0,35	0,25	0,39
GXYLT2	1,226	2,85E-04	0,16	0,38	0,22	0,39
CLDN14	0,877	3,35E-03	0,15	0,28	0,20	0,25
CHST6	0,461	3,30E-02	0,15	0,21	0,15	0,21
SNX22	0,983	6,88E-03	0,14	0,29	0,16	0,18
ACHE	0,801	4,26E-03	0,13	0,23	0,14	0,22
IL11	0,997	8,34E-03	0,10	0,21	0,12	0,18
PTGES3L	1,020	1,79E-02	0,10	0,20	0,15	0,16
PLA1A	1,472	1,66E-06	0,10	0,27	0,14	0,24
C1S	1,036	4,83E-02	0,09	0,17	0,15	0,20
BEST1	3,000	3,23E-02	0,08	0,53	0,13	0,17
THBS2	0,836	1,44E-02	0,08	0,14	0,13	0,14
HAS2	1,050	6,88E-03	0,07	0,15	0,08	0,14
LRG1	0,915	3,23E-02	0,07	0,13	0,11	0,13
MAP6	0,992	5,88E-03	0,07	0,14	0,08	0,09
RAB7B	1,191	6,46E-03	0,05	0,12	0,08	0,10
RPL23AP87	2,313	3,21E-02	0,04	0,13	0,10	0,09

ADAM12	1,044	5,51E-03	0,04	0,08	0,04	0,07
MX2	2,548	8,60E-07	0,02	0,13	0,08	0,13
AL358472.7	20,830	1,46E-05	0,00	0,08	0,15	0,14

Supplementary Table S8: Genes downregulated by LPS exclusively in cells that do not express APEX1(1-20). To identify genes downregulated by LPS specifically in cells transduced with the empty virus, but not in cells expressing moderate levels of APEX1(1-20), the results of the DGE analysis of both cells populations after treatment with detoxified (con) or active LPS (LPS) were combined. The L2FC (Log 2-fold change) states the average difference in gene expression between both treatments, negative values denote downregulation by LPS treatment. Wald test from DESeq2 was used to calculate the significance of the change in the expression. The adjusted p-values take the number of tested genes into account, the threshold for the adjusted p-value was 0.05. Mean expression levels per sample group are stated in transcripts per million (TPM), calculated during quasi-mapping with the tool salmon. The list is sorted by gene expression.

gene name	L2FC	adjusted p-value	mean TPM empty virus con	mean TPM empty virus LPS	mean TPM APEX1(1-20) con	mean TPM APEX1(1-20) LPS
RGS5	-0,291	4,54E-02	1386,54	1138,17	1251,47	1178,35
MMRN1	-0,492	2,43E-02	888,40	637,40	859,18	699,02
VAPA	-0,205	3,21E-03	313,94	271,48	297,11	303,08
CKS2	-0,336	8,89E-03	287,78	228,74	288,97	258,79
PTTG1	-0,362	3,05E-02	285,06	221,31	276,16	228,63
NUCKS1	-0,368	3,27E-04	284,56	220,50	261,59	233,58
CNN3	-0,234	1,04E-02	273,16	231,87	274,05	257,51
CAPN2	-0,289	2,95E-06	260,46	212,68	252,84	228,05
PDCD6IP	-0,363	9,81E-04	189,22	147,31	181,29	183,72
IGF2BP3	-0,313	3,19E-02	182,15	146,90	163,66	171,08
ARL6IP1	-0,280	1,03E-02	162,45	133,86	160,85	137,37
SNX6	-0,454	3,97E-02	159,65	118,82	151,27	147,95
MCFD2	-0,277	7,05E-04	157,06	129,31	155,90	143,20
IPO5	-0,156	2,63E-02	149,62	133,94	146,54	145,32
LAMP2	-0,141	3,91E-02	147,87	133,68	145,02	147,45
PTK2	-0,273	4,98E-02	145,61	121,03	138,06	135,72
ARHGAP29	-0,385	4,42E-02	141,45	109,71	132,43	135,02
HP1BP3	-0,314	1,81E-02	139,47	112,32	131,88	120,54
RGS4	-0,258	5,00E-02	114,80	95,98	117,02	111,04
PRRC2B	-0,252	3,23E-02	112,97	94,70	107,19	104,11
CKAP5	-0,220	1,40E-02	107,89	92,55	102,33	94,75
VPS26A	-0,298	4,96E-02	107,19	87,14	98,37	102,76
TM7SF3	-0,245	1,94E-02	106,30	89,77	104,10	90,06
AHNAK	-0,388	1,41E-02	101,72	77,57	93,38	81,88
THOC3	-0,528	2,78E-02	101,44	70,86	81,58	81,55
NUDT4B	-0,160	4,73E-02	92,42	82,58	90,47	93,70
FAM114A1	-0,168	4,83E-02	92,21	81,82	91,47	90,41
ELK3	-0,267	3,36E-02	91,79	76,37	93,11	78,44
FLI1	-0,212	3,98E-02	90,93	78,68	90,90	82,08
MAPK1	-0,294	1,72E-02	88,64	72,59	86,09	85,87
SULT1B1	-0,498	7,96E-03	86,27	62,34	85,35	79,53
RAB14	-0,247	2,01E-03	85,29	71,61	83,80	80,96
DLGAP5	-0,621	7,41E-06	84,10	55,05	72,73	62,97
KPNA1	-0,182	4,83E-02	80,12	70,56	80,77	79,17
TMPO	-0,320	1,16E-03	79,02	63,21	73,14	75,58
AGFG1	-0,166	3,60E-02	78,64	69,89	77,52	78,78
PRR11	-0,326	5,24E-05	74,01	58,87	71,40	62,27
ARHGAP17	-0,465	2,43E-02	71,96	53,09	76,26	67,74
PTP4A1	-0,335	2,09E-02	71,32	56,77	71,78	69,82
AKT3	-0,276	3,23E-02	71,04	58,58	66,66	64,85
STEAP1B	-0,254	3,71E-02	70,66	59,27	73,25	67,94
FCF1	-0,213	3,43E-02	69,65	59,97	67,01	66,79
PGM2	-0,220	4,75E-02	67,65	58,03	64,30	59,35
NSD2	-0,239	1,18E-02	67,24	56,91	65,10	62,85
TOP2A	-0,435	2,01E-03	67,10	49,88	58,96	54,26

GLCE	-0,244	3,37E-02	66,72	56,47	67,09	61,35
EMCN	-0,524	2,95E-03	65,39	45,79	65,19	55,42
STEAP1	-0,346	7,86E-03	65,27	51,70	64,46	60,41
CD109	-0,318	4,92E-02	63,96	51,58	63,33	60,06
PRKAR2B	-0,307	4,99E-02	62,84	50,99	58,45	55,49
MYO5A	-0,276	8,91E-03	61,34	50,76	56,95	55,68
MSMO1	-0,536	6,33E-03	61,34	42,78	64,09	49,27
CDKN3	-0,614	2,21E-07	60,40	40,00	55,86	45,06
DOCK4	-0,288	3,91E-02	56,86	46,75	51,87	53,14
NPAS2	-0,270	4,45E-02	56,84	47,48	55,26	51,55
ASAP1	-0,339	8,50E-04	56,74	45,02	56,96	51,04
CKAP2	-0,456	3,39E-04	55,75	40,66	49,92	48,53
SPTLC1P1	-0,705	1,91E-03	54,20	33,52	41,77	47,38
UBA6	-0,346	3,56E-02	52,07	41,00	44,69	50,22
HNRNPLL	-0,211	2,37E-02	51,91	44,76	50,54	49,68
TM4SF18	-0,366	1,12E-02	51,79	40,24	51,66	46,59
PIGK	-0,369	8,75E-04	51,64	40,01	46,42	47,87
NDE1	-0,219	3,10E-02	49,68	42,66	48,99	43,31
CCNA2	-0,400	5,75E-03	48,48	36,81	47,63	40,45
MYH10	-0,217	9,83E-03	48,08	41,28	50,00	46,94
WDFY3	-0,381	6,18E-03	47,37	36,63	43,32	43,83
ARHGAP11A	-0,412	1,18E-02	46,93	35,56	40,52	42,96
R3HDM1	-0,468	1,00E-03	46,32	33,74	44,19	42,73
KNSTRN	-0,257	2,04E-02	45,96	38,50	43,46	40,62
CEP55	-0,538	2,21E-04	45,55	31,76	40,39	35,62
PBK	-0,449	1,23E-02	45,20	33,75	41,98	40,13
ARL5A	-0,701	2,40E-03	42,77	27,15	36,22	42,71
SQLE	-0,304	4,39E-02	42,63	34,49	42,79	37,29
CCNYL1	-0,395	5,43E-03	42,60	32,58	42,60	38,88
DHCR7	-0,348	3,00E-02	42,48	33,78	41,52	38,78
NRG1	-0,397	8,48E-03	42,39	31,95	35,24	34,48
NUSAP1	-0,257	4,10E-02	41,51	34,85	39,71	36,20
GLRX	-0,240	5,05E-03	41,14	34,71	39,91	36,15
NUF2	-0,646	2,35E-03	39,75	25,91	35,09	30,36
INSIG1	-0,278	5,37E-03	37,34	30,79	38,85	33,24
DARS2	-0,281	4,92E-02	37,20	30,55	34,90	34,55
SMAD5	-0,472	1,88E-02	36,84	26,75	32,33	33,09
ALDH3A2	-0,186	4,27E-02	36,02	31,66	37,27	34,20
EFCAB14	-0,243	7,20E-03	35,82	30,23	34,90	34,58
LPCAT2	-0,362	5,05E-03	35,25	27,55	35,88	32,97
SULT1E1	-0,482	1,43E-02	34,24	24,97	35,22	29,34
WASHC5	-0,200	3,11E-02	34,07	29,64	32,50	32,76
HMMR	-0,747	7,92E-04	33,34	20,52	27,10	24,57
MKI67	-0,525	2,87E-05	33,20	23,00	30,42	26,99
RACGAP1	-0,327	2,97E-02	32,94	26,26	30,63	28,43
POGLUT3	-0,247	4,29E-02	32,88	27,71	32,13	32,03
HIBCH	-0,436	4,24E-03	32,79	24,29	29,19	28,38
CENPF	-0,557	7,76E-04	32,77	22,82	24,86	24,63
PPP3CA	-0,232	3,15E-02	32,64	27,74	30,29	30,65
PHACTR4	-0,233	2,36E-02	31,22	26,47	30,90	27,69
NCEH1	-0,174	3,69E-02	31,00	27,51	29,64	29,31
SAMHD1	-0,369	3,92E-02	30,58	23,65	26,32	30,88
ACER3	-0,213	9,46E-03	28,85	24,84	27,65	28,00

YAP1	-0,249	4,42E-02	28,09	23,68	27,82	24,13
RBL2	-0,287	1,74E-02	28,00	22,97	27,75	25,92
MEF2A	-0,344	4,52E-02	25,86	20,49	26,06	24,22
DIAPH3	-0,353	2,53E-03	25,40	19,87	24,43	23,94
QTRT2	-0,279	6,99E-03	23,60	19,39	23,54	22,84
MLIP	-0,301	1,12E-02	23,51	19,05	21,92	19,99
MTMR10	-0,375	4,79E-04	23,37	17,98	25,88	21,54
INCENP	-0,443	6,18E-04	23,10	17,10	21,45	22,00
MPHOSPH9	-0,464	6,44E-03	23,10	16,83	19,80	20,44
SUV39H2	-0,517	1,93E-02	23,08	16,34	20,77	22,76
DEPDC1	-0,581	3,66E-02	22,60	15,59	20,95	18,12
FEM1B	-0,299	3,20E-02	22,23	18,09	20,12	20,75
CENPA	-0,407	1,53E-03	22,03	16,54	20,40	17,89
NEK2	-0,489	1,14E-03	22,02	15,84	19,40	16,29
ASPM	-0,784	1,93E-03	21,79	12,83	18,01	15,52
HMGCR	-0,321	3,30E-03	21,56	17,27	21,49	18,02
AFF1	-0,327	5,05E-03	21,49	17,22	20,68	20,16
SPAG5	-0,278	1,44E-02	21,35	17,53	20,53	18,15
VPS8	-0,319	3,23E-02	21,08	16,88	19,50	18,19
GPSM2	-0,652	2,34E-08	20,91	13,27	19,09	15,31
NECTIN3	-0,470	4,92E-03	20,80	15,17	19,88	18,09
RMND5A	-0,187	3,74E-02	20,62	18,11	19,45	20,02
WASF3	-0,313	1,93E-06	20,17	16,22	20,19	17,88
FNBP1	-0,269	1,05E-02	19,95	16,55	20,06	18,57
AC087721.2	-0,375	1,11E-03	19,71	15,18	18,38	16,98
RNMT	-0,425	6,33E-03	18,73	14,07	17,75	17,81
DAW1	-0,338	1,90E-02	18,59	14,68	18,49	15,57
APPBP2	-0,365	3,76E-02	18,50	14,48	17,97	17,14
LATS2	-0,211	1,24E-02	18,14	15,67	17,89	16,95
HSPE1-MOB4	-0,483	1,91E-03	18,08	12,83	14,01	17,11
TNRC18	-0,235	3,23E-02	17,96	15,27	16,98	16,51
COBLL1	-0,381	1,95E-03	17,94	13,75	18,11	18,74
KIF4A	-0,318	6,88E-03	17,68	14,14	16,63	14,60
ANGEL2	-0,371	2,33E-02	16,97	13,21	16,56	15,22
MEF2C	-0,347	5,59E-03	16,44	12,92	14,48	14,42
CEP70	-0,520	1,39E-02	16,00	11,25	14,09	12,74
GAS2L3	-0,436	2,59E-02	15,94	11,94	14,95	13,15
C2CD2	-0,279	2,28E-02	15,93	13,14	16,95	14,32
PIMREG	-0,446	9,83E-03	15,83	11,56	15,40	12,08
KNL1	-0,713	6,93E-04	15,79	9,70	13,00	12,47
ZNF800	-0,353	1,45E-02	15,76	12,34	15,31	14,62
LZTFL1	-0,296	4,42E-02	15,70	12,77	15,16	14,56
WASF1	-0,307	1,77E-02	14,78	11,94	15,34	14,30
PARPBP	-0,421	4,42E-02	14,56	11,09	13,45	13,05
SGO2	-0,656	1,49E-02	14,22	9,35	12,05	10,84
DEPDC1B	-0,341	1,19E-03	13,96	11,04	13,50	12,07
SENP1	-0,270	2,11E-02	13,76	11,38	12,95	13,53
RBBP9	-0,332	8,48E-03	13,73	10,93	14,11	13,07
COMMD3-BMI1	-0,606	3,22E-02	13,41	8,90	10,52	14,74
DIS3L	-0,276	3,98E-02	13,08	10,84	12,61	11,80
OIP5	-0,352	8,05E-03	12,74	9,96	12,37	10,39
CRYBG1	-0,333	8,42E-06	12,65	10,01	11,88	11,12
MGME1	-0,250	1,42E-03	12,53	10,52	12,16	11,54

ZCCHC2	-0,507	1,42E-04	12,17	8,65	11,66	9,51
SAMD8	-0,225	4,66E-02	12,12	10,39	12,15	11,68
CENPE	-0,750	3,78E-03	12,09	7,32	8,56	8,59
APAF1	-0,294	3,35E-03	10,95	8,93	10,43	10,60
SCLT1	-0,365	4,88E-02	10,30	8,06	9,18	8,74
SGO1	-0,365	2,94E-02	10,21	7,94	9,42	8,92
SMG1P3	-0,283	1,90E-02	9,83	8,09	9,21	8,92
BORA	-0,605	1,48E-03	9,52	6,33	8,54	7,95
GPD1L	-0,209	4,48E-02	9,38	8,12	9,50	8,38
SMG1P1	-0,304	4,00E-02	9,06	7,37	8,81	8,74
AC241640.1	-1,539	1,62E-02	8,80	3,10	10,71	4,34
ZNF791	-0,512	3,90E-04	8,68	6,12	8,47	8,46
PDE3A	-0,239	2,67E-02	8,68	7,37	8,38	7,77
HIVEP1	-0,366	1,74E-02	8,05	6,25	7,82	7,46
PLAC8	-0,413	2,19E-02	7,95	5,97	7,64	5,83
DPP4	-0,347	2,35E-03	7,75	6,08	7,84	6,65
CCDC190	-0,264	4,92E-02	7,46	6,19	7,29	6,82
IL1R1	-0,282	4,65E-02	7,25	6,00	7,21	7,81
KIF14	-0,564	6,99E-03	6,75	4,64	5,68	5,25
CXADR	-0,411	5,93E-04	6,35	4,78	5,87	5,17
MAP3K5	-0,280	3,78E-02	6,08	5,00	5,82	5,62
SYNJ1	-0,312	2,94E-03	6,07	4,89	5,73	5,43
TMSB15A	-0,521	1,77E-02	5,77	4,02	5,31	4,62
SFRP1	-0,311	1,62E-02	5,72	4,60	5,47	5,14
CDK19	-0,377	2,47E-02	5,68	4,36	5,76	4,81
ZBTB21	-0,333	4,44E-02	5,66	4,49	5,06	4,70
AP000295.1	-0,791	4,42E-02	5,60	3,52	5,37	5,08
MAP2K6	-0,373	1,13E-04	5,41	4,17	4,89	4,17
SPIN2B	-0,244	4,45E-02	5,22	4,40	5,07	4,63
RAB11FIP2	-0,544	9,61E-03	5,03	3,47	4,19	4,91
PIF1	-0,318	4,39E-02	5,01	4,02	4,92	4,13
MCM9	-0,297	2,33E-02	5,00	4,07	4,95	4,26
OCLN	-0,336	2,46E-02	4,99	3,94	5,14	4,58
RSC1A1	-0,388	3,96E-02	4,95	3,84	4,36	4,90
PIK3CG	-0,918	2,74E-02	4,87	2,59	3,73	3,36
KAT2B	-0,353	4,42E-02	4,34	3,43	4,45	3,95
ARNTL	-0,285	2,61E-02	4,25	3,48	3,91	3,68
ARHGAP11B	-0,429	1,57E-02	3,88	2,91	3,64	3,51
ELMOD1	-0,476	6,64E-04	3,50	2,52	3,34	2,71
ABCA8	-0,677	2,53E-03	3,31	2,07	3,08	2,19
MMP28	-1,256	3,11E-02	2,82	1,09	1,94	2,33
MYO5C	-0,322	2,37E-02	2,76	2,20	2,83	2,46
AL109918.1	-0,486	4,80E-04	2,58	1,85	2,46	2,03
UBN2	-0,561	1,44E-02	2,39	1,62	1,92	1,96
AC079594.2	-0,631	1,73E-02	2,29	1,48	1,89	2,29
SESN3	-0,641	1,72E-02	1,87	1,23	1,74	1,40
SMIM10	-0,426	4,12E-02	1,87	1,39	1,72	1,62
NBPF10	-0,326	7,85E-03	1,84	1,46	1,61	1,56
AC087632.2	-1,660	3,23E-04	1,79	0,53	1,83	1,71
CFAP69	-0,585	1,86E-02	1,66	1,12	1,54	1,45
RMDN2	-0,550	1,13E-02	1,65	1,14	1,48	1,52
H2AC6	-0,697	6,98E-03	1,58	0,98	1,56	1,14
SELP	-0,676	3,81E-02	1,48	0,93	1,36	0,99

CLDN10	-0,387	3,36E-02	1,16	0,89	1,25	0,96
SH3TC2	-0,555	2,35E-02	0,92	0,62	0,84	0,67
AMOT	-0,550	2,22E-02	0,72	0,49	0,64	0,53
ADAMTS12	-0,546	2,74E-02	0,71	0,49	0,67	0,62
CPA4	-0,847	1,94E-02	0,66	0,37	0,50	0,41
KCNJ15	-0,746	1,39E-03	0,61	0,36	0,34	0,37
WNK3	-0,654	1,77E-02	0,60	0,38	0,54	0,48
ADAM32	-1,239	8,91E-03	0,58	0,23	0,47	0,32
LPAR1	-0,631	2,38E-02	0,52	0,34	0,55	0,37
AC139530.2	-30,000	3,86E-10	0,41	0,00	0,28	0,21
H2AC11	-0,650	1,32E-02	0,34	0,22	0,33	0,22
SLC26A4	-0,719	3,05E-02	0,34	0,21	0,33	0,22
SCUBE3	-0,411	2,69E-02	0,25	0,19	0,26	0,20
GP1BB	-22,691	1,38E-06	0,23	0,00	0,34	0,21
SPTA1	-1,154	2,10E-02	0,17	0,08	0,11	0,10
FBXO15	-1,172	2,43E-02	0,16	0,07	0,14	0,11
CMKLR1	-1,002	4,91E-02	0,13	0,07	0,10	0,07
DNM1P47	-0,477	2,40E-02	0,12	0,09	0,10	0,10

Supplementary Table S9: Genes upregulated by LPS exclusively in cells that express APEX1(1-20). To identify genes upregulated by LPS specifically in cells expressing moderate levels of APEX1(1-20), but not in cells transduced with the empty virus, the results of the DGE analysis of both cells populations after treatment with detoxified (control) or active LPS (LPS) were com-bined. The L2FC (Log 2-fold change) states the average difference in gene expression between both treatments, positive values denote upregulation by LPS treatment. Wald test from DESeq2 was used to calculate the significance of the change in the expression. The adjusted p-values take the number of tested genes into account, the threshold for the adjusted p-value was 0.05. Mean expression levels per sample group are stated in transcripts per million (TPM), calculated during quasi-mapping with the tool salmon. The list is sorted by gene expression.

gene name	L2FC	adjusted p-value	mean TPM empty virus con	mean TPM empty virus LPS	mean TPM APEX1(1-20) con	mean TPM APEX1(1-20) LPS
IL1RL1	0,254	4,90E-03	186,63	200,07	175,35	209,27
SELENOT	0,254	3,59E-03	139,92	144,17	139,26	165,99
PXDN	0,668	1,34E-08	130,73	158,35	107,72	171,11
YIPF5	0,269	4,19E-03	85,82	92,90	86,53	104,21
DPYSL3	0,257	2,43E-02	88,43	94,98	83,51	99,79
NPTN	0,193	6,51E-03	67,85	72,68	67,70	77,38
COLGALT1	0,367	8,71E-03	55,94	68,32	56,83	73,29
PLSCR1	0,208	3,55E-02	49,76	53,82	50,49	58,32
ABI3BP	0,365	1,22E-02	42,83	48,38	48,73	62,49
CLEC1A	0,182	4,06E-02	49,73	54,56	48,64	55,20
CD44	0,503	5,30E-03	54,57	62,30	47,62	68,26
TUSC3	0,294	6,19E-03	41,13	44,21	39,24	48,10
ANGPT2	0,361	8,20E-05	38,50	43,80	34,41	44,26
DUXAP9	0,284	2,13E-02	18,14	19,50	18,29	22,28
NUAK1	0,442	3,93E-02	21,46	20,17	17,49	23,93
QPCT	0,564	1,72E-03	19,62	20,56	16,30	24,34
ATAD2	0,366	2,64E-02	14,35	15,01	13,40	17,11
IFI44	0,499	1,71E-02	12,54	15,99	12,14	17,09
HPSE	0,245	6,15E-03	10,00	11,08	9,86	11,67
PRIM1	0,506	6,36E-04	12,13	12,56	9,75	13,82
AK4	0,170	2,29E-02	9,80	10,28	9,68	10,88
CHAF1A	0,466	2,83E-02	9,93	11,66	9,48	13,05
NID2	0,901	9,23E-06	12,01	15,22	8,98	16,73
LRP12	0,252	2,81E-02	8,67	9,31	8,70	10,36
RGS2	0,398	4,63E-02	9,44	10,39	8,45	11,13
ARSK	0,211	4,04E-02	8,45	8,43	8,09	9,35
GK	0,285	2,52E-02	7,60	8,71	7,35	8,95
ZFPM2	0,369	3,39E-02	7,57	8,13	6,70	8,72
IL7R	0,419	2,96E-04	6,01	6,97	5,92	7,92
CLSPN	0,378	3,55E-02	5,33	6,04	5,66	7,33
EXO1	0,511	1,98E-03	5,92	6,37	5,28	7,53
CENPBD1	0,199	3,14E-02	4,71	4,52	4,22	4,85
CREB5	0,326	5,89E-04	2,77	3,01	2,82	3,52
PDE1C	0,280	4,63E-02	2,55	3,03	2,57	3,12
DNAH11	0,366	3,50E-02	2,47	2,47	2,19	2,81
AUNIP	0,412	4,00E-02	1,93	2,39	1,88	2,50
ALDH1L2	0,311	1,70E-02	2,04	2,30	1,85	2,29
LY75-CD302	0,547	1,38E-02	2,12	1,73	1,78	2,57
CACHD1	0,277	2,91E-02	1,81	2,00	1,76	2,13
SH3BP1	0,715	6,40E-03	1,32	1,89	1,40	2,31
CHRNA1	0,426	1,79E-02	1,13	1,44	1,26	1,69
TUBB2B	0,445	4,84E-02	1,12	1,35	1,08	1,47
TCF7	0,391	1,78E-02	1,07	1,19	1,05	1,38
NLRC3	0,376	1,24E-03	0,86	1,03	0,83	1,08
ARHGEF26	0,351	4,67E-02	0,63	0,64	0,58	0,74

RASGRF2	0,347	3,88E-02	0,57	0,71	0,56	0,71
SLC6A15	0,655	1,04E-02	0,37	0,53	0,40	0,64
AMPD3	0,780	2,81E-02	0,38	0,39	0,37	0,66
SLIT3	0,552	1,16E-02	0,23	0,31	0,25	0,36
AFF3	1,033	9,24E-03	0,30	0,35	0,23	0,46
PRRT2	2,229	2,83E-02	0,18	0,23	0,17	1,00
MYPN	0,620	2,17E-02	0,11	0,15	0,09	0,14
OASL	1,044	1,05E-02	0,07	0,09	0,08	0,17
PAPPA2	1,562	1,69E-04	0,06	0,09	0,04	0,12
PLA2G5	1,414	2,80E-02	0,02	0,08	0,03	0,08
TMEM184A	1,991	6,69E-04	0,04	0,05	0,02	0,06
AC019117.4	8,471	1,17E-02	0,47	0,18	0,00	0,26
CR354443.1	32,453	1,50E-11	0,08	0,18	0,00	0,20
H3P6	30,910	1,34E-10	1,80	3,13	0,00	13,28
SRP9P1	25,646	5,29E-07	20,60	15,67	0,00	8,97
AC244260.1	8,622	1,48E-02	0,10	0,20	0,00	0,21

Supplementary Table S10: Genes downregulated by LPS exclusively in cells that express APEX1(1-20). To identify genes downregulated by LPS specifically in cells expressing moderate levels of APEX1(1-20), but not in cells transduced with the empty virus, the results of the DGE analysis of both cells populations after treatment with detoxified (con) or active LPS (LPS) were combined. The L2FC (Log 2-fold change) states the average difference in gene expression between both treatments, negative values denote downregulation by LPS treatment. Wald test from DESeq2 was used to calculate the significance of the change in the expression. The adjusted p-values take the number of tested genes into account, the threshold for the adjusted p-value was 0.05. Mean expression levels per sample group are stated in transcripts per million (TPM), calculated during quasi-mapping with the tool salmon. The list is sorted by gene expression.

gene name	L2FC	adjusted p-value	mean TPM empty virus con	mean TPM empty virus LPS	mean TPM APEX1(1-20) con	mean TPM APEX1(1-20) LPS
NQO1	-0,281	1,26E-02	511,43	442,40	520,05	427,72
PIR	-0,566	2,25E-02	239,69	198,51	259,77	176,08
IGFBP4	-0,294	1,95E-04	187,16	172,64	197,36	160,86
CLEC14A	-0,190	1,99E-02	174,69	168,66	185,74	162,74
SOX18	-0,314	1,70E-05	54,38	50,61	57,60	46,31
TCN2	-0,295	4,29E-02	35,46	32,01	35,93	29,35
BTG2	-0,190	4,93E-02	30,69	28,95	32,58	28,57
CDC25B	-0,240	3,55E-02	28,01	24,68	28,15	23,83
ATP2B4	-0,175	2,48E-02	26,61	24,37	26,48	23,44
NOS3	-0,330	1,99E-02	25,85	21,96	25,64	20,42
GIMAP8	-0,227	3,68E-02	22,98	20,67	24,54	20,96
GGT5	-0,353	3,66E-03	22,00	20,89	24,12	18,92
SHE	-0,219	3,05E-02	22,25	20,13	22,92	19,69
ENOSF1	-0,301	2,71E-02	20,15	17,83	22,46	18,19
C1orf115	-0,180	3,90E-02	20,75	19,57	20,95	18,48
GJA4	-0,568	1,75E-04	14,65	12,07	19,24	12,98
KLF2	-0,494	4,28E-07	13,78	14,54	16,08	11,40
BTD	-0,185	4,29E-02	14,47	12,87	14,48	12,75
RAMP2	-0,465	4,90E-03	11,52	10,04	14,27	10,32
GIMAP1	-0,265	1,26E-02	11,67	11,04	12,66	10,53
BCAM	-0,275	1,74E-02	11,25	10,30	11,90	9,84
ABCG2	-0,578	1,24E-03	9,23	7,10	11,11	7,46
CYP1A1	-0,508	1,91E-02	10,46	8,05	10,60	7,45
IFT122	-0,270	2,29E-02	9,27	8,45	10,30	8,58
NFIA	-0,403	3,63E-02	7,98	7,49	9,43	7,14
MXD3	-0,387	4,04E-02	7,99	6,69	8,09	6,15
TM7SF2	-0,335	3,14E-02	6,80	6,27	6,85	5,42
ZNF467	-0,453	3,40E-03	5,68	4,91	6,20	4,54
HSPB6	-0,351	2,83E-02	4,44	4,25	5,03	3,95
MRAP2	-0,384	4,81E-03	3,70	3,13	4,15	3,17
ZNF219	-0,385	2,52E-02	3,65	2,93	3,90	2,98
SPACA6	-0,405	9,24E-03	3,56	3,10	3,69	2,80
LRTOMT	-0,402	5,51E-03	2,33	2,41	3,68	2,78
ANKRD44	-0,767	3,45E-02	2,23	2,28	3,61	2,12
GPX3	-0,573	3,61E-03	2,36	2,07	3,17	2,13
ASS1	-0,446	4,39E-03	2,43	2,14	2,98	2,19
GSTM2	-0,342	2,92E-02	2,59	2,20	2,86	2,26
MAP3K14	-0,384	1,70E-02	2,62	2,14	2,78	2,13
NRROS	-0,303	9,64E-04	2,48	2,40	2,65	2,15
STC1	-0,462	2,58E-02	2,79	2,23	2,33	1,69
FAM221A	-0,310	3,55E-02	2,04	1,88	2,23	1,80
CRACR2B	-0,419	1,65E-04	1,73	1,72	1,98	1,48
PARD6A	-0,362	3,74E-02	1,79	1,69	1,86	1,44
SLCO2A1	-0,674	2,74E-02	1,48	1,32	1,82	1,15
LRRC75A	-0,393	1,30E-03	1,45	1,25	1,58	1,20

GUCY1A1	-0,911	1,65E-02	1,09	0,83	1,55	0,84
SMIM3	-0,424	6,42E-03	1,27	1,14	1,40	1,05
NTSR1	-0,347	3,46E-02	1,41	1,20	1,33	1,05
C20orf204	-0,498	1,04E-02	1,08	0,97	1,17	0,83
TCF15	-0,467	7,58E-03	1,05	0,97	1,13	0,82
LHX6	-0,471	1,15E-02	1,04	0,83	1,05	0,76
FCF1P2	-23,428	3,30E-11	1,19	1,42	1,05	0,00
AP005018.2	-23,882	3,43E-06	0,91	1,50	1,03	0,00
CCL23	-0,826	3,88E-02	0,99	0,74	1,02	0,57
COL1A2	-0,415	1,87E-03	0,77	0,64	1,01	0,76
CASKIN1	-2,314	1,30E-02	0,36	0,10	0,91	0,29
WNT9A	-0,439	2,83E-02	0,74	0,63	0,85	0,63
MATN2	-0,529	4,63E-02	0,58	0,43	0,76	0,53
DLL1	-0,370	2,69E-02	0,63	0,58	0,70	0,54
C4B	-1,377	7,99E-03	0,51	0,53	0,67	0,25
CD36	-0,760	2,93E-02	0,49	0,31	0,58	0,34
EIF3CL	-0,720	9,24E-03	0,43	0,30	0,54	0,32
FBLN2	-0,677	1,05E-02	0,44	0,32	0,51	0,32
ABCC2	-0,663	1,63E-02	0,38	0,36	0,50	0,32
CA4	-1,172	1,37E-02	0,28	0,19	0,41	0,19
EGLN3	-1,171	1,62E-03	0,31	0,25	0,38	0,17
ARL14EPL	-0,995	4,63E-02	0,29	0,23	0,38	0,19
CDH4	-0,476	1,48E-02	0,33	0,26	0,37	0,26
INHBB	-0,814	1,69E-04	0,22	0,18	0,30	0,17
CLEC3B	-1,195	2,74E-02	0,17	0,11	0,28	0,12
AC005520.3	-1,051	5,63E-03	0,25	0,19	0,26	0,14
KCNN4	-0,792	3,04E-02	0,20	0,17	0,24	0,14
ABLIM2	-1,741	7,58E-03	0,17	0,13	0,24	0,07
CAMSAP3	-0,935	1,63E-02	0,07	0,08	0,17	0,09
SYT7	-0,953	3,29E-02	0,15	0,10	0,16	0,08
TBC1D3K	-30,254	2,79E-10	0,06	0,08	0,08	0,00
RASSF10	-1,470	2,80E-02	0,03	0,02	0,06	0,02
SCNN1B	-2,117	1,78E-02	0,04	0,03	0,04	0,01
ADAMTS15	-1,383	1,02E-03	0,03	0,02	0,04	0,02
NOS1	-2,260	2,64E-02	0,00	0,00	0,02	0,00
RTN4RL1	-2,401	3,55E-02	0,01	0,01	0,01	0,00

Caffeine Inhibits Oxidative Stress- and Low Dose Endotoxemia-Induced Senescence – Role of Thioredoxin-1

Merk D*, **Greulich J***, Vierkant A, Cox F, Eckermann O, von Ameln F, Dyballa-Rukes N, Altschmied J, Ale-Agha N[#], Jakobs P[#], Haendeler J[#]

Antioxidants. 2023; 12, 1244

*gleichberechtigte Erstautoren, [#]gleichberechtigete Seniorautoren

Publikation V

Beteiligung der Autoren:

Merk D: Erstautor, war an der Planung und Durchführung der Versuche beteiligt, führte die Datenanalyse durch und war zudem am Entwurf des Manuskripts beteiligt.

Greulich J: Erstautor, war an der Planung und Durchführung der Versuche beteiligt, führte die Datenanalyse durch und war zudem am Entwurf des Manuskripts beteiligt.

Vierkant A: Führte die Seneszenzinduktionsversuche mit H_2O_2 und Koffein durch.

Cox F: Führte und Immunfluoreszenzfärbungen durch.

Eckermann O: Führte Produktion und Titration lentiviraler Partikel sowie lentivirale Transduktionen durch.

von Ameln F: Führte RNA-Isolierungen transduzierter Zellen und PCR-Analysen durch.

Dyballa-Rukes N: Führte Immunoblots durch.

Altschmied J: Konzipierte Klonierung von Expressionsvektoren, betreute lentivirale Transduktionen, erstellte Abbildungen.

Ale-Agha N: Seniorautorin, war an der Konzeption der Studie federführend beteiligt, war an der Versuchsplanung beteiligt, schrieb und finalisierte das Manuskript.

Jakobs P: Seniorautor, war an der Konzeption der Studie federführend beteiligt, schrieb und finalisierte das Manuskript.

Haendeler J: Seniorautorin, hatte die Idee zur Studie, war an der Versuchsplanung beteiligt, schrieb und finalisierte das Manuskript.

antioxidants

MDPI

Article

Caffeine Inhibits Oxidative Stress- and Low Dose Endotoxemia-Induced Senescence—Role of Thioredoxin-1

Dennis Merk [1,†], Jan Greulich [2,†], Annika Vierkant [2], Fiona Cox [1,3], Olaf Eckermann [1,2], Florian von Ameln [2], Nadine Dyballa-Rukes [1,2], Joachim Altschmied [2,4], Niloofar Ale-Agha [1,4,*], Philipp Jakobs [1,*] and Judith Haendeler [1,4,*]

[1] Cardiovascular Degeneration, Haendeler Group, Clinical Chemistry and Laboratory Diagnostics, Medical Faculty, University Hospital, Heinrich-Heine University Duesseldorf, 40225 Duesseldorf, Germany; dennis.merk@hhu.de (D.M.); fiona.cox@hhu.de (F.C.); olaf.eckermann@hhu.de (O.E.); nadine.dyballa@hhu.de (N.D.-R.)

[2] Cardiovascular Degeneration, Altschmied Group, Clinical Chemistry and Laboratory Diagnostics, Medical Faculty, University Hospital, Heinrich-Heine University Duesseldorf, 40225 Duesseldorf, Germany; jan.greulich@hhu.de (J.G.); annika.vierkant@hhu.de (A.V.); florian.ameln@hhu.de (F.v.A.); joalt001@hhu.de (J.A.)

[3] Institute for Translational Pharmacology, Medical Faculty, University Hospital, Heinrich-Heine University Duesseldorf, 40225 Duesseldorf, Germany

[4] CARID, Cardiovascular Research Institute Düsseldorf, Medical Faculty, University Hospital, Heinrich-Heine University Duesseldorf, 40225 Duesseldorf, Germany

* Correspondence: niale001@hhu.de (N.A.-A.); philipp.jakobs@hhu.de (P.J.); juhae001@hhu.de (J.H.); Tel.: +49-211-8112200 (N.A.-A.); +49-211-8112207 (P.J.); +49-211-8112008 (J.H.)

† These authors contributed equally to this work.

Abstract: The maintenance of Thioredoxin-1 (Trx-1) levels, and thus of cellular redox homeostasis, is vital for endothelial cells (ECs) to prevent senescence induction. One hallmark of EC functionality, their migratory capacity, which depends on intact mitochondria, is reduced in senescence. Caffeine improves the migratory capacity and mitochondrial functionality of ECs. However, the impact of caffeine on EC senescence has never been investigated. Moreover, a high-fat diet, which can induce EC senescence, results in approximately 1 ng/mL lipopolysaccharide (LPS) in the blood. Therefore, we investigated if low dose endotoxemia induces EC senescence and concomitantly reduces Trx-1 levels, and if caffeine prevents or even reverses senescence. We show that caffeine precludes H_2O_2-triggered senescence induction by maintaining endothelial NO synthase (eNOS) levels and preventing the elevation of p21. Notably, 1 ng/mL LPS also increases p21 levels and reduces eNOS and Trx-1 amounts. These effects are completely blocked by co-treatment with caffeine. This prevention of senescence induction is similarly accomplished by the permanent expression of mitochondrial p27, a downstream effector of caffeine. Most importantly, after senescence induction by LPS, a single bolus of caffeine inhibits the increase in p21. This treatment also blocks Trx-1 degradation, suggesting that the reversion of senescence is intimately associated with a normalized redox balance.

Keywords: caffeine; endothelial cells (EC); lipopolysaccharide; senescence; Thioredoxin-1

Citation: Merk, D.; Greulich, J.; Vierkant, A.; Cox, F.; Eckermann, O.; von Ameln, F.; Dyballa-Rukes, N.; Altschmied, J.; Ale-Agha, N.; Jakobs, P.; et al. Caffeine Inhibits Oxidative Stress- and Low Dose Endotoxemia-Induced Senescence—Role of Thioredoxin-1. *Antioxidants* **2023**, *12*, 1244. https://doi.org/10.3390/antiox12061244

Academic Editors: José Godoy and Luciana Azevedo

Received: 21 April 2023
Revised: 2 June 2023
Accepted: 6 June 2023
Published: 9 June 2023

1. Introduction

During the aging process and in a variety of diseases, there is an increase in reactive oxygen species (ROS, e.g., O_2^- and H_2O_2), which can lead to senescent endothelial cells (ECs) in humans [1]. Thioredoxin-1 (Trx-1) is a ubiquitously expressed oxidoreductase, which reduces ROS in concert with peroxiredoxins. Trx-1 also interacts with several proteins in different compartments of the cell and thereby modulates their functions [2,3]. In ECs, Trx-1 is one of the most important anti-oxidative proteins [4,5]. In a previous study, we demonstrated in an oxidative-stress-induced senescence model (using H_2O_2) that the amount of Trx-1 protein is decreased in those senescent ECs and that the levels

of the ROS-generating enzyme NADPH oxidase 4 are elevated, suggesting that disturbed redox homeostasis is linked to senescence induction. Along these lines, senescence induction could be blocked by the permanent expression of Trx-1 [6], demonstrating a causal relationship between the loss of Trx-1 and the appearance of cellular senescence.

Moreover, we were able to show that—in addition to ROS—100 mg/dL low-density lipoprotein (LDL) as well as ultrafine carbon nanoparticles also induce senescence in primary ECs [7].

One important feature of EC functionality is their ability to migrate, which is compromised in senescent ECs [7,8]. We found that the migratory capacity of ECs depends on intact mitochondria [8,9]. Moreover, short-term treatment with caffeine in concentrations up to 50 µM, which corresponds to 4–6 cups of coffee per day [9,10], improves the migratory capacity of ECs [9]. Interestingly, positive effects of caffeine in these doses were also shown in several cohort studies, in which an association was found between coffee consumption and a reduced mortality rate for several diseases affecting the cardiovascular system, most of which are associated with endothelial dysfunction. In these studies, the number of deaths from heart and respiratory diseases, stroke, and type II diabetes correlated negatively with coffee consumption, and the mortality risk was reduced by consumption of 4–6 cups a day compared to lower intake [11]. Altogether, these data suggest that caffeine could sustain EC functionality by counteracting processes leading to their dysfunction, which is a hallmark of senescent cells.

Recently, we unraveled the molecular mechanism explaining the protective role of caffeine. We demonstrated that caffeine increased the translocation of p27, a cell cycle inhibitor, into the mitochondria, leading to improved mitochondrial functionality. In p27-deficient mice, electron transport chain activity was reduced compared to their wild-type littermates and could not be improved with caffeine. This clearly demonstrated that the caffeine effects are mediated through an increase in mitochondrial p27. In addition, we found that caffeine was able to increase the functionality of mitochondria isolated from 24-month-old mice to the level of 6-month-old animals [12] and thus reverse the aging-associated functional decline of these organelles.

So far, we have shown that the maintenance of Trx-1 protein levels, and thus cellular redox homeostasis, has important beneficial effects on ECs by preventing senescence induction. Moreover, caffeine treatment results in functional improvements. However, the effects of caffeine on EC senescence have never been investigated. Furthermore, a high-fat diet has been shown to result in approximately 1 ng/mL lipopolysaccharide (LPS) in the blood [13]. Our finding that a simulated high-fat diet with elevated LDL levels induces EC senescence [7] suggests that low dose LPS might have a similar effect, although this has so far not been analyzed. Therefore, we investigated if low dose endotoxemia can induce EC senescence and concomitantly reduce Trx-1 levels, and if caffeine can counteract induction or even reverse senescence.

2. Materials and Methods

2.1. Cell Culture

Primary human ECs were supplied by LONZA (Cologne, Germany), and human embryonic kidney cells (HEK293T) were supplied by Invitrogen (Darmstadt, Germany). ECs and HEK293T were cultured as previously described [14,15]. In detail, ECs were cultured in endothelial basal medium supplemented with 50 ng/mL amphotericin B, 1 µg/mL hydrocortisone, 50 µg/mL gentamicin, 12 µg/mL bovine brain extract, 10 ng/mL epidermal growth factor (LONZA, Cologne, Germany), and 10% fetal bovine serum until the third passage was reached. Cells were grown for at least 20 h after detachment with trypsin. HEK293T cells were cultured in DMEM GlutaMAX™ (Invitrogen, Darmstadt, Germany) supplemented with 10% heat-inactivated fetal bovine serum and 1% penicillin/streptomycin.

2.2. Lentiviral Production and Transduction

VSV-G pseudotyped lentiviral particles were generated as previously described [6]. In detail, HEK293T cells were co-transfected with a transfer vector and expression vectors for the VSV-G envelope protein and lentiviral Gag/Pol, using the Calcium Phosphate Transfection Kit (Invitrogen, Darmstadt, Germany) according to the manufacturer's instructions. Viral particles containing supernatant were collected over three days, then filtered through a 0.45 µm PVDF membrane (Millipore, Burlington, MA, USA) and concentrated using Vivacell 100 ultrafiltration units with a PES membrane and a 100,000 MW cutoff (Sartorius, Goettingen, Germany). Concentrated virus particles were stored in aliquots at −80 °C. Viral titer was determined with the QuickTiter Lentivirus Titer Kit (Lentivirus-Associated HIV p24) (Cell Biolabs, San Diego, CA, USA). ECs were transduced with lentiviral expression vectors for mitochondrial p27 [12] with a multiplicity of infection of 50. The cells were washed 3 times 24 h after transduction.

2.3. Transient Transfection of ECs

Transient transfections of ECs with plasmid DNA were performed using Effectene (Qiagen, Hilden, Germany). In detail, ECs were transfected on 6 cm culture dishes with 2.5 µg plasmid DNA, 20 µL enhancer, and 25 µL Effectene in 150 µL buffer, with the subsequent addition of 1 mL cell culture medium.

2.4. Migration Assay

Migration was quantitated with a scratch wound assay, as previously described [12]. In detail, wounds were set by scraping cell monolayers with a sterile disposable rubber policeman. For that purpose, ECs were cultivated on 6 cm dishes, which were labeled with a trace line before setting the wound. After applying them to the injury, non-attached cells were removed by gentle washing with culture medium. Quantification of EC migration from the edge of the injured monolayer was performed by staining the cells with 500 ng/mL 4′,6-diamidino-2-phenylindole (DAPI) (Carl Roth, Karlsruhe, Germany) in PBS after the cells were fixed with 4% paraformaldehyde for 15 min at room temperature. Microscopic pictures were taken using an Axio Observer Z (Zeiss, Jena, Germany) using a 200× magnification. The cells which had invaded the wound from the trace line were automatically counted using the particle analysis feature of Image J 1.52a after watershed separation of overlapping nuclei.

2.5. Immunoblotting

Immunoblotting was performed as previously described [16]. In detail, cells were detached from the culture surface with a rubber policeman, centrifuged at 800× *g*, and washed twice with ice-cold PBS. After final centrifugation at 800× *g* and removal of the supernatant, cells were resuspended in radioimmunoprecipitation assay (RIPA) buffer (50 mM Tris-HCl pH 8.0, 150 mM NaCl, 1% (*v*/*v*) IGEPAL®-CA630, 0.1% (*w*/*v*) SDS, and 0.5% (*w*/*v*) Na-Deoxycholate) supplemented with 1/100 volume of a protease inhibitor cocktail and phosphatase inhibitor cocktail (Bimake, Munich, Germany) and lysed for 30 min on ice. Then, the lysates were centrifuged at 18,000× *g* and 4 °C for 15 min and the supernatant was transferred to a fresh tube. Proteins were separated by sodium dodecyl sulfate–polyacrylamide gel electrophoresis according to standard procedures. After the transfer of the proteins onto polyvinylidene difluoride membranes and blocking with 5% milk powder in TBS (200 mM Tris-HCl pH 8.0, 300 mM NaCl, and 100 mM KCl) with 0.1% (*v*/*v*) Tween-20 (TBS-T) for 1 h at room temperature, membranes were incubated with antibodies directed against GAPDH (1:50.000), Trx-1 (1:500), eNOS (1:500) (all three from Abcam, Cambridge, UK), p21 (1:500), and Src (1:1000) (both from Cell Signaling Technologies, Frankfurt, Germany). Antibodies were incubated overnight at 4 °C. The following day, membranes were washed three times with TBS-T and incubated with secondary antibodies coupled to horseradish peroxidase (ECL anti-rabbit or anti-mouse IgG, horseradish-peroxidase-linked whole antibody (from sheep) (1:5000) (Cytiva, Marlborough,

MA, USA). Detection was performed using ECL substrate (Cytiva, Marlborough, MA, USA) and X-ray films. Semi-quantitative analyses were performed on scanned X-ray films using Image J [17].

2.6. Immunostaining of ECs

Immunostaining of ECs was performed as previously described [12]. In detail, cells were fixed with 4% formaldehyde for 15 min and were blocked and permeabilized for 15 min at room temperature with 3% (*v*/*v*) normal goat serum (Sigma-Aldrich, Deisenhofen, Germany) diluted in PBS containing 0.3% (*v*/*v*) Triton X-100. Afterward, the cells were incubated with primary antibodies against a myc-tag or p21 (all from Cell Signaling Technologies, Frankfurt, Germany), each 1:100, overnight at 4 °C. The antibody against TIM23 (BD BioSciences, Heidelberg, Germany) was diluted 1:150 and incubated overnight at 4 °C. Subsequently, cells were washed three times with PBS and incubated with an Alexa Fluor® 594 coupled anti-mouse or anti-rabbit secondary antibody (1:500) (Santa Cruz Biotechnology, Heidelberg, Germany) for 1 h at room temperature. Nuclei were counterstained with DAPI (500 ng/mL) (Carl Roth, Karlsruhe, Germany) in PBS for 5 min at room temperature and the cells were mounted with ProLong™ Diamond Antifade Mountant (Invitrogen, Darmstadt, Germany). Images were taken using Zeiss microscopes (Axio Observer Z or Axio Imager M2, Zeiss, Jena, Germany) using a 400× or 200× magnification. Pixel intensities were measured with Image J [17].

2.7. Measurement of Intracellular ROS by Fluorescence Microscopy

ROS levels were quantitatively assessed using dihydroethidine (DHE) and MitoSOX™-Red, and mitochondria were co-stained with MitoTracker® Green FM (all purchased from Molecular Probes, Eugene, OR, USA). Cells were washed with endothelial basal medium and incubated with either 10 µM DHE or 5 µM MitoSOX™-Red combined with 100 nM MitoTracker® Green FM for 30 min at 37 °C. Afterward, cells were washed twice with endothelial basal medium, and images were taken with an Axio Observer Z (Zeiss, Jena, Germany) using a 200× magnification. Fluorescence intensity was calculated with Image J and normalized to the cell number.

2.8. Total Cellular RNA Isolation

Total cellular RNA was isolated as previously described [18]. In detail, TRIzol (Thermo Fisher Scientific, Dreieich, Germany) was used to extract total RNA from ECs according to the manufacturer's instructions. Further purification of RNA was achieved by using the RNeasy® Mini kit (Qiagen, Hilden, Germany) and concentrations were measured using a NanoDropTM 2000c (Thermo Fisher Scientific, Dreieich, Germany). RNA integrity and purity were analyzed by agarose gel electrophoresis.

2.9. cDNA Synthesis

cDNA was synthesized as previously described [18]. In detail, total cellular RNA was reverse transcribed using the QuantiTect Reverse Transcription kit (Qiagen, Hilden Germany) according to the manufacturer's instructions. For the verification of the expression of transgenes after lentiviral transduction, cDNA was synthesized with or, as a control for residual genomic DNA containing proviral genomes, without reverse transcriptase.

2.10. Polymerase Chain Reaction (PCR)

Endpoint PCRs were performed with MyTaq™ HS DNA Polymerase (Biocat, Heidelberg, Germany) and primers for RPL32 (hm RPL32 Ex02 for1 5′-GTGAAGCCCAAGATCGTCAA-3′ and hm RPL32 Ex03 rev1 5′-TTGTTGCACATCAGCAGCAC-3′) and mito p27 (hCDKN1B Ex01 for1 5′-GGTTAGCGGAGCAATGCG-3′ and myc-tag rev2 5′-TCCTCTTCTGAGATGA GTTTTTGTTC-3′) according to manufacturer's recommen-dations in a Bio-Rad T100 Thermal Cycler (BioRad, Feldkirchen Germany). The reaction products were visualized on standard agarose gels.

Semi-quantitative real-time PCRs were used to determine the relative transcript levels of Trx-1 with corresponding primers (hm TXN1 Ex01 for1 5′-TGGTGAAGCAGATCGAGAGC-3′ and hm TXN1 Ex03/04 rev1 5′-ACATCCTGACAGTCATCCACAT-3′), cDNA as a template, and the primaQUANT 2x qPCR SYBR-Green-MasterMix (Steinbrenner, Wiesenbach, Germany) in a Rotor-Gene Q instrument (Qiagen, Hilden, Germany). Relative expression was calculated by the ΔC_t method with RPL32 as a reference [19].

2.11. Statistics

The number of experiments (n) represents independent biological replicates. The data presented are mean ± SEM. Normal distribution was confirmed by the Shapiro–Wilk test and homogeneity of variances (from means) was verified by Levene's test. Since all data sets represented normal distribution, the multiple comparisons were performed using one-way ANOVA with the post hoc Tukey LSD test. Pairwise comparisons were performed with a paired Student's *t*-test on the raw data.

3. Results

3.1. Caffeine Prevents Stress-Induced Senescence in Endothelial Cells

In previous work, we demonstrated that stress-induced senescence of ECs entails an increase in the cell cycle inhibitor p21 and a decrease in the levels of eNOS, the enzyme constitutively producing NO to preserve the NO bioavailability and functionality of ECs. Moreover, the amount of Trx-1, which is essential for cellular redox homeostasis, was decreased and the migratory capacity of ECs was compromised. Lentiviral re-expression of Trx-1 in this model inhibited senescence induction, underscoring the importance of Trx-1 [6]. We also demonstrated that 100 mg/dL LDL induces EC senescence, reduces mitochondrial functionality, including ATP production, and impairs migration [8]. Interestingly, caffeine induces EC migration [9], enhances mitochondrial functionality in old mouse hearts, and improves the outcomes after myocardial infarction in prediabetic mice [12]. Thus, one could speculate that caffeine could be beneficial in stress-induced senescence in ECs.

To investigate the role of caffeine in stress-induced senescence in ECs, we used an established model [6]. In detail, we treated primary human ECs with 50 µM H_2O_2 and 10 µM caffeine every two days for two weeks (Figure 1A). As expected and previously published [6], H_2O_2-treatment-induced senescence in ECs was shown by an increase in p21. Interestingly, this effect was completely blocked by the co-treatment, while caffeine alone did not affect the p21 levels (Figure 1B,C,E). As a second marker of EC senescence, we investigated the levels of eNOS in this model. Repetitive treatment with H_2O_2 led to a significant decrease in eNOS protein levels, as observed previously [6]. However, the additional treatment with caffeine prevented the H_2O_2-induced loss of eNOS. As for p21, caffeine alone had no effect on eNOS protein levels (Figure 1B,D).

3.2. Caffeine Counteracts Low Dose Endotoxemia-Induced Senescence in Endothelial Cells

After having shown that caffeine is able to inhibit H_2O_2-induced senescence in ECs, we wanted to use a potentially more relevant inducer of EC senescence. In our hands, senescence could also be induced with 100 mg/dL LDL [7]. As it had been demonstrated that a high-fat diet, which leads to diabetes and insulin resistance, results in up to 1 ng/mL LPS in the blood [13], we next investigated if low dose endotoxemia can also induce senescence in ECs, and if this could be prevented with caffeine. Therefore, we treated human ECs repetitively with 1 ng/mL LPS every second day for a total of two weeks and co-incubated those cells with 10 µM caffeine (Figure 2A). As a control, we used LPS from the same *E. coli* serotype that had been partially delipidated by alkaline hydrolysis. This detoxified LPS has an endotoxin level about 10,000 times lower than the parent LPS. In this setting, we demonstrate here for the first time that 1 ng/mL LPS is able to induce a senescent phenotype in ECs, as shown by an increase in p21 (Figure 2B,C,E,F). Moreover, we found that this dose of LPS induces ROS (Supplementary Figure S1). Co-treatment with caffeine prevented this upregulation of p21 (Figure 2B,C,E,F), while caffeine alone had no effect. Next, we analyzed

whether LPS also affects eNOS levels. Repetitive low doses of LPS reduced the amount of eNOS significantly (Figure 2B,D) and this effect was inhibited by caffeine. As before, caffeine alone had no effect on eNOS protein levels. Next, we determined the levels of Trx-1 as an indicator of the cellular redox status. LPS significantly reduced the amount of Trx-1 (Figure 2G,H) comparable to the reduction shown with H_2O_2 in our previous study [6]. On the mRNA level, neither H_2O_2 nor LPS affected Trx-1 (Supplementary Figure S2), indicating that low dose endotoxemia—like oxidative stress—induces the degradation of the protein. Interestingly, co-treatment with caffeine completely restored Trx-1 protein levels (Figure 2G,H). As a functional cellular read-out, we determined the migratory capacity of ECs under this low dose endotoxemia by performing scratch wound assays. The LPS treatment dramatically reduced migration, and this detrimental effect was blocked by caffeine treatment (Figure 2I,J). We had previously shown that caffeine enhances the import of p27 into mitochondria and that the pro-migratory effect of caffeine in ECs completely depends on mitochondrial p27 [12]. Thus, it was tempting to speculate that the protective effects of caffeine in LPS-induced senescence are mediated through mitochondrial p27.

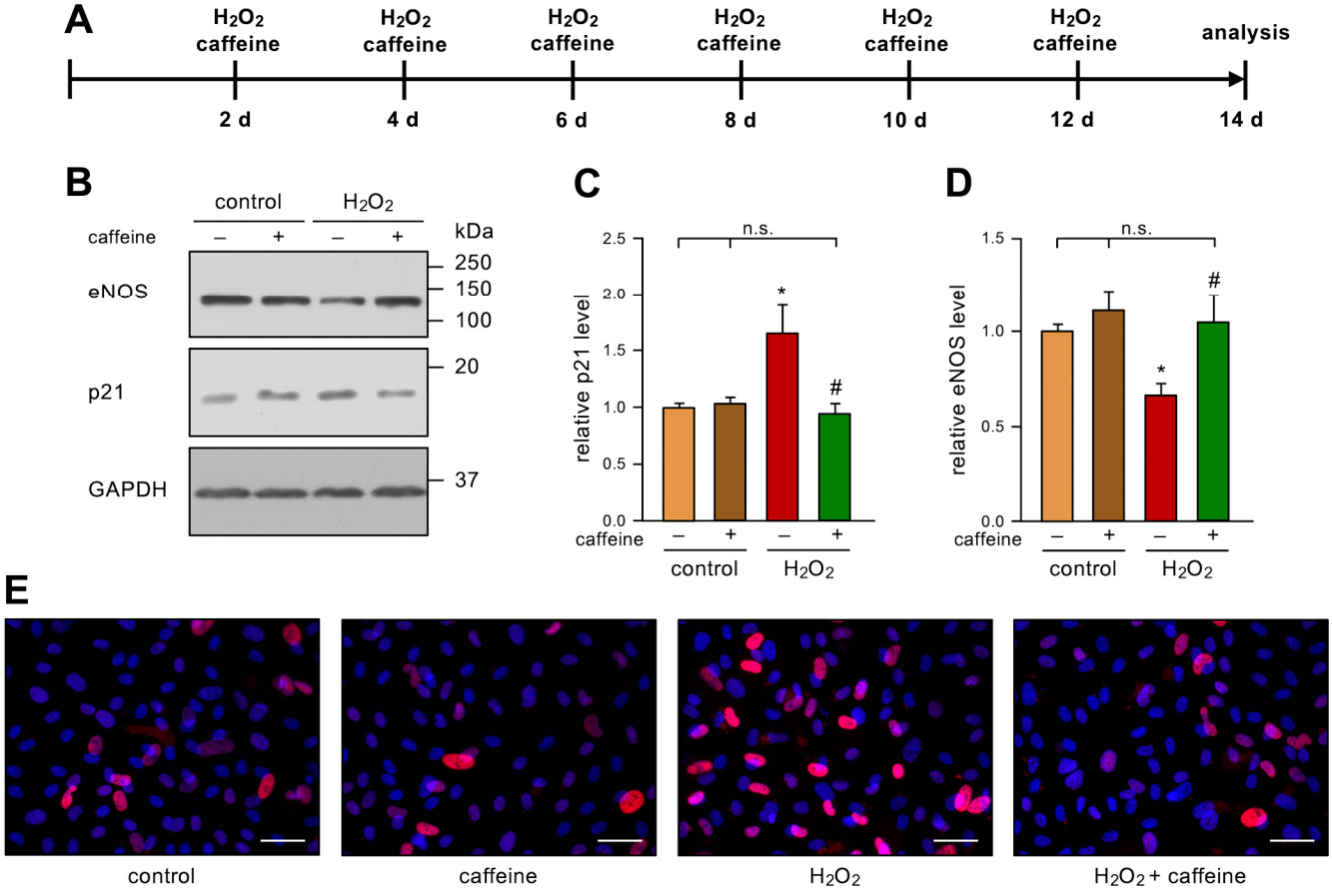

Figure 1. Caffeine prevents H_2O_2-induced senescence. (**A**–**E**) ECs were treated with 50 µM H_2O_2 and 10 µM caffeine every second day for two weeks. (**A**) Schematic representation of the treatment. (**B**–**D**) p21 and eNOS were detected by immunoblot, and GAPDH served as loading control. The untreated controls and the H_2O_2-treated group received caffeine (+) or not (−), as indicated. (**B**) Representative immunoblots for p21 (middle panel), eNOS (upper panel), and GAPDH (lower panel). (**C**,**D**) Semi-quantitative analysis of relative amounts of p21 (**C**) and eNOS (**D**) (data are mean ± SEM, n = 5, * $p < 0.05$ vs. control, $^{\#}$ $p < 0.05$ vs. H_2O_2 without caffeine, n.s. = not significant, and one-way ANOVA with post hoc Tukey LSD test). (**E**) p21 was detected by fluorescence microscopy. ECs were stained with an anti-p21 antibody (red) and nuclei were counterstained with DAPI (blue). Shown is a representative immunostaining (scale bar = 50 µm).

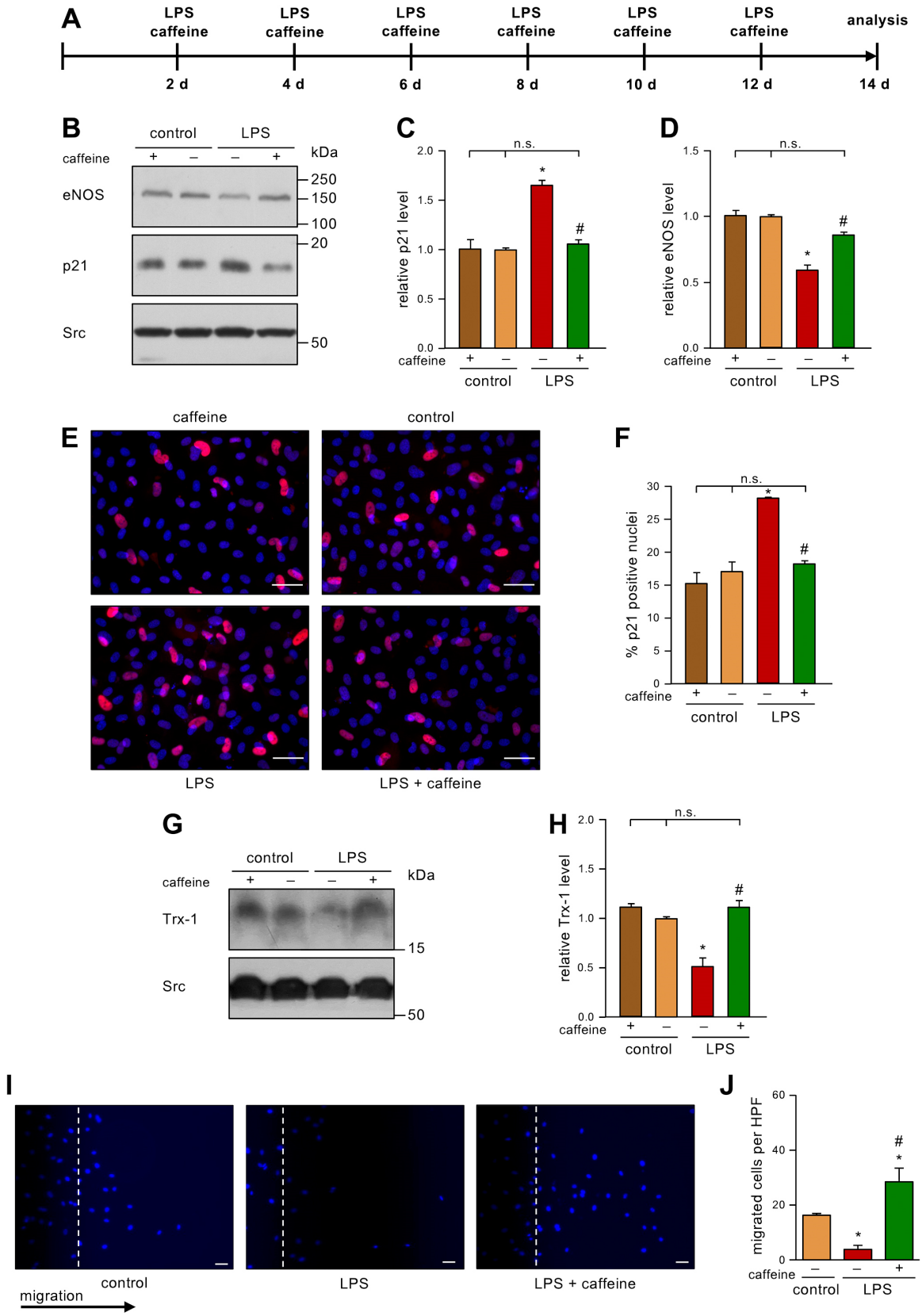

Figure 2. Caffeine counteracts LPS-induced senescence, maintains Trx-1 levels, and increases migratory capacity. (**A**–**J**) ECs were treated with 1 ng/mL detoxified (control) or active LPS (LPS) and 10 μM caffeine every second day for two weeks. (**A**) Schematic representation of the treatment. (**B**–**J**) The controls treated with detoxified LPS and the LPS-treated group received caffeine (+) or not

(−), as indicated. (**B**–**D**) p21 and eNOS were detected by immunoblot, and Src served as a loading control. (**B**) Representative immunoblots for p21 (middle panel), eNOS (upper panel), and Src (lower panel). (**C**,**D**) Semi-quantitative analysis of the relative amounts of p21 (**C**) and eNOS (**D**) (data are mean ± SEM, n = 4, *$p < 0.05$ vs. control, $^{\#}$ $p < 0.05$ vs. LPS without caffeine, n.s. = not significant, and one-way ANOVA with post hoc Tukey LSD test). (**E**,**F**) p21 was detected by fluorescence microscopy. Cells were stained with an anti-p21 antibody (red) and nuclei were counterstained with DAPI (blue). (**E**) Representative immunostainings (scale bar = 50 µm). (**F**) Image J analyses of the percentage of p21 positive nuclei (data are mean ± SEM, n = 4, * $p < 0.05$ vs. control, $^{\#}$ $p < 0.05$ vs. LPS without caffeine, n.s. = not significant, and one-way ANOVA with post hoc Tukey LSD test). (**G**,**H**) Trx-1 was detected by immunoblot and Src served as a loading control. (**G**) Representative immunoblots for Trx-1 (upper panel) and Src (lower panel). (**H**) Semi-quantitative analysis of the relative amounts of Trx-1 (data are mean ± SEM, n = 4, * $p < 0.05$ vs. control, $^{\#}$ $p < 0.05$ vs. LPS without caffeine, n.s. = not significant, and one-way ANOVA with post hoc Tukey LSD test). (**I**,**J**) Migratory capacity was detected by scratch wound assays. Cell nuclei were stained with DAPI. (**I**) Representative DAPI staining (scale bar = 50 µm). (**J**) Semi-quantitative analysis of migrated cells per high-power field (HPF) (data are mean ± SEM, n = 4, * $p < 0.05$ vs. control, $^{\#}$ $p < 0.05$ vs. LPS without caffeine, and one-way ANOVA with post hoc Tukey LSD test).

3.3. Permanent Expression of Mitochondrial p27 in Endothelial Cells Inhibits Senescence Induction by Low dose Endotoxemia

To investigate the impact of permanently elevated levels of mitochondrial p27 on LPS-induced EC senescence, we expressed mitochondrially-targeted p27 (mito p27) with a lentiviral vector [12] before repetitive treatment with LPS. After first confirming exclusive mitochondrial localization (Figure 3A), we showed that LPS treatment affected neither the transcript (Figure 3B) nor the protein levels (Figure 3C) of the lentivirally expressed mitochondrial p27. Next, we measured p21 protein levels by immunoblotting. In the control group transduced with an empty virus, the levels of p21 protein were elevated by LPS treatment. The transduction with the lentiviral mito p27 expression vector did not change p21 protein levels in cells not treated with LPS. Even more interestingly, p21 levels were not increased after repetitive LPS treatment when mitochondrial p27 levels were sustained (Figure 3D,E). Similar results were found by p21 immunostaining (Figure 3F,G). Along the same lines, Trx-1 protein levels were reduced by LPS treatment in the control group, yet transduction with a lentiviral mito p27 expression vector blocked LPS-induced Trx-1 degradation (Figure 3H,I). These data clearly demonstrate a protective effect of mitochondrial p27 as a downstream effector of caffeine in senescence induction in ECs, possibly by maintaining cellular redox homeostasis.

3.4. Caffeine Can Reverse Low dose endotoxemia-Induced Senescence in Endothelial Cells

Finally, we were interested in a therapeutic approach, to address the question of whether caffeine can reverse an already established senescent cellular phenotype. Therefore, we first induced senescence by LPS treatment as before and gave a single bolus of 50 µM caffeine after 12 days of LPS treatment (Figure 4A). This dose was chosen since we had already demonstrated that this concentration induces EC migration as a read-out for proper functionality. Moreover, 0.1% caffeine given with the drinking water resulted in a similar serum concentration in mice [9] and this regimen improved the respiratory chain activity in the heart mitochondria of 24-month-old mice to the level observed in mitochondria from 6-month-old animals [12]. As shown before, LPS treatment led to elevated p21 levels, and, interestingly, the single treatment with caffeine was sufficient to inhibit this increase in p21 (Figure 4B,C). These results were confirmed by immunostaining for p21 (Figure 4D,E). Similar to the results shown for the preventive treatment with caffeine (Figure 2G,H), the single treatment with caffeine blocked Trx-1 degradation induced by LPS (Figure 4F,G), suggesting that the reversion of senescence is intimately associated with a normalized redox balance.

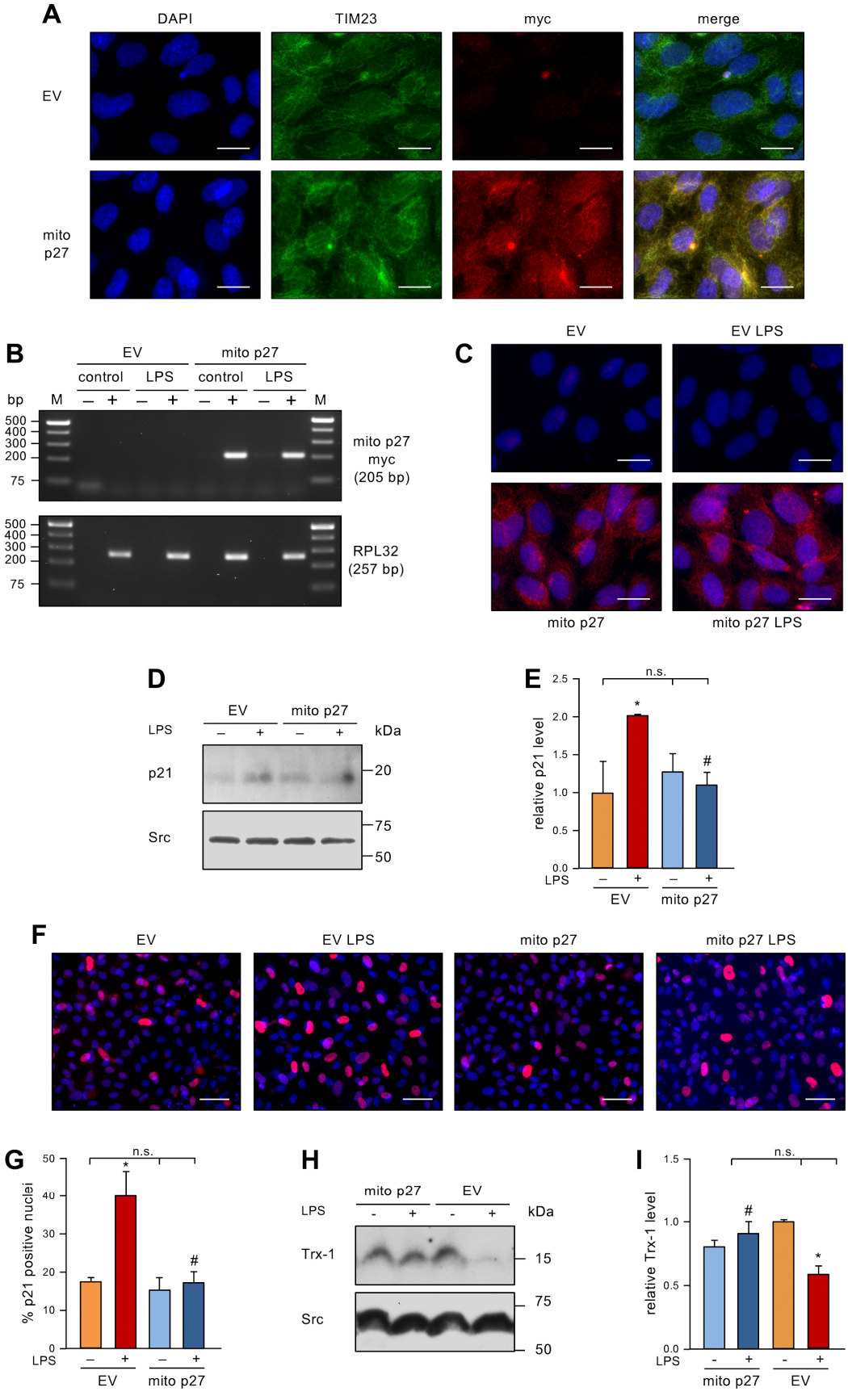

Figure 3. Mitochondrial p27 counteracts LPS-induced senescence and maintains Trx-1 levels. (**A**) ECs were transduced with a lentiviral expression vector for mitochondrially targeted p27 with a C-terminal

myc epitope tag (mito p27) or a corresponding empty virus (EV) and after two weeks localization of mito p27 was examined by fluorescence microscopy. ECs were stained with antibodies directed against the myc-tag on mito p27 (red) and the translocase of inner mitochondrial membrane 23 (TIM23, green), and the nuclei were counterstained with DAPI (blue); shown are representative immunostainings (scale bar = 20 μm). (**B**–**I**) ECs were transduced with a lentiviral expression vector for mitochondrially targeted p27 with a C-terminal myc epitope tag (mito p27) or a corresponding empty virus (EV) and subsequently treated with 1 ng/mL detoxified (control/−) or active LPS (LPS/+) every second day for two weeks. (**B**) Expression of mito p27 was analyzed by reverse transcription polymerase chain reaction. For that purpose, RNA was isolated from the transduced cells, and cDNA was synthesized in the presence (+) or absence (−) of reverse transcriptase. Amplification was performed with primers specifically detecting the mito p27 myc transcript, while the housekeeping gene RPL32 served as control. Amplification products were resolved by agarose gel electrophoresis; the expected fragment sizes are specified, and the numbers on the left indicate DNA size markers (M). (**C**–**E**) p21 was detected by immunoblot and immunostaining. (**C**) ECs were stained with an anti-myc antibody (red), and nuclei were counterstained with DAPI (blue); shown are representative immunostainings (scale bar = 20 μm). (**D**,**E**) p21 was detected by immunoblot and Src served as a loading control. (**D**) Representative immunoblots for p21 (upper panel) and Src (lower panel). (**E**) Semi-quantitative analysis of relative amounts of p21 (data are mean ± SEM, n = 3, * $p < 0.05$ vs. EV without LPS, $^{\#}$ $p < 0.05$ vs. EV + LPS, n.s. = not significant, and one-way ANOVA with post hoc Tukey LSD test). (**F**,**G**) p21 was detected by immunostaining and fluorescence microscopy. Cells were stained with an anti-p21 antibody (red), and nuclei were counterstained with DAPI (blue). (**F**) Representative immunostainings (scale bar = 50 μm). (**G**) Image J analyses of the percentage of p21 positive nuclei (data are mean ± SEM, n = 3, * $p < 0.05$ vs. EV without LPS, $^{\#}$ $p < 0.05$ vs. EV + LPS, n.s. = not significant, and one-way ANOVA with post hoc Tukey LSD test). (**H**,**I**) Trx-1 was detected by immunoblot and Src served as a loading control. (**H**) Representative immunoblots for Trx-1 (upper panel) and Src (lower panel). (**I**) Semi-quantitative analysis of the relative amounts of Trx-1 (data are mean ± SEM, n = 3, * $p < 0.05$ vs. EV without LPS, $^{\#}$ $p < 0.05$ vs. EV + LPS, n.s. = not significant, and one-way ANOVA with post hoc Tukey LSD test).

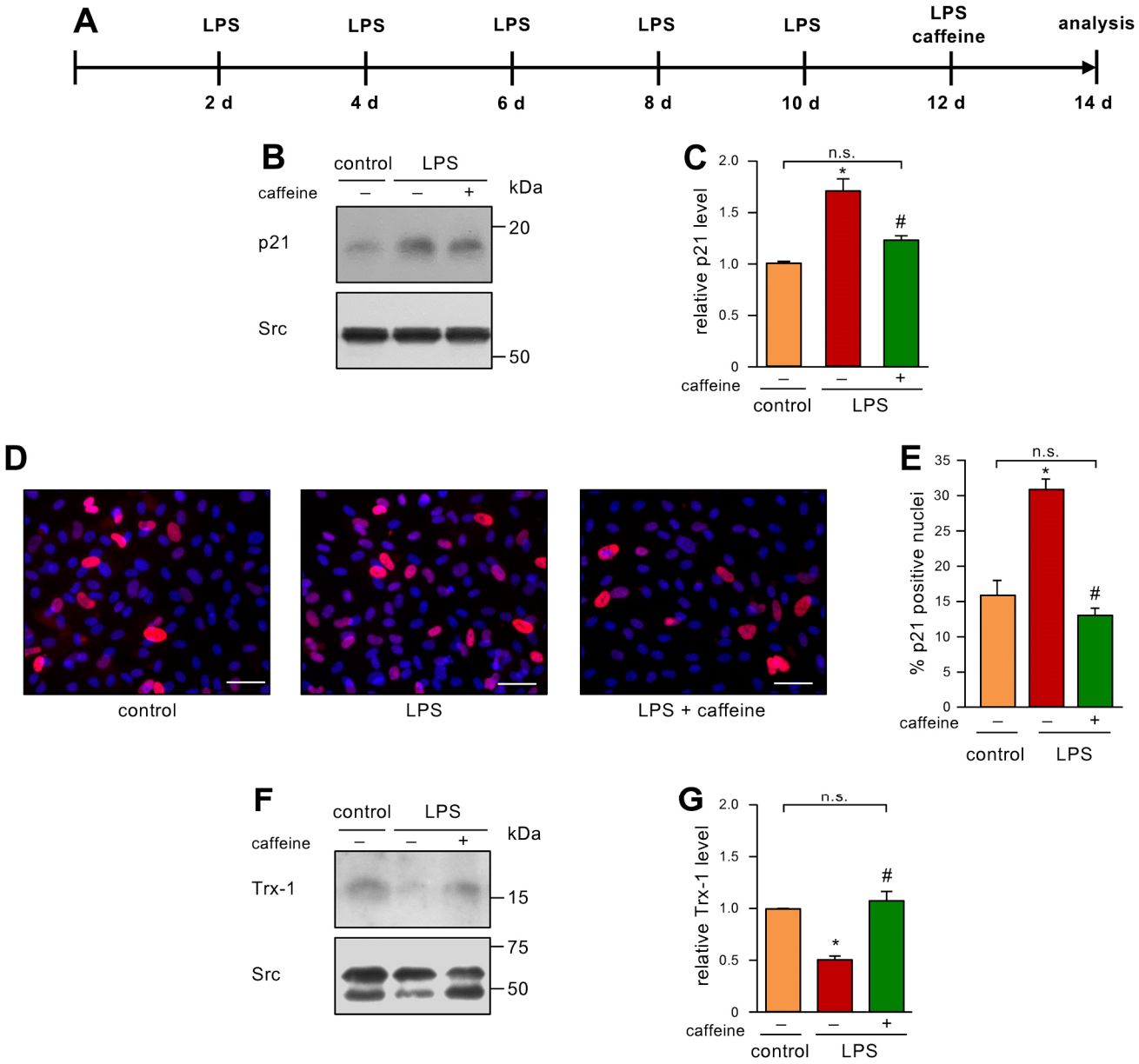

Figure 4. A single caffeine bolus reverses LPS-induced senescence and restores Trx-1 levels. (**A**–**G**) ECs were treated with 1 ng/mL detoxified (control) or active LPS (LPS) every second day for two weeks with a single bolus of 50 µM caffeine on the last treatment day. (**A**) Schematic representation of the treatment. (**B**–**G**) The LPS-treated group received caffeine (+) or not (−), as indicated. (**B**,**C**) p21 was detected by immunoblot and Src served as a loading control. (**B**) Representative immunoblots for p21 (upper panel) and Src (lower panel). (**C**) Semi-quantitative analysis of relative amounts of p21 (data are mean ± SEM, n = 5, * $p < 0.05$ vs. control, $^{\#}$ $p < 0.05$ vs. LPS without caffeine, n.s. = not significant, and one-way ANOVA with post hoc Tukey LSD test). (**D**,**E**) p21 was detected by immunostaining and fluorescence microscopy. Cells were stained with an anti-p21 antibody (red), and nuclei were counterstained with DAPI (blue). (**D**) Representative immunostainings (scale bar = 50 µm). (**E**) Image J analyses of the percentage of p21 positive nuclei (data are mean ± SEM, n = 4, * $p < 0.05$ vs. control, $^{\#}$ $p < 0.05$ vs. LPS without caffeine, n.s. = not significant, and one-way ANOVA with post hoc Tukey LSD test). (**F**,**G**) Trx-1 was detected by immunoblot and Src served as a loading control. (**F**) Representative immunoblots for Trx-1 (upper panel) and Src (lower panel). (**G**) Semi-quantitative analysis of relative amounts of Trx-1 (data are mean ± SEM, n = 4, * $p < 0.05$ vs. control, $^{\#}$ $p < 0.05$ vs. LPS without caffeine, n.s. = not significant, and one-way ANOVA with post hoc Tukey LSD test).

4. Discussion

The major findings of the present study are the prevention and, even more importantly, the reversion of low dose endotoxemia-induced EC senescence by caffeine. Here we show for the first time that caffeine precludes senescence in ECs by preventing the loss of Trx-1 and eNOS, proteins vital for cellular redox homeostasis and NO bioavailability, respectively, and thereby, for the proper functionality of ECs. Moreover, we established a model for senescence induction by repetitive treatment with LPS in a low concentration. Indeed, in this low dose endotoxemia model, co-incubation with caffeine prevented the occurrence of senescence. Even more important, in a therapeutic setting, a single bolus of caffeine given on day 12 of senescence induction by LPS reversed senescence and the loss of Trx-1 protein.

Our data demonstrate that treatment of primary human ECs with 1 ng/mL LPS results in the onset of senescence and loss of EC functionality. This LPS concentration was chosen as several studies in mice and humans demonstrated that a high-fat diet leads to an increase in LPS levels in the blood. In mice, feeding a high-fat diet for 4 weeks increased the plasma LPS concentrations up to three times to a concentration of approximately 1.2 ng/mL [13]. Similarly, in healthy humans, a high fat, high carbohydrate meal resulted in elevated LPS levels in the blood when compared with humans consuming a high fiber and fruit meal [20]. The consumption of Western-type calorie rich diets combined with chronic overnutrition and a sedentary lifestyle represents a rising public health problem, as this often results in, for instance, type 2 diabetes and atherosclerosis. Given the fact that a high-fat diet leads to low dose endotoxemia, it is tempting to speculate that the senescent ECs found in human atherosclerotic plaques [1] are induced by increased LPS in the blood, as our findings here demonstrate that this low dose endotoxemia induces senescence in human ECs.

Senescence and aging are associated with mitochondrial dysfunction [21]. Here, we show that low dose endotoxemia reduces the migratory capacity of ECs. As previous studies demonstrated that the migration of ECs depends on intact mitochondria [9] and functional oxidative phosphorylation [8], one could assume that LPS treatment impairs electron transport chain activity and, thereby, diminishes migratory capacity. This would be in line with the findings of Deshpande et al. demonstrating that induction of senescence by constitutive active Rac1 results in increased mitochondrial ROS and decreased electron transport chain activity in ECs [22]. Similarly, we demonstrated that treatment of ECs with 100 mg/dL LDL results in senescence induction [7] and in a loss of mitochondrial ATP production [8]. Thus, mitochondrial functionality and EC senescence are intimately interwoven. Therefore, a substance that improves mitochondrial functions and, thus, endothelial functionality would be of great interest to prevent or delay endothelial dysfunction.

We have shown that caffeine in serum concentrations, which are reached after consumption of 4–6 cups of coffee, increases the migratory capacity of human ECs [9,10]. A few years ago, we unraveled the mechanisms underlying the promigratory effect of caffeine. We demonstrated that caffeine induces the translocation of p27 into the mitochondria and that the migratory capacity of ECs—also after stimulation with caffeine—is completely dependent on mitochondrial p27. Caffeine in the drinking water improved the respiratory chain activity in the hearts of wild-type mice, but not in p27-deficient littermates. More importantly, caffeine was able to increase the electron transport chain activity in the hearts of 24-month-old animals to the levels measured in adult, 6-month-old mice, suggesting an anti-aging effect of caffeine [12]. Here, we demonstrate that caffeine indeed inhibits senescence induction in ECs, possibly by improving mitochondrial functionality as the permanent expression of mitochondrially targeted p27 had the same effect. Caffeine also counteracted the loss of Trx-1 and, moreover, even when given in a therapeutic setting, i.e., after senescence induction by LPS, restored Trx-1 levels.

Since the maintenance of Trx-1 protein levels is important for preserving redox homeostasis as well as the ability to store NO in ECs, it is interesting to note that H_2O_2- as well as low dose LPS-induced senescence lead to the degradation of Trx-1 and increase in ROS ([6] and Supplementary Figure S1, respectively). Thus, one has to assume that disturbed redox homeostasis is a hallmark of senescence induction in ECs and thus, of

endothelial dysfunction. Since caffeine is able to restore Trx-1 levels and inhibit senescence, it would be interesting to understand how caffeine is capable of doing so. The loss of Trx-1 in senescent ECs goes along with the elevated activity of cathepsin D [6], the major lysosomal protease, which is responsible for Trx-1 degradation [23,24]. As it is known that mitochondrial respiration controls lysosomal function and that impairment of respiration leads to an increase in the lysosomal compartment [25], it is tempting to speculate that caffeine reduces lysosomal activity. This is beyond the scope of this study but will be investigated in the future. However, it has to be noted that low dose endotoxemia, but also the treatment of ECs with 150 ng/mL LPS for 24 h does not change Trx-1 mRNA levels (Supplementary Figure S2 and [18]). Those data suggest that it is not the downregulation of Trx-1 expression, but rather enhanced degradation that leads to the decrease in Trx-1 levels in senescent ECs. Having shown that treatment with low dose LPS led to a degradation of Trx-1, and that caffeine, which improves mitochondrial functionality [12], counteracts Trx-1 degradation, it would be interesting to investigate if LPS and caffeine have similar effects on Thioredoxin-2, the mitochondrial Thioredoxin, in a future study.

5. Conclusions

In conclusions, the observation that caffeine interferes with senescence induction in ECs, which would lead to endothelial dysfunction that is observed in nearly all cardiovascular diseases [26], might at least partially explain the beneficial effects of moderate coffee consumption on mortality risk in elderly people [11,27].

Supplementary Materials: The following supporting information can be downloaded at: https://www.mdpi.com/article/10.3390/antiox12061244/s1, Figure S1: Low dose endotoxemia increases ROS levels; Figure S2: Senescence induction does not change the Trx-1 transcript level.

Author Contributions: Conceptualization, D.M., N.A.-A., P.J., and J.H.; formal analysis, D.M., A.V., F.C., O.E., F.v.A., and N.D.-R.; investigation, J.G. and J.H.; methodology, J.G., F.C., O.E., and F.v.A.; software, F.v.A.; supervision, J.H.; validation, O.E., J.A., N.A.-A., and J.H.; writing—original draft, J.A., P.J., and J.H. All authors have read and agreed to the published version of the manuscript.

Funding: This study was in part funded by the Deutsche Forschungsgemeinschaft (DFG), IRTG1902-2 to J.A. and J.H.; D.M., J.G. and A.V. are stipend holders of IRTG1902-2. This study was also in part funded by Bayer Grant4Target (2019-08-2427) to J.H. and by intramural funding (9772727) of the University Hospital of the Heinrich-Heine University to J.H.

Institutional Review Board Statement: Not applicable.

Informed Consent Statement: Not applicable.

Data Availability Statement: Data are contained within the article. All further information will be provided by the corresponding authors upon request.

Conflicts of Interest: The authors declare no conflict of interest. The funders had no role in the design of the study; in the collection, analyses, or interpretation of data; in the writing of the manuscript; or in the decision to publish the results.

References

1. Minamino, T.; Miyauchi, H.; Yoshida, T.; Ishida, Y.; Yoshida, H.; Komuro, I. Endothelial cell senescence in human atherosclerosis: Role of telomere in endothelial dysfunction. *Circulation* **2002**, *105*, 1541–1544. [CrossRef] [PubMed]
2. Holmgren, A. Antioxidant function of thioredoxin and glutaredoxin systems. *Antioxid. Redox Signal.* **2000**, *2*, 811–820. [CrossRef]
3. Zschauer, T.C.; Matsushima, S.; Altschmied, J.; Shao, D.; Sadoshima, J.; Haendeler, J. Interacting with thioredoxin-1--disease or no disease? *Antioxid. Redox Signal.* **2013**, *18*, 1053–1062. [CrossRef]
4. Altschmied, J.; Haendeler, J. Thioredoxin-1 and endothelial cell aging: Role in cardiovascular diseases. *Antioxid. Redox Signal.* **2009**, *11*, 1733–1740. [CrossRef]
5. Haendeler, J. Thioredoxin-1 and posttranslational modifications. *Antioxid. Redox Signal.* **2006**, *8*, 1723–1728. [CrossRef]
6. Goy, C.; Czypiorski, P.; Altschmied, J.; Jakob, S.; Rabanter, L.L.; Brewer, A.C.; Ale-Agha, N.; Dyballa-Rukes, N.; Shah, A.M.; Haendeler, J. The imbalanced redox status in senescent endothelial cells is due to dysregulated Thioredoxin-1 and NADPH oxidase 4. *Exp. Gerontol.* **2014**, *56*, 45–52. [CrossRef]

7. Buchner, N.; Ale-Agha, N.; Jakob, S.; Sydlik, U.; Kunze, K.; Unfried, K.; Altschmied, J.; Haendeler, J. Unhealthy diet and ultrafine carbon black particles induce senescence and disease associated phenotypic changes. *Exp. Gerontol.* **2013**, *48*, 8–16. [CrossRef]
8. Gonnissen, S.; Ptok, J.; Goy, C.; Jander, K.; Jakobs, P.; Eckermann, O.; Kaisers, W.; von Ameln, F.; Timm, J.; Ale-Agha, N.; et al. High Concentration of Low-Density Lipoprotein Results in Disturbances in Mitochondrial Transcription and Functionality in Endothelial Cells. *Oxid. Med. Cell Longev.* **2019**, *2019*, 7976382. [CrossRef]
9. Spyridopoulos, I.; Fichtlscherer, S.; Popp, R.; Toennes, S.W.; Fisslthaler, B.; Trepels, T.; Zernecke, A.; Liehn, E.A.; Weber, C.; Zeiher, A.M.; et al. Caffeine enhances endothelial repair by an AMPK-dependent mechanism. *Arter. Thromb. Vasc. Biol.* **2008**, *28*, 1967–1974. [CrossRef] [PubMed]
10. Ohmichi, T.; Kasai, T.; Shinomoto, M.; Matsuura, J.; Koizumi, T.; Kitani-Morii, F.; Tatebe, H.; Sasaki, H.; Mizuno, T.; Tokuda, T. Quantification of Blood Caffeine Levels in Patients With Parkinson's Disease and Multiple System Atrophy by Caffeine ELISA. *Front. Neurol.* **2020**, *11*, 580127. [CrossRef] [PubMed]
11. Freedman, N.D.; Park, Y.; Abnet, C.C.; Hollenbeck, A.R.; Sinha, R. Association of coffee drinking with total and cause-specific mortality. *N Engl. J. Med.* **2012**, *366*, 1891–1904. [CrossRef]
12. Ale-Agha, N.; Goy, C.; Jakobs, P.; Spyridopoulos, I.; Gonnissen, S.; Dyballa-Rukes, N.; Aufenvenne, K.; von Ameln, F.; Zurek, M.; Spannbrucker, T.; et al. CDKN1B/p27 is localized in mitochondria and improves respiration-dependent processes in the cardiovascular system-New mode of action for caffeine. *PLoS Biol.* **2018**, *16*, e2004408. [CrossRef]
13. Cani, P.D.; Amar, J.; Iglesias, M.A.; Poggi, M.; Knauf, C.; Bastelica, D.; Neyrinck, A.M.; Fava, F.; Tuohy, K.M.; Chabo, C.; et al. Metabolic endotoxemia initiates obesity and insulin resistance. *Diabetes* **2007**, *56*, 1761–1772. [CrossRef] [PubMed]
14. Haendeler, J.; Hoffmann, J.; Tischler, V.; Berk, B.C.; Zeiher, A.M.; Dimmeler, S. Redox regulatory and anti-apoptotic functions of thioredoxin depend on S-nitrosylation at cysteine 69. *Nat. Cell Biol.* **2002**, *4*, 743–749. [CrossRef]
15. Jakob, S.; Schroeder, P.; Lukosz, M.; Buchner, N.; Spyridopoulos, I.; Altschmied, J.; Haendeler, J. Nuclear protein tyrosine phosphatase Shp-2 is one important negative regulator of nuclear export of telomerase reverse transcriptase. *J. Biol. Chem.* **2008**, *283*, 33155–33161. [CrossRef] [PubMed]
16. Jander, K.; Greulich, J.; Gonnissen, S.; Ale-Agha, N.; Goy, C.; Jakobs, P.; Farrokh, S.; Marziano, C.; Sonkusare, S.K.; Haendeler, J.; et al. Extra-Nuclear Functions of the Transcription Factor Grainyhead-Like 3 in the Endothelium-Interaction with Endothelial Nitric Oxide Synthase. *Antioxidants* **2021**, *10*, 428. [CrossRef] [PubMed]
17. Schindelin, J.; Arganda-Carreras, I.; Frise, E.; Kaynig, V.; Longair, M.; Pietzsch, T.; Preibisch, S.; Rueden, C.; Saalfeld, S.; Schmid, B.; et al. Fiji: An open-source platform for biological-image analysis. *Nat. Methods* **2012**, *9*, 676–682. [CrossRef] [PubMed]
18. Merk, D.; Ptok, J.; Jakobs, P.; von Ameln, F.; Greulich, J.; Kluge, P.; Semperowitsch, K.; Eckermann, O.; Schaal, H.; Ale-Agha, N.; et al. Selenoprotein T Protects Endothelial Cells against Lipopolysaccharide-Induced Activation and Apoptosis. *Antioxidants* **2021**, *10*, 1427. [CrossRef]
19. Pfaffl, M.W. A new mathematical model for relative quantification in real-time RT-PCR. *Nucleic. Acids Res.* **2001**, *29*, e45. [CrossRef]
20. Ghanim, H.; Abuaysheh, S.; Sia, C.L.; Korzeniewski, K.; Chaudhuri, A.; Fernandez-Real, J.M.; Dandona, P. Increase in plasma endotoxin concentrations and the expression of Toll-like receptors and suppressor of cytokine signaling-3 in mononuclear cells after a high-fat, high-carbohydrate meal: Implications for insulin resistance. *Diabetes Care* **2009**, *32*, 2281–2287. [CrossRef]
21. Lopez-Otin, C.; Blasco, M.A.; Partridge, L.; Serrano, M.; Kroemer, G. The hallmarks of aging. *Cell* **2013**, *153*, 1194–1217. [CrossRef] [PubMed]
22. Deshpande, S.S.; Qi, B.; Park, Y.C.; Irani, K. Constitutive activation of rac1 results in mitochondrial oxidative stress and induces premature endothelial cell senescence. *Arterioscler. Thromb. Vasc. Biol.* **2003**, *23*, e1–e6. [CrossRef] [PubMed]
23. Dyballa-Rukes, N.; Jakobs, P.; Eckers, A.; Ale-Agha, N.; Serbulea, V.; Aufenvenne, K.; Zschauer, T.C.; Rabanter, L.L.; Jakob, S.; von Ameln, F.; et al. The Anti-Apoptotic Properties of APEX1 in the Endothelium Require the First 20 Amino Acids and Converge on Thioredoxin-1. *Antioxid. Redox Signal.* **2017**, *26*, 616–629. [CrossRef] [PubMed]
24. Haendeler, J.; Popp, R.; Goy, C.; Tischler, V.; Zeiher, A.M.; Dimmeler, S. Cathepsin D and H_2O_2 stimulate degradation of thioredoxin-1: Implication for endothelial cell apoptosis. *J. Biol. Chem.* **2005**, *280*, 42945–42951. [CrossRef]
25. Baixauli, F.; Acin-Perez, R.; Villarroya-Beltri, C.; Mazzeo, C.; Nunez-Andrade, N.; Gabande-Rodriguez, E.; Ledesma, M.D.; Blazquez, A.; Martin, M.A.; Falcon-Perez, J.M.; et al. Mitochondrial Respiration Controls Lysosomal Function during Inflammatory T Cell Responses. *Cell Metab.* **2015**, *22*, 485–498. [CrossRef]
26. Cai, H.; Harrison, D.G. Endothelial dysfunction in cardiovascular diseases: The role of oxidant stress. *Circ Res* **2000**, *87*, 840–844. [CrossRef]
27. Greenberg, J.A.; Chow, G.; Ziegelstein, R.C. Caffeinated coffee consumption, cardiovascular disease, and heart valve disease in the elderly (from the Framingham Study). *Am. J. Cardiol.* **2008**, *102*, 1502–1508. [CrossRef]

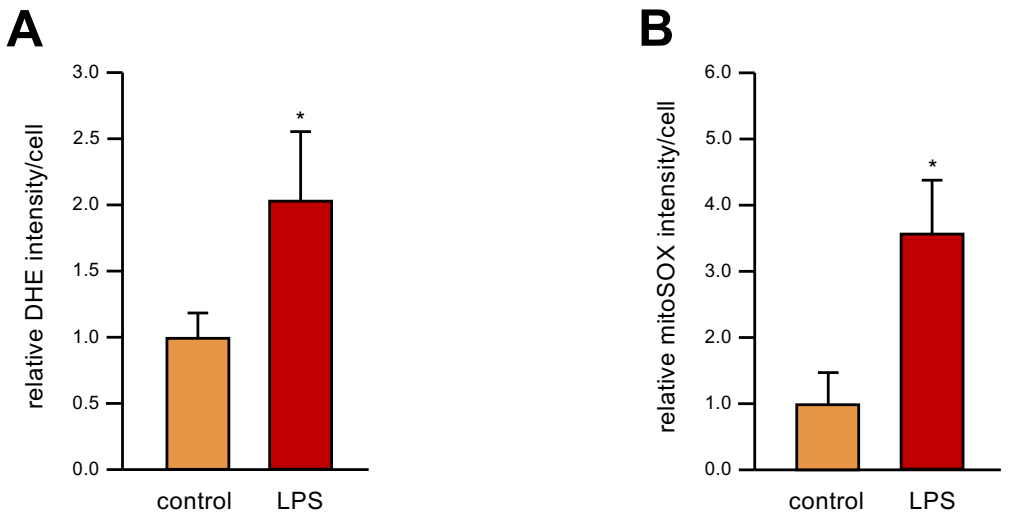

Supplementary figure S1: Low dose endotoxemia increases ROS levels. EC were treated with 1 ng/mL detoxified (control) or active LPS (LPS) every second day for two weeks. Rela-tive DHE (A) or mitoSOX (B) intensities were analyzed by Image J using total cell count for normalization (data are mean ± SEM, n = 3, *p < 0.05 vs control, two sided paired t-Test).

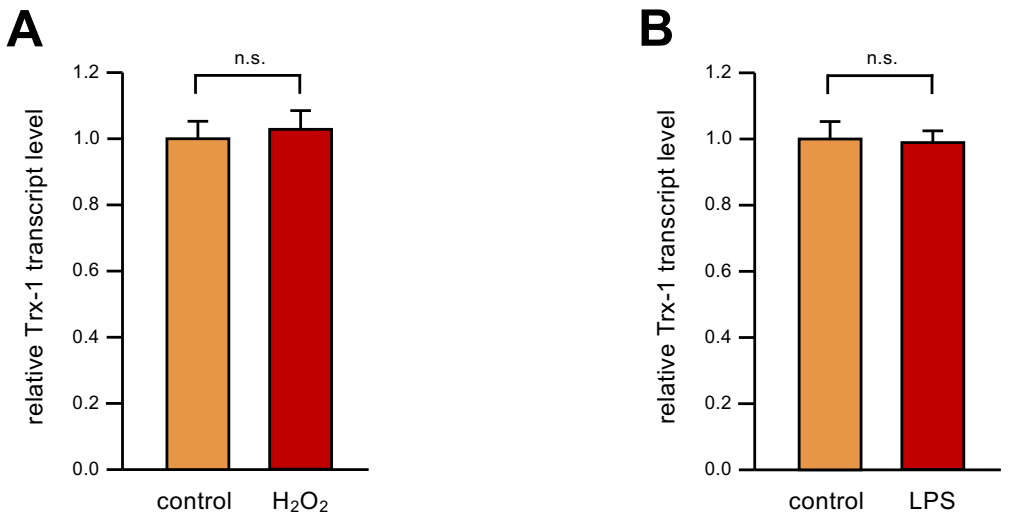

Supplementary figure S 2: Senescence induction does not change the Trx-1 transcript level. (A) EC were treated with 50 µM H_2O_2 every day for two weeks or left untreated (control). (B) In a low dose endotoxemia model, EC were treated with 1 ng/mL detoxified (control) or active LPS (LPS) every second day for two weeks. (A, B) Trx-1 transcript levels were ana-lyzed by semi-quantitative real-time PCR using RPL32 for normalization (data are mean ± SEM, n = 6, n.s. = not significant, two sided paired t-Test).

Extra-Nuclear Functions of the Transcription Factor Grainyhead-Like 3 in the Endothelium-Interaction with Endothelial Nitric Oxide Synthase

Jander K*, **Greulich J***, Gonnissen S*, Ale-Agha N, Goy C, Jakobs P, Farrokh S, Marziano C, Sonkusare SK, Haendeler J#, Altschmied J#

Antioxidants. 2021; 10, 428

*gleichberechtigte Erstautoren, #gleichberechtigete Seniorautoren

Publikation VI

Beteiligung der Autoren:

Jander K: Erstautorin, war an der Planung und Durchführung der Versuche beteiligt, führte die Datenanalyse durch und war zudem am Entwurf des Manuskripts beteiligt. Führte die *en face* Färbungen zusammen mit Frau Marziano durch.

Greulich J: Erstautor, war an der Planung und Durchführung der Versuche beteiligt, führte die Datenanalyse durch und war zudem am Entwurf des Manuskripts beteiligt.

Gonnissen S: Erstautorin, war an der Planung und Durchführung der Versuche beteiligt, führte die Datenanalyse durch und war zudem am Entwurf des Manuskripts beteiligt.

Ale-Agha N: Führte Immunfluoreszenzfärbungen durch.

Goy C: Führte Griess assays durch.

Jakobs P: Führte Immunoblots und Migrationsversuche durch.

Farrokh S: Generierte Expressionsvektoren für GRHL3 Deletionsmutanten.

Marziano C: Führte die *en face* Färbungen zusammen mit Frau Jander durch.

Sonkusare SK: Konzipierte und betreute die *en face* Färbungen; erstellte Videoanimationen.

Haendeler J: Seniorautor, war an der Konzeption der Studie federführend beteiligt, war an der Versuchsplanung beteiligt, schrieb und finalisierte das Manuskript.

Altschmied J: Seniorautor, konzipierte die Studie, war an der Versuchsplanung beteiligt, schrieb und finalisierte das Manuskript.

antioxidants

Article

Extra-Nuclear Functions of the Transcription Factor Grainyhead-Like 3 in the Endothelium—Interaction with Endothelial Nitric Oxide Synthase

Kirsten Jander [1,2,†], Jan Greulich [1,†], Stefanie Gonnissen [1,†], Niloofar Ale-Agha [2], Christine Goy [1], Philipp Jakobs [2], Sabrina Farrokh [1], Corina Marziano [3], Swapnil K. Sonkusare [3], Judith Haendeler [2,*] and Joachim Altschmied [1,2,*]

1 IUF-Leibniz Research Institute for Environmental Medicine, 40225 Düsseldorf, Germany; kirsten.jander89@gmx.de (K.J.); jan.greulich@hhu.de (J.G.); stefanie@gonnissen.de (S.G.); christinegoy100@posteo.eu (C.G.); sabrina.farrokh@googlemail.com (S.F.)
2 Environmentally-Induced Cardiovascular Degeneration, Clinical Chemistry and Laboratory Diagnostics, Medical Faculty, University Clinics, Heinrich-Heine-University, 40225 Düsseldorf, Germany; aleagha@hhu.de (N.A.-A.); philipp.jakobs@hhu.de (P.J.)
3 Robert M. Berne Cardiovascular Research Center, Department of Pharmacology, University of Virginia-School of Medicine, Charlottesville, VA 22908, USA; cm3xe@virginia.edu (C.M.); sks2n@virginia.edu (S.K.S.)
* Correspondence: juhae001@hhu.de (J.H.); joalt001@hhu.de (J.A.); Tel.: +49-211-3389-291 (J.H. & J.A.); Fax: +49-211-3389-331 (J.H. & J.A.)
† K.J., J.G. and S.G. contributed equally to the work.

check for updates

Citation: Jander, K.; Greulich, J.; Gonnissen, S.; Ale-Agha, N.; Goy, C.; Jakobs, P.; Farrokh, S.; Marziano, C.; Sonkusare, S.K.; Haendeler, J.; et al. Extra-Nuclear Functions of the Transcription Factor Grainyhead-Like 3 in the Endothelium—Interaction with Endothelial Nitric Oxide Synthase. *Antioxidants* **2021**, *10*, 428. https://doi.org/10.3390/antiox10030428

Academic Editors: Eric E. Kelley and Adam C. Straub

Received: 7 January 2021
Accepted: 9 March 2021
Published: 11 March 2021

Abstract: We previously demonstrated that the transcription factor Grainyhead-like 3 (GRHL3) has essential functions in endothelial cells by inhibiting apoptosis and promoting migration as well as activation of endothelial nitric oxide synthase (eNOS). We now show that a large portion of the protein is localized to myo-endothelial projections of murine arteries suggesting extra-nuclear functions. Therefore, we generated various deletion mutants to identify the nuclear localization signal (NLS) of GRHL3 and assessed potential extra-nuclear functions. Several large-scale deletion mutants were incapable of activating a GRHL3-dependent reporter construct, which could either be due to deficiencies in transcriptional activation or to impaired nuclear import. One of these mutants encompassed a predicted bipartite NLS whose deletion led to the retention of GRHL3 outside the nucleus. Interestingly, this mutant retained functions of the full-length protein as it could still inhibit pathways inducing endothelial cell apoptosis. As apoptosis protection by GRHL3 depends on NO-production, we examined whether GRHL3 could interact with eNOS and showed a direct interaction, which was enhanced with the extra-nuclear GRHL3 variant. The observation that endogenous GRHL3 also interacts with eNOS in intact murine arteries corroborated these findings and substantiated the notion that GRHL3 has important extra-nuclear functions in the endothelium.

Keywords: grainyhead-like 3; endothelium; migration; apoptosis; endothelial NO synthase

1. Introduction

The endothelium—the innermost layer of the vessel wall—is a single layer of cells that line the inside of blood vessels. They form a selective barrier between vessels and tissues and control the flow of substances into and out of a tissue. Nitric oxide (NO) produced by endothelial cells is essential for their functionality as well as for the maintenance of vascular homeostasis. In endothelial cells, NO is produced constitutively by the endothelial NO Synthase (eNOS). Impaired endothelial cell functionality is observed in nearly all cardiovascular diseases and is typically referred to as endothelial dysfunction. It is characterized by reduced NO bioavailability and migratory capacity as well as increased sensitivity towards apoptotic stimuli [1].

The transcription factor Grainyhead-like 3 (GRHL3) has been shown to be critical in wound healing and epidermal barrier function. It is also required for proper neural tube closure during embryonic development; therefore, GRHL3-deficient mice die shortly after birth due to an open back (spina bifida) [2,3]. Knockdown experiments in keratinocytes isolated from GRHL3-deficient mice revealed the involvement of GRHL3 in the migration of epidermal cells [4]. While mice express only a single GRHL3 protein, three different isoforms are found in humans, with isoform 2 being the direct homolog of the mouse protein. The two other isoforms are derived from a transcript with a different first exon that is not present in the mouse genome and an additional alternative splicing event, including or skipping exon 2; all other exons are identical in the three isoforms [5]. Previously, we found all GRHL3 isoforms to be expressed in primary human endothelial cells (EC) ex vivo [6,7]. There, isoforms 1 (GRHL3-1) and 2 (GRHL3-2) increased the migratory capacity and inhibited induction of apoptosis, whereas the N-terminally truncated isoform 3 (GRHL3-3) had opposite effects [6–8]. We have demonstrated that apoptosis protection by isoforms 1 and 2 and the pro-migratory effect of isoform 1 are NO-dependent. Although isoform 2 enhances endothelial migration and is critical for this process [6,8], the evidence for NO-dependent migration induction by this protein is only circumstantial. While it does not affect VEGF levels, it increases NO bioavailability by increasing phosphorylation of eNOS on serine 1177 [6] and endogenously produced NO has long been known to promote endothelial cell migration.

The underlying mechanisms leading to increased NO bioavailability and improved endothelial cell functionality are not completely understood. Moreover, the expression of GRHL3 in the vascular wall in vivo has not been studied so far. Therefore, the aim of this study was to analyze GRHL3 localization in murine arteries and to determine the mechanisms leading to improved endothelial cell functionality.

To our surprise, we found a relatively large portion of the transcription factor GRHL3 outside the nucleus in endothelial cells in vivo, mostly at myoendothelial projections, suggesting extra-nuclear functions. After delineation of the nuclear localization signal (NLS), we demonstrated that the extra-nuclear protein improves endothelial cell functionality. Moreover, GRHL3 interacted with eNOS outside the nucleus and thereby increased NO bioavailability, which probably explains the increased endothelial cell functionality.

In conclusion, GRHL3 is a new interaction partner of eNOS ex vivo and in vivo, and their interplay seems to be critical for vascular homeostasis and, thus, functions.

2. Materials and Methods

2.1. Cell Culture

Primary human endothelial cells (EC) were supplied from LONZA (Cologne, Germany), and human embryonic kidney cells (HEK293) were supplied from Invitrogen (Darmstadt, Germany). EC and HEK293 were cultured as previously described [9,10]. In detail, EC were cultured in endothelial basal medium supplemented with 1 µg/mL hydrocortisone, 12 µg/mL bovine brain extract, 50 µg/mL gentamicin, 50 ng/mL amphotericin B, 10 ng/mL epidermal growth factor (LONZA, Cologne, Germany), and 10% fetal bovine serum until the third passage. After detachment with trypsin, cells were grown for at least 20 h. HEK293 were cultured in DMEM GlutaMAX™ supplemented with 10% heat-inactivated fetal bovine serum and 1% penicillin/streptomycin.

2.2. Plasmids

To generate an expression vector for human full-length GRHL3 with a C-terminal myc-tag, the GRHL3 coding sequence from the original vector carrying a V5-tag [8] was amplified by PCR and inserted into pcDNA3.1/Myc-His(-) A (Invitrogen/Life Technologies, Darmstadt, Germany) opened with Xho I and Hind III using the Gibson Assembly® Cloning Kit according to the manufacturer's protocol (New England Biolabs, Frankfurt, Germany). Starting from this plasmid, the expression vectors for the GRHL3 deletion mutants were generated by Gibson Assembly. All constructs were verified by DNA se-

quencing. Cloning details and complete plasmid sequences are available upon request. The GRHL3-specific luciferase reporter plasmid has been described previously [6].

2.3. Transfection

Transient transfections with plasmid DNA in EC were performed using SuperFect (Qiagen, Hilden, Germany) as previously described [9,10]. In detail, EC were transfected on 6 cm culture dishes with 3 µg plasmid DNA and 22.5 µL SuperFect, or in 6-well plates with 1.2 µg plasmid DNA and 12 µL SuperFect per well. Transient transfections of HEK293 were performed using Lipofectamine® 3000 transfection reagent (Thermo Fisher Scientific, Schwerte, Germany) according to the manufacturer's instructions.

2.4. Migration Assays

Migration assays were performed with a scratch wound assay as previously described [11] or with a Boyden chamber Transwell migration assay. For detection of cell migration via scratch wound assay, wounds were set by scraping confluent cell monolayers with a sterile disposable rubber policeman. Therefore, endothelial cells were cultivated on 6 cm dishes, which were labeled with a trace line prior to setting the wound. After the injury, non-attached cells were removed by gentle washing with culture medium. The wound was created 5 h after transfection. Endothelial cell migration from the edge of the injured monolayer was quantified by staining the cells with 500 ng/mL 4′,6-diamidino-2-phenylindole (DAPI, Carl Roth, Karlsruhe, Germany) in PBS after the cells were fixed with 4% paraformaldehyde for 15 min at room temperature and microscopic pictures were taken using a Zeiss Axiovert 100. The cells, which had invaded the wound from the trace line, were automatically counted using the particle analysis feature of Image J 1.52a after watershed separation of overlapping nuclei.

For detection of cell migration via a Boyden chamber Transwell migration assay, cells were seeded and transfected on 6 cm dishes. 5 h after transfection, cells were detached with trypsin from the surface of the dishes and 2.6×10^5 cells were transferred on Transwell inserts placed in 6-well plates (Corning Inc., Corning, NY, USA) containing culture medium with 20% fetal bovine serum, with etched coverslips on the bottom of the wells. Endothelial cell migration from the Transwell insert onto the edged coverslips was quantified by staining the migrated cells on the coverslips with 500 ng/mL DAPI (Carl Roth, Karlsruhe, Germany) in PBS after the cells were fixed with 4% paraformaldehyde for 15 min at room temperature and microscopic pictures were taken using a Zeiss Axiovert 100. The cells, which migrated through the Transwell insert, were automatically counted as described above.

2.5. Immunoblotting

After transfer of the proteins from polyacrylamide gels onto polyvinylidene difluoride membranes and blocking, membranes were incubated with antibodies directed against myc-tag (1:500), phospho-eNOS (S1177, 1:500) and Caspase-3 (1:3000 for full-length protein; 1:250 for the cleaved protein), all from Cell Signaling Technology, Frankfurt, Germany), GAPDH (1:70,000), eNOS (1:500) both from Abcam, Cambridge, UK, Topoisomerase I (1:200, Santa Cruz Biotechnology, Heidelberg, Germany), Tubulin (1:10,000; Sigma-Aldrich, Deisenhofen, Germany). Antibodies were incubated overnight at 4 °C. On the following day, membranes were incubated with secondary antibodies coupled to horseradish peroxidase, and detection was performed using ECL substrate (GE Healthcare, Solingen, Germany) and X-ray films.

2.6. Luciferase Reporter Gene Assay

Luciferase activity was measured as described [7]. In detail, after transfection, cells were lysed with Reporter Lysis Buffer (Promega, Mannheim, Germany) according to the manufacturer's instructions. For HEK293, protein content was determined prior to the

experiment, then a total of 10 µg protein was used. For EC, 10 µL of cell lysate was used, and protein content was determined and used for normalization.

2.7. S-NO Content

S-NO content in EC was measured as described previously [12,13] with one alteration: instead of 3.75 mM, p-chloromercuribenzosulfonic acid, 10 mM $CuSO_4$ was used. In detail, cells were lysed in Griess lysis buffer (50 mM Tris-HCl, pH 8.0, 150 mM NaCl, 5 mM KCl, 1% Igepal CA630, 1 mM phenylmethylsulfonyl fluoride, 1 mM bathocuproinedisulfonic acid, 1 mM diethylenetriaminepenta-acetic acid, 10 mM N-ethylmaleimide), and 80 µg of cell lysate were incubated with 1% sulfanilamide and 0.1% N-(1-naphthyl)ethylenediamine in the presence or absence of 10 mM $CuSO_4$ for 20 min. S-NO content was measured photometrically at 540 nm. The amount was calculated using defined GSNO concentrations as a standard.

2.8. Biochemical Fractionation

EC were lysed and fractionated using the NE-PER™ Nuclear and Cytoplasmic Extraction Reagent according to the manufacturer's protocol (Life Technologies, Darmstadt, Germany). The purity of the nuclear and cytosolic fractions was confirmed by immunoblotting with antibodies against Topoisomerase I (nuclear protein fraction) and GAPDH (cytosolic protein fraction).

2.9. Cyclic GMP Detection Assay

Cyclic GMP (cGMP) content in EC was determined using the cGMP Complete ELISA Kit according to the manufacturer's instructions (Enzo Life Sciences, Lörrach, Germany). In brief, cells were lysed in 0.1 M HCl, and cell lysates, as well as cGMP conjugated to alkaline phosphatase, were added to the 96-well plate containing antibody against cGMP, binding the cGMP in the lysates and the conjugate competitively. After the addition of a substrate for the alkaline phosphatase, the absorbance was measured photometrically at 405 nm. The cGMP concentrations in the lysates were determined using the provided cGMP standards. All samples and standards were acetylated for increased sensitivity.

2.10. Immunostaining of EC

EC were fixed and permeabilized as described previously [11]. Cells were incubated with a primary antibody against the C-terminal myc-tag (1:50; Biomol, Hamburg, Germany) overnight at 4 °C and with an Alexa Fluor® 488 coupled anti-mouse secondary antibody (1:500; Santa Cruz Biotechnology, Heidelberg, Germany) for 1 h at room temperature. Nuclei were stained with DAPI (500 ng/mL, Roche, Mannheim, Germany) for 5 min, and the actin cytoskeleton was stained with Phalloidin CF® 488 (1:70; Biotium, Fremont, CA, USA) for 20 min. Images were taken using Zeiss microscopes (Axio Observer D1 or Axio Imager M2, magnification 40× oil).

2.11. Proximity Ligation Assay in EC

EC were seeded on acidified glass slides and transfected. 18 h after transfection, cells were fixed and permeabilized as described under immunostaining of EC. After overnight incubation at 4 °C with primary antibodies against the myc-tag or Akt1 (both: 1:100; Cell Signaling Technology, Frankfurt, Germany) and eNOS (1:100; BD Biosciences, Heidelberg, Germany), cells were treated with the components of the Duolink® In Situ detection kit (Sigma-Aldrich, Deisenhofen, Germany) according to the manufacturer's instructions. The actin cytoskeleton was stained with Phalloidin CF® 488 1:70 for 20 min; nuclei were stained with DAPI 500 ng/mL for 5 min.

2.12. Immunostaining of Murine Mesenteric Arteries and Aorta

Immunostaining was performed on en face third-order mesenteric arteries or aorta as described previously [14,15]. In short, mesenteric arteries or thoracic aortas were isolated

from 10–12 week old C57BL6 mice (Jackson Laboratories, Bar Harbor, ME, USA) and pinned down on a SYLGARD block. The arteries were fixed with 4% paraformaldehyde for 15 min at room temperature. Fixed arteries were washed three times for 5 min with phosphate-buffered saline (PBS). The arteries were then treated with 0.2% Triton-X/PBS for 30 min at room temperature on a rocker. Following this permeabilization step, arteries were treated with 5% normal goat serum (Abcam PLC, Cambridge, MA, USA) for 1 h at room temperature and subsequently incubated overnight with antibodies against GRHL3 (1:1,000; Merck Millipore, Darmstadt, Germany). Arteries were then washed three times with PBS and incubated with Alexa Fluor® 568 goat anti-rabbit secondary antibody (1:500; Invitrogen/Life Technologies, Darmstadt, Germany) at room temperature for 1 h in the dark. Thereafter, arteries were washed three times with PBS and incubated with 0.3 µM DAPI (Invitrogen, Carlsbad, CA, USA) for 10 min at room temperature in the dark to stain nuclei. Images were obtained using the Andor Revolution WD (with Borealis) spinning-disk confocal imaging system (Andor Technology, Belfast, UK) comprising an upright microscope (Nikon, Tokyo, Japan) with a 60× water-dipping objective (numerical aperture, 1.0) and an electron-multiplying charge-coupled device camera, as described previously [16]. Consecutive images were taken along the z-axis at a slice thickness of 0.1 µm from the top surface of ECs to the bottom surface of SMCs. GRHL3 immunostaining was imaged by exciting at 561 nm and collecting the emitted fluorescence with a 607/36 nm band-pass filter. DAPI immunostaining was imaged by excitation with 409 nm and collecting the emitted fluorescence with a 447/60 nm band-pass filter. Autofluorescence of the internal elastic lamina was imaged using an excitation wavelength of 488 nm and a 525/36 nm band-pass emission filter.

2.13. Proximity Ligation Assay in Murine Mesenteric Arteries

Proximity ligation assay was performed on en face mesenteric arteries pinned on SYLGARD blocks as described previously [14]. Interaction between GRHL3 and eNOS was determined using primary antibodies against GRHL3 (as described above) and eNOS (1:100; BD Biosciences, Franklin Lakes, NJ, USA) and subsequently applying the DuoLink® In Situ detection kit (Sigma-Aldrich, Deisenhofen, Germany) according to the manufacturer's instructions.

2.14. Statistics

The number of experiments (n) given in figure legends represents independent biological replicates; the data shown are mean ± SEM. Normal distribution for all data sets was confirmed by Shapiro–Wilk test; homogeneity of variances (from means) between groups was verified by Levene's test. Pairwise comparisons were performed with two-sided, unpaired Student's *t*-tests on raw data. Multiple comparisons were performed using one-way ANOVA with post hoc Tukey's LSD test.

3. Results

3.1. Localization of GRHL3 In Vivo

We were the first to describe that the transcription factor GRHL3 is expressed in primary human endothelial cells ex vivo [6,7]. After generating an antibody against GRHL3 in cooperation with Merck Millipore, which is now commercially available, we performed en face staining of the murine aorta, which is a conduit artery, and resistance-sized mesenteric arteries to investigate whether GRHL3 is also expressed in endothelial cells in vivo. GRHL3 is detectable in the endothelium but not in the smooth muscle cell layer of those arteries (Figure 1). To our surprise, a large portion of the protein was localized outside the nucleus, which is unexpected for a transcription factor. Moreover, the majority of the extra-nuclear GRHL3 was found in myoendothelial projections (MEPs) (Figure 1 and Supplementary Videos). These MEPs are protrusions of endothelial cells reaching through the internal elastic lamina [17], thereby directly contacting the adjacent smooth muscle cells.

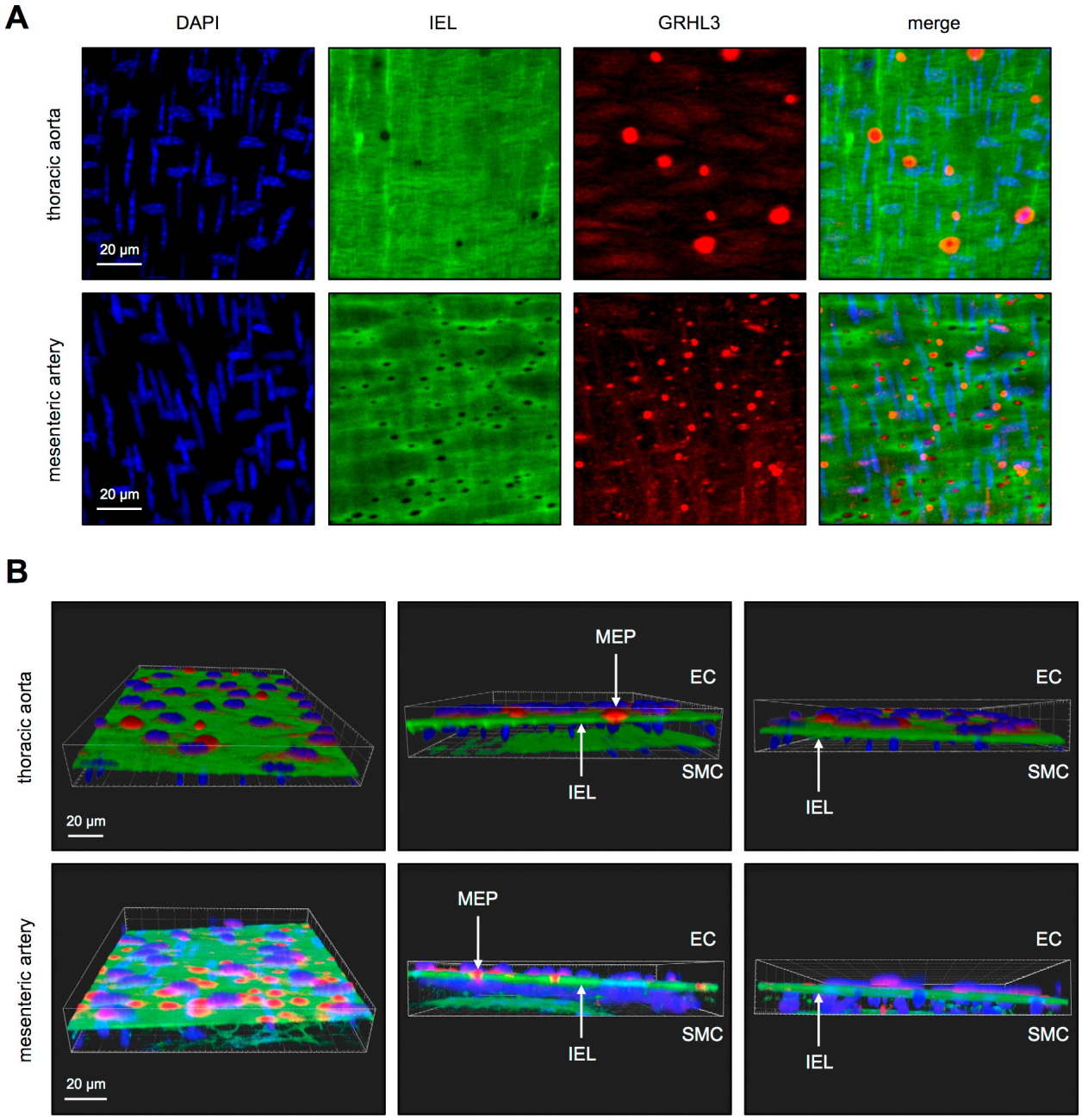

Figure 1. Transcription factor Grainyhead-like 3 (GRHL3) localization in the murine aorta and mesenteric arteries. (**A**) En face staining of the aorta (thoracic) and mesenteric arteries with an antibody against GRHL3 (red). Nuclei were counterstained with 4′,6-diamidino-2-phenylindole (DAPI) (blue). Horizontally-oriented nuclei are from endothelial cells and vertically oriented nuclei from smooth muscle cells. The internal elastic lamina (IEL) appears green due to autofluorescence. Black wholes in the IEL represent myoendothelial projections (MEP). Merge is the overlay of all channels. (**B**) Single frames from animated three-dimensional reconstructions of the aorta and mesenteric artery staining (see also Supplementary Videos). The endothelial cell layer (EC, top) is separated from the smooth muscle cell layer (SMC, bottom) by the internal elastic lamina (IEL). In the middle panels, MEPs are highlighted. Red staining represents GRHL3, which is only present in the endothelial cell layer, and blue shows the cell nuclei stained with DAPI.

3.2. Identification of the Nuclear Localization Signal within Human GRHL3

On the basis of the unexpected finding that the transcription factor GRHL3 is also localized outside the nucleus and in MEPs, we hypothesized that GRHL3 has an up to now unknown non-nuclear function. To investigate this hypothesis, we first wanted to identify

the NLS in GRHL3 to examine putative extra-nuclear functions of GRHL3 ex vivo, using the human isoform 2 that is the direct homolog of the mouse protein.

Therefore, we generated large-scale deletion mutants of GRHL3 (Figure 2A) based on the predicted functional domains [5] and our own previous experiments [7]. We then measured the transcriptional activation of a GRHL3-specific luciferase reporter [6] by these mutants in HEK 293 cells as this is strictly dependent on the nuclear localization of the transcription factor. In mutant ΔA (deletion of amino acids 1–230, Δ1–230), we deleted the predicted activation domain and the following sequences up to the DNA-binding domain, as we had previously shown that a splice variant that is translated into the N-terminally truncated isoform 3, which lacks the first 93 amino acids, but is still a fully active transcription factor [7]. Mutant ΔB (Δ231–348) lacks the DNA-binding domain (DBD) and thus, serves as a control, which is expected to be incapable of transcriptional activation. In ΔC (Δ350–492), we deleted the region between the DBD and a putative bipartite nuclear localization signal predicted by the software package cNLS Mapper [18], which is highly conserved between the human and the mouse protein and is missing in ΔbiNLS (Δ485–515). The last mutant, ΔCT (Δ514–602), does not contain the C-terminus of the protein with the majority of its dimerization domain (DD).

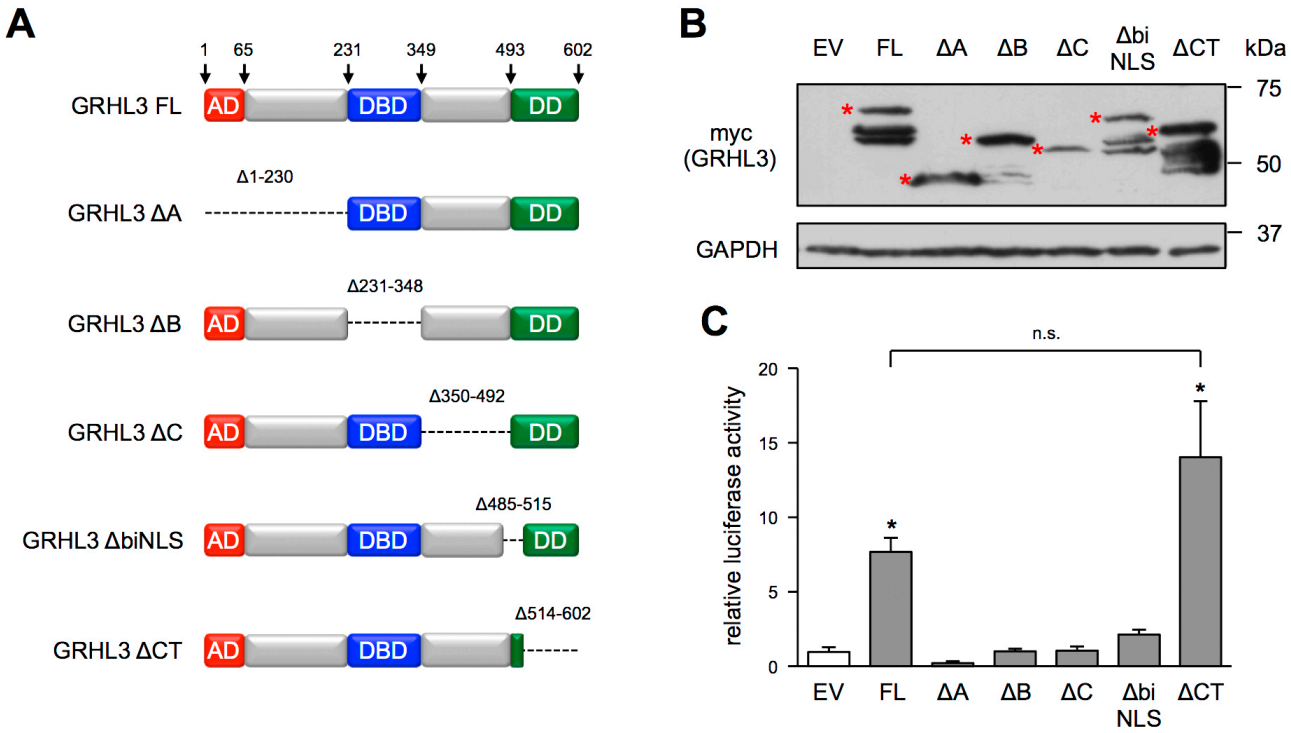

Figure 2. Transcriptional activity of full-length GRHL3 (GRHL3 FL) and of various deletion mutants in HEK293 cells. (**A**) Schematic representation of the GRHL3 variants Δ denotes the deleted amino acids (AD = predicted activation domain; DBD = predicted DNA-binding domain; DD = predicted dimerization domain). (**B**,**C**) HEK293 cells were co-transfected with a GRHL3-specific luciferase reporter construct and expression vectors for the GRHL3 variants shown in (**A**). (**B**) Expression of the different GRHL3 variants was verified by immunoblot (upper panel, * marks proteins of the expected sizes), GAPDH served as a loading control (lower panel). (**C**) Luciferase activity was measured in cell lysates and is shown relative to cells co-transfected with an empty vector (EV) instead of GRHL3 variants (data are mean ± SEM, n = 4–10, * $p < 0.05$ vs. EV).

The full-length GRHL3 protein (FL) and ΔCT could activate the GRHL3-specific reporter to the same extent, suggesting that the dimerization domain is not essential for the transcription factor activity of GRHL3. In contrast, all other mutants, although expressed to similar levels (Figure 2B), did not show measurable transcription factor activity when compared to an empty vector, which was transfected as a negative control (Figure 2C).

This could be either due to a lack of an as yet unknown activation domain or to impaired nuclear import as a consequence of the deletion of the NLS, which could be the most likely explanation for the ΔbiNLS mutant.

Assuming that GRHL3 ΔbiNLS is retained in the cytosol, we next expressed this mutant and GRHL3 FL in EC and measured their transactivation potential with the same luciferase reporter as above. While the transcriptional activation by the full-length protein can easily be measured, EC expressing GRHL3 ΔbiNLS showed no higher luciferase activity than cells transfected with an empty vector (Figure 3A). Therefore, we next determined the intracellular localization of GRHL3 FL and GRHL3 ΔbiNLS. Immunostaining and biochemical fractionation revealed that GRHL3 ΔbiNLS is only localized in the cytosol, clearly indicating that the deletion encompasses the NLS of GRHL3. In contrast, GRHL3 FL is detectable in the nucleus as well as in the cytosol (Figure 3B,C), confirming the results obtained in murine arteries (Figure 1).

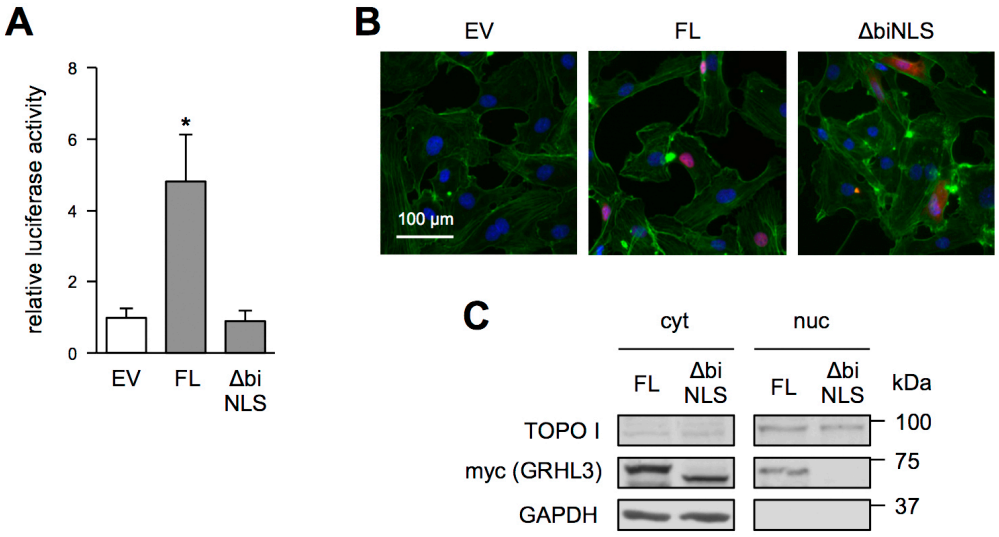

Figure 3. Transcriptional activity and intracellular localization of GRHL3 FL and GRHL3 ΔbiNLS in EC. (**A**,**B**) EC were transfected with an empty vector (EV), GRHL3 FL (FL) or GRHL3 ΔbiNLS (ΔbiNLS) plasmids. (**A**) Relative luciferase activity was measured in lysates of cells co-transfected with the GRHL3-specific luciferase reporter plasmid (data are mean ± SEM, $n = 5$, * $p < 0.05$ vs. EV). (**B**) Representative immunostainings. Nuclei were stained with DAPI (blue), GRHL3 FL and GRHL3 ΔbiNLS were detected with an antibody against the myc-tag (red), the actin cytoskeleton was stained with Phalloidin (green). The merge of all channels is shown. (**C**) EC were transfected with GRHL3 FL (FL) or GRHL3 ΔbiNLS (ΔbiNLS) plasmids. Representative immunoblots. Biochemical fractionation in cytosolic (cyt) and nuclear (nuc) fractions. Topoisomerase I (TOPO I, upper panels) and GAPDH (lower panels) served as purity controls of nuclear and cytosolic fractions, respectively. Myc represents the detection of the C-terminal myc-tag of GRHL3 FL and GRHL3 ΔbiNLS (middle panels).

3.3. Role of Extra-Nuclear GRHL3 in Endothelial Cell Functionality, NO Bioavailability, eNOS Phosphorylation and Interaction of Akt1 and eNOS

To understand the role of extra-nuclear localized GRHL3 in EC, we compared GRHL3 ΔbiNLS and GRHL3 FL in their ability to inhibit apoptosis and to enhance migratory capacity. We had previously demonstrated that GRHL3 inhibits apoptosis and enhances migration [6,7], both in a NO-dependent manner. We had also shown that GRHL3 enhances NO bioavailability and the phosphorylation of eNOS on serine 1177 [6,7]. Therefore, EC were transfected with an empty vector, GRHL3 FL or GRHL3 ΔbiNLS plasmids. First, comparable overexpression of GRHL3 FL and GRHL3 ΔbiNLS in EC was controlled by immunoblotting (Figure 4A). Then, apoptosis was measured using the amount of cleaved Caspase-3 as a standard marker. GRHL3 FL inhibited apoptosis as published previously by

us [6,7]. Interestingly, the extra-nuclear localized GRHL3 ΔbiNLS blocked apoptosis more pronounced than GRHL3 FL (Figure 4A,B). Next, we investigated the migratory capacity of EC using a Boyden chamber and a scratch wound assay. As shown in Figure 4C–E, GRHL3 FL enhanced migration of EC when compared to empty vector-transfected cells; however, migration was enhanced even stronger when GRHL3 ΔbiNLS was expressed. Thus, the functionality of endothelial cells is even more improved when GRHL3 is outside of the nucleus. Since apoptosis protection and migratory capacity of endothelial cells depend on the bioavailability of NO, we next measured the S-NO content, which is used as a surrogate marker for NO bioavailability [10].

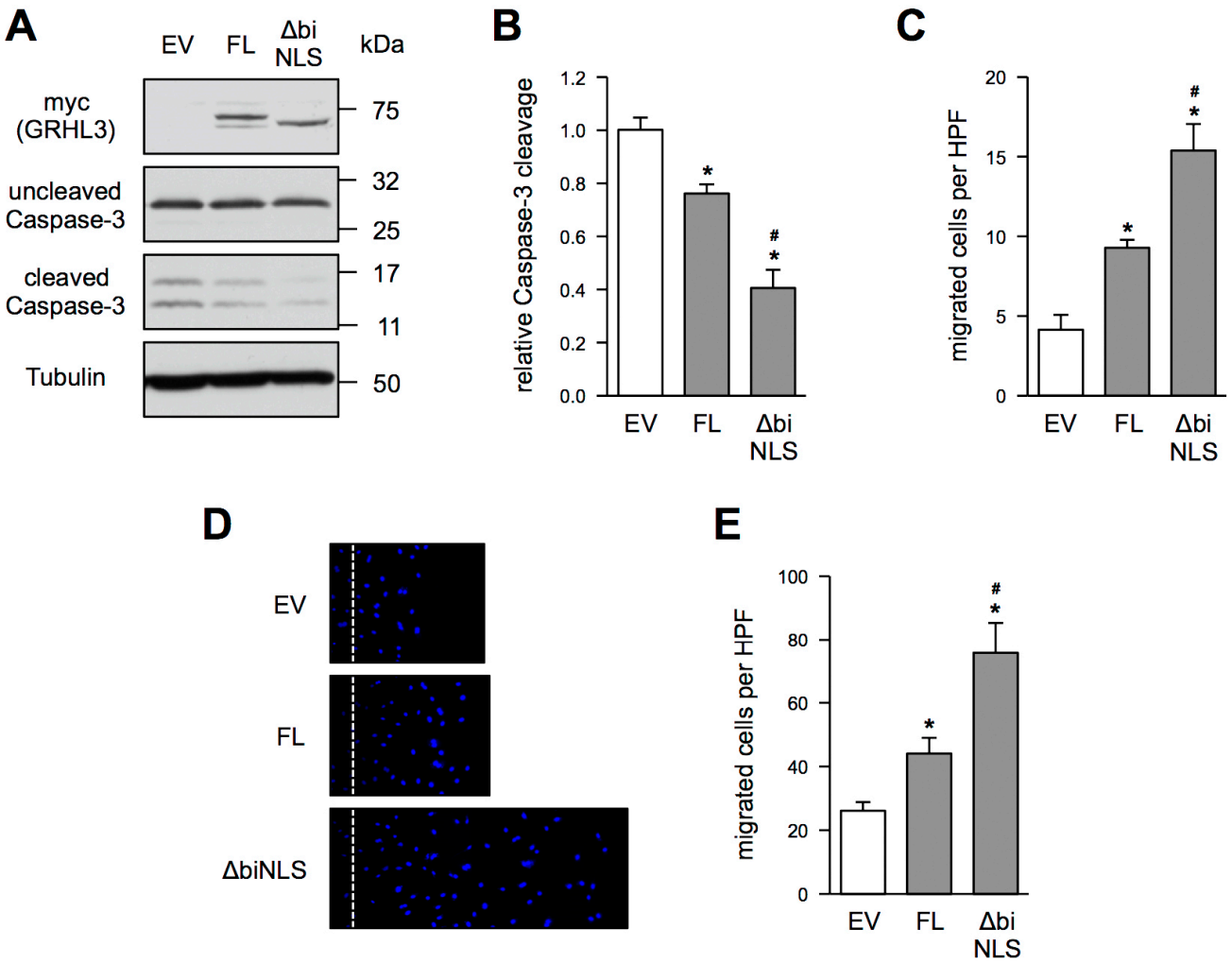

Figure 4. Effects of GRHL3 FL and GRHL3 ΔbiNLS on apoptosis and migration in EC. (**A**–**E**) EC were transfected with an empty vector (EV), GRHL3 FL or GRHL3 ΔbiNLS plasmids. (**A**) Representative immunoblot. Myc represents the expression of GRHL3 FL, and GRHL3 ΔbiNLS (upper panel), uncleaved Caspase-3 (upper, middle panel), cleaved Caspase-3 (lower, middle panel), Tubulin served as a loading control (lower panel). (**B**) Semiquantitative analyses of the relative amount of cleaved Caspase-3 (data are mean ± SEM, $n = 6$, * $p < 0.05$ vs. EV, # $p < 0.05$ vs. FL). (**C**) Migratory capacity was measured in a Boyden chamber assay. Image J analyses of migrated cells per high-power field (HPF) (data are mean ± SEM, $n = 5$, * $p < 0.05$ vs. EV, # $p < 0.05$ vs. FL). (**D**,**E**) Migratory capacity was measured in a scratch-wound assay. (**D**) Representative DAPI staining. Wounds were set at the scattered lines; left of the lines are the unwounded areas. The areas right to the lines show the wounds with the cells that had migrated into them. Nuclei were stained with DAPI. (**E**) Image J analyses of migrated cells per high-power field (HPF) (data are mean ± SEM, $n = 5$, * $p < 0.05$ vs. EV, # $p < 0.05$ vs. FL).

In agreement with the improved endothelial cell functionality in EC overexpressing GRHL3 ΔbiNLS, this extra-nuclear GRHL3 variant increased the S-NO content significantly

when compared with GRHL3 FL (Figure 5A). Therefore, we also determined whether GRHL3 ΔbiNLS improves phosphorylation of eNOS on serine 1177, which activates the enzyme. As expected and previously published by us, GRHL3 FL enhanced phosphorylation of eNOS on serine 1177 (Figure 5B) [6,7]. Corroborating the S-NO content data, GRHL3 ΔbiNLS overexpressing EC showed significantly more phosphorylation on serine 1177 when compared to GRHL3 FL (Figure 5B,C). This increase in intracellular, bioavailable NO could result in increased cyclic GMP (cGMP) levels. However, cGMP measurements revealed no differences in EC transfected with empty vector, GRHL3 FL and GRHL3 ΔbiNLS plasmids (EV: 0.183 +/− 0.04 pmol/mL, GRHL3 FL: 0.155 +/− 0.04 pmol/mL, GRHL3 ΔbiNLS: 0.154 +/− 0.02, data are mean ± SEM, n = 3–4, n.s.). An increase in eNOS phosphorylation on serine 1177 could also be explained by an increase in the interaction between Akt1 and eNOS. Therefore, we performed proximity ligation assays for Akt1 and eNOS in EC transfected with an empty vector or the GRHL3 expression plasmids. As demonstrated in Figure 5D, the interaction between Akt1 and eNOS is more pronounced in cells overexpressing GRHL3 ΔbiNLS than in GRHL3 FL overexpressing EC.

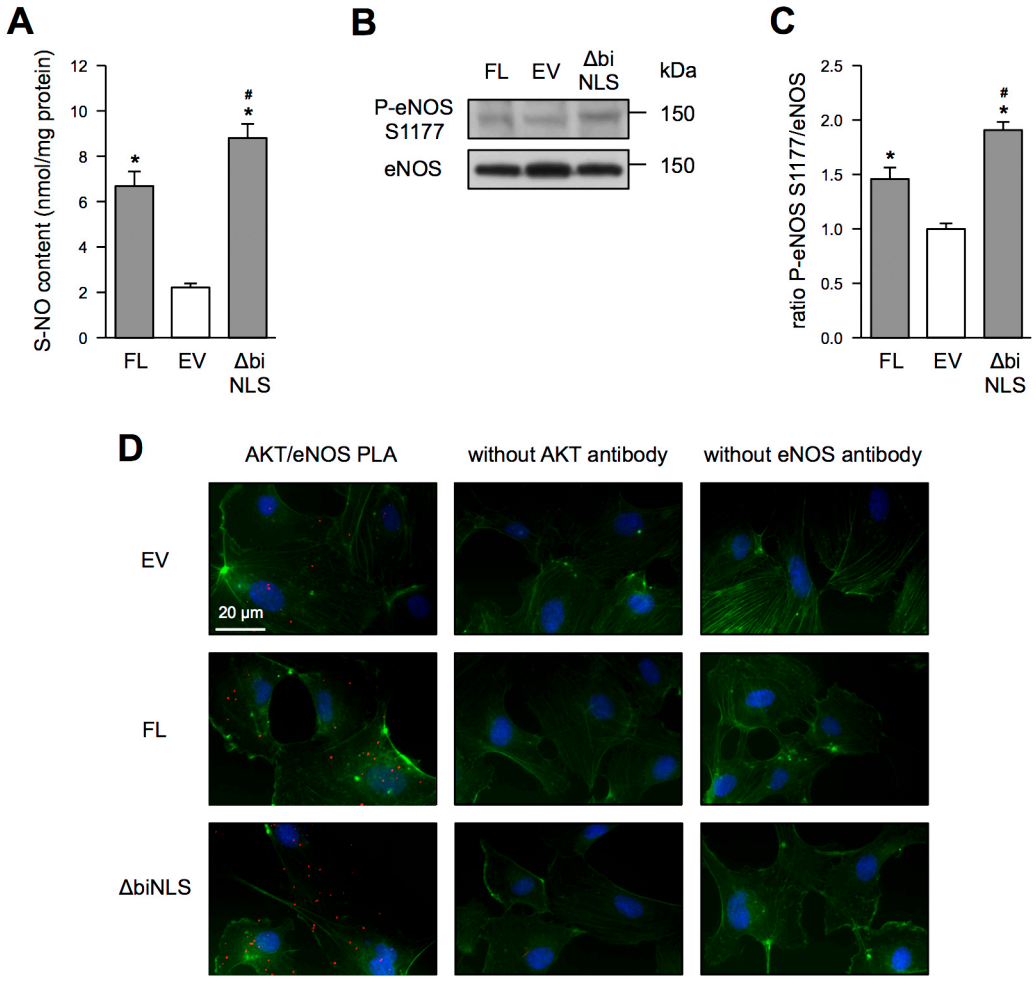

Figure 5. Effects of GRHL3 FL and GRHL3 ΔbiNLS on NO bioavailability, eNOS phosphorylation and interaction of Akt1 and eNOS. (**A**–**D**) EC were transfected with an empty vector (EV), GRHL3 FL or GRHL3 ΔbiNLS plasmids. (**A**) S-NO content was measured at 405 nm and calculated as nmol/mg protein (data are mean ± SEM, n = 5, * p < 0.05 vs. EV, # p < 0.05 vs. FL). (**B**,**C**) Phosphorylation of eNOS on serine 1177 was measured by immunoblot. (**B**) Representative immunoblot. The upper panel shows phosphorylation of eNOS on serine 1177. The lower panel shows comparable levels of total eNOS. (**C**) Semiquantitative analyses of the ratio of phosphorylated eNOS on serine 1177 to total eNOS (data are mean ± SEM, n = 5, * p < 0.05 vs. EV, # p < 0.05 vs. FL). (**D**) Proximity ligation assay (PLA) was performed with antibodies against AKT and eNOS (AKT/eNOS PLA, left panels). As negative controls, PLAs were performed, omitting either the AKT antibody (middle panels) or the eNOS antibody (right panels). Red dots represent AKT and eNOS interactions. The actin cytoskeleton was stained with Phalloidin (green) and nuclei with DAPI (blue).

3.4. GRHL3 eNOS Interaction Ex Vivo and In Vivo

The S-NO content in EC depends on the production of NO by eNOS, and eNOS is mainly localized outside the nucleus and notably also in MEPs [16]. Therefore, we hypothesized that GRHL3 and eNOS could be in close proximity to each other and that one extra-nuclear function of GRHL3 is the interaction with eNOS resulting in activation of the enzyme and, thus, increased NO bioavailability. To test this hypothesis, we first performed immunostainings in EC overexpressing GRHL3 FL or GRHL3 ΔbiNLS using antibodies against eNOS and the myc-tag to specifically detect GRHL3 FL as well as GRHL3 ΔbiNLS. As shown in Figure 6A, GRHL3 and eNOS colocalize. To further investigate whether GRHL3 and eNOS are in so close proximity that they interact with each other, proximity ligation assays were performed. Indeed, GRHL3 and eNOS interact with each other (Figure 6B). Interestingly, the interaction between eNOS and GRHL3 ΔbiNLS is more pronounced than the interaction between eNOS and GRHL3 FL. Thus, one could assume that the increase in S-NO content shown in Figure 5A is due to enhanced interaction between extra-nuclear GRHL3 and eNOS.

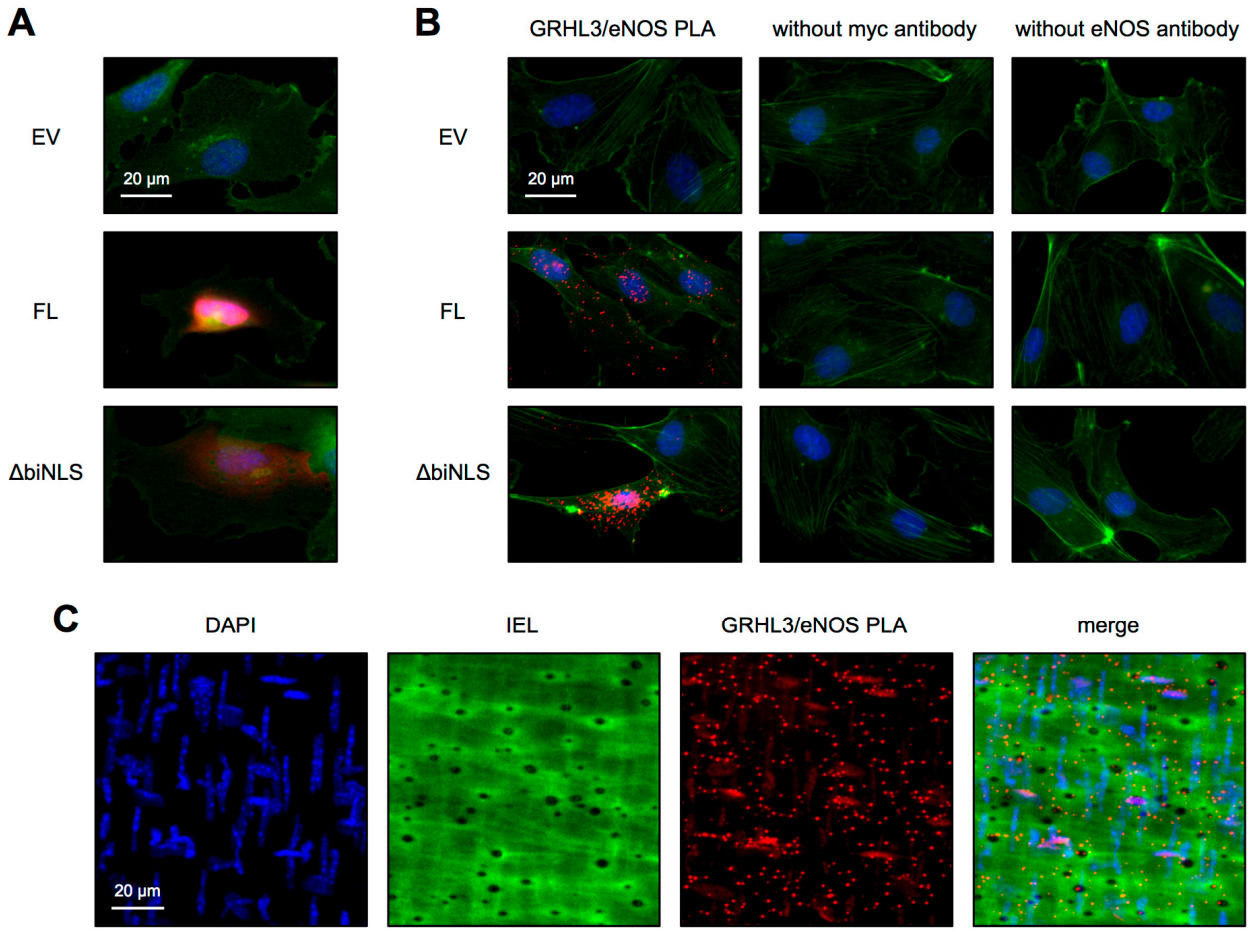

Figure 6. GRHL3 and eNOS interaction ex vivo and in vivo. (**A**,**B**) EC were transfected with an empty vector, GRHL3 FL or GRHL3 ΔbiNLS plasmids. (**A**) Representative immunostainings. Co-immunostainings with an anti-myc-tag antibody and an eNOS antibody were performed. Myc-tag represents GRHL3 variants (red), eNOS is shown in green, nuclei were stained with DAPI (blue). (**B**) Proximity ligation assay (PLA) was performed with an antibody against the myc-tag and an eNOS antibody (GRHL3/eNOS PLA, left panels). As negative controls, PLAs were performed, omitting either the myc antibody (middle panels) or the eNOS antibody (right panels). Red dots represent eNOS and GRHL3 interactions. The actin cytoskeleton was stained with Phalloidin (green) and nuclei with DAPI (blue). (**C**) Proximity ligation assay (PLA) in the mesenteric artery using GRHL3 and eNOS antibodies. Nuclei were counterstained with DAPI. Horizontally-oriented nuclei are from endothelial cells, and vertically oriented nuclei are from smooth muscle cells. Shown are nuclear stains with DAPI (blue). The autofluorescence of the internal elastic lamina (IEL) is shown in green. Black holes in the IEL represent myoendothelial projections (MEP). Red dots represent eNOS and GRHL3 interactions. Merge is the overlay of all channels.

Finally, we also performed in situ proximity ligation assays in the murine mesenteric arteries using antibodies against eNOS and GRHL3 to determine whether our results in cells also hold true in vivo. As shown in Figure 6C, GRHL3 also showed nanometer proximity with eNOS in the endothelium of murine mesenteric arteries in situ.

Thus, GRHL3 is a new interaction partner for eNOS ex vivo and in vivo, and its extra-nuclear localization leads to enhanced endothelial cell functionality, probably by improving NO production.

4. Discussion

The major finding of the present study is that the transcription factor GRHL3 has an extra-nuclear function in primary human endothelial cells. Extra-nuclear GRHL3 interacts with eNOS in EC and murine arteries. It improves NO bioavailability and migratory capacity and inhibits apoptosis.

Transcription factors normally exert their function by binding to DNA and activating their target genes within the nucleus. However, several studies have demonstrated that transcription factors can have functions outside the nucleus independent of target gene activation. In contrast to GRHL3, which inhibits apoptosis in endothelial cells, the transcription factor p53 has been shown to induce apoptosis upon DNA damage. Within the nucleus, p53 induces the expression of target genes leading to apoptosis induction. However, p53 also has extra-nuclear functions. In the cytoplasm, it induces the release of Cytochrome C from the mitochondria into the cytosol, which increases the apoptotic process [19]. Thus, the activation of target genes by p53 and its extra-nuclear function are both intimately involved in apoptosis induction. Along the same lines, but with opposite outcome in endothelial cells, nuclear GRHL3-1 induces expression of Bcl-X_L [7], an anti-apoptotic protein, which protects the outer mitochondrial membrane from damage, among other organs also in the cardiovascular system [20]. Here, we demonstrate that extra-nuclear GRHL3-2 enhances the bioavailability of NO and, thus, inhibits apoptosis. Due to the very short coding part of the two different first exons in the transcripts coding for GRHL3-1 and GRHL3-2, these proteins differ only in very few amino acids at their extreme N-terminus, with the first 11 amino acids in isoform 1 being different from the first six amino acids in isoform 2, while the remainder of the two proteins is identical. Thus, it seems reasonable to assume that both protective isoforms of GRHL3 function in the same manner. Therefore, one could hypothesize that activation of gene transcription by GRHL3-1 and GRHL3-2 as well as their extra-nuclear function are both required for apoptosis protection. It is also worth speculating that, dependent on the external stimuli hitting the endothelium, fast protection could be required, and under such circumstances, GRHL3-2, and most likely also GRHL3-1, is exported from the nucleus to increase the GRHL3/eNOS interaction and thus, NO bioavailability. Increased intracellular NO would lead to inhibition of, e.g., Caspase-3 activation, since increased NO leads to enhanced S-nitrosation of cysteine 163 in Caspase-3, which prevents the generation of the fully active enzyme [21]. This is in line with findings in our study here, demonstrating that increased extra-nuclear GRHL3 leads to higher S-NO content and to reduced cleaved Caspase-3. Besides an increase in the S-NO content, we also found enhanced active phosphorylation of eNOS and interaction of Akt1 and eNOS. Thus, one could assume that the resulting increase in intracellular NO would lead to S-nitrosation of several proteins besides Caspase-3, which are important in apoptosis protection, like, for instance, Thioredoxin-1 [9,10]. However, further studies are required to determine which S-nitrosated proteins may be involved in apoptosis protection conferred by GRHL3 in EC.

Another example of the interplay between nuclear and extra-nuclear GRHL3 is the induction of migration. We have previously published that GRHL3-1 activates transcription and protein expression of Akt2. Akt2, as a master regulator of other Akt isoforms, phosphorylates Akt1, which in turn activates eNOS [7]. Moreover, Akt2 is intimately connected to enhanced cell migration [22]. On the other hand, we demonstrate here that isoform 2 lacking the NLS has a more pronounced effect on migration than the full-length protein, which must be independent of transcription. Thus, one could hypothesize that, as

eluded to above, the induction of endothelial cell migration by GRHL3-1 and GRHL3-2 requires concerted action inside and outside the nucleus.

It must be noted that the enhanced effects of GRHL3 ΔbiNLS on the different outputs in EC could simply be due to the fact that all of the overexpressed protein is excluded from the nucleus. Thereby, the cytosolic concentration of GRHL3 is higher than when the full-length protein is expressed such that the extra-nuclear functions are more pronounced.

We demonstrate here for the first time that GRHL3 interacts with eNOS. It has been demonstrated that eNOS forms a complex with the Heat-shock protein 90 (Hsp90). The binding of Hsp90 to eNOS enhances the activation of eNOS [23], most likely through phosphorylation on serine 1177 by Akt1. Since Hsp90 is a chaperone, it is tempting to speculate that Hsp90, eNOS, Akt1 and GRHL3 form a larger complex and that GRHL3 contributes to increased activation of eNOS. However, further studies are needed to delineate the nature of the interactions between those proteins.

Another new finding of our study is the presence of GRHL3 in MEPs. MEPs are protuberances of the plasma membrane of the endothelium to generate close contact to the subjacent smooth muscle cells. Recently, it has been demonstrated that eNOS is also localized in MEPs. Within those MEPs, eNOS cooperates with Transient Receptor Potential Vanilloid 4 (TRPV4) ion-channels to enhance vasodilation. The increase in calcium ions by the TRPV4 ion-channels leads to activation of eNOS and NO production [16]. Thus, one could speculate that the interaction of eNOS with GRHL3 also in these MEPs will further enhance NO production and, thus, contribute to vasodilation.

5. Conclusions

In conclusion, our study shows for the first time that the transcription factor GRHL3 has extra-nuclear functions. Moreover, GRHL3 is a new interaction partner of eNOS in EC and in murine arteries. An increase in extra-nuclear GRHL3 results in enhanced migratory capacity and NO bioavailability, and reduced apoptosis. Thus, not only the transcriptional activity of GRHL3 but also its extra-nuclear actions contribute to improved functionality of endothelial cells.

Supplementary Materials: The following are available online at https://www.mdpi.com/2076-3921/10/3/428/s1, Video S1: 3D reconstruction aorta, Video S2: 3D reconstruction mesenteric artery.

Author Contributions: Conceptualization, J.H. and J.A.; data curation, J.H. and J.A.; formal analysis, K.J., J.G., S.G., C.M., S.K.S., J.H. and J.A.; funding acquisition, S.K.S., J.H. and J.A.; investigation, K.J., J.G., S.G., N.A.-A., C.G., P.J., S.F. and C.M.; methodology, K.J., J.G., S.G., N.A.-A., C.G., P.J., S.F., C.M. and S.K.S.; project administration, J.H. and J.A.; resources, S.K.S., J.H. and J.A.; supervision, S.K.S., J.H. and J.A.; validation, K.J., J.G., S.G., C.G., P.J. and S.F.; visualization, K.J., N.A.-A. and S.K.S.; writing—original draft, K.J., J.G. and S.G.; writing—review and editing, J.H. and J.A. All authors have read and agreed to the published version of the manuscript.

Funding: This research was funded by the Deutsche Forschungsgemeinschaft (DFG), IRTG1902-1 and IRTG1902-2 to J.H. and J.A.; K.J., S.G. and P.J. were stipend holders of the IRTG1902; J.G. is stipend holder of the IRTG1902.

Institutional Review Board Statement: Not applicable.

Informed Consent Statement: Not applicable.

Data Availability Statement: Raw data will be made available by the corresponding authors upon reasonable request.

Acknowledgments: We thank Florian von Ameln and Olaf Eckermann for their excellent technical support.

Conflicts of Interest: The authors declare no conflict of interest.

References

1. Haendeler, J. Nitric oxide and endothelial cell aging. *Eur. J. Clin Pharmacol.* **2006**, *62* (Suppl. 13), 137–140. [CrossRef]
2. Ting, S.B.; Wilanowski, T.; Auden, A.; Hall, M.; Voss, A.K.; Thomas, T.; Parekh, V.; Cunningham, J.M.; Jane, S.M. Inositol- and folate-resistant neural tube defects in mice lacking the epithelial-specific factor grhl-3. *Nat. Med.* **2003**, *9*, 1513–1519. [CrossRef]
3. Ting, S.B.; Caddy, J.; Hislop, N.; Wilanowski, T.; Auden, A.; Zhao, L.L.; Ellis, S.; Kaur, P.; Uchida, Y.; Holleran, W.M.; et al. A homolog of drosophila grainy head is essential for epidermal integrity in mice. *Science* **2005**, *308*, 411–413. [CrossRef]
4. Caddy, J.; Wilanowski, T.; Darido, C.; Dworkin, S.; Ting, S.B.; Zhao, Q.; Rank, G.; Auden, A.; Srivastava, S.; Papenfuss, T.A.; et al. Epidermal wound repair is regulated by the planar cell polarity signaling pathway. *Dev. Cell* **2010**, *19*, 138–147. [CrossRef] [PubMed]
5. Ting, S.B.; Wilanowski, T.; Cerruti, L.; Zhao, L.L.; Cunningham, J.M.; Jane, S.M. The identification and characterization of human sister-of-mammalian grainyhead (som) expands the grainyhead-like family of developmental transcription factors. *Biochem. J.* **2003**, *370*, 953–962. [CrossRef]
6. Lukosz, M.; Mlynek, A.; Czypiorski, P.; Altschmied, J.; Haendeler, J. The transcription factor grainyhead like 3 (grhl3) affects endothelial cell apoptosis and migration in a no-dependent manner. *Biochem. Biophys. Res. Commun.* **2011**, *412*, 648–653. [CrossRef] [PubMed]
7. Haendeler, J.; Mlynek, A.; Buchner, N.; Lukosz, M.; Graf, M.; Guettler, C.; Jakob, S.; Farrokh, S.; Kunze, K.; Goy, C.; et al. Two isoforms of sister-of-mammalian grainyhead have opposing functions in endothelial cells and in vivo. *Arterioscler Thromb. Vasc. Biol.* **2013**, *33*, 1639–1646. [CrossRef]
8. Guardiola-Serrano, F.; Haendeler, J.; Lukosz, M.; Sturm, K.; Melchner, H.; Altschmied, J. Gene trapping identifies a putative tumor suppressor and a new inducer of cell migration. *Biochem. Biophys. Res. Commun.* **2008**, *376*, 748–752. [CrossRef]
9. Jakob, S.; Schroeder, P.; Lukosz, M.; Buchner, N.; Spyridopoulos, I.; Altschmied, J.; Haendeler, J. Nuclear protein tyrosine phosphatase shp-2 is one important negative regulator of nuclear export of telomerase reverse transcriptase. *J. Biol. Chem.* **2008**, *283*, 33155–33161. [CrossRef] [PubMed]
10. Haendeler, J.; Hoffmann, J.; Tischler, V.; Berk, B.C.; Zeiher, A.M.; Dimmeler, S. Redox regulatory and anti-apoptotic functions of thioredoxin depend on s-nitrosylation at cysteine 69. *Nat. Cell Biol.* **2002**, *4*, 743–749. [CrossRef]
11. Ale-Agha, N.; Goy, C.; Jakobs, P.; Spyridopoulos, I.; Gonnissen, S.; Dyballa-Rukes, N.; Aufenvenne, K.; von Ameln, F.; Zurek, M.; Spannbrucker, T.; et al. Cdkn1b/p27 is localized in mitochondria and improves respiration-dependent processes in the cardiovascular system-new mode of action for caffeine. *PLoS Biol.* **2018**, *16*, e2004408–e2004410. [CrossRef]
12. Hoffmann, J.; Haendeler, J.; Zeiher, A.M.; Dimmeler, S. Tnfalpha and oxldl reduce protein s-nitrosylation in endothelial cells. *J. Biol. Chem.* **2001**, *276*, 41383–41387. [CrossRef]
13. Hoffmann, J.; Haendeler, J.; Aicher, A.; Rossig, L.; Vasa, M.; Zeiher, A.M.; Dimmeler, S. Aging enhances the sensitivity of endothelial cells toward apoptotic stimuli: Important role of nitric oxide. *Circ. Res.* **2001**, *89*, 709–715. [CrossRef]
14. Ottolini, M.; Hong, K.; Cope, E.L.; Daneva, Z.; DeLalio, L.J.; Sokolowski, J.D.; Marziano, C.; Nguyen, N.Y.; Altschmied, J.; Haendeler, J.; et al. Local peroxynitrite impairs endothelial trpv4 channels and elevates blood pressure in obesity. *Circulation* **2020**. [CrossRef] [PubMed]
15. Sonkusare, S.K.; Dalsgaard, T.; Bonev, A.D.; Hill-Eubanks, D.C.; Kotlikoff, M.I.; Scott, J.D.; Santana, L.F.; Nelson, M.T. Akap150-dependent cooperative trpv4 channel gating is central to endothelium-dependent vasodilation and is disrupted in hypertension. *Sci. Signal.* **2014**, *7*, ra66. [CrossRef] [PubMed]
16. Marziano, C.; Hong, K.; Cope, E.L.; Kotlikoff, M.I.; Isakson, B.E.; Sonkusare, S.K. Nitric oxide-dependent feedback loop regulates transient receptor potential vanilloid 4 (trpv4) channel cooperativity and endothelial function in small pulmonary arteries. *J. Am. Heart Assoc.* **2017**, *6*. [CrossRef] [PubMed]
17. Straub, A.C.; Zeigler, A.C.; Isakson, B.E. The myoendothelial junction: Connections that deliver the message. *Physiology (Bethesda)* **2014**, *29*, 242–249. [CrossRef]
18. Kosugi, S.; Hasebe, M.; Tomita, M.; Yanagawa, H. Systematic identification of cell cycle-dependent yeast nucleocytoplasmic shuttling proteins by prediction of composite motifs. *Proc. Natl. Acad. Sci. USA* **2009**, *106*, 10171–10176. [CrossRef] [PubMed]
19. Green, D.R.; Kroemer, G. Cytoplasmic functions of the tumour suppressor p53. *Nature* **2009**, *458*, 1127–1130. [CrossRef]
20. Rohrbach, S.; Niemann, B.; Abushouk, A.M.; Holtz, J. Caloric restriction and mitochondrial function in the ageing myocardium. *Exp. Gerontol.* **2006**, *41*, 525–531. [CrossRef]
21. Dimmeler, S.; Haendeler, J.; Nehls, M.; Zeiher, A.M. Suppression of apoptosis by nitric oxide via inhibition of interleukin-1beta-converting enzyme (ice)-like and cysteine protease protein (cpp)-32-like proteases. *J. Exp. Med.* **1997**, *185*, 601–607. [CrossRef]
22. Fan, Y.; Gong, Y.; Ghosh, P.K.; Graham, L.M.; Fox, P.L. Spatial coordination of actin polymerization and ilk-akt2 activity during endothelial cell migration. *Dev. Cell* **2009**, *16*, 661–674. [CrossRef] [PubMed]
23. Garcia-Cardena, G.; Fan, R.; Shah, V.; Sorrentino, R.; Cirino, G.; Papapetropoulos, A.; Sessa, W.C. Dynamic activation of endothelial nitric oxide synthase by hsp90. *Nature* **1998**, *392*, 821–824. [CrossRef] [PubMed]

Danksagung

Ich möchte mich an erster Stelle von ganzem Herzen bei Yogi Altschmied und Jojo Haendeler für die Möglichkeit bedanken, meine Doktorarbeit an so einem spannenden Thema und unter eurer Aufsicht anzufertigen. Die Zeit war sowohl wissenschaftlich als auch persönlich enorm lehrreich, nie langweilig und hat mir immer viel Spaß bereitet. Danke für alles, was ihr mir beigebracht habt und all die Chancen, die ihr mir eröffnet habt. Ich habe stets eure Leidenschaft für die Forschung und für die Lehre bewundert und wertgeschätzt.

Außerdem danke ich Herrn Prof. Dr. William F. Martin für die Übernahme des Zweitgutachtens.

Danke auch an meine gesamte Arbeitsgruppe, die mich während meiner Zeit dort stets in allen Aspekten unterstützt hat, vor allem aber auch die Zeit dort mit Spaß und Freude gefüllt hat. Ich möchte mich ganz herzlich bei Dennis, Fiona, Olaf, Philipp, Nilo, Nadine, Flo, Kirsten, und Fee bedanken. Mit euch ist neben der Arbeit auch vor allem der Spaß nie zu kurz gekommen.

Des Weiteren möchte ich mich bei allen Mitgliedern des IRTG1902 bedanken, in dessen Rahmen ich meine Promotion anfertigen durfte. Ein wichtiger Teil davon war auch mein sechsmonatiger Austausch an der Universität von Virginia, wo ich in den Laboren von Norbert Leitinger und Brant Isakson forschen durfte und denen auch besonderer Dank gilt. Die Zeit war sehr prägend und aufregend, und ich denke gerne an all die schönen und aufregenden Momente zurück. In diesem Sinne danke ich auch der DFG, welche mir die Promotion und den Austausch ermöglicht und finanziert hat. An dieser Stelle auch ein besonderer Dank an Sandra Berger, welche als Koordinatorin des IRTG stets ein offenes Ohr für alle Problene hatte und vor allem auch viele Unternehmungen des IRTG organisiert hat, die immer viel Spaß gemacht haben.

Ein riesiges Danke an meine Freunde, die mich stets abzulenken und aufzumuntern wussten. Selbst in den stressigsten Situationen wusste ich, dass ich mich auf euch verlassen kann und immer ein offenes Ohr habe. Ich könnte mir keine besseren Freunde vorstellen.

Ein ganz besonderer Dank gilt meiner Familie. Ohne euch wäre ich nicht da, wo ich heute bin und auch nicht die Person, zu der ich mich entwickelt habe. Ihr habt stets meine Wünsche und Pläne unterstützt und wart in jeder erdenklichen Lebenslage für mich da. Auf euch ist immer Verlass und ohne euch hätte ich diese Arbeit nicht anfertigen können. Danke!